Search for Dark Matter and Vacuum Quantum Gravity Fluctuations using Gravitational Wave Experiments

Thesis by
Vincent Sze Him Lee

In Partial Fulfillment of the Requirements for the
Degree of
Doctor of Philosophy

CALIFORNIA INSTITUTE OF TECHNOLOGY
Pasadena, California

2025
Defended May 20, 2024

Vincent Sze Him Lee
ORCID: 0000-0002-3481-3590

ACKNOWLEDGEMENTS

The past five years has been an incredible journey for me that would not have been possible without the help and supports from my family, friends, and colleagues. First and foremost, I want to thank my parents and sister for their unwavering encouragement in my decision to pursue a Ph.D. in a foreign city, sixteen-hour of flight away from home. Despite the distance, they have remained deeply connected with me, bringing me immense joy and warmth.

I would like to thank my advisor, Kathryn Zurek, for introducing me to the field of high energy phenomenology and the realm of publication-level physics research. Her way of thinking about physics and analyzing phenomena has been a constant inspiration. I have also been fortunate enough to have the opportunity to collaborate with a number of outstanding professors and postdocs: Steve Taylor, Sergei Gukov, Yanbei Chen, and Moira Gresham; Andrea Mitridate, Yikun Wang, Kim Berghaus, and Leonardo Badurina.

On a personal note, I extend my thanks to Caltech Performing and Visual Arts and all the musicians with whom I've had the pleasure of playing music. Music has been a cherished hobbyof mine, providing a welcome break from the rigors of physics. Additionally, I want to express my appreciation to Carol Silberstein, our 4th-floor administrative assistant, who has helped me in countless ways since my arrival at Caltech five years ago.

Finally, I want to express my gratitude to all the theory graduate students on the 4th floor. The weekly grad socials and impromptu physics discussions have brought me immense joy and a sense of belonging.

ABSTRACT

The biggest physics discoveries of recent decades—the detection of the Higgs at the Large Hadron Collider (LHC) in 2012 and the observation of gravitational waves by the Laser Interferometer Gravitational-Wave Observatory (LIGO) in 2015—are often celebrated as two monumental yet distinct discoveries. While the potential of gravitational wave experiments to illuminate particle physics has been acknowledged, its full scope has not been fully appreciated. In this dissertation, we explore various methods to utilize experiments designed for gravitational wave observations in the pursuit of understanding physics beyond the standard model. Specifically, we study two pressing aspects of particle physics: dark matter and quantum gravity, examining their potential signatures in these experiments.

Pulsars, due to their stable periods, are exceptionally suited for gravitational wave observations. Recently, the North American Nanohertz Observatory for Gravitational Waves (NANOGrav) reported positive evidence of a stochastic gravitational wave background in 2023. While the application of pulsar timing measurements in gravitational wave detection is well established, they also offer avenues to study various properties of dark matter, such as the small-scale power spectrum and gravitational wave signatures from a cosmological phase transition. We will discuss search strategies for dark matter using realistic pulsar timing array data, current constraints, and future prospects.

Laser interferometry-based gravitational wave detectors like LIGO also offer a potential pathway for dark matter detection. With their high precision in measuring laser phase fluctuations, even feeble interactions between dark matter and standard model particles can produce signals of potentially measurable size. This includes gravitational interactions as well as other long-range forces, such as scalar or vector mediated Yukawa interactions. We will explore the spectral shape of such signals and their detection prospects.

Finally, recent proposals suggest that vacuum quantum gravity effects may manifest as observable phenomena at low energies in laser interferometers. Planck-sized fluctuations arising from quantum gravity are amplified by the large number of degrees of freedom on the horizon of the causal diamond, corresponding to its entropy. Although LIGO is nominally sensitive to these signatures, its lack of sensitivity at the free-spectral range frequency of the cavities renders it ill-suited for

detecting such phenomena, highlighting the need for additional experimental setups. We will discuss one approach to estimate the size of these fluctuations by drawing connections between a four-dimensional causal diamond and known solutions of two-dimensional Jackiw–Teitelboim (JT) gravity, as well as the experimental implications.

PUBLISHED CONTENT AND CONTRIBUTIONS

[1] Vincent S. H. Lee, Kathryn M. Zurek, and Yanbei Chen. "Astronomical image blurring from transversely correlated quantum gravity fluctuations". In: *Phys. Rev. D* 109.8 (2024), p. 084005. DOI: 10.1103/PhysRevD.109.084005. arXiv: 2312.06757 [gr-qc].
VL participated in the conception of the project, aided in the derivation of the blurring effects in astronomical images, produced all figures and participated in the writing of the manuscript.

[2] Sander M. Vermeulen et al. "Photon Counting Interferometry to Detect Geontropic Space-Time Fluctuations with GQuEST". Apr. 2024. arXiv: 2404.07524 [gr-qc].
VL estimated the expected photon count per second in the benchmark pixellon model during the early stage of the project.

[3] Adeela Afzal et al. "The NANOGrav 15 yr Data Set: Search for Signals from New Physics". In: *Astrophys. J. Lett.* 951.1 (2023), p. L11. DOI: 10.3847/2041-8213/acdc91. arXiv: 2306.16219 [astro-ph.HE].
VL aided in the analysis of dark matter substructure search (Sec. 6.2), participated in writing the relevant discussion, and produced Fig. 17 and Fig. 18.

[4] Yufeng Du, Vincent S. H. Lee, Yikun Wang, and Kathryn M. Zurek. "Macroscopic dark matter detection with gravitational wave experiments". In: *Phys. Rev. D* 108.12 (2023), p. 122003. DOI: 10.1103/PhysRevD.108.122003. arXiv: 2306.13122 [astro-ph.CO].
VL aided in the derivation of the dark matter signal spectrums, computed the projected sensitivity of various current and future gravitational wave eexperiments, produced Fig. 1-5, and participated in the writing of the manuscript.

[5] Moira I. Gresham, Vincent S. H. Lee, and Kathryn M. Zurek. "Astrophysical observations of a dark matter-Baryon fifth force". In: *JCAP* 02 (2023), p. 048. DOI: 10.1088/1475-7516/2023/02/048. arXiv: 2209.03963 [astro-ph.HE].
VL aided in the derivation of the kinetic heating and weak equivalent principle tests constraints, performed the analysis on pulsar timing measurements, produced Fig. 1, Fig. 3 and Fig. 4, and participated in the writing of the manuscript.

[6] Sergei Gukov, Vincent S. H. Lee, and Kathryn M. Zurek. "Near-horizon quantum dynamics of 4D Einstein gravity from 2D Jackiw-Teitelboim gravity". In: *Phys. Rev. D* 107.1 (2023), p. 016004. DOI: 10.1103/PhysRevD.107.016004. arXiv: 2205.02233 [hep-th].
VL participated in the conception of the project, aided in establishing the

connection between Einstein gravity near a causal diamond horizon and JT gravity, aided in the derivation of the four-dimensional photon travel time using existing result from JT gravity, produced all figures and participated in the writing of the manuscript.

[7] Dongjun Li, Vincent S. H. Lee, Yanbei Chen, and Kathryn M. Zurek. "Interferometer response to geontropic fluctuations". In: *Phys. Rev. D* 107.2 (2023), p. 024002. DOI: 10.1103/PhysRevD.107.024002. arXiv: 2209.07543 [gr-qc].
VL participated in the conception of the project, computed the existing and projected constraints on the pixellon model in laboratory-sized interferometer experiments, created Fig. 6 and participated in the writing of the manuscript.

[8] Zaven Arzoumanian et al. "Searching for Gravitational Waves from Cosmological Phase Transitions with the NANOGrav 12.5-Year Dataset". In: *Phys. Rev. Lett.* 127.25 (2021), p. 251302. DOI: 10.1103/PhysRevLett.127.251302. arXiv: 2104.13930 [astro-ph.CO].
VL performed the numerical search in gravitational waves originating from a cosmological phase transition using the NANOGrav 12.5-Year Dataset, and participated in the writing of the manuscript.

[9] Vincent S. H. Lee, Andrea Mitridate, Tanner Trickle, and Kathryn M. Zurek. "Probing Small-Scale Power Spectra with Pulsar Timing Arrays". In: *JHEP* 06 (2021), p. 028. DOI: 10.1007/JHEP06(2021)028. arXiv: 2012.09857 [astro-ph.CO].
VL helped in developing the Monte Carlo code for computing the SNR from transiting dark matter substructure in pulsar timing experiments, aided in computing the projected reach for different dark matter models, produced Fig. 1-2 and Fig. 6-10, and participated in the writing of the manuscript.

[10] Vincent S. H. Lee, Stephen R. Taylor, Tanner Trickle, and Kathryn M. Zurek. "Bayesian Forecasts for Dark Matter Substructure Searches with Mock Pulsar Timing Data". In: *JCAP* 08 (2021), p. 025. DOI: 10.1088/1475-7516/2021/08/025. arXiv: 2104.05717 [astro-ph.CO].
VL developed the Bayesian pipeline of merging existing Monte Carlo simulations on dark matter substructure with the software used by the PTA community in searching for gravitational waves (`enterprise`), computed the projected reach using realistic PTA mock data, produced all figures, and participated in the writing of the manuscript.

TABLE OF CONTENTS

LIST OF ILLUSTRATIONS

Number *Page*

LIST OF TABLES

Number *Page*

Chapter 1

INTRODUCTION

sinc

The field of high-energy phenomenology has undergone a gradual shift in focus over the past decade. Throughout the 20th century, the concerted efforts of theorists and experimentalists yielded the highly successful formulation of the standard model of particle physics. This culminated with the discovery of the Higgs at the Large Hadron Collider (LHC) at CERN [12]. The standard model is highly celebrated for its accurate description of nature and its elegant structure imposed by symmetry. However, with its completion, attention has turned towards the quest for physics beyond the standard model (BSM), largely motivated by considerations of naturalness [13]. Key among these motivations are the hierarchy problem, the cosmological constant problem, and the strong CP problem. Notably, a significant ongoing endeavor at the LHC involves probing the Higgs sector with high precision, aiming to shed light on the hierarchy problem [14].

Naturalness serves as both a physical principle and a pragmatic guide in pursuing new physics, historically guiding significant discoveries. Many quantities within the standard model agree with reasoning inspired by naturalness [15]. However, it is imperative to acknowledge that naturalness issues are fundamentally fine-tuning problems, and new physics isn't inherently bound by naturalness arguments. In particular, there are two avenues where BSM phenomena are *known* to exist:

- **Dark matter**: The most unequivocal evidence of BSM physics comes from the existence of dark matter (DM). The first evidence of DM comes from the observation of galaxy rotation curves [16], where the mass density in the galaxy is found to exceed ordinary luminous matter, thus inferring the existence of *dark* matter. Additional evidence of dark matter are subsequently provided by observation of anisotropies in the cosmic microwave background (CMB) as a result of baryon acoustic oscillation (BAO) [17] and observation of bullet cluster [18] (more about dark matter will be discussed in Sec. 1.2. An important open question in physics is to understand the particle nature of dark matter and any possible interaction with standard model particles.

- **Quantum gravity**: The general theory of relativity proposed by Einstein has been a highly successful theory in describing astrophysical observations, with the latest landmark being the observation of gravitational waves from a binary black hole merger by the Laser Interferometer Gravitational-Wave Observatory (LIGO) [19], an effort led by both Caltech and MIT. This incredibly elegant theory, however, is incompatible with quantum field theory at high energy scales, the very building block of the standard model. In particular, quantum gravity is non-renormalizable [20], hence an infinite number of counter terms are needed to cancel all the divergences, leading to no sensible predictions from the theory itself. The energy scale associated with quantum effects from gravity is the Planck mass, $M_{\rm pl} = \sqrt{\hbar c/G} \sim 10^{19}$ GeV, far beyond the energy scales that the LHC can probe. On the other hand, when the spacetime curvature is small, we can classically quantize gravity coupled to field theory under the framework of *effective field theory* into a coherent theory [21]. However, there are compelling reasons to suspect that this approach is insufficient, even in the low-energy realm. For instance, Hawking's semiclassical treatment near black hole horizons predicts black hole evaporation, which is inconsistent with quantum mechanics principles that pure states should evolve to pure states [22, 23]. This is known as the black hole information paradox [24]. Moreover, applying semiclassical methods to eternal inflation leads to conflicting probability interpretations [25]. These expose the inadequacies of semiclassical quantum gravity in its naive application. To the best of the author's knowledge, low energy effects of quantum gravity have never been measured experimentally, leaving vast uncharted territory within the landscape of BSM physics.

Remarkably, the technological advancements developed to observe and detect gravitational waves in recent decades have significant implications for understanding both dark matter and quantum gravity, in ways not previously anticipated. LIGO achieves remarkable sensitivity by precisely controlling experimental setups and suppressing noise from various backgrounds, enabling detection of length fluctuations as small as 10^{-19} m [26]. In addition to conventional interferometry-based detectors like LIGO, pulsar timing arrays offer another avenue for gravitational wave detection. [27], with the ability to measure deviations in pulse arrival times as small as $\sim \mu$s. The recent report of positive evidence for a stochastic gravitational wave background at the nano-Hertz level by NANOGrav has generated significant excite-

ment within both the astrophysics and particle physics communities [28]. These highly sensitive instruments and observations allow us to potentially measure feeble interactions between dark matter and ordinary matter, providing insights into the various particle properties of dark matter. On the quantum gravity front, while Dyson famously noted the impossibility of detecting gravitons with LIGO [29], recent proposals suggest that quantum gravity effects may be boosted by the large number of degrees of freedom associated with the entropy of a causal diamond horizon, lead to sizable fluctuations in low energy accessible to laser interferometer systems [30], which is further facilitated by recent advancements in photon-counting technologies [2].

The thesis aims to explore the possibilities to detect signatures from dark matter and quantum gravity using technologies developed for gravitational wave detection, including both laser interferometers and pulsar timing arrays.

1.1 Gravitational Wave Experiments

gravitational wave detectors

This subsection is based on

[1] Vincent S. H. Lee and Kathryn M. Zurek. "Proper Time Observables of General Gravitational Perturbations in Laser Interferometry-based Gravitational Wave Detectors". In: (Aug. 2024). arXiv: 2408.03363 [hep-ph].

.

Here, we provide an overview of the operational principles behind laser-interferometer-based gravitational wave detectors like LIGO [31]. Specifically, we identify the physics observable of *any* gravitational perturbation in an interferometer system, such as simple Michelson interferometers [32], to be the *proper time* elapsed as measured by the *beamsplitter*, between the moments when a photon first passes through the beamsplitter and when the same photon returns. Denoting the beamsplitter's worldline as x^μ_B, its change in proper time is related to the Nambu-Goto action:

$$\Delta\tau_a = \int \sqrt{-g_{\mu\nu} dx^\mu_B dx^\nu_B}\,. \tag{1.1}$$

Here the subscript a labels the interferometer arms and runs from $1, 2$. The interference pattern observed by collecting the laser from the beamsplitter to the detector is determined by the *difference* of proper time elapsed between the two arms, *i.e.*

$$\Delta\tau = \Delta\tau_1 - \Delta\tau_2\,. \tag{1.2}$$

and the strain is given by

$$h = \frac{\Delta\tau}{2L}\,, \tag{1.3}$$

where L is the length of the interferometer arms. The interference pattern observed when the lasers are recollected to the photon detector is determined by the relative phase shift between the two arms, which can be related to the proper time observable as follows. Consider a continuous stream of photons, with frequency $\omega_{\rm laser}$, arriving at the beamsplitter from the laser source. Two particular photons pass through the beamsplitter at two (possibly different) proper times, τ_1 and τ_2 (as measured by the beamsplitter), along the two interferometer arms and recombine at the beamsplitter at the same proper time. Each photon admits a phase, $\exp(i\omega_{\rm laser}\tau_1)$ and $\exp(i\omega_{\rm laser}\tau_2)$, respectively, which are conserved along the wavefront (up to a π-phase shift due to reflection at the far mirror) until they recombine at the beamsplitter. Their superposition thus admits a relative phase of $\Delta\phi = \omega_{\rm laser}(\tau_2 - \tau_1) = \omega_{\rm laser}\Delta\tau$ from Eq. (1.2). Note that the shift in laser frequency coincides with the frequency of the metric perturbation (see, *e.g.*, Ref. [33]), which is much smaller than the laser frequency in any realistic experimental setup, and is thus neglected. Since the proper time as defined in Eq. (1.1) is a scalar, it is manifestly invariant under diffeomorphisms on the metric perturbation. It might be surprising at first that the physical observable is a time shift quantity as measured by the beamsplitter, not the photons[1]. However, any deviation in the photon trajectories will alter the proper time measured by the beamsplitter by changing the integration limits of Eq. (1.1). Specifically, for GW signals, as we will later show, the proper time observable is equivalent to the commonly quoted detector strain, which is well known to be gauge-invariant by calculations in both the transverse-traceless (TT) gauge and the proper detector frame [34][2]. Furthermore, perturbations on the photons and the beamsplitter (as well as the far mirror) can be shuffled into each other by a generic gauge transformation, while the sum of all effects remains gauge-invariant. We will explicitly verify these statements in later sections.

[1] One might be tempted to attribute the physical interferometer observable to either the change in *proper distance* between the beamsplitter and the far mirror, or the change in *proper time* for the light propagating between them. However, neither description is entirely satisfying. Proper distances are only defined between two spacelike-separated events, which cannot generally be measured by null geodesics unless the proper distance does not change substantially within a photon roundtrip time (which holds for long-wavelength GWs but is not true in general). On the other hand, proper times are ill-defined for photons as they travel in null geodesics (*i.e.* $ds^2 = 0$).

[2] A calculation of GW measurements with laser interferometers in a general gauge, assuming slowly varying scalar and vector perturbations along a photon roundtrip, is recently performed in Ref. [35].

The goal of this *Letter* is to fully develop the idea of proper time as a physical observable, focused on the case of a simple Michelson interferometer. We provide a simple recipe for computing the observable given a generic metric perturbation in any gauge, and show that, for any metric perturbation, the beamsplitter proper time elapsed can be written as a sum of Doppler, Shapiro and Einstein delays. This latter result is consistent with previous work [36, 7], though now we are able to show explicitly that this sum is the proper time elapse of the beamsplitter observer. This recipe can now be applied to any metric perturbation, beyond the usual GW treatment. Readers interested in computing this gauge-invariant observable can directly refer to Eqs. (1.2)-(1.3) and Eqs. (1.8)-(1.13).

A laser interferometer consists of two arms linked by a beamsplitter. We schematically depict a single arm of a laser interferometer in Fig. 10.1. For a single measurement, there are three notable physical events:

i) **Emission** ($\mathcal{E}$): The laser reaches the beamsplitter and split into two beams, each traversing along separate arms.

ii) **Reflection** ($\mathcal{R}$): The beams encounter the mirrors at the far ends, and reflect back towards the beamsplitter.

iii) **Observation** ($\mathcal{O}$): The beams return to the beamsplitter, and finally reconverge at the detection port. The intensity of the laser is then measured to determine the phase difference between the two laser beams.

Suppose the metric is perturbed as $g_{\mu\nu} = \eta_{\mu\nu} + h_{\mu\nu}$, where $\eta_{\mu\nu} = \text{diag}(-1, +1, +1, +1)$ is the metric of flat Minkowski spacetime in the mostly positive convention. When the perturbation is small, we apply the linearized gravity limit and only terms with leading order in $h_{\mu\nu}$ are retained.

A general gauge transformation on the metric perturbation is defined as

$$h_{\mu\nu} \to h'_{\mu\nu} = h_{\mu\nu} - \partial_\mu \xi_\nu - \partial_\nu \xi_\mu \,, \tag{1.4}$$

for a general vector field ξ^μ. The physical observable must be a quantity that is invariant under a transformation as defined in Eq. (1.4). One such quantity is given by the proper time elapsed, as measured by the photon detector, between photon emission at the beamsplitter ($\mathcal{E}$) and when the photon is reflected back to the beamsplitter and sent to the detection port ($\mathcal{O}$). Here, we assume that the

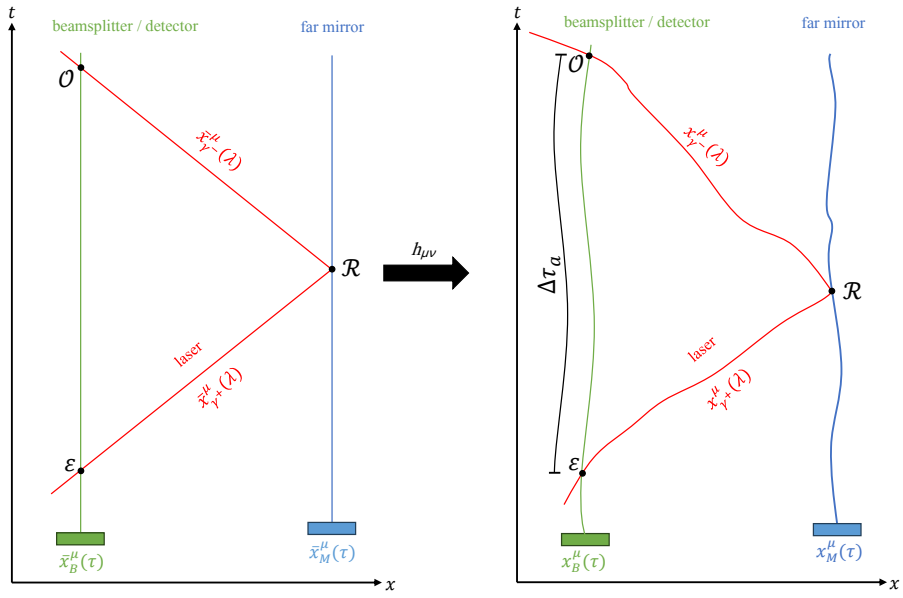

Figure 1.1: Schematic spacetime diagram of a single arm in a GW detector. The left/right diagram corresponds to the unperturbed/perturbed system. The worldlines of the beamsplitter, far mirror, and the photon are represented by green, blue, and red lines, and denoted by $x^\mu_B(\tau)$, $x^\mu_M(\tau)$, and $x^\mu_{\gamma^\pm}(\lambda)$, respectively. The physical events, emission ($\mathcal{E}$), reflection ($\mathcal{R}$), and observation ($\mathcal{O}$), are defined by intersections of worldlines (see description of each event in the main text). The proper time observable for each arm, $\Delta\tau_a$, is defined to be the proper time elapsed at the beamsplitter between $\mathcal{E}$ and $\mathcal{O}$. Quantities defined in the unperturbed system are denoted by an overbar.

detection port and the mirrors close to the beamsplitter are positioned closely to the beamsplitter itself (in comparison to the interferometer arm length), and thus can all be regarded as the same point in spacetime.

We first consider a single arm in the interferometer oriented towards the unit vector $\hat{\mathbf{n}}$. The proper time elapsed, as measured by the detector, is given by:

$$\Delta\tau_a = \int_{\tau_\mathcal{E}}^{\tau_\mathcal{O}} d\tau = \tau_\mathcal{O} - \tau_\mathcal{E} \,. \tag{1.5}$$

where $\tau_\mathcal{E}$ and $\tau_\mathcal{O}$ denote the detector proper times when the photon is emitted from the beamsplitter and observed by the detector, respectively. Note that $\tau_\mathcal{E}$ is independent of the metric perturbation, since it simply marks the starting (proper) time of a measurement. However, $\tau_\mathcal{O}$ will change under a metric perturbation, determined

by the intersection of worldlines between the detector and the photon. In a general perturbed metric, the (3+1)-dimensional worldlines do not necessarily intersect with each other. Nevertheless, in a realistic experimental setup, the beamsplitter and the mirrors have finite extents, which are usually neglected since they are much shorter than the interferometer arm length. In the $h_{\mu\nu} \ll 1$ limit, the photons should be considered as coinciding with the detector / mirrors as long as the projections of their worldlines on the $\hat{\mathbf{n}}$ direction overlap. Denoting the outgoing and incoming photon worldlines by $x^\mu_{\gamma^+}(\lambda)$ and $x^\mu_{\gamma^-}(\lambda)$ respectively with λ being an affine parameter, and the detector and far mirror worldlines by $x^\mu_B(\tau)$ and $x^\mu_M(\tau)$ respectively, these intersections are then obtained by solving the system of equations

$$\begin{aligned}
\mathcal{E}: &\begin{cases} x^0_B(\tau_\mathcal{E}) = x^0_{\gamma^+}(\lambda_\mathcal{E}) \\ \hat{\mathbf{n}}\cdot\mathbf{x}_B(\tau_\mathcal{E}) = \hat{\mathbf{n}}\cdot\mathbf{x}_{\gamma^+}(\lambda_\mathcal{E}) \end{cases} \\
\mathcal{R}: &\begin{cases} x^0_M(\tau_\mathcal{R}) = x^0_{\gamma^+}(\lambda_\mathcal{R}) = x^0_{\gamma^-}(\lambda_\mathcal{R}) \\ \hat{\mathbf{n}}\cdot\mathbf{x}_M(\tau_\mathcal{R}) = \hat{\mathbf{n}}\cdot\mathbf{x}_{\gamma^+}(\lambda_\mathcal{R}) = \hat{\mathbf{n}}\cdot\mathbf{x}_{\gamma^+}(\lambda_\mathcal{R}) \end{cases} \\
O: &\begin{cases} x^0_B(\tau_O) = x^0_{\gamma^-}(\lambda_O) \\ \hat{\mathbf{n}}\cdot\mathbf{x}_B(\tau_O) = \hat{\mathbf{n}}\cdot\mathbf{x}_{\gamma^-}(\lambda_O)\,, \end{cases}
\end{aligned} \tag{1.6}$$

where $\tau_\mathcal{R}$ is the mirror proper time when it reflects the photon, and $\lambda_\mathcal{E}$, $\lambda_\mathcal{R}$ and λ_O are the photon affine parameters when it is emitted, reflected and observed, respectively. In general, Eq. (1.6) needs to be solved by finding the intersections of geodesics under a general metric. In linearized gravity, however, we can solve for worldline intersections order by order. Denoting unperturbed worldline trajectories and time quantities by an overbar and perturbation by δ, we can expand a generic timelike geodesic in the leading order of h as $x^\mu_{B,M}(\tau) = \bar{x}^\mu_{B,M}(\bar{\tau}) + \delta\tau\,\bar{v}^\mu_{B,M}(\bar{\tau}) + \delta x^\mu_{B,M}(\bar{\tau})$ with $\tau = \bar{\tau} + \delta\tau$, $\bar{v}^\mu_{B,M}(\tau) = (d/d\tau)\bar{x}^\mu_{B,M}(\tau)$, and analogous equations for the null geodesics. Hence, Eq. (1.6) becomes

$$\begin{aligned}
\mathcal{E}: &\begin{cases} \delta x^0_B(\tau_\mathcal{E}) = \delta x^0_{\gamma^+}(\lambda_\mathcal{E}) \\ \hat{\mathbf{n}}\cdot\delta\mathbf{x}_B(\tau_\mathcal{E}) = \hat{\mathbf{n}}\cdot\delta\mathbf{x}_{\gamma^+}(\lambda_\mathcal{E}) \end{cases} \\
\mathcal{R}: &\begin{cases} \delta x^0_B(\bar{\tau}_\mathcal{R}) + \delta\tau_\mathcal{R} = \delta x^0_{\gamma^+}(\bar{\lambda}_\mathcal{R}) + \delta\lambda_\mathcal{R} = \delta x^0_{\gamma^-}(\bar{\lambda}_\mathcal{R}) + \delta\lambda_\mathcal{R} \\ \hat{\mathbf{n}}\cdot\delta\mathbf{x}_M(\bar{\tau}_\mathcal{R}) = \hat{\mathbf{n}}\cdot\delta\mathbf{x}_{\gamma^+}(\bar{\lambda}_\mathcal{R}) + \delta\lambda_\mathcal{R} = \hat{\mathbf{n}}\cdot\delta\mathbf{x}_{\gamma^+}(\bar{\lambda}_\mathcal{R}) - \delta\lambda_\mathcal{R} \end{cases} \\
O: &\begin{cases} \delta x^0_B(\bar{\tau}_O) + \delta\tau_O = \delta x^0_{\gamma^-}(\bar{\lambda}_O) + \delta\lambda_O \\ \hat{\mathbf{n}}\cdot\delta\mathbf{x}_B(\bar{\tau}_O) = \hat{\mathbf{n}}\cdot\delta\mathbf{x}_{\gamma^-}(\bar{\lambda}_O) - \delta\lambda_O \end{cases},
\end{aligned} \tag{1.7}$$

where we used the expressions for the unperturbed worldlines

$$\begin{aligned}
\bar{x}^\mu_B(\tau) &= (\tau, \bar{\mathbf{x}}_B) \\
\bar{x}^\mu_M(\tau) &= (\tau, \bar{\mathbf{x}}_M) \\
\bar{x}^\mu_{\gamma^+}(\lambda) &= (\lambda, (\lambda - \lambda_{\mathcal{E}})\hat{\mathbf{n}} + \bar{\mathbf{x}}_B) \\
\bar{x}^\mu_{\gamma^-}(\lambda) &= (\lambda, -(\lambda - \bar{\lambda}_{\mathcal{O}})\hat{\mathbf{n}} + \bar{\mathbf{x}}_B)\,.
\end{aligned} \tag{1.8}$$

We note that the asymmetry between the emission equations (first two) and the observation equations (last two) in Eq. (1.7) originates from the fact that $\delta\tau_{\mathcal{E}} = 0$ (*i.e.* the emission proper time is unperturbed) while $\delta\tau_{\mathcal{O}} \neq 0$.

The perturbed worldlines of the detector and the far mirror are given by solving the geodesic equation, $d^2x^\rho_{B,M}/d\tau^2 + \Gamma^\rho_{\mu\nu}(dx^\mu_{B,M}/d\tau)(dx^\nu_{B,M}/d\tau) = 0$, which in linearized gravity gives

$$\frac{d^2}{d\tau^2}\delta x^i_{B,M}(\tau) = \eta^{ij}\left(-\partial_0 h_{0j} + \frac{1}{2}\partial_j h_{00}\right)\Big|_{\bar{x}^\mu_{B,M}(\tau)}\,. \tag{1.9}$$

The time component of the worldlines are determined by $ds^2 = g_{\mu\nu}dx^\mu_{B,M}dx^\nu_{B,M} = -1$ for timelike geodesics

$$\frac{d}{d\tau}\delta x^0_{B,M}(\tau) = \frac{1}{2}h_{00}\Big|_{\bar{x}^\mu_{B,M}(\tau)}\,. \tag{1.10}$$

In Eqs. (1.9)-(1.10), the metric derivatives on the RHS are evaluated at the unperturbed detector and mirror worldlines, $\bar{x}^\mu_B(\tau)$ an $\bar{x}^\mu_M(\tau)$, as defined in Eq. (1.8), respectively. These differential equations are solved by integrating the RHS of in τ. The photon geodesics are solved by setting $ds^2 = g_{\mu\nu}dx^\mu_{\gamma^\pm}dx^\nu_{\gamma^\pm} = 0$, which becomes

$$n^\pm_\mu \delta v^\mu_{\gamma^\pm}(\lambda) = -\frac{1}{2}\left[h_{00} \pm 2n^i h_{0i} + n^i n^j h_{ij}\right]\Big|_{\bar{x}^\mu_{\bar{\gamma}^\pm}(\lambda)}\,, \tag{1.11}$$

where we defined $v^\mu_{\gamma^\pm}(\lambda) = (d/d\lambda)x^\mu_{\gamma^\pm}(\lambda)$, $n^\mu_\pm = (1, \pm n^i)$, and the perturbed metric in the RHS are evaluated at the unperturbed photon trajectories, $\bar{x}^\mu_{\gamma^\pm}(\lambda)$, as defined in Eq. (1.8), respectively.

Finally, rearranging Eq. (1.7) to solve for $\Delta\tau_a = \tau_{\mathcal{O}} - \tau_{\mathcal{E}} = 2L + \delta\tau_{\mathcal{O}}$, we find that Eq. (1.5) can be written in a compact form

$$\Delta\tau_a = 2L + \Delta\tau_a^{(\text{Doppler})} + \Delta\tau_a^{(\text{Shapiro})} + \Delta\tau^{(\text{Einstein})}\,, \tag{1.12}$$

where we have written the shift in proper time elapsed as a sum of three individual contributions, defined as

$$\begin{aligned}
\Delta\tau_a^{(\text{Doppler})} &= -\hat{\mathbf{n}}\cdot\left[\delta\mathbf{x}_B(\tau_{\mathcal{E}}) - 2\delta\mathbf{x}_M(\tau_{\mathcal{E}}+L) + \delta\mathbf{x}_B(\tau_{\mathcal{E}}+2L)\right] \\
\Delta\tau_a^{(\text{Shapiro})} &= -\int_{\lambda_{\mathcal{E}}}^{\lambda_{\mathcal{E}}+L} d\lambda\, n_\mu^+ \delta v_{\gamma^+}^\mu(\lambda) - \int_{\lambda_{\mathcal{E}}+L}^{\lambda_{\mathcal{E}}+2L} d\lambda\, n_\mu^- \delta v_{\gamma^-}^\mu(\lambda) \\
\Delta\tau^{(\text{Einstein})} &= -\int_{\tau_{\mathcal{E}}}^{\tau_{\mathcal{E}}+2L} d\tau \left[\frac{d}{d\tau}\delta x_B^0(\tau)\right],
\end{aligned} \tag{1.13}$$

where $\lambda_{\mathcal{E}} = \tau_{\mathcal{E}}$, and the expressions for the worldlines are given in Eqs. (1.8)-(1.11). Here we used $\bar{\tau}_{\mathcal{O}} = \tau_{\mathcal{E}} + 2L$ and $\bar{\tau}_{\mathcal{R}} = \tau_{\mathcal{E}} + L$. The difference in proper time elapsed between two arms is then given by Eq. (1.2), Eq. (1.12) and Eq. (1.13). An analogous decomposition has also been identified in Ref. [36] for the special case of interferometer response to GWs in the proper detector frame, in which that the sum is shown to be translationally invariant.

We briefly describe the physical meanings of the Doppler, Shapiro, and Einstein terms defined in Eq. (1.13). The Doppler term corresponds to the motion of the detector and the far mirror, akin to the Doppler effect, where the motion of the emitter or observer of a wave affects the apparent frequency. The Shapiro term accounts for the integrated shifts in velocity in the photon trajectories, similar to a Shapiro delay for light waves propagating under the influence of a gravitational field. Lastly, the Einstein term corresponds to the time dilation of the clock at the detector.

Since the proper time elapsed defined in Eq. (1.5) is a scalar, it is by construction a gauge-invariant quantity. Although one could attribute physical meanings to the individual components in Eq. (1.12) such as proper motion and time delay, they are ultimately coordinate-dependent quantities, and by themselves do not constitute a true physical observable as measured by a realistic experiment.

We conclude this section with several remarks. Firstly, observe that the Einstein term does not depend on the arm orientation $\hat{\mathbf{n}}$, and hence is completely canceled when the proper time difference across the two arms is computed. Secondly, the time variable of this measurement can be identified as final time of the light-pulse sequence. Therefore, the power spectrum of the signal is obtained by Fourier transforming the proper time elapsed with respect to $\tau_{\mathcal{O}} = \tau_{\mathcal{E}} + 2L + O(h)$, the time of observation, *i.e.* [37]

$$\tilde{h}(f) = \frac{1}{2L}\int_{-\infty}^{\infty} d\tau_{\mathcal{E}}\, e^{-2\pi i f(\tau_{\mathcal{E}}+2L)}\Delta\tau\,. \tag{1.14}$$

Finally, as an example, we compute the proper time observable as defined above for a classical GW. Assuming that the wave passes through the interferometer at $t = 0$ in the $\hat{\mathbf{z}}$ direction while the two interferometer arms are oriented in the $\hat{\mathbf{x}}$ and $\hat{\mathbf{y}}$ directions and the beamsplitter set at the origin, the metric perturbation, in the TT gauge, can be written as $h^{TT}_{xx} = -h^{TT}_{yy} = h_+ \cos(\omega_{\rm GW} t - k_{\rm GW} z)$ and $h^{TT}_{xy} = h^{TT}_{yx} = h_\times \cos(\omega_{\rm GW} t - k_{\rm GW} z)$, where h_+ and $h_\times$ are the plus-polarization and cross-polarization strains, and $\omega_{\rm GW}$ and $k_{\rm GW}$ are the angular frequency and wavenumber of the GW. It is immediately clear from Eqs. (1.9)-(1.11) that the only term in Eq. (1.13) that contributes to the proper time shift is the Shapiro term, which evaluates to (using Eqs. (1.11)-(1.13) and Eq. (1.2))

$$\Delta\tau^{(\rm GW)} = 2Lh_+ \left(\omega_{\rm GW} L\right) \cos\left(\omega_{\rm GW}(\tau_{\mathcal{E}} + L)\right) \ . \tag{1.15}$$

The strain as derived from the proper time observable by putting Eq. (1.15) into Eq. (1.3) is then given by the familiar relation, $h^{(\rm GW)}(t) \approx h_+ \cos(\omega_{\rm GW} t)$ [38] in the long-wavelength limit, $\omega_{\rm GW} L \ll 1$. We have thus shown that the proper time observable is equivalent to the detector strain for GWs. Consequently, when discussing GW signatures in TT gauge, one can focus solely on the photon time delay across a round-trip as a simplified definition of the observable.

As a sanity check, we repeat the above calculation in the proper detector frame. Using results from Ref. [39], the only non-vanishing and relevant component is given by $h^{PD}_{00}\Big|_{z=0} = -(1/2)\omega^2_{\rm GW}\left[h_+(x^2 - y^2) + 2h_\times xy\right]\cos(\omega_{\rm GW} t)$ [40]. One finds that both Doppler and Shapiro terms contribute, with (*cf.* Eqs. (1.11)-(1.13) and Eq. (1.2))

$$\begin{aligned}
\Delta\tau^{(\rm GW,Doppler)} &= 2Lh_+ \cos(\omega_{\rm GW}(\tau_{\mathcal{E}} + L)) \\
\Delta\tau^{(\rm GW,Shapiro)} &= -2Lh_+ \cos(\omega_{\rm GW}(\tau_{\mathcal{E}} + L))\left[1 - (\omega_{\rm GW} L)\right] \ ,
\end{aligned} \tag{1.16}$$

which reproduces the TT-gauge result in Eq. (1.15). We note that in the proper detector frame, the mirror motion (*i.e.* Doppler term) is the dominant contribution if $\omega_{\rm GW} L \ll 1$, in agreement with the literature [34].

pulsar timing arrays

Precision timing measurement of pulses emitted from rapidly rotating neutron stars known as pulsars provides us with another way of detecting gravitational waves. The advantage of pulsar timing measurements comes from the incredible stability of millisecond pulsars, often with an intrinsic spindown rate potentially as small

$\dot{P} \sim 10^{-21}$ where P is the pulsar period [41][3]. This remarkable stability facilitates the detection of gravitational waves by minimizing the uncertainties originating from the pulsar itself, thereby enhancing our ability to accurately detect and measure gravitational wave signals. Additionally, timing measurements from a large collection of pulsars at different locations in the celestial sphere allows us to measure the cross-correlation of any timing deviations, which provide a smoking-gun signature of gravitational waves passing through the entire array of pulsars.

We provide a brief introduction to measuring gravitational perturbations using pulsar timing arrays. Our treatment here mostly follows Ref. [42]. The intrinsic phase of a pulsar is modeled by the timing model

$$\phi(t) = \phi_0 + \nu t + \frac{1}{2}\dot{\nu} t^2 \,, \tag{1.17}$$

where ϕ_0, ν and $\dot{\nu}$ are the pulsar phase constant, angular frequency and spindown. In the presence of any gravitational perturbation, the pulsar phase will be modulated, leading to a phase residual

$$s(t) = \phi(t) - \phi_{\text{fitted}}(t) \,, \tag{1.18}$$

where $\phi_{\text{fitted}}(t)$ is obtained by fitting the measured pulsar phase with a quadratic polynomial in time as Eq. (1.17). Any components of the timing residuals $s(t)$ that are not attributed to noise can then potentially be signatures due to gravitational waves, dark matter, or other phenomena that can alter pulsar timings. This also shows that any perturbations in pulsar timing that are at most linear in time will be completely degenerate with the timing model, and hence are cannot be discovered by pulsar timing measurements (although they are still constrained to be smaller in magnitude than the experimental fitted values).

Dark matter signatures can manifest in pulsar timing measurements in various ways. Here we name a few as an illustration. First, dark matter substructure in the universe can gravitationally accelerate pulsars, leading to an apparent Doppler shift in the observed phase [43]. Second, gravitational field due to dark matter substructure can lead to Shapiro time delay in the observed pulses [44]. Finally, a strong first-order cosmological phase transition in the dark sector can produce a stochastic gravitational wave background, which can in turned be measured by pulsar timing arrays [45]. This is particularly important if the dark sector is completely secluded

[3] While individual pulse profile can suffer from random fluctuations, the pulse profile averaged over rotations can be extraordinarily stable across long timescales [27].

from the standard model, then gravitational signatures will be the only observables accessible to experiments.

1.2 Dark Matter

This section provides a concise overview of the field of dark matter research relevant to this thesis, while not exhaustively covering all recent developments. Detailed reviews discussing various evidence of dark matter and detection techniques are available in TASI lectures [46, 47, 48, 49, 50, 51, 52] as well as the recent Snowmass paper [53]. In summary, the current open questions about dark matter are:

- What is the particle nature (*e.g.*, mass) of dark matter?
- How does dark matter interact with standard model particles?
- What is the origin of dark matter?

evidence of dark matter and alternative explanations

As mentioned in the introduction, dark matter was originally proposed to explain galaxy rotation curves [54]. The inference of dark matter's existence from these curves relies on the assumption that general relativity holds on larger scales than those currently subjected to precision tests. Consequently, there have been proposals to explain rotation curves by modifying gravity on a large scale, thus avoiding the need for dark matter [55, 56, 57]. Additionally, alternative proposals inspired by string theory, black hole information theory, and quantum information theory suggest that gravity contains an additional "dark" force at the scale of the cosmological horizon. This concept is commonly known as "emergent" or "entropic" gravity [58].

While these alternative proposals can often also explain galaxy rotation curves, sometimes with even better agreement with experimental data (see Refs. [59, 60]), they also need to be capable of reproducing other empirical evidence of dark matter without the introduction of extra matter content. This includes observations of the anisotropies in the cosmic microwave background [61], gravitational lensing observations of bullet clusters [61, 62], abundance of light elements from big bang nucleosynthesis [63], and large scale structure observations [64], all of which align well with the standard ΛCDM (dark energy + cold dark matter) paradigm [65]. Tensions with observational data on small scales can generally be attributed to baryonic effects [66]. In particular, studies have demonstrated that for any generic theory of modified gravity that is isotropic and conserves both matter and momentum, to

match observations of the large-scale distribution of structure [67], the corresponding acceleration law needs to switch sign at around ~ 150 Mpc scale [68], a feature absent in any current proposed theories of modified gravity. Therefore, dark matter remains the simplest and most coherent explanation of cosmological observations on both large and small scales, with modified gravity (without the addition of any other matter content) being a possibility that is intriguing, yet challenging to be reconciled with the vast diversity of existing observations.

properties of dark matter

Here we summarize the known properties of dark matter.

- Mass: The mass of dark matter is constrained within $10^{-19}\,\mathrm{eV} \lesssim m_\chi \lesssim 10^2\,M_\odot$ [69], where the lower bound is derived from observations of ultrafaint dwarf galaxies [70], and the upper bound is determined from microlensing observations [71]. Fermionic dark matter particles are required to be heavier than ~keV to fit into a dwarf galaxy while satisfying the Fermi exclusion principle [72]. Additionally, it is noted that dark matter heavier than the Planck mass exists as either black holes or bound-states [52].

- Phase space distribution: The dark matter velocity in the solar neighborhood is often approximated with the standard halo, which is a Maxwell-Boltzmann distribution, $f(\mathbf{v}) \propto \exp(-\mathbf{v}^2/v_0^2)$, truncated at the escape velocity of $v_{\rm esp} \approx 600$ km/s, with a scale velocity of $v_0 \approx 220$ km/s, and boosted to the Earth frame by the solar system velocity $v_\odot \approx 240$ km/s [73]. However, recent studies using stellar observations of SDSS-Gaia reveal substantial deviation of the dark matter velocity distribution from the standard halo model, with important implications on direct prospects [74]. On the other hand, the density profile of dark matter in the galaxy can generically be modeled by the Navarro-Frenk-White (NFW) profile [65, 75], $\rho(r) \propto (r/r_s)^{-1}(1 + r/r_s)^{-2}$, where r is the radial distance from the galactic center and $r_s \approx 8$ kpc is the scale radius [76].

- Interaction: To date, the only known interaction between dark matter and standard model particles is gravity. Any additional interactions must be feeble to evade existing experimental constraints. For instance, interactions between dark matter and photons are constrained by observation of cosmic background radiation intensity in the microwave, infrared, optical, ultraviolet,

x-ray and gamma-ray bands [77]. On the other hand, dark matter is allowed to self-interact with cross-section limited by the upper bound, $\sigma/m_\chi \lesssim \mathrm{cm}^2/\mathrm{g}$, set by bullet cluster observation [78, 79].

detection strategies

Traditional endeavors in dark matter direct detection have predominantly focused on weakly interacting massive particles (WIMPs), widely regarded as the most well-motivated model of dark matter [80]. It has been proposed that WIMPs initially existed in thermal equilibrium with the standard model plasma in the early universe. As the universe expanded, the thermal bath cooled, leading to an exponential suppression in the dark matter number density as $\exp(-m_\chi/T)$ until the Hubble expansion rate surpassed the dark matter annihilation rate. Subsequently, dark matter underwent “freeze-out" from thermal equilibrium, resulting in a constant comoving density. Studies have indicated that within this framework, the mass of dark matter must fall within the range $\mathrm{MeV} \lesssim m_\chi \lesssim 100, \mathrm{TeV}$ to comply with constraints from big bang nucleosynthesis and to avoid overproduction. Additionally, standard thermodynamic calculations suggest that for dark matter with a mass of ~ 100 GeV, the requisite dark matter abundance observed today necessitates an annihilation cross-section of approximately $\langle \sigma v \rangle \sim 10^{-26}\ \mathrm{cm}^3/\mathrm{s}$ [50]. This notion, commonly referred to as the "WIMP miracle," proposes that weak-scale particle dark matter must undergo annihilation with a strength comparable to the weak interaction. Despite this success, efforts in direct detection of WIMPs have thus far yielded no conclusive evidence, despite significant advancements in experimental sensitivity.

Over the past decade, there has been significant progress in the direct detection of light dark matter, particularly sub-GeV dark matter. Unlike their counterparts, these dark matter candidates were not initially in thermal equilibrium with the standard model bath. Instead, they attained their observed abundance through inefficient production via a small coupling with the standard model, a phenomenon termed “freeze-in" [81, 82]. Given that sub-GeV dark matter particles are not heavy enough to induce measurable nuclear recoil effects, direct detection hinges on the excitation of collective modes in condensed matter systems [83, 84].

While direct detection experiments are an indispensable element of the search for dark matter, it is also important to recognize that targeted experimental searches for any particular model or class of models might eventually yield no conclusive results. The importance of “casting a wider net" has gained recognition within the

community [85], particularly with the increasing number of well-motivated dark matter models. Specifically, if dark matter is not a single particle but part of a more complex dark sector with its own dynamics, then designing a targeted experiment for each variant of the model will be highly inefficient. It has long been recognized that astrophysical systems offer an excellent avenue to explore the dark matter parameter space due to their often extreme environments (*e.g.*, gravitational and magnetic field strengths). Additionally, as to be discussed in Sec. 1.1, gravitational wave experiments have achieved remarkable precision in recent years, providing another promising method for probing feeble interactions between dark matter and standard model particles, including purely gravitational interaction, and potentially dark-sector mediated long-range Yukawa interaction.

1.3 Quantum Gravity

It is conventional wisdom that quantum gravity effects can never be measured with realistic experimental setups. Indeed, by traditional power counting under the effective field theory framework, the size of any physical process that is both "quantum" and "gravitational" is expected to be proportional to certain positive powers of both the reduced Planck constant, $\hbar$, and the Newtonian constant, G_N (here we temporarily restore units that are otherwise dimensionless in natural units to illustrate the physical sizes). If the observable is a length quantity, then the physical size should be given by the only product of fundamental constants that give a length quantity, i.e the Planck length $l_p = \sqrt{G_N \hbar / c^3} \sim 10^{-34}$ m, which is far too small to be measured by any interferometer systems.

However, there are reasons to believe that the vacuum fluctuations can be much bigger than anticipated. A recent review is given by Ref. [86]. The photon trajectory traces a causal diamond, which is a null surface that causally separates two regions of spacetime, *i.e.* the exterior and the interior of the diamond. This is analogous to a black hole horizon, which is also a null surface. The Berkenstein-Hawking entropy of a black hole is given by the famous formula [87, 88, 89],

$$S = \frac{A}{4G_N}\,, \tag{1.19}$$

where A is the area of the black hole horizon. This suggests a thermodynamic description of the black hole. In particular, this also suggests that the IR scale of the system, *i.e.* the horizon size, enters into the number of degree of freedom in the horizon.

In fact, it has been long speculated that length fluctuations near a black hole horizon can be much larger than the size as predicted by a naive application of EFT. Marolf argued that fluctuations of low energy modes near a black hole horizon provide the horizon with a non-zero quantum mechanical width. The width in four spacetime dimensions is estimated to be [90]

$$\Delta L \sim \sqrt{l_p L}\,. \tag{1.20}$$

A recent paper by Bousso and Penington demonstrated that EFT radically breakdown as evident of information located in an entanglement island reconstructed non-perturbatively from distant radiation [91]. The length scale where EFT breaks down also has the same scaling relation as Eq. (1.20) in four spacetime dimensions. While these results cannot be directly translated into interferometer observables, they serve as examples that EFT can break down near a black hole horizon, which is a region with weak gravitational field and one would assume that EFT is still valid.

Part I

Dark Matter

Chapter 2

PROBING DARK MATTER SUBSTRUCTURE WITH PULSAR TIMING ARRAYS: FORMALISM AND PROJECTED COSNTRAINTS

This chapter is based on

[1] Vincent S. H. Lee, Andrea Mitridate, Tanner Trickle, and Kathryn M. Zurek. "Probing Small-Scale Power Spectra with Pulsar Timing Arrays". In: *JHEP* 06 (2021), p. 028. DOI: 10.1007/JHEP06(2021)028. arXiv: 2012.09857 [astro-ph.CO].

2.1 Introduction

Dark Matter (DM) is one of the pillars of the standard cosmological model. Perturbations in the DM density field generated by inflation provide the seeds for the hierarchical structure formation we observe in the Universe. On large scales the matter power spectrum of these primordial perturbations can be inferred from the anisotropies in the cosmic microwave background (CMB). These observations indicate a nearly scale-invariant spectrum of primordial fluctuations, which is compatible with the large scale structures we observe on galactic and extra-galactic scales.

However on smaller length scales, $k \gtrsim \text{pc}^{-1}$, different theories of DM leave unique fingerprints on the primordial perturbations and/or their evolution. Here we focus on four theories which produce different small scale structures, avoid current experimental bounds, and are theoretically well motivated:

- **ΛCDM**: A nearly scale invariant spectrum of adiabatic perturbations is produced at the end of infaltion [92, 93].
- **Post-inflationary QCD axion**: The $U(1)_{\text{PQ}}$ symmetry is broken after inflation. The decay of axion field defects at the QCD phase transition then induces large amplitude isocurvature fluctuations on scales smaller than the horizon at the QCD epoch [94, 95].

- **Early Matter Domination**: Adiabatic perturbations which are within the horizon during an early stage of matter domination grow linearly instead of logarithmically, enhancing the amount structure on these scales [96, 97].
- **Vector DM Produced During Inflation**: If the DM is a massive spin-1 particle, the longitudinal modes produced at the end of inflation can peak the power spectrum at small scales, with the location of the peak determined by the DM mass [98].

These model specific features in the primordial seeds, and their evolution, translate to different predictions for the amount, and properties, of sub-galactic DM halos (subhalos). Therefore measuring this population of subhalos can be a powerful tool in pinning down the model of DM.

Unfortunately DM subhalos are elusive objects, mostly because they are expected to contain very little baryonic matter and are therefore nearly invisible (assuming a weak indirect detection signal). Because of this, gravitational probes are the natural candidate to look for them. Many such probes have been proposed (*e.g.* Refs. [99, 100, 101, 102]), however their discovery potential depends on the subhalo mass and density profile (usually parameterized with a concentration parameter). At small masses ($M \lesssim 10^{-2} M_\odot$), where these probes lose sensitivity, Pulsar Timing Arrays (PTAs) may be powerful and complementary probes [44, 103, 104, 105, 43, 42]. The ability to test extremely light ($M \gtrsim 10^{-13}$) subhalos with low concentration parameters ($c \gtrsim 10$) makes PTA searches particularly interesting.

The signals DM subhalos can induce in a PTA measurement of the pulsar phase have been studied in depth [43, 42]. Each subhalo induces a shift to the residual phase measurement which can be non-degenerate with the timing model. Previous works [43, 42] have used analytic approximations of the signal, denoted as *static*, *dynamic*, and *stochastic* limits. These correspond to three different limits where the timescale, τ, for a typical subhalo to transit the line-of-sight is much greater than the observing time T ($\tau \gg T$, static), is much less than the observing time ($\tau \ll T$), but the signal is dominated by a single transiting subhalo (dynamic) or many transiting subhalos (stochastic). Here we will limit these simplifications by generating the full time series produced by a population of DM halos by using a Monte Carlo (MC) simulation. One goal of this paper is to develop this numeric tool, which we make publicly available on GitHub .

The second goal of this work is to use this MC to generate the PTA signal that would be produced by the subhalo populations predicted by the four DM models listed above. To obtain an estimate of the local population of DM subhalos, one needs to know how primordial perturbations evolve from the early Universe until today. This is a complex problem, especially at the sub-galactic scales relevant for PTA searches where non-linearities and tidal effects play a crucial role. The Press-Schechter formalism [106] is known to give a reasonably good analytic description of the non-linear physics related to the clustering of DM overdensities (at least for the case of ΛCDM, where a direct comparison with numerical simulations is possible). We then use this model, together with semi-analytic description of tidal effects, to relate the primordial power of primordial perturbations to the local population of DM subhalos. We should caution that a number of the methods we are using have not be tested against N-body simulations for such low mass and high density subhalos. We leave for future work validating and calibrating the analytic results for small scale DM subhalos.

The outline of the paper is as follows. In Section 2.2 we review the derivation of the PTA signal induced by a population of DM subhalos, along with the signal-to-noise ratio, and discuss the MC algorithm used to compute it. In Section 2.3 we illustrate the semi-analytic procedure used to relate the primordial power of density perturbation to the local subhalo population. In Section 2.4 we apply these results to the benchmark scenarios discussed above, and derive constraints for planned [107], and future PTAs. Finally, in Section 9.5 we conclude.

2.2 Dark Matter Subhalo Signatures in Pulsar Timing Arrays

We begin with a discussion of the signal induced in PTAs by DM subhalos, how we generate this signal with the Monte Carlo, and the signal-to-noise ratio (SNR) of such a signal. Many of the formulae presented here were previously derived in Refs. [43, 42] and we review them here for completeness. Previously both the Doppler effect (acceleration induced by a DM subhalo of either the Earth or a pulsar (called the *Earth* or *pulsar* terms, respectively)), and Shapiro effect (a change in the light arrival time due to the DM subhalo gravitational potential) were considered. Here we will only consider signals from the Doppler effect, which is dominant over the Shapiro effect for subhalos with mass below $M \lesssim 10^{-3} M_\odot$ for any concentration parameter (see Ref. [42]).

Phase Shifts from Dark Matter Subhalos

Pulsars are rotating, highly magnetized neutron stars that emit beams of electromagnetic radiation from their magnetic poles. Given a misalignment between the rotation and magnetic axes, the pulsar rotation can cause the radiation beam to sweep across Earth. If this happens, a pulsar will appear to an Earth observer as a periodic emitter. When a DM subhalo approaches either the Earth, or a pulsar, in the array it will cause an acceleration and therefore change the observed pulsar frequency, ν. This frequency shift, $\delta\nu$, for a subhalo passing with position $\mathbf{r} = \mathbf{r}_0 + \mathbf{v}t$, where $\mathbf{r}_0$ is the initial position and $\mathbf{v}$ is the velocity, is given by

$$\delta\nu\,(t; \mathbf{r}_0, \mathbf{v}) = \nu\,\hat{\mathbf{d}} \cdot \int_0^t \nabla\Phi(\mathbf{r}(t'))\,dt'\,, \tag{2.1}$$

where Φ is the subhalo gravitational potential. The coordinate system for the Earth (pulsar) term is chosen with the Earth (pulsar) at the origin, with $\hat{\mathbf{d}}$ pointing from the Earth to the pulsar (pulsar to Earth). We also parameterize the position vector as $\mathbf{r}(t) = \mathbf{b} + \mathbf{v}(t - \bar{t})$, where $\mathbf{b} = \mathbf{r}_0 + \mathbf{v}\bar{t}$ is the impact parameter, and $\bar{t} = -\mathbf{r}_0 \cdot \mathbf{v}/v^2$ is the time to reach the point of closest approach. The phase shift, $\delta\phi$, is then simply

$$\delta\phi(t) = \int_0^t \delta\nu(t')\,dt'\,. \tag{2.2}$$

For spherically symmetric halos, the gradient of gravitational potential appearing in (2.1) can be written in terms of a form factor $\mathcal{F}(s, c)$ as

$$\nabla\Phi(\mathbf{r}, M) = \frac{GM}{r^3}\mathcal{F}(r/r_v, c)\,\mathbf{r}, \tag{2.3}$$

where M is the virial mass defined as the subhalo mass contained inside the virial radius r_v, the radius within which the mean halo density is 200 times the critical density of the Universe, ρ_c. In the following we will assume that DM subhalos have an NFW density profile

$$\rho(r) = \frac{4\rho_s}{(r/r_s)\,(1 + r/r_s)^2}, \tag{2.4}$$

where r_s is the scale radius, and $\rho_s \equiv \rho(r_s)$. For NFW subhalos the form factor is

$$\mathcal{F}(s, c) = \frac{\ln(1 + c\,s) - c\,s/(1 + c\,s)}{\ln(1 + c) - c/(1 + c)}, \tag{2.5}$$

where we have introduced the concentration parameter, $c \equiv r_v/r_s$, related to the subhalo scale density by

$$\rho_s = \frac{50\,c^3\rho_c}{3\,(\ln(1 + c) - c/(1 + c))}\,. \tag{2.6}$$

We see that for very compact halos, $c \to \infty$, the form factor reduces to one and subhalos behave as point-like object. We will refer to this as the 'PBH' limit since when $\mathcal{F} \to 1$ the gravitational potential reduces to that of a primordial black hole (PBH).

In the PBH limit Eq. (2.2) can be simplified to [43][1]

$$\delta\phi_{\rm PBH}(t; M, \mathbf{r}_0, \mathbf{v}) = \frac{GM\nu}{v^2}\hat{\mathbf{d}} \cdot \left(\sqrt{1+x^2}\,\hat{\mathbf{b}} - \sinh^{-1}(x)\,\hat{\mathbf{v}}\right), \tag{2.7}$$

where $x = (t - \bar{t})/\tau$ is a normalized time variable, and $\tau = b/v$.

For an $\mathcal{F}$ given by Eq. (2.5), $\delta\phi$ can be challenging to compute analytically due to the discontinous derivatve in $\mathcal{F}$ at $s = 1$ which can be important if the subhalo passes from $s > 1$ to $s < 1$. In principle, one could perform the integrations numerically, though this becomes intensive with a large number of subhalos. We instead use a conservative estimate of the signal size by substituting $\mathcal{F}(r/r_v, c)$ with $\mathcal{F}^*(c) \equiv \mathcal{F}(r_{\rm min}/r_v, c)$, where $r_{\rm min}$ is the distance of closest approach over the observation time. This approximation changes the amplitude by $\mathcal{O}(10\%)$ for $c \sim 100$ but quickly shrinks to $\mathcal{O}(1\%)$ for $c \sim 10^4$. Using this conservative estimate the phase shift for an NFW subhalo is simply

$$\delta\phi(t; M, c, \mathbf{r}_0, \mathbf{v}) = \frac{GM\mathcal{F}^*(c)\nu}{v^2}\,\hat{\mathbf{d}} \cdot \left(\sqrt{1+x^2}\,\hat{\mathbf{b}} - \sinh^{-1}(x)\,\hat{\mathbf{v}}\right). \tag{2.8}$$

This effect is now easily generalized to a PTA with N_P pulsars, each of which is influenced by N subhalos. In this case the phase shift of the I^{th} pulsar is given by

$$\Delta\phi_I(t) = \sum_{i=1}^{N} \delta\phi(t; M_i, c_i, \mathbf{r}_0^i, \mathbf{v}^i), \tag{2.9}$$

where the sum runs over all of the DM subhalos affecting the $I^{\rm th}$ pulsar.

As discussed in detail in Ref. [42], the phase shift itself is not directly observable. This is because the shift induced by transiting DM subhalos can be partially degenerate with the phase shift induced by the 'natural' evolution of the pulsar frequency, described by the timing model

$$\phi(t) = \phi^0 + \nu t + \frac{1}{2}\dot{\nu}t^2, \tag{2.10}$$

[1]Indefinite integrals were used in deriving Eq. (2.7) from Eq. (2.1). This will not affect any observable since any dependence on reference times will be removed in the fit to the residual phase shift.

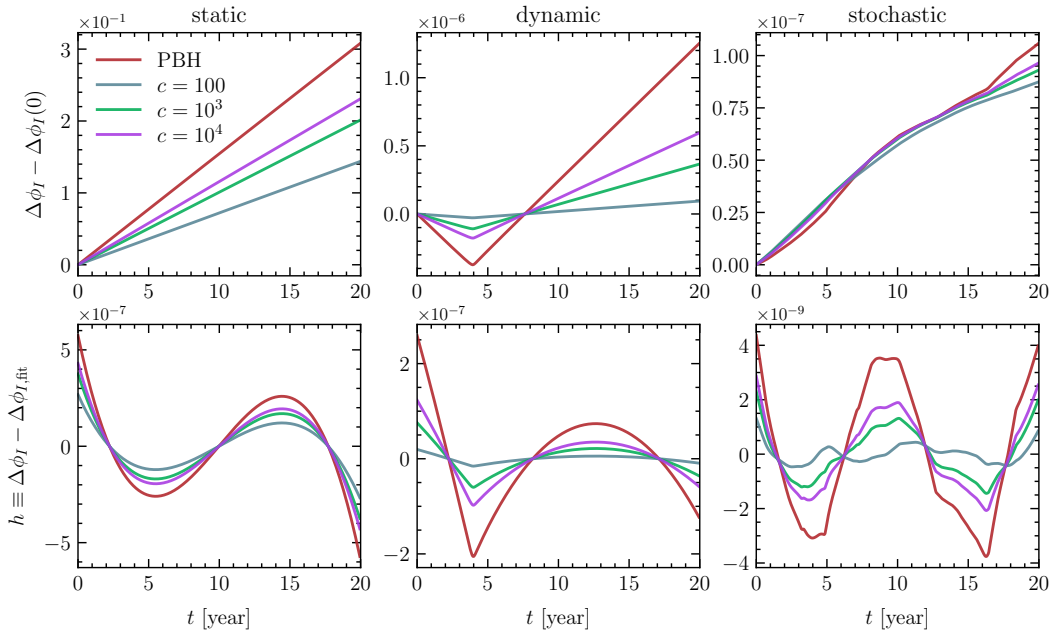

Figure 2.1: Sample signal shapes of the static (left column), dynamic (middle column) and stochastic (right column) signals from DM subhalos with $c = 100, 10^3, 10^4$ and the Primordial Black Hole limit $c \to \infty$. The top row shows the unsubtracted signal shapes, computed from Eqs. (2.8) and (2.9), while the bottom row shows the subtracted signal shapes after the terms degenerate with the timing model have been removed. The first two columns show the phase shift $\delta\phi(t)$, Eq. (2.8), from a single transiting subhalo and the last is the signal shape from multiple transiting subhalos, $\Delta\phi$, in Eq. (2.9). The signal shapes are taken from a realization of the Monte Carlo. The mass of the subhalos are $10^{-2}\ M_\odot$, $10^{-11}\ M_\odot$ and $10^{-14}\ M_\odot$ for the static, dynamic and stochastic signals respectively. Only the closest subhalo is kept for the static and dynamic signals, while all subhalos are kept for the stochastic signal.

where ϕ_0, ν, $\dot{\nu}$ are the phase offset, pulsar frequency, and its first time derivative. In general, if a DM signal is present, each pulsar measures a total residual phase shift, s_I, given by the sum of signal, h_I, and noise, n_I:

$$s_I(t) \equiv h_I(t) + n_I(t)\,. \tag{2.11}$$

The DM signal, h_I, is defined as the part of the phase shift, $\Delta\phi_I$, that is not absorbed by the pulsar timing model,

$$h_I(t) \equiv \Delta\phi_I(t) - \Delta\phi_{I,fit}(t), \tag{2.12}$$

where

$$\Delta\phi_{I,\mathrm{fit}} = \frac{1}{T}\sum_{n=0}^{2} f_n(t) \int_0^T f_n(t')\Delta\phi_I(t')\,dt', \tag{2.13}$$

with $f_n = \sqrt{2n+1}P_n(2t/T-1)$, P_n the n$^{\text{th}}$ Legendre polynomials, and $\phi(t)$ given by Eq. (5.37). Similarly, the post-fit residual noise, $n_I(t)$, is given by the intrinsic pulsar phase evolution that is not reabsorbed by the timing model.

Sample unsubtracted and subtracted signal shapes (*i.e.* before and after fitting for ϕ^0, ν, and $\dot{\nu}$) are shown in Fig. 2.1. The left and middle columns show the signal shapes from a single subhalo. Depending on the timescale of the interaction, τ, we classify the signals as either "static" ($\tau \gg T$, left column) or "dynamic" ($\tau \ll T$, right column). Both limits allow for simplifications of Eq. (2.8). In the static limit $\delta\phi$ can be Taylor expanded in t/τ. The total $\delta\phi$, in the top row, then looks nearly linear, while the measurable subtracted signal, the bottom row, is $\propto f_3(t)$, defined below Eq. (2.13), due to the timing model fit of ϕ^0, ν and $\dot{\nu}$. A dynamic signal, on the other hand, has a more characteristic signal shape. Expanding the term $\propto \mathbf{b}\cdot\mathbf{d}$ in Eq. (2.8) for small τ leads to $\delta\phi \propto |t-t_0|$, which explains the kink in the upper middle panel in Fig. 2.1. This parameterization can be simplified further, since the terms $\propto t$ will be subtracted, to $\delta\phi(t) \sim (t-\bar{t})\Theta(t-\bar{t})$, and therefore the signal can be parameterized in terms of two variables: an amplitude and $\bar{t}$. Lastly, the stochastic signal in the right column is the sum of a large number of individual subhalos with $\tau \lesssim T$ and we see that the signal has no simple parameterization.

Constructing the SNR

With the signal defined, we now discuss the signal significance relative to noise, or SNR. As done in Refs. [43, 42] we will use a matched filter procedure [37, 108, 109]. As discussed previously, each pulsar in the PTA measures the residual phase shift, s_I, given in (2.11) which is the sum of signal, h_I, and noise, n_I. Naively one would expect that the signal is only significant if $|h_I| > |n_I|$. However if we know the form of the signal, we can filter the noise and boost the significance. The optimal scenario for this filtering procedure is the one where the shape of the signal is known *a priori*, or can be parameterized by a computationally searchable space of parameters. In this case the best test statistic is $\mathcal{T} \equiv \sum_I \int dt\, s_I(t) Q_I^{opt}(t)$, where the signal of each pulsar is convolved with its own *optimal* filter, $\widetilde{Q}_I^{\text{opt}} = \widetilde{h}_I/\widetilde{N}_I$, where $\sim$ denotes the Fourier transform and $\widetilde{N}_I$ is the noise power spectrum of the I^{th} pulsar. We will assume the noise is white, so that we have

$$\widetilde{N}_I = \nu_I^2 t_{\text{rms}}^2 \Delta t\,, \tag{2.14}$$

where t_{rms} is the root mean square residual timing noise, and Δt is the time between measurements (the cadence). However to know, or find through a Markov Chain

Monte Carlo, the optimal filter for all the pulsars in the array is not always possible. We discuss alternatives for both the pulsar and Earth terms.

We start by discussing the pulsar term. For a generic pulsar in the array, many transiting events contribute to the signal $s_I(t)$. This makes unfeasible to look for the optimal filter of a generic pulsar, given the large number of parameters needed to describe the signal shape. However, we expect the largest signal in the array to be dominated by a single halo transiting very close to the pulsar. Therefore, the largest signal is expected to have the simple parametrization discussed below (2.13), which makes the search for its optimal filter feasible. We therefore define the *P*ulsar SNR, SNR_P, to be the largest across the array:

$$\mathrm{SNR}_P^2 = \max_I \left\{\mathrm{SNR}_I^2\right\} = \max_I \left\{ \frac{\left| \int df\, \widetilde{s}_I(f) \widetilde{Q}^*(f) \right|^2}{\int df\, \widetilde{N}_I(f) \widetilde{Q}^*(f) \widetilde{Q}(f)} \right\} . \tag{2.15}$$

Concretely, to place a constraint on a model we would generate an array of filters with different values of the parameters in the signal model (e.g. an amplitude for the static signal, and an amplitude plus epoch, $\bar{t}$, for the dynamic signal), use these as the filter Q in Eq. (2.15), and then place constraints with the largest SNR_P.[2] In practice, we assume we can select a filter which is arbitrarily close to Q^{opt}, and compute the expected maximum SNR from it,

$$\overline{\mathrm{SNR}}_P^2 = \max_I \left\{ \frac{1}{\widetilde{N}_I} \int dt\, h_I^2 \right\} . \tag{2.16}$$

The statistical significance of a given SNR, for the purposes of limit setting, is discussed in Appendix C. The h_I's are generated with the MC which will be discussed in more detail below, as well as in Appendix A. The resulting constraints for a monochromatic population of subhalos are labeled “Closest only" in the right panel of Fig. 2.2, where only the signal from the closest subhalo is kept. To verify this approximation we also show the constraints obtained by taking h_I to be the sum of the signals from all the subhalos around each pulsar, they are labelled “All.” in the right panel of Fig. 2.2.

The second signal, labelled “Earth” in the left panel of Fig. 2.2, originates from a large flux of subhalos transiting near the Earth. Since the signal is generated

[2] This is not the only way the analysis could be done. Since the signal shapes are known the best fit signal parameters could be searched for with an Markov Chain Monte Carlo (MCMC), such as Enterprise [110], and then compared to this distribution predicted by the MC presented here. We plan to explore this in a future work.

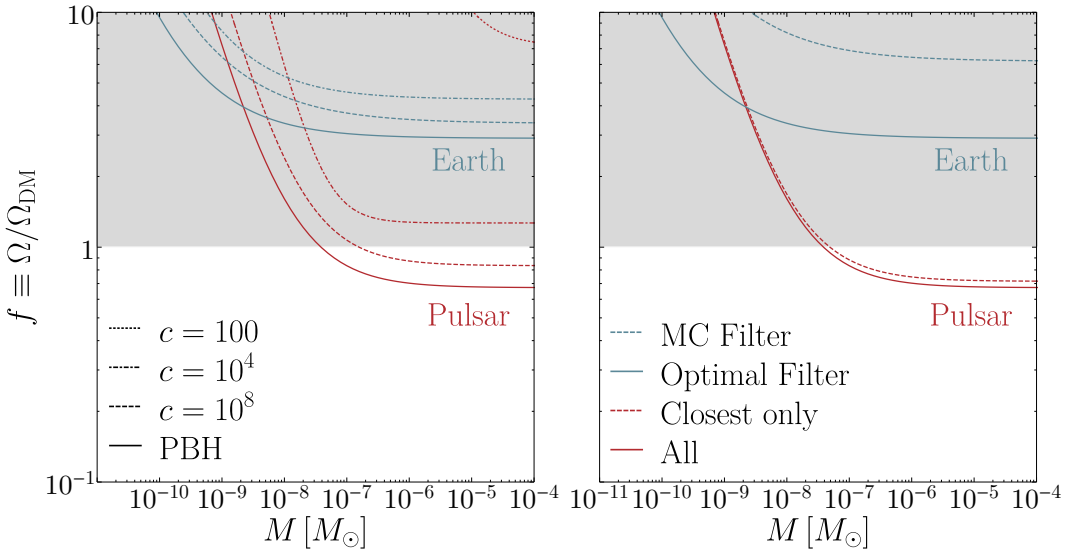

Figure 2.2: Limits from PTAs on the dark matter mass fraction $f = \Omega/\Omega_{\rm DM}$ in subhalos of mass M. The left panel compares different subhalo concentration parameters, $c = 100$, 10^4, 10^8, and the PBH limit, $c \to \infty$, as well as the different search types, "Earth" and "Pulsar". The right panel shows how the constraints change when different assumptions are used when computing the SNR for the Earth and the Pulsar terms discussed in Sec. 2.2. For the pulsar term we compare the constraints from keeping only the closest subhalo around each pulsar, labelled "Closest only", to the constraint obtained from keeping all of the subhalo contributions, "All". For the Earth term we compare the optimal filter to the one generated by the MC to understand the *mis-filtering* effect. The PTA parameters used were $N_P = 200$, $\Delta t = 2$ wk, $t_{\rm rms} = 50$ ns and $T = 20$ years.

by an acceleration of the Earth it will leave an imprint across the entire array with correlations between pulsars, similar to the correlations in the stochastic gravitational wave background [111, 112]. This signal is generated stochastically by many passing subhalos; as such, the optimal filter is not easily reconstructed. One can, however, parameterize the signal autocorrelator, $R_{IJ}(t,t') \equiv \langle h_I(t) h_J(t') \rangle$, where $\langle\rangle$ denotes an ensemble average. As in Ref. [42], we then define the SNR in terms of the signal correlator, $s_I(t)s_J(t')$,

$$\mathrm{SNR}_E^2 = \frac{1}{2} \frac{\left| \sum_{I \neq J} \int df df'\, S_{IJ}(f,f') \widetilde{Q}^*_{IJ}(f,f') \right|^2}{\sum_{I \neq J} \int df df'\, \widetilde{N}_I(f) \widetilde{N}_J(f') \widetilde{Q}^*_{IJ}(f,f') \widetilde{Q}_{IJ}(f,f')}, \tag{2.17}$$

where $S_{IJ}(f,f') = \widetilde{s}_I(f)\widetilde{s}_J(f')$. If $\widetilde{s}_I(f)$ is known *a priori* then the optimal filter to use is $\widetilde{Q}^{\rm opt}_{IJ} = \widetilde{s}_I(f)\widetilde{s}_J(f')/\left(\widetilde{N}_I \widetilde{N}_J\right)$. Since this is not the case, we use a filter based on the expected signal, $Q_{IJ} = \widetilde{R}_{IJ}/\left(\widetilde{N}_I \widetilde{N}_J\right)$, where $\widetilde{R}_{IJ} = \langle \widetilde{h}_I(f) h_J(f') \rangle$. Since the

expected filter will not be optimal, this introduces a *mis-filtering* effect. In the right panel of Fig. 2.2 we illustrate the effect that mis-filtering has on the constraints, lowering them by an $\mathcal{O}(1)$ number. We compute this constraint by using the MC to generate $S_{IJ}(f, f')$ in numerous realizations, taking the ensemble average $\widetilde{R}_{IJ}(f, f')$ over all the realizations, re-labelling it to $Q_{IJ}(f, f')$ and computing the SNR of the signal from new realizations using Eq. (2.17). We will take the latter, more conservative, limits below.

As discussed in detail in Appendix A, to generate signals for monochromatic halo mass functions, as shown in Fig. 2.2, the MC first generates the pulsar positions uniformly on a sphere. Then, for the Pulsar (Earth) term, around each pulsar (the Earth), subhalo initial positions $\mathbf{r}_i^0$ and velocities $\mathbf{v}_i$ are generated and used to compute the signal in Eq. (2.9). The initial positions are assumed to be uniformly distributed throughout space with density fixed to be $0.46\ \mathrm{GeV/cm^3}$, and the velocities drawn from a Maxwell-Boltzmann distribution with RMS velocity $v_0 = 325$ km/s. The relevant SNR is then computed in 1000 realizations and constraints are placed setting the 10^{th} percentile SNR equal to 4 which, as detailed in Appendix C, correspond to a signal significance of $\sigma_{\text{significance}} \sim 2$.

2.3 From Primordial Perturbations to the Local Subhalo Population

As we have seen in the previous section, PTAs are a powerful tool to constrain the abundance of Milky Way (MW) DM subhalos. These sub-galactic structures are seeded by the primordial perturbations on scales much smaller than the ones tested by CMB observables, where DM models can leave unique fingerprints. In principle, once the power spectrum of primordial perturbations is known the abundance of these DM subhalos can be derived. In practice, however, this is an intricate problem where non-linearities, tidal effects, and baryonic feedback play an important role. For the ΛCDM model we can rely on numerical simulations which have been well-tested with semi-analytic fits. For other models of DM we need to employ motivated analytic estimates. The goal of this section is to illustrate the analytic prescription that we will adopt in the rest of this work to compute the subhalo mass function (sHMF) and concentration parameters.

We start by writing the dimensionless primordial power spectrum for DM density perturbations, $\Delta^2(k)$, as

$$\Delta^2(k) = \Delta^2_{SI}(k) + \Delta^2_{MD}(k) \tag{2.18}$$

where $\Delta^2_{MD}(k)$ is the model dependent contribution to the small scale power, and

$\Delta^2_{SI}(k)$ is the scale-invariant primordial power spectrum for adiabatic perturbations as extracted from CMB measurements (and extrapolated to smaller scales) [113]:

$$\Delta^2_{SI}(k) = A_s \left(\frac{k}{k_0}\right)^{n_s - 1}, \tag{2.19}$$

with $n_s = 0.9665$, $A_s = 2.101 \times 10^{-9}$, and pivot scale $k_0 = 5 \times 10^{-3}\,\mathrm{Mpc}^{-1}$. Following the standard assumption of linear evolution of the density perturbations, we relate this primordial power spectrum to its late-time value by means of transfer, $T(k)$, and growth, $D(z)$, functions:

$$\Delta^2(k, z < z_{eq}) = T^2(k) D^2(z) \Delta^2_{SI}(k) + T^2_{MD}(k) D^2_{MD}(z) \Delta^2_{MD}(k), \tag{2.20}$$

where $z_{eq} \simeq 3.3 \times 10^3$ is the redshift at matter-radiation equality, and we allow Δ_{SI} and Δ_{MD} to have different transfer and growth functions.

The first category of models we consider modifies ΛCDM by increasing the amplitude of small-scale perturbations (*i.e.* $\Delta^2_{MD}(k) \neq 0$). The post-inflationary axion and vector DM models, discussed in Secs. 2.4 and 2.4 respectively, belong to this category. The second category of models preserves the primordial power of ΛCDM (*i.e.* $\Delta^2_{MD}(k) = 0$) but modifies the growth of small-scale perturbations in the early Universe, *i.e.* an enhanced, non-standard $T(k)$. Models featuring an early stage of matter domination, discussed in Sec. 2.4, belong to this category. The net effect of both of these categories is similar: they enhance the power of matter density fluctuations on small scales, as shown in Fig. 2.3. We will discuss these figures in more detail below, but simply note that the models under consideration feature a large enhancement of density fluctuations at scales well below what is currently measured with large scale structure surveys.

Halo Mass Function

The first quantity we derive from $\Delta^2(k, z)$ is the global Halo Mass Function (HMF), a function that gives the comoving number density of isolated halos in the Universe as a function of mass. Despite the non-linear nature of the problem, the analytic approach pioneered by Press & Schechter [106] has been proven to well-approximate numerical N-body simulations (at least for the standard ΛCDM).

In the Press-Schechter (PS) formalism, overdense regions are expected to detach from the Hubble flow and gravitationally collapse when their average overdensity, $\delta \equiv \delta\rho/\rho$, becomes larger than a critical value, δ_c (which in a flat Universe is

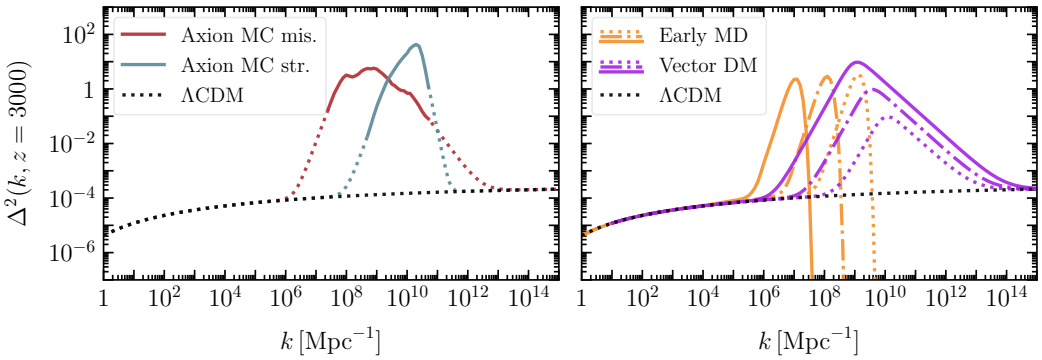

Figure 2.3: **Left:** dimensionless power spectrum at recombination for ΛCDM (black) compared to the post inflationary axion models (red for the misalignment dominated scenario, blue for the string dominated one). Dashed lines indicate regions where, due to lack of numerical or experimental results, the power spectra has been extrapolated. **Right:** similar to the left panel, except for the vector DM (purple), and early matter domination (orange) models replacing the post inflationary axion. For the early MD model we show the power spectrum obtained with three different choices of the reheating temperature: $T_{RH} = 10\,\mathrm{MeV}$ (solid), $T_{RH} = 0.1\,\mathrm{GeV}$ (dashdot), and $T_{RH} = 1\,\mathrm{GeV}$ (dotted). For the vector DM model we fix the inflationary scale at $H_I = 10^{14}\,\mathrm{GeV}$ and consider three DM masses: $m = 10^{-15}\,\mathrm{GeV}$ (solid), $m = 10^{-14}\,\mathrm{GeV}$ (dashdot), and $m = 10^{-13}\,\mathrm{GeV}$ (dotted).

found to be $\delta_c \simeq 1.686$).[3] Therefore, for Gaussian perturbations, the probability an overdense region of mass scale M is collapsed by redshift z is given by

$$f(M,z) = \frac{2}{\sqrt{2\pi}\sigma(M,z)} \int_{\delta_c}^{\infty} d\delta\; e^{-\delta^2/2\sigma^2(M,z)} \tag{2.21}$$

where $\sigma(M,z)$ is the variance of density perturbations smoothed over a sphere of size $R(M) = (3M/4\pi\rho_m)^{1/3}$:

$$\sigma^2(M,z) = \int_0^{\infty} \frac{dk}{k}\, \Delta^2(k,z) W^2\left(k\, R(M)\right), \tag{2.22}$$

where $W(x)$ is the window function of choice, and ρ_m is the background matter density of the universe today. In the following, unless otherwise specified, we will use a top-hat window function, $W(x) = 3x^{-3}(\sin(x) - x\cos(x))$.

The fact that a region of size $R(M)$ is collapsed does not prejudice against being part of a larger overdensity which has also collapsed. The HMF only counts collapsed

[3] For gravitational collapse during the radiation dominated epoch the critical overdensity becomes redshift dependent: $\delta_c(z) \simeq 1.686 \left(\frac{3}{2}\frac{z}{z_{eq}}\right)$ [114, 115].

objects which are not contained within larger halos; to obtain the comoving number density of these we differentiate Eq. (2.21) with respect to M and multiply by the average number density, ρ_m/M,

$$\frac{dn(M,z)}{d\ln M} = \frac{\rho_m}{M}\frac{df(M,z)}{d\ln M}\,, \tag{2.23}$$

with the mass fraction per logarithmic interval, $df/d\ln M$, is

$$\frac{df(M,z)}{d\ln M} = \sqrt{\frac{2}{\pi}}\nu(M,z)\exp\left(-\frac{\nu^2(M,z)}{2}\right)\frac{d\ln\sigma(M,z)}{d\ln M}\,, \tag{2.24}$$

where we have defined $\nu(M,z) \equiv \delta_c/\sigma(M,z)$.

The PS formalism has been validated against numerical simulations for ΛCDM cosmology [116, 117]. But whether it is still a good approximation for models that, on small scales, differ vastly from ΛCDM has yet to be studied in detail. We plan to study this question in future work, but for the moment we limit our discussion to PS predictions and compare them to numerical results available for the case of axion miniclusters [118]. The results of this comparison, shown in Appendix B, suggest that – at least for axion miniclusters – PS still provides a good estimate of the HMF. All the following results are based on this assumption.

Subhalo Mass Function

As already mentioned, the target of PTA searches are pulsars within a radius of $O(5\,\mathrm{kpc})$ from our solar system. Because of this, PTAs can only detect signals generated by the local population of MW DM subhalos, and not from the cosmological population described by the HMF. Unfortunately, estimating the local subhalo density is a much more complicated problem than deriving the HMF. Indeed, in the galactic environment these subhalos are exposed to tidal forces that strip part of their mass, and which may ultimately lead to their complete disruption.

We divide the problem of deriving the subhalo mass function (sHMF), $d\tilde{n}/d\log M$, in two steps. First we derive its value at infall: $d\tilde{n}/d\log M_{acc}$, where M_{acc} is the subhalo mass at the moment of its accretion into the MW and before tidal effects may reduce its value. Then, we analytically estimate the impact of tidal effects and derive the relation between the infall and final subhalo mass

$$M \equiv f_b(M_{acc})M_{acc}, \tag{2.25}$$

where we have implicitly defined the bound fraction, $f_b(M_{acc})$, as the fraction of the infall subhalo mass that survives tidal effects. Finally, by using (2.25), we relate

the infall sHMF to its final value,

$$\frac{d\tilde{n}}{d\log M} = \int d\log M_{acc} \frac{d\tilde{n}}{d\log M_{acc}} \delta\left(1 - \frac{f_b(M_{acc})M_{acc}}{M}\right), \tag{2.26}$$

where here and in the following, we adopt a $\sim$ notation to distinguish between the local sHMF and the global HMF.

As we will see, the density profile plays a key role in determining the impact of tidal effects. Subhalos are expected to have a radial density profile which is well described by the usual NFW profile given in Eq. (2.4). The characteristic density of the subhalo, Eq. (2.4), is set by the Universe's energy density at the time of collapse,

$$\rho_s = C_\rho \rho_c \left[\Omega_{\rm DM}(1+z_{col})^3 + \Omega_r(1+z_{col})^4\right], \tag{2.27}$$

where C_ρ is a free parameter that encodes the growth of the halo density during the virialization processes, and z_{col} is the collapse redshift. We fix the value of C_ρ by fitting (2.27) against N-body simulations. For ΛCDM halos (for which $z_{col} \simeq 10$) we use the results in [119] and find $C_\rho \sim 600$, for axion miniclusters (for which $z_{col} \gtrsim 10^3$) we use the results of [118] and find $C_\rho \sim 9 \times 10^4$. In the following we use a z_{col}-dependent C_ρ which smoothly interpolates between these two values.

Following Ref. [65], we define z_{col} for a subhalo of final mass M as the redshift at which half of its final mass is contained in progenitors more massive than ϵM. Using the extended Press-Schechter model [120], this redshift can be estimated by

$$\mathrm{erfc}\left[X(z_{col}) - X(0)\right] = \frac{1}{2}, \tag{2.28}$$

where

$$X(z) = \frac{\delta_c}{\sqrt{2\left[\sigma^2(\epsilon M, z) - \sigma^2(M, z)\right]}}, \tag{2.29}$$

and the best fit to ΛCDM halos is found for $\epsilon = 0.01$. In the following we will assume that the same value of ϵ provides a good estimate also for different DM models. The typical concentration parameters, as a function of mass, are shown in the lower panels of Fig. 2.4, where (2.6) was used to relate ρ_s to the concentration parameter. As expected, larger amplitude primordial perturbations lead to an earlier collapse and in turn larger concentration parameters.

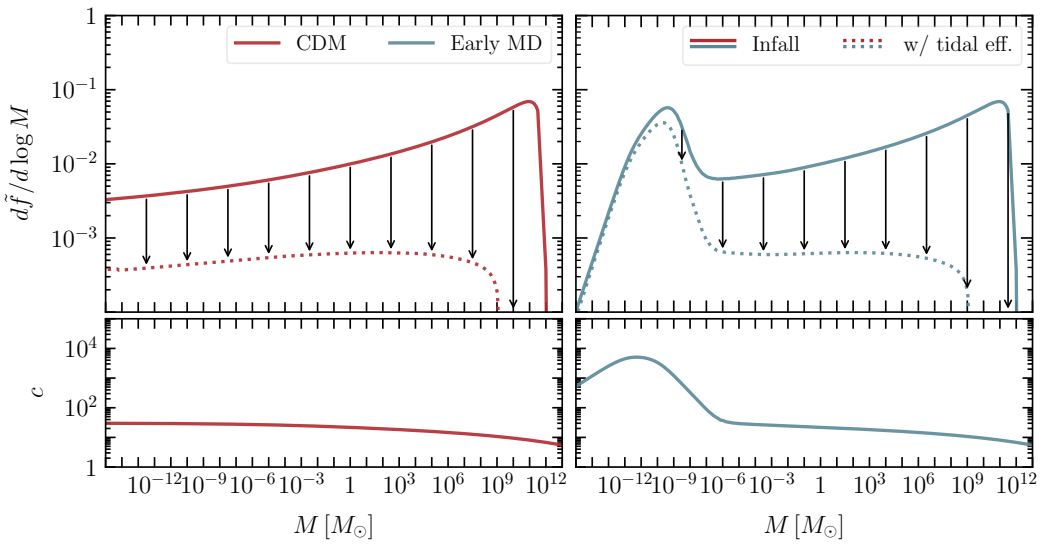

Figure 2.4: Illustrative example of the impact of tidal effects on the subhalo mass fraction. Upper: subhalo mass fraction before (solid) and after (dotted) tidal disruption for standard ΛCDM (red), and early MD (blue) with reheating temperature $T_{RH} = 10\,\mathrm{MeV}$ (for more details see Sec. 2.4). Lower: typical concentration parameter as a function of the subhalo mass. Additional power on small scales leads to an early collapse and therefore a larger concentration parameter for light halos.

sHMF at infall

In the PS formalism the probability that a halo of mass M at redshift z will be part of a larger halo of mass M_0 at redshift z_0 is given by [120, 121]

$$\tilde{f}(M, z; M_0, z_0) = \frac{1}{\sqrt{2\pi}} \frac{\delta_c(z - z_0)}{(s - S)^{3/2}} \exp\left(-\frac{\delta_c^2 (z - z_0)^2}{s - S}\right), \tag{2.30}$$

where $s \equiv \sigma^2(M, 0)$ and $S \equiv \sigma^2(M_0, 0)$. Therefore, as a proxy for the sHMF at infall we can use

$$\frac{d\tilde{n}}{d\log M_{acc}} = \frac{\rho_{\rm DM}}{M_{acc}} \frac{d\tilde{f}(M_{acc}, z_{MW}; M_{200}^{MW}, 0)}{d\log M_{acc}}, \tag{2.31}$$

where $\rho_{\rm DM}$ is the local DM energy density, $M_{200}^{MW} \approx 1.5 \times 10^{12} M_\odot$ is the MW virial mass, and z_{MW} is the MW collapse time, derived from (2.28).

Tidal effects

Subhalos in the MW can experience different kinds of tidal forces. Subhalos on nearly circular orbits are subjected to an almost constant tidal pull from the galactic

halo. The effect of this gravitational pull is to strip away the halo mass contained beyond its *tidal radius*, r_t, defined as the distance from the subhalo center at which the gravitational pull of the galaxy is stronger than the self-gravity of the subhalo [122]:

$$r_t = r_\oplus \left[\frac{M_{acc}(r < r_t)/M_{MW}(r < r_\oplus)}{3 - \frac{d \ln M_{MW}}{d \ln R}|_{r_\oplus}} \right] \tag{2.32}$$

where $r_\oplus$ is the radius of the Earth's circular orbit (assumed to be the distance between the solar system and the center of the galaxy, 8 kpc), $M_{MW}(r < r_\oplus)$ is the Milky Way mass enclosed within radius $r_\oplus$, and $M_{\rm acc}(r < r_t)$ is the accreted mass within r_t. For an NFW profile, the enclosed mass is given by $M(r < r^*) = M\mathcal{F}(r^*/r_v, c)$, where $\mathcal{F}$ is defined in Eq. (2.5), and M is the total mass. Assuming that the mass outside the tidal radius is instantaneously stripped away, the halo bound fraction surviving tidal stripping is[4]

$$f_b(M_{acc}) = \frac{M_{acc}(r < r_t)}{M_{acc}} \,. \tag{2.33}$$

The treatment of tidal effects performed in this analysis should be seen as a simple order of magnitude estimate whose main goal is to take into account the large tidal disruption suffered by the standard ΛCDM halos. To accurately estimate the smaller impact that tidal effects have on high concentration subhalos a more sophisticated analysis is needed. Specifically, additional processes like subhalo-subhalo encounters and interactions with MW stars can be the dominant disruption mechanism for high density subhalos, and need to be considered. A detailed study of these effects would require dedicated numerical simulation that we leave for future works. However, we do not expect these effects to change our results drastically, as also suggested by the recent results of Ref. [123].

2.4 Constraints on Primordial Power Spectra

In this section we use the tools developed to derive the discovery potential of PTAs for four benchmark DM models. However before discussing model-specific results, we want to give a rough idea of the constraints that PTAs can place on the DM primordial power spectrum. Assuming this spectrum is locally scale invariant, it can be shown [126] that

$$\sigma^2(M, z) \sim \Delta^2(1/R(M), z) \tag{2.34}$$

[4] In reality, tidal stripping happens over several orbits. However, if compared with numerical simulations of ΛCDM halos, the instantaneous stripping assumption seems to be accurate up to $O(1)$ factors [122].

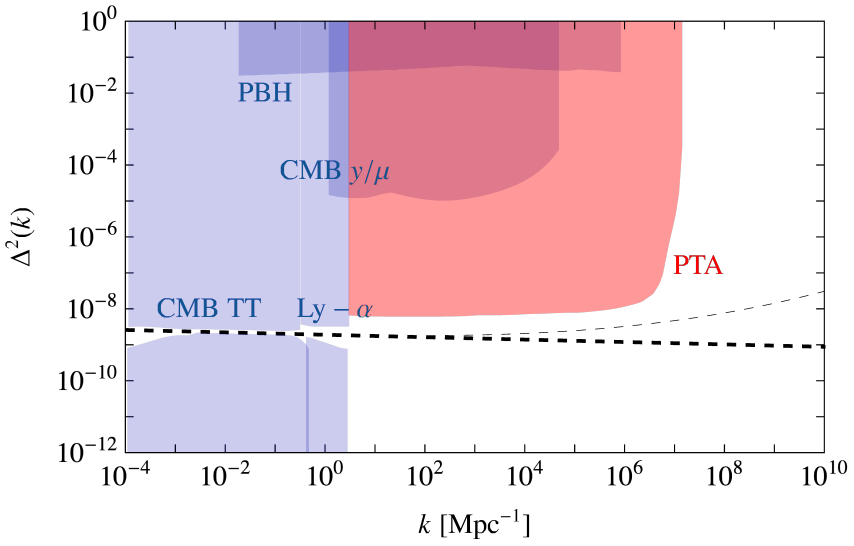

Figure 2.5: Limits on the dimensionless primordial power of curvature fluctuations. PTA limits (red) are compared to constraints from a combination of CMB [124] and Ly-α [125] observables, together with limits on primordial black holes (PBH) (all in blue). The thick dashed line is the Planck best fit, assuming a constant spectral index, while the thin dashed line is the best fit obtained allowing the spectral index to have a k dependence.

where, as before, R and M are related by $R(M) = (3M/4\pi\rho_m)^{1/3}$. This implies that there is an approximate one-to-one correspondence between the power of perturbations on scales $1/R(M)$ and the collapse probability, $f(M,z)$, given by (2.21). Assuming that the population of subhalos is not drastically altered by their merger history, the fraction of the local DM energy density in subhalos of a given mass is $f(M,z)f_b(M)$, where $f_b(M)$ is the bound fraction, Eq. (2.33), which accounts for tidal effects that these subhalos experience once accreted into the MW halo. In general these subhalos will not be isolated objects but will form substructure of larger subhalos, meaning $f(M,z=0)$ is certainly an overestimate of the mass fraction of subhalos of mass M. Bearing in mind these assumptions, we can say that PTA searches will be sensitive to a given amount of primordial power on scales $1/R(M)$ when

$$f(M,z=0)f_b(M) > f_{mono}(M,c)\,, \tag{2.35}$$

where the constraints for a monochromatic population of subhalos, $f_{mono}(M,c)$, are shown in Fig. 2.2. Assuming the transfer function is the one predicted by ΛCDM, and $r_\oplus = 8.2\,\mathrm{kpc}$, the constraints on the dimensionless primordial power are shown in Fig. 2.5. It is clear from this figure that PTA searches can strongly

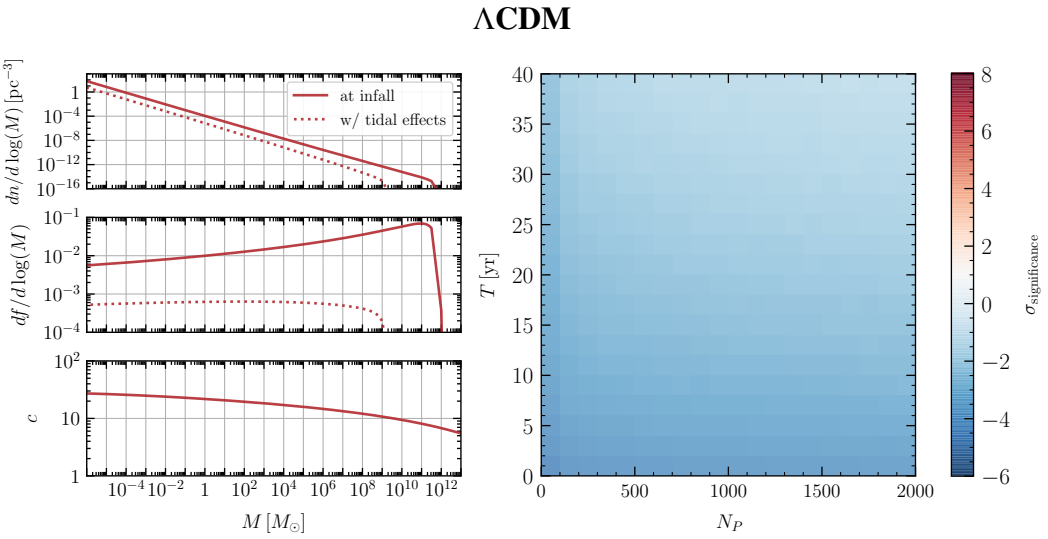

Figure 2.6: **Left:** sHMF (top panel), and mass fraction per logarithmic interval (center panel) before (solid) and after (dashed) the inclusion of tidal effects. The lower panel shows the typical subhalo concentration parameter as a function of their mass. **Right:** Discovery significance for different values of the observation time and number of pulsars in the array. The residual timing noise and observation cadence have being fixed to $t_{rms} = 10\,\text{ns}$ and $\Delta t = 1\,week$.

constrain models that have a small scale power spectrum that is enhanced compared to ΛCDM. However, standard ΛCDM subhalos, being almost completely disrupted by tidal effects (see Fig. 2.4), are a much more challenging target (as discussed in Sec. 2.4).

ΛCDM

The ΛCDM model is reproduced taking $\Delta^2_{MD}(k) = 0$ in (2.18), and the standard growth and transfer functions in (2.20). Specifically, we use the BBKS transfer function [127],

$$T(x \equiv k/k_{eq}) = \frac{12x^2}{5}\frac{\ln(1+0.171x)}{0.171x}\Big[1+0.284x+(1.18x)^2+(0.399x)^3+(0.490x)^4\Big]^{-1/4}, \tag{2.36}$$

and a linear growth function,

$$D(z) = g(\Omega_m, \Omega_\Lambda)\frac{1+z_{eq}}{1+z}. \tag{2.37}$$

Here $a_{eq} \simeq 3\times10^{-4}$ is the scale factor at matter radiation equality, $k_{eq} \simeq 0.01\,\text{Mpc}^{-1}$ the largest scale that enters the horizon before equality, and we use the approximated

growth factor given in [128]:

$$g(\Omega_m, \Omega_\Lambda) \approx \frac{5\,\Omega_m}{2\left[\Omega_m^{4/7} - \Omega_\Lambda + (1 - \Omega_m/2)(1 + \Omega_\Lambda/70)\right]}, \tag{2.38}$$

where Ω_m and Ω_Λ are the matter and vacuum energy densities, normalized to the critical density, ρ_c, respectively.

The sHMF for standard CDM halos has been computed in the mass range $(10^{-5} - 10^{12})M_\odot$ [119] but little is known for lighter subhalos. Because of this, we compute the sHMF at infall by using Eq. (2.30). As expected, the result is compatible with the numerical simulations, and the sHMF at infall is well fitted by

$$\frac{d\tilde{n}}{d\log M_{acc}} = \mathcal{N}(M_{max}, M_{min})\left(\frac{M_{acc}}{M_0}\right)^{\alpha} \Theta(M_{max} - M_{acc})\Theta(M_{acc} - M_{min}), \tag{2.39}$$

with a slope of $\alpha = -0.95$, truncated at the DM free streaming scale, M_{min}, and a host mass $M_{max} \approx 10^{12} M_\odot$. The normalization constant

$$\mathcal{N}(M_{max}, M_{min}) = \frac{\rho_{\rm DM}}{1+\alpha}\left(M_{max}^{1+\alpha} - M_{min}^{1+\alpha}\right) \tag{2.40}$$

is derived by requiring that, before tidal disruption takes place, DM subhalos account for all the local DM energy density. The final sHMF, including tidal effects, is derived following the prescription described in the previous section; the results of this procedure are shown in the left panels of Fig. 2.6.

We then use the MC to simulate the PTA signal that this population of DM subhalos would induce in a PTA. The statistical significance of this signal is shown in the right panel of Fig. 2.6 for different values of the observation time and number of pulsars in the array, while the timing residual noise and cadence have been fixed to $t_{rms} = 10\,$ns and $\Delta t = 1$ week. Despite the optimistic PTA parameters, the strong impact of tidal effects, which almost completely erase the local population of ΛCDM subhalos, makes the model impossible to test in present and future PTA experiments.

Axions with PQ Symmetry Breaking After Inflation

If the PQ symmetry breaks after inflation ($f_a \lesssim H_I$), the Universe is populated by casually disconnected patches each containing different values of the axion field. These patches are separated by a network of strings and domain walls which evolve through axion radiation until the QCD phase transition. At this point the PQ symmetry is explicitly broken, the network of topological defects decays, and the

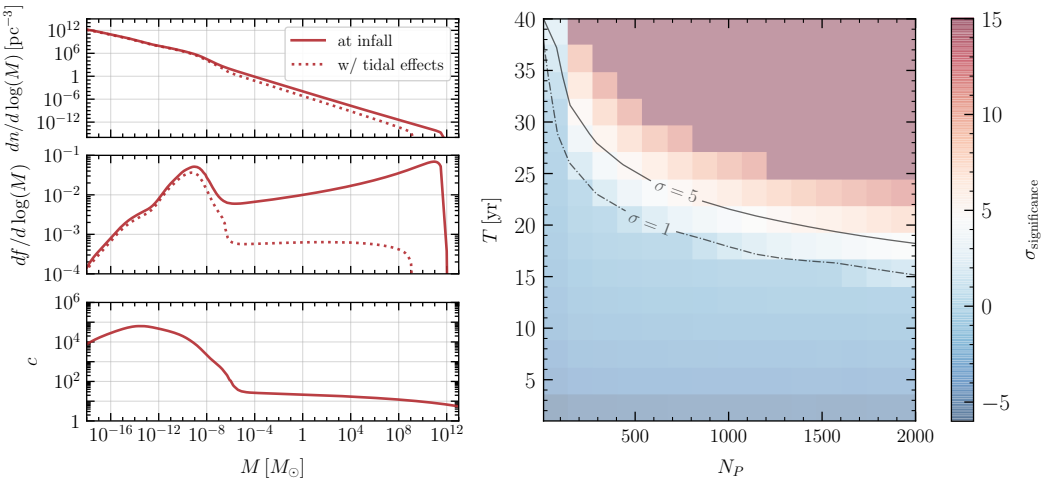

Figure 2.7: **Left:** sHMF (top panel), and mass fraction per logaritmich interval (center panel) before (solid) and after (dashed) the inclusion of tidal effects. The lower panel shows the typical subhalo concentration parameter as a function of their mass. **Right:** Discovery significance for different values of the observation time and number of pulsars in the array. The residual timing noise and observation cadence have being fixed to $t_{rms} = 10\,\mathrm{ns}$ and $\Delta t = 1\,week$. The dashed (solid) line shows the 1σ (5σ) significance contour.

axion starts to oscillate around its minimum. From this point on the axion behaves as CDM and perturbations in the density field evolve as those of a collisionless fluid.

The evolution of the PQ field down to the QCD phase transition has been studied numerically in [129, 130]. These simulations need to resolve string cores and contain a few Hubble patches at the same time. These two scales are respectively fixed by the mass of the radial mode, $m_r \approx f_a$, and $1/H \approx M_{Pl}/T^2$. At the QCD phase transition the scale separation is $\log(M_{Pl} f_a/\Lambda^2_{QCD}) \approx 70$, which makes numerical progress to evolve from the PQ to QCD phase transition nearly impossible. Luckily strings are expected to enter a scaling regime, during which their length per Hubble patch remains constant, soon after the PQ phase transition. Therefore simulations can be stopped for reasonable values of $\log(m_r/H)$ and extrapolated to the QCD era. However, the authors of [131] recently pointed out that large logarithmic corrections to this scaling regime are present, the extrapolation of which suggests that axions from strings may dominate the axion relic density contrary to what is assumed in [129, 130]. This would not only change the predicted axion mass but also the spectrum of its primordial perturbations. In the following we will set constraints

assuming that the axion relic density is dominated by the misalignment contribution, with the possibility of updating the results in case the conclusion of reference [131] is confirmed.

Given this assumption we use the primordial spectrum for the axion field derived in [129]. Since isocurvature perturbations are expected to experience a very small logarithmic growth during radiation domination, and linearly evolve afterwards, in (2.20) we take

$$T_{MD}(k) \approx 1 \qquad and \qquad D_{MD}(z) \simeq \left(1 + \frac{3}{2}\frac{1+z_{eq}}{1+z}\right), \tag{2.41}$$

while for the transfer and growth function of the scale invariant part of the spectrum ($T(k)$ and $D(z)$) we use the same conventions described in the previous subsection. The properties of the resulting local population of DM subhalos are shown in the left panels of Fig. 2.7.

As before we use the MC to simulate the local population of DM subhalos and derive the induced PTA signal with the methods discussed in Sec. 2.2, and the results are shown in the right panel of Fig. 2.7. For SKA parameters the detection of axion MC appears to be challenging, but more futuristic PTA experiments should be able to test this model.

Similarly to the axion case, models featuring a cosmological phase transition in the early Universe can boost the DM power spectrum on small scales [132] and be tested by PTAs. Interestingly, if the phase transition happens at low enough temperatures ($T \lesssim 1$ GeV), these models are also expected to generate a background of gravitational waves which could be searched for in PTAs (see for example [133]). We leave to future works a detailed study of these scenarios.

Early matter domination

Models with an early stage of matter domination (MD) are another class of models potentially testable by PTAs. Here, after the end of inflation, the Universe's energy density is dominated by a non-relativistic spectator field. Sub-horizon perturbations of this field then grow linearly with the scale factor during this early stage of MD. When the spectator field decays and reheats the Universe, these density fluctuations are inherited by the DM density field. This primordial growth of matter perturbations can be parametrized in terms of a modified matter transfer function, $T_{\rm MD}$. Following

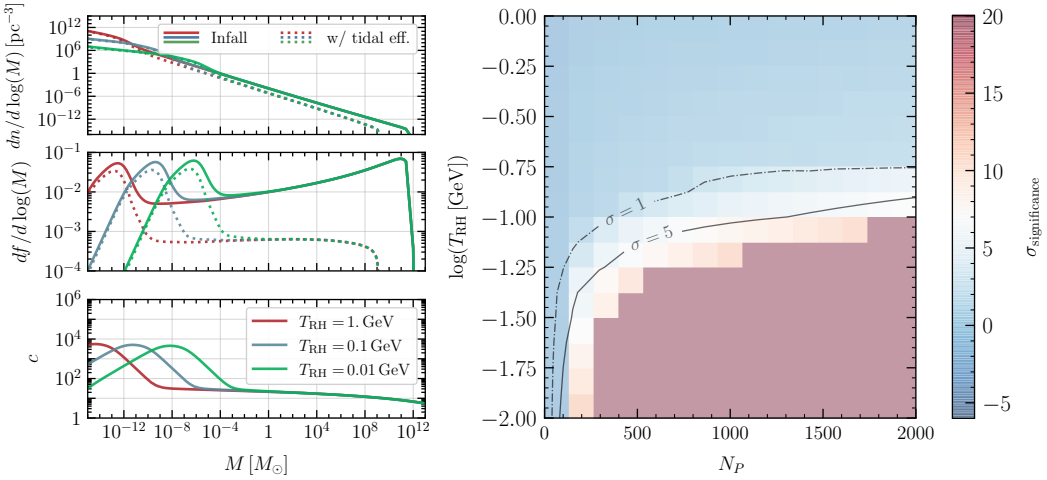

Figure 2.8: **Left:** sHMF (top panel), and mass fraction per logarithmic mass interval (center panel) before (solid) and after (dashed) the inclusion of tidal effects. The lower panel shows the typical subhalo concentration parameter as a function of subhalo mass. All curves are shown for three values of the reheating temperature, $T_{\rm RH} = 10\,\text{MeV}, 100\,\text{MeV}, 1\,\text{GeV}$. **Right:** Discovery significance for different values of the reheating temperature and number of pulsars in the PTA. The residual timing noise, observation cadence, and observation time are $10\,\text{ns}$, $1\,week$, and $30\,yr$, respectively. The dashed (solid) line shows the 1σ (5σ) significance contour.

[96], we include a period of early MD by modifying the transfer function,

$$T_{\rm MD}(k) = R(k)T(k)\exp\left(-\frac{k^2}{2k_{fs}^2}\right), \tag{2.42}$$

where $T(k)$ is the standard BBKS transfer function, $R(k)$ encodes the modifications induced by the early matter domination era, and the exponential is given by the free streaming scale, induced by the finite velocity of the DM when it is produced from the decay of the spectator field. Large scales are not affected by the early matter domination so $R(k < 0.05\ k_{RH}) = 1$, where k_{RH} is the wave number of the mode that enters the horizon at reheating,

$$\frac{k_{RH}}{k_{eq}} = 1.72\times10^{11}\left(\frac{T_{RH}}{100\,\text{GeV}}\right)\left(\frac{g_*}{100}\right)^{1/6}, \tag{2.43}$$

with $k_{eq} \simeq 0.01\,\text{Mpc}^{-1}$ the largest scale that enters the horizon before matter-radiation equality, T_{RH} the temperature at which the spectator field decays (*i.e.* the reheating temperature), and g_* the number of relativistic species at the time of

reheating. On small scales, $k > 0.05\ k_{RH}$, early matter domination enhances the growth of perturbations such that [96],

$$R(k > 0.05\ k_{RH}) = \frac{A(k/k_{RH}) \ln\left[\left(\frac{4}{e^3}\right)^{f_2/f_1} \frac{B(k/k_{RH}) a_{eq}}{a_{hor}(k)}\right]}{9.11 \ln\left[\left(\frac{4}{e^3}\right)^{f_2/f_1} 0.594 \frac{\sqrt{2}k}{k_{eq}}\right]}, \tag{2.44}$$

with $a_{hor}(k)$ the scale factor at reheating and horizon crossing, and f_1 and f_2 related to the baryon fraction $f_b \equiv \rho_b/(\rho_b + \rho_{\rm DM})$ by

$$f_1 = 1 - 0.568 f_b + 0.094 f_b^2 \qquad f_2 = 1 - 1.156 f_b + 0.149 f_b^2 - 0.074 f_b^3 \,. \tag{2.45}$$

On small scales, the functions $A(x)$ and $B(x)$ are fit according to

$$\begin{aligned} A(x) &= \exp\left[\frac{0.609}{\left(1 + 2.15(\log x - 1.52)^2\right)^{1.38}}\right]\left[9.11\,\mathcal{S}(5.02 - x) + \frac{3}{5}x^2\mathcal{S}(x - 5.02)\right] \\ B(x) &= \exp\left[\log(0.594)\mathcal{S}(5.02 - x) + \mathcal{S}(x - 0.52)\log\left(\frac{e}{x^2}\right)\right] , \end{aligned} \tag{2.46}$$

where $\mathcal{S}(y) = [\tanh(y/2) + 1]/2$. Finally, ignoring DM interactions, the free-streaming scale, k_{fs}, appearing in (2.42) is approximately given by

$$\frac{k_{RH}}{k_{fs}} \approx \frac{\langle v_{RH}\rangle}{0.06} \tag{2.47}$$

where v_{RH} is the DM velocity at reheating. In deriving our results we have assumed that $\langle v_{RH}\rangle = 10^{-3}$. For smaller values of $\langle v_{\rm RH}\rangle$ the results shown in Fig. 2.8 remain almost unchanged. However if the DM is produced with $\langle v_{\rm RH}\rangle \gtrsim 0.06$ then $k_{\rm RH} \gtrsim k_{\rm fs}$ and free streaming erases the small scale perturbations of the scalar field entirely. In this case PTAs will not be able to set constraints.

The properties of the subhalo population resulting from this modified transfer function are shown in the left panels of Fig. 2.8. While the significance of the predicted signal is reported on the right panel of the same figure. We see that, assuming optimistic PTA parameters, the model can be tested for $T_{RH} \lesssim 1\,\text{GeV}$. For higher reheating temperatures typical subhalo masses become too small to induce a large enough signal and sensitivity is lost.

Vector DM

As shown in [98], massive vector bosons can be produced by quantum fluctuations during inflation. The relic abundance of particles produced in this way is given by

$$\Omega \simeq \Omega_{\rm DM}\sqrt{\frac{m}{6\times 10^{-6}\,\text{eV}}}\left(\frac{H_I}{10^{14}\,\text{GeV}}\right)^2 , \tag{2.48}$$

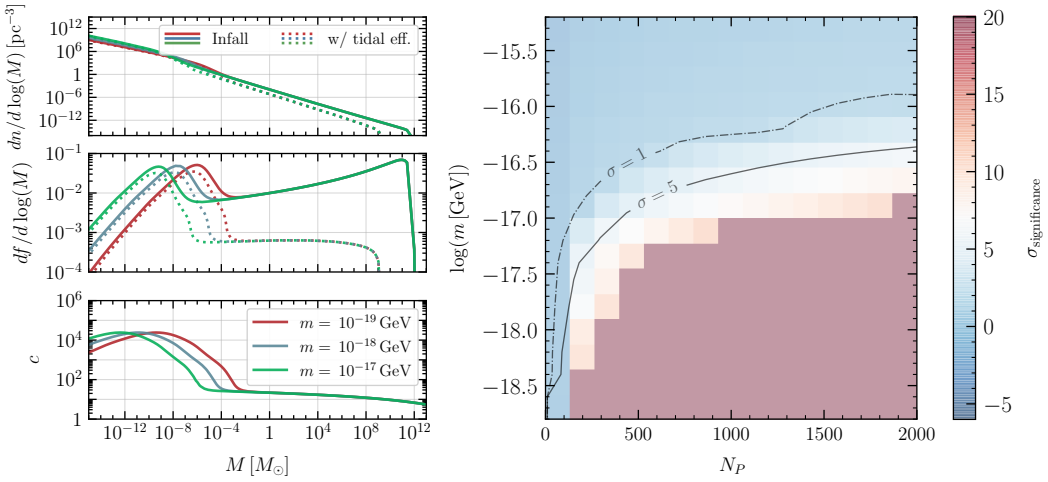

Figure 2.9: **Left:** sHMF (top panel), and mass fraction per logarithmic mass interval (center panel) before (solid) and after (dashed) the inclusion of tidal effects. The lower panel shows the typical subhalo concentration parameter as a function of their mass. All curves are shown for three values of the DM mass, $m = 10^{-17}, 10^{-18}, 10^{-19}\,\mathrm{GeV}$. **Right:** Discovery significance for different values of the DM mass and number of pulsars in the array. The inflationary scale, H_I, has been fixed in order to reproduce the DM relic density according to (2.48). The residual timing noise, observation cadence, and observation time have being fixed to $t_{rms} = 10\,\mathrm{ns}$, $\Delta t = 1\,week$, and $T = 30\,yr$. The dashed (solid) line shows the 1σ (5σ) significance contour.

where $\Omega_{\mathrm{DM}} \simeq 0.265$ is the observed DM relic density, m is the mass of the boson, and H_I is the Hubble rate during inflation. In addition to the adiabatic and scale invariant fluctuations inherited from perturbations in the inflaton field, the inflationary production generates isocurvature fluctuations on small scales. Specifically, the primordial power spectrum of the field amplitude is [98]

$$\Delta_A^2(k) = \left(\frac{kH_I}{2\pi m}\right)^2 . \tag{2.49}$$

Notice that this is not the power spectrum for DM density perturbations; we will discuss shortly how the two are related. At late times the small-scale power spectrum for the field amplitude has the usual relation

$$\Delta_A^2(k, z < z_{\mathrm{eq.}}) = T_A^2(k) D^2(z) \Delta_A^2(k), \tag{2.50}$$

where $D(z)$ is the standard growth function, while the transfer function is

$$\tilde{T}_A(k) = \sqrt{\frac{k_*}{m\, a_{eq}}} \times \begin{cases} 1 & for\ k < k_* \\ \left(\frac{k_*}{k}\right)^{3/2} & for\ k > k_* \end{cases}, \tag{2.51}$$

and $k_* = a_{eq}\sqrt{H_{eq} m}$, with $a_{eq} = 3 \times 10^{-4}$ and $H_{eq} \simeq 10^{-29}\,\text{eV}$ the value of the scale factor and Hubble rate at equality. Finally, the small-scale power spectrum for density perturbations is given by [98]:

$$\Delta^2_{MD}(k,z) = \frac{k^2}{4\langle A^2\rangle^2} \int_{|q-k|<p<q+k} \frac{(k^2-q^2-p^2)^2}{q^4 p^4} \Delta^2_A(p,z)\Delta^2_A(q,z)\, dpdq \tag{2.52}$$

where $\langle A^2\rangle = \int d\ln k\, \Delta^2_A(k,z)$.

In Fig. 2.9 we show the properties of the subhalo population predicted by this model (left panel), and the significance of the signal that it would produce (right panel). We see that future PTA experiments will have a good sensitivity for DM masses below $10^{-16}\,\text{GeV}$.

2.5 Conclusions

We have studied the detectability in Pulsar Timing Arrays of a variety of well motivated DM models of substructure including: standard ΛCDM, axion models where the PQ symmetry breaks after inflation, early matter domination, and vector DM. Given the low concentration, ΛCDM subhalos are particularly susceptible to tidal effects which drastically reduces their local abundance. As a result, we found that ΛCDM will not be testable by present or (near-)future PTAs. The other models, which feature subhalos with much larger concentration parameters, and hence much lower tidal disruption, are better candidates for detection. Specifically, we found that models featuring an early stage of matter domination ending at temperatures lower than 1 GeV will be testable by PTAs with SKA-like capabilities. Similarly, vector DM candidates produced during inflation with a mass smaller than $10^{-16}\,\text{GeV}$ are within the reach of PTAs with SKA-like parameters. Finally, axions whose PQ symmetry breaks after inflation (if the production is dominated by misalignment) are out of reach for an SKA-like experiment, but could be probe by a slightly more optimistic set of experimental parameters.

To generate the signals we have developed a Python Monte Carlo tool that, given the subhalo mass function, DM velocity distribution, and concentration parameters,

generates a population of subhalos and computes the acceleration of the Earth, or pulsar, induced, and the resulting shift on the phase of the pulse time-of-arrival. We make the code publicly available on GitHub .

In future works we plan to improve the present analysis in two ways. First, by performing dedicated N-body simulations to more precisely describe the impact of tidal effects on high-density subhalos. Second, by performing a more realistic treatment of the background noise through the NANOGrav software Enterprise [110].

Chapter 3

PIPELINE FOR DARK MATTER SUBSTRUCTURE SEARCHES WITH REALISTIC PULSAR TIMING DATA

This chapter is based on

[1] Vincent S. H. Lee, Stephen R. Taylor, Tanner Trickle, and Kathryn M. Zurek. "Bayesian Forecasts for Dark Matter Substructure Searches with Mock Pulsar Timing Data". In: *JCAP* 08 (2021), p. 025. DOI: 10.1088/1475-7516/2021/08/025. arXiv: 2104.05717 [astro-ph.CO].

3.1 Introduction

Dark matter, despite being one of the most important components of standard cosmology, is not well-constrained on sub-galactic scales. The lack of observational constraints is problematic because many well-motivated models of dark matter predict unique structures on these small scales. For example, the Lambda Cold Dark Matter (ΛCDM) model with inflation produces a nearly scale invariant spectrum of adiabatic perturbations [64, 134] down to the free streaming scale corresponding to about $10^{-6}\,M_\odot$ for Weakly Interacting Massive Particle (WIMP) dark matter [135]. The QCD axion, if the Peccei-Quinn (PQ) symmetry [136] breaks after inflation, induces large isocurvature fluctuations on scales smaller than the QCD epoch horizon [94, 95, 132, 130, 137, 118, 138]. Primordial black holes (PBHs) are generically formed by increasing the power of density fluctuations on small scales [139] which then collapse.

To date, general substructure constraints only extend down to mass scales $\sim 10\,M_\odot$, coming predominantly from gravitational microlensing of stars in the Large Magellanic Cloud and Andromeda [140, 141, 142, 143] as well as stars in the local neighborhood [144, 145, 99]. Constraints on PBHs extend further down in mass due to their exceptionally high density. Non-evaporation from Hawking radiation requires $M \gtrsim 10^{-16}\,M_\odot$ [146], and microlensing currently constrains PBHs to be a subcomponent of dark matter for $M \gtrsim 10^{-10}\,M_\odot$ [147, 148, 149, 141].

It has been shown that pulsar timing arrays (PTAs) are potentially a powerful tool to search for dark matter substructure [44, 150, 103, 151, 104, 105, 43, 152, 42, 9] via *Doppler* and *Shapiro* effects. The Doppler effect is the change of observed pulsar

frequency due to the acceleration of the pulsar as it is pulled by passing substructures gravitationally, while the Shapiro effect is a gravitational redshift effect due to the metric perturbations on the photon geodesic along the line of sight [44]. The signals can be further classified as *static* (*dynamic*) if the characteristic time scale of transiting dark matter, τ, is much smaller (larger) than the pulsar observation time, T. A dynamic signal will be observed as a blip in the pulsar phase time series, whereas a static signal is observed as a long time scale perturbation. Generally static (dynamic) signals originate from heavier (lighter) dark matter, due to the smaller (larger) number density.

In this paper, we develop techniques to detect signals from dark matter substructure that can be applied to real PTA data. Our purpose is to bridge the gap between the theoretically exhaustive analyses of Refs. [43, 42, 9] and an application to real PTA data. We will focus our attention on monochromatic PBH dark matter since it is the simplest to study. As noted previously [43, 42, 9], PTAs are sensitive to much less compact subhalos (such as axion miniclusters) than other lensing searches. To perform our analysis we use the software `enterprise` [153] developed by the North American Nanohertz Observatory for Gravitational Waves (NANOGrav) [154]. `enterprise` utilizes a Bayesian inference framework to study how compatible pulsar phase models are with the measured data and noise sources. Since we are concerned not only with current PTAs but also future PTAs, such as the Square Kilometer Array (SKA) [155], we use realistic mock data which allows us to change certain PTA parameters, such as the number of pulsars or the observation time. Generally we find quite good agreement with the frequentist, signal-to-noise ratio (SNR) analysis performed previously in Refs. [43, 42, 9] with the exception of PBHs with masses 10^{-4}–$10^{-2}\ M_\odot$ for the Shapiro search where the present constraint is closer to an order of magnitude weaker than the previous predicted constraints, mostly due to an approximation of the signal in the static regime necessary for carrying out the Bayesian analysis.[1] Note that we restrict our work to the case of PBH dark matter, though, utilizing previous work [43, 42, 9], our conclusions can be generalized to more diffuse substructures such as axion miniclusters.

To search for a dark matter signal with `enterprise`, a simple, parametrized form of

[1] We leave for future work how to better approximate the Shapiro signal outside of the static regime. Note that the Shapiro dynamic signal rapidly becomes weak even for moderately lower halo concentration relative to a PBH [42], making the Shapiro dynamic search of limited utility for a broad range of dark matter models.

the phase shift must be known. This precludes carrying out a fully general analysis, across static and dynamic signals which have dramatically different time series as discussed in Refs. [43, 42, 9]. We must break the analysis up into different regimes where a simple polynomial form of the signal dominates; we will nevertheless find that the three separate analyses we carry out with `enterprise` agree well across more than ten orders of magnitude in PBH mass with the frequentist approach carried out in Refs. [43, 42, 9].

In particular, we parametrize the dark matter induced phase shift using an amplitude and at most one shape parameter. Schematically the detection pipeline consists of the following steps:

i) Search for the dark matter amplitude inside the PTA data.

ii) Compute the theoretical prediction of the dark matter amplitude.

iii) Compare the distributions of the amplitude from i) and ii) for consistency.

The PTA data in i) are analyzed with `enterprise` while the theoretical predictions in ii) are computed numerically using the Monte Carlo (MC) simulations developed in Ref. [9], which produces the probability distribution of the signal amplitudes.

Most importantly, we find that the leading order difference between the previous theoretical analyses and what can be realistically concluded with future PTA data will depend on how well a gravitational wave background (GWB) is separated and mitigated from a dark matter signal. Signals from GWBs are of primary interest for the PTA community. For instance, NANOGrav recently reported [156] strong evidence for a common-spectrum low-frequency stochastic process that is consistent with the characteristic strain spectrum from supermassive black hole binaries (SMBHBs [157, 158]). If handled naively over the entire frequency range of the data, and with no spatial correlation information included, we find that it will swamp a dark matter signal. While beyond the scope of this work, separating today's signals (such as the GWB) from signals of future interest (such as dark matter) will be crucial for the future science program of PTAs. The present work strongly motivates a focus on this type of background mitigation.

The outline of the paper is as follows. In Sec. 3.2 we describe the form of the PTA signal injected by dark matter substructure, paying close attention to describing

the needed approximations. In Sec. 3.3 we perform the Bayesian analysis with `enterprise` to derive the posterior distribution of dark matter amplitude in PTA data, and detail how to detect, or constrain, dark matter with this data. In Sec. 3.4 we apply these detection techniques to mock data and compare the constraints with our previous sensitivity projections in [9] and [42]. Finally, in Sec. 9.5 we conclude.

3.2 Dark Matter Signals

Pulsars are excellent tools for studying astrophysical phenomena because they are exceptionally stable clocks [159]. Although the pulsar periods can fluctuate on shorter time scales, these fluctuations do not accumulate [160]. The intrinsic pulsar phase, $\phi(t)$, can then be modelled, to leading orders, by

$$\phi(t) = \phi_0 + \nu t + \frac{1}{2}\dot{\nu}t^2\,, \tag{3.1}$$

where ϕ_0 is the phase offset, ν is the pulsar frequency and $\dot{\nu}$ is its first derivative. This is called the *timing model* of the pulsar. Since the second derivative of the pulsar frequency is small (typically $\ddot{\nu}/\nu \lesssim 10^{-31}\ Hz^2$ [161]), terms of order $\mathcal{O}(t^3)$ or higher are not included in the model. Any process that produces terms that are not in Eq. (5.37) (e.g. a term $\propto t^3$) can be observed or constrained. In this section we focus on parametrizing additions to the pulsar phase due to a single dark matter subhalo.

The phase modification, $\delta\phi(t)$, induced by a dark matter subhalo can be written as

$$\delta\phi(t) = \int_0^t \delta\nu(t')dt'\,, \tag{3.2}$$

where $\delta\nu$ is the induced frequency shift. The frequency shift due to Doppler and Shapiro effects were studied in Ref. [43], and are given by

$$\left(\frac{\delta\nu}{\nu}\right)_D = \hat{\mathbf{d}}\cdot\int \nabla\Phi(\mathbf{r}, M)dt \tag{3.3}$$

$$\left(\frac{\delta\nu}{\nu}\right)_S = -2\int \mathbf{v}\cdot\nabla\Phi(\mathbf{r}, M)dz\,, \tag{3.4}$$

where $\hat{\mathbf{d}}$ is the unit vector pointing from Earth to the pulsar, Φ is the dark matter gravitational potential, M and $\mathbf{v}$ are the mass and the velocity of the dark matter, respectively, and z parameterizes the path that the photon travels from the pulsar to Earth. To further simplify these expressions, we write the position of the dark matter

as $\mathbf{r}(t) = \mathbf{r}_0 + \mathbf{v}t$ where $\mathbf{r}_0$ is the initial position.[2] For the Shapiro signal, it is useful to define $\mathbf{r}_\times \equiv \mathbf{r}_0 \times \hat{\mathbf{d}}$ and $\mathbf{v}_\times \equiv \mathbf{v} \times \hat{\mathbf{d}}$. Then the time for the dark matter to reach its point of closest approach is given by $t_{D,0} \equiv -\mathbf{r}_0 \cdot \mathbf{v}/v^2$ and $t_{S,0} \equiv -\mathbf{r}_\times \cdot \mathbf{v}_\times/v_\times^2$, while the width of the signal is given by $\tau_D \equiv |\mathbf{r}_0 \times \mathbf{v}|/v^2$ and $\tau_S \equiv |\mathbf{r}_\times \times \mathbf{v}_\times|/v_\times^2$. The impact parameter is $\mathbf{b}_D \equiv \mathbf{r}_0 + \mathbf{v}t_{D,0}$ and $\mathbf{b}_S \equiv \hat{\mathbf{d}} \times (\mathbf{r}_\times + \mathbf{v}_\times t_{S,0})$. The explicit expressions for $\delta\phi(t)$ in the PBH limit, the main focus of this work, have been previously derived in Refs. [43, 9], and are given by

$$\delta\phi_D(t) = \frac{GM\nu}{v^2}\hat{\mathbf{d}} \cdot \left(\sqrt{1+x_D^2}\hat{\mathbf{b}}_D - \sinh^{-1}(x)\hat{\mathbf{v}}\right) \tag{3.5}$$

$$\delta\phi_S(t) = 2GM\nu \log(1+x_S^2)\,, \tag{3.6}$$

where we define $x_D \equiv (t - t_{D,0})/\tau_D$ and $x_S \equiv (t - t_{S,0})/\tau_S$ as normalized time variables. We have also dropped all terms in Eq. (3.5) and Eq. (3.6) that are independent, linear or quadratic in time t since they are completely degenerate with the timing model in Eq. (5.37), and hence unobservable.

Static and Dynamic Signals

`enterprise` primarily uses a Markov Chain Monte Carlo (MCMC) to search over the parameter space in a signal model, which here is the dark matter signal. However such methods can become overwhelmed with too many variables, enhancing the search space dimensions, or variables degenerate in their effects, e.g. two variables describing the amplitude of a signal. This makes the expressions in Eq. (3.5) and Eq. (3.6) too cumbersome, and to facilitate the analysis, expressions of $\delta\phi(t)$ with fewer parameters are necessary. As discussed in Sec. 10.1, the signals can be further classified into static ($\tau \gg T$) and dynamic ($\tau \ll T$) signals. If the mass of the dark matter is large, the number density $n = \rho_{\rm dm}/M$ will be smaller, leading to a larger impact parameter. This translates to a large signal width since $\tau = b/v$. On the other hand, if the dark matter mass is small, the signal width τ will be small (precise definitions of 'large' and 'small' can be found in the discussion of the different length scales in Ref. [42]).

We start by discussing the Doppler effect. In the static limit, we can expand Eq. (3.5) in a power series of τ/T. Since all terms up to $O(t^2)$ are degenerate with the timing

[2] We assume the dark matter subhalo travels in a straight line; a valid approximation when the orbital eccentricity $e \gg 1$. This requires $b \gg G(M+M_P)/v^2$ [162] where M_P is the pulsar mass. Since $M_P \approx 1\,M_\odot$ [163], the impact parameter must satisfy $b \gg 10^{-8}\ pc$, for $M \lesssim 1\,M_\odot$, which is indeed the case for the mass range considered in this work.

model, we can effectively parametrize the measurable signal as

$$\frac{\delta\phi_{D,\,\mathrm{stat}}(t)}{\nu} = \frac{A_{D,\,\mathrm{stat}}}{yr^2}t^3\,, \tag{3.7}$$

where $A_{D,\,\mathrm{stat}}$ is a dimensionless parameter that characterizes the amplitude of the Doppler static signal and is given by

$$A_{D,\,\mathrm{stat}} = yr^2\frac{GM}{2v^2}\hat{\mathbf{d}}\cdot\left[\frac{t_{D,0}}{\tau_D^4}\frac{1}{(1+t_{D,0}^2/\tau_D^2)^{5/2}}\hat{\mathbf{b}}_D + \frac{1}{3\tau_D^3}\frac{1-2t_{D,0}^2/\tau_D^2}{(1+t_{D,0}^2/\tau_D^2)^{5/2}}\hat{\mathbf{v}}\right]. \tag{3.8}$$

We see that the static signal can be described by using only one parameter (i.e. $A_{D,\,\mathrm{stat}}$). In the dynamic limit, by observing that $\sqrt{1+x_D^2} \propto |t-t_{D,0}|$ when $\tau_D \ll T$, it is clear that up to a linear term in x_D, the phase shift is parametrized by

$$\frac{\delta\phi_{D,\,\mathrm{dyn}}(t)}{\nu} = A_{D,\,\mathrm{dyn}}(t-t_{D,0})\Theta(t-t_{D,0})\,, \tag{3.9}$$

where Θ is the Heaviside step function and $A_{D,\,\mathrm{dyn}}$ characterizes the amplitude of the Doppler dynamic signal, which is given by[3]

$$A_{D,\,\mathrm{dyn}} = \frac{2GM}{v^2\tau_D}\hat{\mathbf{d}}\cdot\hat{\mathbf{b}}_D. \tag{3.10}$$

We see that in contrast to the static signal, we need two different parameters ($A_{D,\,\mathrm{dyn}}$ and $t_{D,0}$) to fully describe the dynamic signal.

We now turn our attention to the Shapiro effect. In a completely analogous way to the Doppler effect, we can parametrize the static Shapiro signal by a term $\propto t^3$

$$\frac{\delta\phi_{S,\,\mathrm{stat}}(t)}{\nu} = \frac{A_{S,\,\mathrm{stat}}}{yr^2}t^3\,, \tag{3.11}$$

where $A_{S,\,\mathrm{stat}}$ is the amplitude of the signal given by

$$A_{S,\,\mathrm{stat}} = -\,yr^2\frac{4GM}{3}\frac{t_{S,0}}{\tau_S^4}\frac{3-t_{S,0}^2/\tau_S^2}{1+t_{S,0}^2/\tau_S^2}\,. \tag{3.12}$$

Parametrizing the Shapiro signal in the dynamic limit is tricky, since Eq. (3.6) does not reduce to any simple expressions when $\tau_S \ll T$. On the other hand, in Refs. [42, 9], another type of signal known as the *stochastic* signal is also considered. In the limit of extremely light substructure mass, a large number of events could collectively

[3]For simplicity, only the term $\propto \hat{\mathbf{b}}$ in Eq. (3.5) is kept since it dominates over the term $\propto \hat{\mathbf{v}}$ in the dynamic limit.

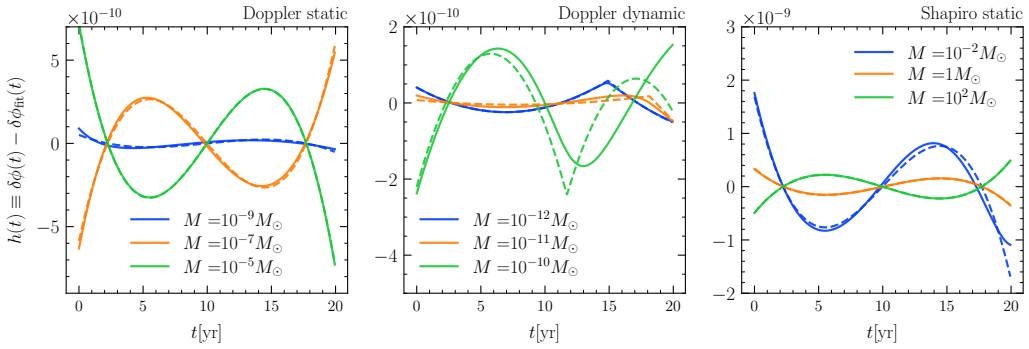

Figure 3.1: Comparison between the numerical and analytic subtracted timing residuals $h(t)$. The solid lines are generated from the MC with a single PBH using Eqs. (3.5)-(3.6) while the dashed lines are computed using the analytic formulas in Eqs. (5.42), (3.9) and (3.11). Both sets of signals are subtracted, meaning that the timing residual $\delta\phi(t)$ is first fitted to a second order polynomial in time. The fitted signal, $\delta\phi_{\rm fit}(t)$, is then subtracted from $\delta\phi(t)$.

generate sizable signals. Moreover, the stochastic signal induces angular correlations between pulsars for the Earth term (similar to the GWB), which enhances the signal-to-noise ratio. However, parametrizing the stochastic signal is challenging (both in real and frequency space), and the Earth term analysis requires the construction of the likelihood function with non-square covariance matrices, which is computationally demanding. In light of these challenges, we do not search for these signals in this work and leave the analyses for future work.

In Fig. 3.1 we show some characteristic signal shapes of the timing residuals generated from the MC[4] after numerically fitting away all terms of order $O(t^2)$ or less in the time series. For the static searches, we observe that the subtracted signals closely resemble a cubic polynomial in t, which justifies the t^3 parametrization that we have taken. For the Doppler dynamic case, the timing residuals have a rather abrupt turn at $t = t_{D,0}$, which matches with our prediction of the signal behaving like a step function in this limit. As shown in the figure, we find good agreement between the numerical results and the analytic approximations.

The important physical parameters are the dark matter mass, M, and mass fraction, $f_{\rm dm} \equiv \Omega/\Omega_{\rm dm}$, where $\Omega_{\rm dm} \equiv \rho_{\rm dm}/\rho_{\rm crit}$ is the local dark matter density parameter and $\Omega \equiv \rho/\rho_{\rm crit}$ is the local density parameter of the dark matter of interest (PBHs

[4]Not to be confused with the MCMC introduced earlier in this subsection, which is a sampling scheme used to explore the parameter space and compute the posterior distribution.

in this work). The relations between these parameters and the signal amplitudes A are obtained using MC simulations described in Ref. [9]. While the MC simulations can generate signals from general dark matter subhalos, we focus on the PBH case here. We first randomly distribute PBHs with mass M, density $\rho_{\rm dm} f_{\rm dm}$ ($\rho_{\rm dm} = 0.46\,{\rm GeV/cm^3}$ [164]), and a Maxwell-Boltzmann velocity distribution with $v_0 = 325\,{\rm km/s}$, $v_{\rm esc} = 600\,{\rm km/s}$ and isotropic angular dependence.[5] The simulation volume is taken to be a sphere for the Doppler search and a cylinder with height d for the Shapiro search, where d is the distance between the pulsar and Earth. The center of the simulation volume is taken to be the position of the pulsar. The PBHs are then classified as dynamic if they satisfy $T - \tau > t_0 > \tau$ and static otherwise [43]. This condition ensures that the pulsar phase shift behaves approximately like Eq. (3.9) for the dynamic PBHs. To compute $A_{\rm stat}$, we first evaluate the total pulsar phase shift (as a function of time) due to all the static PBHs using Eq. (3.5) and Eq. (3.6) for the Doppler and the Shapiro case respectively. Then we fit the phase shift to a cubic polynomial in time to extract the coefficient of the t^3 term, which gives us $A_{D,\,\rm stat}$ and $A_{S,\,\rm stat}$ in accordance with Eq. (5.42) and Eq. (3.11). To compute $A_{D,\,\rm dyn}$, we use Eq. (3.9) for the dynamic PBH that has the smallest τ_D. Finally, we repeat the simulation for numerous realizations to obtain the conditional probability distributions $P(A_{D,\,\rm stat}|f_{\rm dm})$, $P(A_{D,\,\rm dyn}|f_{\rm dm})$ and $P(A_{S,\,\rm stat}|f_{\rm dm})$ for each choice of M.[6]

3.3 Bayesian Analysis of Dark Matter Signals in PTAs

We now develop the Bayesian framework for detecting dark matter subhalos with PTAs. For clarity, we will collectively refer the dark matter signal amplitudes for the different types of signals $A_{D,\,\rm stat}$, $A_{D,\,\rm dyn}$ and $A_{S,\,\rm stat}$ defined in Eq. (5.42), Eq. (3.9) and Eq. (3.11) as A.

[5] We have taken a dark matter velocity spread, v_0, higher than the often quoted value $v_0 \approx 230\,{\rm km/s}$. This is to eliminate the velocity anisotropy due to the relative motion between the pulsar and the galactic rest frame. Since we do not expect such anisotropy to be observable, we ignore this effect and boost the distribution with a larger v_0 value.

[6] We have suppressed the PBH mass M inside the conditional probability for notational convenience in later sections. A larger $f_{\rm dm}$ implies a larger signal amplitude A, so it is conceptually more natural to draw upper limits on $f_{\rm dm}$ for each choice of M instead of deriving the two dimensional posterior distribution for both parameters simultaneously.

Noise Modeling and Likelihood

Our modeling and analysis of PTA data closely follows Refs. [165, 166], and we refer the reader to those papers for a full discussion of the PTA data model. We summarize several of the salient features here. Let $N_{\rm TOA}$ be the number of pulsar times of arrival (TOAs). The timing residuals of a pulsar correspond to the raw TOA data with the best-fit timing model subtracted. By definition, any unmodeled phenomena or noise fluctuations should be encapsulated in the residuals, which we model as

$$\delta\mathbf{t} = M\epsilon + F\mathbf{a} + \delta\mathbf{t}_{\rm dm} + \mathbf{n}\,. \tag{3.13}$$

The matrix M is the timing model design matrix corresponding to partial derivatives of the TOAs with respect to timing model parameters, and the vector ϵ denote small linear parameter offsets. Together $M\epsilon$ represents the inaccuracies in the subtraction in the timing model.

The term $F\mathbf{a}$ represents a Fourier series of low-frequency ('red') timing deviations, where F is an $N_{\rm TOA}\times 2N_{\rm modes}$ matrix with alternating columns of sines and cosines in harmonics of the base frequency $1/T$, and $\mathbf{a}$ are the Fourier coefficients of each mode. Sources of pulsar intrinsic red noise include spin instability noise, secular pulse profile changes, and time-dependent dispersion measure variations [167, 168, 169] (although the latter has a known dependence on the observed radio frequency). Inter-pulsar correlated red noise may derive from Roemer-delay errors when barycentering the pulse TOAs (inducing dipolar correlations) [170], long-timescale drifts in clock standards (inducing monopolar correlations) [170], and a stochastic GWB that is generated from a population of sources such as SMBHBs (inducing quadrupolar-dominated Hellings & Downs correlations [112]) [*e.g.*, 158, and references therein]. We do not consider barycentering or clock errors here, nor do we leverage the Hellings & Downs correlations between pulsars for the GWB; for the sake of computational convenience, the GWB is modeled as an uncorrelated common-spectrum red process amongst all pulsars, as in the NANOGrav 12.5yr Dataset analysis [156].

Red noise of any source is modeled as a stationary Gaussian process with a power-law power spectral density of timing deviations:

$$P_{\rm red}(f) = \frac{A_{\rm red}^2}{12\pi^2}\left(\frac{f}{yr^{-1}}\right)^{-\gamma_{\rm red}} yr^3\,, \tag{3.14}$$

where $A_{\rm red}$ and $\gamma_{\rm red}$ are the red noise amplitude and the spectral index respectively. For a GWB produced by a population of SMBHBs evolving solely through GW emission, $\gamma = 13/3$ [171].

The term $\mathbf{n}$ denotes white noise that has equal power across all frequencies in the residual time series, and which is uncorrelated amongst pulsars. This noise is heteroscedastic with a per-TOA uncertainty dominated by the pulse template-fitting uncertainties. These uncertainties are then scaled. NANOGrav also computes many near-simultaneous sub-banded TOAs, producing white noise that is correlated across sub-bands, but uncorrelated in time. Once all of these effects are accounted for, the white noise covariance matrix has a block-diagonal structure in epoch blocks.

The term $\delta\mathbf{t}_{\rm dm}$ denotes a putative dark matter signal, which we model as a deterministic process. Grouping the timing model offsets and red noise together into the matrix-vector product $T\mathbf{b}_{\rm lat}$, we form model-dependent white noise residuals, $\mathbf{r}_{\rm res} = \delta\mathbf{t} - T\mathbf{b}_{\rm lat} - \delta\mathbf{t}_{\rm dm}$. The likelihood is then simply a Gaussian distribution in all the data with zero mean and a covariance matrix given by the modeled white-noise. However, we are typically not interested explicitly in the latent parameters $\mathbf{b}_{\rm lat}$, such that we analytically marginalize over these parameters with Gaussian priors described by the unbounded variance of the timing model offsets and the power spectral density (PSD) of the red noise. The resulting likelihood function is then

$$p(\delta\mathbf{t}|\eta,\theta) = \frac{\exp(-\frac{1}{2}(\delta\mathbf{t} - \delta\mathbf{t}_{\rm dm}(\theta))^T C(\eta)^{-1}(\delta\mathbf{t} - \delta\mathbf{t}_{\rm dm}(\theta)))}{\sqrt{\det(2\pi C(\eta))}}\,. \tag{3.15}$$

where η are hyper-parameters describing the spectral models of the intrinsic pulsar red noise and GWB; C is the model-dependent covariance matrix of white noise, red noise, and timing offsets; and θ are parameters of the dark matter signal. This likelihood is constructed using the `enterprise` [153] and `enterprise_extensions` [172] software packages, and the Bayesian posterior distributions of all parameters are sampled using MCMC techniques implemented with the `PTMCMCSampler` package [173]. To compute the posterior distribution of the dark matter amplitude, we numerically marginalize the MCMC chain over all parameters except this amplitude. For the Doppler dynamic search, the time of arrival t_0 is also marginalized over. In every case, we obtain the posterior distribution of the dark matter amplitude $P(A|\delta\mathbf{t})$.

Posterior Distribution of the Dark Matter Abundance

As stated in the previous section, the physical parameters that we are interested in are the dark matter mass M and mass fraction, $f_{\rm dm} \equiv \Omega/\Omega_{\rm dm}$. This subsection describes the translation from the posterior distribution on the amplitude A, $P(A|f_{\rm dm}, M)$ to a statement on the dark matter abundance.

Single Pulsar

We begin with the simple case of a single pulsar, and fix the dark matter subhalo mass M for the remainder of this subsection. Even for a fixed $f_{\rm dm}$, the amplitude A is a random variable since both $\mathbf{r}_0$ and $\mathbf{v}$ are random variables. The conditional probability $P(A|f_{\rm dm})$ can be computed using the MC simulation described in Sec. 3.2. The marginalized posterior distribution of $f_{\rm dm}$, given the measured data $\delta\mathbf{t}$, is

$$P(f_{\rm dm}|\delta\mathbf{t}) = \int_{-\infty}^{\infty} P(f_{\rm dm}|A)P(A|\delta\mathbf{t})dA\,. \tag{3.16}$$

Using Bayes' theorem, we can invert the conditional probability

$$P(f_{\rm dm}|A) = \frac{P(A|f_{\rm dm})P(f_{\rm dm})}{P(A)}\,, \tag{3.17}$$

and assuming uniform priors on both $f_{\rm dm}$ and A, we can write

$$P(f_{\rm dm}|A) \propto P(A|f_{\rm dm})\,. \tag{3.18}$$

Substituting Eq. (3.18) into Eq. (3.16) gives

$$P(f_{\rm dm}|\delta\mathbf{t}) \propto \int_{-\infty}^{\infty} P(A|f_{\rm dm})P(A|\delta\mathbf{t})dA\,, \tag{3.19}$$

subjected to the normalization condition, $\int_0^\infty P(f_{\rm dm}|\delta\mathbf{t})df_{\rm dm} = 1$.

Multiple Pulsars

The above analysis is easily generalized to multiple pulsars. The marginalized posterior distribution of $f_{\rm dm}$ for multiple pulsars can be formulated in two non-equivalent, but equally valid, ways. First, we write the collection of the amplitude in each pulsar as $\mathbf{A} = (A_1, A_2, \cdots, A_{N_P})$ where N_P is the number of pulsars. Then $P(f_{\rm dm}|\delta\mathbf{t})$ is given by

$$P(f_{\rm dm}|\delta\mathbf{t}) = \int_{-\infty}^{\infty} P(f_{\rm dm}|\mathbf{A})P(\mathbf{A}|\delta\mathbf{t})d^{N_P}A\,. \tag{3.20}$$

Since all the pulsars are independent from each other, we can factorize the likelihood function and hence the joint posterior distribution of $\mathbf{A}$ (since $\mathbf{A}$ has a uniform prior)

$$P(\mathbf{A}|\delta\mathbf{t}) = P(A_1|\delta\mathbf{t})P(A_2|\delta\mathbf{t})\cdots P(A_{N_P}|\delta\mathbf{t})\,. \tag{3.21}$$

Following the same steps in Sec. 3.3, the final expression of $P(f_{\rm dm}|\delta\mathbf{t})$, labelled 'all' because it includes all the pulsars directly, is

$$P_{\rm all}(f_{\rm dm}|\delta\mathbf{t}) \propto \prod_{i=1}^{N_P}\int_{-\infty}^{\infty} P(A_i|f_{\rm dm})P(A_i|\delta\mathbf{t})dA_i\,, \tag{3.22}$$

which must also be normalized to one. We emphasize that since Eq. (5.43) is merely a product of N_P integrals (instead of an N_P-dimensional integral), it is computationally inexpensive to evaluate.

Alternatively, instead of using the amplitudes from all pulsars, we can compute $P(f_{\rm dm}|\delta\mathbf{t})$ using only the pulsar with the maximum amplitude, labelled 'max',

$$P_{\rm max}(f_{\rm dm}|\delta\mathbf{t}) \propto \int_{-\infty}^{\infty} P(A_{\rm max}|f_{\rm dm})P(A_{\rm max}|\delta\mathbf{t})dA_{\rm max}\,, \tag{3.23}$$

where $A_{\rm max} \equiv \max_i A_i$. The upper limits placed on $f_{\rm dm}$ for these two different ways of formulating $P(f_{\rm dm}|\delta\mathbf{t})$ scale differently with N_P. If we use the amplitudes from all pulsars, it is clear from Eq. (5.43) that $P_{\rm all}(f_{\rm dm}|\delta\mathbf{t})$ we obtain from considering N_P pulsars is effectively raising the single pulsar posterior by a factor of N_P (up to normalization, assuming identical pulsars), which always results in a lower $90^{\rm th}$ percentile on $f_{\rm dm}$. On the other hand, if we only consider the pulsar with the maximum amplitude, since $A_{\rm max} \geq A_i$ for all i, $P_{\rm max}(f_{\rm dm}|\delta\mathbf{t})$ will also be shifted to lower $f_{\rm dm}$. Hence we get a more stringent upper limit on $f_{\rm dm}$ with larger N_P for both treatments, but they do not necessarily scale with the same power of N_P. Since both $\mathbf{A}$ and $A_{\rm max}$ are well defined statistical variables, we have the freedom to draw upper limits on $f_{\rm dm}$ using either of them (despite the fact that they give different results). These treatments can now be repeated for all choices of M to obtain $P(f_{\rm dm}|\delta\mathbf{t})$ for each M.

3.4 Mock Data

To demonstrate the formalism developed in the previous sections we place the upper limits on the dark matter abundance in PBHs with standard mock pulsar data.

	N_P	d [kpc]	T [yr]	Δt [week]	$t_{\rm rms}$ [ns]
SKA	200	5	20	2	50
Optimistic	1000	10	30	1	10

Table 3.1: PTA parameters assumed when generating the mock pulsars. Here N_P is the number of pulsars, d is the pulsar-Earth distance, T is the observation time, Δt is the cadence and $t_{\rm rms}$ is the root-mean-square timing residuals.

Dataset

The mock pulsars in our analyses originated from the International Pulsar Timing Array (IPTA) First Mock Data Challenge (MDC) [174]. Using the python wrapper `libstempo` [175] to the pulsar timing package `TEMPO2` [176, 177], we generate mock data from the MDC `.par` files with zero timing residuals (i.e. perfect fit of the timing model). We then prepare two sets of mock pulsars with the pulsar parameters consistent with the predicted parameters for future PTA experiments, which are summarized in Table 3.1.

Then, for each set of mock pulsars, we inject noise into the timing residuals. To compare with our previous works [42, 9], our main result uses mock pulsars with only white noise injected. In addition, we also prepare a separate set of mock pulsars with both white noise and red noise injected. The spectral index of the red noise is chosen to be $\gamma_{\rm red} = 13/3$, which is the theoretical prediction of a stochastic gravitational wave background (GWB) signal due to a population of inspiraling SMBHBs in circular orbits [171]. To investigate the effects of red noise with different amplitudes, we carried out the analysis using mock data with $A_{\rm red} = 10^{-17}$, 10^{-16}, 10^{-15} and 10^{-14}.

Results

To generate the posterior distribution of the dark matter signal amplitude, A, we closely follow the Bayesian inference procedure described in Ref. [165] using the software `enterprise` [153]. We marginalize over all the timing model and noise parameters with an MCMC using the package `PTMCMCSampler` [173]. The time of closest approach $t_{D,0}$ for the Doppler dynamic search is also marginalized over. Since the signals we are interested in are pulsar independent, we carry out the analysis independently for each pulsar.

The parameters and their priors are listed in Table 5.1. In particular, we use uniform

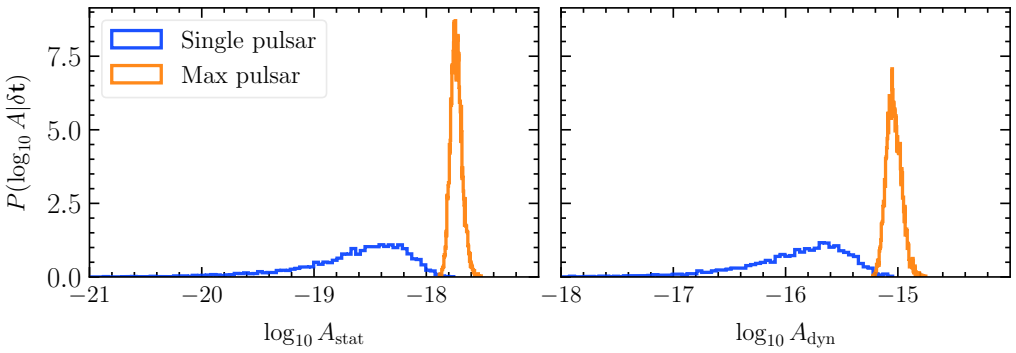

Figure 3.2: Posterior distribution of $\log_{10} A_{\rm stat}$ and $\log_{10} A_{\rm dyn}$ for mock pulsars with white noise only assuming SKA parameters. Both the single pulsar posterior and the posterior of the maximum amplitude across all $N_P = 200$ pulsars are shown.

(instead of log-uniform) priors for the dark matter amplitudes and we justify our choices as follows. For detection purpose, if the signal amplitude can span across several orders of magnitude, the prior is often chosen to be log-uniform to yield an unbiased parameter estimation. However, for the purpose of setting upper limits, uniform priors are often used for the signal amplitude since the prior of A has to be finite at $A = 0$. Otherwise, if a log-uniform prior is used instead, the prior will diverge at $A = 0$ and the precise value of the upper limit on A will depend on the lower-cut of A [165]. Considering that the data are consistent with $A = 0$ (i.e. no signal), no physically motivated values can be chosen for the lower-cut of A, rendering such dependence undesirable. Since the main objective of this work is to place constraints of dark matter (rather than claiming detection), we use uniform priors on A. Note that this does skew the posterior distribution into higher values of A, which indicates that the upper limits that we obtain are conservative bounds. The red-noise amplitude, however, does not have such restriction. It has been shown that using uniform priors on the red noise amplitude can lead to overstated Bayesian upper limits by transferring the signal power to the red noise process [178], so we choose to use log-uniform priors instead. We show the posterior distribution of the dark matter amplitude of one of the pulsars and the maximum amplitude across the entire PTA in Fig. 3.2.

To place an upper limit on the PBH dark matter abundance $f_{\rm dm}$, we first use the MC simulations described in Sec. 3.2 to compute the conditional probability $P(A|f_{\rm dm})$ for different choices of M and the same pulsar parameters as the mock data. We show

Parameter	Description	Prior
Red noise		
$A_{\rm red}$	Red noise power-law amplitude	Log-Uniform $[-19, -12]$
$\gamma_{\rm red}$	Red noise power-law spectral index	Uniform $[0, 7]$
Dark Matter		
$A_{\rm stat}$	Static dark matter amplitude	Uniform $\pm[10^{-21}, 10^{-13}]$
$A_{\rm dyn}$	Dynamic dark matter amplitude	Uniform $\pm[10^{-20}, 10^{-12}]$
t_0/T	Dynamic dark time of arrival	Uniform $[0.1, 0.9]$

Table 3.2: Parameters and priors used in the mock data analysis. The notation Uniform $\pm[\dots]$ stands for the union of Uniform $[+\dots]$ and Uniform $[-\dots]$. The effects of white noise are accounted for by marginalizing over a multiplicative factor in front of the errors on the timing residuals.

the probability for some choices of $f_{\rm dm}$ and M in Fig. 3.3. We see that higher values of $f_{\rm dm}$ lead to larger amplitudes. The inferred posterior distributions of $f_{\rm dm}$ are then computed using Eqs. (5.43)-(3.23), and are shown in Fig. 3.4.[7] By comparing Fig. 3.2 and Fig. 3.3, we observe that if $f_{\rm dm}$ is either too large or too small, the two probability distributions in Eqs. (5.43)-(3.23) do not overlap at all, leading to $P(f_{\rm dm}|\delta\mathbf{t}) = 0$. Hence the posterior distributions of $f_{\rm dm}$ shrink to zero on both ends similar to the posterior distributions of A in Fig. 3.2. The $p^{\rm th}$ percentile upper limit constraints on $f_{\rm dm}$, f_p, are then derived by requiring $\int_0^{f_p} P(f_{\rm dm}|\delta\mathbf{t}) df_{\rm dm} = 100 \times p$.

Finally, the $90^{\rm th}$ percentile upper limits on $f_{\rm dm}$ for PBHs are shown in Fig. 3.5. These results are compared to the sensitivity projection in our previous works described in Refs. [42, 9] using the same pulsar parameters. Our previous works use a matched-filter procedure to compute the signal-to-noise ratio (SNR) from PBHs relative to white noise, and derive the upper limits on $f_{\rm dm}$ by putting an appropriate cut on the SNR. We see that with both SKA and optimistic pulsar parameters, the constraints agree with each other to within a factor of two for most PBH masses. The only mass range where the results significantly differ from each other is 10^{-3}–$10^{-1}\ M_\odot$ (SKA)

[7] Shaded regions in Figs. 3.4-3.6 correspond to $f_{\rm dm} > 1$, which are unphysical if gravitation is the only interaction between the pulsar and the dark matter, but can be possible in the presence of additional forces.

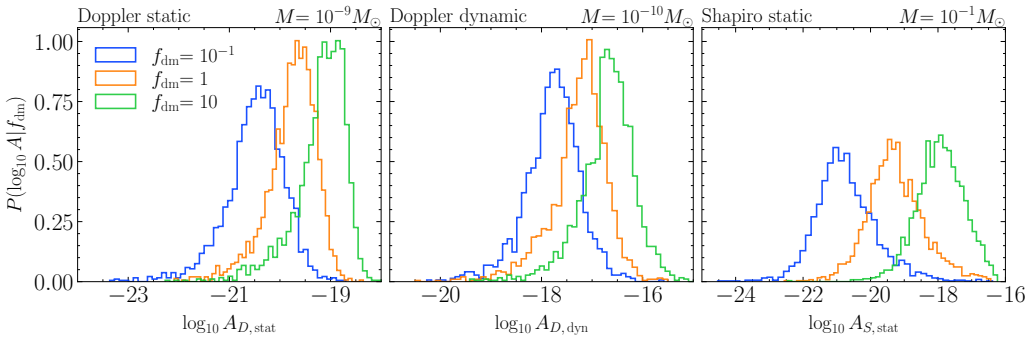

Figure 3.3: Conditional probability $P(\log_{10} A|f_{\rm dm})$ obtained by the MC for different values of $f_{\rm dm}$, assuming SKA parameters. The three panels correspond to Doppler static, Doppler dynamic and Shapiro static respectively.

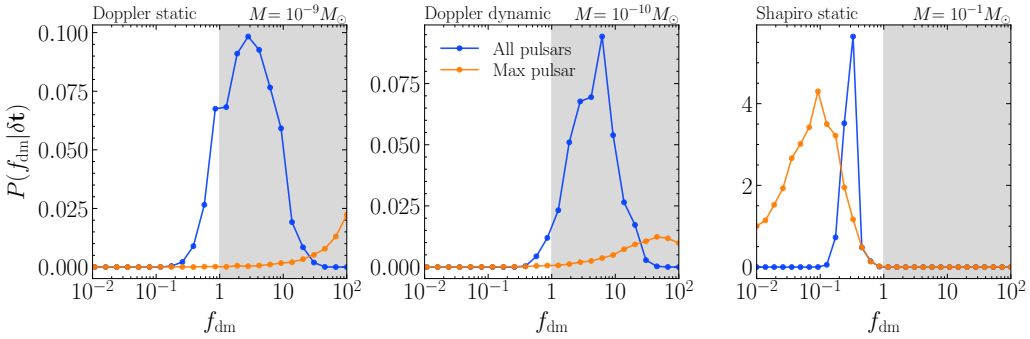

Figure 3.4: Posterior probability $P(f_{\rm dm}|\delta\mathbf{t})$ assuming SKA parameters and only white noise in the mock pulsars. The three panels show the results for Doppler static, Doppler dynamic and Shapiro static respectively. The lines labelled 'All pulsars' use Eq. (5.43) to compute the posterior distribution, while the lines labelled 'Max pulsar' use Eq. (3.23).

and 10^{-4}–$10^{-2}\,M_\odot$ (optimistic) for the Shapiro search, where our constraints on $f_{\rm dm}$ are weaker by around an order of magnitude. We also show the most stringent upper limits (for a given PBH mass) on $f_{\rm dm}$ from both the 'max/all pulsar' searches in Fig. 3.6.

Here we summarize the differences between our previous works and this work. First, our previous work draws constraints using the SNR, which is a frequentist interpretation of the data. This work derives the constraints using the posterior distribution, which is Bayesian in nature. It is not uncommon for results from frequentist and Bayesian inferences to differ from each other by $O(1)$ numbers. Second, the latest iteration of our previous work [9] does not distinguish the static and dynamic signals,

because a Monte Carlo was used to generate the signals and smoothly interpolate between dynamic and static regimes. In this work, we must divide the signal into static and dynamic signals for the ease of signal parameterization in the data. This leads to a deterioration of the constraints when the mass M falls under the transition region between the static and the dynamic regimes. For the Doppler case, this deterioration is not significant. However, for the Shapiro case, since we do not carry out the Shapiro dynamic analysis, the constraint is significantly weakened at the edge of the static mass regime (as commented in the previous paragraph). While this weakening is due to calculational limitations in the Bayesian analysis is unfortunate, we also note the limited utility of the Shapiro searches for even moderately lower concentration dark matter subhalos [42], suggesting that for a broad range of dark matter models, Doppler searches will be the dominant tool. Finally, our previous work only draws constraints using the maximum SNR among all the pulsars, while in this work we also consider the possibility of studying the dark matter signals in all the pulsars simultaneously. As indicated in Fig. 3.5, this leads to a better reach for some mass ranges (e.g. $M < 10^{-2}\, M_\odot$ for the Shapiro signal with SKA parameters).

Effects of Red Noise

Realistic PTA data contain red noise. Some pulsars contain intrinsic red noise, while a stochastic GWB can also induce a red noise process correlated among all pulsars. For instance, a common red noise process with median amplitude $A = 1.92 \times 10^{-15}$ and spectral index $\gamma = 13/3$ is reported by NANOGrav in Ref. [156]. For completeness, we briefly consider the effect of red noise, such as the SMBHB background, on a PTA's ability to detect dark matter.

Instead of the upper limits on $f_{\rm dm}$, we report the effects of red noise on the posterior distribution of the dark matter amplitudes $A_{\rm stat}$ and $A_{\rm dyn}$ in Fig. 3.7. The presence of the red noise shifts the posterior distribution towards large amplitudes, implying that the constraints on the amplitudes (hence $f_{\rm dm}$) worsen. To quantify the effects, we show the $90^{\rm th}$ percentile of $A_{\rm stat}$ and $A_{\rm dyn}$. As shown in Fig. 3.7, a red noise process with $A_{\rm red} = 10^{-15}$ would increase the upper limits on $A_{\rm stat}$ and $A_{\rm dyn}$ by 2 and 1.5 orders of magnitude respectively. The PBH dark matter abundance $f_{\rm dm}$ scales as $A_{D,\,\rm stat}$, $A^2_{D,\,\rm dyn}$ and $A^{2/3}_{S,\,\rm stat}$ respectively, meaning that, in any case, the upper limits on $f_{\rm dm}$ worsen by over an order of magnitude when red noise is present in the data.[8]

[8] In practice, instead of only considering the upper limits on A, one would have to perform the

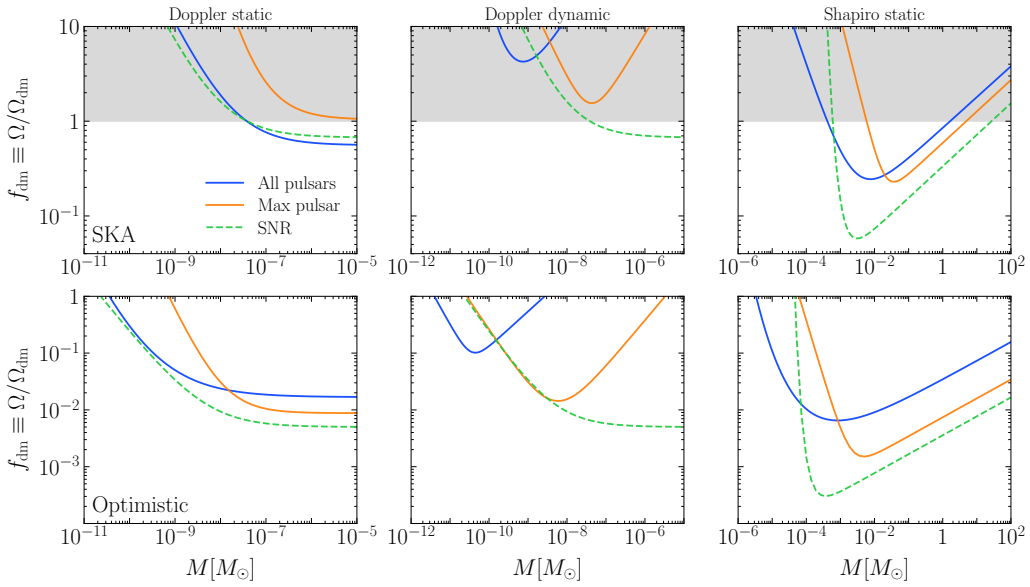

Figure 3.5: The 90$^{\rm th}$ percentile upper limits on the PBH dark matter abundance $f_{\rm dm} \equiv \Omega/\Omega_{\rm dm}$ for different PBH masses, M. The top and bottom rows correspond to the SKA and optimistic parameters defined in Table 3.1, while the three columns corresponding to the Doppler static, Doppler dynamic and Shapiro static searches, respectively. The results for this work are shown in solid lines while the dotted lines denote the projected sensitivity using the frequentist formalism developed in Refs. [42, 9]. Note that the previous results quoted here do not distinguish between static and dynamic searches. The lines labelled 'All pulsars' and 'Max pulsar' labels show the upper limits derived using all pulsars and only the pulsar with maximum signal amplitude respectively.

3.5 Conclusions

In this work, we have provided a Bayesian framework for detecting dark matter substructure with Pulsar Timing Arrays, which bridges the gap between our previous work [43, 42, 9] and realistic PTA data. Using mock data with well-motivated pulsar parameters, we found that for mock pulsars with white noise only, the upper limits placed on the PBH dark matter abundance agree with our previous results up to a factor of two for all mass ranges for the Doppler search and most mass ranges for the Shapiro search. This implies that non-negligible constraints on PBHs with mass 10^{-8}–$10^{2}\,M_\odot$ and mass 10^{-11}–$10^{2}\,M_\odot$ can be placed in the next decade and

overlapping integrals using Eqs. (5.43)-(3.23) to compute the posterior distribution of $f_{\rm dm}$. Hence this analysis is an order of magnitude estimate of the effects of $A_{\rm red}$ on $f_{\rm dm}$. We did not perform a full analysis on mock data with red noise since that would require us to run the MC simulations with unrealistically high $f_{\rm dm}$, which is computationally challenging.

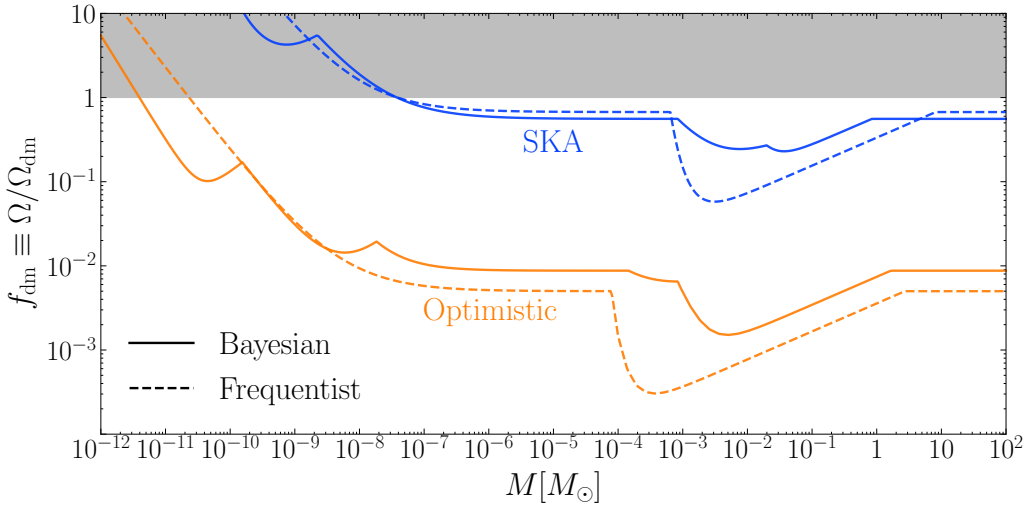

Figure 3.6: The most stringent 90$^{\rm th}$ percentile upper limits on the PBH dark matter abundance $f_{\rm dm} \equiv \Omega/\Omega_{\rm dm}$ for different PBH masses, M. The results in the present work are labelled as 'Bayesian' while the sensitivity projections in Refs. [42, 9] are labelled as 'Frequentist'.

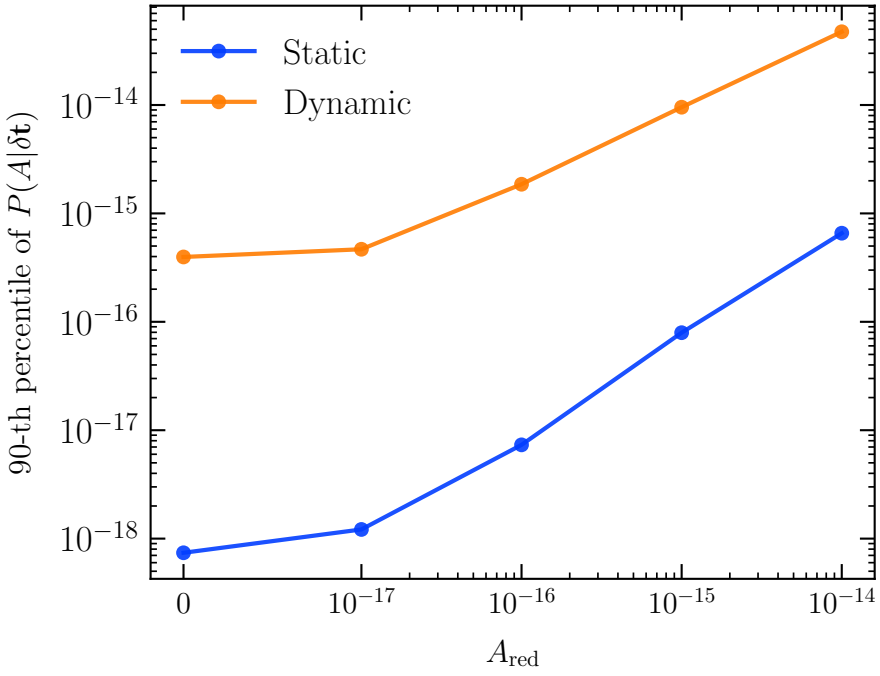

Figure 3.7: The 90$^{\rm th}$ percentile of $A_{\rm stat}$ and $A_{\rm dyn}$ in the presence of different red noise amplitudes. The data point for $A_{\rm red} = 0$ corresponds to no red noise at all.

the decade after respectively.

We have also investigated the effects of red noise on the sensitivity of dark matter signals, where we found that the upper limits on the PBH dark matter abundance $f_{\rm dm}$ weaken by over an order of magnitude when red noise from supermassive black hole binaries is introduced in the present framework. While this might eliminate any hope of detecting dark matter with PTAs in the near future, we note that significant progress is being made by the PTA community in separating signals from different physical processes. In particular, if the timing residuals due to red noise (pulsar intrinsic or pulsar correlated) are identified to high precision (instead of only the amplitude and the spectral index in frequency space), we will be able to subtract the contribution from red noise and mitigate its effects, since the dark matter signal shape studied here is not degenerate with the red noise. We hope that this work will motivate future work in the PTA community in separating signals of different sources.

This work only formulates the detection of PBHs and PBH-like substructures. To distinguish between different dark matter models, it is important to also develop a formalism that works for dark matter substructure with general halo mass functions and density profiles. In addition, many dark matter models include additional couplings between dark matter and the standard model beyond gravitational interactions. Such classes of dark matter also produce signals that can be potentially detected by PTAs [179]. We leave these analyses for future work.

bibliography

Chapter 4

SEARCHING FOR GRAVITATIONAL WAVES FROM COSMOLOGICAL PHASE TRANSITIONS WITH THE NANOGRAV 12.5-YEAR DATASET

This chapter is based on

[1] Zaven Arzoumanian et al. "Searching for Gravitational Waves from Cosmological Phase Transitions with the NANOGrav 12.5-Year Dataset". In: *Phys. Rev. Lett.* 127.25 (2021), p. 251302. DOI: 10.1103/PhysRevLett.127.251302. arXiv: 2104.13930 [astro-ph.CO].

4.1 Introduction

The search for gravitational waves (GWs) spans many orders of magnitude and encapsulates a plethora of source phenomena. At very-low frequencies ($\sim 1-100$ nHz), pulsar-timing arrays (PTAs; [180, 181, 182]) aim to detect GWs through the presence of correlated deviations to radio-pulse arrival times across an ensemble of precisely-timed Milky Way millisecond pulsars. There are three PTA collaborations that currently have decadal-length timing data from an ensemble of pulsars: The North American Nanohertz Observatory for Gravitational Waves (NANOGrav; [183]), the European Pulsar Timing Array (EPTA; [184]), and the Parkes Pulsar Timing Array (PPTA; [185]). These three, in addition to the Indian PTA (InPTA; [186]), are synthesized into the International Pulsar Timing Array (IPTA; [187]). There are also emerging efforts in China (CPTA; [188]), as well as some telescope-centered timing programs (MeerKAT; [189]; CHIME; [190]).

The dominant GW signals at such low frequencies frequencies are expected to be from a cosmic population of tightly-bound inspiralling supermassive binary black holes (SMBHBs; [191, 192]), producing an aggregate incoherent signal that we search for as a stochastic GW background (GWB), and also individual binary signals that we attempt to resolve out of this stochastic confusion background. However, other more speculative GW sources in the PTA frequency range include cosmic strings [193, 194], a primordial GWB produced by quantum fluctuations of the gravitational field in the early universe, amplified by inflation [195, 196, 197], and cosmological phase transitions [198, 199, 200, 201, 202], the latter of which is the subject this study.

The most recent PTA results are from NANOGrav's analysis of 12.5 years of precision timing data from 47 pulsars [203, hereafter], of which 45 exceeded a timing baseline of 3 years and were analysed in a search for a stochastic GWB [204, hereafter]. NANOGrav reported strong evidence for a common-spectrum low-frequency stochastic process in its array of 45 analyzed pulsars, where $\sim$ 10 of those pulsars are strongly supportive, most are ambivalent, and a few seem to disfavor the process (although not significantly). No evidence for the characteristic inter-pulsar correlation signature imparted by GWs was found. At low frequencies the shape of the characteristic strain spectrum was well matched to a power-law, with an amplitude and slope consistent with theoretical models of SMBHB populations. Under a model that assumes the origin of the GWB is a population of SMBHBs, the median characteristic strain amplitude at a frequency of $1/\text{year}$ is 1.92×10^{-15}. Interpretations of this common-spectrum process as a GWB from SMBHBs have since appeared in the literature, showing that, if it is indeed so, robust evidence of the distinctive inter-pulsar correlations should accrue within the next several years, followed by characterization of the strain spectrum and astrophysical probes of the underlying population [205, 206]. However, the Bayesian posterior probability distributions of the strain-spectrum amplitude and slope are broad enough to entertain a variety of different source interpretations, many of which have since appeared in the literature [e.g. 207, 208, 209, 210].

In this Letter we consider gravitational waves produced by first-order cosmological phase transitions, both as an alternative origin of the common process measured in the NANOGrav 12.5 year Dataset [211, 212, 213, 214, 215, 216, 217, 218], and as a sub-dominant signal to that produced by SMBHBs. The frequency range to which NANOGrav is sensitive corresponds to phase transitions at temperatures below the electroweak phase transitions of the Standard Model (*i.e.* $T \lesssim 100\,\text{GeV}$). This has led many to consider higher frequency GW observatories, such as LISA and LIGO, as the dominant instruments to search for phase transitions. However, phase transitions may occur at much lower temperatures in particular in *hidden sectors* [219, 220, 45]. Hidden sectors/valleys feature rich dynamics, with multiple matter fields and forces, independent of the dynamics of the Standard Model. They appear generically in top-down constructions like string theory, and in some solutions to the so-called hierarchy problem. In many cases, they may be difficult to detect via their particle interactions with the Standard Model, but gravity is an irreducible messenger. In this regard, PTAs provide a powerful complementary probe to the dynamics of hidden sectors already being explored through many terrestrial, astrophysical and

cosmological probes (see Ref. [221] for a recent summary).

Previous studies on cosmological first order phase transition in the context of the NANOGrav results were carried out in [216, 222, 223, 212]. Our analysis presents two main novelties compared to these works: first, we properly include the relevant noise sources and discuss the impact of backgrounds (like the one generated by SMBHBs); second, we discuss how the results are affected by the theoretical uncertainties on the GW spectrum produced by first order phase transitions.

The outline of this Letter is as follows. In the next section we briefly summarize the signature of GWs from the dominant background of SMBH mergers. We then dive into the main subject of this Letter, GWs from a first-order phase transition, where we discuss the relevant parameters characterizing the signal. We then carry out an analysis with the NANOGrav 12.5 year dataset, finding that the data can be modeled in terms of a strong phase transition with a transition temperature around 10 MeV. The dataset and data model for these analyses are exactly as described in NG12 and NG12gwb, respectively. All common processes (whether interpreted as being of SMBHB or phase-transition origin) are modeled within the five lowest sampling frequencies of the array time series, corresponding to $\sim 2.5 - 12$ nHz. Finally, we discuss theoretical uncertainties, and compare the PT interpretation of the data to the standard interpretation in terms of SMBHB finding no strong preference for one over the other.

4.2 GW from SMBHBs Mergers

Regardless of origin, the energy density of GWs as a fraction of closure density is related to the GW characteristic strain spectrum by [224]

$$\Omega_{GW}(f) = \frac{2\pi^2}{3H_0^2} f^2 h_c^2(f), \tag{4.1}$$

where H_0 is the Hubble constant (set here to be 67 km/s/Mpc [225]), and the GWB characteristic strain spectrum $h_c(f)$ is often described by a power-law function for astrophysical and cosmological sources:

$$h_c(f) = A_{\rm GWB} \left(\frac{f}{yr^{-1}} \right)^{\alpha}, \tag{4.2}$$

where $A_{\rm GWB}$ is the amplitude at a reference frequency of 1/year, and α is an exponent that depends on the origin of the GWB. For a population of inspiraling SMBHBs, this is $\alpha = -2/3$ [226]. The cross-power spectral density of GW-induced timing

	Bubbles [228]	Sound Waves [229]
$\Delta(v_w)$	$\dfrac{0.48 v_w^3}{1 + 5.3 v_w^2 + 5 v_w^4}$	$0.513\, v_w$
κ	κ_ϕ	κ_{sw}
p	2	2
q	2	1
$\mathcal{S}(x)$	$\dfrac{(a+b)^c}{\left[b x^{-a/c} + a x^{b/c}\right]^c}$	$x^3 \left(\dfrac{7}{4+3x^2}\right)^{7/2}$
f_*/β	$\dfrac{0.35}{1 + 0.07 v_w + 0.69 v_w^4}$	$\dfrac{0.536}{v_w}$

Table 4.1: Parameters for the gravitational wave spectrum of eq. (4.4). The values of the parameters (a, b, c) in the spectral shape of the bubble contribution are reported in Table 4.2.

deviations between two pulsars a and b can be written as

$$S_{ab}(f) = \Gamma_{ab} \frac{A^2_{\rm GWB}}{12\pi^2} \left(\frac{f}{yr^{-1}}\right)^{-\gamma} yr^3 \,, \tag{4.3}$$

where $\gamma \equiv 3 - 2\alpha = 13/3$ for SMBHBs, and Γ_{ab} is the Hellings-Downs [227] correlation coefficient between pulsar a and pulsar b.

4.3 GWs from First-order Phase Transition

A first-order phase transition (PT) occurs when the true minimum of a potential is separated from a false minimum by a barrier through which a field must locally tunnel. This can occur in either weakly coupled (where a scalar field tunnels) or strongly coupled (where a vacuum condensate corresponds to the scalar field) theory. Such transitions are known to proceed through nucleation of bubbles of true vacuum which, if sufficiently large, expand in the background plasma (still in the false vacuum). Collisions of these bubbles, as well as interactions between the expanding bubble walls and the surrounding plasma, can be efficient sources of GWs.

We characterize the phase transition in terms of four parameters:

- T_* – the Universe temperature at which the phase transition takes place.

	Envelope	Semi-analytic	Numerical
a	3	1 – 2.2	1.6 – 0.7
b	1	2.6 – 2.9	1.4 – 2.3
c	1.5	1.5 – 3.5	1
f_*/β	$\dfrac{0.35}{1+0.07v_w+0.69v_w^2}$	0.1	0.2

Table 4.2: Comparison of the bubble spectral shape parameters derived using the envelope and thin wall approximation [228] (left column), the semi-analytic approach of reference [230] (middle column), and lattice simulations [231] (right column). For numerical and semi-analytic results the values of the parameters depend on the choice of the scalar field potential, we report the range of values obtained for the different scalar field potentials considered in the above mentioned works.

- α_* – the strength of the phase transition, defined as the ratio of the vacuum and relativistic energy density at the time of the phase transition.
- β/H_* – the bubble nucleation rate in units of the Hubble rate at the time of the phase transition, H_*.
- v_w – the velocity of the bubble walls.

The three main sources of GWs associated with a first-order phase transition are: (i) collisions of bubble walls, (ii) collisions of the sound waves generated in the background plasma by the bubbles expansion, and (iii) turbulence in the plasma generated by expansion and collisions of the sound-wave. However, in this analysis we will not include the turbulence contribution as it usually is subleading compared to the sound-wave one, and also affected by the largest theory uncertanties (see for example [232, 233, 234] for recent developments).

The contribution to the total GW spectrum from bubbles and sound waves collisions can be parametrized as [235, 232]

$$h^2\Omega(f) = \mathcal{R}\,\Delta(v_w)\left(\frac{\kappa\,\alpha_*}{1+\alpha_*}\right)^p\left(\frac{H_*}{\beta}\right)^q \mathcal{S}\left(f/f_*^0\right), \tag{4.4}$$

where the prefactor $\mathcal{R} \simeq 7.69\times10^{-5} g_*^{-1/3}$ accounts for the redshift of the GW energy density, $\mathcal{S}(\cdot)$ parametrizes the spectral shape, and $\Delta(v_w)$ is a normalization factor

which depends on the bubble wall velocity, v_w. The value of the peak frequency today, f_*^0, is related to the value of the peak frequency at emission, f_*, by:

$$f_*^0 \simeq 1.13 \times 10^{-10}\, Hz \left(\frac{f_*}{\beta}\right)\left(\frac{\beta}{H_*}\right)\left(\frac{T_*}{MeV}\right)\left(\frac{g_*}{10}\right)^{1/6}, \tag{4.5}$$

where g_* denotes the number of relativistic degrees of freedom at the time of the phase transition. The values of the peak frequency at emission, the spectral shape, the normalization factor, and the exponents p and q are reported in Table 4.1 for all the production mechanisms considered in this work. Due to the finite lifetime [236, 237] of the sound waves, to derive Ω_{sw} eq. (4.4) needs to be multiplied by a suppression factor $\Upsilon(\tau_{sw})$ given by [236]:

$$\Upsilon(\tau_{sw}) = 1 - (1 + 2\tau_{sw}H_*)^{-1/2} \tag{4.6}$$

where the sound-wave lifetime is usually taken to be the timescale for the onset of turbulent behaviors in the plasma [238]: $\tau_{sw} \approx R_*/\bar{U}_f$, where the average bubble separation is given by $R_* = (8\pi)^{1/3}\beta^{-1}Max(v_w, c_s)$ [239], and $\bar{U}_f^2 \approx 3\kappa_{sw}\alpha/[4(1+\alpha_*)]$ [238].

Generally both the production mechanism contribute to the GW spectrum. However, if the bubble walls interacts with the surrounding plasma most of the energy released in the PT is expected to be transferred to the plasma so that the sound waves (and possibly the turbulence) contribution dominates the GW spectrum. An exception to this scenario is provided by models in which the bubble walls do not interact with the plasma, or by models where the energy released in the PT is large enough that the friction exerted by the plasma is not enough to stop the walls from keep accelerating (runaway scenario). However, determining wether or not the runaway regime is realized is either model dependent or affected by large theoretical uncertainties. Therefore, we perform two separate of analyses. A sound-wave-only (SWO) analysis, where we assume that the runaway regime is not reached and that the sound wave and turbulence contributions dominate the GW spectrum; therefore we set $\kappa_\phi = 0$, and use the results of reference [240] to derive κ_{sw} as a function of v_w and α_*. A bubble-only (BO) analysis, where we assume that the runaway regime is reached and that bubble collisions dominate the GW spectrum; we then set $v_w = 1$, $\kappa_{sw} = 0$ and $\kappa_\phi = 1$.

We conclude this section emphasizing that, despite recent progress, large theoretical uncertainties still affect the prediction of the GW signal produced in cosmological phase transitions. To get an idea of the impact that these uncertainties have on our

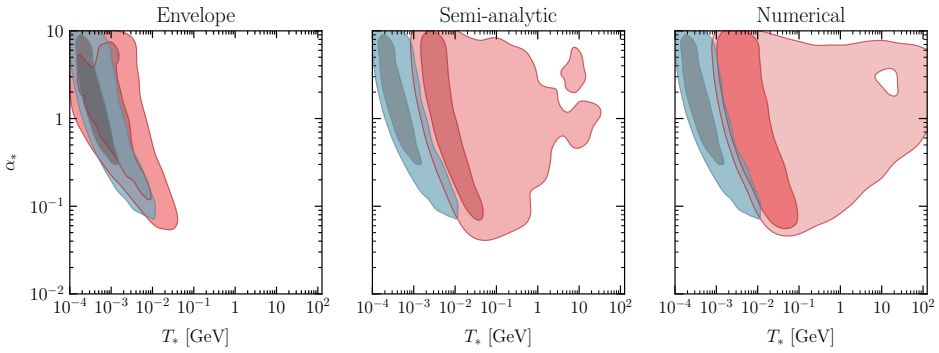

Figure 4.1: In red (blue) the 1-σ (68% posterior credible level), and 2-σ (95% posterior credible level) contours for the two-dimensional posterior distributions in the (T_*, α_*) plane obtained in the BO (SWO). The BO analysis has been performed with the spectral shape computed by using the envelope approximation (left panel), semi-analytic results (central panel), and numerical results (right panel). Specifically, we use $(a, b, c) = (1, 2.61, 1.5)$ for the semi-analytic results, and $(a, b, c) = (0.7, 2.3, 1)$ for the numerical results.

results we will study how the BO analysis is impacted by them. Similar, if not larger, uncertainties affect the sound wave contribution and would impact the results of the SWO analysis.

Assuming that the stress energy density of the expanding bubbles is localized in an infinitesimally thin shell near the bubble wall (thin shell approximation), and that it instantaneously decays to zero after two bubbles collide (envelope approximation), the bubble spectral shape can be derived analytically [241, 228]. The spectral shape parameters obtained in this way are reported in the left column of Table 4.2. To go beyond these approximations, 3D lattice simulations are needed. These simulations are extremely expensive given the hierarchy between the large simulation volume needed to include multiple bubbles, and the small lattice spacing needed to resolve the thin walls. Because of the relativistic contraction of the wall width, this separation of scales becomes increasingly large for increasing wall velocities, making it impossible to simulate ultra-relativistic walls. However, the GW spectrum can be simulated at lower velocities and the results extrapolated to larger values. This is the approach taken in Refs. [242, 231], where the authors show that at high frequencies the GW spectrum is much steeper than predicted by the envelope approximation ($b \sim 1.4 - 2.3$ depending on the form of the scalar field potential). An alternative approach to the problem has been taken by the authors of Refs. [243, 230]. In these works a parametric form for the evolution of the scalar field during bubble colli-

sions is found by using two-bubble simulations. This parametric form is then used in many-bubble simulations to derive the GW spectrum. They also find a steeper high frequency slope ($b \sim 2.6 - 2.9$) compared to the prediction of the envelope approximation. Similar discrepancies are found at low frequencies, where both the numerical and semi-analytic results find a shallower spectrum compared to the envelope approximation (see Tab. 4.2). To probe the theoretical uncertainty associated with the bubble contribution, we will carry out three separate BO analyses utilizing each approach and compare the constraint on the phase transition temperature and strength.

4.4 Results

We now report our results for the BO and SWO analyses. For either of them we consider both the case where the only GW signal is the one produced by the PT, and the one in which the PT signal is superimposed to an astrophysical background produced by SMBHB. This latter analyses will give an indication of how difficult it will be to disentangle a signal from a phase transition from the SMBHB background. The prior distributions for the model parameters of all these analyses, in addition to other noise characterization parameters, are listed in Table 4.3.

The two parameters that we can constrain the most are the transition temperature, T_*, and the phase transition strength, α_*. Their 2D posterior distributions for the PT-only searches are shown in Fig. 4.1. To assess the impact of theoretical uncertainties related to the bubble spectrum, for the BO analysis we report the results obtained by using the three different estimates of the bubble contribution to the GW spectrum described in the previous section (envelope, semi-analytic, and numerical). We can see that at the 1-σ (68% posterior credible) level all the searches prefer a strong PT, $\alpha_* \gtrsim 0.1$, with low transition temperature, $T_* \lesssim 10\,MeV$. At 2-σ (95% posterior credible) level the posteriors for the semi-analytical and numerical results have support at much higher temperatures, while the envelope results still prefer relatively low values. The preference for small values of T_* at the 1-σ level can be understood by noticing (see Fig. 4.2) that the data prefer GW spectra that are peaked at frequencies below the NANOGrav sensitivity window (*i.e.* $f_*^0 \lesssim 10^{-9}\,Hz$). And, by setting $\beta/H_* = 1$ in (4.5), we see that this requirement corresponds to $T_* \lesssim 10\,MeV$. The low-frequency part of the numerical and semi-analytical GW spectra is shallow enough that, at the 2-σ level, the data can be fitted also by spectra with peak frequencies above the NANOGrav sensitivity window. The same is not true for the envelope results, which have a much steeper low-frequency spectrum;

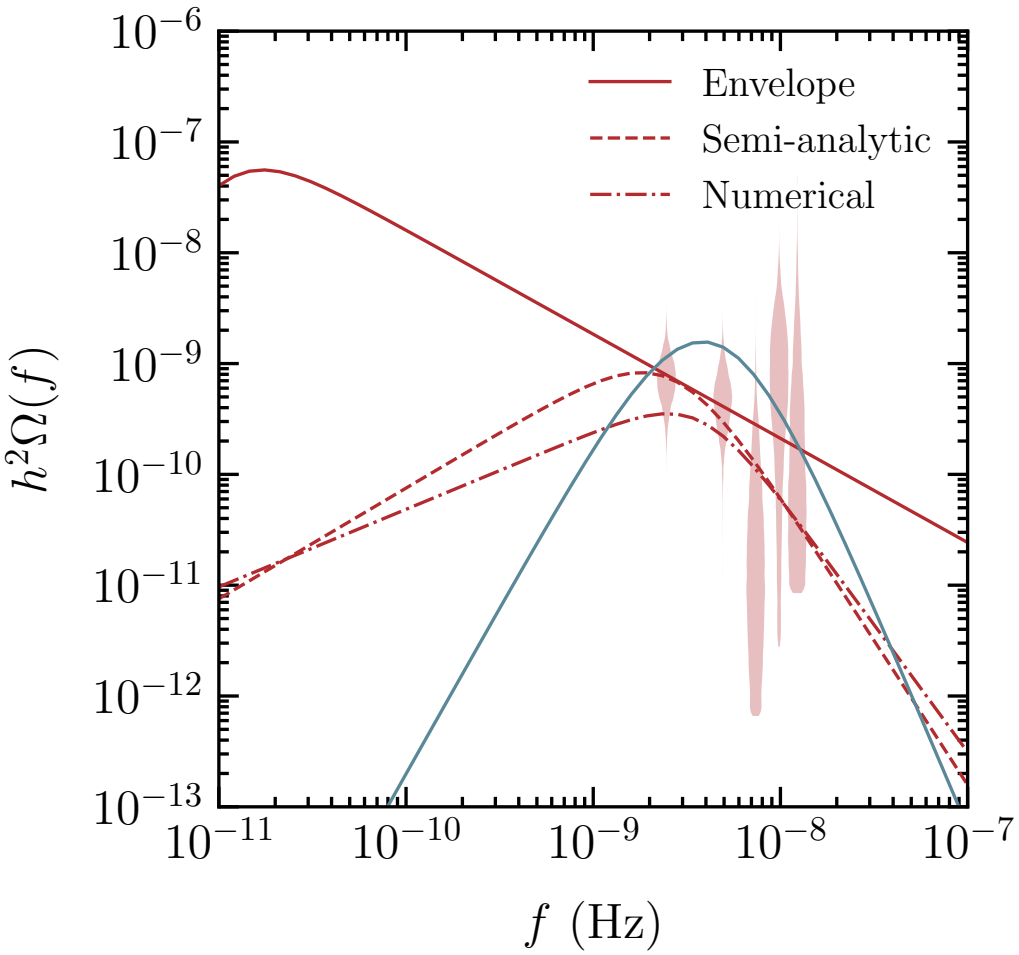

Figure 4.2: Maximum likelihood GWB fractional energy-density spectrum for the BO (red) and SWO (blue) analyses compared with the marginalized posterior for the free power spectrum (independent per-frequency characterization; red violin plot) derived in NG12gwb. For the BO analysis we show the results derived by using the envelope (solid line), semi-analytic (dashed), and numerical (dot-dashed) spectral shapes. For the BO analyses the values of (α_*, T_*) for these maximum likelihood spectra are $(0.28, 0.7\,MeV)$ for the envelope results, $(1.2, 3.4\,MeV)$ for the semi-analytic results, and $(0.13, 14.1\,MeV)$ for the numerical results. While for the SO analysis we get $(6.0, 0.32\,MeV)$.

this is the reason why the 2-σ levels of the envelope results deviate substantially from the other two.

In Fig. 4.2 we show the GWB spectrum predicted for the maximum likelihood parameters of PT-only searches. To better illustrate our results, and how the different parameters and theoretical uncertainties affect the GWB spectrum, we release an interactive version of Fig. 4.2 at this link.

Parameter	Description	Prior
	White Noise	
E_k	EFAC per backend/receiver system	Uniform $[0, 10]$
Q_k [s]	EQUAD per backend/receiver system	log-Uniform $[-8.5, -5]$
J_k [s]	ECORR per backend/receiver system	log-Uniform $[-8.5, -5]$
	Red Noise	
$A_{\rm red}$	red-noise power-law amplitude	log-Uniform $[-20, -11]$
$\gamma_{\rm red}$	red-noise power-law spectral index	Uniform $[0, 7]$
	Phase Transition	
T_* [GeV]	phase transition temperature	log-Uniform $[-4, 3]$
α_*	phase transition strength	log-Uniform $[-1.3, 1]$
H_*/β	bubble nucleation rate	log-Uniform $[-2, 0]$
v_w	bubble wall velocity	log-Uniform $[-2, 1]$
	Supermassive Black Bole Binaries (SMBHB)	
$A_{\rm GWB}$	common process strain amplitude	log-Uniform $[-18, -14]$
$\gamma_{\rm GWB}$	common process power-law spectral index	delta function ($\gamma_{\rm GWB} = 13/3$)

Table 4.3: Priors distributions for the parameters used in all the analyses in this work. The prior for the bubble wall velocity reported in this table is the one used for the SWO analysis, for the BO analyses we use $v_w = 1$ as explained in the text. The white noise parameters are fixed by the single-pulsar analysis. The red noise parameters are independent for each pulsar while the phase transition and SMBHB parameters are common across the entire PTA (except for $\gamma_{\rm GWB}$, which is fixed to 13/3).

To understand how the inclusion of the SMBHB background affects our results, in Fig. 4.3 we show the posterior for the parameters α_* and $A_{\rm GWB}$ obtained in the PT+SMBHB search. As expected, with the inclusion of the SMBHB background, the posteriors for α_* stretch to lower values where most of the signal is provided by the SMBHB contribution.[1] The Bayesian Information Criterion (BIC) [244], defined to be BIC $= k \ln n - 2 \ln \hat{\mathcal{L}}$ where $n = 5$ is the number of data points in the frequency space, k is the number of parameters in the model and $\hat{\mathcal{L}}$ is the maximum likelihood, is also computed. For the BO searches, the differences in BIC between the PT+SMBHB and SMBHB only searches are found to be -0.92, 3.04 and 1.89 for the envelope, semi-analytic and numerical results respectively;

[1] The posterior stops around $\alpha_* \simeq 0.05$ because of choice of the prior, otherwise it woiuld extend down to $\alpha_* \sim 0$.

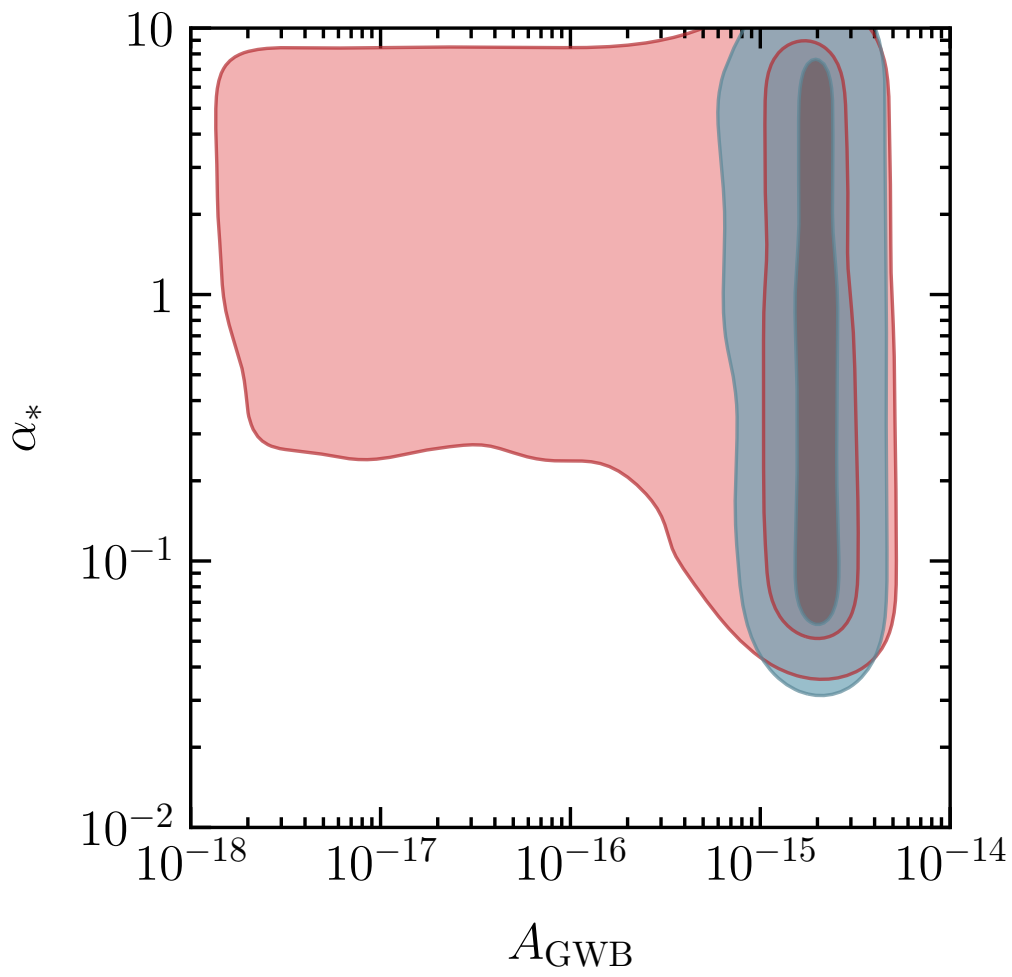

Figure 4.3: 1-σ (68% posterior credible level), and 2-σ (95% posterior credible level) contours for the parameters $A_{\rm GWB}$ and α_* in the PT+SMBHB search. In red (blue) the results for the BO (SWO) analyses. In this figure we have used the semi-analytic results for the bubble spectrum. The posteriors do not extend to lower values of α_* because of our choice for the α_* prior: log-Uniform $[-1.3, 1]$.

similarly the BIC differences between the PT-only and SMBHB-only searches are -1.82, -3.18, -1.28. For the SWO analysis, the difference in BIC between the PT+SMBHB and SMBHB only searches is -4.56, while we get -2.19 for the difference between the PT-only and SMBHB-only searches. We can then conclude that that the PT+SMBHB and PT-only models were neither strongly favored nor disfavored compared to the SMBHB only model [245].

A complete set of posteriors for the parameters of the PT-only searches (derived by using the semi-analytic spectrum for the BO analysis) are shown in Fig. 4.4. As

noted previously, at 1-σ level the data prefer a strongly first-order phase transition ($\alpha_* \gtrsim 0.1$) taking place at temperature $T_* \lesssim 10\,MeV$; while no strong constraints on v_w or H_*/β is observed. We can also notice that the higher values of T_* allowed in the 2-σ region are accompanied by slower nucleation rates (large H_*/β). We should caution, however, that numerical simulation have been performed for phase transition strengths up to $\alpha_* \sim 0.5$ [246], and that our results for $\alpha_* \gtrsim 0.5$ are derived by extrapolating the results of these simulations. A similar remark should be made for H_*/β, numerical simulations with values of this parameter close to unity have not been performed yet.

Given the low value of T_*, and the strong constraints on new physics at such low scales, we expect the phase transition to take place in a dark sector with only feeble interactions with the Standard Model (SM). In order to be consistent with the Hubble parameter constraints during the era of Big Bang Nucleosynthesis (BBN) [247], the energy of this dark sector must be transferred to the SM before the onset of BBN at $T \sim 1\,MeV$. This leaves an allowed range of values for the transition temperature given by $T_* \sim 1\,MeV - 100\,\mathrm{GeV}$. The next data release, which adds multiple years of observations and extends the the sensitivity window to lower frequency, should begin to resolve the peak of the spectrum or additionally shrink the range of allowed values for T_*.

4.5 Conclusions

We performed a search for a stochastic gravitational wave background from first-order phase transitions in the 12.5 year NANOGrav dataset. While previous NANOGrav analysis found no evidence yet for the inter-pulsar correlation signature of a GWB, the evidence for a common-spectrum process was significant. We found that the data can be modeled by a strong ($\alpha_* > 0.1$) phase transition taking place at temperatures below the electroweak scale. However, the data do not show any strong preference between an SMBHB and a PT generated signal, but we expect to gain additional discriminating power with future datasets, improving the signal to noise ratio and extending the sensitivity window to lower frequencies. In particular, data from the International Pulsar Timing Array will allow the baseline of observations to be significantly extended, and the number of monitored pulsars to be greatly expanded. The present quality of the data is such that our results are not strongly affected by theoretical uncertainties on the GW spectral shape. However, methodological improvements on determining the origin of the GWB spectrum will be needed for future datasets in order to separate the signal from a first-order PT

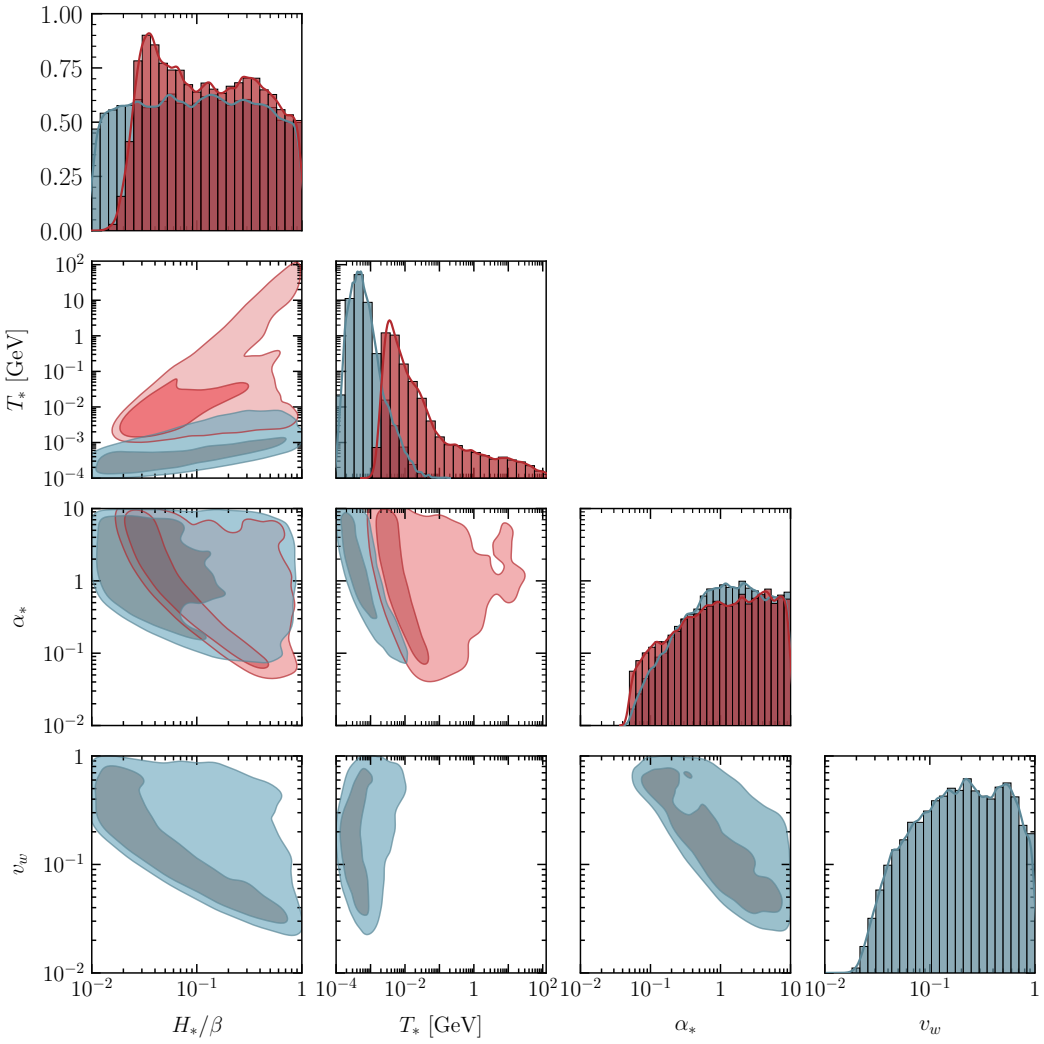

Figure 4.4: Corner plot showing the 1D and 2D posterior distributions for the parameters of the PT-only search. In red (blue) the results for the BO (SWO) analyses. In deriving these results we have used the semi-analytic bubble spectral shape with $(a, b, c) = (1, 2.61, 1.5)$.

from the SMBHB background, as well as to constrain the microscopic origins of the PT.

4.6 Facilities and Software Used in the Analysis

Facilities Arecibo, GBT

Software — `ENTERPRISE` [248], `enterprise_extensions` [172], `HASASIA` [249], `libstempo` [250], `matplotlib` [251], `PTMCMC` [252], `tempo` [253], `tempo2` [254], `PINT` [255]

Chapter 5

OBSERVATIONS OF A LONG-RANGE DARK MATTER-BARYON INTERACTION USING NEUTRON STAR KINETIC HEATING AND PULSAR TIMING ARRAYS

This chapter is based on

[1] Moira I. Gresham, Vincent S. H. Lee, and Kathryn M. Zurek. "Astrophysical observations of a dark matter-Baryon fifth force". In: *JCAP* 02 (2023), p. 048. DOI: 10.1088/1475-7516/2023/02/048. arXiv: 2209.03963 [astro-ph.HE].

5.1 Introduction

A long-range fifth force between baryonic matter has long been the focus of both theoretical and experimental inquiry, as reviewed in Ref. [256]. If DM also interacts with baryons via an attractive fifth force, it induces a potential,

$$V_{\rm Yuk}(r) = -\tilde{\alpha}\frac{GMm_X}{r}e^{-r/\lambda}, \tag{5.1}$$

where m_X and M are the masses of the DM and a macroscopic baryonic object, respectively, when the sizes of both objects are much smaller than the force range, λ, and separation, r. This potential can arise from an effective interaction $\mathcal{L} \supset g_X\phi\bar{X}X + g_n\phi\bar{n}n$ where X and n are the effective DM and nucleon fields, and ϕ can be either a massive but very light scalar or vector field. The effective coupling in this simplified model is

$$\tilde{\alpha} \approx \frac{g_n g_X}{4\pi G m_n m_X}, \tag{5.2}$$

where the approximation holds well when the fifth force and gravitational binding energies are subdominant contributors to the mass, M. Here we have in mind that m_X could be the mass of a DM particle, or a macroscopic DM object such as a nugget of asymmetric DM [257, 258, 259, 260, 261, 262, 263, 264].

The goal of this paper is to consider the astrophysical observables of such a DM-baryon fifth force [1], focusing on a few simple tests that constrain such an interaction. Focusing on astrophysical tests implies that we are interested in force ranges $20\,\text{km} \ll \lambda \ll$ kpc, corresponding to (ultralight) mediator masses

[1] A recent work on long-range DM-baryon fifth force with a different set-up can be found in [265].

$10^{-11}\,\mathrm{eV} \gg m_\phi \gg 10^{-26}\,\mathrm{eV}$.[2] Firstly, one must consider the constraints separately on g_n and g_X, which are dominated by the MICROSOPE mission's weak equivalence principle (WEP) test [266, 267] and DM self-interactions [78, 79, 268], respectively. Combining these constraints allows one to derive a bound on $\tilde{\alpha}$, shown in Fig. 5.1 as "bullet cluster + WEP" for two different astrophysical force ranges. Note, importantly, that this combination of bounds will lift quickly for a DM sub-component, only weakly constrained by observations of DM halos.

The majority of this paper will focus on a pair of constraints that weaken only linearly with the DM density for a DM sub-component. These come from heating of neutron stars (NSs) from DM capture, and pulsar timing measurements of transiting DM clumps, where DM passing near pulsars enhance the Doppler effect on the pulsar frequencies [269, 270, 151, 271, 272, 273, 274, 103, 43, 42, 9, 10]. These two constraints on the DM-baryon fifth force, which we derive in detail below, are summarized in Fig. 5.1, labeled as "heating" and "PTA." The heating constraints are further shown for two different limits: first, where the DM interactions beyond gravity are only via the fifth force (labeled as "tidal"), and, second, where the DM has not only the fifth force to focus it onto the NS but also a short range interaction to capture it with high efficiency (labeled as "maximal"). In Fig. 5.1 we also show constraints from microlensing surveys, which rule out DM with $M > 10^{-11}\,M_\odot$ and radii less than ~ 0.1 solar radius [147]. This is relevant for our kinetic heating analysis, since we assume that each DM is smaller than the size of a typical NS. The PTA constraints, however, are unaffected by the microlensing bounds, since the PTA analysis only assumes DM to be smaller than the impact parameter relative to the NS, which are at least $b > 2.5 \times 10^4$ solar radii for $M > 10^{-11}\,M_\odot$ (cf. Eq. (5.41)), and thus cannot be effectively constrained by microlensing studies.

Heating of NSs via DM capture has been considered previously for the case of a short-range interaction, such as for WIMPs and hidden sector DM [275, 276, 277, 278, 279, 280, 281, 282, 283, 284, 285, 286, 287, 286, 288, 289, 290, 291, 292, 293, 294]. However, when the force range is longer than a typical NS diameter, $\lambda > 20\,\mathrm{km}$ ($m_\phi < 10^{-11}\,\mathrm{eV}$), a DM-baryon force accelerates and focusses DM more than through gravity alone, leading to observable effects via two different mechanisms which we compute in detail. First, more DM is focussed on the NS due to the fifth force. Second, the DM is more energetic when it arrives at the NS surface, which we show then dominantly heats the NS via seismic oscillations.

[2] Above the kpc scale, torsion balance tests of differential accelerations toward the galactic center limit the baryon-DM force to be weaker than gravity. The lower limit is set by neutron star diameters.

We then extract the heating constraints utilizing the coldest observed NS (PSR J2144-3933, from Hubble Space Telescope) by requiring that the kinetic energy of all the captured DM raise the temperature by an amount less than the observed (unredshifted surface) temperature, $T_s < 42,000$ K [295].

The rest of the paper is devoted to deriving in detail the constraints on the DM-baryon fifth force coupling $\tilde{\alpha}$ outlined in Fig. 5.1. In Sec. 5.2, we derive the kinetic heating rate and resulting NS luminosity in the presence of a fifth force interaction. Some of the details are relegated to Appendices. In Sec. 5.3, we outline the procedure for deriving fifth force constraints with PTA observations, and show the results using the 11-year dataset [296, 297] by NANOGrav [298]. In Sec. 5.4, we consider observations from WEP tests and the bullet cluster, and derive indirect upper limits on the DM-baryon interaction. Finally, in Sec. 5.5, we conclude.

5.2 Limits from NS Temperature Observations

Transiting DM can heat NSs to higher-than-expected temperatures observable by the next generation of infrared telescopes, including the James Webb Space Telescope (JWST) [275]. As discussed in [275], if the energy deposited by DM passing near a NS is dissipated through black-body radiation, then in the local rest frame of the NS, the thermal photon luminosity due to dark kinetic heating is $L_\gamma^{\rm DM} = \dot{E}_{\rm kin}$. Given an unredshifted surface temperature measurement $T_{{\rm s},i} \leq T_{{\rm s},i_{\rm max}^{\rm meas}}$ for a particular NS, i, with radius, R, we can infer a limit on the factors contributing to $\dot{E}_{\rm kin}$ through[3]

$$\dot{E}_{\rm kin} < \sigma_{\rm B} 4\pi R^2 \left(T_{{\rm s},i_{\rm max}^{\rm meas}}\right)^4, \tag{5.3}$$

where the heating rate is schematically given by

$$\dot{E}_{\rm kin} \approx \dot{N} \Delta E, \tag{5.4}$$

with $\dot{N}$ and ΔE being the relevant DM flux and single-DM energy transfer, respectively.

All previous analyses of DM kinetic heating of NSs have focused on short-range DM interactions. As explained in [275], in this case, DM can deposit energy on a NS only if it intersects the NS, requiring impact parameters less than $b_{\rm max}^{\rm grav} = v^{-1}\sqrt{2GMR/(1-2GM/R)}$. At a maximum, an order one fraction of DM that intersects the NS is captured and deposits all of its kinetic energy at the NS surface,

[3] Redshifted surface temperature, T^∞, is related to unredshifted temperature, T, through $T = \frac{T^\infty}{\sqrt{1-\frac{2GM}{R}}}$.

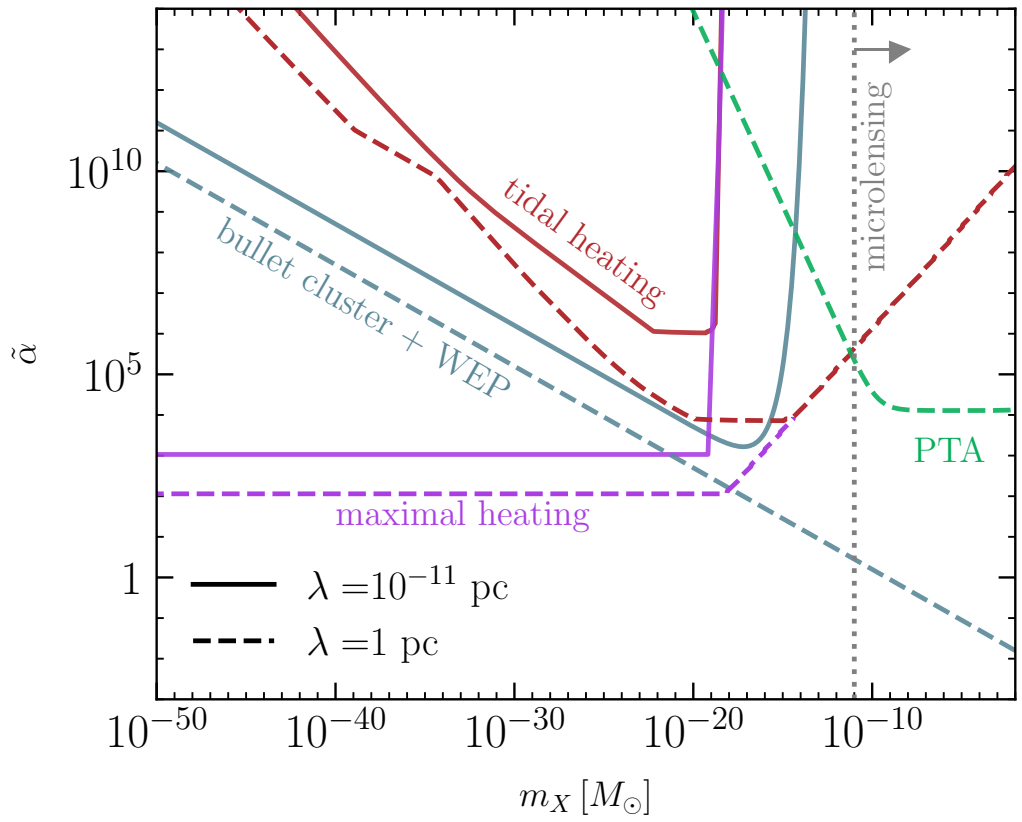

Figure 5.1: Summary of the bounds derived in this paper on the DM-baryon fifth force to gravitational force strength ratio, $\tilde{\alpha}$, as defined in Eq. 5.1, for force ranges, λ, at the two extremes of the range we consider. The relevant equations for tidal heating, maximal heating, PTA, and bullet cluster + WEP are derived in Sec. 5.2-5.2, Sec. 5.2, Sec. 5.3, and Sec. 5.4 respectively. Bound from microlensing surveys is shown in a gray line, which apply to compact DM with radii less than ~ 0.1 solar radius [147].

also known as the gravitational binding energy released in the capture process. Hence $\Delta E^{\rm grav}_{\rm max} \approx GMm_X/R$ and $\dot{N}^{\rm grav}_{\rm max} \approx (\rho_X/m_X)\pi\langle b^2_{\rm max} v\rangle$, leading to a maximum heating rate from DM focused by gravity onto typical NSs near our galactic radius ($GM/R \sim 0.2$, $\langle v\rangle \sim 10^{-3}$, $\rho_X \sim 0.4\,{\rm GeV/\,cm^3}$),

$$\dot{E}^{\rm grav}_{\rm kin,\,max} \approx \frac{GMm_X}{R}\pi\frac{\rho_X}{m_X}\langle \left(b^{\rm grav}_{\rm max}\right)^2 v\rangle \approx 4\pi R^2\sigma_{\rm B}(2000{\rm K})^4. \tag{5.5}$$

Therefore measured (unredshifted) surface temperatures of nearby NSs below about 2000K can start to constrain short-range interactions of DM with NS matter. Conversely, finding several old isolated neutron stars with temperatures of order 2000K and greater near our Galactic radius—with higher temperatures in DM-rich regions—could be a sign of DM kinetic heating.

We now consider a long-range ($> 20\,\mathrm{km}$) fifth force, which changes the heating rate calculation, Eq. (5.4), in three ways. First, more DM is focussed and potentially captured by the NS (larger $b_{\max}$).[4] Second, the DM's kinetic energy near the NS surface—roughly equivalent to the DM-NS binding energy—is larger, meaning more energy is dissipated in a DM capture process (larger ΔE).[5] Third, the energy deposition mechanism is qualitatively different due both to the long-range force and ultrarelativistic DM speeds at the NS surface; collective excitations of NS matter are particularly important.

We divide DM contributing to heating into two groups:

A. *Grazing* DM, including NS-transiting DM that is not gravitationally captured, as well as gravitationally bound DM whose first orbital period after capture is greater than the NS lifetime, implying no subsequent energy deposits within the NS's lifetime.

B. *Captured* DM, which deposits sufficient energy to become gravitationally bound on its first transit and deposits further energy on subsequent transits within the NS lifespan.

The total heating rate for a long-range interaction is thus

$$\dot{E}_{\mathrm{kin}} \approx \dot{E}_{\mathrm{graze}} + \dot{E}_{\mathrm{cap}} \tag{5.6}$$

with $\dot{E}_{\mathrm{graze}} \approx \dot{N}_{\mathrm{graze}} \Delta E_{\mathrm{graze}}$ and $\dot{E}_{\mathrm{cap}} \approx \dot{N}_{\mathrm{cap}} \Delta E_{\mathrm{cap}}$. Below in Secs. 5.2-5.2, we derive explicit estimates of $\Delta E_{\mathrm{graze}}$, $\dot{N}_{\mathrm{graze}}$, ΔE_{cap}, and $\dot{N}_{\mathrm{cap}}$ in Eqs. 5.7, 5.12, 5.16, and 5.19, respectively. Then in Sec. 5.2 we discuss the maximal heating rate, analogous to Eq. 5.5, requiring assistance by additional short-range forces. In Sec. 5.2 we estimate when heating is effectively continuous and possibly destructive to the NS, which is relevant at the higher mass scales we consider. Finally, in Sec. 5.2, we present limits based on our estimates and Eq. 5.3.

Grazing heating rate

$\Delta E_{\mathrm{graze}}$

Two stars in a close encounter can become bound by sinking energy and angular momentum into seismic oscillations of the stars through gravitational tidal forces

[4] A repulsive interaction would defocus DM and reduce the maximum possible kinetic heating rate. Here we focus on the attractive case.

[5] Similar effects on Earth could be relevant for direct detection, and were discussed in [299, 300].

[301, 302]. Pani and Loeb [303] considered a similar capture mechanism for primordial black holes (PBHs) by NSs. They modeled PBHs as point-like objects that remain intact as they transit the NS, and found that tidally deposited energy exceeds energy deposit through dynamical friction by several orders of magnitude. A small, compact DM object should behave similarly, and an additional Yukawa force with range much larger than the NS radius will simply effectively increase the strength of the gravitational tidal forces by a factor $1 + \tilde{\alpha}$.

Based on [303], we estimate the energy deposited through tidal excitation of NS seismic oscillations by DM that transits an NS as

$$\Delta E_{\rm graze} \approx \frac{G m_X^2 (1+\tilde{\alpha})^2}{R} 4\sqrt{l_{\rm max}} \tag{5.7}$$

where $l_{\rm max}$ corresponds to the largest spherical seismic mode excited in the NS. Qualitatively, thinking of the NS like a spring, the energy goes as the square of the amplitude of the oscillation, which is set by the maximum tidal force at close approach—proportional to $(1 + \tilde{\alpha})m_X$. The stiffness of the NS equation of state determines the nontrivial dependence on mode number. We refer the reader to [303] for details.

Ref. [303] considers many possible cutoffs for $l_{\rm max}$. The limiting cutoffs come from demanding the particle size, R_X, is smaller than the mode's wavelength, leading to $l_{\rm max} < R/R_X$, and that the DM crossing time, $\tau_{\rm cross} \sim R/\beta_R \sim R$, is short compared to the shear viscosity oscillation damping timescale [304],

$$\tau_\eta \approx \frac{\rho R^2/\eta}{(l-1)(2l+1)}, \tag{5.8}$$

where η is the shear viscosity, and ρ is the mass density of the NS. For cold NSs with $T < 10^8$K, in which neutrons and protons are expected to be superfluid (at least outside the inner core of the NS, where the tidally-induced oscillations are supported) the dominant source of viscosity is from electron scattering, η_e [305]. To within an order of magnitude, for a given temperature, the maximal value of η_e/ρ occurs around $\rho \sim 10^{10}$–$4 \times 10^{14} \frac{\rm g}{\rm cm^3}$, and is [306, 307]

$$\left(\frac{\eta_e}{\rho}\right)_{\rm max} \approx \left(\frac{T}{10^8 {\rm K}}\right)^{-2} 10^4 {\rm cm}^2/{\rm sec}, \tag{5.9}$$

leading to an estimate

$$l_{\rm max} \sim \min\left(10^2 \left(\frac{T}{10^4 {\rm K}}\right), \frac{R}{R_X}\right) \tag{5.10}$$

for DM that is relativistic (and ultrarelativistic) at the NS surface, with the consistency requirement, $l_{\max} > 1$. For simplicity and consistency, we consider only DM and NSs with

$$\frac{R_X}{R} < 10^{-2}\frac{10^4\mathrm{K}}{T} < 1 \qquad \text{and} \qquad T < 10^8\mathrm{K} \tag{5.11}$$

such that the shear viscosity timescale determines the highest excited mode number. For maximally compact (i.e. $\frac{Gm_X}{R} \sim 1/2$) DM objects, this requires $m_X \lesssim 10^{-2}\frac{10^4\mathrm{K}}{T}M_\odot < M_\odot$. The cutoff occurs at lower mass for less compact DM.

A few other factors deserve mention. First, our estimate based on [303] is consistent only if both the DM and NS survive the DM's transit. For DM to survive, the Roche distance—where the tidal forces on the DM from the NS start to exceed the binding forces—must be smaller than the NS radius. Depending on the forces binding the DM, the DM must be sufficiently compact.[6] Energy deposits comparable to a few percent of the NS's gravitational binding energy could also destroy the NS. We discuss this case further in Secs. 5.2 and 5.2.

Second, the estimate Eq. 5.7 is based on analyzing a particle's infall from rest. But as discussed in [303], it should be a decent estimate for particles with other trajectories as long as they breach or come close to breaching the NS surface. On the other hand, at distances, r, large compared to R, the tidal force falls off as r^{-3} and effective crossing times lengthen when $r_{\min} \gg R$. Indeed estimates of gravitational tidal capture for close star encounters as in [301] apply in this case, and the moral is that a good estimate of heating and capture comes from counting only DM that intersects the NS, with $\Delta E_{\mathrm{graze}}$ as in Eqs. 5.7 and 5.10 for all such DM.

$\dot{N}_{\mathrm{graze}}$

The number of DM particles of mass m_X and asymptotic mass density ρ_X passing through a given NS per time—the flux—is

$$\dot{N}_{\mathrm{graze}} = \frac{\rho_X}{m_X}\pi\langle b_{\max}^2 v\rangle. \tag{5.12}$$

Given focusing through gravity alone, $\dot{N}_{\mathrm{graze}} \sim \frac{10^{-24}}{\mathrm{yr}}\frac{\rho_X}{0.4\,\mathrm{GeV/\,cm^3}}\left\langle\frac{10^{-3}}{v}\right\rangle\frac{M_\odot}{m_X}\frac{R}{10\,\mathrm{km}}\frac{GM}{2\,\mathrm{km}}$. An attractive DM-NS fifth force focuses more DM onto a NS, leading to a significantly larger flux via larger $b_{\max}$. For moderate $\tilde{\alpha}$ and $\lambda \gg R$, compared to focusing

[6] Modeling the DM binding force per mass as proportional to $\frac{(\tilde{\alpha}_{X,\mathrm{eff}}+1)Gm_X}{R_X^2}$ on the DM surface, given $R_X \ll R$, the Roche distance is approximately $r_{\mathrm{Roche}} \sim \left(4\frac{(1+\tilde{\alpha})M}{(1+\tilde{\alpha}_{X,\mathrm{eff}})m_X}\right)^{1/3}R_X$, and in terms of the DM and NS compactnesses, the DM can survive only if $\frac{Gm_X}{R_X} > 4\frac{(1+\tilde{\alpha})}{(1+\tilde{\alpha}_{X,\mathrm{eff}})}\frac{GM}{R}\left(\frac{R_X}{R}\right)^2$.

through gravity alone, $b_{\max}$ is larger by a factor $\sqrt{1+\tilde{\alpha}}$. When $\tilde{\alpha} \gg 1$, $b_{\max}$ grows linearly with $\tilde{\alpha}$ until a cutoff where an *outer* centrifugal barrier at $r > \lambda$ from the exponential turn-on of the fifth force becomes stronger than the always-present *inner* centrifugal barrier. More specifically, when $\tilde{\alpha} \gg 1$,

$$b_{\max} v \sim \begin{cases} GM\tilde{\alpha} & \text{inner barrier} \\ \sqrt{2GM\lambda \log\left(\tilde{\alpha} \log \tilde{\alpha}\right)} & \text{outer barrier when } \tilde{\alpha} e^{-GM/\lambda v^2} < 1 \\ \lambda v \log\left(\frac{\tilde{\alpha} GM}{\lambda v^2}\right) & \text{outer barrier otherwise,} \end{cases} \tag{5.13}$$

with $b_{\max} = \min(b_{\max,\,inner}, b_{\max,\,outer})$ if $\tilde{\alpha} GM/\lambda v^2 \gtrsim e$ and $b_{\max} = b_{\max,\,inner}$ otherwise. In Appendix D, we derive the general relativistic equation of motion that determines $b_{\max}$ in Eqs. D.2-D.5 along with analytic approximations in Eqs. D.6-D.8; Fig. D.2 shows our analytic approximations alongside numerical solutions to the exact barrier-determining expressions.

Captured heating rate

$\Delta E_{\rm cap}$

The energy deposited per DM particle captured is approximately the DM kinetic energy at the NS surface,

$$E_{\rm DM,\,kin}(R) \approx m_X(\gamma_R - 1). \tag{5.14}$$

with

$$\gamma_R = \frac{\frac{1}{\sqrt{1-v^2}} + \tilde{\alpha}\frac{GM}{R} e^{-R/\lambda}}{\sqrt{1-\frac{2GM}{R}}} \approx \frac{1 + \frac{GM}{R}\tilde{\alpha} e^{-R/\lambda}}{\sqrt{1-\frac{2GM}{R}}} \approx 1 + \frac{GM}{R}\left(1 + \tilde{\alpha} e^{-R/\lambda}\right) \tag{5.15}$$

as measured in a locally flat frame at the NS surface. Since DM asymptotic speeds, v, are generally much less than the escape speed at the NS surface, the energy deposit is essentially independent of v. Without a fifth force, γ_R is given by Eq. (5.15) but with $\tilde{\alpha} = 0$, which for typical neutron stars and DM with $v \ll 1$, is $\gamma_R \sim (1 - \frac{2GM}{R})^{-1/2} \sim \sqrt{5/3}$. With a fifth force, $\gamma_R - 1$ is larger by about a factor of $1 + \tilde{\alpha} e^{-R/\lambda}$.

If the period of the first orbit after capture, Δt_1, is greater than NS lifetime, then the DM deposits only energy $\Delta E_{\rm graze}$ within the NS lifetime. Hence, we cannot simply use the expression for $E_{\rm DM,\,kin}(R)$ in Eq. (5.14) for $\Delta E_{\rm cap}$. Instead, we use an empirical formula for $\Delta E_{\rm cap}$ to smoothly interpolate between different limits of

$\Delta t_1/t_{\rm NS}$, written as

$$\Delta E_{\rm cap} \approx \left(\frac{\Delta E_{\rm graze}}{E_{\rm DM,\,kin}(R)}\right)^{\Delta t_1/t_{\rm NS}} E_{\rm DM,\,kin}(R) \qquad (\text{when } \Delta E_{\rm graze} \ll E_{\rm DM,\,kin}(R))\,. \tag{5.16}$$

We now justify this expression. If $\Delta t_1 \gg t_{\rm NS}$, then DM would not have enough time to deposit energy into NS, and we expect $\Delta E_{\rm cap} \to 0$. In the opposite limit where $\Delta t_1 \ll t_{\rm NS}$, DM has ample time to transfer all its energy and be completely captured by the NS, hence one expects $\Delta E_{\rm cap} = E_{\rm DM,\,kin}(R)$. Finally, if $\Delta t_1 \sim t_{\rm NS}$, then we expect DM to deposit some but not all of its kinetic energy to the NS, since the DM is not fully captured by NS. Effectively, the DM grazes the NS once. It is thus appropriate to approximate $\Delta E_{\rm cap} \sim \Delta E_{\rm graze}$ in this scenario. One can easily check that the empirical formula in Eq. (5.16) is a smooth function that reduces to these three limits. In the case where $\Delta t_1 \gtrsim t_{\rm NS}$, the DM is counted as "grazing" DM.[7] We estimate the orbital period in Appendix E; see Δt_1 in Eqs. (E.4)-(E.5).

Using Eqs. 5.7, 5.10, 5.14, and 5.15, we see $\Delta E_{\rm graze} < E_{\rm DM,\,kin}(R)$ as long as $\frac{m_X}{M}(1+\tilde{\alpha})40\sqrt{\frac{T}{10^4{\rm K}}} < 1$. The condition saturates when $\Delta E_{\rm graze} \approx E_{\rm DM,\,kin}(R) \approx \sqrt{\frac{10^4{\rm K}}{T}}\frac{1}{40}\frac{GM^2}{R}$, or when the energy deposit is about 10% of the NS binding energy ($\sim \frac{3}{5}\frac{GM^2}{R}$) given $T \sim 42,000{\rm K}$. We expect such an energy deposit to destroy the NS rather than "heat" it, as we will discuss further in Sec. 5.2. Therefore $\Delta E_{\rm graze} < E_{\rm DM,\,kin}(R)$ holds as long as the kinetic heating limit is relevant.

$\dot{N}_{\rm cap}$

To become gravitationally bound to the NS, DM must lose sufficient energy when it first grazes the NS surface. Thus the capture rate is approximately

$$\dot{N}_{\rm cap} \approx \frac{\rho_X}{m_X}\pi\langle b_{\rm max}^2 v\rangle_{v<v_{\rm cap}}, \tag{5.17}$$

where the average is over asymptotic DM speeds up to a the maximum speed of DM that is captured:

$$v_{\rm cap} = \sqrt{2\Delta E_{\rm graze}/m_X}. \tag{5.18}$$

Given a Maxwellian velocity distribution with peak speed v_p, since $(b_{\rm max}v)$ is nearly constant as function of v—increasing negligibly for most or our parameter range of

[7] Note the first energy deposit of captured DM is double counted in $\dot{E}_{\rm graze}$ and $\dot{E}_{\rm cap}$, which is acceptable for an order-of-magnitude estimate since it will at most overestimate the heating effect by a factor of two, and in most cases by a only a tiny fraction over one.

interest and less than linearly in the entire range—to reasonable approximation,

$$\dot{N}_{\rm cap} \approx \frac{\rho_X}{m_X}\pi(b_{\rm max}v)^2|_{v\to\min(v_p,v_{\rm cap})}\frac{2}{\sqrt{\pi}v_p}f \tag{5.19}$$

where

$$f \approx \left(1 - e^{-v_{\rm cap}^2/v_p^2}\right) \tag{5.20}$$

roughly represents the fraction of surface-breaching DM that is captured. We can also use Eq. (5.19) to estimate $\dot{N}_{\rm graze}$ by taking $v_{\rm cap} \to 1$.

Capture assisted by short-range interactions

We have just described a capture mechanism through DM's tidal force excitation of seismic oscillations in an NS—classical collective modes stretching over the entire NS. In contrast, most previous treatments of kinetic heating have focussed on effectively local interactions of DM with one or more individual nucleons or leptons within the NS during a transit [275, 276, 277, 278, 279, 280, 281, 282, 283, 284, 285, 286, 287, 286, 288, 289, 290, 291, 292, 293, 294]. A notable exception is [308], which focuses specifically on collective effects within dense stellar media in DM scattering.

Relative to the case without a fifth force, when the fifth force increases DM's speeds in the NS rest frame (c.f. Eq. 5.15), the kinematic upper limit on energy transfer to nucleons in elastic DM-nucleon interactions also increases. At the same time, length contraction of the NS in the DM-nucleon CM frame can be significant, so it is easier for the de Broglie wavelength of the CM motion ($q^{-1} \sim 1/\sqrt{2m_n\Delta E_{\rm graze}}$) to be larger than the inter-nucleon distance along the direction of motion in the CM frame. Thus while the increased CM energy might naively increase nucleon-DM elastic cross sections, the range of kinematically allowed energies where nucleons are effectively free is also narrower. When the DM is ultrarelativistic at the NS surface, we expect proper treatment of collective effects in NS matter to be particularly important in a treatment of DM scattering via short-range forces.

Rather than trying to model specific short-range interactions and account for the relevant microscopic NS physics that determines the probability of capture, we consider maximal heating, where an order one fraction of transiting DM is captured. In this case,

$$\dot{E}_{\rm kin,\,max} \approx E_{\rm DM,\,kin}(R)\dot{N}_{\rm graze} \tag{5.21}$$

with $E_{\rm DM,\,kin}(R)$ given by Eq. 5.14 and $\dot{N}_{\rm graze}$ by Eq. 5.12.

Cooling timescale and continuous heating approximation

NSs are born with internal temperatures of order 10^{11} K and rapidly cool through neutrino and photon emission to under 10^7 K within about 1000 years. Without additional sources of heating, NSs are expected to cool to under 1000 K within about 20 Myr (see *e.g.* [309, 310]). Under temperatures of order 10^6 K, photon emission dominates, and nucleons in at least the inner crust and outer core of such cold stars are thought to be superfluid. The heat capacity (per unit volume) of such very cold NS's is dominated by ultrarelativistic, degenerate electrons, and is given by [311]

$$c_{V,e} \approx \frac{p_{\mathrm{F}e}^2 k_{\mathrm{B}}^2 T}{3} = \frac{(3\pi^2 n_e)^{2/3} k_{\mathrm{B}}^2 T}{3}. \tag{5.22}$$

Given heating only through DM kinetic heating, and black-body-radiation-dominated cooling, the NS temperature evolves in time according to

$$C_V \frac{dT}{dt} = \dot{E}_{\mathrm{kin}} - 4\pi R^2 \sigma_B T^4. \tag{5.23}$$

Without a heat source, using the relations above and approximating the NS as roughly uniform temperature throughout, we approximate the timescale to cool from a higher temperature T_h to a lower temperature of order T_l below 10^6K as

$$t_{\mathrm{c}}(T_l) \sim \frac{R(3\pi^2 n_e)^{2/3} k_{\mathrm{B}}^2}{18\sigma_B T_l^2}\left(1 - \left(\frac{T_l}{T_h}\right)^2\right) \sim 10^4\,\mathrm{yr}\left(\frac{10^4\mathrm{K}}{T_l}\right)^2\left(1 - \left(\frac{T_l}{T_h}\right)^2\right) \tag{5.24}$$

where we set the electron density to a typical value in the NS outer core, $n_e \sim 0.01\mathrm{fm}^{-3}$. To set a kinetic heating limit based on a maximum temperature, T, we require a deposit rate (flux) comparable to or greater than one per cooling time, $\dot{N} \gtrsim 1/t_c(T)$.

Going the other way, the temperature, T_h, to which a NS is heated from temperature T_l through an energy deposit ΔE is given by

$$\Delta E = \int C_V dT \sim \frac{4\pi R^3}{3}\frac{(3\pi^2 n_e)^{2/3} k_{\mathrm{B}}^2}{6}(T_h^2 - T_l^2) \sim 5\times 10^{-14}\frac{GM^2}{R}\frac{T_h^2 - T_l^2}{(10^6\mathrm{K})^2} \tag{5.25}$$

where the last expressions apply when both temperatures are below 10^6 K. The heat capacity rises by a factor of 20 or so at higher temperatures, and we can see that $\Delta E \gtrsim 10^{-2}\frac{GM^2}{R}$, approaching the gravitational binding energy of a NS, roughly heats a NS back above its temperature at birth ($\sim 10^{11}$ K). We expect a single energy deposit of order $10^{-2}\frac{GM^2}{R}$ or greater to destroy a NS. So the mere existence of a cold

NS of age $t_{\rm NS} > \dot{N}_{\rm cap}^{-1}$ limits

$$\frac{\Delta E_{\rm graze}}{10^{-2} G M^2/R} \sim 10^4 \left(\frac{m_X}{M}\right)^2 (1+\tilde{\alpha})^2 \sqrt{\frac{T}{4.2{\rm kK}}} < \frac{E_{\rm DM,\,kin}(R)}{10^{-2} G M^2/R} \sim 10^2 \frac{m_X}{M}(1+\tilde{\alpha}) < 1. \tag{5.26}$$

Limits

Here we present limits based on Eq. 5.3 for the coldest presently known NS [295], a slow, isolated pulsar located about 170 pc from Earth, with the observation upper limit on temperature $T_{{\rm s},i_{\rm max}^{\rm meas}} = 42,000$ K and age $t_{\rm NS} = 0.3$ Gyr. Without additional sources of heating, this NS should have cooled to temperatures below 1000 K within the first 10% of its life. Here we emphasize that the value $T_{{\rm s},i_{\rm max}^{\rm meas}} = 42,000$ K is an upper limit based on telescope observations, and is expected to tighten as observational techniques improve. The four panels in Fig. 5.2 show limits for four different force ranges, λ, spanning our range of interest. The thick black *tidal heating* limit lines result from our estimate of $\dot{E}_{\rm kin}$ in Eq. 5.6, as described in Secs. 5.2-5.2. The thick red *maximal kinetic heating* line results when an order one fraction of NS-transiting DM deposit their entire available energy over a NS lifetime, with a heating rate as in Eq. 5.21, requiring assistance from short-range forces as described in Sec. 5.2. We employed our analytic estimate of the impact parameter in Eqs. D.6-D.8 to calculate the relevant fluxes (Eqs. 5.12 and 5.19), and the limits assume asymptotic DM density $\rho_X = 0.4\,{\rm GeV/\,cm^3}$, a Maxwellian speed distribution peaked at $v_p \sim 10^{-3}$, and typical NS parameters $\frac{GM}{R} \approx 0.2$, $R \approx 10\,{\rm km}$. Below we explain the scaling of the limits, starting with the high-mass behavior and working to lower masses.

To set a limit based on Eq. 5.3 for a given maximum NS temperature T, we require the frequency of energy deposit events, $\dot{N}$, to be comparable to or greater than the inverse cooling timescale, $1/t_{\rm c}(T)$, in Eq. 5.24. This requirement determines the high-mass cut-off for the limit, shown by the thin purple "flux <1/(cooling time)" lines in Fig. 5.2. Using Eq. 5.12, and assuming a Maxwellian speed distribution with peak speed v_p, the high-mass limit reads,

$$\dot{N}_{\rm graze} t_{\rm c} \sim 6 \times 10^{-22} \left(\frac{t_c}{500\,yr}\right) \left(\frac{R}{10\,km}\right)^2 \left(\frac{10^{-3}}{v_p}\right) \left(\frac{M_\odot}{m_X}\right) \left(\frac{(b_{\rm max} v)|_{v_p}}{R}\right)^2 < 1. \tag{5.27}$$

where fiducial quantities in the parentheses are used to obtain our Fig. 5.2 and we have taken here (and throughout) $\rho_X = 0.4\,{\rm GeV/cm^3}$. Note that $t_c(T_l = 42\,kK) \sim$

500 years according to Eq. 5.24. Here, $b_{\rm max}$ is given in Eqs. D.6-D.8 and Fig. D.2, and its scaling with $\tilde{\alpha}$ depends on whether it is determined by the inner or outer barrier, as indicated by the brown horizontal dashed lines in the figure.[8] Eq. 5.13 gives the scaling of $b_{\rm max}$ in various regimes.

The grazing and capture fluxes are approximately equal at the highest constrained masses, where $v_{\rm cap} \sim 5(1+\tilde{\alpha}) \left(\frac{m_X}{M_\odot}\right)^{1/2} \left(\frac{T}{42\,kK}\right)^{1/4} \left(\frac{10\,km}{R}\right)^{1/2} \gtrsim v_p$ (see Eqs. 5.7, 5.10, and 5.18). The tidal heating limit curves break away from the $\dot{N}_{\rm graze} = 1/t_{\rm c}$ curves where $v_{\rm cap} < v_p$, below the dashed blue lines in Fig. 5.2. When $v_{\rm cap} < v_p$, the flux-limited limit follows

$$\begin{aligned} &\dot{N}_{\rm cap} t_{\rm c} \\ &\sim 10^{-14}(1+\tilde{\alpha})^2 \left(\frac{t_c}{500\,yr}\right)\left(\frac{R}{10\,km}\right)\left(\frac{T}{42\,kK}\right)^{1/2}\left(\frac{10^{-3}}{v_p}\right)^3\left(\frac{(b_{\rm max}v)|_{v_{\rm cap}}}{R}\right)^2 < 1\,. \end{aligned} \tag{5.28}$$

For lower masses, the limit applies in parameter regions with continuous heating, and when $\dot{E}_{\rm cap} \gg \dot{E}_{\rm graze}$ (see Eqs. 5.6, 5.7, 5.12, 5.16, and 5.19), the limit reads

$$\begin{aligned} &\frac{\dot{E}_{\rm cap}}{L_\circ} \\ &\sim 2\times 10^2 (1+\tilde{\alpha})^3 \left(\frac{M}{1.4\,M_\odot}\right)\left(\frac{T}{42\,kK}\right)^{1/2}\left(\frac{10\,km}{R}\right)^2\left(\frac{10^{-3}}{v_p}\right)^3\left(\frac{m_X}{M_\odot}\right)\left(\frac{(b_{\rm max}v)|_{v_{\rm cap}}}{R}\right)^2 \\ &< \left(\frac{T_{{\rm s},i\,{\rm max}}^{\rm meas}}{42{\rm kK}}\right)^4, \end{aligned} \tag{5.29}$$

where $L_\circ = 4\pi R^2 \sigma_B (42{\rm kK})^4$, and the scaling of $(b_{\rm max}v)|_{v_{\rm cap}}$ with $\tilde{\alpha}$ again depends on whether the outer or inner barrier determines $b_{\rm max}$. For Fig. 5.2, the relevant relationships are $b_{\rm max}v \sim GM\tilde{\alpha}$ for the inner barrier and $b_{\rm max}v \sim \sqrt{2GM\lambda \log(\tilde{\alpha}\log\tilde{\alpha})}$ for the outer.

The thin green "period > NS age" lines in Fig. 5.2 are the contours $\Delta t_1 = t_{\rm NS}$ with Δt_1 as in Eq. E.6. Heating from captured DM goes to zero when $\Delta t_1 > t_{\rm NS}$ (c.f. Eq. 5.16), explaining why the limit asymptotes to this contour in the first three panels of Fig. 5.2 at low DM masses. Using the results in Appendix E, for

[8] In the first three panels, we show the transition for $b_{\rm max}|_{v_{\rm cap}}$ and in the last the dashed line corresponds to the transition for $b_{\rm max}|_{v_p}$.

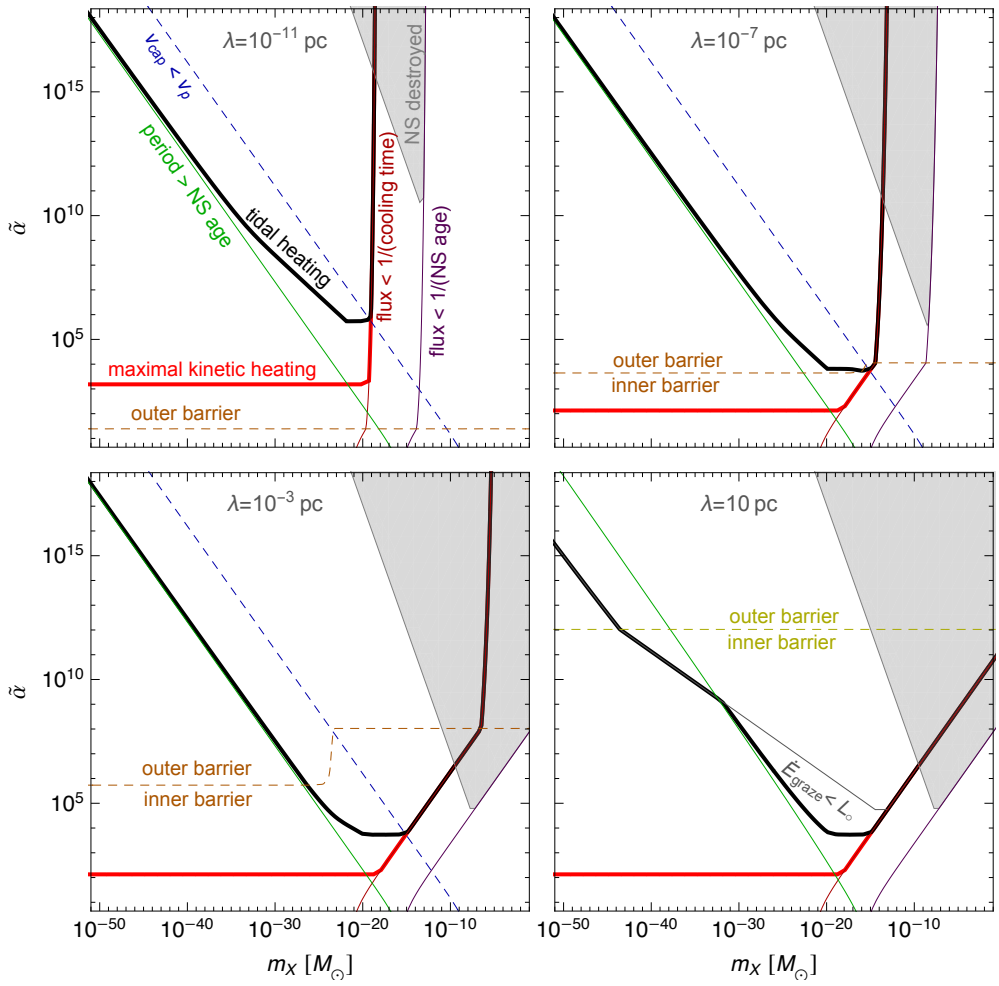

Figure 5.2: Limit on an attractive NS-DM fifth force (Eq. 5.1) for four representative force ranges, λ, from *tidal* kinetic *heating* of the coldest known NS with temperature $T < 4.2$kK and age 0.3 Gyr (black). In Sec. 5.2 we explicitly explain how limits were derived in several regimes, beginning at high mass. Eqs. 5.27, 5.28, 5.29, and 5.30 determine the limits in the first three panels from high to low mass, respectively, and Eq. 5.31 applies at the lowest masses in the last panel. The thick red *maximal kinetic heating* curve assumes 100% of transiting DM is captured and deposits energy quickly through additional short-range forces, leading to Eq. 5.32 at low masses. In the gray regions, the old NS would have been destroyed by a single DM encounter (see Eq. 5.26).

$\lambda \ll (\sqrt{GM}t_{\rm NS})^{2/3} \sim 10\,{\rm pc}\left(\frac{t_{\rm NS}}{\rm Gyr}\right)^{2/3}$, the $\Delta t_1 > t_{\rm NS}$ asymptote corresponds to

$$\begin{aligned}\frac{t_{\rm NS}}{\Delta t_1} &= \frac{t_{\rm NS}}{GM}\frac{\sqrt{2}}{\pi}\left(\frac{\Delta E_{\rm graze}}{m_X}\right)^{3/2} \\ &\approx 3\times 10^{22}(1+\tilde{\alpha})^3\left(\frac{T}{42\,kK}\right)^{3/4}\left(\frac{1.4\,M_\odot}{M}\right)\left(\frac{10\,km}{R}\right)^{3/2}\left(\frac{t_{\rm NS}}{0.3\,{\rm Gyr}}\right)\left(\frac{m_X}{M_\odot}\right)^{3/2} \\ &< 1. \end{aligned} \tag{5.30}$$

In the last panel, at low masses the contour is instead controlled by heating from grazing encounters. When $\dot{E}_{\rm graze} \gg \dot{E}_{\rm cap}$, the limit is,

$$\begin{aligned}&\frac{\dot{E}_{\rm graze}}{L_\circ} \\ &\sim 4\times 10^{-4}(1+\tilde{\alpha})^2\left(\frac{T}{42\,kK}\right)^{1/2}\left(\frac{10\,km}{R}\right)\left(\frac{10^{-3}}{v_p}\right)\left(\frac{m_X}{M_\odot}\right)\left(\frac{(b_{\rm max}v)|_{v_p}}{R}\right)^2 \\ &< \left(\frac{T_{{\rm s},i}^{\rm meas}{}_{\rm max}}{42{\rm kK}}\right)^4 \end{aligned} \tag{5.31}$$

with $(b_{\rm max}v)|_{v_p}$ as in Eq. 5.13 for large $\tilde{\alpha}$. The thin gray "$\dot{E}_{\rm graze} < L_\circ$" contour in the last panel corresponds to saturation of Eq. 5.31 evaluated at the fiducial parameters.

When an order one fraction of transiting DM is captured and deposits its available energy quickly, kinetic heating is "maximal." When $\lambda \gg R$ and $\dot{N}_{\rm graze}t_{\rm c} > 1$, the limit reads

$$\begin{aligned}\frac{\dot{E}_{\rm kin,\,max}}{L_\circ} &\sim 6\times 10^{-6}(1+\tilde{\alpha})\left(\frac{M}{1.4\,M_\odot}\right)\left(\frac{10\,km}{R}\right)\left(\frac{10^{-3}}{v_p}\right)\left(\frac{(b_{\rm max}v)|_{v_p}}{R}\right)^2 \\ &< \left(\frac{T_{{\rm s},i}^{\rm meas}{}_{\rm max}}{42{\rm kK}}\right)^4. \end{aligned} \tag{5.32}$$

To one significant figure the maximal kinetic heating limit shown in red in Fig. 5.2 corresponds to

$$\tilde{\alpha} < 150 \qquad \text{when } \lambda \gtrsim 10^{-10}{\rm pc}, \tag{5.33}$$

$$\frac{\lambda}{R}\tilde{\alpha}\log\left(\tilde{\alpha}\log(\tilde{\alpha})\right) < 4\times 10^5 \qquad \text{when } R < \lambda \lesssim 10^{-10}{\rm pc}. \tag{5.34}$$

In Appendix F, we show that the kinetic heating limit above also rules out the possibility of observable pulsar glitches caused by angular momentum deposits of transiting DM.

Near-future measurements with infrared telescopes such as JWST should be able to improve NS surface temperature measurements by a factor of ten or better (see [275]). For smaller force ranges, tidal heating limits will not change much because they are bounded by the flux and energy deposit timescales (see Eqs. 5.27, 5.28 and 5.30) except in a narrow mass range, where Eq. 5.29 applies. The bound for larger λ will tighten at lower masses, according to Eq. 5.31. If the temperature of a cold NS were an order of magnitude lower, so $T_s \sim 4,200$K, the maximal kinetic heating limit (Eq. 5.32) becomes $\tilde{\alpha} \lesssim 2$ for all $\lambda \gtrsim R$. Recalling that the maximum heating rate of a typical local NS by DM focussed through gravity alone corresponds to $T_s \sim 2,000$K (see Eq. 5.5), we expected maximal kinetic heating to constrain a fifth force to gravitational strength or weaker for temperatures approaching this infrared range.

We now highlight some important caveats. First, DM-DM interactions become important to NS capture and heating at time $t_{\rm eq}$ when the effective charge of captured DM is comparable to the effective charge of baryons in the NS:[9] $\dot{N}_{\rm cap} t_{\rm eq} g_X = \frac{M}{m_n} g_n$. Accelerated (decelerated) capture and heating start just before $t_{\rm eq}$ given scalar (vector) mediation. Therefore scalar-mediated constraints should tighten and vector mediated constraints should loosen when

$$\frac{t_{\rm NS}}{t_{\rm eq}} = \frac{m_X}{M} \frac{\tilde{\alpha}}{\tilde{\alpha}_n} \dot{N}_{\rm cap} t_{\rm NS} > 1. \tag{5.35}$$

When this inequality is satisfied, time dependence of capture and heating rates should be taken into account. More specifically, the capture luminosity constraint, $E_{\rm DM,\,kin}(R)\dot{N}_{\rm cap} \approx m_X \frac{GM}{R}(1+\tilde{\alpha})\dot{N}_{\rm cap} < L_\circ \left(\frac{T_{\rm max}}{42{\rm kK}}\right)^4$, is saturated in a region of parameter space with $t_{\rm eq} < t_{\rm NS}$ when

$$\frac{1+\tilde{\alpha}}{\tilde{\alpha}} \tilde{\alpha}_n < \frac{L_\circ t_{\rm NS}}{GM^2/R} \left(\frac{T_{\rm max}}{42{\rm kK}}\right)^4 \approx 4 \times 10^{-11} \left(\frac{t_{\rm NS}}{0.3\,{\rm Gyr}}\right) \left(\frac{T_{\rm max}}{42{\rm kK}}\right)^4. \tag{5.36}$$

Since WEP tests suggest $\tilde{\alpha}_n \lesssim 10^{-11}$ when $\lambda \gtrsim 2R_{\rm Earth}$ [312, 266, 267], DM-DM interactions may thus be relevant when $\tilde{\alpha}_n$ is significantly below this bound. Our kinetic heating limits which neglect DM-DM interactions are thus conservative in the scalar-mediated case since captured DM could further accelerate capturing more DM. On the other hand our bounds could lift in the vector-mediated case if the DM-DM repulsive interaction was sufficiently strong compared to the attractive

[9] This expression assumes the charge-to-mass ratio of captured DM is similar to that of halo DM. If this were untrue, additional heat would be released (absorbed) in the capture process, leading to larger (smaller) DM charge-to-mass ratios.

DM-baryon interaction. Furthermore, heating that appears to accelerate (decelerate) at a characteristic timescale depending on local DM density and NS age could be a smoking gun signal of a scalar (vector) mediated long-range force.

We also remind the reader of restrictions necessary for consistency of our tidal heating estimate discussed in Secs. 5.2-5.2. First, the DM must be sufficiently compact to survive an NS transit and to tidally excite modes up to the cutoff determined by shear viscous damping (see Sec. 5.2). Second, tidal energy deposits approach the expected maximum $E_{\rm DM,\,kin}(R)$ at approximately the same $\tilde{\alpha}, m_X$ parameter range as they approach a few percent of the NS gravitational binding energy, where we expect transiting DM to destroy rather than heat the NS (see Eq. 5.26). Fig. 5.2 shows this region in gray.

5.3 Limits from Pulsar Timing Arrays

The use of PTAs to probe DM substructure has been extensively studied [269, 270, 103, 151, 271, 273, 43, 152, 42]. To set upper limits on the fifth force strength, we analyse the data collected by NANOGrav [298] in their 11-year dataset [296, 297]. This analysis utilizes the software `enterprise` [153] developed by NANOGrav and closely follows the Bayesian inference framework developed in our previous work [10].

We commence with deriving the phase shift signals measured by an observer on Earth due to a transiting DM. The intrinsic pulsar phase, $\phi(t)$, is often modelled as a truncated power series in t

$$\phi(t) = \phi_0 + \nu t + \frac{1}{2}\dot{\nu} t^2 \,, \tag{5.37}$$

where ϕ_0 is the phase offset, ν is the pulsar frequency and $\dot{\nu}$ is its first derivative. Astrophysical signals such as Doppler shifts due to transiting DM manifest as deviations from the above timing model.

The phase shift $\delta\phi(t)$ is related to the frequency shift $\delta\nu(t)$ by $\delta\phi(t) = \int_0^t \delta\nu(t')dt'$. In the presence of an external potential Φ, the acceleration of the pulsar induces an observed frequency shift due to the Doppler effect, which is given by [43]

$$\frac{\delta\nu}{\nu} = \hat{d} \cdot \int \nabla\Phi dt \,, \tag{5.38}$$

where $\hat{d}$ is the unit vector pointing from Earth to the pulsar. The fifth force potential is given by Eq. (5.1) and $\Phi(r) = V_{\rm Yuk}(r)/M$, and its gradient is

$$\nabla\Phi(r) = \frac{G m_X}{r^2}\left[1 + \tilde{\alpha}(1 + r/\lambda)e^{-r/\lambda}\right]\hat{r} \,. \tag{5.39}$$

To simplify these expressions, we perform the analysis in the pulsar rest frame and place the pulsar at the origin. We then write the DM position as $\vec{r}(t) = \vec{r}_0 + \vec{v}t$ with $\vec{v}$ being the DM velocity. The two important timescales in this system are the time of closest approach, $t_0 = -\vec{r}_0 \cdot \vec{v}/v^2$, and the signal width, $\tau = |\vec{r}_0 \times \vec{v}|/v^2$. The impact parameter is given by $\vec{b} = \vec{r}_0 + \vec{v}t_0 = v\tau$. Defining the dimensionless time variable, $x \equiv (t - t_0)/\tau$, we write $\vec{r} = b(\hat{b} + x\hat{v})$ and $r = b\sqrt{1+x^2}$. Using these variables, the frequency shift due to the fifth force can be written as

$$\left(\frac{\delta\nu}{\nu}\right)_{\text{fifth}} = \tilde{\alpha} G m_X \frac{1}{v^2\tau}\hat{d} \cdot \int \frac{1}{(1+x^2)^{3/2}} \left(1 + \frac{b}{\lambda}\sqrt{1+x^2}\right) e^{-(b/\lambda)\sqrt{1+x^2}} (\hat{b} + x\hat{v}) dx \,. \tag{5.40}$$

The equivalent expression for gravitation is given by Eq. 5.40 but with $\tilde{\alpha} = 1$ and $\lambda \to \infty$. In general the integral in Eq. 5.40 has to be computed numerically. An additional integration over time gives the phase shift $\delta\phi(t)$.

The above analysis assumes that the DM trajectory is approximately a straight line, which has been shown to hold for the DM mass range that we are interested in for gravity only [10]. In the presence of a fifth force, the deviation in DM paths is small if and only if $b \approx r_{\min}$ where $r_{\min}$ is the distance of closest approach. Eq. D.4 implies $b \approx r_{\min}$ iff $\frac{GM}{bv^2}(1 + \tilde{\alpha}e^{-b/\lambda}) \ll 1$. One can estimate the minimum impact parameter of all passing DMs to be

$$b_{\min} \sim \left(\frac{3}{4\pi}\frac{m_X}{\rho_X}\right)^{1/3} \sim 3\,\text{pc}\left(\frac{m_X}{M_\odot}\right)^{1/3} . \tag{5.41}$$

If the aforementioned condition is not satisfied, then DMs will substantially converge to the pulsar, which will lead to a larger amplitude for the timing deviation. Hence our constraints based on the straight-trajectory approximation serve as a conservative estimate. We leave a detailed analysis of PTA constraints accounting for full DM orbit information as a potential direction for future work.

To search for the DM signal in experimental data, similar to the static analysis in Ref. [10], we parametrize the signal with the leading order perturbation of the timing model

$$\frac{\delta\phi(t)}{\nu} = \frac{A}{\text{yr}^2}t^3 \,, \tag{5.42}$$

where A characterizes the signal amplitude. Terms of order t^2 or less are degenerate with the timing model and have no observable consequences. We search for the signal in Eq. 5.42 using `enterprise` and compute the Bayesian posterior distribution of the DM amplitude, $P(A|\vec{\delta t})$, using the Markov Chain Monte Carlo sampling

Parameter	Description	Prior
Comments		
	Red noise	
$A_{\rm red}$	Red noise power-law amplitude	Log-Uniform $[-20, -11]$
$\gamma_{\rm red}$	Red noise power-law spectral index	Uniform $[0, 7]$
Dark Matter		
A	Dark matter amplitude	Uniform $\pm[10^{-20}, 10^{-11}]$

Table 5.1: Parameters and priors used in the PTA analysis with the 11-yr dataset from NANOGrav. The notation Uniform $\pm[\dots]$ stands for the union of Uniform $[+\dots]$ and Uniform $[-\dots]$. We account for the effects from white noise by marginalizing over a multiplicative pre-factor of the timing residual errors. Errors from Solar System ephemeris (SSE) modeling are corrected using BayesEphem, as described in [297].

techniques with the `PTMCMCSampler` package [173]. The parameters and priors are listed in Table. 5.1. In particular, we adopt a uniform (instead of log-uniform) prior on the DM amplitude A, which is a standard procedure for upper-limit setting [313, 10]. For the red noise amplitude, however, we use a uniform prior to avoid the transfer of signal power to the red noise process, which has been shown to lead to overstated Bayesian upper limits [314].

We now fix a choice of λ. To relate the posterior distribution $P(A|\delta\vec{t})$ to the fifth force parameters $\tilde{\alpha}$, we use a Monte Carlo simulation described in Ref. [10] to compute the conditional probability $P(A|\tilde{\alpha})$. In particular, we randomly distribute DMs in a sphere and compute the total $\delta\phi(t)$ using Eq. 5.40. We then numerically fit $\delta\phi(t)$ with a third order polynomial in t to extract the t^3 coefficient and hence A. This procedure is repeated for numerous realizations to obtain the required distribution $P(A|\tilde{\alpha})$. The final posterior distribution on $\tilde{\alpha}$ is then given by [10]

$$P(\tilde{\alpha}|\delta\vec{t}) \propto \prod_{i=1}^{N_P} \int_{-\infty}^{\infty} P(A_i|\tilde{\alpha}) P(A_i|\delta\vec{t}) dA_i \tag{5.43}$$

where N_P is the number of pulsars.[10] The posterior distribution satisfies the normalization condition $\int d\tilde{\alpha} P(\tilde{\alpha}|\delta\vec{t}) = 1$.

[10] In Ref. [10] we also considered the possibility of deriving upper limits using the maximum amplitude among all pulsars (instead of using the amplitude in every single pulsar), but the limits turn out to be less stringent than the present results.

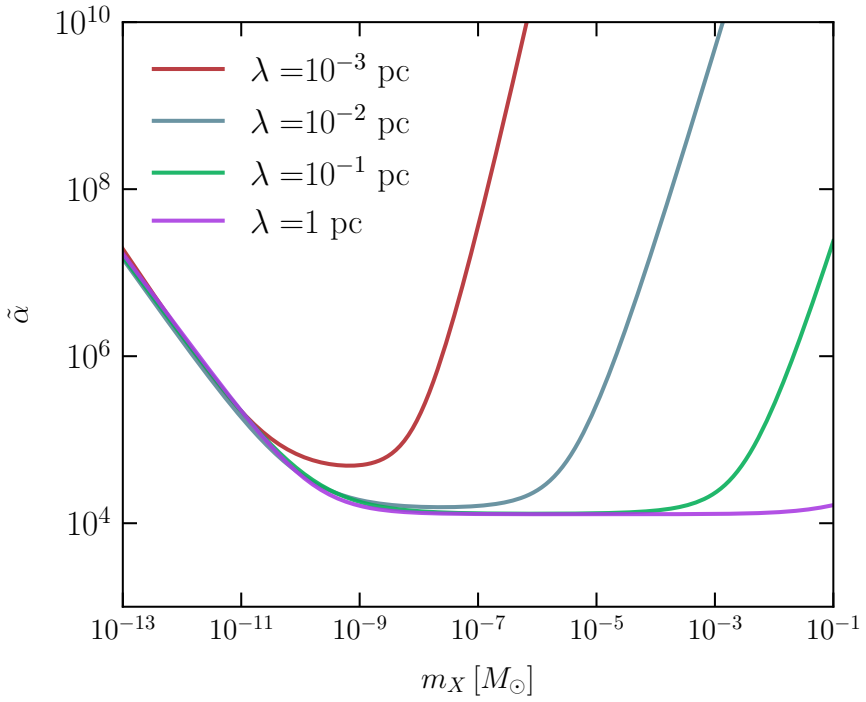

Figure 5.3: The 90$^{\text{th}}$ percentile upper limits on the fifth force strength $\tilde{\alpha}$ derived from the NANOGrav 11-year dataset. The constraints are shown for different DM mass m_X and range λ.

Finally, we compute the 90$^{\text{th}}$ percentile upper limit on $\tilde{\alpha}$ for each choice of λ, which is shown in Fig. 5.3. In the large mass limit, the constraints degrade since b_{min} becomes larger than λ, hence the phase shift is dominated by gravitational effects only, which is not sufficient to produce an observable signal. On the other hand, in the low mass limit, we have $b_{\text{min}} \lesssim \lambda$, but the constraints also become less stringent, since the fifth force and gravitational strength weaken with the DM mass. For adequately large force ranges (i.e. $\lambda \gtrsim 10^{-2}$ pc), there is an intermediate mass regime where $b_{\text{min}} \lesssim \lambda$ so the fifth force effectively modifies the gravitational constant by $G \to (1+\tilde{\alpha})G$, but its strength is not enough to perturb the DM path, hence the constraints exhibit a plateau behavior similar to the gravity-only analyses in Ref. [10].

5.4 Inferred Limits from Equivalence Principle Tests and the Bullet Cluster

In this section we consider indirect constraints on a fifth force between NS matter and DM from a combination of weak equivalence principle (WEP) tests [256, 312], which can constrain composition-dependent forces to be weaker than gravitational

limit	ref	test	$\Delta((B-L)/(M/m_n))$	$\Delta(B/(M/m_n))$
$\lvert\frac{\Delta a}{a_{\rm tot}}\rvert \lesssim 3\times10^{-4}$	[315]	perihelion precession	0.37	~ 0
$\lvert\frac{\Delta a}{a_{\rm tot}}\rvert \lesssim 0.004$	[316]	binary pulsar	0.69	0.19
$\lvert\frac{\Delta a}{a_{\rm tot}}\rvert \lesssim 10^{-5}$	[312]	lunar laser ranging	0.012	~ 0
$\lvert\frac{\Delta a}{a_{\rm tot}}\rvert \lesssim 10^{-4}$	[312]	torsion pendula	0.013, 0.036	0.0024, 0.0020

Table 5.2: Collection of limits on the differential acceleration of two baryonic test objects toward the galactic center. The B and $B-L$ number to mass ratios are based on Table II in [315] and Table 1 in [312]. The magnitude of the gravitational acceleration field due to galactic dark matter at Earth was taken as 5×10^{-11} m/ s^2 in [312], following [317]; this is the value assumed in calculating $\lvert\frac{\Delta a}{a_{\rm tot}}\rvert$ for the last two entries.

at macroscopic scales, and the bullet cluster bound on DM self-interactions [78, 79]. In Sec. 5.4 we translate a WEP bound on the differential acceleration of two baryonic bodies toward our Galaxy's center to a limit on $\tilde{\alpha}$ and λ when $\lambda \ll$ kpc. We then combine bullet cluster limits on $\tilde{\alpha}_X = g_X^2/4\pi G m_X^2$ with the very strong WEP constraints on $\tilde{\alpha}_n = g_n^2/4\pi G m_n^2$ at Earth and solar system scales ($\lambda \gtrsim 1000\,$km) to infer a limit on $\tilde{\alpha} = \sqrt{\tilde{\alpha}_X\tilde{\alpha}_n}$ in Sec. 5.4. Our results are shown in Fig. 5.4.

Weak Equivalence Principle Tests

Most DM-baryonic matter WEP tests constrain the difference in acceleration between two baryonic test bodies (which we will label as A and B) toward the galactic center, divided by the total acceleration:[11] $\frac{\Delta a}{a_{\rm tot}}$. When the total acceleration is dominated by gravity and the fifth force is Coulombic, assuming the DM charge-to-mass ratio is constant for DM throughout the halo, it is given by[12]

$$\frac{\Delta a_{\rm Coul}}{a_{\rm tot}} = \tilde{\alpha}\left[\left(\frac{Q}{M/m_n}\right)_A - \left(\frac{Q}{M/m_n}\right)_B\right], \tag{5.44}$$

where Q is the effective charge of the body in units of g_n. The difference in charge-to-mass ratio for the test bodies must be nonzero in order to obtain a non-trivial constraint. For normal matter, we consider couplings to baryon number or to $B-L$—i.e. $Q = B$ or $B-L$, but other combinations lead to similar constraints.

To include range dependence in the differential acceleration calculation, we integrate over the force times DM distribution and correct Eq. 5.44 with the ratio

[11] See Ref. [312] for one of the most highly cited treatments/reviews from the last decade.

[12] We neglect the difference between the atomic mass unit, u, and the neutron mass, m_n, throughout.

$\frac{|\Delta\vec{a}_{\rm Yuk}(\vec{r})|}{|\Delta\vec{a}_{\rm Coul}(\vec{r})|}$. Given a spherically symmetric DM halo mass distribution, $\rho_{halo}(r')$, and a uniform DM charge-to-mass ratio, the net acceleration due to a Coulombic force from halo DM on object i at position $\vec{r}$ relative to the halo's center is $\vec{a}_{\rm Coul}(\vec{r}) = \tilde{\alpha} G \frac{Q_i}{M_i/m_n} \frac{\hat{r}}{r^2} \int_0^r \rho_{halo}(r') d^3\vec{r}\,'$. For a Yukawa force, when $\lambda \ll r$, we find[13]

$$\begin{aligned}\vec{a}_{\rm Yuk}(\vec{r}) &= -\tilde{\alpha} G \frac{Q_i}{M_i/m_n} \vec{\nabla} \int_{\rm DM\ halo} \frac{\rho_{halo}(r') e^{-|\vec{r}-\vec{r}\,'|/\lambda}}{|\vec{r}-\vec{r}\,'|} d^3\vec{r}\,' \\ &\approx -4\pi\tilde{\alpha} G \lambda^2 \frac{Q_i}{M_i/m_n} \rho'_{halo}(r)\hat{r}\,. \end{aligned} \tag{5.45}$$

Therefore when $\lambda \ll r$ the ratio of Yukawa to Coulomb differential accelerations for test objects near the same radial distance, r, from the halo center is given by

$$\frac{|\Delta\vec{a}_{\rm Yuk}(\vec{r})|}{|\Delta\vec{a}_{\rm Coul}(\vec{r})|} \approx \frac{-4\pi r^4 \rho'_{halo}(r)}{\int_0^r \rho_{halo}(r') d^3\vec{r}\,'} \left(\frac{\lambda}{r}\right)^2 . \tag{5.46}$$

Given an NFW DM halo profile [65],

$$\rho_{halo}(r) = \frac{\rho_{halo,0}}{r/r_s(1+r/r_s)^2}, \tag{5.47}$$

with scale radius r_s, the expression in Eq. (5.46) becomes

$$\frac{|\Delta\vec{a}_{\rm Yuk}(\vec{r})|}{|\Delta\vec{a}_{\rm Coul}(\vec{r})|} = \frac{(r/r_s)^2(1+3r/r_s)}{(1+r/r_s)^2\left[(1+r/r_s)\log(1+r/r_s) - r/r_s\right]} \left(\frac{\lambda}{r}\right)^2 . \tag{5.48}$$

The coefficient in Eq. (5.48) lies between 2.4 and 2.6 when $0.23 < \frac{r}{r_s} < 2$, with the maximum of about 2.6 occurring near $\frac{r}{r_s} = 0.8$. For concreteness we take $r = 8\,\text{kpc}$ and set the coefficient to 2.5, which is within 4% of the exact value when $4\,\text{kpc} < r_s < 35\,\text{kpc}$, well within agreement with recent fits [318, 73]. The constraint on a Yukawa fifth-force then reads,

$$\left|\frac{\Delta a_{\rm Yuk}}{a_{\rm tot}}\right| \approx 2.5\,\tilde{\alpha}\left(\frac{\lambda}{r}\right)^2 \left[\left(\frac{Q}{M/m_n}\right)_A - \left(\frac{Q}{M/m_n}\right)_B\right] < \left|\frac{\Delta a}{a_{\rm tot}}\right|^{\rm max} . \tag{5.49}$$

Table 5.2 shows a variety of recent limits on differential accelerations, along with the difference in B- and $(B-L)$-to-mass ratios for the test objects. The strongest limit given $Q = B$ corresponds to $|\frac{\Delta a}{a_{\rm tot}}|/|\Delta[Q/(M/m_n)]| \lesssim 0.02$. The best limit given $Q = B - L$ is more than an order of magnitude stronger. Therefore the limit

[13] We dropped terms suppressed by $e^{-r/\lambda}$ and higher powers of $\frac{\lambda}{r}$. More precisely, we assumed $\lambda\rho'_{halo}(r) \gg e^{-r/\lambda}\rho_{halo}(r), \frac{e^{-r/\lambda}}{r\lambda}\int e^{-r'/\lambda}\rho_{halo}(r')\,r'dr', \frac{\lambda}{r}\lambda^2\rho''_{halo}(r), \ldots$

on a Yukawa fifth force coupling to baryon number from equivalence principle tests is roughly,

$$2.5\,\tilde{\alpha}\left(\frac{\lambda}{8\,\mathrm{kpc}}\right)^2 \lesssim 0.02 \qquad \text{when} \quad \left(\frac{m_X}{\rho_X}\right)^{1/3} \ll \lambda \ll 8\,\mathrm{kpc}, \tag{5.50}$$

where the conditions on λ are necessary for consistency of our spherically symmetric fluid approximation for the DM distribution near Earth, where the inter-DM spacing is estimated as $\left(\frac{m_X}{\rho_X}\right)^{1/3}$ and we set Earth's galactic radius to $r \approx 8\,\mathrm{kpc}$.

Bullet Cluster limit

Following Ref. [268], the momentum transfer cross section for a long-range DM-DM interaction can be approximated as $\sigma_T \approx 4\pi d_C^2$ where d_C is the distance of closest approach given a repulsive Yukawa interaction, $V_{\mathrm{Yuk}} = \frac{G m_X^2 \tilde{\alpha}_X}{r} e^{-r/\lambda}$. For simplicity we assume an order one fraction of the DM by mass takes the form of objects with roughly the same size. Assuming the Yukawa DM-DM interaction is much stronger than the gravitational DM-DM interaction at closest approach, $\frac{d_C}{\lambda} = W\left(\frac{4G\tilde{\alpha}_X m_X}{\lambda v^2}\right)$, where W is the Lambert W function satisfying $W(z)e^{W(z)} = z$ and v is the relative speed of the interacting DM pair. Note that σ_T thus depends on the DM velocity v. Observation of the bullet cluster sets the rough limit $\frac{\sigma_T}{m_X} = \frac{4\pi d_C^2}{m_X} < \frac{\mathrm{cm}^2}{\mathrm{g}}$, translating to a limit

$$\frac{4G\tilde{\alpha}_X m_X}{v^2} < \sqrt{\frac{1}{4\pi}\frac{m_X}{\mathrm{g}}}\, e^{\sqrt{\frac{1}{4\pi}\frac{m_X}{\mathrm{g}}}\frac{\mathrm{cm}}{\lambda}}\,\mathrm{cm} \tag{5.51}$$

or

$$\tilde{\alpha}_X\sqrt{\frac{m_X}{M_\odot}} < 2\times 10^6\left(\frac{v}{10^{-2}}\right)^2 e^{4\times 10^{-3}\sqrt{\frac{m_X}{M_\odot}}\frac{\mathrm{pc}}{\lambda}}. \tag{5.52}$$

The limit becomes very weak when the interaction range, λ, is comparable or small compared to the scattering length $\sqrt{\frac{m_X}{\mathrm{g}}}\,\mathrm{cm} = 10^{-2}\sqrt{\frac{m_X}{M_\odot}}\,\mathrm{pc}$.[14] The constraint on $\tilde{\alpha}_X$ is clearly consistent with our assumption that $\tilde{\alpha}_X \gg 1$ when $m_X \lesssim M_\odot$.

Now consider the indirect constraint on $\tilde{\alpha}$. If the DM and B fifth force charge to mass ratios are approximately independent of environment, then

$$\tilde{\alpha} \approx \sqrt{\tilde{\alpha}_n \tilde{\alpha}_X}. \tag{5.53}$$

Therefore the bullet cluster constraint plus a constraint on $\tilde{\alpha}_n$ lead to a constraint on $\tilde{\alpha}$:

$$\tilde{\alpha} < 5\times 10^{-3}\left(\frac{\tilde{\alpha}_n^{\max}}{10^{-11}}\right)^{1/2}\left(\frac{M_\odot}{m_X}\right)^{1/4}\left(\frac{v}{10^{-2}}\right) e^{2\times 10^{-3}\sqrt{\frac{m_X}{M_\odot}}\frac{\mathrm{pc}}{\lambda}}. \tag{5.54}$$

[14] Conversely, the limit is very insensitive to λ as long as $\lambda \gg 10^{-2}\sqrt{\frac{m_X}{M_\odot}}\,\mathrm{pc}$.

We choose a fiducial value of 10^{-11} for $\tilde{\alpha}_n^{\max}$ based on the MICROSCOPE limit [266, 267] but note that a more conservative limit based on inverse-square-law tests corresponds to $\tilde{\alpha}_n^{\max} \sim 10^{-1}$ - 10^{-10} in the km to pc force range [256]. Furthermore, both the inverse square law and MICROSCOPE limits come from measuring accelerations on Earth and in our solar system—very different from the bullet cluster environment. A more conservative approach would not combine the limits at all. Furthermore, we note that the bullet cluster limit on DM subcomponents weakens precipitously.

The limits in Eqs. 5.52 (red), 5.54 (purple), and 5.50 (blue) are represented in Fig. 5.4, along with the best constraint on $\tilde{\alpha}_n$, from Fig. 1 of [266] (green) for two force ranges at the boundaries of our range of interest. The inferred limit on $\tilde{\alpha}$ is just the geometric mean of the limits on $\tilde{\alpha}_X$ and $\tilde{\alpha}_n$.

5.5 Summary and Conclusions

We investigated probes of a long-range DM-baryon interaction. First, we derived limits on the interaction strength and range as functions of NS temperature and DM mass, density, and asymptotic speed distribution. This work extends the dark kinetic heating analysis of [275] to long-range forces and draws on the PBH gravitational tidal capture analysis of [303]. Fig. 5.2 shows our limit based on the coldest known NS. Next, extending the work in [10], we considered effects of a long-range fifth force on Doppler shifts of pulsar frequencies, and derived a limit based on the 11-yr NANOGrav PTA timing dataset, shown in Fig. 5.3. Finally, we considered *indirect* limits from weak equivalence principle tests and the bullet cluster, shown in Fig. 5.4. The three sets of constraints are shown together in Fig. 5.1. The indirect bullet cluster + WEP bound is stronger than the direct tidal heating and PTA bounds by an order of magnitude or more for all of the parameter space we considered. However, the tidal heating and PTA constraints are still interesting since they are direct phenomenological probes on DM-baryon interactions, independent of the microscopic origin of such a force. Moreover, if additional short-range interactions assist DM capture by NSs (allowing "maximal kinetic heating") or if only a subcomponent of DM interacts through the long-range fifth force, the kinetic heating and PTA limits dominate.

Imminent improvements on NS temperature and pulsar timing observations from, e.g., the James Webb Space Telescope [319] and Square Kilometer Array [320] will extend the reach of NSs as probes of a long-range DM-baryon fifth force.

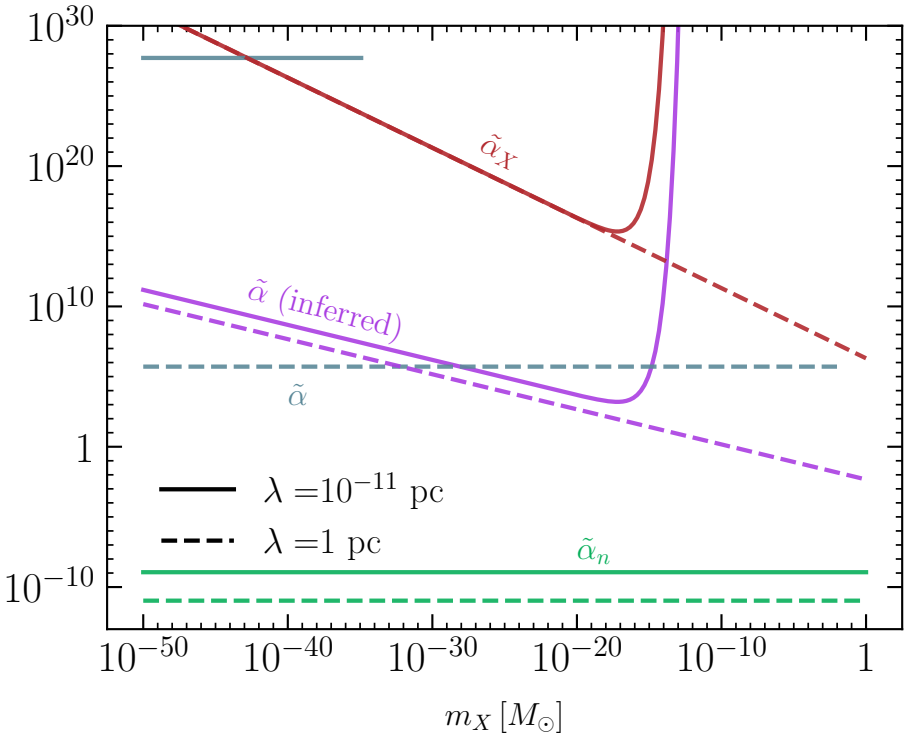

Figure 5.4: Constraints on the fifth force to gravitational force strength ratios for baryonic matter self-interactions ($\tilde{\alpha}_n$), DM-baryon interactions ($\tilde{\alpha}$), and DM self-interactions ($\tilde{\alpha}_X$), from MICROSCOPE (Fig. 1 of [266]), weak equivalence principle tests constraining accelerations toward the galactic center (Eq. 5.50 and Table 5.2), and the bullet cluster (Eq. 5.52), respectively, for force ranges at the extremes of those we consider. The inferred constraint on $\tilde{\alpha}$ (purple) is derived by combining the MICROSCOPE (green) and bullet cluster (red) limits, using $\tilde{\alpha}^{\rm max} = \sqrt{\tilde{\alpha}_n^{\rm max}\tilde{\alpha}_X^{\rm max}}$ (Eq. 5.54). We have assumed that all of the DM in the Milky Way halo and in the bullet cluster takes the form of compact, effectively point-like states with approximately the same mass, m_X.

In addition, the requirement for the NS cooling timescale to be smaller than the encounter timescale can be potentially relaxed by surveying a large population of NSs and searching for a fraction of them that are still cooling down after recent DM encounters [294]. On the other hand, higher than expected temperatures of isolated old NSs could be a sign of DM kinetic heating; if those temperatures are higher than can be explained given kinetic heating through short-range interactions (c.f. [275] and Eq. 5.21 with $\tilde{\alpha} = 0$), a long-range force could be part of the explanation. So could DM annihilation (see e.g. [321, 322, 323, 324, 325]) or other DM-induced exothermic processes (see e.g. [326, 290]). An unexpected NS temperature age dependence for old NSs in otherwise similar environments is another potential

signature of a long-range force, since the heating rate can dramatically change once the effective charge of captured DM becomes comparable to that of the NS at birth. As discussed at the end of Sec. 5.2, scalar-mediated interactions would lead to accelerated heating and vector-mediated to decelerated heating at late times. We leave detailed analyses of such possibilities for future work, should any observational hints arise.

Chapter 6

SEARCHING FOR SIGNATURES FROM DARK MATTER SUBSTRUCTURE AND COSMOLOGICAL PHASE TRANSITIONS WITH THE NANOGRAV 15-YEAR DATA SET

This chapter is based on

[1] Adeela Afzal et al. "The NANOGrav 15 yr Data Set: Search for Signals from New Physics". In: *Astrophys. J. Lett.* 951.1 (2023), p. L11. DOI: 10.3847/2041-8213/acdc91. arXiv: 2306.16219 [astro-ph.HE].

6.1 Introduction

The Standard Model (SM) of particle physics currently provides our best description of the laws governing the universe at subatomic scales. However, it fails to explain several observed properties of our universe, such as the origin of the matter–antimatter asymmetry, the nature of dark matter (DM) and dark energy, and the origin of neutrino masses. These shortcomings have motivated the development of several theories for physics beyond the SM, or BSM theories for short, accompanied by a rich experimental program trying to test them. The generation of gravitational waves (GWs) is a ubiquitous feature of many BSM theories [327, 328, 329]. These GWs form a stochastic background and propagate essentially unimpeded over cosmic distances to be detected today, whereas electromagnetic radiation does not start free streaming until after recombination. Thus, detecting a stochastic GW background (GWB) of cosmological origin would offer a unique and direct glimpse into the very early universe and herald a new era for using GWs to study fundamental physics.

Cosmological GWBs can be produced by a number of particle physics models of the early universe. Notably, cosmic inflation generically produces GWs [330], which may be observable at nanohertz frequencies if their energy density spectrum is sufficiently blue-tilted. Similarly, an enhanced spectrum of short-wavelength scalar perturbations produced during inflation can source so-called scalar-induced GWs [SIGWs; 331, 332]. Another potential source of GWs are cosmological first-order phase transitions [333, 334, 335], which proceed through bubble nucleation; bubble collisions and bubble interactions with the primordial plasma giving rise to sound waves contribute to GW production. Finally, topological defects left behind

by cosmological phase transitions, such as cosmic strings and domain walls [336, 337, 338], can radiate GWs and hence contribute to the GWB.

The North American Nanohertz Observatory for Gravitational Waves [NANOGrav; 339] has recently found the first convincing evidence for a stochastic GWB signal, as detailed in [340]. Analyzing 15-year of pulsar timing observations, NANOGrav has detected a red-noise process whose spectral properties are common among all pulsars and that is spatially correlated among pulsar pairs in a manner consistent with an isotropic GWB. In the following, we will refer to this observation as "the NANOGrav signal," "the GWB signal," or simply "the signal," keeping in mind the level of statistical significance at which the GW nature of the signal has been demonstrated in [340]. While the GWB is primarily expected to arise from a population of inspiraling supermassive black hole binaries [SMBHBs; 341, 342, 343, 157, 158], cosmological sources may also contribute to it.

The SMBHB interpretation of the signal is considered in [344]. In this paper, we analyze the NANOGrav 15-year data set [345] to investigate the possibility that the observed signal is cosmological in nature or that it arises from a combination of SMBHBs and a cosmological source. In particular, we consider phenomenological models of cosmic inflation, SIGWs, first-order phase transitions, cosmic strings (stable, metastable, and superstrings), and domain walls. We find that all of these models, except for stable cosmic strings of field theory origin, are consistent with the observed GWB signal. Many models provide in fact a better fit of the NANOGrav data than the baseline SMBHB model, which is reflected in the outcome of a comprehensive Bayesian model comparison analysis that we perform: several new-physics models result in Bayes factors between 10 and 100. We also consider composite models where the GWB spectrum receives contributions from new physics and SMBHBs. Comparing these composite models to the SMBHB reference model leads to comparable results, again with many Bayes factors falling into the range from 10 to 100. Cosmic superstrings, as predicted by string theory, are among the models that provide a good fit of the data, while stable cosmic strings of field theory origin only result in Bayes factors in the range from 0.1 to 1.

The reason that some of the Bayes factors reach large values is that the SMBHB signal expected from the theoretical model used in this analysis agrees somewhat poorly (only at the level of 95% regions) with the observed data, leaving room for improvement by adding additional sources or better noise modeling. It is perhaps an intriguing idea that this disagreement may point to the presence of a cosmological

source, but the present evidence is quite weak. We stress that Bayes factors for additional models beyond the SMBHB interpretation are highly dependent on the range of priors with which these models are introduced. Thus, one should not assign too much meaning to the exact numerical values of the Bayes factors reported in this work.

In many models, there are ranges of parameter values that would produce signals in conflict with the NG15 data. In those cases, we show the excluded regions and give numerical upper limits for individual parameters. We do so in terms of a new statistical test, introducing what we call the K ratio. These parameter constraints are independent of the origin of the signal in the NG15 data and a testament to the constraining power of PTA data in the search for new physics. In our parameter plots, we label the K-ratio constraints by NG15, and where applicable, we compare them to other existing bounds. In many cases, the NG15 bounds are complementary to existing bounds, highlighting the fact that new-physics searches at the PTA frontier venture into previously unexplored regions of parameter space.

Aside from cosmological GWBs, signals of new physics can appear in GW detectors in a deterministic manner. Although pulsar timing arrays (PTAs) are primarily used to search for a GWB, we can also leverage their remarkable sensitivity to search for these deterministic signals. Specifically, DM substructures within the Milky Way can produce a Doppler effect by accelerating the Earth or a pulsar [150], or a Shapiro delay of the photons' arrival times by perturbing the metric along the photon geodesic [44]. PTAs can also probe models of ultralight DM (ULDM), which can cause shifts in the observed pulse timing via metric fluctuations [346, 347] or via couplings between ULDM and SM particles [348, 349]. We search for both of these deterministic signals, and after finding no evidence for either of them, we derive new bounds on both these models.

This paper is organized as follows. We describe the NG15 data set in Section 6.2 and our general analysis methods in Section 6.3. In Section 6.4, we discuss the GWB expected from SMBHBs. We present the analysis and results for new-physics models that generate a cosmological GWB in Section 6.5 and for models that produce deterministic signals in Section 6.6. We conclude in Section 6.7. Additionally, we include a list of parameters for each model, the prior ranges we use in our analysis, and the corresponding recovered posterior ranges in Appendix G. We provide supplementary material for specific models in Appendix H .

6.2 PTA data

The NANOGrav 15-year (NG15) data set consists of observations of 68 millisecond pulsars made between 2004 July and 2020 August. This updated data set adds 21 pulsars and 3 yr of observations to the previous 12.5 yr data set [350]. One pulsar, J0614–3329, was observed for less than 3 yr, which is why it is not included in our analysis. The remaining 67 pulsars were all observed for more than 3 yr with an approximate cadence of 1 month (with the exception of six pulsars that were observed weekly as part of a high-cadence campaign, which started in 2013 at the Green Bank Telescope and in 2015 at the Arecibo Observatory).

The pulse times of arrival (TOAs) were generated from the raw data following the procedure discussed in [166, 351] and [350]. The resulting cleaned TOAs were fit to a timing model that accounts for the pulsar's period and spin period derivative, sky location, proper motion, and parallax. For pulsars in a binary system, we included in the timing model five Keplerian binary parameters and an additional non-Keplerian parameter if they improved the fit as determined by an F-test. Pulse dispersion was modeled as a piecewise constant with the inclusion of DMX parameters [166, 169]. The timing model fits were performed using the TT(BIPM2019) timescale and the JPL Solar System Ephemeris model DE440 [352]. Additional detail about the data set and the processing of the TOAs can be found in [345] and [353].

6.3 Data Analysis Methods

The statistical tools needed to describe noise sources, GWBs, and deterministic signals in pulsar timing data have already been extensively discussed in the literature [see, e.g., 165, 354]. In the following brief overview, we focus on the implementation of new-physics signals within this framework.

Likelihood

Our search for a new-physics signal utilizes the pulsars' timing residuals, $\boldsymbol{\delta t}$. These timing residuals measure the discrepancy between the observed TOAs and the ones predicted by the pulsar timing model described in [345] and briefly summarized in Section 6.2. There are three main contributions to these timing residuals: white noise, time-correlated stochastic processes (also known as red noise), and small errors in the fit to the timing-ephemeris parameters [355]. Specifically, we can model the timing residuals as

$$\boldsymbol{\delta t} = \boldsymbol{n} + F\,\boldsymbol{a} + M\,\boldsymbol{\epsilon}\,. \tag{6.1}$$

In the remainder of this section, we will define and discuss each of these three terms and define the PTA likelihood.

The first term on the right-hand side of Eq. (6.1), $\boldsymbol{n}$, describes the white noise that is assumed to be left in each of the N_{TOA} timing residuals after subtracting all known systematics. White noise is assumed to be a zero mean normal random variable, fully characterized by its covariance. For the receiver/back-end combination I, the white-noise covariance matrix reads

$$\langle n_i n_j \rangle = \mathcal{F}_I^2 \left[\sigma_{i\,S/N}^2 + \mathcal{Q}_I^2 \right] \delta_{ij} + \mathcal{J}_I^2 \, \mathcal{U}_{ij} \,, \tag{6.2}$$

where i and j index the TOAs, $\sigma_{i\,S/N}$ is the TOA uncertainty for the ith observation, $\mathcal{F}_I$ is the Extra FACtor (EFAC) parameter, $\mathcal{Q}_I$ is the Extra QUADrature (EQUAD) parameter, and $\mathcal{J}_I$ is the ECORR parameter. ECORR is modeled using a block diagonal matrix, $\mathcal{U}$, with values of 1 for TOAs from the same observing epoch and zeros for all other entries. Following the approach of previous works [165, 354], we fix all white-noise parameters to their values at the maxima in the posterior probability distributions recovered from single pulsar noise studies in order to increase computational efficiency [353].

Time-correlated stochastic processes, like pulsar-intrinsic red noise and GWB signals, are modeled using a Fourier basis of frequencies i/T_{obs}, where i indexes the harmonics of the basis and T_{obs} is the timing baseline, extending from the first to the last recorded TOA in the full PTA data set. Since we are generally interested in processes that exhibit long-timescale correlations, the expansion is truncated after N_f frequency bins. In this paper, we use $N_f = 30$ for pulsar-intrinsic red noise and $N_f = 14$ for GWBs. The latter choice stems from the observation that most of the evidence for a GWB comes from the first 14 frequency bins. More specifically, fitting a common-spectrum uncorrelated red-noise process with a broken power-law spectral shape to the NG15 data, the posterior distribution for the break frequency reaches it maximum around the 14th frequency bin [340]. This set of $2N_f$ sine–cosine pairs evaluated at the different observation times is contained in the Fourier design matrix, F. The Fourier coefficients of this expansion, $\boldsymbol{a}$, are assumed to be normally distributed random variables with zero mean and covariance matrix, $\langle \boldsymbol{a}\boldsymbol{a}^{\mathrm{T}} \rangle = \phi$, given by

$$[\phi]_{(ak)(bj)} = \delta_{ij} \left(\Gamma_{ab} \Phi_i + \delta_{ab} \varphi_{a,i} \right) \tag{6.3}$$

where a and b index the pulsars, i and j index the frequency harmonics, and Γ_{ab} is the GWB overlap reduction function, which describes average correlations between

pulsars a and b as a function of their angular separation in the sky. For an isotropic and unpolarized GWB, Γ_{ab} is given by the Hellings & Downs correlation [356], also known as "quadrupolar" or "HD" correlation.

The first term on the right-hand side of Eq. (6.3) parameterizes the contribution to the timing residuals induced by a GWB in terms of the model-dependent coefficients Φ_i. In this work, we consider two kinds of GWB sources: one of astrophysical origin, namely a population of inspiraling SMBHBs (discussed in section 6.4), and one of cosmological origin, induced by one of the exotic new-physics models under consideration (discussed in section 6.5). The last term in Eq. (6.3) models pulsar-intrinsic red-noise in terms of the coefficients $\varphi_{a,i}$, where

$$\varphi_a(f) = \frac{A_a^2}{12\pi^2}\frac{1}{T_{\rm obs}}\left(\frac{f}{1\,yr^{-1}}\right)^{-\gamma_a} yr^3 \tag{6.4}$$

and $\varphi_{a,i} = \varphi_a(i/T_{\rm obs})$ for all N_f frequencies. The priors for the red noise parameters are reported in Table G.1.

Finally, deviations from the initial best-fit values of the m timing-ephemeris parameters are accounted for by the term $M\boldsymbol{\epsilon}$. The design matrix, M, is an $N_{TOA}\times m$ matrix containing the partial derivatives of the TOAs with respect to each timing-ephemeris parameter (evaluated at the initial best-fit value), and $\boldsymbol{\epsilon}$ is a vector containing the linear offset from these best-fit parameters.

Since in this analysis we are not interested in the specific realization of the noise but only in its statistical properties, we can analytically marginalize over all the possible noise realizations (i.e., integrate over all the possible values of $\boldsymbol{a}$ and $\boldsymbol{\epsilon}$). This leaves us with a marginalized likelihood that depends only on the (unknown) parameters describing the red-noise covariance matrix [i.e., A_a, γ_a, plus any other parameters describing Φ_i; 357, 358]:

$$p(\boldsymbol{\delta t}|\phi) = \frac{\exp\left(-\frac{1}{2}\boldsymbol{\delta t}^T C^{-1}\boldsymbol{\delta t}\right)}{\sqrt{det(2\pi C)}}\,, \tag{6.5}$$

where $C = N + TBT^T$. Here N is the covariance matrix of white noise, $T = [M, F]$, and $B = diag(\infty, \phi)$, where ∞ is a diagonal matrix of infinities, which effectively means that we assume flat priors for the parameters in $\boldsymbol{\epsilon}$. Since in our calculations we always deal with the inverse of B, all these infinities reduce to zeros.

Eq. (6.5) can be easily generalized to take into account deterministic signals (like the ones that will be discussed in Section 6.6). In the presence of a deterministic signal,

$\boldsymbol{h}(\boldsymbol{\theta})$, which depends on a set of parameters $\boldsymbol{\theta}$, we just need to shift the residuals, $\boldsymbol{\delta t} \to \boldsymbol{\delta t} - \boldsymbol{h}(\boldsymbol{\theta})$.

Finally, we relate our characterization of the GWB given in Eq. (6.3) in terms of Φ_i to the commonly adopted spectral representation in terms of the GWB energy density per logarithmic frequency interval, $d\rho_{GW}/d\ln f$, as a fraction of the closure density, i.e., the total energy density of our universe, ρ_c [109]

$$\Omega_{GW}(f) \equiv \frac{1}{\rho_c}\frac{d\rho_{GW}(f)}{d\ln f} = \frac{8\pi^4 f^5}{H_0^2}\frac{\Phi(f)}{\Delta f}\,. \tag{6.6}$$

Here H_0 is the present-day value of the Hubble rate, $\Delta f = 1/T_{\rm obs}$ is the separation between the N_f frequency bins, and $\Phi(f)$ determines the coefficients Φ_i in Eq. (6.3), i.e., $\Phi_i = \Phi\,(i/T_{\rm obs})$. Note that $\Phi(f)$ is identical to the timing residual power spectral density (PSD), $S(f) = \Phi(f)/\Delta f$, up to the constant factor of $1/\Delta f$. In the remainder of this paper, we will often work with $h^2\Omega_{GW}$ instead of Ω_{GW}, where h is the dimensionless Hubble constant, $H_0 = h \times 100\,\mathrm{kms}^{-1}\mathrm{Mpc}^{-1}$, such that the explicit value of H_0 cancels in the product $h^2\Omega_{GW}$.

Bayesian analysis

The goal of this work is to investigate a series of cosmological interpretations of the GWB signal in our data. Specifically, we would like to answer two questions. First, what is the region in the parameter space of the new-physics models that could produce the observed GWB? And second, is there any preference between the astrophysical and cosmological interpretations of the signal?

To answer these questions, we make use of Bayesian inference. Bayesian inference is a statistical method in which Bayes' rule of conditional probabilities is used to update one's knowledge as observations are acquired. Given a model $\mathcal{H}$, a set of parameters Θ, and data $\mathcal{D}$, we can use Bayes' rule to write

$$P(\Theta|\mathcal{D},\mathcal{H}) = \frac{P(\mathcal{D}|\Theta,\mathcal{H})P(\Theta|\mathcal{H})}{P(\mathcal{D}|\mathcal{H})}\,, \tag{6.7}$$

where $P(\Theta|\mathcal{D},\mathcal{H})$ is the posterior probability distribution for the model parameters, $P(\mathcal{D}|\Theta,\mathcal{H})$ is the likelihood, $P(\Theta|\mathcal{H})$ is the prior probability distribution, and

$$\mathcal{Z} \equiv P(\mathcal{D}|\mathcal{H}) = \int \mathrm{d}\Theta\, P(\mathcal{D}|\Theta,\mathcal{H})P(\Theta|\mathcal{H}) \tag{6.8}$$

is the marginalized likelihood, or evidence. In the context of this work, $\mathcal{H}$ is the timing residual model given in Eq. (6.1), Θ contains the parameter describing

the covariance matrix ϕ, and the data are the timing residuals $\boldsymbol{\delta t}$. The likelihood function for our analysis is given by Eq. (6.5) and implemented using the [153] and `ENTEPRISE_EXTENSIONS` [248] packages. Our prior choices are summarized in Tables G.1 and G.2.

The posterior distribution on the left-hand side of Eq. (6.7) is the central result of the Bayesian analysis and contains all the information needed to answer our two original questions. Indeed, integrating over all the model parameters except one (two) allows us to derive marginalized distributions that can be used to obtain 1D (2D) credible intervals. At the same time, given two models $\mathcal{H}_0$ and $\mathcal{H}_1$, we can perform model selection by calculating the Bayes factor defined as

$$\mathcal{B}_{10}(\mathcal{D}) = \frac{\mathcal{Z}_1}{\mathcal{Z}_0} = \frac{P(\mathcal{D}|\mathcal{H}_1)}{P(\mathcal{D}|\mathcal{H}_0)} \,. \tag{6.9}$$

The numerical value of the Bayes factor for a given model comparison can then be interpreted as evidence against or in favor of model hypothesis $\mathcal{H}_1$ according to the Jeffreys scale [359]: $\mathcal{B}_{10} < 1$ means that $\mathcal{H}_1$ is disfavored, while $\mathcal{B}_{10}$ values in the ranges $[10^{0.0}, 10^{0.5}]$, $[10^{0.5}, 10^{1.0}]$, $[10^{1.0}, 10^{1.5}]$, $[10^{1.5}, 10^{2.0}]$, $[10^{2.0}, \infty)$ are interpreted as negligibly small, substantial, strong, very strong, and decisive evidence in favor of $\mathcal{H}_1$, respectively.

Given the large number of parameters, the integration required to derive marginalized distributions and Bayes factors needs to be performed through Monte Carlo sampling. Specifically, we use the Markov Chain Monte Carlo (MCMC) tools implemented in the `PTMCMCSampler` package [360] to sample from the posterior distributions. The marginalized posterior densities shown in our plots are then derived by applying kernel density estimates to the MCMC samples via the methods implemented in the `GetDist` package [361].

In order to compute the Bayes factor between two models, we use product space methods [362, 363, 364], instead of calculating the evidence $\mathcal{Z}$ for each model separately. This procedure recasts model selection as a parameter estimation problem, introducing a model indexing variable that is sampled along with the parameters of the competing models and controls which model likelihood is active at each MCMC iteration. The ratio of samples spent in each bin of the model indexing variable returns the posterior odds ratio between models, which coincides with the Bayes factor for equal model priors, $P(\mathcal{H}_1) = P(\mathcal{H}_0)$. The Monte Carlo sampling uncertainties associated with this derivation of the Bayes factors can be estimated through statistical bootstrapping [365]. Bootstrapping creates new sets of Monte

Carlo draws by resampling (with replacement) the original set of draws. These sets of draws act as independent realizations of the sampling procedure and allow us to obtain a distribution for the Bayes factors from which we derive point values and uncertainties on our Bayes factors corresponding to mean and standard deviation. Specifically, the central values and corresponding errors quoted in the following for the Bayes factors were derived by creating 5×10^4 realizations of our Monte Carlo draws.

From Eq. (6.8), it is evident that models' evidence and, therefore, Bayes factors depend on the prior choice. In our analysis, we will often restrict priors to the region of parameter space for which cosmological models produce an observable signal in the PTA frequency band. However, a more appropriate prior choice would cover the entire allowed region of parameter space. Nonetheless, when working with flat priors, it is easy to rescale the Bayes factors to account for wider prior ranges. Specifically, if the priors are extended to a region of parameter space for which the likelihood $P(\mathcal{D}|\Theta, \mathcal{H})$ is approximately zero, the Bayes factors decrease by a factor proportional to the increase in prior volume.

For each model $\mathcal{H}$ considered in our analysis, we use the reconstructed posterior distribution, $P(\Theta|\mathcal{D}, \mathcal{H})$, to identify relevant parameter ranges and set upper limits. Specifically, we identify 68% (95%) Bayesian credible intervals [367] by integrating the posterior over the regions of highest density until the integral covers 68% (95%) of the posterior probability. Moreover, we give upper limits above which the additional model is "strongly disfavored" according to the Jeffreys scale [359]. For instance, to place a bound on a single parameter θ, we first marginalize over all other model parameters and then determine the parameter value at which the likelihood ratio

$$K(\theta) = \frac{P(\mathcal{D}|\theta, \mathcal{H})}{P(\mathcal{D}|\theta_0, \mathcal{H})}\,, \tag{6.10}$$

has dropped to $K = 110$. Here θ_0 refers to the parameter limit in which the new-physics contribution to the total signal becomes negligible and $P(\mathcal{D}|\theta, \mathcal{H})$ no longer depends on the exact value of θ. Graphing $P(\mathcal{D}|\theta, \mathcal{H})$ as a function of θ, this parameter region appears as a plateau, with $P(\mathcal{D}|\theta_0, \mathcal{H})$ denoting the height of this plateau. Assuming a flat prior on θ, the ratio in Eq. (6.10) is identical to the corresponding ratio of marginalized posteriors. Furthermore, multiplying and dividing by the prior on θ,

$$K(\theta) = \frac{P(\theta|\mathcal{H})}{P(\theta_0|\mathcal{D}, \mathcal{H})} \frac{P(\theta|\mathcal{D}, \mathcal{H})}{P(\theta|\mathcal{H})}\,. \tag{6.11}$$

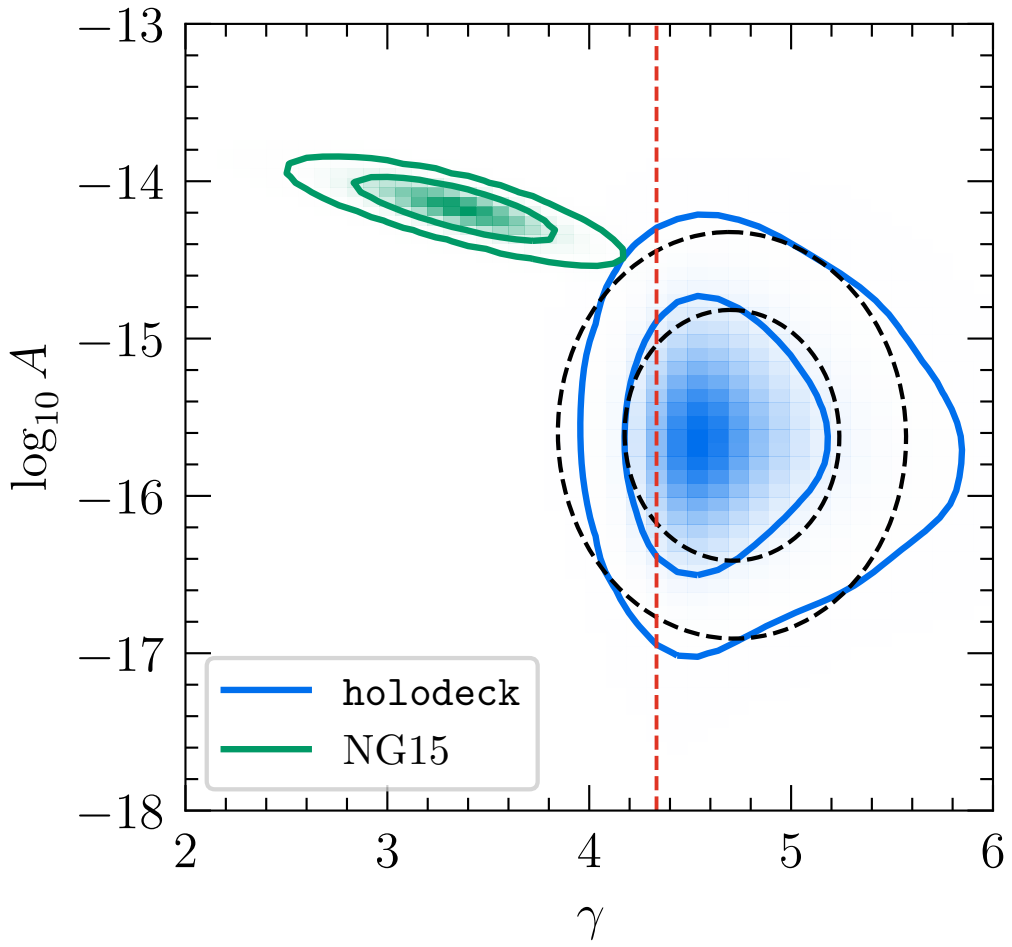

Figure 6.1: Comparison of the 68% and 95% probability regions for the amplitude and slope of a power-law fit to the observed GWB signal (green contours) and predicted for purely GW-driven SMBHB populations with circular orbits [blue contours; 344]. The black dashed lines represent a 2D Gaussian fit of the blue contours. The vertical red line indicates $\gamma = 13/3$, the naive expectation for a GWB produced by a GW-driven SMBHB population [366].

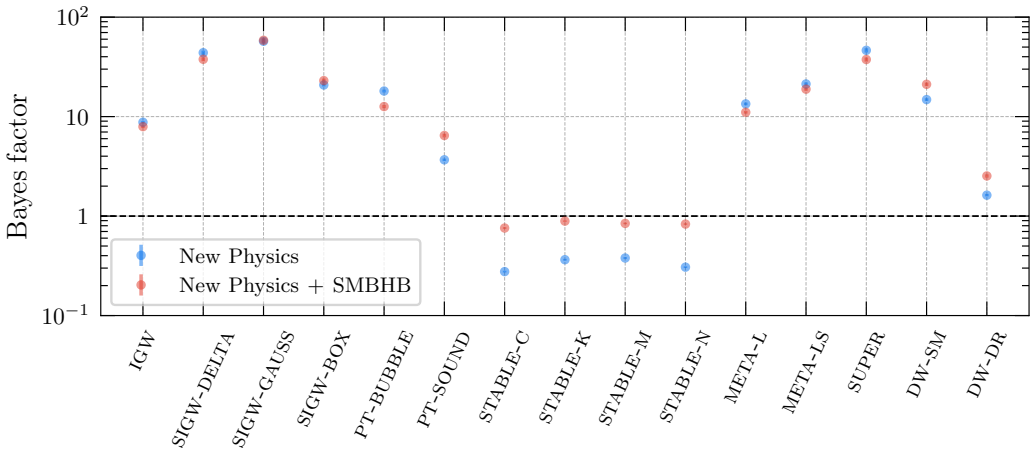

Figure 6.2: Bayes factors for the model comparisons between the new-physics interpretations of the signal considered in this work and the interpretation in terms of SMBHBs alone. Blue points are for the new physics alone, and red points are for the new physics in combination with the SMBHB signal. We also plot the error bars of all Bayes factors, which we obtain following the bootstrapping method outlined in Section 6.3. In most cases, however, these error bars are small and not visible.

The first factor is the Savage–Dickey density ratio and can hence be identified as the Bayes factor $\mathcal{B} = P(\mathcal{D}|\mathcal{H})/P(\mathcal{D}|\mathcal{H}_0)$, where $\mathcal{H}_0$ is the model that results from model $\mathcal{H}$ when omitting the signal contribution controlled by the parameter θ. The K ratio can thus be written as the product of the global Bayes factor and the local posterior-to-prior ratio for the parameter θ,

$$K(\theta) = \mathcal{B}\,\frac{P(\theta|\mathcal{D},\mathcal{H})}{P(\theta|\mathcal{H})}\,. \tag{6.12}$$

Once $\mathcal{B}$ is known, it is straightforward to evaluate Eq. (6.12) and determine the K-ratio bound on θ. Eq. (6.12) is useful for numerically evaluating K, as it automatically encodes the height of the plateau in the marginalized posterior, $P(\theta_0|\mathcal{D},\mathcal{H}) = P(\theta|\mathcal{H})/\mathcal{B}$, which we would otherwise have to obtain from a fit to our MCMC data. However, we stress that K is defined as a likelihood ratio, which renders it immune to prior effects [prior choice, range, etc.; 368]. For more than one parameter dimension, we proceed analogously and derive bounds based on the criterion $K(\Theta) > 110$.

All Bayesian inference analyses discussed in this work were implemented into via a newly developed wrapper that we call `PTArcade` [369, 370]. This wrapper is intended to allow easy implementation of new-physics searches in PTA data. We make this wrapper publicly available at https://doi.org/10.5281/zenodo.

7876429. Similarly, all MCMC chains analyzed in this work can be downloaded at https://zenodo.org/record/8010909.

6.4 GWB Signal from SMBHBs

Most galaxies are expected to host a supermassive black hole (SMBH) at their center [371, 372]. During the hierarchical merging of galaxies taking place in the course of structure formation [373], these black holes are expected to sink to the center of the merger remnants, eventually forming binary systems [374]. The gravitational radiation emitted by this population of inspiraling SMBHBs forms a GWB in the PTA band [341, 342, 343] and is a natural candidate for the source of the signal observed in our data.

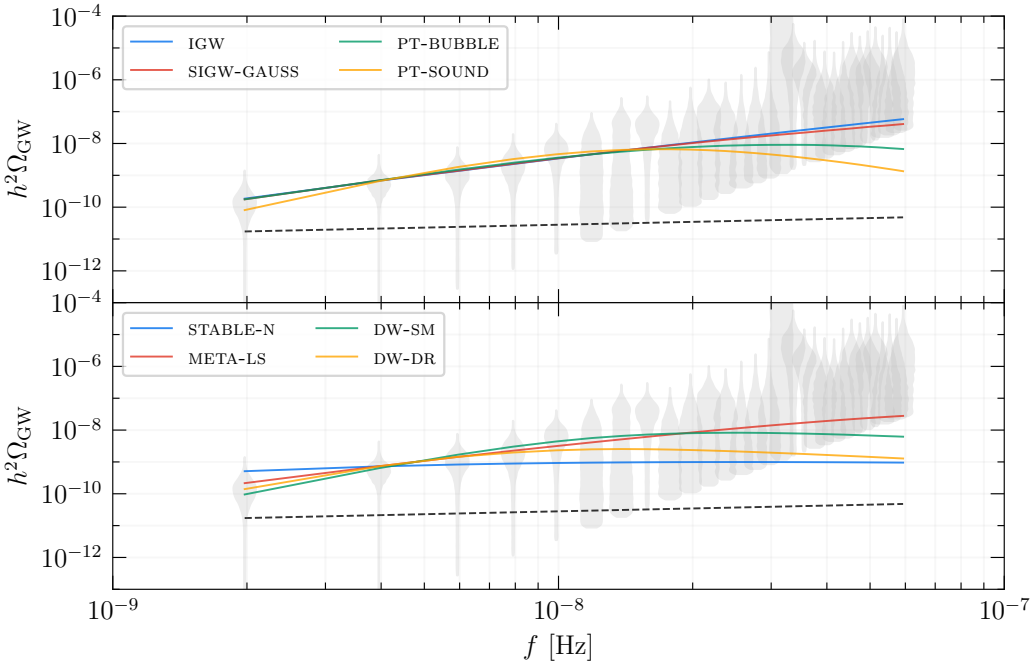

Figure 6.3: Median GWB spectra produced by a subset of the new-physics models, which we construct by mapping our model parameter posterior distributions to $h^2\Omega_{GW}$ distributions at every frequency f (see Figs. G.1 and G.2 for the models not included here). We also show the periodogram for an HD-correlated free spectral process (gray violins) and the GWB spectrum produced by an astrophysical population of inspiraling SMBHBs with the parameters $A_{\rm BHB}$ and $\gamma_{\rm BHB}$ fixed at the central values $\boldsymbol{\mu}_{BHB}$ of the 2D Gaussian prior distribution specified in Eq. (G.1) (black dashed line).

The shape and normalization of this GWB depend on the properties of the SMBHB population and on its dynamical evolution [375, 376, 377, 378]. As discussed

in [344], the normalization is primarily controlled by the typical masses and abundance of SMBHBs, while the shape of the spectrum is determined by subparsec-scale binary evolution, which is currently unconstrained by observations. For a population of binaries whose orbital evolution is driven purely by GW emission, the resulting timing residual PSD is a power law with a spectral index (defined below in Eq. (6.13)) of $-\gamma_{\rm BHB} = -13/3$ [366], produced by the increasing rate of inspiral and decreasing number of binaries emitting over each frequency interval. However, as GW emission alone is typically insufficient to merge SMBHBs within a Hubble time, the number of binaries emitting in the PTA band depends on interactions between binaries and their local galactic environment to extract orbital energy and drive systems toward merger [374]. If these environmental effects extend into the PTA band, or if binary orbits are substantially eccentric, then the GWB spectrum can flatten at low frequencies [typically expected at $f \ll 1\, yr^{-1}$; 377]. At high frequencies, once the expected number of binaries dominating the GWB approaches unity, the spectrum steepens below 13/3 [typically expected at $f \gg 1\, yr^{-1}$; 376].

Unfortunately, current observations and numerical simulations provide only weak constraints on the spectral amplitude or the specific locations and strengths of power-law deviations. Despite these uncertainties, the sensitivity range of PTAs is sufficiently narrowband that it is reasonable, to first approximation, to model the signal by a power law in this frequency range:

$$\Phi_{\rm BHB}(f) = \frac{A^2_{\rm BHB}}{12\pi^2}\frac{1}{T_{\rm obs}}\left(\frac{f}{\rm yr^{-1}}\right)^{-\gamma_{\rm BHB}} {\rm yr}^3\,, \tag{6.13}$$

where $\Phi_{BHB}/\Delta f$ is the timing residual PSD (see Eq. (6.6)).

Following [379], we can gain some insight into the allowed range of values for the amplitude, $A_{\rm BHB}$, and slope, $\gamma_{\rm BHB}$, of this power law by simulating a large number of SMBHB populations covering the entire range of allowed astrophysical parameters. Specifically, we consider the SMBHB populations contained in the `GWOnly-Ext` library generated as part of the [344] analysis (and discussed in additional detail there). This library was constructed with the `holodeck` package [380] using semianalytic models of SMBHB mergers. These models use simple, parameterized forms of galaxy stellar mass functions, pair fractions, merger rates, and SMBH-mass versus galaxy-mass relations to produce binary populations and derived GWB spectra. While some parameters in these models are fairly well known (e.g., concerning the galaxy stellar mass function), others are almost entirely unconstrained—particularly those governing the dynamical evolution of SMBHBs on subparsec scales [374].

The `GWOnly-Ext` library assumes purely GW-driven binary evolution and uses relatively narrow distributions of model parameters based on literature constraints from galaxy-merger observations [e.g., 381] in addition to more detailed numerical studies of SMBHB evolution [e.g., 382].

For each population contained in the `GWOnly-Ext` library, we perform a power-law fit of the corresponding GWB spectrum across the first 14 frequency bins that we use in our analysis. The distribution for $A_{\rm BHB}$ and $\gamma_{\rm BHB}$ obtained in this way is reported in Fig. 6.1 (blue contours) and compared to the results of a simple power-law fit to the GWB signal in the NG15 data set (green contours). The 95% regions of the two distributions barely overlap, signaling a mild tension between the astrophysical prediction and the reconstructed spectral shape of the GWB. In view of this observation, we stress again that while these simulated populations are consistent with systematic investigations of the GWB spectrum [e.g., 382], they assume circular orbits and GW-only driven evolution. Adopting models that include either significant coupling between binaries and their local environments or very high eccentricities could serve to flatten the spectral shape and lead to SMBHB signals that better align with the observed data (see [344] for an extended discussion). Neither of these effects, however, is expected to significantly impact the amplitudes of the predicted spectra that, for expected values of astrophysical parameters, remain in mild tension with observed data. As discussed in [344], in order to reproduce the observed amplitude, SMBHB models require one or more of the astrophysical parameters describing the binaries' population to differ from expected values. For the present analysis, the spectra derived from the `GWOnly-Ext` library thus represent a convenient benchmark that is simple, well defined, and easy to use. By using theory-motivated priors, our reference model constitutes an important step toward a more realistic modeling of the GWB spectrum from inspiraling SMBHBs that goes beyond a power-law parameterization with spectral index $\gamma_{\rm BHB} = 13/3$, which has been the standard reference model in much of the PTA literature over the past decades.

The black dashed contours in Fig. 6.1 show the results of a 2D Gaussian fit to the distribution of $A_{\rm BHB}$ and $\gamma_{\rm BHB}$ values derived from the simulated SMBHB populations (see Eq. (G.1) in Appendix G for the parameters of this Gaussian distribution). This fitted distribution is what we adopt as a prior distribution for $A_{\rm BHB}$ and $\gamma_{\rm BHB}$ in all parts of the analysis described in this paper.

6.5 GWB Signals from New Physics

In this section, we discuss the GWB produced by various new-physics models and investigate each model alone and in combination with the SMBHB signal as a possible explanation of the observed GWB signal. For each model, we give a brief review of the mechanism behind the GWB production and discuss the parametrization of its signal prediction. We report the reconstructed posterior distributions of the model parameters and compute the Bayes factors against the baseline SMBHB interpretation. In Fig. 6.2, we show a summary of these Bayes factors; in Fig. 6.3, we present median reconstructed GWB spectra in the PTA band for a number of select new-physics models.

As discussed in Section 6.4 and in more detail in [344], there is a mild tension between the NG15 data and the predictions of SMBHB models. The models generally prefer a weaker and less blue-tilted $h^2\Omega_{GW}$ spectrum than the data. This discrepancy presents an opportunity for new-physics models to fit the data better than the conventional SMBHB signal. Eventually, this tension may grow to the point of giving strong evidence for new physics, or it may be resolved with better modeling and more data. Specifically, models of SMBHB evolution with a significant coupling between binaries and their local environment could lead to a signal that better aligns with the data and reduce the evidence for new physics. For all these reasons, we caution against over-interpreting the observed evidence in favor of some of the new-physics models discussed in the following sections.

Cosmological phase transitions

Model description

In the cosmological context, first-order phase transitions take place when a potential barrier separates the true and false minima of scalar field potential.[1] The phase transition is triggered by quantum or thermal fluctuations that cause the scalar field to tunnel through or fluctuate over the barrier, which results in the nucleation of bubbles within which the scalar field is in the true vacuum configuration. If sufficiently large, these bubbles expand in the surrounding plasma where the scalar field still resides in the false vacuum. The expansion and collision of these bubbles [241, 383, 384, 385, 386, 387], together with sound waves generated in the plasma [388, 389, 390,

[1] The scalar field can either be an elementary field of a weakly coupled theory or correspond to the vacuum condensate of a strongly coupled theory. Scenarios with several scalars are also possible.

391], can source a primordial GWB (see [392, 199] for seminal work).[2] For earlier Bayesian searches for a phase transition signal in PTA data, see [8, 393].

Generally, the GWB produced during the phase transition is a superposition of the bubble and sound-wave contributions. However, if the bubble walls interact with the surrounding plasma, most of the energy released in the phase transition is expected to be converted to plasma motion, causing the sound-wave contribution to dominate the resulting GWB. An exception to this scenario is provided by models in which there are no (or only very feeble) interactions between the bubble walls and the plasma, or by models where the energy released in the phase transition is large enough that the friction exerted by the plasma is not enough to stop the walls from accelerating (runaway scenario). However, determining whether or not the runaway regime is reached is either model dependent or affected by large theoretical uncertainties (see, e.g., [394, 395, 396] for recent work on this topic). Therefore, in this work, we perform two separate analyses: a sound-wave-only analysis (PT-SOUND), where we assume that the runaway regime is not reached and sound waves dominate the GW spectrum, and a bubble-collisions-only analysis (PT-BUBBLE), where we assume that the runaway regime is reached and bubble collisions dominate the GW spectrum.

We parameterize the GWB produced by both sound waves and bubble collisions in a model-independent way in terms of the following phase transition parameters:

• T_*, the percolation temperature, i.e., the temperature of the universe when $\sim 34\%$ of its volume has been converted to the true vacuum [397]. For weak transitions, this temperature coincides with the temperature at the time of bubble nucleation, $T_n \sim T_*$. Conversely, for supercooled transitions, we typically have $T_n \ll T_*$. Barring the case of extremely strong transitions, $\alpha_* \ggg 1$ (see below), which we do not consider in this work, T_* also determines the reheating temperature after percolation, $T_{rh} \sim T_*$ [397].

• α_*, the strength of the transition, i.e., the ratio of the change in the trace of the energy–momentum tensor across the transition and the radiation energy density at percolation [334, 398].

• $H_* R_* = R_*/H_*^{-1}$, the average bubble separation in units of the Hubble radius at percolation, H_*^{-1}. For relativistic bubble velocities, which is what we consider

[2] Turbulent motion of the plasma can also source GWs; however, its contribution is usually subleading compared to the two other contributions (see the discussion in [334]). Therefore, we ignore GWs sourced by turbulence in our analysis.

in the following, R_* is related to the bubble nucleation rate, β, by the relation $H_* R_* = (8\pi)^{1/3} H_*/\beta$.

In addition to the parameters T_*, α_*, and $H_* R_*$, the GWB produced by a phase transition also depends on the velocity of the expanding bubble walls, v_w. However, deriving the precise value of this quantity is an open theoretical problem, which depends on model-dependent quantities, such as the strength of the interactions between the bubble walls and the SM plasma. Therefore, in our analysis, we fix the bubble velocity to unity (i.e., the speed of light in natural units). This assumption is well justified for strong phase transitions [399], which, realistically, are the only ones that could lead to a detectable signal in our current data. In particular, we fix $v_w = 1$ for both phase transition scenarios that we are interested in, PT-SOUND and PT-BUBBLE. In the latter case, $v_w \to 1$ is automatically implied by the runaway behavior of the phase transition; in the former case, one actually expects a subluminal terminal velocity, $v_w < 1$. In this sense, our decision to fix $v_w = 1$ amounts to the optimistic assumption that this terminal velocity is numerically close to $v_w = 1$. A similar approach is followed by the authors of the LISA review paper [334] who work with $v_w = 0.95$ throughout most of their analysis in the absence of more detailed microphysical calculations. Finally, we point out that the parametrization of the GWB signal in terms of $H_* R_* = (8\pi)^{1/3}\, v_w\, H_*/\beta$ already absorbs a large part of the dependence on the bubble wall velocity. The remaining v_w dependence is mostly contained in the efficiency factor κ_s (see below). However, in the regime of large α_* values, $\alpha_* \sim 0.3 \cdots 10$, which turn out to be preferred by the NG15 data (see Fig. 6.4), this dependence is rather weak (see Fig. 13 in [400]), which justifies again to keeping v_w fixed.

The GWB spectrum sourced by bubbles and sound waves can be written in terms of these parameters as

$$\Omega_b(f) = \mathcal{D}\, \tilde{\Omega}_b \left(\frac{\alpha_*}{1+\alpha_*}\right)^2 (H_* R_*)^2\, \mathcal{S}(f/f_b) \tag{6.14}$$

$$\Omega_s(f) = \mathcal{D}\, \tilde{\Omega}_s\, \Upsilon(\tau_{sw}) \left(\frac{\kappa_s\, \alpha_*}{1+\alpha_*}\right)^2 (H_* R_*)\, \mathcal{S}(f/f_s)\,. \tag{6.15}$$

Here $\tilde{\Omega}_b = 0.0049$ [401] and $\tilde{\Omega}_s = 0.036$ [402]; the efficiency factor $\kappa_s = \alpha_*/(0.73 + 0.083\sqrt{\alpha_*} + \alpha_*)$ [400] gives the fraction of the released energy that is transferred to plasma motion in the form of sound waves, and $\mathcal{D}$ accounts for the redshift of the

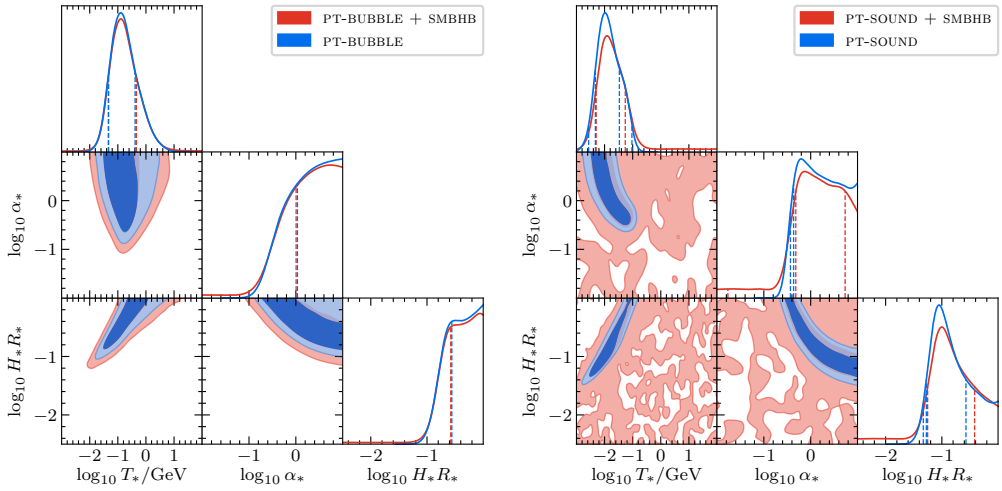

Figure 6.4: Reconstructed posterior distributions for the PT-BUBBLE (left panel) and PT-SOUND model (right panel). Fig. H.1 in Appendix H shows the same plots but with the parameter a fixed by causality, $a = 3$. Figs. H.2 and H.3 in Appendix H show extended versions of the two plots that include the spectral shape parameters a, b, c and the SMBHB parameters $A_{\rm BHB}$ and $\gamma_{\rm BHB}$.

GW energy density,

$$\mathcal{D} = \frac{\pi^2}{90}\frac{T_0^4}{M_{Pl}^2 H_0^2}\, g_* \left(\frac{g_{*,s}^{eq}}{g_{*,s}}\right)^{4/3} \simeq 1.67\times 10^{-5}\,. \tag{6.16}$$

We recall that T_0 and H_0 denote the photon temperature and Hubble rate today. The degrees of freedom g_* and $g_{*,s}$ in Eq. (6.16) are evaluated at $T = T_*$, and $g_{*,s}^{eq}$ is the number of degrees of freedom contributing to the radiation entropy at the time of matter–radiation equality. The production of GWs from sound waves stops after a period τ_{sw}, when the plasma motion turns turbulent [397, 398, 403, 404]. In Eq. (6.15), this effect is taken into account by the suppression factor

$$\Upsilon(\tau_{sw}) = 1 - (1 + 2\tau_{sw} H_*)^{-1/2}, \tag{6.17}$$

where the shock formation time scale, τ_{sw}, can be written in terms of the phase transition parameters as $\tau_{sw} \approx R_*/\bar{U}_f$, with $\bar{U}_f^2 \approx 3\kappa_s\alpha_*/[4(1+\alpha_*)]$ [238].

The functions $\mathcal{S}_{b,s}$ describe the spectral shape of the GWB and are expected to peak at the frequencies

$$f_{b,s} \simeq 48.5\, nHz\; g_*^{1/2}\left(\frac{g_{*,s}^{eq}}{g_{*,s}}\right)^{1/3}\left(\frac{T_*}{1\,GeV}\right)\frac{f_{b,s}^* R_*}{H_* R_*}\,, \tag{6.18}$$

where the values of the peak frequencies at the time of GW emission are given by $f_b^* = 0.58/R_*$ [401] and $f_s^* = 1.58/R_*$ [402]. In passing, we mention that the numerical factors in these estimates may still change in the future, as our understanding of cosmological phase transitions improves. However, at the level of our Bayesian fit analysis, changes in these prefactors can be absorbed in the temperature scale T_*, which in its role as an independent fit parameter only controls the peak frequencies in Eq. (6.18). A similar argument applies to the numerical factors in Eqs. (6.14) and (6.15): changes in these prefactors can always be absorbed in a rescaled version of the fit parameter α_*, which only appears in the expressions for the peak amplitudes of the GWB signal.

The shape of the spectral functions can be usually approximated with a broken power law of the form

$$\mathcal{S}(x) = \frac{1}{\mathcal{N}} \frac{(a+b)^c}{(bx^{-a/c} + ax^{b/c})^c} \,. \tag{6.19}$$

Here a and b are two real and positive numbers that give the slope of the spectrum at low and high frequencies, respectively; c parametrizes the width of the peak. The normalization constant, $\mathcal{N}$, ensures that the logarithmic integral of $\mathcal{S}$ is normalized to unity and is given by

$$\mathcal{N} = \left(\frac{b}{a}\right)^{a/n} \left(\frac{nc}{b}\right)^c \frac{\Gamma\left(a/n\right)\,\Gamma\left(b/n\right)}{n\,\Gamma(c)} \,, \tag{6.20}$$

where $n = (a+b)/c$ and Γ denotes the gamma function. While the values of the coefficients a, b, and c can in principle be estimated from numerical simulations, we allow them to float within the prior ranges given in Table G.2. These prior ranges were chosen to roughly reflect the typical uncertainties of numerical simulations and any possible model dependency of these coefficients (see, e.g., [402, 335, 405, 406, 407, 408]).[3]

Results and discussion

The reconstructed posterior distributions for the parameters α_*, T_* and H_*R_* of the PT-SOUND and PT-BUBBLE models are reported in Fig. 6.4, both for the case where the phase transition is assumed to be the only source of GWs (blue contours) and

[3] Causality fixes the spectral index of the phase transition GWB signal to $a = 3$ in the low-frequency limit. However, given the simple power-law parametrization adopted in this work, double-peak features observed in the results of numerical simulations [402, 409] can appear as a deviation from this behavior near the peak frequency. Nonetheless, in Appendix H, we also report the results of an analysis in which the low-frequency slope is fixed to $a = 3$.

for the scenario where we consider the superposition of the phase transition and SMBHB signals (red contours).[4] Corner plots including the posterior distributions for the spectral shape parameters a, b, c and SMBHB parameters $A_{\rm BHB}$ and $\gamma_{\rm BHB}$ are reported in Figs. H.2 and H.3 in Appendix H.

In all analyses, the data prefer a relatively strong and slow phase transition. Specifically, for PT-BUBBLE, we find $\alpha_* > 1.1$ (0.29) and $H_*R_* > 0.28$ (0.14) at the 68% (95%) credible level. When the SMBHB signal is added on top of the GWB predicted by PT-BUBBLE, we find $\alpha_* > 1.0$ (0.23) and $H_*R_* > 0.26$ (0.11) at the 68% (95%) credible level. For the PT-SOUND model, we find $\alpha_* > 0.42$ (0.37) and $H_*R_* \in [0.053, 0.27]$ ($[0.046, 0.89]$) at the 68% (95%) credible level. Including the SMBHB signal on top of the one predicted by PT-SOUND, we find $\alpha_* \in [0.46, 5.4]$ (> 0.16) and $H_*R_* \in [0.054, 0.35]$ (> 0.0015) at the 68% (95%) credible level.

As can be seen in Fig. 6.3, for both phase transition models, the reconstructed GWB spectrum tends to peak around the higher frequency bins and fit the signal in the lower frequency bins with the left tail of the spectrum. Specifically, for the PT-BUBBLE model we find $T_* \in [0.047, 0.41]$ ($[0.023, 1.75]$) GeV at the 68% (95%) credible level, whereas for the PT-SOUND model we get $T_* \in [4.7, 33]$ ($[2.7, 93]$) MeV at the 68% (95%) credible level. The shift between these T_* intervals is partially explained by the different numerical factors in the frequencies f_s^* and f_b^* (see Eq. (6.18)). As explained below Eq. (6.18), any change in these numerical factors can be reabsorbed in a redefinition of the fit parameter T_*.

The inclusion of the SMBHB signal, by adding power to the lowest frequency bins, allows the T_* posterior for the PT-SOUND model to extend to higher values. In this case, we find that $T_* \in [4.9, 50]$ ($[0.8, 2 \times 10^6]$) MeV at the 68% (95%) credible level. Here the increase in the 68% upper limit is reflected in the slight shift between the red and blue dashed vertical lines in the 1D marginalized posterior distribution for T_* in the right panel of Fig. 6.4. The drastic increase in the 95% upper limit, on the other hand, is related to the fact that adding the SMBHB signal to the GWB results in a flat plateau region in the posterior distribution of the PT-SOUND model parameters where the NANOGrav signal is mostly explained by the SMBHB contribution to the GWB. The 95% credible regions for the PT-SOUND+SMBHB model cover much of this plateau, which explains their large extent and noisy appearance in Fig. 6.4. For

[4]The noise in the 95% credible regions of the posterior distributions of the PT-SOUND+SMBHB model is due to the presence of an extended plateau region in the posterior distribution, which renders the kernel density reconstruction sensitive to Poisson fluctuations in the binned MCMC data.

the PT-BUBBLE model, the inclusion of the SMBHB signal is less significant, and we find $T_* \in [0.046, 0.46]$ ($[0.017, 3.27]$) GeV at the 68% (95%) credible level.

The larger phase transition temperatures observed for the PT-BUBBLE model are a consequence of the smaller value of the peak frequency at the time of emission, f_b^*, but also of the lower prior range for the low-frequency spectral index adopted for the PT-BUBBLE model. Indeed, a shallower low-frequency tail allows spectra with a higher peak frequency to still produce a sizable signal in the lowest frequency bins. In Appendix H, we report the results of the analysis in which the low-frequency slope is set to the value predicted by causality ($a = 3$). In this case, as expected, the reconstructed phase transition temperatures for the two phase transition models are closer to each other.

The corner plots in Fig. 6.4 also illustrate that, as expected from the expression for the peak frequency in Eq. (6.18), there is an approximately linear correlation between $\log_{10} T_*$ and $\log_{10} H_* R_*$. For $\alpha_* \lesssim 1$, we instead find $\alpha_* \sim 1/(H_* R_*)$ for the PT-BUBBLE model and $\alpha_*^2 \sim 1/(H_* R_*)$ for the PT-SOUND model as expected from the factors in Eq. (6.14) and Eq. (6.15).

We also notice that, for both models, the posterior distribution for T_* is peaked at significantly larger values compared to what was derived in the 12.5 yr analysis [8]. This shift results from the reconstructed $h^2\Omega_{GW}$ spectrum being bluer than the one derived for the common process observed in the 12.5 yr data set. As a result, the lowest frequency bins, which were fit by the high-frequency tail of the phase transition spectrum in the 12.5 yr analysis, are now fit by the low-frequency tail of the spectrum. This then translates into a higher peak frequency and therefore a higher transition temperature. Incidentally, the larger reconstructed value for the transition temperature allows the phase transition signal to safely evade bounds from BBN and CMB observations [410, 411] for both the PT-BUBBLE and PT-SOUND models, which constrain the phase transition parameter space at temperatures around $T_* \sim 1$ MeV.

Instead, we conclude that the reconstructed posterior distribution of T_* is compatible with phase transition scenarios that have been discussed in the literature as a possible source of GWs in the PTA band: (i) BSM models in which the chiral-symmetry-breaking phase transition in quantum chromodynamics (QCD) is a strong first-order phase transition (see, e.g., [412, 222]) and (ii) strong first-order phase transitions in a dark sector composed of new BSM degrees of freedom (see, e.g., [413, 133]). In view of the NG15 data, both of these options for the particle physics origin of the phase transition signal remain viable. A third option may consist in a strongly

supercooled first-order electroweak phase transition [414].

Finally, we report that that the phase transition models provide a better fit of the NG15 data than the base SMBHB model. The Bayes factors for PT-BUBBLE and PT-SOUND versus SMBHB are $\mathcal{B} = 18.1 \pm 0.6$ and $\mathcal{B} = 3.7 \pm 0.1$, respectively, while the Bayes factors for PT-BUBBLE+SMBHB and PT-SOUND+SMBHB versus SMBHB are $\mathcal{B} = 12.6 \pm 0.5$ and $\mathcal{B} = 6.5 \pm 0.3$, respectively. An interesting observation in view of these results is that adding the SMBHB contribution to the GWB signal does not help to improve the quality of the fit for PT-BUBBLE—in this case, we find again a decrease in the Bayes factor going from PT-BUBBLE to PT-BUBBLE+SMBHB because of the larger prior volume—but it does lead to a better fit for PT-SOUND. This model benefits from the additional SMBHB contribution because it can add power to the low frequency bins in the GW spectrum that the PT-SOUND model alone struggles to fit well on its own (see Fig. 6.3). The reason for this, in turn, is the prior range for the spectral index at low frequencies, a, which can as be as low as $a = 1$ for PT-BUBBLE, but which we require to be at least $a = 3$ for PT-SOUND (see Table G.2). Another consequence of this interplay between the phase transition and SMBHB signals is that the NANOGrav signal may in fact be dominated by SMBHBs. This possibility is realized when the PT-SOUND model parameters fall into the plateau region in Fig. 6.4 (i.e., the red 95% credible regions in the right panel) and the SMBHB parameters are close to $\log_{10} A_{\rm BHB} \sim -(15 \cdots 14)$ and $\gamma_{\rm BHB} \sim 3 \cdots 4$ (see Fig. H.3).

6.6 Deterministic Signals from New Physics

In addition to the GWB signals discussed previously, there are several new-physics theories that can imprint a deterministic signal, described by a time series $\boldsymbol{h}$, in pulsar timing data. In this section, we consider the deterministic signals induced by DM substructures. After finding no statistically significant evidence for such signals in our data, we report upper limits on the allowed strength of these signals.

Dark matter substructures

Model description

In the ΛCDM model, the structures we observe in the universe are seeded by primordial curvature fluctuations generated during inflation and then imprinted onto the DM density field. CMB observations indicate that these fluctuations have a nearly scale-invariant power spectrum on large scales (i.e., for comoving wavenumbers $k \simeq Mpc^{-1}$). However, on smaller scales, various theories of DM

leave unique fingerprints on primordial perturbations or their evolution, resulting in different predictions for the amount of subgalactic DM substructures. Consequently, measuring local DM substructures could be crucial in determining the correct model of DM.

PBHs are perhaps the simplest example of such small-scale DM substructures. They can be formed in inflationary theories that create large density fluctuations on small scales. Several studies investigated the possibility of identifying a galactic PBH population by analyzing the Doppler and Shapiro signals they can leave in PTA data [150, 44, 43, 42, 9, 10]. In this analysis, we will closely follow the method outlined by [10] to constrain the local PBH abundance.[5]

The Doppler signal results from the apparent shift in the pulsar spin frequency, generated by the acceleration induced by the gravitational pull of a passing PBH. According to the timescale of the transit event, τ, the signal can be further classified as dynamic (static) if τ is much smaller (larger) than the observation time, $T_{\rm obs}$. In the static regime, the leading-order term of the Doppler signal that is not degenerate with the timing model is given by [42, 9, 10]

$$h_{D,sta}(t) = \frac{A_{D,sta}}{yr^2}\, t^3\,, \tag{6.21}$$

where $A_{D,sta}$ is a dimensionless parameter that can be related to the kinematic parameters of the transiting event (see Appendix H for more details). In the dynamic limit, and assuming that the signal is dominated by the closest transiting PBH, we get

$$h_{D,\rm dyn}(t) = A_{D,\rm dyn}\,(t - t_0)\,\Theta(t - t_0)\,, \tag{6.22}$$

where Θ is the Heaviside step function, $A_{D,\rm dyn}$ is a dimensionless amplitude that can be related to kinematic parameters of the transiting event, and t_0 is the time of closest approach (see Appendix H for more details).

The Shapiro signal refers to shifts in the TOAs caused by metric perturbations along the photon geodesic produced by PBHs transiting along the observer's line of sight. In the static limit, and after subtracting away degeneracies with timing model parameters, the leading-order term of this signal can be parameterized as

$$h_{S,sta}(t) = \frac{A_{S,sta}}{yr^2}\, t^3\,, \tag{6.23}$$

[5] A similar approach could be applied to set constraints on the local abundance of DM subhalos. However, we do not consider this case, since our constraints for PBHs are already quite weak. Constraints on DM subhalos would likely be even weaker, making it a less promising target for future PTAs.

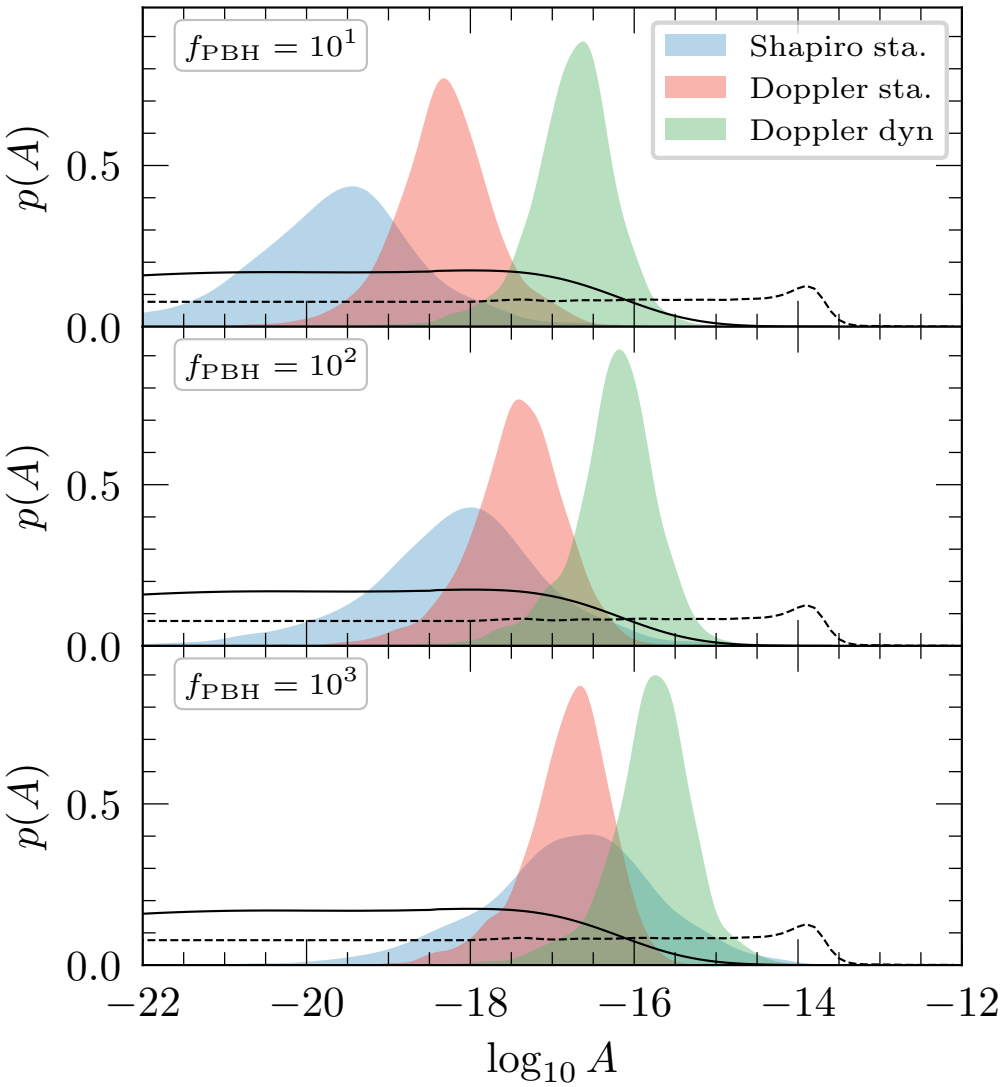

Figure 6.5: The black solid (dashed) lines show the posterior distributions $p(\log_{10} A_{sta}|\boldsymbol{\delta t})$ ($p(\log_{10} A_{\rm dyn}|\boldsymbol{\delta t})$) for a representative pulsar (J1909-3744). The filled distributions show the conditional probability distributions $p(\log_{10} A|f_{\rm PBH})$ for the same pulsar and different values of $f_{\rm PBH}$. In this plot, $M = 10^{-6}$ (10^{-10}) $M_\odot$ for the Doppler static (dynamic) signal, and $M = 10M_\odot$ for the Shapiro static signal.

where, as for the Doppler case, $A_{S,sta}$ is a dimensionless parameter that can be related to the kinematic parameters of the transiting event (see Appendix H for more details). In the dynamic limit, there is no simple parametrization of the Shapiro signal; therefore, we do not search for this signal.

Assuming a monochromatic PBH population, our goal is to derive a posterior distribution for the PBH mass fraction, $f_{\rm PBH} \equiv \Omega_{\rm PBH}/\Omega_{DM}$, as a function of the PBH mass, M: $p(f_{\rm PBH}|\boldsymbol{\delta t}, M)$. We do this as follows:

• For each given value of $f_{\rm PBH}$ and M, we use the Monte Carlo code developed by [9] to generate a PBH population surrounding each of the pulsars in our array. From this distribution, we derive the amplitude of the static Doppler and Shapiro signals generated by the entire PBH population and the amplitude for the dynamic Doppler signal generated by the closest transiting PBH. Finally, we repeat this procedure for 2.5×10^3 realizations to obtain the conditional probability distributions $p(\log_{10} A_I|f_{\rm PBH})$, where I indexes pulsars in the array and A refers to any of the PBH signal amplitudes introduced in Eqs. (6.21), (6.22), and (6.23). In Fig. 6.5 we report some of the distributions derived in this way.[6]

• One at a time, we include the PBH signals given in Eqs. (6.21), (6.22), and (6.23) in the timing model, and we analyze our data to derive the posterior distributions for the various PBH signal amplitudes, $p(\log_{10} \boldsymbol{A}|\boldsymbol{\delta t})$. Since the PBH signal in different pulsars is assumed to be independent, these distributions can be factorized as

$$p(\log_{10} \boldsymbol{A}|\boldsymbol{\delta t}) = \prod_{I=1}^{N_P} p(\log_{10} A_I|\boldsymbol{\delta t}) \,. \tag{6.24}$$

Some of the $p(\log_{10} A_I|\boldsymbol{\delta t})$ are reported in Fig. 6.5.

• Finally, we can write

$$\begin{aligned} p(f_{\rm PBH}|\boldsymbol{\delta t}) &= \prod_{I=1}^{N_P} \int d\log_{10} A_I \; p(f_{\rm PBH}|\log_{10} A_I) p(\log_{10} A_I|\boldsymbol{\delta t}) \\ &\propto \prod_{I=1}^{N_P} \int d\log_{10} A_I \; p(\log_{10} A_I|f_{\rm PBH}) p(\log_{10} A_I|\boldsymbol{\delta t}) \end{aligned} \tag{6.25}$$

where, in the second step, we used Bayes theorem and assumed uniform priors on $\log_{10} A_I$ and $f_{\rm PBH}$. More details on each of these three steps can be found in Appendix H or in [10].

[6] From now on, we suppress the PBH mass, M, in the expressions for the conditional probabilities for the sake of notation.

DM substructures can also possess macroscopic charges and interact with baryonic matter via long-range Yukawa interactions. These interactions can be modeled by a potential of the form

$$V_{\rm fifth}(r) = -\tilde{\alpha}\frac{GMM_P}{r}e^{-r/\lambda}\,, \tag{6.26}$$

where M and M_P are the masses of the DM and pulsar, respectively, λ is the range of the interaction, and $\tilde{\alpha}$ is the effective DM-barion coupling, normalized against the gravitational coupling (also known as the Yukawa parameter). Here the DM can be either a particle or a macroscopic object such as a nugget of asymmetric DM ([259, 260, 257, 258, 262, 261]). These Yukawa interactions can arise from an effective Lagrangian of the form $\mathcal{L} \supset g_X\phi\bar{X}X + g_n\phi\bar{n}n$, where X and n are the effective DM and neutron fields, and ϕ is a massive (but potentially light) scalar or vector field. The effective coupling is related to the coupling constants by $\tilde{\alpha} \approx \frac{g_n g_X}{4\pi G m_X m_n}$, where m_n is the neutron mass. These interactions are constrained to be weaker than gravity for the mass range $M \lesssim 100$ GeV by the CMB, Lyman-α forest [415], and direct detection experiments such as X-ray Quantum Calorimeter (XQC) [416] and Cryogenic Rare Event Search with Superconducting Thermometers (CRESST) [417] (for a review on these constraints see [418]). However, stronger-than-gravity fifth forces are allowed if $M \gg 100$ GeV, even when X accounts for the entirety of the DM population.

If present, these Yukawa interactions will contribute to the pulsar's acceleration induced by a transiting DM substructure and contribute to the Doppler signal discussed before (the expression for the Yukawa contribution to the Doppler signal can be found in Appendix H). Therefore, as shown by [5], following a procedure similar to the one used to constrain the abundance of PBHs, we can constrain the value of the Yukawa parameter, $\tilde{\alpha}$. Specifically, for each given value of $\tilde{\alpha}$ and M, we use the Monte Carlo code developed by [9] to generate a population of DM substructure surrounding each of the pulsars in our array. From this distribution, we derive the amplitude of the static Doppler signal generated by the closest transiting substructure by considering the acceleration induced by both the gravitational and Yukawa interaction. By repeating this procedure for multiple populations of DM substructure, we derive the distribution $p(\log_{10} A_I|\tilde{\alpha})$. By plugging this quantity into an expression similar to the one given in Eq. (6.25), we can derive $p(\tilde{\alpha}|\boldsymbol{\delta t})$ and use this quantity to constrain $\tilde{\alpha}$.

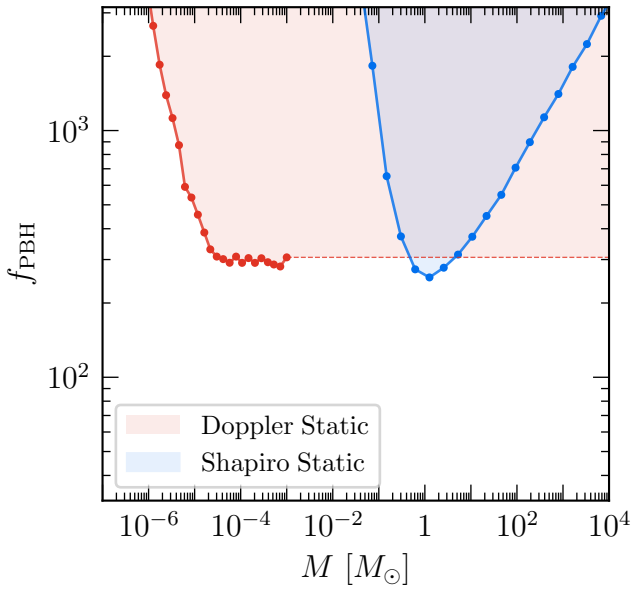

Figure 6.6: Constraints at the 95% credible level on the local PBH abundance derived from the search for static Doppler (red shaded region) and static Shapiro signals (blue shaded region). The solid lines interpolate between the PBH masses simulated in this work, while the red dashed line shows an extrapolation of the constraints to higher masses.

Results and discussion

We start by searching for PBH signals on top of a GWB that we model as a power law with amplitude and spectral index allowed to float within the following prior ranges: $\log_{10} A_{GWB} \in [-11, -18]$ and $\gamma_{GWB} \in [0, 7]$. We find no statistically significant evidence for any of the PBH signals described in the previous section. Therefore, we proceed to set constraints on the local PBH abundance. The prior distributions used for the PBH signal parameters are reported in Table G.2.

The 95% upper limits on $f_{\rm PBH}$ derived from the static Doppler and Shapiro signals are reported in Fig. 6.6. The dynamic Doppler signal is too weak to produce any detectable signal for any of the $f_{\rm PBH}$ values considered. These are the first constraints on $f_{\rm PBH}$ derived using real PTA data. As expected, our constraints are much weaker compared to the projections that were derived by [10] using mock data and including only white noise. Indeed, as already discussed by [10], the presence of a common red-noise process significantly reduces the sensitivity to PBH signals.

Finally, in Fig. 6.7 we show the constraints on $\tilde{\alpha}$ set by NG15 data. These constraints are compared with several other constraints that can be placed on $\tilde{\alpha}$. Specifically,

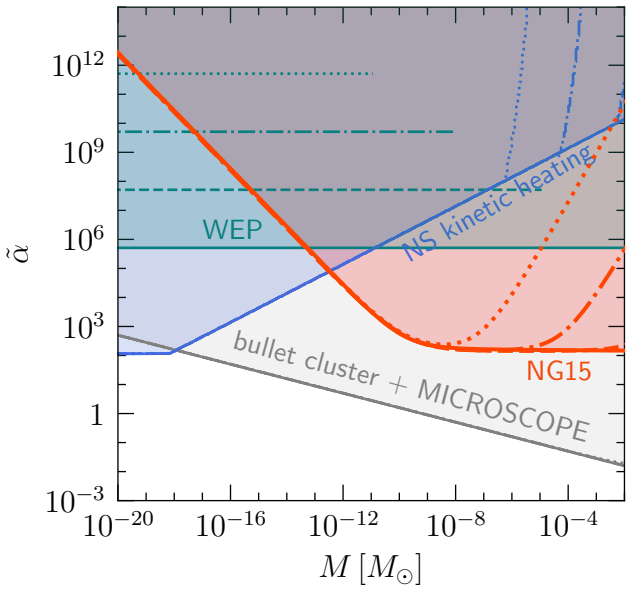

Figure 6.7: The 95% credible level for the fifth-force strength $\tilde{\alpha}$ derived from the NG15 data (red lines) is compared with constraints from NS kinetic heating (blue lines), equivalence principle constraints (green lines), and Bullet Cluster + equivalence principle constraints (gray line). Solid (dashed) lines are deriving assuming $\lambda = 1\ pc$ ($\lambda = 10^{-1}\ pc$), while dashed-dotted (dotted) lines are derived assuming $\lambda = 10^{-2}\ pc$ ($\lambda = 10^{-3}\ pc$).

in teal we show weak equivalence principle (WEP) constraints [312, 316, 315] (properly rescaled to take into account the finite range of the interaction [5]) derived by considering differential acceleration of baryonic test bodies toward the galactic center. In blue we report constraints from neutron star (NS) heating (assuming additional short-range DM-baryon interaction) induced by DM capture [5], derived from the coldest known NS to date - PSR J2144-3933 [295]. And in gray we report the indirect constraints that can be derived by combining the fifth-force constraints on baryon-baryon interactions [266, 267], and Bullet Cluster constraints on DM-DM interactions [78, 79] (see [268, 5]). We find that the NG15 constraints are competitive with WEP and NS kinetic heating, especially in the $M \gtrsim 10^{-12}\ M_\odot$ regime. However, the combined constraint from the Bullet Cluster and MICROSCOPE dominates over all other constraints in the entire mass range of interest. We note, however, that the combined constraint is an indirect probe of the Yukawa parameter and depends on the specific form of the light mediator coupling to DM and baryons. Specifically, in deriving the combined constraints, we have assumed that the Yukawa DM-baryon interaction arises from a Lagrangian of the form $\mathcal{L} \supset g_X \phi \bar{X} X + g_n \phi \bar{n} n$.

In addition, if only a subcomponent of DM interacts through the long-range fifth force, then the Bullet Cluster constraint will quickly lift, while the other constraints only deteriorate linearly with the DM fraction.

6.7 Discussion

The analysis of the NANOGrav 15-year data set has produced the first convincing evidence for a stochastic background of GWs in the nanohertz frequency range. The origin of this background is still unknown. In this work, we considered various cosmological sources and compared them to the commonly studied astrophysical signal produced by a population of inspiraling supermassive black-hole binaries. Specifically, we considered the signals produced by nonminimal inflation scenarios, scalar-induced GWs, cosmological phase transitions, several cosmic-string models, and domain walls.

For each of these models, we identified regions of the parameter space that are compatible with the observed signal. We find that, with the exception of stable cosmic strings of field theory origin, all new-physics models considered in this analysis are capable of reproducing the GWB signal. Many models allow us in fact to fit the signal better than the SMBHB reference model, which is reflected in Bayes factors ranging from 10 to 100 (see Fig. 6.2). When the new-physics signals are combined with the astrophysical one, we obtain comparable results. More precisely, in several models, the addition of the SMBHB signal leads to a slight decrease of the Bayes factor, which indicates that the SMBHB contribution does not help to improve the quality of the fit but merely increases the prior volume. In other models, on the other hand, such as PT-SOUND and DW-DR, adding the SMBHB signal on top of the new-physics signal can lead to a slight increase of the Bayes factor, indicating that the SMBHB signal can in fact play a dominant role in the total GW spectrum. For all four stable-string models, we find Bayes factors between 0.1 and 1. Cosmic superstrings, on the other hand, which are also stable but not of field theory origin, can explain the data at a level comparable to other new-physics sources.

Despite the fact that some of the Bayes factors derived in this paper might suggest that a purely astrophysical interpretation of the signal is disfavored by the data, we caution against this interpretation. The Bayes factors do not account for the full range of uncertainties in both the cosmological and astrophysical signals and are prior dependent. It is conceivable that, as our understanding of SMBHB signals and our noise models improve, the tension between observations and astrophysical pre-

dictions will decrease, potentially weakening the evidence in favor of cosmological signals.

Future data sets will improve the spectral characterization of the signal and improve our ability to discriminate cosmological sources from the SMBHB signal. Unfortunately, similarities in the spectral shape and theoretical uncertainties will make it challenging to definitively determine the origin of the background using power spectrum characterization alone. However, the observation of anisotropies could eventually resolve this debate, as the expected anisotropies generated by black hole binaries are significantly larger than those produced by most cosmological sources. Similarly, the detection of a continuous wave from a single binary would provide convincing evidence in favor of an astrophysical origin of the signal. Ultimately, measurements of the GWB spectral shape and angular power spectrum may be complemented by observations of its polarization content and possible deviations from Gaussian statistics, which can again help to discriminate between an astrophysical and a cosmological origin of the signal.

It is worth emphasizing that in all parts of our analysis we described cosmological signals using effective parameters, e.g., T_*, α_*, and H_*R_*, for the phase transition models. Moving forward, it will be crucial to identify microscopic models that can reproduce the values of these parameters that we found to best fit the GWB signal. That is, in order to shed more light on the various cosmological interpretations of the signal, we require a better understanding of how the NANOGrav signal could possibly result from the fundamental parameters of a particle physics Lagrangian that describes the generation of GWs in the early universe.

Along with searching for a cosmological GWB, we also analyze our data to search for deterministic signals generated by models of ULDM and DM substructures. We do not find significant evidence for either of these signals. Nonetheless, we are able to place constraints on the parameters space of these models. For a wide range of ULDM models, our constraints compete or outperform laboratory constraints in the $10^{-23}\,\mathrm{eV} \lesssim m_\phi \lesssim 10^{-20}\,\mathrm{eV}$ mass window. The signal from DM substructures is harder to detect; as a consequence, we are able to set very weak constraints on the local abundance of these objects. Future data sets will improve our reach, but a better characterization of the GWB will be needed to probe realistic models of DM substructures.

The discovery of a GWB will lead to significant breakthroughs in our understanding of cosmology and particle physics. As future PTA data sets become available,

we will establish the origin of the GWB. Regardless of whether the signal is of cosmological origin, we have shown how PTAs will undoubtedly contribute to exploring new physics, either as a discovery tool or as a new way to constrain the parameter space of BSM models.

Chapter 7

DETECTION OF MACROSCOPIC DARK MATTER WITH GRAVITATIONAL WAVE EXPERIMENTS

This chapter is based on

[1] Yufeng Du, Vincent S. H. Lee, Yikun Wang, and Kathryn M. Zurek. "Macroscopic dark matter detection with gravitational wave experiments". In: *Phys. Rev. D* 108.12 (2023), p. 122003. DOI: 10.1103/PhysRevD.108.122003. arXiv: 2306.13122 [astro-ph.CO].

7.1 Introduction

Astrophysical and cosmological evidence points to the existence of dark matter (DM), but little has been determined about its microscopic nature, with even its possible mass consistent with observation in the large range of 10^{-22} eV to $10^{4}\,M_{\odot}$ (see Ref. [419] for a recent review). Direct detection of dark matter in terrestrial experiments has focused on DM particles whose interactions with the Standard Model particles are determined by the DM abundance in the Universe. Such DM typically has mass $\lesssim$ 340 TeV [420], and has been the subject of a range of experiments searching both for single particle interactions (see Ref. [421] for a review) and collective wavelike phenomena [422, 423].

On the other hand, the direct detection of ultra-heavy dark matter (UHDM) is relatively unexplored, with primordial black holes (PBHs) [424] being the most well-studied DM candidate in this category. While unitarity bounds limit DM production through thermal mechanisms above $\sim$ 100 TeV, UHDM can be a composite state synthesized in a way similar to SM nuclei [425, 260, 261, 262]. Such UHDM can be searched for by direct scattering [268] or quantum mechanical sensors [426, 427].

In this work, we consider the detection of UHDM beyond $M_{\rm Pl}$ via long-range forces, whether gravity or a new fifth force between baryons and DM. Alongside LIGO's success in detecting gravitational waves (GWs) from a binary black hole merger [428], a myriad of laser interferometer experiments are either in operation or are planned to commence operation in the near future [429]. DM transiting in the solar system produces a weak gravitational potential, and can in principle be observed by laser interferometers. These effects have been analyzed previously in

the context of pulsar timing arrays (PTAs) [44, 103, 42, 9, 10, 5]. In addition, laser interferometer experiments with shorter ($\sim$ m) baselines, designed to measure quantum gravity signature in causal diamonds (see Ref. [86] for a review), can also be sensitive to transiting DM, which includes the past experiment Holometer [430, 431], and an upcoming experiment commissioned by Caltech and Fermilab under the Gravity from the Quantum Entanglement of Space-Time (GQuEST) collaboration [432]. These GW detectors generally operate at high frequency $\gtrsim$ 10 Hz, which corresponds to sensitivity towards DM with mass $M \lesssim$ kg assuming that the DM saturates the local dark matter density.

Detection of UHDM with laser interferometers has been considered elsewhere in the literature [433, 434, 435]. Other works model GW detectors as simple accelerometers and derive the sensitivity due to transiting DM from mirror acceleration [436, 437, 438, 439]. In this work, we take a more careful approach and formally derive the gauge invariant observable on laser interferometers [7] from transiting DM. In addition to the Doppler effect (which is usually the sole effect considered in the literature), the Shapiro delay and Einstein delay are also derived. Moreover, we discuss the statistical formalism for detecting both single events and a stochastic background of events. For other types of GW detectors, we give an overview of those sensitive to transiting DM and project the sensitivity assuming an accelerometer signal.

Finally, we also consider the possibility that the DM and baryon are coupled with an additional long-range Yukawa interaction, also known as a fifth force [440]. Such an interaction can arise very generally from an effective Lagrangian with a scalar/vector/tensor mediator between DM and baryons and is only weakly unconstrained by cosmology for heavy DM with force range $\lambda \lesssim 10^6$ m, even with stronger-than-gravity coupling. The existence of a long-range fifth force can have profound implications in DM searches, such as the creation of DM evaporation barriers in celestial bodies [441]. Various experiments searching for weak equivalence principle violating forces have put constraints on specific models, such as coupling through massive scalars [442, 443]. Here we consider a more general scenario without the assumption of the specific microscopic interaction. We find that high-frequency detectors are able to constrain the Yukawa coupling constant to be $\lesssim 10^3$ for a force range $\lambda > 10^6$ m and $M \sim$ kg within one year of integration time, which is roughly consistent with the findings of Refs. [438, 435].

Our paper is organized as follows. In Section 7.2, we provide a description of the gauge invariant strain from transiting macroscopic DM and discuss various aspects

of the signal. In Section 7.3, we provide a detailed derivation of the signal spectrum. In Section 7.4, we derive the constraints from a stochastic signal, where individual DM might be insufficient to produce a detector signature, but the collective behavior from all DM passing by the detector can be detectable. In Section 7.5 we discuss the various experiments we consider in this work and their sensitivity curves to the signal. In Section 7.6 we place our results into context and conclude.

7.2 Description of Macroscopic Dark Matter Signals in Interferometry-Based Gravitational Wave Detectors

Transiting DM induces a gravitational field as a metric perturbation $h_{\mu\nu}$. This produces a strain in a GW detector, $h(t) = \Delta L/L$ (where L is the interferometer arm length), which is the sum of three individual contributions

i) Doppler effect: acceleration of the mirrors

ii) Shapiro delay: change in the photon travel time within the interferometer arm

iii) Einstein delay: time dilation of the clock proper time (also known as gravitational redshift)

The total strain can be written in the general form

$$h(t, \hat{\mathbf{n}}) = h_{\text{Doppler}}(t, \hat{\mathbf{n}}) + h_{\text{Shapiro}}(t, \hat{\mathbf{n}}) + h_{\text{Einstein}}(t)\,, \tag{7.1}$$

where $\hat{\mathbf{n}}$ is the unit vector along the interferometer arm. Note that the Einstein delay does not depend on the arm orientation. A Michelson-Morley laser interferometer consists of two arms and measures the *difference* between the two arms

$$h(t, \hat{\mathbf{n}}_1, \hat{\mathbf{n}}_2) = h(t, \hat{\mathbf{n}}_1) - h(t, \hat{\mathbf{n}}_2)\,, \tag{7.2}$$

where $\hat{\mathbf{n}}_1$ and $\hat{\mathbf{n}}_2$ are the orientation of the two arms respectively. We quickly see that the Einstein delay contribution vanishes for laser interferometers, but can be present in single-arm interferometers, such as PTAs and long-baseline atom interferometers. In the following sections, we will suppress the unit vector dependence for simplicity. We emphasize that individual contributions from Eq. (7.1) are frame-dependent, and only the sum is gauge invariant and is hence an acceptable experimental observable [7], which will be formally derived in Sec. 7.3.

In Fig. 7.1 we show the Fourier transformed strain, $\tilde{h}_X(f) \equiv \int dt \exp(-2\pi i f t) h_X(t)$, for each contribution (X = Doppler, Shapiro or Einstein) and some choices of the

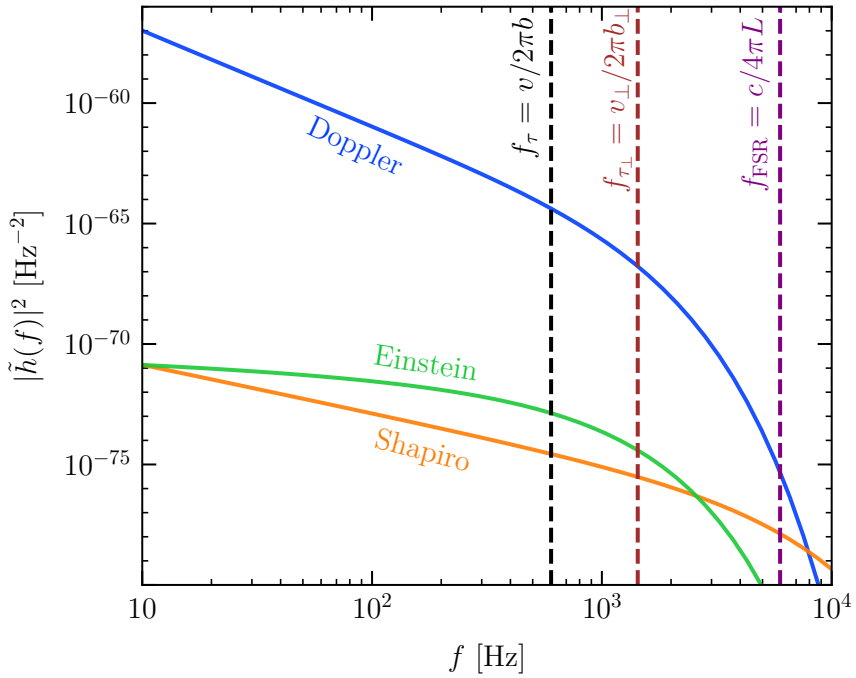

Figure 7.1: Signal spectrum $|h_X(f)|^2$ for Doppler effect, Shapiro delay and Einstein delay. Here we choose $M = 10^{-4}$ kg, $b = 90$ m, $v = 340$ km/s, $b_\perp = 30$ m, $v_\perp = 270$ km/s, $L = 4$ km, and assume a single-arm GW detector for illustration purposes. See the discussion of different length scales in Sec. 7.2. The analytic expressions for the signal spectrum are taken from Eq. (7.26) (Doppler), Eq. (7.32) (Shapiro), and Eq. (7.37) (Einstein).

DM mass M, velocity v, and impact parameter b, as specified in the figure caption. Analytic formulae for the spectrum are derived in Sec. 7.3. We observe that the signal is a simple power law in the frequency f when $f \lesssim f_\tau$, and rapidly drops to zero as $f \gtrsim f_\tau$, where $f_\tau \equiv 1/(2\pi\tau)$ is the characteristic frequency of a transiting DM as given by the characteristic timescale $\tau \equiv b/v$, or in the $b \lesssim L/2$ limit of the Shapiro delay, $\tau_\perp \equiv b_\perp/v_\perp$ with $b_\perp$ and $v_\perp$ being the perpendicular impact parameter and velocity with respect to the interferometer arm, respectively. In general, the signal spectrum can be parameterized as

$$|\tilde{h}_X(f)|^2 = A_X^2 \left|\tilde{q}_X\left(\frac{f}{f_{\rm FSR}}\right)\right|^2 \left|\tilde{s}_X\left(\frac{f}{f_\tau}\right)\right|^2 , \tag{7.3}$$

where $f_{\rm FSR} \equiv c/4\pi L$ is the detector's free-spectral-range (FSR) frequency, characterizing the time needed for the photon to complete a roundtrip within the interferometer, $\tilde{q}_X(x)$ is its associated spectral shape, and $\tilde{s}_X(x)$ is the spectral shape of the

DM signal. The constant coefficient A_X characterizes the amplitude of the signal. Explicit forms of each component are derived in Sec. 7.3.

Most laser interferometers designed to measure GWs such as LIGO utilize Fabry–Pérot (FP) cavities to increase interaction time between photons and the GW. A direct consequence is that the detector peak sensitivity is displaced from the FSR frequency by the cavity quality factor $Q \gg 1$, *i.e.* $f_{\rm peak}/f_{\rm FSR} \sim 1/Q$. As we will derive in Sec. 7.3, the effect of finite photon travel time produces corrections to the signal spectrum in powers of $(f/f_{\rm FSR})$ (Eq. (7.26), Eq. (7.32), and Eq. (7.37)), and hence can be safely ignored for these experiments. However, experimental apparatus designed to measure quantum gravity effects such as Holometer and GQuEST generally do not have FP cavities, since the peak frequency of quantum gravity signatures is naturally the frequency associated with the photon travel time in the physical interferometer arm, *i.e.* the FSR frequency [7]. Hence these quantum gravity detectors generally are most sensitive to signals that peak at $f_{\rm FSR}$, and the photon travel time within the apparatus cannot be neglected.

Distance Scales

We first summarize various relevant distance scales for the DM signals. For Doppler and Einstein delay, since the DM effect only acts on a point (the mirrors or the clock), the relevant distance scale is b. For Shapiro delay, if the DM is sufficiently distant ($\gtrsim L/2$) from the detector, then the entire interferometer arm is effectively a point and the relevant distance is still b. However, for nearby DM ($b \lesssim L/2$), the relevant scale for Shapiro delay is the DM's closest encounter to any point along the arm rather than a specific point, denoted as $b_\perp$ (note that $b_\perp \leq b$ by definition). The local statistical distribution of b and $b_\perp$ of DM has been studied and derived in the appendix of Ref. [43]. In particular, the 90$^{\rm th}$ percentile minimum DM impact parameters, $b_{\rm min}$ and $b_{\perp,\rm min}$, are given by

$$\begin{aligned} b_{\rm min} &= \sqrt{-\frac{\log(1-p)}{\pi n \bar{v} T}} = 9\,{\rm km}\left(\frac{M}{\rm kg}\right)^{1/2} f_{\rm DM}^{-1/2}\left(\frac{340\ {\rm km/s}}{\bar{v}}\right)^{1/2}\left(\frac{\rm yr}{T}\right)^{1/2}, \\ b_{\perp,\rm min} &= -\frac{\log(1-p)}{n \bar{v}_\perp T L} = 300\,{\rm km}\left(\frac{M}{\rm kg}\right) f_{\rm DM}^{-1}\left(\frac{\rm km}{L}\right)\left(\frac{270\ {\rm km/s}}{\bar{v}_\perp}\right)\left(\frac{\rm yr}{T}\right), \end{aligned} \tag{7.4}$$

where p is the percentile of the minimal impact parameters (taken to be 0.9 for the numerical estimate above), $n = \rho_{\rm DM} f_{\rm DM}/M$ is the local DM number density, with $\rho_{\rm DM} = 0.46\,{\rm GeV}/c^2/{\rm cm}^3$, $f_{\rm DM}$ the DM fraction in mass M, $\bar{v}$ and $\bar{v}_\perp$ are the average DM velocity and perpendicular velocity respectively, and the estimate for $b_{\perp,\rm min}$ only holds when $b_{\rm min} < L$. In Fig. 7.2 we show the distance scales from LISA,

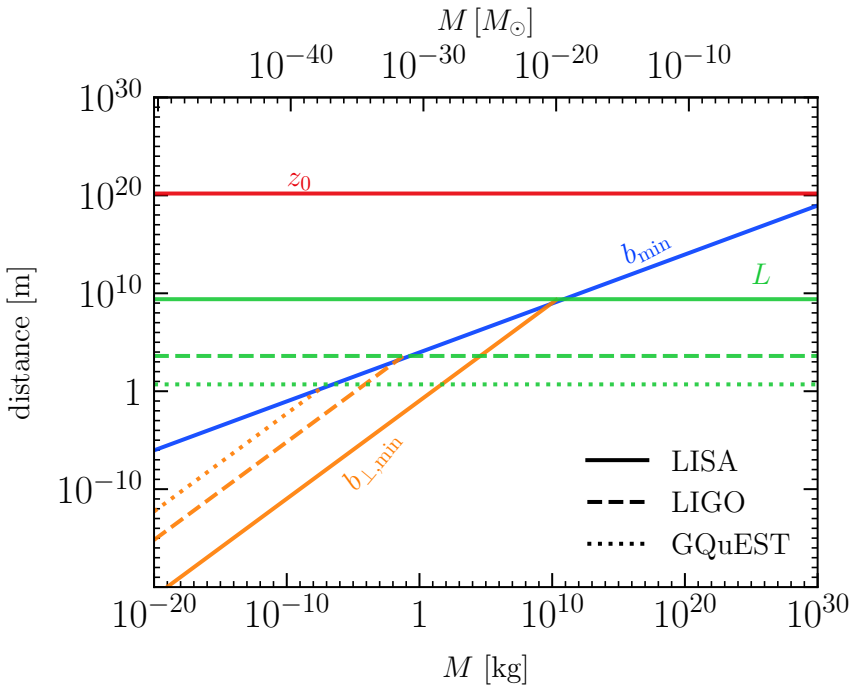

Figure 7.2: Relevant distance scales for measuring transiting DM signals as a function of DM mass M, assuming $f_{\rm DM} = 1$ and a local DM mass density of $\rho_{\rm DM} = 0.46\,{\rm GeV}/c^2/{\rm cm}^3$. The length scale for Doppler and Einstein effect is $b_{\rm min}$, while the length scale for Shapiro is $b_{\rm min}$ if $b_{\rm min} \gtrsim L/2$ and $b_{\perp,\rm min}$ otherwise. Note that $b_{\perp,\rm min}$ depends on the length scale of the detector baseline, for which we choose three experiments with diverse baselines (LISA, LIGO, and GQuEST) for illustration purposes. For reference we also show a typical pulsar-Earth distance, $z_0 \sim 5$ kpc, which is the largest distance scale for PTA searches when $M < 10^2\,M_\odot$.

LIGO, and GQuEST for different choices of DM mass M. As will be discussed in the next subsection and carefully verified in Sec. 7.3, only DM with impact parameter $b \lesssim L$ can potentially generate sizable signals. We see that $b_{\rm min}$ and $b_{\perp,\rm min}$ coincide at $\sim L$. At those lower mass ranges, the Shapiro effect is boosted by the fact that $b_\perp < b$, but as we will see in the next section (cf. Eq. (7.32)), the Shapiro delay in the $b < L/2$ limit suffers a suppression factor of v/c. These competing factors lead to the dominance of the Doppler effect in most experiments, but the Shapiro effect has a slight edge for specific values of L and M.

For reference, we also show the typical distance between Earth and a pulsar observed in PTA experiments, $z_0 \sim 5$ kpc. For $M \lesssim 10\,M_\odot$, which is the mass range considered in most previous works on PTA [43, 42, 9, 10, 5], z_0 is the largest distance scale. This shows a natural mass cut-off when extending the previous PTA

results for DM with mass $M \gtrsim 10 M_\odot$, as we do not expect DM to give measurable signatures in PTAs if $b \gtrsim z_0$.

Tidal and Q-Suppression

Laser interferometers are mostly sensitive to DM with impact parameter $b \lesssim L$. The main reason is that if $b \gtrsim L$, the peak frequency of the signal $f_\tau \lesssim 2(v/c) f_{\rm FSR} \sim 10^{-3} f_{\rm FSR}$. Thus unless the Q-factor is sufficiently large ($Q > 10^3$), the peak DM frequency typically falls below the sensitivity window of the GW detector. Notice that the DM signal drops exponentially above such a signal peak frequency. In addition, the strain due to DM with $b \gtrsim L$ suffers suppression from two other effects, which we will see explicitly from the derivation in Sec. 7.3.:

- *Tidal suppression.* Since an interferometer measures differential quantities, when $b \gtrsim L$, the interferometer behaves like a dipole under a gravitational field, and thus the signal can be suppressed by a factor of L/b, which is commonly known as the tidal effect.

- *Q-suppression.* When $b \gtrsim L$, the signal can evade tidal suppression since the interferometer measures the differential strain at slightly different times, creating an envelope in Fourier space that is peaked at $f_{\rm FSR}$ [1]. When the signal is evaluated at the detector peak sensitivity f_{peak}, the signal picks up a factor of $1/Q$.

When the signal with $b > L$ is evaluated at frequency $f = f_\tau$, since $(1/Q)(f_\tau/f_{peak}) = f_\tau/f_{\rm FSR} = 2(v/c)(L/b)$, we see that the Q-suppressed term is always weaker than the tidally-suppressed term for laser interferometers as $v \ll c$. However, for some types of interferometers, such as atom interferometers, the speed of the probe can be much slower than the DM speed. In that case $f_\tau > f_{\rm FSR}$ is possible even when $b > L$, and the Q-suppressed term can dominate over the tidally-suppressed term. We leave the detailed treatment of these types of experiments for future work.

Projected Sensitivity

To set the projected sensitivity for various current and future GW detectors, we assume that the detector noise is stationary and Gaussian with a one-sided PSD $S_n(f)$ (in units of $\rm Hz^{-1}$). The deterministic signal-to-noise ratio (SNR), assuming

[1] Effects of finite photon travel time in the context of ultralight DM are discussed in Ref. [444]

optimal filtering in a matched filtering procedure, is given by [34]

$$\mathrm{SNR}^2_{\mathrm{det}} = 4\int_0^\infty df \frac{|\tilde{h}(f)|^2}{S_n(f)}\,. \tag{7.5}$$

For narrowband GW detectors, the deterministic SNR can be approximated as $\mathrm{SNR}^2_{\mathrm{det}} \approx (4\Delta f/S_n)|\tilde{h}(f_{\mathrm{peak}})|^2$, where Δf is the narrow frequency bandwidth.

On the signal side, the spectrum in Eq. (7.3) can be greatly simplified assuming $b < L$ for the purpose of computing the SNR, which takes much simpler forms truncated at $f = f_\tau$. Here we quote the results from Sec. 7.3, and take the $f \ll f_\tau$ limit of Eq. (7.26), Eq. (7.32) and Eq. (7.37)

$$\begin{aligned}
|\tilde{h}_{\mathrm{Doppler}}(f)|^2 &\approx \frac{4}{3}\left(\frac{8GML}{c^2 bv}\right)^2\left(\frac{f_{\mathrm{FSR}}}{f}\right)^4\cos^2\left(\frac{f}{2f_{\mathrm{FSR}}}\right)\Theta(f_\tau - f),\\
|\tilde{h}_{\mathrm{Shapiro}}(f)|^2 &\approx \left(\frac{8\pi GM}{c^3}\right)^2\left(\frac{f_{\mathrm{FSR}}}{f}\right)^2\cos^2\left(\frac{f}{4f_{\mathrm{FSR}}}\right)\Theta(f_{\tau_\perp} - f),\\
|\tilde{h}_{\mathrm{Einstein}}(f)|^2 &\approx \left(\frac{8GM}{c^2 v}\right)^2\left(\frac{f_{\mathrm{FSR}}}{f}\right)^2\sin^2\left(\frac{f}{2f_{\mathrm{FSR}}}\right)\log^2\left(\frac{f}{f_\tau}\right)\Theta(f_\tau - f)\,,
\end{aligned} \tag{7.6}$$

for one-arm detectors. For two-arm interferometers $|\tilde{h}_{\mathrm{Doppler}}(f)|^2$ should pick up a factor of $4\sin^2(\Delta\theta/2)$, where $\Delta\theta$ is the angle between the two arms, $|\tilde{h}_{\mathrm{Shapiro}}(f)|^2$ does not receive a correction when $b < L/2$ and $\Delta\theta \sim O(1)$, and $|\tilde{h}_{\mathrm{Einstein}}(f)|^2 = 0$. The simplified spectrum is very accurate for the lower mass range where $b < L$, but can underestimate the upper limits on f_{DM} by $\lesssim 4$ orders of magnitude on the higher mass range.

The 90^{th} percentile upper limit on f_{DM} is derived by requiring $b_{min} > L$ (in the high mass limit), and the 10^{th} percentile SNR to be less than two (in the low mass limit), where the SNR is produced by DM with impact parameter given by Eq. (7.4). Computing $\mathrm{SNR}_{\mathrm{det}}$ in Eq. (7.5) using the simplified signal strain in Eq. (7.6), the constraints on f_{DM} are then roughly given by

$$\begin{aligned}
f^L_{\mathrm{DM,Doppler}} &\lesssim 2\times 10^{16}\left(\frac{\mathrm{kg}}{M}\right)\left(\frac{\mathrm{yr}}{T}\right)\left(\frac{\bar{v}}{340\ \mathrm{km/s}}\right)\left(\frac{\mathrm{km}}{L}\right)^2\left(\frac{1}{Q}\right)^4\left(\frac{S_n}{10^{-46}\ \mathrm{Hz}^{-1}}\right)\left(\frac{\mathrm{kHz}}{\Delta f}\right),\\
f^R_{\mathrm{DM,Doppler}} &\lesssim 80\left(\frac{M}{\mathrm{kg}}\right)\left(\frac{\mathrm{yr}}{T}\right)\left(\frac{340\ \mathrm{km/s}}{\bar{v}}\right)\left(\frac{\mathrm{km}}{L}\right)^2,\\
M^L_{\mathrm{Shapiro}} &\lesssim 5\times 10^9\ \mathrm{kg}\left(\frac{1}{Q}\right)\left(\frac{S_n}{10^{-46}\ \mathrm{Hz}^{-1}}\right)^{1/2}\left(\frac{\mathrm{kHz}}{\Delta f}\right)^{1/2},\\
f^R_{\mathrm{DM,Shapiro}} &\lesssim 3\times 10^2\left(\frac{M}{\mathrm{kg}}\right)\left(\frac{\mathrm{yr}}{T}\right)\left(\frac{270\ \mathrm{km/s}}{\bar{v}_\perp}\right)\left(\frac{\mathrm{km}}{L}\right)^2.
\end{aligned} \tag{7.7}$$

Here L and R denote the low and high mass regions of the parameter space, respectively. Note that in the low mass regime, the SNR for the Shapiro effect becomes independent of $f_{\rm DM}$, for which case we show the constraint on the DM mass M instead.

In Fig. 7.3 we show the projected constraints for several existing and proposed GW experiments based on laser interferometery, assuming $T = 1$ yr of observation time. These experiments are discussed in Sec. 7.5 in more detail, with the noise spectral densities plotted together in Fig. 7.6. We derive the projections using a Monte Carlo simulation to sample the DM initial conditions, compute the SNR with the exact strain as derived and shown in Sec. 7.3, and set the SNR to two. In the Monte Carlo simulation, the DM impact parameters are randomly sampled, properly normalized to the local DM density, while the velocity distribution is taken to be the Standard Halo Model (SHM), *i.e.* an isotropic Maxwell-Boltzmann distribution with $v_0 = 220$ km/s, boosted by the solar system speed $v_0 = 220$ km/s, and truncated at the escape velocity $v_{\rm esc} = 600$ km/s. The mean DM velocities are $\bar{v} = 340$ km/s and $\bar{v}_\perp = 270$ km/s [42]. The DM trajectories are then given by Eq. (7.16) and Eq. (7.17) for the Doppler and Shapiro signal respectively (see discussion in Sec. 7.3). The constraints are reported in terms of $f_{\rm DM}$, defined to be the fraction of DM as transiting point masses. We find that for laser interferometers, the Doppler effect is dominant over the Shapiro delay except for the high mass range in Holometer and GQuEST (which appears as bumps in the constraint curves). We see that gravitational signals from transiting DM are out-of-reach for laser interferometry-based GW detectors, even if the DM local density is saturated. However, if there exists an additional long-range fifth force between DM and baryonic matter, GW detectors can be sensitive to a fifth force $\sim 10^3$ times stronger than gravity within a year of observation, which will be elaborated in Sec. 7.2. On the same plot, we show projections from other types of high-frequency GW detectors, which are modeled as accelerometers for simplicity. More specifics are explained in Sec. 7.5.

Fifth Force

In the presence of a long-range DM-baryon Yukawa force (also known as a fifth force), the potential can be written as

$$\Phi_{\rm fifth}(r) = -\tilde{\alpha}\frac{GM}{r}e^{-r/\lambda}\,, \tag{7.8}$$

where $\tilde{\alpha}$ is the coupling strength (normalized against gravity), and λ is the force range. The effect of the fifth force can be estimated using the same signal spectrum

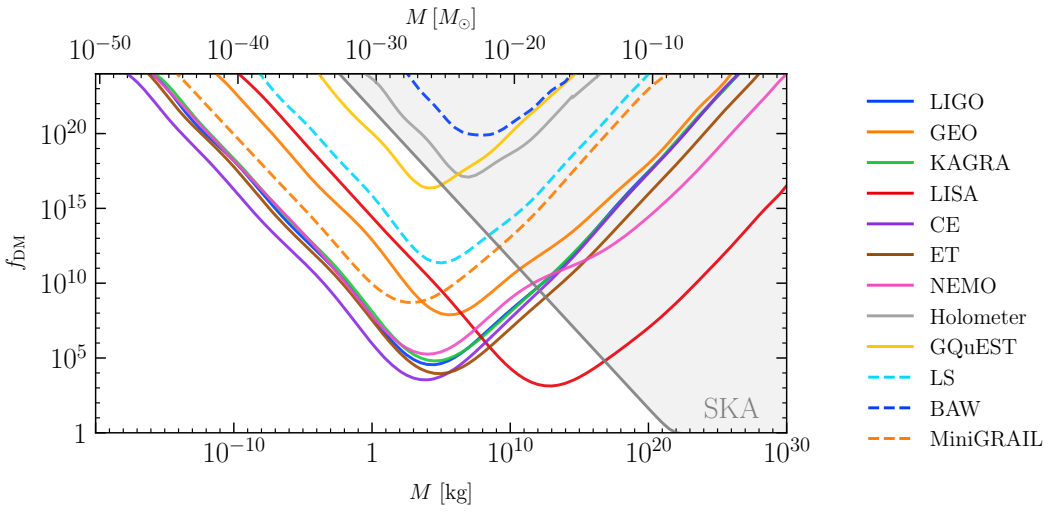

Figure 7.3: Projected 90$^{\rm th}$-percentile upper limits on transiting DM fraction from several existing and proposed GW detectors based on laser interferometry, assuming $T = 1$ yr of observation time and local DM density $\rho_{\rm DM} = 0.46\ {\rm GeV}/c^2/{\rm cm}^3$. The limits are derived by setting the 10$^{\rm th}$-percentile SNR defined in Eq. (7.5) to be two, and the DM initial conditions are sampled using a Monte Carlo simulation. Projections from other types of high-frequency GW experiments are shown with dashed colored lines. See Sec. 7.5 for a description of the experiments.

in Eq. (7.3) but truncated at $b \gtrsim \lambda$ for Doppler effect (note that a fifth force coupled to B or $B-L$ induces no Shapiro delay). In Fig. 7.4 we show the resulting projected constraints from the Monte Carlo simulation on $\tilde{\alpha}$ for $\lambda = 1$ m and $\lambda = 10^6$ m, alongside several existing fifth force constraints. The finite force range introduces a cutoff mass corresponding to $b_{\rm min} \sim \lambda$. We observe that constraints on $\tilde{\alpha}$ for experiments with long baselines such as LISA and LIGO significantly weaken when the force range λ drops below the interferometer length. However, experiments with shorter baselines such as Holometer and GQuEST are less insensitive to the shorter force range as long as $\lambda \gtrsim 1$ m, since the peak sensitivity of these experiments corresponds to the $b \sim 1$ m scale.

Astrophysical constraints on the DM-baryon fifth force include weak equivalence principle (WEP) tests, which measure the differential acceleration of two baryonic bodies toward the galactic center. Several existing WEP analyses include perihelion precession (Sun-Mercury) [315], binary pulsar (NS-WD) [445], lunar laser ranging (Earth-Moon) and torsion pendula (Be-Ti, Be-Al) [446], but have been shown to be subdominant (upper limits on $\tilde{\alpha} > 10^{20}$) for $\lambda < 10^6$ m [5]. Observation of neutron star (NS) surface temperature can also place upper limits on the Yukawa

coupling constant since a large DM-baryon interaction leads to a high NS temperature due to kinetic heating [5]. An indirect bound on DM-baryon interaction comes from combining [268] upper limits on DM self-interaction from bullet cluster observation [447, 448], and bounds on baryon-baryon fifth force measured in Eötvös experiments such as MICROSCOPE [449, 450], which is shown in Fig. 7.4. While the bullet cluster + MICROSCOPE bound is dominant over the GW detector bounds for most mass ranges, if only a sub-component (say 1%) of DM is charged under the fifth force, then the bullet cluster bound on DM self-interaction does not exist, while the GW detector bounds will only deteriorate linearly with the sub-component fraction.

7.3 Derivation of the Signal

To understand the general interferometry signals induced by a passing massive object, we analyze the gauge invariant quantity proposed in Ref. [7] in three parts, corresponding to the Doppler effect, the Shapiro effect, and the Einstein time delay, as conventionally seen in the literature. Here we briefly summarize the gauge invariant quantity and show that it can be separated into the above mentioned effects. Then, we restrict ourselves to the scenario of a point-like transiting DM and explicitly derive the strain for each effect.

In the presence of a general metric perturbation

$$ds^2 = -(1-\mathcal{H}_0)dt^2 + (1+\mathcal{H}_2)dr^2 + 2\mathcal{H}_1 dt dr ..., \tag{7.9}$$

the total photon travel time within a roundtrip, T_γ, in an interferometer centering at the origin can be computed by including effects from the clock rate change, mirror motion, and gravitational redshift in the photon geodesic [7]:

$$\begin{aligned} T_\gamma(t) = T_\gamma^{\rm out}(t) + T_\gamma^{\rm in}(t) = \delta\tau &+ \frac{1}{c}\int_{r_{\rm M}(t,0)}^{L+r_{\rm M}(t+\frac{L}{c},L)} dr \left(1+\frac{1}{2}\mathcal{H}^{\rm out}\left(t+\frac{r}{c},r\right)\right) \\ &- \frac{1}{c}\int_{L+r_{\rm M}\left(t+\frac{L}{c},L\right)}^{r_{\rm M}\left(t+\frac{2L}{c},0\right)} dr \left(1+\frac{1}{2}\mathcal{H}^{\rm in}\left(t+\frac{2L-r}{c},r\right)\right) \end{aligned} \tag{7.10}$$

where t is the time when the photon leaves from the beamsplitter. Here $\mathcal{H}^{\rm out/in} \equiv \mathcal{H}_0 + \mathcal{H}_2 \pm 2\mathcal{H}_1$, $r_M(t', r')$ denotes the mirror position at time t' with r' being its spatial coordinate in the absence of metric perturbations, and $\delta\tau$ is the clock rate change, corresponding to the Einstein time delay. Keeping the linear terms, one can

obtain the total time delay:

$$c\delta T_\gamma \equiv cT_\gamma - 2L = \underbrace{c\delta\tau}_{\text{Einstein}} \underbrace{+2r_{\rm M}\left(t+\frac{L}{c},L\right) - r_{\rm M}\left(t,0\right) - r_{\rm M}\left(t+\frac{2L}{c},0\right)}_{\text{Doppler}} \underbrace{+\frac{1}{2}\int_0^L dr\mathcal{H}^{\rm out}\left(t+\frac{r}{c},r\right) - \frac{1}{2}\int_L^0 dr\mathcal{H}^{\rm in}\left(t+\frac{2L-r}{c},r\right)}_{\text{Shapiro}}. \tag{7.11}$$

The second line shows the gravitational redshift experienced by the photon between two unperturbed mirrors, which corresponds to the definition of the Shapiro effect in the literature [451, 44]. The contribution from mirror motion, corresponding to the Doppler effect, is the differential position shift between the two mirrors during one photon roundtrip obtained by solving the mirror geodesic equations, which, to leading order, can be written as [103]:

$$r_{\rm M}(t,r) \approx \frac{1}{2}\int^t dt' \int^{t'} dt''\partial_r\mathcal{H}_0(t'',r). \tag{7.12}$$

The choice of initial conditions in the above time integrals can be subtle depending on the gauge choice, so it is more convenient to work with the mirror acceleration instead. The Doppler strain, which is a displacement quantity, is related to the mirror acceleration, $\tilde{a}(f)$, in the frequency domain via $|\tilde{h}_{\rm Doppler}(f)|^2 \sim (2\pi f)^{-4}L^{-2}|\tilde{a}(f)|^2$ [452], circumventing the need to specify the mirrors' initial conditions. This is to be contrasted with the treatment of the Doppler effect in PTAs, where the accelerations of the pulsars / Earth are explicitly integrated over time to obtain the shift in the pulsar phase [43, 42, 9, 10].

The total time delay in Eq. (7.11) is shown to be invariant under general gauge transformations [7]. Equipped with this well-defined observable, we specialize to the case of a transiting DM and compute each effect individually.

To compute the individual contributions, one has to fix a gauge. We work with the harmonic gauge, where the metric perturbation due to a non-relativistic ($v \ll c$) point particle is given by [453]

$$ds^2 = -\left(1+\frac{2\Phi(t,\mathbf{x})}{c^2}\right)c^2dt^2 + \left(1-\frac{2\Phi(t,\mathbf{x})}{c^2}\right)(dx^2+dy^2+dz^2), \tag{7.13}$$

where Φ is the DM Newtonian potential

$$\Phi(t,\mathbf{x}) = -\frac{GM}{|\mathbf{x}-\mathbf{r}_{\rm DM}(t)|}, \tag{7.14}$$

with $\mathbf{r}_{\rm DM}(t)$ being the DM trajectory. Assuming a straight-line motion, we can completely specify $\mathbf{r}_{\rm DM}(t)$ using six phase space parameters, $\{\mathbf{r}_0, \mathbf{v}\}$

$$\mathbf{r}_{\rm DM}(t) = \mathbf{r}_0 + \mathbf{v}t\,, \tag{7.15}$$

where $\mathbf{r}_0$ and $\mathbf{v}$ are the three-dimensional DM initial position and velocity. While Eq. (7.15) is intuitive, it is inconvenient to use in practice, since it does not explicitly show the DM time of closest approach, when the signal is maximized. For DM signals induced on a spatial point of the detector (*i.e.* Doppler effect and Einstein delay), a more convenient parameterization of Eq. (7.14) is [43]

$$\mathbf{r}_{\rm DM}(t) = \mathbf{b} + \mathbf{v}(t - t_0)\,, \tag{7.16}$$

where $\mathbf{b}$ is the impact parameter, and t_0 can be interpreted as the DM "arrival time". Note that $\mathbf{b}$ is constrained to be perpendicular to $\mathbf{v}$, hence the total number of phase space parameters $\{\mathbf{b}, \mathbf{v}, t_0\}$ is still six, and for an experiment with total observation time T, only DM with arrival time within the range $-T/2 \leq t_0 \leq T/2$ can be feasibly detected. One can rewrite Eq. (7.16) as $\mathbf{r}_{\rm DM}(t) = b(\hat{\mathbf{b}} + \eta\hat{\mathbf{v}})$, where $\eta \equiv (t - t_0)/\tau$ is a dimensionless time parameter and $\tau \equiv b/v$.

Finally, if the DM signal depends on the closest distance between $\mathbf{r}_{\rm DM}$ and the experiment baseline (*i.e.* Shapiro delay in the small impact parameter limit, see Sec. 7.3), assumed to be aligned in $\hat{\mathbf{n}}$, then the most convenient parameterization of Eq. (7.15) is

$$\mathbf{r}_{\rm DM}(t) = \mathbf{b}_\perp + b_\parallel\hat{\mathbf{n}} + \mathbf{v}(t - t_{0,\perp})\,, \tag{7.17}$$

where $\mathbf{b}_\perp$ and $b_\parallel$ are the perpendicular and parallel impact parameter respectively, and $t_{0,\perp}$ is the time when the DM reaches $\mathbf{b}_\perp$. The phase space parameters are $\{\mathbf{b}_\perp, b_\parallel, \mathbf{v}, t_{0,\perp}\}$, where $b_\perp$ is constrained to be perpendicular to both $\hat{\mathbf{n}}$ and $\hat{\mathbf{v}}$, giving again a total of six independent parameters, as expected. The perpendicular DM distance is $r_\perp(t) \equiv |\mathbf{r}_{\rm DM}(t)\times\hat{\mathbf{n}}| = b_\perp\sqrt{1+\eta_\perp^2}$, where $\eta_\perp \equiv (t-t_{0,\perp})/\tau_\perp$, $\tau_\perp \equiv b_\perp/v_\perp$ and $v_\perp \equiv |\mathbf{v}\times\hat{\mathbf{n}}|$.

Doppler Effect

We start by studying the Doppler effect, focusing on a one-arm GW detector. The Doppler effect is often the only component of transiting DM signals considered in the literature, such as Refs. [433, 438], since it is the most dominant contribution in most mass ranges. When unperturbed, suppose the two mirrors are located at $\mathbf{r}_{M_1}$ (an inner mirror close to the beamsplitter) and $\mathbf{r}_{M_2}$ (an exterior mirror at the edge of

the arm), which are separated by a distance of $\mathbf{r}_{M_2} - \mathbf{r}_{M_1} = L\hat{\mathbf{n}}$. The laser measures the distance between the two free-falling mirrors, with trajectories given by $\mathbf{r}_{M_1}(t)$ and $\mathbf{r}_{M_2}(t)$ (with arguments), evaluated at times separated by the photon transverse time.

$$h_{\rm Doppler}(t) = \frac{\hat{\mathbf{n}}}{L} \cdot \left\{ \left[\mathbf{r}_{M_2}\left(t + \frac{L}{c}\right) - \mathbf{r}_{M_1}(t) \right] - \left[\mathbf{r}_{M_1}\left(t + \frac{2L}{c}\right) - \mathbf{r}_{M_2}\left(t + \frac{L}{c}\right) \right] \right\} . \tag{7.18}$$

This corresponds to the mirror motion term in Eq. (7.11). It is in fact more natural to consider the Doppler signal as the acceleration of the mirrors caused by the transiting DM. The strain, which is a displacement quantity, is related to the mirror acceleration along the interferometer arm, $a_{M_a}(t) = \hat{\mathbf{n}} \cdot \frac{d^2}{dt^2}\mathbf{r}_{M_a}(t)$ for $a = 1, 2$, by

$$\frac{d^2}{dt^2} h_{\rm Doppler}(t) = \frac{1}{L} \left\{ \left[a_{M_2}\left(t + \frac{L}{c}\right) - a_{M_1}(t) \right] - \left[a_{M_1}\left(t + \frac{2L}{c}\right) - a_{M_2}\left(t + \frac{L}{c}\right) \right] \right\} . \tag{7.19}$$

In the Newtonian limit, it is clear that the mirror accelerations are simply given by the gravitational potential from the DM. Alternatively, to more explicitly relate to the gauge invariant formalism developed in Ref. [7], one can also derive the mirror acceleration using the metric perturbation in Eq. (7.13), which is a standard general relativity calculation that we briefly review. The mirrors free fall in accordance with the geodesic equation parameterized by the coordinate time, which is $\frac{d^2}{dt^2} r^\mu_{M_a}(t) + \Gamma^\mu_{\rho\sigma}[dr^\rho_{M_a}(t)/dt][dr^\sigma_{M_a}(t)/dt] = 0$. For the metric in Eq. (7.13), when the source is moving slowly ($v \ll c$), the Christoffel symbols are $\Gamma^0_{0i} = \Gamma^i_{00} = \partial_i\Phi/c^2$ and $\Gamma^i_{jk} = (\delta_{jk}\partial_i\Phi - \delta_{ik}\partial_j\Phi - \delta_{ij}\partial_k\Phi)/c^2$ [453]. In the limit where the mirror is moving very slowly ($\dot{r}_{M_a} \ll c$), the leading order geodesic equation is $(d^2/dt^2) r^i_{M_a}(t) + c^2\Gamma^i_{00} = 0$, and thus the mirror acceleration is given by the gradient of the potential

$$a_{M_a}(t) = -\frac{GM}{\Delta r^2_{M_a}(t)} \Delta\hat{\mathbf{r}}_{M_a}(t) \cdot \hat{\mathbf{n}} , \tag{7.20}$$

where we define the distance between the mirrors and the DM, $\Delta\mathbf{r}_{M_a}(t) \equiv \mathbf{r}_{M_a} - \mathbf{r}_{\rm DM}(t)$. This is of course the gravitational force that the DM exerts on the mirrors. We now take the DM trajectory in Eq. (7.16) choosing the unperturbed beamsplitter location as the coordinate origin. Then the acceleration of the first mirror in Eq. (7.20) is given by $a_{M_1}(t) = -\hat{\mathbf{n}} \cdot (GM/b^2)(\hat{\mathbf{b}} + \eta\hat{\mathbf{v}})/(1+\eta^2)^{3/2}$ with the Fourier

transform

$$\tilde{a}_{M_1}(f) = -\frac{GM}{bv} e^{-2\pi i f t_0} \tilde{s}_{M_1}\left(\frac{f}{f_\tau}\right) \quad with \quad \tilde{s}_{M_1}(x) \equiv 2x\left[K_1(x)\hat{\mathbf{b}} - iK_0(x)\hat{\mathbf{v}}\right]\cdot\hat{\mathbf{n}}\,, \tag{7.21}$$

where we separated the magnitude and the signal shape for clarity. The Doppler acceleration has a sharp peak at $\eta = 0$ in real space, corresponding to the DM time of arrival as expected. In Fourier space, the Doppler acceleration has a weak log-dependence on the frequency for $f < f_\tau$, but quickly drops to zero when $f > f_\tau$. This behavior is in fact general for all three types of signals, as we will see shortly.

The acceleration of the second mirror can be computed using Eq. (7.15), Eq. (7.20) and $\Delta\mathbf{r}_{M_2}(t) = \Delta\mathbf{r}_{M_1}(t) + L\hat{\mathbf{n}}$,

$$a_{M_2}(t) \approx \begin{cases} -\dfrac{GM}{L^2}, & \text{if } b \ll L \\ a_{M_1}(t) + \dfrac{GML}{b^3}\left[\dfrac{3(\hat{\mathbf{b}}\cdot\hat{\mathbf{n}} + \eta\hat{\mathbf{v}}\cdot\hat{\mathbf{n}})^2}{(1+\eta^2)^{5/2}} - \dfrac{1}{(1+\eta^2)^{3/2}}\right], & \text{if } b \gg L \end{cases}. \tag{7.22}$$

The Fourier transform is given by

$$\tilde{a}_{M_2}(f) \approx \begin{cases} 0, & \text{if } b \ll L \\ \tilde{a}_{M_1}(f) + \left(\dfrac{L}{b}\right)\tilde{a}_{\text{tidal}}(f), & \text{if } b \gg L \end{cases}, \tag{7.23}$$

where we have approximated $\delta(f) \sim 0$ and

$$\begin{aligned} \tilde{a}_{\text{tidal}}(f) &= \frac{GM}{bv} e^{-2\pi i f t_0}\tilde{s}_{\text{tidal}}\left(\frac{f}{f_\tau}\right) \\ \tilde{s}_{\text{tidal}}(x) &\equiv 2x\Big\{\left[(\hat{\mathbf{b}}\cdot\hat{\mathbf{n}})^2 - (\hat{\mathbf{v}}\cdot\hat{\mathbf{n}})^2\right] xK_0(x) \\ &\quad + \left[\left(2(\hat{\mathbf{b}}\cdot\hat{\mathbf{n}})^2 + (\hat{\mathbf{v}}\cdot\hat{\mathbf{n}})^2 - 1\right) - 2i(\hat{\mathbf{b}}\cdot\hat{\mathbf{n}})(\hat{\mathbf{v}}\cdot\hat{\mathbf{n}})x\right] K_1(x)\Big\}\,. \end{aligned} \tag{7.24}$$

The total Doppler effect can be computed by Fourier transforming Eq. (7.19) and,

using Eq. (7.23), we have

$$\tilde{h}_{\rm Doppler}(f) \approx -\frac{2}{(2\pi f)^2 L} e^{-if/2f_{\rm FSR}} \times \begin{cases} \cos\left(\frac{f}{2f_{\rm FSR}}\right)\tilde{a}_{M_1}(f), & \text{if } b \ll L \\ \underbrace{2\sin^2\left(\frac{f}{4f_{\rm FSR}}\right)\tilde{a}_{M_1}(f)}_{\text{Q-suppressed}} - \underbrace{\left(\frac{L}{b}\right)\tilde{a}_{\rm tidal}(f)}_{\text{tidal-suppressed}}, & \text{if } b \gg L \end{cases} . \tag{7.25}$$

Eq. (7.25) is illuminating, as it shows that we can safely ignore the contribution from the second mirror if $b \ll L$ since the acceleration of the first mirror is much greater than the second mirror. However, if $b \gg L$, then both mirrors experience similar acceleration from the same transiting DM. This leads to a suppression factor of (L/b), known as the tidal factor as alluded to in Sec. 7.2, which is well-studied in the literature of accelerometers [434, 438]. However, an additional piece of the power spectrum is not suppressed by the tidal factor, but arises from the fact that a laser interferometer measures the differential acceleration between the mirrors at a slightly different time. Defining $Q_f \equiv f_{\rm FSR}/f$, the Doppler signal is thus

$$|\tilde{h}_{\rm Doppler}(f)|^2 \approx \left(\frac{8GML}{c^2 bv}\right)^2 \left(\frac{f_{\rm FSR}}{f}\right)^4 \times \begin{cases} \cos^2\left(\frac{f}{2f_{\rm FSR}}\right)\left|\tilde{s}_{M_1}\left(\frac{f}{f_\tau}\right)\right|^2, & \text{if } b \ll L \\ 4\sin^4\left(\frac{f}{4f_{\rm FSR}}\right)\left|\tilde{s}_{M_1}\left(\frac{f}{f_\tau}\right)\right|^2, & \text{if } b \gg L \text{ and } 1/Q_f \gg L/b \\ \left(\frac{L}{b}\right)^2\left|\tilde{s}_{\rm tidal}\left(\frac{f}{f_\tau}\right)\right|^2, & \text{if } b \gg L \text{ and } 1/Q_f \ll L/b \end{cases} , \tag{7.26}$$

where we assume that either the Q-suppressed or the tidal-suppressed term dominates when $b \gg L$. Previous studies in the literature [437, 438] that treated a laser interferometer as a simple accelerometer have generally neglected the sines and cosines of $\sim (f/f_{\rm FSR})$ (which originate from the finite photon travel time within the interferometer), the second term of Eq. (7.26), and estimated $\tilde{s}_{\rm tidal}(f/f_\tau) \approx \tilde{s}_{M_1}(f/f_\tau)$. The treatment is well-justified for GW detectors that utilize FP cavities with $Q \gg 1$ such as LIGO, but does not apply to other laser interferometers such as Holometer and GQuEST.

The average signal shape can be computed by taking the amplitude squared of Eq. (7.21) and Eq. (7.24) while substituting the angular factors derived in App. I

(see Eq. (I.2) and Eq. (I.4))

$$\left\langle |\tilde{s}_{M_1}(x)|^2 \right\rangle = \frac{4}{3}x^2\left[K_0^2(x)+K_1^2(x)\right] \approx \frac{4}{3}\begin{cases}1, & \text{if } x \ll 1\\ \pi x e^{-2x}, & \text{if } x \gg 1\end{cases}$$

$$\left\langle |\tilde{s}_{\rm tidal}(x)|^2 \right\rangle = \sum_{i,j,k} c_{ij,k}x^k K_i(x)K_j(x) \approx \frac{16}{15}\begin{cases}1, & \text{if } x \ll 1\\ \pi x^3 e^{-2x}, & \text{if } x \gg 1\end{cases}, \tag{7.27}$$

where $c_{ij,k}$ are some $O(1)$ coefficients.

We observe that $\left\langle |\tilde{s}_{\rm tidal}(x)|^2 \right\rangle \sim (4/5)\left\langle |\tilde{s}_{M_1}(x)|^2 \right\rangle$. The spectral shapes of the tidal-suppressed piece and the Q-suppressed piece are in fact very similar to each other (constant until f_τ and then exponential decay), but are suppressed by factors of different physical origins. To set an upper limit on the DM fraction, we compute the $10^{\rm th}$ percentile $|\tilde{h}_{\rm Doppler}(f)|^2$ using Eq. (7.26) with impact parameter given by Eq. (7.4), while taking the mean value of the angular factors and v. In the limit where $b \ll L$, one recovers Eq. (7.6). On the other hand, if the interferometer has two arms separated by an angle of $\Delta\theta$, then we replace the angular factors in Eq. (7.27) with the two-arm angular factors in Eq. (I.5), while removing the $\hat{\mathbf{n}}$-independent term in Eq. (7.24), giving, up to $O(1)$ factors, a factor of $4\sin^2(\Delta\theta/2)$ in Eq. (7.26).

Shapiro Delay

The Shapiro delay has been studied extensively for transiting DM signals in PTAs [44, 43, 42]. A pulsar located at a distance of z_0 from Earth has a long baseline of $L \sim$ kpc, which is greater than the DM impact parameter even for DM as heavy as 10 $M_\odot$. Hence most PTA works compute the Shapiro signal assuming $z_0 > b$, in which case it has been shown that the relevant impact parameter is defined relative to the line-of-sight between Earth and the pulsar, *i.e.* $b_\perp$. For laser interferometers, however, the baseline L can, in general, be smaller than the DM impact parameter, b. In this section, we show that if $b > L$, then the relevant impact parameter is, in fact, b as the length scale of the detector becomes negligible and the detector becomes "point-like", which is consistent with Ref. [44]. In the opposite limit where $b < L$, an interferometer becomes similar to the pulsar-Earth system, and the relevant impact parameter is $b_\perp$.

We choose the midpoint of the interferometer arm as the coordinate origin in Eq. (7.17) . The total Shapiro delay is given by the change in the proper length of the interferometer arm, measured over a photon roundtrip

$$h_{\rm Shapiro}(t) = \frac{1}{L}\left[\Delta l\left(t+\frac{L}{2c}\right)+\Delta l\left(t+\frac{3L}{2c}\right)\right], \tag{7.28}$$

where $\Delta l(t)$ is the shift in the proper arm length, measured by a photon that passes through the midpoint of the arm, $\mathbf{r}_{\rm mid}$, at time t, *i.e.*

$\Delta l(t) = \frac{1}{2}\int_{-L/2}^{L/2} dz\, h_{ij}\left(t+\frac{z}{c}, \mathbf{r}_{\rm mid} + z\hat{\mathbf{n}}\right) n^i n^j$. Under the DM gravitational field in Eq. (7.13) and Eq. (7.14), and assuming that DM moves in a straight line with a constant velocity according to Eq. (7.15), the motion of $\mathbf{r}_{\rm DM}(t)$ within a one-way photon travel time can be simply treated as $\mathbf{r}_{\rm DM}(t+(z/c)) = \mathbf{r}_{\rm DM}(t) + (z/c)\mathbf{v}$, and hence [44]

$$\Delta l(t) = \frac{GM}{c^2}\int_{-L/2}^{L/2} dz \frac{1}{\sqrt{(z-r_\parallel)^2 + r_\perp^2}}\,, \tag{7.29}$$

where we defined the parallel and perpendicular distance of DM, relative to the arm midpoint, $r_\perp \equiv |[\mathbf{r}_{\rm DM}(t) - \mathbf{r}_{\rm mid}]\times\hat{\mathbf{n}}|$ and $r_\parallel \equiv [\mathbf{r}_{\rm DM}(t) - \mathbf{r}_{\rm mid}]\cdot\hat{\mathbf{n}}$, and used the non-relativistic limit $\hat{\mathbf{n}} - (v/c)\hat{\mathbf{v}} \approx \hat{\mathbf{n}}$. The integral in Eq. (7.29) can now be computed analytically [44]

$$\begin{aligned}\Delta l(t) &= \frac{GM}{c^2}\log\left(\frac{r_\parallel + (L/2) + \sqrt{r_\perp^2 + [r_\parallel + (L/2)]^2}}{r_\parallel - (L/2) + \sqrt{r_\perp^2 + [r_\parallel - (L/2)]^2}}\right) \approx \frac{GM}{c^2} \\ &\times \begin{cases} \log\left(\dfrac{L^2}{r_\perp^2}\right), & \text{if } \sqrt{r_\perp^2 + r_\parallel^2} \lesssim L/2 \\ \dfrac{L}{\sqrt{r_\perp^2 + r_\parallel^2}}, & \text{if } \sqrt{r_\perp^2 + r_\parallel^2} \gtrsim L/2 \end{cases},\end{aligned} \tag{7.30}$$

taking a simpler form in the two different limits. We observe that when $b \gtrsim L/2$, then the Shapiro delay depends on the magnitude of $\mathbf{b}$, similar to the Doppler effect. However when $b \lesssim L/2$, the effect only depends on the perpendicular component and has a weak log boost from the small distance (as opposed to the Doppler case). Using the parameterization in Eqs. (7.16)-(7.17) for the upper and lower entries of Eq. (7.30) and performing a Fourier transform, we find [2]

$$\Delta\tilde{l}(f) \approx \frac{GM}{c^2}\begin{cases} \dfrac{1}{f}e^{-2\pi i f t_{0,\perp}} e^{-f/f_{\tau_\perp}}, & \text{if } b \lesssim L/2 \\ \dfrac{2L}{v}e^{-2\pi i f t_0} K_0\left(\dfrac{f}{f_\tau}\right), & \text{if } b \gtrsim L/2 \end{cases}. \tag{7.31}$$

[2] Useful Fourier transform integral: $\int_{-\infty}^{\infty} dx e^{-ikx}\log\left(\frac{1}{\alpha x^2+\beta x+\gamma}\right) = \frac{2\pi}{|k|}e^{ik\frac{\beta}{2\alpha}}e^{-\frac{\sqrt{-\Delta}}{2\alpha}|k|}$, where $\alpha, \beta\,\gamma \in \mathbb{R}$, $\alpha > 0$, $\gamma > 0$, and $\Delta \equiv \beta^2 - 4\alpha\gamma < 0$. We dropped all delta functions as usual.

We then Fourier transform the total Shapiro delay in Eq. (7.28)

$$|\tilde{h}_{\rm Shapiro}(f)|^2 = \left(\frac{8\pi GM}{c^3}\right)^2 \cos^2\left(\frac{f}{4f_{\rm FSR}}\right) \begin{cases} \left(\frac{f_{\rm FSR}}{f}\right)^2 e^{-2f/f_{\tau_\perp}}, & \text{if } b \lesssim L/2 \\ \left(\frac{c}{2\pi v}\right)^2 K_0^2\left(\frac{f}{f_\tau}\right), & \text{if } b \gtrsim L/2 \end{cases} . \tag{7.32}$$

We emphasize that Eq. (7.32) should be read with caution. The two entries of Eq. (7.32) are decided by the relative magnitude between b and $L/2$. If $b \gtrsim L/2$, then the Shapiro signal is cut off at the frequency corresponding to b. Otherwise if $b \lesssim L/2$, then the Shapiro spectrum is suppressed by factors of v/c compared to the Doppler spectrum in Eq. (7.26), and is cut off at the frequency corresponding to $b_\perp$.

In a two-arm interferometer system with an $O(1)$ (in radians) arm separation angle, the total Shapiro strain is the difference between individual arm strains. If $b \ll L/2$, then the Shapiro delay for one of the arms should be much stronger than that of the second arm (it is statistically unlikely that the DM with the smallest $b_{\perp,1}$ for one arm also has a comparably small $b_{\perp,2}$ relative to the second arm unless the angle between the two arms is very small, which is in general not true for any realistic GW detector). Otherwise, if $b \gg L/2$, then the two interferometer arms effectively become two point detectors oriented towards directions $\hat{\mathbf{n}}_1$ and $\hat{\mathbf{n}}_2$, and the total strain suffers a tidal suppression factor of L/b, similar to the Doppler effect in Eq. (7.22). Using Eq. (7.30), we find

$$\Delta l(t, \hat{\mathbf{n}}_1) - \Delta l(t, \hat{\mathbf{n}}_2) \approx \frac{GM}{c^2} \begin{cases} \log\left(\frac{L^2}{|\mathbf{r}_{\rm DM}(t) \times \hat{\mathbf{n}}_1|^2}\right), & \text{if } b \lesssim L/2 \\ \frac{L^2}{2r_{\rm DM}^2(t)} \hat{\mathbf{r}}_{\rm DM}(t) \cdot (\hat{\mathbf{n}}_1 - \hat{\mathbf{n}}_2), & \text{if } b \gtrsim L/2 \end{cases} . \tag{7.33}$$

Taking the Fourier transform of Eq. (7.33) using Eq. (7.17) and Eq. (7.28), the total Shapiro strain is

$$\begin{aligned} |\tilde{h}_{\rm Shapiro}(f)|^2 = &\left(\frac{8\pi GM}{c^3}\right)^2 \cos^2\left(\frac{f}{4f_{\rm FSR}}\right) \\ &\times \begin{cases} \left(\frac{f_{\rm FSR}}{f}\right)^2 e^{-2f/f_{\tau_\perp}}, & \text{if } b \lesssim L/2 \\ \left(\frac{L}{8b}\right)^2 \left(\frac{c}{2\pi v}\right)^2 \left|\tilde{s}_{M_1}\left(\frac{f}{f_\tau}\right)\right|^2, & \text{if } b \gtrsim L/2 \end{cases} , \end{aligned} \tag{7.34}$$

where $\tilde{s}_{M_1}(x)$ is defined in Eq. (7.21), but with $\hat{\mathbf{n}}$ replaced by $\hat{\mathbf{n}}_1 - \hat{\mathbf{n}}_2$. Comparing Eq. (7.34) with Eq. (7.32), we see that the Shapiro spectrum for a two-arm interferometer is identical to that of a one-arm detector for $b \lesssim L/2$, but picks up a suppression factor of $4\sin^2(\Delta\theta/2)(L/8b)^2$ when $b \gtrsim L/2$.

Einstein Delay

The gravitational effect due to the Einstein delay is given by the difference of the clock proper time τ at the beamsplitter over a photon roundtrip time

$$h_{\rm Einstein}(t) = \frac{c}{L}\left[\tau\left(t + \frac{2L}{c}\right) - \tau(t)\right] . \tag{7.35}$$

The proper and coordinate times are related by $d\tau(t)/dt = 1 - (1/2)h_{00}$, so that using Eq. (7.13) and Eq. (7.35), we write

$$\frac{d}{dt}h_{\rm Einstein}(t) = \frac{1}{cL}\left[\Phi\left(t + \frac{2L}{c}\right) - \Phi(t)\right] , \tag{7.36}$$

where the DM gravitational potential Φ is evaluated at the beamsplitter. Putting the DM trajectory in Eq. (7.15) with the beamsplitter location chosen as the coordinate origin into the potential, one finds $\Phi(t) = -(GM/b)(1+\eta^2)^{-1/2}$ with the Fourier transform $\tilde{\Phi}(f) = -(2GM/v)e^{-2\pi i f t_0}K_0(f/f_\tau)$, giving the Einstein strain

$$|\tilde{h}_{\rm Einstein}(f)|^2 = \left(\frac{8GM}{c^2 v}\right)^2\left(\frac{f_{\rm FSR}}{f}\right)^2 \sin^2\left(\frac{f}{2f_{\rm FSR}}\right) K_0^2\left(\frac{f}{f_\tau}\right) . \tag{7.37}$$

Note that the impact parameter only enters the spectrum through the peak frequency $f_{\rm peak}$, but not the amplitude.

If the interferometer has two arms, then the Einstein delay contribution cancels between the two interferometer arms, and thus the effect vanishes.

7.4 Stochastic Signal

In the small DM mass limit, it is possible that each individual DM is not sufficient to produce a sizable signal, but the collective effect due to all DM passing by the detector might be large enough to be measured. In this limit, DM behaves collectively like a stochastic background. The total strain $h(t)$ is given by summing over strains $h_a(t)$ from all individual DM:

$$h(t) = \sum_a h_a(t) . \tag{7.38}$$

Correlations from the stochastic DM field have been previously studied in Ref. [42] in the context of PTAs.

Doppler Effect

For a given $\hat{\mathbf{v}}$, the differential volume of an element in a cylinder is $dV = vbdbd\varphi dt_0$, where φ is the polar angle of $\mathbf{b}$ on the plane perpendicular to $\mathbf{v}$. We have assumed monochromatic DM masses. Using the parameterization in Eq. (7.16), the auto-correlation function of $\tilde{h}_{\rm Doppler}(f)$ is then given by integrating over the volume

$$\langle \tilde{h}(f)\tilde{h}^*(f')\rangle = \frac{n}{4\pi}\int_{b_{\rm min}}^{\infty} bdb \int_0^{2\pi} d\varphi \int_{-T/2}^{T/2} dt_0 \times \int_0^{v_{\rm esc}} v f_v(v) dv \int_0^{\pi} \sin\theta d\theta \int_0^{2\pi} d\phi\, \tilde{h}(f)\tilde{h}^*(f')\,, \tag{7.39}$$

where $f_v(v)$ is the Maxwell-Boltzmann distribution for the velocity, and θ and ϕ are the polar and azimuthal angles for $\mathbf{v}$ respectively. The factor of $1/(4\pi)$ comes from normalization of the angular integration over θ and ϕ. Note that we also set the lower limit of the integral over b to $b_{\rm min}$ as defined in the RHS of Eq. (7.4). The integral is formally divergent if we allow $b \to 0$, which is a case of statistical outliers skewing the mean of a distribution. Following the treatment of Ref. [42] in the context of PTAs, the divergence can be regulated by truncating the integral at the 90$^{\rm th}$-percentile of minimum impact parameter among DM particles, which is insensitive to statistical outliers.

Since the DM trajectory in Eq. (7.15) is a function of $t - t_0$, the strain in Fourier space $\tilde{h}(f)$ can only depend on t_0 through a phase factor $\exp(-2\pi i f t_0)$. Integrating over t_0 thus evaluates to a delta function in $f - f'$ in the limit when $fT \gg 1$: $\langle \tilde{h}_{\rm Doppler}(f)\tilde{h}_{\rm Doppler}(f')\rangle = S_{\rm Doppler}(f)\delta(f-f')$, indicating that the stochastic signal is stationary when the observation time is sufficiently large. The strain power spectrum reads

$$S_{\rm Doppler}(f) = \frac{n}{4\pi}\int_{b_{\rm min}}^{\infty} bdb \int_0^{2\pi} d\varphi \int_0^{v_{\rm esc}} v f_v(v) dv \int_0^{\pi} \sin\theta d\theta \int_0^{2\pi} d\phi\, |\tilde{h}(f)|^2\,. \tag{7.40}$$

Anticipating that the signal's dependence on the velocity is going to be weak, we set the velocity to $\bar{v}$, while integrating over angular factors of $\hat{\mathbf{b}}\cdot\hat{\mathbf{n}}$ and $\hat{\mathbf{v}}\cdot\hat{\mathbf{n}}$ using Eq. (I.2). We show the analytic form for the Doppler effect and extend the spectrum result for $b < L$ to $b \to \infty$, since we expect the detector to only be sensitive to

$b < L$. Then integrating Eq. (7.40) with Eq. (7.26), we find [3]

$$S_{\rm Doppler}(f) = B_{\rm Doppler}\left(\frac{f_{\rm FSR}}{f}\right)^4 \cos^2\left(\frac{f}{2f_{\rm FSR}}\right)\left(\frac{f}{f_{\tau_{\rm min}}}\right) K_0\left(\frac{f}{f_{\tau_{\rm min}}}\right) K_1\left(\frac{f}{f_{\tau_{\rm min}}}\right), \tag{7.41}$$

where $f_{\tau_{\rm min}} \equiv v/(2\pi b_{\rm min})$, and

$$\begin{aligned} B_{\rm Doppler} &\equiv \frac{128\pi L^2 G^2 M \rho_{\rm DM} f_{\rm DM}}{3c^4 \bar{v}} \\ &= 2\times 10^{-73}\ {\rm Hz}^{-1}\left(\frac{M}{\rm kg}\right) f_{\rm DM}\left(\frac{340\ {\rm km/s}}{\bar{v}}\right)\left(\frac{L}{\rm km}\right)^2 . \end{aligned} \tag{7.42}$$

For stationary signals, considering the cross-correlation between two detectors and the optimal matched filtering, the stochastic SNR is given by

$${\rm SNR}^2_{\rm X,stoc} = 2T\int_0^\infty df\,\Gamma^2(f)\,\frac{S_X^2(f)}{S_{n_1}(f)S_{n_2}(f)}, \tag{7.43}$$

where $S_{n_{1,2}}(f)$ are the one-sided auto-correlated PSD of the two detectors $1, 2$, $\Gamma(f)$ is the cross-correlation function across detectors, and X can correspond to the Doppler, Shapiro or Einstein effect. For simplicity, we assume $\Gamma(f) \sim 1$, *i.e.* the two detectors are co-located and aligned without correlated noise, and $S_{n_1}(f) = S_{n_2}(f) = S_n(f)$. Note that if there is only one detector, then due to the random nature of both the signal and the noise, no matched filtering can be applied.

In the first panel of Fig. 7.5, we show constraints on the DM fraction f_{DM} for LIGO, LISA, GQuEST, and Holometer, which all have two detectors. For the mass range and experimental parameters considered in this work, the Doppler stochastic reach is subdominant compared to the deterministic reach, which is consistent with the conclusion of Ref. [433]. This can be explicitly shown by estimating the SNR assuming both the signal and the noise are constant within the experiment's frequency window Δf, using Eqs. (7.26) and (7.41), one observes

$$\begin{aligned} \frac{{\rm SNR}_{,\,\rm Doppler}}{({\rm SNR}_{det,\,\rm Doppler})^2} &\approx \frac{1}{\sqrt{T\Delta f}}\left.\frac{K_0(x)K_1(x)}{x[K_0(x)^2+K_1(x)^2]}\right|_{x=f_{peak}/f_\tau} \\ &\approx -\frac{1}{\sqrt{T\Delta f}}\log(f_{peak}/f_\tau), \end{aligned} \tag{7.44}$$

in the limit $f_{peak} \ll f_\tau$, showing that the stochastic constraint grows logarithmically for lower masses. As for all GW detectors considered in this work, including

[3] Useful integral: $\int_a^\infty x[K_0^2(x)+K_1^2(x)]dx = aK_0(a)K_1(a)$ for $a > 0$.

LIGO, LISA, GQuEST and Holometer, $T\Delta f \gg 1$, and hence the stochastic limit is subdominant for the whole mass range as shown in Fig. 7.5. Notice that for PTAs, for example, $T\Delta f \sim 1$ thus the stochastic constraint can take over at a relevant mass range [42].

Shapiro Delay

The stochastic Shapiro delay can be derived in a similar manner. Recall from Sec. 7.3 that in the $b \ll L$ limit, the impact parameter relative to the interferometer arm sets the size of the signal. The volume of a differential element is given by $dV = v_\perp db_\perp db_\parallel dt_{0,\perp}$ [42]. The stochastic Shapiro power spectrum is thus given by integrating the Shapiro strain in Eq. (7.32) with the parameterization in Eq. (7.17) over volume

$$S_{\rm Shapiro}(f) = \frac{n}{4\pi}\int_0^\infty db_\perp \int_{-L/2}^{L/2} db_\parallel \times \int_0^{v_{\rm esc}} v_\perp f_{v_\perp}(v_\perp) dv \int_0^\pi \sin\theta d\theta \int_0^{2\pi} d\phi \, |\tilde{h}_{\rm Shapiro}(f)|^2 \,, \tag{7.45}$$

where we again assume that $\mathbf{v}$ points at a direction of (θ, ϕ), $f_{v_\perp}(v_\perp)$ is the perpendicular (relative to the interferometer arm) velocity distribution, and we performed the integral over $t_{0,\perp}$ assuming $fT \gg 1$. Anticipating that DM with $b_\perp < L/2$ will dominate the stochastic signal, we perform the integral in Eq. (7.45) using the upper entry of Eq. (7.32) and find

$$S_{\rm Shapiro}(f) = B_{\rm Shapiro}\left(\frac{f_{\rm FSR}}{f}\right)^3 \cos^2\left(\frac{f}{4f_{\rm FSR}}\right)\left(1 - e^{-(f/2f_{\rm FSR})(c/v_\perp)}\right)\Theta(L - b_{\perp,\rm min}) \,, \tag{7.46}$$

where

$$B_{\rm Shapiro} \equiv \frac{64\pi^2 L^2 G^2 M \rho_{\rm DM} f_{\rm DM} \bar{v}_\perp^2}{c^7} = 8\times 10^{-82}\ {\rm Hz}^{-1}\left(\frac{M}{\rm kg}\right) f_{\rm DM}\left(\frac{\bar{v}_\perp}{270\ {\rm km/s}}\right)^2\left(\frac{L}{\rm km}\right)^2 \,, \tag{7.47}$$

and we substituted the mean value, $\bar{v}_\perp$, of the velocity distribution, and introduced a cut-off requiring $b_{\perp,\rm min} < L$ to ensure that there are non-zero number of DM with $b_\perp < L$.

The projected reach of the stochastic Shapiro signal is shown in the second panel of Fig. 7.5, and is derived by setting the SNR in Eq. (7.43) with the spectrum in Eqs. (7.46)-(7.47) to be two. Unlike the Doppler effect, the stochastic Shapiro signal

can actually have better reach than the deterministic signal in the lower DM mass range, such as $M \lesssim 10^6$ kg for LIGO, for example. This can be traced to the fact that the Shapiro deterministic signal amplitude is independent of the DM mass once the DM impact parameter becomes less than L. However, the stochastic Shapiro spectrum scales lienarly with the DM mass, as evident in Eq. (7.47), resulting in a larger SNR for the relevant mass range.

The stochastic signal derived in this section in general agrees with the results in Ref. [42] studied in the context of PTAs. In particular, the stochastic spectrum in Eq. (7.42) and Eq. (7.46) have the same scaling relations of M, $f_{\rm DM}$, $\rho_{\rm DM}$, $\bar{v}$, $\bar{v}_\perp$ and L (up to the definition of the observable) as the spectrum derived in Ref. [42]. A notable difference is that Ref. [42] presented the stochastic signal as a non-stationary process, with a power spectrum that is a function of both f and f', as opposed to the stationary signal we derived in this section, where the power spectrum is only a function of f, similar to a stochastic GW background [329]. As discussed in Sec. 7.4, one can explicitly demonstrate that the stochastic DM signal is stationary by integrating over the DM arrival time, t_0 (Doppler) or $t_{0,\perp}$ (Shapiro), over the experimental time T. In the limit $fT \gg 1$, which holds for all GW detectors considered in this work with $T = 1$ year, one finds that $\langle \tilde{h}(f)\tilde{h}(f')\rangle$ is proportional to $\delta(f - f')$, which is the definition of a stationary process. Physically, this demonstrates that for a sufficiently long observation time, DM can arrive at any time during the experiment, which is a uniformly random variable, and hence the signal produced is stationary in nature.

7.5 Gravitational Wave Experiments and Noise Curves

In this section, we discuss various types of GW experiments that are sensitive to transiting macroscopic DM signals, with a focus on laser interferometers.

A collection of noise spectral densities for such experiments can be found in Fig. 7.6.

Laser Interferometers

Gravitational waves were first detected by LIGO and Virgo [428]. Since then, laser interferometry laboratories, both ongoing and proposed, have expanded their coverage to encompass a broader range of signal frequencies. At higher frequencies ($\gtrsim Hz$), the advanced LIGO and Virgo are to be joined by Cosmic Explorer [454], Einstein Telescope [455, 456] and proposals such as NEMO [457] and LIGO Voyager [458]. On the other hand, LISA [459] is proposed to operate at lower frequencies below Hz. At the same time, experimental apparatus proposed mainly to detect

quantum gravity effects, such as Holometer [431] and GQuEST [432], are sensitive to signals at high frequencies in the MHz range.

The peak sensitivity frequency is typically set by the arm length L and the quality factor Q of the FP cavity (if any), $f_{peak} \simeq c/(4\pi QL)$. Throughout the paper, for laser interferometers, we consider the sensitivity as obtained by a two-arm configuration. The angle between the two arms is given by the proposed detector geometry. Throughout this work, We have used the published noise curves for all experiments as shown in Fig. 7.6 unless otherwise specified. Holometer and GQuEST are in principle narrowband detectors.

Other Types of Gravitational Wave Detectors

Optically levitated sensors with tunable frequencies have been proposed to detect GWs at high frequencies in the $\sim [10, 300]\, kHz$ range [460, 461]. Such a device consists of a nano- or micro-scale sensor (sphere or disk) levitated optically and placed at an antinode of a tunable trapping laser inside an FP cavity. An interferometer-like configuration [461] further increases the sensitivity by noise cancellation between its two arms. A one-meter prototype of the detector is under construction. The optically levitated sensor is a resonant detector, where the motion of a dielectric nanoparticle suspended at an antinode of the cavity can be detected. The operating frequency is determined by the tunable trapping frequency of the nanoparticle: $\omega_0^2 = \frac{1}{m_s}\frac{d^2U}{dx^2}|_{x=x_0}$, where m_s is the nanoparticle mass, U is the optical potential, and x_0 is the antinode location. The dominant noise source is from the Brownian thermal motion of photon scattering from the nanoparticle, which is suppressed at higher frequencies and cryogenic temperatures. For such resonant sensors, we assume the TM to be free over the interaction timescale, so the characteristic frequency of the signal is larger than the trapping frequency, $2\pi f_\tau \gtrsim \omega_0$.

In a local Lorentz frame with the inner mirror at the origin, we treat both the levitated object and the end mirror as free objects within one measurement, initially at x_s and ℓ_m. The relevant quantity measured is the displacement of the levitated object from the antinode of the trapping laser, $\Delta x = \delta x_{\rm min} - \delta x_s = \delta\ell_m - \delta x_s$. A detector specialized to probe GW signals would benefit from having x_s as small as possible [460], so here we also work in the limit where $x_s \ll \ell_m$, treating the device as an interferometer with two mirrors separated by a distance of $\sim \ell_m$. We use the strain sensitivity quoted in Ref. [461] to calculate the SNR, without a careful treatment of the cavity response. The cavity response might boost the signal on the higher

frequency end up to an order of magnitude (for the 100 m stack detector). In addition to the classical Doppler acceleration, we also consider the Shapiro effect, which can displace the minimum of the optical potential and hence the sensor location. We estimate the Shapiro strain using formulas derived for laser interferometers in Sec. 7.3. We emphasize that the interferometry treatment here is an approximation, where the effects are not gauge invariant in the setup of an optically levitated sensor with a trapping potential. We leave a more detailed calculation for future work.

We note that there are experiments with standalone levitated or trapped test masses not included in this paper [462, 463, 464, 465, 466, 467, 468, 469]. They either operate at lower frequencies comparable to laser interferometers or with lower acceleration sensitivities than the apparatus considered. Another recent proposal involving an array of levitated mechanical sensors and the projected sensitivity to composite DM can be found in Ref. [470].

Resonant mass detectors have their origins at the beginning of experimental GW physics, *i.e.* the Weber bar experiment. In general, resonant vibration modes of the test mass as induced by an external force can be sensed through certain read-out systems. Along one direction of the test mass, considering the fundamental mode, the strain sensitivity of such detectors can be converted to acceleration sensitivity according to $\tilde{h}(f) \sim \tilde{a}(f)/(8Lf^2)$, where L is the length of the resonant mass in such a direction [34]. To estimate the DM sensitivity, we consider the classical Doppler acceleration as given by Eq. (7.21) projected onto one direction. We acknowledge that the exact signal induced by the DM's potential requires a careful calculation that can be done using the metric perturbation formalism. However, as the DM sensitivity for such experiments is suppressed, as shown in Fig. 7.3 and 7.4, we do not attempt to refine the calculation further. *Spherical resonant mass* experiments, such as Mini-GRAIL [471] and Schenberg antenna [472], transform excited mechanical modes to electrical signals. Such experiments operate at $\sim$ kHz frequencies, and the strain sensitivities are typically less than laser interferometers operating at the same frequency. At the same time, a new type of resonant mass detectors, the *Bulk Acoustic Wave* experiment, is designed to operate at higher frequencies in the MHz - GHz range [473, 474]. These experiments generally sense the acoustic waves inside a piezoelectric material along a certain direction (e.g., for a cylinder, along the length) through the SQUID readout. There is a broad range of operating frequencies depending on the acoustic eigenmode. The strain sensitivity is improved with a large mode quality factor and cryogenic temperatures. Note that

such experiments employ higher resonance modes to achieve broadband sensitivity. To convert the strain sensitivity, we have assumed the fundamental mode. Notice that at a similar frequency range, membrane optomechanical experiments based on optical cavities (see e.g. [475]) can reach a similar acceleration sensitivity of $\sim 10^{-5}\, m/s^2/\sqrt{Hz}$. We do not make explicit projections for such experiments and refer the readers to the BAW projection as a reference.

Long-baseline atom interferometers are another venue for both GW and DM direct detection. There has been a growing interest in such detectors and active proposals. Long-baseline atom interferometers consisting of two spatially separated single atom interferometers are proposed to close the mid-band window between the low-frequency LISA (~ 0.01 Hz) and ground-based laser interferometers (~ 1 Hz). The operation frequency is limited by gravity gradient noise on the lower end and the rate of relaunching cold atoms on the higher end. With improved noise models and space-based designs, some missions can cover lower frequency range even beyond LISA (see Ref. [476] for a review). A long-baseline atom interferometer, such as Magis [477, 478], AEDGE [479], or AION [480], resembles a single-arm laser interferometer that can perform differential phase measurements at any given time and benefit from noise cancellation between the two devices. Although a single atom interferometer can also serve as an accelerometer, the tidal effect is determined by the rather small wavepacket separation, typically $\lesssim 1$ m, that would generally suppress the sensitivity. Here we briefly discuss the prospects for long-baseline atom interferometers and leave detailed studies for both types of proposals for future work. A long-baseline atom interferometer precisely measures the light traveling time between the two atom interferometers distantly separated by a baseline length L. The two atom interferometers are run by a common laser. The laser drives the atomic transition between the ground and excited states and transfers $2\pi\hbar/\lambda$ momentum to the atoms at each pulse, where λ is the laser wavelength. Laser pulses applied at different times serve as “mirrors" and the “beamsplitter" for the interferometer. The phase of the interference fringe at each atom interferometer depends both on the laser phase and the phase accumulated by the atoms themselves. The pair of atom interferometers serve as both precise inertia and laser frequency reference. For the single-photon transition scheme, the relative interference phase between the two atom interferometers is given by $\Delta\phi = \omega_A\,(2L/c)$, where ω_A is the atomic transition frequency, and the baseline length determines the light traveling time. Thus, naively, the strain on the baseline length $h(t) \sim \Delta L/L$, as induced by the transiting DM interacting with the atom cloud and the traversing photon through

the Newtonian potential, can be sensed by such detectors. However, the exact phase shift as induced by the transiting DM depends on the internal mechanism of the atom interferometry, as well as how the photon propagates with space-time fluctuations. For example, the Shapiro effect can be dominant in the high DM mass regime, and cannot be captured by the classical accelerometer projection based on the Doppler effect. The strain sensitivity of proposed long-baseline atom interferometers can be comparable to laser interferometers. Thus, we postpone the study of the gauge invariant phase calculation to future work.

Pulsar timing arrays have been studied as powerful and complementary probes to DM subhalos at small masses ($M < 10^2 M_\odot$) [44, 103, 104, 43, 42, 9]. In this work, we appropriately extend the results from [9] to lower masses using analytic results, assuming observations of 200 pulsars across 20 years of observational time, 2 weeks of cadence, and 50 ns of white noise in the timing data, which corresponds to an estimated scenario of the Square Kilometer Array (SKA) experiment [155].

7.6 Discussion and Conclusion

In this paper, we consider the effects of transiting macroscopic dark matter on GW experiments, particularly laser interferometers. Gravitational interaction and an additional Yukawa interaction are both considered. We applied the formal gauge invariant observable for laser interferometers to the case of transiting DM. Importantly, in addition to the Dopper effect, which is the only effect considered in existing literature, the Shapiro effect and Einstein delay may also be present for a generic interferometer design. The Shapiro effect is the change in the messenger travel time along the interferometer arm. The Einstein delay is the time dilation of the clock's proper time, which cancels between arms for a two or multi-baseline interferometer. We show that, for most operating and proposed laser interferometers, the Shapiro effect is subdominant compared to the Doppler effect. However, we also observe that depending on the experimental parameters, the Shapiro effect may take over for higher DM masses.

In general, GW experiments operating at higher frequencies are sensitive to macroscopic DM with lower masses. Across the landscape of experiments included in this paper, apart from PTAs in the very low-frequency range, for laser interferometers in the $10^{-4}\,Hz - kHZ$ range and high-frequency apparatus (including Holometer and GQuEST) in the $kHZ - GHz$ range, the projections peak at DM masses in the range of $\sim 1 - 10^{15}$ kg. The signal is dominated by transiting DM with an impact

parameter smaller than the interferometer baseline length, *i.e.* $b < L$. This is a result of several effects, such as the peak frequency of the DM signal compared to that of the experiment, the tidal effect, and the time differential effect of the strain measurement. Typically the peak frequency is the dominant factor. However, for experiments with a large quality factor, the tidal effect may be the most relevant suppression for DM with large impact parameters.

We have also investigated constraints from the stochastic signal produced by an ensemble of transiting DM. We found that for the Doppler effect, the constraints from stochastic signals are always weaker than the deterministic constraints. On the other hand, for the Shapiro effect, the stochastic signal could dominate over the deterministic signal in the low mass regime.

Lastly, we have left out the analysis of an important type of GW experiment, *i.e.* atom interferometers, as the exact gauge invariant observable induced by transiting DM is different than that of laser interferometers. We postpone such a study for future work.

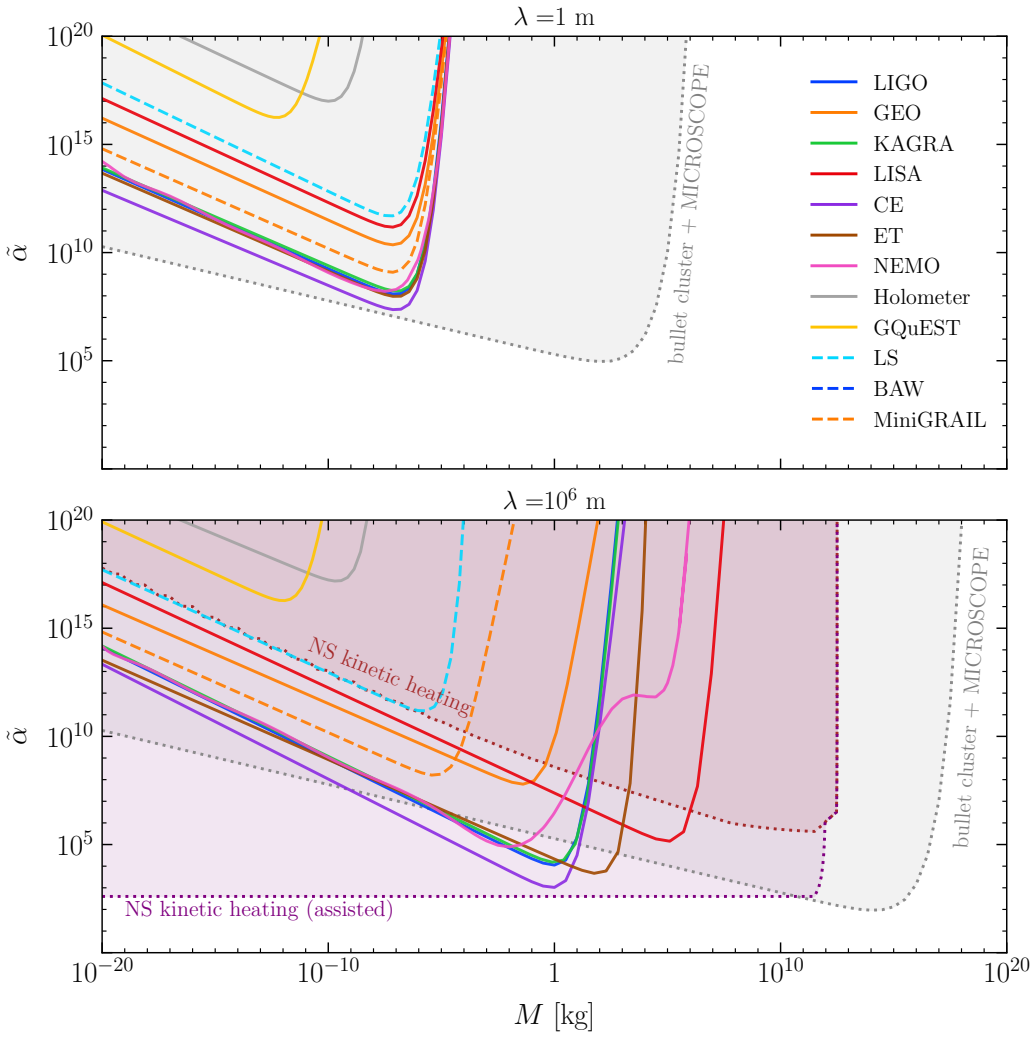

Figure 7.4: Projected 90$^{\text{th}}$-percentile upper limits on the fifth force Yukawa parameter from several existing and proposed GW detectors based on laser interferometry, assuming $T = 1$ yr of observation time and two choices of force range, $\lambda = 1$ m and $\lambda = 10^6$ m. Existing constraints are shown in dotted lines. The grey line is the combined constraint from bullet cluster observation [447, 448] and the MICROSCOPE experiment [449, 450], while the purple (red) lines are constraints from neutron star kinetic heating [5] with (without) additional short-range DM-baryon interactions to facilitate energy transfer. The limits are derived by setting the 10$^{\text{th}}$-percentile SNR defined in Eq. (7.5) to be two, and the DM initial conditions are sampled using a Monte Carlo simulation. Projections from other types of high-frequency GW experiments are shown with dashed colored lines. See Sec. 7.2 for a summary of existing fifth force constraints, and Sec. 7.5 for a description of the experiments.

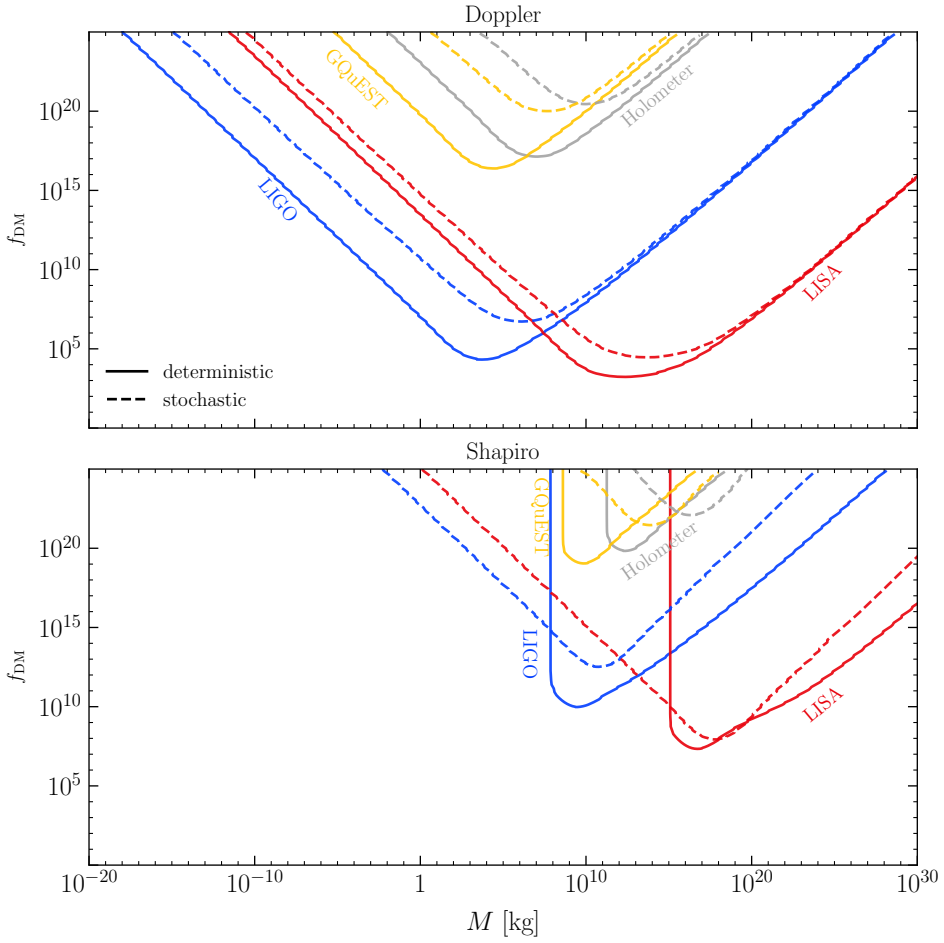

Figure 7.5: Projected 90$^{\rm th}$-percentile upper limits on stochastic DM signals from LIGO, LISA, GQuEST, and Holometer, assuming $T = 1$ year of observation time and local DM density $\rho_{\rm DM} = 0.46\,{\rm GeV}/c^2/{\rm cm}^3$. The limits are derived by setting the 10$^{\rm th}$-percentile SNR defined in Eq. (7.43) to be two. See Sec. 7.5 for a description of the experiments.

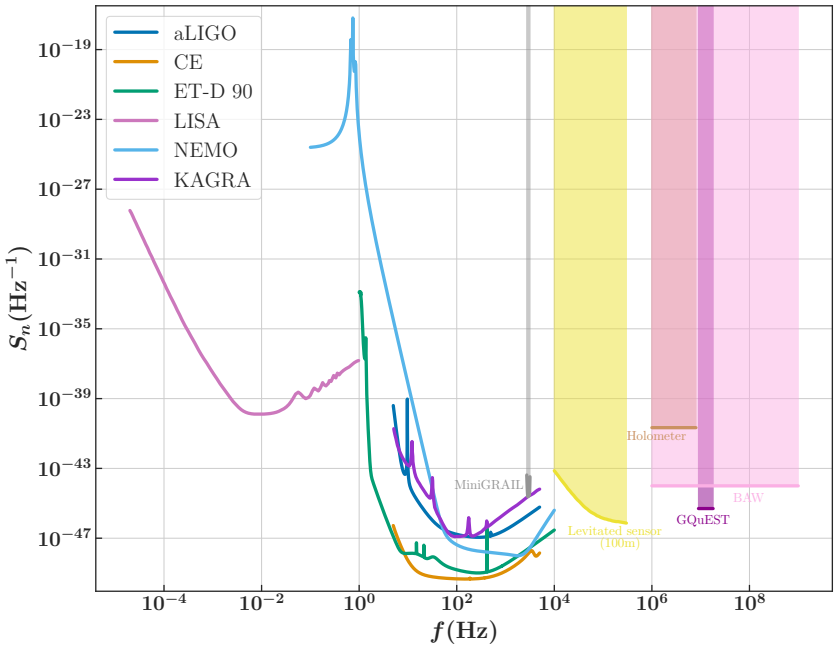

Figure 7.6: Sensitivity curves of GW experiments. The projected noise spectral densities for laser interferometers are plotted in solid lines. Strain sensitivities for narrowband detectors are shown in shaded regions within the quoted bandwidths. Note that the presented frequency range for the levitated sensor corresponds to the tunable frequency range of the trapping potential, rather than the measurement bandwidth. See Sec. 7.5 for a description of experiments.

Part II

Quantum Gravity

Chapter 8

NEAR-HORIZON QUANTUM DYNAMICS OF 4-D EINSTEIN GRAVITY FROM 2-D JT GRAVITY

This chapter is based on

[1] Sergei Gukov, Vincent S. H. Lee, and Kathryn M. Zurek. "Near-horizon quantum dynamics of 4D Einstein gravity from 2D Jackiw-Teitelboim gravity". In: *Phys. Rev. D* 107.1 (2023), p. 016004. DOI: 10.1103/PhysRevD.107.016004. arXiv: 2205.02233 [hep-th].

8.1 Introduction

Dimensional reduction has long played an important role in understanding the behavior of higher dimensional gravitational theories, in particular in the study of black hole horizons. When a higher-dimensional theory is reduced to a two-dimensional system associated with the light-cone directions, the area of the transverse directions becomes the dilaton field. In the near-horizon limit the dilaton is conformal (see *e.g.* [481]), and by studying the conformal states of the action and using Cardy's formula the correct expression for the black hole entropy can be derived.

While the conformal description of near-horizon states has been widely applied to black hole horizons, there is reason to think that a similar formalism may apply to light sheet horizons more generally [482]. The interior of a causal diamond in many generic spacetimes can be represented by a topological black hole metric:

$$ds^2 = -f(R)dT^2 + \frac{dR^2}{f(R)} + \rho(T,R)^2 d\Sigma_{d-2}^2. \tag{8.1}$$

For example, for boundary anchored diamonds in AdS, $f(R) = R^2/L^2 - 1$, with L the AdS curvature, while in empty Minkowski, $f(R) = 1 - R/R_h$, where R_h is the radius of the bifurcate horizon. The representation of the causal diamond has an associated modular Hamiltonian, K, that characterizes the density matrix of the diamond, $\rho_{\text{diamond}} = e^{-K}/\text{tr}(e^{-K})$. If one conjectures that the near-horizon states of a light-sheet horizon are described by a conformal field theory, one is able to immediately write down the form of the partition function (see discussion in [482]),

$$\log Z = \log\left(\int dE\ e^{B\sqrt{E}-\beta E}\right), \tag{8.2}$$

from which one can derive both the expectation value of K, $\langle K\rangle = -\beta\partial_\beta \log Z + \log Z = \beta\langle E\rangle + \log Z = S$, and its fluctuations, $\langle \Delta K^2\rangle = \beta^2\partial_\beta^2 \log Z = \beta^2\langle \Delta E^2\rangle$, finding $\langle \Delta K^2\rangle = \langle K\rangle$. This result agrees with previous calculations for Ryu-Takayanagi diamonds in AdS/CFT [483, 484]. These modular fluctuations generate metric fluctuations, inducing a quantum uncertainty in the horizon of the causal diamond. The authors of previous works [482, 484, 30] suggested that these fluctuations might be observably large.

Here, we put a new twist on these ideas by showing that Einstein gravity on a causal diamond in flat 4-d spacetime, at least in the near-horizon limit, exactly dimensionally reduces to Jackiw-Teitelboim (JT) gravity [485, 486] in 2 dimensions. In particular, the parent 4-d theory can be Weyl-rescaled to a dilaton theory on $AdS_2 \times S^2$, as shown in Fig. 8.1. The dynamics of the dilaton (shown by a dashed line) controls both the size of the S^2 and the relative position of the horizon with respect to the boundary. As has also been noted by others, the dilaton is expected to have an effective hydrodynamic description [487].

This implies that, if we are interested only in observables defined on a light sheet horizon, we can make use of a vast literature studying the JT theory. In turn, this allows us to potentially draw connection between experimental observables and theoretical calculations in the vast field of quantum gravity. We will make use, in particular, of the solutions presented in Ref. [487], which features a 2-sided AdS_2 spacetime. These authors computed the quantum uncertainty in a geodesic distance controlled by the dilaton. We will show that the quantum uncertainty in this geodesic distance computed in the 2-sided 2-d JT theory is directly related to the uncertainty in the travel time for a photon to be fired from a boundary to the bulk, reflected by a mirror, and returned to the boundary. The relation is illustrated in Fig. 8.1, which will be described in more detail in the main text. The original 4-d spacetime has a flat metric

$$ds^2_{\text{Mink}} = -dt^2 + dr^2 + r^2 d\Omega_2^2\,, \tag{8.3}$$

which is conformally equivalent to the product metric on $AdS_2 \times S^2$:

$$ds^2_{\text{Mink}} = \frac{\rho^2}{L^2}\left(L^2\frac{-dt^2+dr^2}{r^2} + L^2 d\Omega_2^2\right)\,, \tag{8.4}$$

where we treat $\rho = r$ as a scalar field, and L is a positive constant which we identify with the AdS_2 radius (as well as the radius of the sphere S^2). This closely resembles the near-horizon limit of a 4-d near-extremal Reissner-Nordström black hole. In the limit $l_p \to 0$, such that the magnetic charge and temperature are kept

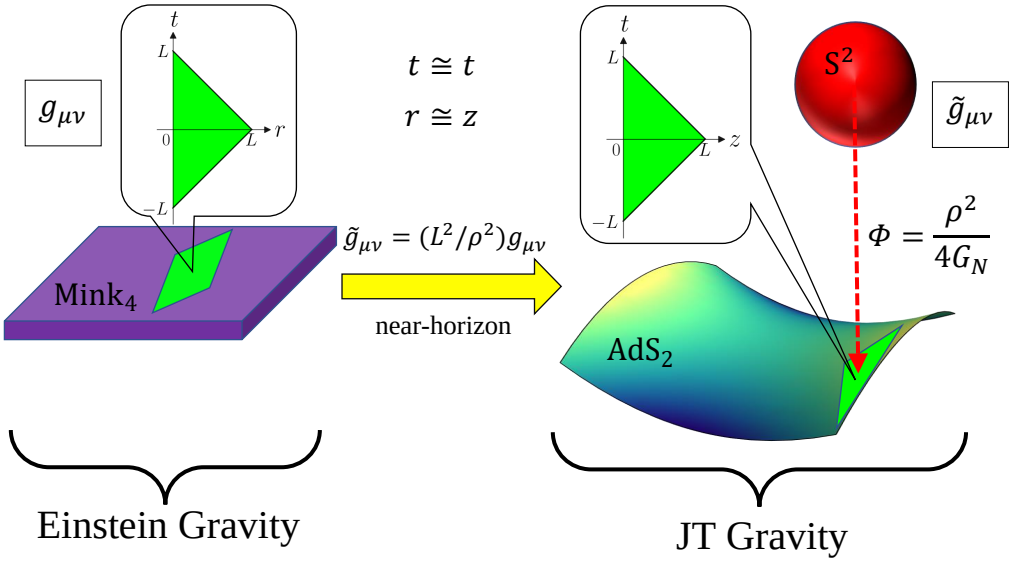

Figure 8.1: The metric on Mink$_4$ is conformally equivalent to that on AdS$_2$×S^2. Inserts illustrate spacetime diagrams of the causal diamonds in both geometries.

fixed, this near-horizon geometry becomes AdS$_2$×S^2, while the Einstein-Maxwell action reduces to the JT action [488] after integrating over the angular coordinates. Moreover, Eq. (8.4) demonstrates that the Minkowski spacetime variables, t and r, naturally become the AdS spacetime variables in Poincarécoordinates, t and z. Motivated by this well known result, in later sections we demonstrate that the Einstein gravity reduces to the JT gravity by a similar procedure and compute the relevant observables.

The causal diamond can be observationally defined by an interferometer set-up, also shown in Fig. 8.1. We align our interferometer arm along the radial direction and denote its length by L. The photon is fired from $r = 0$ at $t = -L$. At time $t = 0$, the photon hits the mirror at the interferometer end ($r = L$) and bounces back. Finally, the photon arrives to its starting position $r = 0$ at $t = L$. The photon trajectory is hence described by $t - r = -L$ and $t + r = L$ for its first and second trip respectively. The spacetime region bounded by the photon trajectory and $r = 0$ is commonly referred to as the causal diamond, where the photon trajectory itself is known as the

horizon since no particles can cross the boundary and escape to infinity, similar to a black hole horizon. Spacetime fluctuations lead to uncertainty in the photon travel time.

At first sight, it seems surprising that JT gravity in 2-sided AdS, such as that solved explicitly in Ref. [487], would have anything to do with photon trajectories in Minkowski space. After all, the JT set-up is in AdS space and has curvature, while Minkowski does not. It is also not immediately clear what a 2-sided geometry has to do with a 1-sided causal diamond. It is important to highlight two subtle, but important points that allow us to utilize the computational tools of JT gravity. First, while AdS clearly has curvature that the parent Minkowski theory does not, in the near horizon limit of the causal diamond relevant for photon trajectories, we will show that these terms in the action which contribute to the curvature are subdominant. Second, while the formal solution to JT gravity that we utilize is in two-sided AdS, we will see that the length of the causal diamond horizon in one-sided Minkowski is identical to that of the two-sided AdS horizon connecting the two boundaries. Hence, one can compute the physical photon roundtrip time by calculating the time for a photon to travel from one AdS boundary to the boundary on the other side of AdS along the horizon. We will see that the other side of AdS serves as a convenient tool for us to compute quantum fluctuations in the physical observable by computing how one side of AdS fluctuates with respect to the other side.

The outline of the paper is as follows. In Sec. 8.2, we discuss how the JT action can be obtained by dimensionally reducing the familiar gravitational action and dropping a subdominant kinetic term in the near-horizon limit. In Sec. 8.3, we study the AdS geometry and introduce various useful coordinate systems. In Sec. 8.4, we define our observable in the context of JT gravity and compute its fluctuations. Finally, in Sec. 10.5, we discuss implications of our results and mention a few future directions.

8.2 Dimensional Reduction to the JT action

We begin by dimensionally reducing the familiar gravitational action in 4-d Minkowski spacetime, in the near-horizon limit, to the 2-d JT action. As advertised above, this calculation is similar to the previous work by one of the authors [482] on small empty diamonds. There are, however, a couple of important differences with these earlier works. First, in line with theories of JT gravity, our dimensionally-reduced

manifold has a boundary. We thus must include the boundary contributions during the dimensional reduction process, which will ultimately lead to the boundary action in JT gravity. This is crucial for our later analysis since the bulk action vanishes on-shell for JT gravity, and thus the boundary term gives rise to the sole degree of freedom. Second, we perform a (different) Weyl rescaling to bring the two-dimensional metric into the AdS_2 form to align with the exact JT gravity setup studied in the literature.

On a 4-manifold M_4, the total action, $I = I_{\rm EH} + I_{\rm GHY}$, is the sum of the bulk Einstein-Hilbert (EH) action and the boundary Gibbons-Hawking-York (GHY) action:

$$\begin{aligned} I_{\rm EH} &= \frac{1}{16\pi G_N}\int_{M_4} d^4x\sqrt{-g_4}R_4 \\ I_{\rm GHY} &= \frac{1}{8\pi G_N}\int_{\partial M_4} d^3x\sqrt{-\gamma_3}K_3 \end{aligned} \tag{8.5}$$

where G_N is the 4-d gravitational constant, γ_3 is the induced metric on the boundary, g_4 is the metric with the Ricci scalar R_4 and the extrinsic curvature K_3 on ∂M_4. The GHY action is needed in gravitational theories with a boundary to make the variational problem well-posed. In particular, the extra boundary term that arises from varying the EH action cancels against the variation of the GHY term. We will see a similar mechanism in action shortly.

We consider spherically-symmetric metrics in the general form

$$ds^2 = g_{ab}(x^0, x^1)dx^a dx^b + \rho^2(x^0, x^1)d\Omega_2^2\,. \tag{8.6}$$

where x^0 and x^1 will be referred to as the light-cone coordinates[1], the radius ρ is a scalar function of x^0 and x^1, and $d\Omega_2^2$ is the line element of a two-dimensional unit sphere. Geometrically speaking, ρ sets the radius of the horizon. As we will see below, ρ^2 plays the role of a dilaton, which corresponds to the horizon area (and hence the entropy).

A generalization of the conformal equivalence $\text{Mink}_4 \cong \text{AdS}_2\times\text{S}^2$ noted in Eqs. (8.3)-(8.4) is a similar relation between a spherically-symmetric metric (8.6) and the space of the form $\tilde{M}_2\times\text{S}^2$:

$$ds^2 = \frac{\rho^2}{L^2}\left(\frac{L^2}{\rho^2}g_{ab}dx^a dx^b + L^2 d\Omega_2^2\right)\,. \tag{8.7}$$

[1] We use Greek letters for bulk coordinates in four dimensions and Latin letters from the early part of the alphabet for the light-cone coordinates.

Ultimately we would like to work with an AdS_2 metric, which motivates us to denote the metric in the parenthesis as $\tilde{g}_{\mu\nu} = (L^2/\rho^2)g_{\mu\nu}$, and compute the action in terms of $\tilde{g}_{\mu\nu}$.

A few remarks are in order:

- Since Einstein gravity is not conformally invariant, $\tilde{g}_{\mu\nu}$ does not satisfy the usual vacuum Einstein equation. However, it still satisfies the equation of motion that follows from action Eq. (8.5) after the contribution of the conformal factor is properly accounted for.
- The conformal relation between $g_{\mu\nu}$ and $\tilde{g}_{\mu\nu}$ in Eq. (8.4) works for any choice of positive L. We find it most convenient to choose L that coincides with the interferometer arm length.
- Weyl transformations do not alter the causal structure of a metric. A null geodesic in $g_{\mu\nu}$ is still a null geodesic in $\tilde{g}_{\mu\nu}$.

Einstein-Hilbert Action

We first consider the EH action. The curvatures of $g_{\mu\nu}$ and $\tilde{g}_{\mu\nu}$ are related by [489]

$$R_4 = L^2(\rho^{-2}\tilde{R}_4 - 6\rho^{-3}\tilde{\Box}\rho)\,, \tag{8.8}$$

while the curvature of the product manifold $\tilde{g}_{\mu\nu}$ in Eq. (8.7) is a simple sum of individual curvatures

$$\tilde{R}_4 = \tilde{R}_2 + \frac{2}{L^2}\,, \tag{8.9}$$

where $\tilde{R}_2$ is the Ricci scalar of $\tilde{g}_{ab}$. This allows us to evaluate the action in Eq. (8.5)[2]

$$\begin{aligned} I_{\rm EH} &= \frac{1}{16\pi G_N}\frac{1}{L^2}\int_{\tilde{M}_4} d^4x\sqrt{-\tilde{g}_4}\left(\rho^2\tilde{R}_2 - 6\rho\tilde{\Box}\rho + \frac{2}{L^2}\rho^2\right) \\ &= \frac{1}{16\pi G_N}\frac{1}{L^2}\int_{\tilde{M}_4} d^4x\sqrt{-\tilde{g}_4}\left(\rho^2\tilde{R}_2 + 6(\tilde{\nabla}\rho)^2 + \frac{2}{L^2}\rho^2\right) \\ &\quad - \frac{1}{16\pi G_N}\frac{3}{L^2}\int_{\partial\tilde{M}_4} d^3x\sqrt{-\tilde{\gamma}_3}\tilde{g}^{\mu\nu}\tilde{n}_\mu\tilde{\nabla}_\nu\rho^2\,. \end{aligned} \tag{8.10}$$

[2]We use the shorthands $\Box\rho = g^{\mu\nu}\nabla_\mu\nabla_\nu\rho$, $(\nabla\rho)^2 = g^{\mu\nu}\nabla_\mu\rho\nabla_\nu\rho$, $\tilde{\Box}\rho = \tilde{g}^{\mu\nu}\tilde{\nabla}_\mu\tilde{\nabla}_\nu\rho$ and $(\tilde{\nabla}\rho)^2 = \tilde{g}^{\mu\nu}\tilde{\nabla}_\mu\rho\tilde{\nabla}_\nu\rho$. Since ρ does not depend on the angular variables, we can also replace the four-dimensional contractions in the above derivatives by just two-dimensional contractions.

The boundary term here comes from the Stokes' theorem[3] that relates a total derivative to a boundary term.

To perform the dimensional reduction, we integrate over the angular directions while keeping in mind that ρ as well as $\tilde{R}_2$ only depend on the light-cone variables. Hence, the EH action becomes

$$I_{\text{EH}} = \frac{1}{4G_N}\int_{\tilde{M}_2} d^2x\sqrt{-\tilde{g}_2}\left(\rho^2\tilde{R}_2 + 6(\tilde{\nabla}\rho)^2 + \frac{2}{L^2}\rho^2\right) - \frac{3}{4G_N}\int_{\partial\tilde{M}_2} dx^0\sqrt{-\tilde{\gamma}_1}\tilde{g}^{ab}\tilde{n}_a\tilde{\nabla}_b\rho^2\,, \tag{8.11}$$

where x^0 is the boundary time.

Gibbons-Hawking-York Action

We now turn our attention to the GHY action. The normal vector of the boundary transforms as $\tilde{n}^\mu = (\rho/L)n^\mu$, hence the extrinsic curvature transforms as

$$\begin{aligned} K_3 &= \nabla_\mu n^\mu \\ &= \frac{1}{\sqrt{-g_4}}\partial_\mu(\sqrt{-g_4}n^\mu) \\ &= \left(\frac{L}{\rho}\right)^4 \frac{1}{\sqrt{-\tilde{g}_4}}\partial_\mu\left(\left(\frac{\rho}{L}\right)^3\sqrt{-\tilde{g}_4}\tilde{n}^\mu\right) \\ &= \frac{L}{\rho}\tilde{K}_3 + 3\frac{L^2}{\rho^2}\tilde{n}^\mu\tilde{\nabla}_\mu\frac{\rho}{L}\,. \end{aligned} \tag{8.12}$$

Putting this into the GHY action in Eq. (8.5) gives

$$I_{\text{GHY}} = \frac{1}{8\pi G_N}\frac{1}{L^2}\int_{\partial\tilde{M}_4} d^3x\sqrt{-\tilde{\gamma}_3}\left(\rho^2\tilde{K}_3 + \frac{3}{2}\tilde{g}^{\mu\nu}\tilde{n}_\mu\tilde{\nabla}_\nu\rho^2\right)\,. \tag{8.13}$$

Since the boundary ∂M_4 is taken to be spherically symmetric, only the light-cone component of the normal vector n^μ is non-zero, which then coincides with n^a, the normal vector to ∂M_2. On the other hand, projection to $\tilde{M}_2$ gives a simple relation $\tilde{K}_3 = \tilde{K}_1$, where $\tilde{K}_1$ is the extrinsic curvature of $\tilde{g}_{ab}$ on $\partial\tilde{M}_2$. This allows us to perform the dimensional reduction

$$I_{\text{GHY}} = \frac{1}{2G_N}\int_{\partial\tilde{M}_2} dx^0\sqrt{-\tilde{\gamma}_1}\rho^2\tilde{K}_1 + \frac{3}{4G_N}\int_{\partial\tilde{M}_2} dx^0\sqrt{-\tilde{\gamma}_1}\tilde{g}^{ab}\tilde{n}_a\tilde{\nabla}_b\rho^2\,. \tag{8.14}$$

[3] We define the normal vector n^μ to the boundary to be pointing outward/inward if it is spacelike/timelike. In this convention, the Stokes' theorem reads $\int_{M_4} d^4x\sqrt{-g_4}\nabla_\mu V^\mu = \int_{\partial M_4} d^3x\sqrt{-\gamma_3}n_\mu V^\mu$ for any vector V^μ regardless of the signature of the boundary. The analogous formula also holds in two dimensions.

We see that the extra boundary term from the EH action precisely cancels the second term in the GHY action. The total action then becomes

$$I = \frac{1}{4G_N}\int_{\tilde{M}_2} d^2x\sqrt{-\tilde{g}_2}\left(\rho^2\tilde{R}_2 + 6(\tilde{\nabla}\rho)^2 + \frac{2}{L^2}\rho^2\right) + \frac{1}{2G_N}\int_{\partial\tilde{M}_2} dx^0\sqrt{-\tilde{\gamma}_1}\rho^2\tilde{K}_1\,. \tag{8.15}$$

Similar cancellations have been noted in Ref. [490] while models with actions similar to Eq. (8.15) have been extensively studied in Ref. [491].

Near-horizon Limit

We now examine the metric and the action near the horizon of a Minkowski causal diamond of size L. The metric in the interior of a causal diamond is obtained from Eq. (8.3) via the transformation [30]

$$\begin{aligned} t &= 2L\sinh\left(\frac{T}{2L}\right)\sqrt{1-\frac{R}{L}} \\ r &= L - 2L\cosh\left(\frac{T}{2L}\right)\sqrt{1-\frac{R}{L}}\,, \end{aligned} \tag{8.16}$$

and the metric can be written in the form of Eq. (8.1)

$$ds^2_{\text{Mink}} = -\left(1-\frac{R}{L}\right)dT^2 + \frac{dR^2}{1-R/L} + \rho^2(T,R)d\Omega_2^2\,, \tag{8.17}$$

where we again identify $\rho = r$. The transformed light-cone variables are T and R. Observe that

$$(t+r-L)(t-r+L) = -4L^2\left(1-\frac{R}{L}\right)\,, \tag{8.18}$$

hence the horizon of the causal diamond described at the end of Sec. 10.1 is located at $R = L$. In the near-horizon limit, $R \to L$, the dilaton is approximately a large positive constant. We can thus expand the dilaton as a small perturbation

$$\rho^2 = \phi_0 + \phi\,, \tag{8.19}$$

where $\phi_0 = L^2$ and $\phi \ll \phi_0$. It is also clear in this coordinate that the classical area of the causal diamond is $A = 4\pi L^2$.

The action we obtained in Eq. (8.15) is almost the action of JT gravity except for the kinetic term $(\tilde{\nabla}\rho)^2$. It has been argued in Ref. [492] that the kinetic term is a subdominant contribution in the context of a near-extremal Reissner-Nordström

black hole. We briefly review the argument and apply it to our set-up. Expanding the kinetic term using Eq. (8.19) gives

$$\int_{\tilde{M}_2} d^2x\sqrt{-\tilde{g}_2}(\tilde{\nabla}\rho)^2 = \frac{1}{4}\int_{\tilde{M}_2} d^2x\sqrt{-\tilde{g}_2}\frac{(\tilde{\nabla}\phi)^2}{\phi_0+\phi}\,. \tag{8.20}$$

Suppose the system is perturbed by coupling to some matter field via $I \to I + I_{\text{matter}}$. Then, the equation of motion associated with the action in Eq. (8.15) can be written as $T_{ab} = T_{ab}^{\text{matter}}$ with $T_{ab} = -\tilde{\nabla}_a\tilde{\nabla}_b\rho^2$, where we have absorbed the dilaton kinetic term into the definition of T_{ab}^{matter}. In the conformal gauge, $d\tilde{s}^2 = -\exp(2\omega(u^+,u^-))du^+du^-$, the $++$ component of the equation of motion turns out to be

$$-e^{2\omega}\partial_+(e^{-2\omega}\partial_+\rho^2) = T_{++}^{\text{matter}} > 0\,. \tag{8.21}$$

Integrating this expression along a line $u^- = 0$ from $u^+ = 0$ to $u^+ = \pi$ then gives

$$\int_0^\pi du^+ e^{-2\omega}T_{++}^{\text{matter}} = [e^{-2\omega}\partial_+\rho^2]|_{u^+\to 0} - [e^{-2\omega}\partial_+\rho^2]|_{u^+\to\pi}\,. \tag{8.22}$$

In AdS_2, the conformal gauge is given by $\exp(-2\omega) \sim \sin^2 u^+$ with the boundaries located at $u^+ = 0$ and $u^+ = \pi$. Requiring the expression in Eq. (8.22) be positive then implies that ρ^2 diverges near at least one of the boundaries [488]

$$\begin{aligned}\rho^2|_{u^+\to 0} &\sim \text{constant} + \frac{1}{u^+}\\ \rho^2|_{u^+\to\pi} &\sim \text{constant} + \frac{1}{u^+-\pi}\,.\end{aligned} \tag{8.23}$$

With this information in hand, we can consider the dilaton kinetic term in Eq. (8.20) using the Poincaré coordinates[4]

$$d\tilde{s}^2 = L^2\frac{-dt^2+dz^2}{z^2}\,, \tag{8.24}$$

where the boundary is located at $z = 0$. Since the dilaton diverges as $\phi \sim 1/z$ near $z = 0$ and has the dimension of $[\text{length}]^2$, by dimensional analysis, one finds $\phi \sim l_p^2L^2E/z$ where E is the energy associated with the causal diamond. The derivatives evaluate to $(\tilde{\nabla}\phi)^2 = g^{zz}\partial_z\phi\partial_z\phi = \phi^2/L^2 \sim \phi^2/\phi_0$. Hence we can evaluate Eq. (8.20)

$$\begin{aligned}\frac{(\tilde{\nabla}\phi)^2}{\phi_0+\phi} &\approx \frac{1}{\phi_0}\frac{1}{1+\phi/\phi_0}\frac{\phi^2}{\phi_0}\\ &= \frac{\phi^2}{\phi_0^2} + O\left(\frac{\phi^3}{\phi_0^3}\right)\,,\end{aligned} \tag{8.25}$$

[4]We use the symbol t for both the Minkowski time and the AdS time in Poincaré coordinates since they can be identified with each other via the Weyl rescaling of Eq. (8.4), while different notations are used for the spatial coordinates, z and r.

which is quadratic in ϕ/ϕ_0 at the leading order, and thus can be omitted in Eq. (8.15). This leaves us with the JT action

$$I = \int_{\tilde{M}_2} d^2x\sqrt{-\tilde{g}_2}\Phi\left(\tilde{R}_2 + \frac{2}{L^2}\right) + 2\int_{\partial\tilde{M}_2} dx^0\sqrt{-\tilde{\gamma}_1}\Phi\tilde{K}_1\,. \tag{8.26}$$

where we have defined the dimensionless dilaton field

$$\Phi = \frac{\rho^2}{4G_N}, \tag{8.27}$$

which controls the size of the S^2. We will also show that this field controls how long it takes for a photon to traverse from the bottom to the top of the causal diamond.

We emphasize that the procedure of dropping the dilaton kinetic term (and hence the correspondence with JT gravity) is only valid near the causal diamond horizon. The classical equations of motion for the metric and dilaton are later derived in Eq. (8.33) using the truncated action Eq. (8.26). If one attempts to directly compute the classical Ricci scalar of the four dimensional metric in Eq. (8.6) and Eq. (8.27), one finds a non-vanishing curvature for $r > 0$. On the other hand, if one retains the kinetic term, than the metric equation of motion would remain the same as Eq. (8.33), but the dilaton solution would simply be $\rho = z = r$, which would completely reproduce the original four dimensional Minkowski metric in Eq. (8.6) with zero curvature. For our purposes, we are interested in the dilaton equation of motion near a null trajectory, where the dilaton kinetic term is subdominant. Dropping the kinetic term, however, comes at a price of introducing a (unphysical) curvature in the parent Minkowski theory. According to our argument above, however, this curvature is irrelevant for the dilaton equations of motion in the near-horizon limit. We thus proceed with the JT theory, in the near-horizon limit, as a good approximation to near-horizon Minkowski spacetime fluctuations.

8.3 The Two-sided AdS Geometry and Classical Dilaton Solution

Before considering the quantum fluctuations, we discuss the classical equations of motion for both the metric field and the dilaton. This will allow us to determine how the dilaton is related to fluctuations in geodesic distances, that we can in turn relate to photon travel times in the original 4-d Minkowski space. The equations of motion read:

$$\begin{aligned} \tilde{R}_2 + \frac{2}{L^2} &= 0 \\ (L^2\tilde{\nabla}_a\tilde{\nabla}_b - \tilde{g}_{ab})\Phi &= 0\,. \end{aligned} \tag{8.28}$$

The first equation shows that the bulk geometry is a slice of AdS while the second equation specifies the classical behavior of the dilaton. To ensure that the variational problem is well defined, we fix the dilaton value at the boundary to be

$$\Phi|_{\text{boundary}} = \frac{\Phi_b \mathfrak{r}_c}{L}\,, \tag{8.29}$$

and the induced metric to be $\gamma_{00}|_{\partial \tilde{M}_2} = \mathfrak{r}_c^2/L^2$, where $\mathfrak{r}_c \to \infty$ is the regularized location of the AdS boundary.

The AdS_2 space can be described as a hypersurface $T_1^2 + T_2^2 - X^2 = L^2$ in the Minkowski spacetime with signature (2,1):

$$ds^2 = -dT_1^2 - dT_2^2 + dX^2\,, \tag{8.30}$$

As shown in Fig. 8.2, this hypersurface is a hyperboloid with one connected component and a reflection symmetry around $X = 0$. The two AdS boundaries are located at $X \to \pm\infty$. We see that the boundaries are disjoint and each associated to a coordinate patch. The most general solution to Eqs. (8.28) has the dilaton profile $\Phi = AT_1 + BT_2 + CX$, with some constants A, B and C. Following Ref. [487], by invoking the SO(2,1) symmetry of the ambient Minkowski spacetime, we can rotate our coordinates such that $B = C = 0$. Hence we can write

$$\Phi = \frac{\Phi_h T_1}{L}, \tag{8.31}$$

where Φ_h will later be identified as the dilaton value at the horizon.

As shown in Fig. 8.3, we will use multiple coordinates to describe the causal diamond in AdS geometry, as we discuss in detail next. We cast the embedding coordinates first in the standard Poincarécoordinates. Then we discuss Schwarzschild coordinates, which have the advantage of making the position of the Rindler horizon explicit, which in turn will be directly related to the value of the dilaton; these coordinates cover only the interior of the causal diamond shown in Fig. 8.3. Finally, we transform to global coordinates, which cover the entire spacetime and will be the coordinate system of choice for computing the Hartle-Hawking wavefunction and partition function. We will also explain how each of these coordinate systems relates to the coordinates in the original Minkowski metric, where actual measurements are supposed to take place.

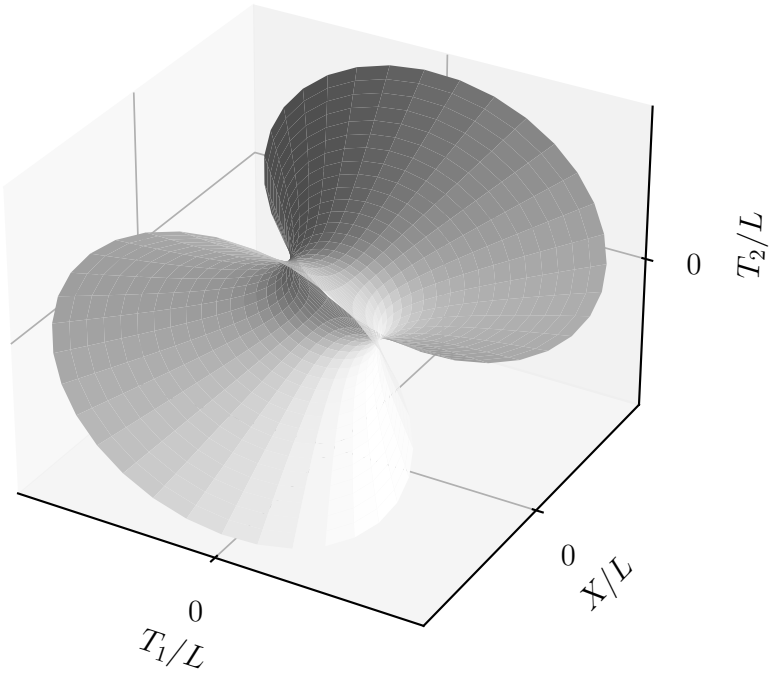

Figure 8.2: Embedding of the the AdS_2 in Minkowski space of signature (2,1). The explicit relation between the coordinate is summarized in Eq. 8.32. In these coordinates, the two AdS_2 boundaries (related by the reflection symmetry) are at $X \to \pm\infty$. In Poincarécoordinates, these boundaries correspond to $z = 0^{\pm}$ shown in Fig. 8.3.

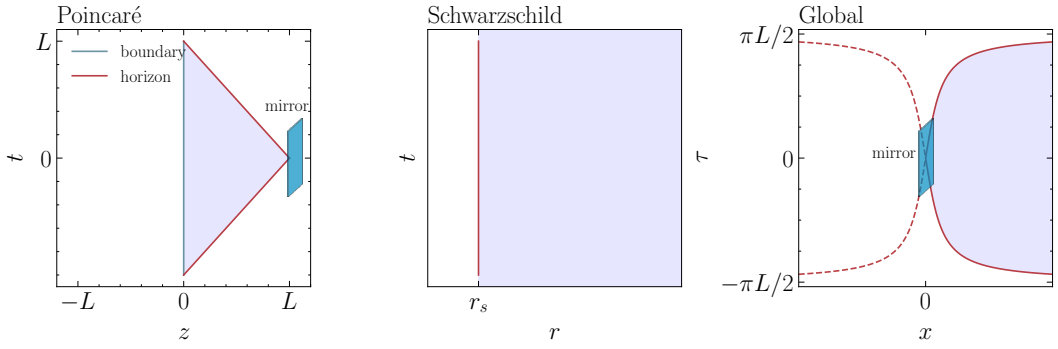

Figure 8.3: Causal diamonds in different AdS coordinates. In all three panels, the shaded region corresponds to a causal diamond in one half of the entire AdS space, which in embedding coordinates is $X \to +\infty$ shown in Fig. 8.2. It is also the shaded region that corresponds to the interior of the causal diamond in the original Minkowski spacetime, which will be the focus of our attention. The causal diamond horizon inherited from the 4-d Minkowski spacetime is indicated as a solid red curve, while the same horizon but on the other side of AdS is indicated as a dashed red curve.

Poincarécoordinates

The most commonly used coordinate system in the AdS spacetime is the aforementioned Poincarécoordinate system, related to the embedding coordinates by

$$\begin{aligned} T_1 &= \frac{L^2 - t^2 + z^2}{2z} \\ T_2 &= L\frac{t}{z} \\ X &= \frac{L^2 + t^2 - z^2}{2z}\,, \end{aligned} \tag{8.32}$$

with the metric and dilaton

$$\begin{aligned} d\tilde{s}^2 &= L^2 \frac{-dt^2 + dz^2}{z^2} \\ \Phi &= \Phi_h \frac{L^2 - t^2 + z^2}{2Lz}\,. \end{aligned} \tag{8.33}$$

The AdS boundaries are located at $z = 0^{\pm}$, shown in the left-hand panel of Fig. 8.3; they corresponds to $X \to \pm\infty$ in the embedding coordinates, shown in Fig. 8.2.

From Eq. (8.4), the (t, z) coordinates in AdS directly translate to (t, r) in Minkowski spacetime, such that the horizon in the original Minkowski spacetime is now at $|t| + z = L$. The shaded regions in Fig. 8.3 thus correspond to the interior of the causal diamond also in the original Minkowski spacetime.

Schwarzschild Coordinates

Since we are interested in the behavior near the horizon, a convenient coordinate system is the so-called "topological black hole," or Schwarzschild system of coordinate $(\mathfrak{t}, \mathfrak{r})$, given by

$$\begin{aligned} T_1 &= L\frac{\mathfrak{r}}{\mathfrak{r}_s} \\ T_2 &= L\sinh\left(\frac{\mathfrak{r}_s \mathfrak{t}}{L^2}\right)\sqrt{\frac{\mathfrak{r}^2}{\mathfrak{r}_s^2} - 1} \\ X &= \pm L\cosh\left(\frac{\mathfrak{r}_s \mathfrak{t}}{L^2}\right)\sqrt{\frac{\mathfrak{r}^2}{\mathfrak{r}_s^2} - 1}\,, \end{aligned} \tag{8.34}$$

where

$$\begin{aligned} d\tilde{s}^2 &= -\frac{\mathfrak{r}^2 - \mathfrak{r}_s^2}{L^2} d\mathfrak{t}^2 + \frac{L^2}{\mathfrak{r}^2 - \mathfrak{r}_s^2} d\mathfrak{r}^2 \\ \Phi &= \Phi_b \frac{\mathfrak{r}}{L}\,, \end{aligned} \tag{8.35}$$

and $\mathfrak{r}_s$ is some constant and the coordinate is only defined for $\mathfrak{r} \geq \mathfrak{r}_s$. The $\pm$ sign in Eq. (8.34) corresponds to the right and left patches of the AdS spacetime. This coordinate system was used in Refs. [493, 484] to study the behavior of light sheet horizons utilizing black hole thermodynamics in the bulk. The relation between Poincaréand Schwarzschild coordinates is

$$\left(\frac{(L+t)^2 - z^2}{2z}\right)\left(\frac{(L-t)^2 - z^2}{2z}\right) = L^2\left(\frac{\mathfrak{r}^2}{\mathfrak{r}_s^2} - 1\right)$$
$$\frac{2Lt}{L^2 + t^2 - z^2} = \pm \tanh \frac{\mathfrak{r}_s \mathfrak{t}}{L^2}\,. \tag{8.36}$$

It is clear from Eq. (8.36) that $\mathfrak{r} = \mathfrak{r}_s$ is the position of the Rindler (bifurcate) horizon, where $X = T_2 = 0$ corresponds to $t = 0, z = L$ in Poincarécoordinates. The AdS boundary is located at $\mathfrak{r} \to \infty$, hence the region $\mathfrak{r} \geq \mathfrak{r}_s$ describes the entirety of the causal diamond interior.

Note that Eq. (8.35) explicitly states that the dilaton controls the position of the Rindler horizon, and evaluating it at the horizon reveals that

$$\mathfrak{r}_s = L\frac{\Phi_h}{\Phi_b}. \tag{8.37}$$

We thus expect dilaton quantum fluctuations to be responsible for the quantum uncertainty in the photon travel time in the original Minkowski theory.

Global Coordinates

Finally, we define a global coordinate system (τ, x) by

$$T_1 = L\sqrt{1 + \frac{x^2}{L^2}}\cos\frac{\tau}{L}$$
$$T_2 = L\sqrt{1 + \frac{x^2}{L^2}}\sin\frac{\tau}{L}$$
$$X = x\,, \tag{8.38}$$

such that

$$d\tilde{s}^2 = -\left(1 + \frac{x^2}{L^2}\right)d\tau^2 + \frac{dx^2}{1 + x^2/L^2}$$
$$\Phi = \Phi_h\sqrt{1 + \frac{x^2}{L^2}}\cos\frac{\tau}{L}\,, \tag{8.39}$$

Following Ref. [487], this is the basis of choice for computing the Hartle-Hawking wavefunctions and the partition function. An important observation is that the

global coordinates cover the entire AdS spacetime, while the Poincaréand (right) Schwarzschild coordinates only cover the region $x \geq 0$, i.e. the right exterior region. This can be easily verified by noting the relation with the Poincarécoordinates

$$\begin{aligned} \tan \frac{\tau}{L} &= \frac{2Lt}{L^2 - t^2 + z^2} \\ x &= \frac{L^2 + t^2 - z^2}{2z} \,. \end{aligned} \tag{8.40}$$

Moreover, one could check that the horizon is located at $x = \pm L \tan(\tau/L)$, while the AdS boundary is at $x \to \pm\infty$. Hence, the causal diamond is a subset of the right coordinate patch, while the global coordinates effectively provide the maximal extension of the patch. An analogous coordinate system can be set up to describe the left exterior region, thus effectively factorizing the system.

With the groundwork laid on the relation between the dilaton and coordinate systems, we can now compute the quantum fluctuations.

8.4 Spacetime Fluctuations in JT Gravity

Our analysis mostly follows Ref. [487], which was originally motivated by the factorization problem [494, 495]. Instead of applications to the factorization problem, we use this framework for constructing the action and its solutions beyond the classical saddle point approximation.

One important feature of the JT gravity is that it can be reduced to a 1-d quantum mechanics on the boundary. The Hamiltonian of the QM problem is obtained by evaluating the stress-energy tensor on each boundary, left and right, using the action in Eq. (8.26):

$$H_L = H_R = \frac{\Phi_h^2}{L\Phi_b} \,. \tag{8.41}$$

The Hamiltonian on the left (resp. right) boundary is conjugate to the time variable t_L (resp. t_R), denoting the Schwarschild time on the respective AdS boundary. Alternatively, on can define conjugate momentum P and length (which we denote L_g to distinguish it from the AdS radius). In these variables, the symplectic form Ω looks like [487]

$$\Omega = d\delta \wedge dH = dL_g \wedge dP \,, \tag{8.42}$$

where $H = H_L + H_R$ is the total Hamiltonian. The two canonical conjugate pairs are (δ, H) and (L_g, P).

Canonical Variables

Since Eq. (8.41) implies that $H_L - H_R = 0$, the only time variable is generated by $H_L + H_R$, and is defined to be

$$\delta = \frac{\mathrm{t}_L + \mathrm{t}_R}{2} \,. \tag{8.43}$$

It is noted in Ref. [487] that δ can be interpreted as a time-shift operator of the Hilbert space spanned by normalized states E, with $\delta = i\partial/\partial E$. Physically, δ is the *time difference* between the two boundaries, which is a quantity that can be measured by an interferometer system. According to Ref. [487], one way to define δ is to examine a geodesic connecting the two boundaries which is orthogonal to surfaces of constant Φ. The fluctuation of the arrival time relative to the starting time is characterized by 2δ [487]. A suitable candidate for such geodesic is simply the horizon of the two-sided AdS, defined by firing a photon from a point at the left boundary, $(-\pi L/2, -\infty)$, and eventually arriving at the right boundary, $(\pi L/2, \infty)$. The horizon is indicated as a red line in the right panel of Fig. 8.3 (ignoring the mirror in the figure for now), combining the dashed and the solid lines in the left and right AdS patch respectively. The equation for this trajectory can be solved by setting $d\tilde{s} = 0$ in Eq. (8.40), which turns out to be $\tau = L \tan^{-1}(x/L)$[5]. The dilaton field along this trajectory can be found by putting this equation into Eq. (8.40), which turns out to be a constant, $\Phi = \Phi_h$, as expected. Since null geodesics are orthogonal to themselves, the horizon (which connects the two boundaries) satisfies the condition quoted from Ref. [487], *i.e.* a geodesic that is orthogonal to curves of constant Φ. Hence we can interpret δ as the relative time between the two boundaries measured by this particular photon path. Note that $\delta = 0$ corresponds to the classical (unperturbed) light trajectory, since the clock on the left and right boundaries runs oppositely, and the time for a photon to traverse from $x = 0$ to either boundary is the same in the unperturbed spacetime, *i.e.* the clocks on each boundary tick at the same pace (but with opposite arrows of time) on either boundary in the absence of quantum fluctuations. *Thus $\delta \neq 0$ indicates a quantum fluctuation in the light trajectory, or equivalently, a quantum fluctuation in rate at which the boundary clocks tick.*

Further, δ is related to the quantum fluctuation in the time of arrival of a photon in the Minkowski interferometer. First, we note that while the two-sided AdS system

[5]Usually it is not possible to shoot a photon from one boundary to the other in a two-sided black hole system, since the two boundaries are causally disconnected. However, in our set-up, the photon trajectory defines the horizon, which is a (and the only) null geodesic that connects the two boundaries, as apparent when the Penrose diagram of the spacetime is inspected. AdS geometries with horizons defined by photon paths are also noted and used in Refs [493, 484].

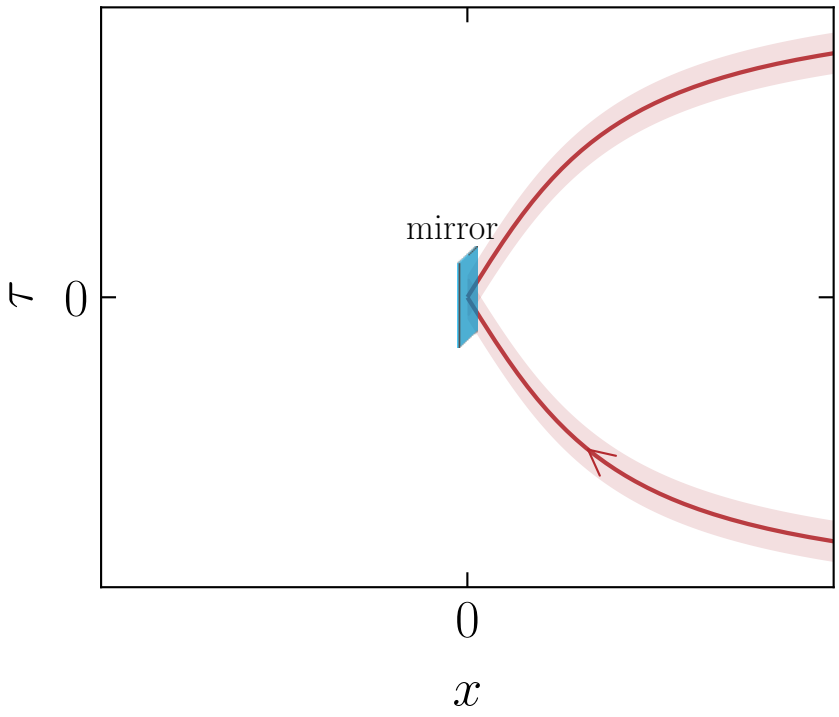

Figure 8.4: The quantum uncertainty in the light trajectory, here depicted by fuzzing of the horizon, is what we seek to compute via the quantum uncertainty in the geodesic distances parameterized by L_g and δ defined in the text. In particular 2δ is the time shift, with respect to a classical unperturbed trajectory, for a photon that is fired from the right boundary and reflected back to its starting position.

is a natural solution to the JT theory, the original Minkowski causal diamond only covers a Poincarépatch as indicated by the shaded regions in Fig. 8.3. However, by putting a mirror at $x = 0$ (*i.e.* the interface between the two AdS sides), one can construct a geodesic that was fired from the right boundary at $(-\pi L/2, \infty)$, reflected by the mirror at $(0, 0)$, and arrives back at the right boundary at $(\pi L/2, \infty)$, as indicated by the solid red line at the right panel of Fig. 8.3. This is simply the horizon of the Minkowski causal diamond. Then, using reflection symmetry around $x = 0$ as discussed in the previous paragraph, the distance traveled by this photon must be identical, in the absence of quantum fluctuations, to the distance traveled by a photon fired from the left boundary and eventually arrives at the right boundary, *i.e.* the two-sided AdS horizon. Then, 2δ is precisely the time shift, with respect to a classical unperturbed trajectory, for a photon that is fired from the right boundary and reflected back to its starting position. This is illustrated in Fig. 8.4.

In this sense, the two-sided AdS serves as a mathematical trick (philosophically

akin to the method of images in electrostatics) for us to compute the physical photon travel time, by allowing us to compute the relative photon travel time in one copy of AdS with respect to the other. Since the photon travel time must be the same on both sides in the absence of quantum fluctuations, δ thus quantifies quantum fluctuations in the time of arrival of the photon in one copy of AdS relative to the reference copy.

We further work with the assumption that the mirror is a probe and hence does not substantially affect the spacetime geometry. This is analogous to calculations of the interferometer response in gravitational wave experiments, which also neglect the back-reaction of the geometry to the mirrors. This treatment can be justified by considering the Schwarzschild radius of the mirror. For a mirror with mass ~ 10 kg, its Schwarzschild radius is $R_{\text{mirror}} = 2G_N M_{\text{mirror}} \sim 10^{-26}$ m, which is much shorter than both the interferometer arm length and the photon wavelength, and hence its back-reaction to the geometry can be ignored. On the other hand, since R_{mirror} is much longer than l_p, we can also ignore the quantum effect of the mirror. We believe that the effect of the mirror could be included more explicitly by incorporating the additional degrees of freedom associated with the reflecting boundary conditions (a la "end-of-the-world brane"), but we leave this implementation to future work.

Now we turn to the other pair of canonically conjugate variables (L_g, P). The renormalized geodesic distance L_g between the two boundaries can be evaluated using the global coordinates in Eq. (8.39), where the boundaries are now regulated by bringing them from $x \to \pm\infty$ to some cut-off at $x = \pm x_c$. The expression for x_c can be found by equating the second lines of Eq. (8.35) and Eq. (8.39) at the boundary

$$\begin{aligned} \Phi|_{\partial \tilde{M}_2} = \Phi_b \frac{\mathfrak{r}_c}{L} &= \Phi_h \sqrt{1 + \frac{x_c^2}{L^2}} \cos\frac{\tau}{L} \\ \implies x_c &\approx \frac{L\mathfrak{r}_c}{\mathfrak{r}_s} \frac{1}{\cos(\tau/L)}, \end{aligned} \tag{8.44}$$

where we used Eq. (8.37) and also assumed $x_c \gg L$. This allows us to define a

"renormalized geodesic distance" [487]

$$\begin{aligned} L_g &= \int_{-x_c}^{x_c} \sqrt{-g_{\tau\tau}\frac{d\tau}{dx}\frac{d\tau}{dx}}dx - 2L\log(2\Phi|_{\partial\tilde{M}_2}) \\ &= \int_{-x_c}^{x_c} \frac{1}{\sqrt{1+x^2/L^2}}dx - 2L\log\left(\frac{2\Phi_b \mathfrak{r}_c}{L}\right) \\ &= 2L\sinh^{-1}\left(\frac{x_c}{L}\right) - 2L\log\left(\frac{2\Phi_b\mathfrak{r}_c}{L}\right) \\ &\approx 2L\log\left(\frac{x_c}{\Phi_b\mathfrak{r}_c}\right) \\ &= 2L\log\left(\frac{L\cosh(\mathfrak{r}_s\delta/L^2)}{\Phi_b\mathfrak{r}_s}\right), \end{aligned} \tag{8.45}$$

where we used $\cos(\tau/L) = 1/\cosh(\mathfrak{r}_s\delta/L^2)$ in the third line [487], which can be found by equating Eq. (8.34) and Eq. (8.38) and taking the $\mathfrak{r}_c \gg \mathfrak{r}_s$ limit. We are interested in computing the Euclidean path integral in terms of L_g, and because we are interested in perturbations about the classical spacetime (where $\delta = 0$), we will expand L_g to its first correction in δ:

$$L_g \approx 2L\left(\log\frac{L}{\Phi_b r_s} + \frac{\mathfrak{r}_s^2\delta^2}{2L^4}\right). \tag{8.46}$$

That L_g depends (at first order) quadratically on δ will have important consequences for fluctuations in the photon travel time.

Euclidean Path Integral

We now turn to the solution to the QM path integral from a saddle point expansion of the Euclidean Path Integral, which gives the thermodynamic fluctuations of the system. The saddle-point geometry in Euclidean signature is given by performing a Wick rotation on Eq. (8.35)

$$d\tilde{s}_E^2 = \frac{\mathfrak{r}^2 - \mathfrak{r}_s^2}{L^2}d\mathfrak{t}_E^2 + \frac{L^2}{\mathfrak{r}^2-\mathfrak{r}_s^2}d\mathfrak{r}^2\,. \tag{8.47}$$

Consider the AdS geometry with one asymptotic boundary. To avoid a conical singularity at $\mathfrak{r} = \mathfrak{r}_s$, we require

$$\mathfrak{r}_s = \frac{2\pi L^2}{\beta}\,. \tag{8.48}$$

We compute the JT action in Eq. (8.26) on an AdS manifold with a disk topology and β as the periodicity of t_E,

$$-I_E = 2\frac{\Phi_b\mathfrak{r}_c}{L}\int_0^\beta d\mathfrak{t}_E\sqrt{\tilde{\gamma}_1}\tilde{K}_1\,, \tag{8.49}$$

where we have used the bulk equation of motion and the dilaton value at the boundary. The Euclidan version of the boundary condition outlined below Eq. (8.28) is $\sqrt{\tilde{\gamma}} = \sqrt{\tilde{\gamma}_{t_E t_E}} = \mathfrak{r}_c/L$. The unit vector normal to the boundary $\mathfrak{r} = \mathfrak{r}_c$ is $\tilde{n}^\mu = (0, \sqrt{\mathfrak{r}^2 - \mathfrak{r}_s^2}/L)$. Hence, the extrinsic curvature in Eq. (8.47) is given by

$$\begin{aligned} \tilde{K}_1 &= \tilde{\nabla}_\mu \tilde{n}^\mu|_{\mathfrak{r}=\mathfrak{r}_c} \\ &= \partial_\mu \tilde{n}^\mu|_{\mathfrak{r}=\mathfrak{r}_c} \\ &= \frac{1}{L}\frac{\mathfrak{r}_c}{\sqrt{\mathfrak{r}_c^2 - \mathfrak{r}_s^2}} \\ &= \frac{1}{L}\left(1 + \frac{1}{2}\frac{\mathfrak{r}_s^2}{\mathfrak{r}_c^2}\right), \end{aligned} \tag{8.50}$$

where we used $\sqrt{\tilde{g}} = 1$ in the second line. Finally, putting Eq. (8.50) and Eq. (8.48) into Eq. (8.49), the action becomes[6]

$$-I_E = 4\pi^2 L \frac{\Phi_b}{\beta}\,. \tag{8.51}$$

The thermal partition function *evaluated at the saddle-point* is given by

$$\begin{aligned} Z[\beta] &= e^{-I_E} \\ &= e^{4\pi^2 L \Phi_b/\beta}\,. \end{aligned} \tag{8.52}$$

This allows to compute the energy and the entropy

$$\begin{aligned} \langle E\rangle &= -\partial_\beta \log Z[\beta] = \frac{1}{L}\frac{\Phi_h^2}{\Phi_b} \\ S &= \log Z[\beta] + \beta\langle E\rangle = 4\pi\Phi_h\,. \end{aligned} \tag{8.53}$$

Here we see the direct connection between the entropy and the value of the dilaton at the horizon.

We can get the leading correction to the saddle-point via

$$Z\,[\beta] \approx \int_0^\infty dE_L e^{S(E_L)-\beta E_L} \approx \int_0^\infty dE_L e^{4\pi\sqrt{L\Phi_b E_L}-\beta E_L}. \tag{8.54}$$

This is the famous "square-root E" behavior of the density of states that appears in many systems. It was shown in Ref. [482] that this density of states gives rise to the relation $\beta^2\partial_\beta^2 \log Z\,[\beta] = -\beta\partial_\beta \log Z\,[\beta] + \log Z\,[\beta]$, which corresponds to

[6] To obtain a finite result in Eq. (8.49), we need to add a holographic renormalization counterterm $-(2/L)\int_{\partial\tilde{M}_2} dx^0\sqrt{-\tilde{\gamma}_1}\Phi$, similar to the one in Ref. [496] where the Schwarzian action is derived from the JT action, but with a different boundary condition.

$\langle \Delta K^2 \rangle = \langle K \rangle$ [483, 484] in the language of AdS/CFT. This also directly follows from the relation $\log Z \sim \beta^{-1}$ at the saddle-point as indicated in Eq. (8.52).

We will later identify the entropy of the system to be the black hole entropy associated with the causal diamond horizon, *i.e.*

$$\begin{aligned} S &= \frac{A}{4G_N} \\ &= \frac{8\pi^2 L^2}{l_p^2} \,. \end{aligned} \tag{8.55}$$

In order to understand the fluctuation in δ, we now turn our attention to the calculation in the (L_g, P) basis with two asymptotic boundaries in global coordinates. Following Ref. [487], this can be achieved by studying the Hartle-Hawking wavefunction, which can be interpreted as a wormhole connecting the two boundaries. Operationally, this amounts to computing the action in Eq. (8.26) with the metric in Eq. (8.47), where the boundaries of the manifold is now the AdS conformal boundary with length $\mathfrak{r}_c \beta/2$ and a bulk boundary Σ. The action in Eq. (8.26) also has to be modified to include contributions from the two corners of the geometry. The result is

$$-I_E = \frac{8L\Phi_b}{\beta}\left(y^2 + \frac{2y}{\tan y}\right) , \tag{8.56}$$

where β is the periodicity of the Euclidean time and

$$\begin{aligned} y &= \frac{r_s \beta}{4L^2} = \frac{1}{4}\frac{\beta \Phi_h}{L\Phi_b} \\ a &= \frac{\sin y}{y} = 4L\Phi_b e^{L_g/2L}\beta^{-1} \,, \end{aligned} \tag{8.57}$$

and $a \leq 1$. We observe that I_E is minimized at $y = \pi/2$, which corresponds to $\delta = 0$ according to Eq. (8.45). Expanding near the peak, one finds [487]

$$\begin{aligned} -I_E &= \text{constant} - \frac{8L\Phi_b}{\beta}\left(y - \frac{\pi}{2}\right)^2 \\ &= \text{constant} - \frac{\pi^2}{2}\frac{\Phi_b}{\beta L}(L_g - L_{g,\text{peak}})^2 \\ &= \text{constant} - \frac{S}{16L^2}(L_g - L_{g,\text{peak}})^2 \,, \end{aligned} \tag{8.58}$$

where in addition to Eq. (8.53), we used Eq. (8.48) in the last line, which is expected to hold at the peak of the wavefunction as required by smoothness at $\mathfrak{r} = \mathfrak{r}_s$ in Eq. (8.35). This suggests that the uncertainty of L_g is

$$\Delta L_g = \frac{2\sqrt{2}L}{\sqrt{S}} \,, \tag{8.59}$$

Using Eq. (8.46), this translates to the variance in δ

$$\Delta\delta^2 = \frac{2\sqrt{2}L^4}{\mathfrak{r}_s^2\sqrt{S}}\,. \tag{8.60}$$

We note that the precise numerical factor here depends on the details of the path integral measure, which we mostly ignored so far in our leading-order analysis. Moreover, at this level of approximation, we can use semiclassical relations between different variables, in particular, between L_g and δ. A more careful treatment would require a Jacobian factor in the path integral, which also can be considered as a part of the integration measure. We expect that all such factors do not considerably change the results of the leading-order saddle point analysis.

8.5 Photon Travel Time

The uncertainty relation in Eq. (8.58) allows us to compute the uncertainty in photon travel time in the interferometer system. Recall that δ measures the time shift between the two AdS boundaries shown in the right-hand panel of Fig. 8.3. When regulated, the boundaries are brought in from $\mathfrak{r} \to \infty$ to a finite value $\mathfrak{r} = \mathfrak{r}_c$ in their respective Schwarzschild patch. To allow for a non-zero value of δ, we must allow the two boundaries to fluctuate independently while keeping Φ_b fixed. Since the experiment is only probing the right exterior region (*i.e.* $z > 0$), we would like to trace out the degrees of freedom in the left patch. This can be achieved by taking the limit where $\mathfrak{r}_c$ in the left is much greater than its right-hand side counterpart. Operationally, we take $\mathfrak{r}_c \to \infty$ at the left while keeping $\mathfrak{r}_c$ at the right finite (but still large). In Poincarécoordinates, this perturbs the boundary from $z = 0^+$ to some small curve $z = z_{\text{boundary}}(t)$. Putting $\mathfrak{r} = \mathfrak{r}_s$ in the first line of Eq. (8.36), one finds

$$\begin{aligned} z_{\text{boudnary}}(t) &= \frac{L - \sqrt{L^2 - (L^2 - t^2)(\mathfrak{r}_s^2/\mathfrak{r}_c^2)}}{\mathfrak{r}_s/\mathfrak{r}_c} \\ &= \frac{L^2 - t^2}{2L}\frac{\mathfrak{r}_s}{\mathfrak{r}_c} + O\left(\frac{\mathfrak{r}_s^3}{\mathfrak{r}_c^3}\right)\,. \end{aligned} \tag{8.61}$$

As expected, if $\mathfrak{r}_c \to \infty$, the boundary would be located at $z = 0$. The regularized boundary $z = z_{\text{boundary}}(t)$ turns out to be a parabola, which we plot in Fig. 8.5. Noting that the left boundary is still at $z = 0$, the boundary times are given by the second line of Eq. (8.36)

$$\begin{aligned} \mathfrak{t}_R &= \frac{L^2}{\mathfrak{r}_s}\tanh^{-1}\frac{2Lt}{L^2 + t^2 - z_{\text{boundary}}^2(t)} \\ \mathfrak{t}_L &= -\frac{L^2}{\mathfrak{r}_s}\tanh^{-1}\frac{2Lt}{L^2 + t^2}\,. \end{aligned} \tag{8.62}$$

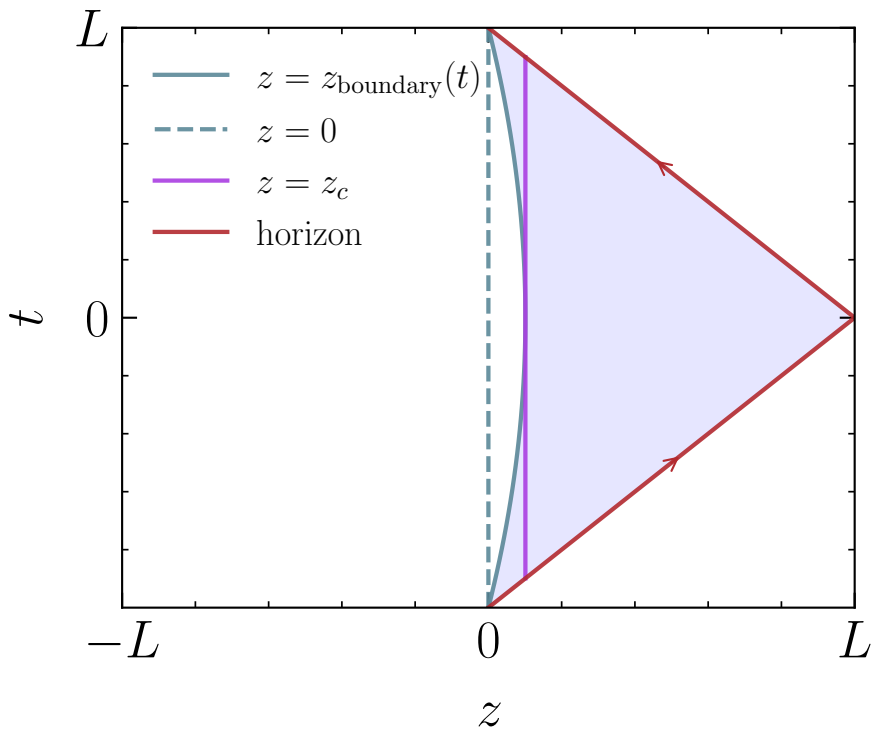

Figure 8.5: Spacetime diagram showing the regularized boundary $z = z_{\text{boundary}}(t)$, the flat brane $z = z_c$ and the photon trajectories. We have chosen $\mathfrak{r}_s/\mathfrak{r}_c = 0.2$ for illustration purpose.

We emphasize that t is the Poincarétime, related to the Minkowski time by a conformal rescaling (as already noted below Eq. (8.4)), while $\mathfrak{t}$ is Schwarzschild time. Hence, we use Eq. (8.61) to evaluate $\delta = (\mathfrak{t}_L + \mathfrak{t}_R)/2$ and obtain

$$\delta = \frac{L\mathfrak{r}_s}{4\mathfrak{r}_c^2} t + \mathcal{O}\left(\frac{\mathfrak{r}_s^3}{\mathfrak{r}_c^3}\right) . \tag{8.63}$$

We see that δ in linear in the Poincarétime.

The interferometer is now placed on a flat brane $z = z_c$ for some constant $z_c \ll L$ such that the brane is barely touching $z_{\text{boundary}}(t)$. This ensures that the brane is as close to the boundary as possible without leaving the domain of the system, which sets the value of z_c to be

$$z_c = \frac{L}{2}\frac{\mathfrak{r}_s}{\mathfrak{r}_c} . \tag{8.64}$$

The location of the brane is also indicated in Fig. 8.5. The photon round-trip time $T_{\text{r.t.}}$ is $2(L - z_c)$ multiplied by a conformal factor in front of the metric L/z_c, which

is approximately

$$T_{\text{r.t.}} = \frac{2L^2}{z_c} = 4L\frac{\mathfrak{r}_c}{\mathfrak{r}_s} . \tag{8.65}$$

Note that the photon travel time diverges if the boundary was not regularized, as noted in Ref. [484]. The fluctuation in photon roundtrip time scales linearly with fluctuations in δ. The ratio $\Delta T_{\text{r.t.}}/T_{\text{r.t.}}$ should be independent of the metric prefactor. Using Eq. (8.63), Eq. (8.60) and Eq. (8.65), we find

$$\begin{aligned}\frac{\Delta T_{\text{r.t.}}^2}{T_{\text{r.t.}}^2} &= \frac{(4\mathfrak{r}_c^2/L\mathfrak{r}_s)^2\Delta\delta^2}{4L^2} \\ &= 8\sqrt{2}\left(\frac{\mathfrak{r}_c}{\mathfrak{r}_s}\right)^4\frac{1}{\sqrt{S}} \\ &= \frac{1}{\sqrt{2}}\left(\frac{T_{\text{r.t.}}}{2L}\right)^4\frac{1}{\sqrt{S}} .\end{aligned} \tag{8.66}$$

Since the experiment is carried out in Minkowski spacetime, the photon measured travel time does not have any conformal factors in it, which allow us to identify $T_{\text{r.t.}} = 2L$. Combined with the entropy relation in Eq. (8.55), we find

$$\begin{aligned}\frac{\Delta T_{\text{r.t.}}^2}{T_{\text{r.t.}}^2} &= \frac{1}{\sqrt{2S}} \\ &= \frac{l_p}{4\pi L} .\end{aligned} \tag{8.67}$$

This scaling relation agrees with the previous work of one of the present authors in Refs. [30, 484, 497, 482], which demonstrated that the two-point correlation function of arm length fluctuations in an interferometer system are proportional to l_p/L. While a small fluctuation, it is measurable with a laboratory scale interferometer.

8.6 Conclusion

The dimensional reduction of Einstein gravity in a causal diamond of the four-dimensional flat Minkowski spacetime can be described by two-dimensional JT gravity with the dilaton field playing the role of the diamond area. By analyzing the Hartle-Hawking wavefunction in JT gravity, we find that the uncertainty in an interferometer arm length scales with the Newton's constant as $\Delta L \sim \sqrt{l_p L}$. This agrees with the previous works [30, 484, 497, 482], where the same scaling was obtained by other methods.

Our result in Sec. 8.4 may appear surprising since it naively violates well-known effective field theory lore, which states that the two-point function of an observable should scale with an integer power of the coupling constant. Our result, however, is not in contradiction with this fact for two reasons. First, our analysis is not based on perturbation theory involving a single graviton. Instead, this is a collective effect that comes from all quantum gravity effects within a causal diamond. This is analogous to hydrodynamic description of diffusion, where the UV scale is the average separation of fluid particles. In hydrodynamics, it is well-known that a particle in the system admits a random walk description, with variance growing linearly in time and with the diffusion coefficient that scales as the square root of the UV scale. Following Refs. [498, 499], relations between JT gravity and hydrodynamics have been noted *e.g.* in Ref. [487]. Establishing a more precise connection between quantum gravity in flat spacetime and hydrodynamics is a possible future development of this work.

The second reason our result is consistent with the effective field theory lore is that the quantity with a traditional EFT scaling $\langle L_g L_g \rangle \sim S^{-1} \sim G_N$ does not correspond to the observable δ relevant for a photon travel time measurement. Rather δ scales as $L_g \sim \delta^2$, implying that it is the four-point of δ with linear scaling in G_N. This behavior is familiar from the study of time-ordered/out-of-time-ordered-correlators, and it is not surprising that such correlators are relevant for systems that display chaotic and hydrodynamic behavior. We leave study of the connection between the observable of interest and hydrodynamic and chaotic behavior for future work.

Chapter 9

INTERFEROMETER RESPONSE TO GEONTROPIC FLUCTUATIONS

This chapter is based on

[1] Dongjun Li, Vincent S. H. Lee, Yanbei Chen, and Kathryn M. Zurek. "Interferometer response to geontropic fluctuations". In: *Phys. Rev. D* 107.2 (2023), p. 024002. DOI: 10.1103/PhysRevD.107.024002. arXiv: 2209.07543 [gr-qc].

9.1 Introduction

Traditional wisdom in effective field theory (EFT) suggests that quantum fluctuations in the fabric of spacetime should be of the order of $\sim l_p = \sqrt{8\pi G\hbar/c^3} \sim 10^{-34}$ m, where G, $\hbar$, c, and l_p are the gravitational constant, reduced Planck constant, speed of light, and Planck length respectively. Fluctuations on such small time and length scales are experimentally undetectable.

It has, however, been recently argued in multiple different contexts that the length scale L of the physical system itself may enter into the observable [30, 484, 482, 497, 6, 500] (see Ref. [86] for a summary)

$$\left\langle \left(\frac{\Delta L}{L}\right)^2 \right\rangle \sim \frac{l_p}{L}\,, \tag{9.1}$$

where ΔL is the quantum fluctuation of L. For example, in Refs. [30, 497], L is the length of interferometer arm in flat spacetime. More generally, L can be the size of a causal diamond in dS, AdS, and flat spacetime [482, 484]. These works argued that the naive EFT reasoning is corrected by long-range correlations in the metric fluctuations–such as are known to occur in holography–which allow the UV fluctuations to accumulate into the infrared. A physical analogue is Brownian motion (discussed in Ref. [86]) where the interactions occur at very short distances but become observable on long timescales as the UV effects accumulate.

While the calculations presented in Refs. [30, 484, 482, 497, 6] are firmly grounded in standard theoretical techniques, such as AdS/CFT, they have not yet provided important, detailed experimental information, such as the power spectral density.

This was the motivation behind the model of Ref. [497], to provide a framework that reproduces important behaviors of the UV-complete theory while also allowing to calculate detailed signatures in the infrared. In the language of the Brownian motion model, while the fluctuations arise from local interactions, the observable is only defined globally. In the language of an interferometer experiment, one cannot measure spacetime fluctuation within a portion of an interferometer arm length, but must wait for a photon to complete a round trip before making a measurement of the global length fluctuation across the entire arm.

In this work, we continue along the lines of Ref. [497], utilizing a scalar field coupled to the metric to model the behavior of the spacetime fluctuations proposed in Refs. [30, 484, 482, 497, 6]. In particular, we propose a model in four dimensions, where the metric appears as a breathing mode of a sphere controlled by a scalar field ϕ:

$$ds^2 = -dt^2 + (1-\phi)(dr^2 + r^2 d\Omega^2)\,. \tag{9.2}$$

Since ϕ effectively controls the area of a spherical surface, it is thus proportional to the entropy of a causal diamond, and may be identified with the dilaton mode studied in Refs. [482, 6]. In the model we consider, ϕ is a scalar field whose quantum fluctuations will be characterized by its occupation number, which we label as σ_{pix}. The subscript denotes "pixellon" following the proposal of Ref. [497], referring to the pixels of spacetime whose fluctuations the scalar field is modeling.

In particular, the quantum fluctuations of the scalar, since they couple to the metric, will give rise to fluctuations in the round-trip time for a photon to traverse from mirror to mirror in an interferometer, as depicted in Fig. 10.1. Similar to Ref. [497], our main goal is to compute the gauge invariant interferometer observable arising from the metric Eq. (9.2), with ϕ being a scalar field having a high occupation number. In contrast to Ref. [497], which calculated length fluctuations utilizing the Feynman-Vernon influence functional in a single interferometer arm, we will use only linearized gravity and the QFT of a scalar field with a given occupation number. We will thus be able to extend the previous work in Ref. [497], calculating both the power spectral density and angular correlations in the interferometer arms in a manifestly gauge invariant way, checking previous claims made in Ref. [30], as well as making new predictions. Note that while the model is not yet uniquely derived from first principles in the ultraviolet (utilizing for example shockwave geometry [500]), we will argue below that it is nevertheless well-motivated from first principles.

More specifically, we consider an interferometer with two arms of equal length L, *i.e.*, with spherical symmetry, and separated by angle θ, as depicted in Fig. 10.1. We assume that the first arm as the reference beam points in the direction $\mathbf{n}_1$, and the second arm as the signal beam points in the direction $\mathbf{n}_2$. We will find that the observable takes the form:

$$\left\langle \frac{\delta T(t_1, n_1)\delta T(t_2, n_2)}{4L^2} \right\rangle = \frac{l_p^2}{4L^2} \int_0^L dr_1 \int_0^L dr_2 \int \frac{d^3\mathbf{p}}{(2\pi)^3} \frac{\sigma_{pix}(\mathbf{p})}{2\omega(\mathbf{p})} F(r_1, r_2, p, \Delta x)\,, \tag{9.3}$$

where $\delta T(t, n)$ denotes the fluctuation of time delay of light beam sent at time $t - L$ along the direction n, and $p = (\omega, p)$, $\Delta x = (\Delta t, \Delta x)$ are four-vectors. The main object of interest in this paper is $F(r_1, r_2, p, \Delta x)$, which encapsulates the response of the interferometer gravitationally coupled to the scalar field ϕ.

The rest of the paper is organized around deriving Eq. (9.3). In Sec. 9.2, we review the pixellon scalar field model, with an occupation number σ_{pix} motivated in particular by [497], but also by work demonstrating that the effect of interest is a breathing mode of the horizon [482, 6]. We then couple this scalar field to the Einstein-Hilbert action and derive its equation of motion. In Sec. 9.3, we perform a linearized gravity calculation and derive the observable. In particular, we compute the interferometer response function $F(r_1, r_2, p, \Delta x)$ from our specific model. In Sec. 9.4, we compute the relevant power spectral density and angular correlation from Eq. (9.3). We then discuss various existing experimental constraints. Finally, in Sec. 9.5, we conclude. Throughout the paper we will work in units $\hbar = c = k_B = 1$ while keeping the gravitational constant $G = l_p^2/(8\pi)$ explicit.

9.2 Scalar Field Quantum Fluctuations in a Causal Diamond

The main goal of this section is to motivate the form of the scalar occupation number, σ_{pix}, that will be coupled to the metric. Our discussion here is mostly based on Ref. [497], though, as mentioned previously, it is also broadly consistent with the dilaton model presented in Ref. [482, 6].

The effect of interest, as presented in Refs. [30, 484] is based on fluctuations in the modular Hamiltonian K

$$K = \int_B T_{\mu\nu}\zeta_K^\mu dB^\nu\,, \tag{9.4}$$

where B is some spatial region with a stress tensor $T_{\mu\nu}$, dB^ν is the volume element of B (with dB^ν pointing in the time direction), and ζ_K^μ is the conformal Killing vector

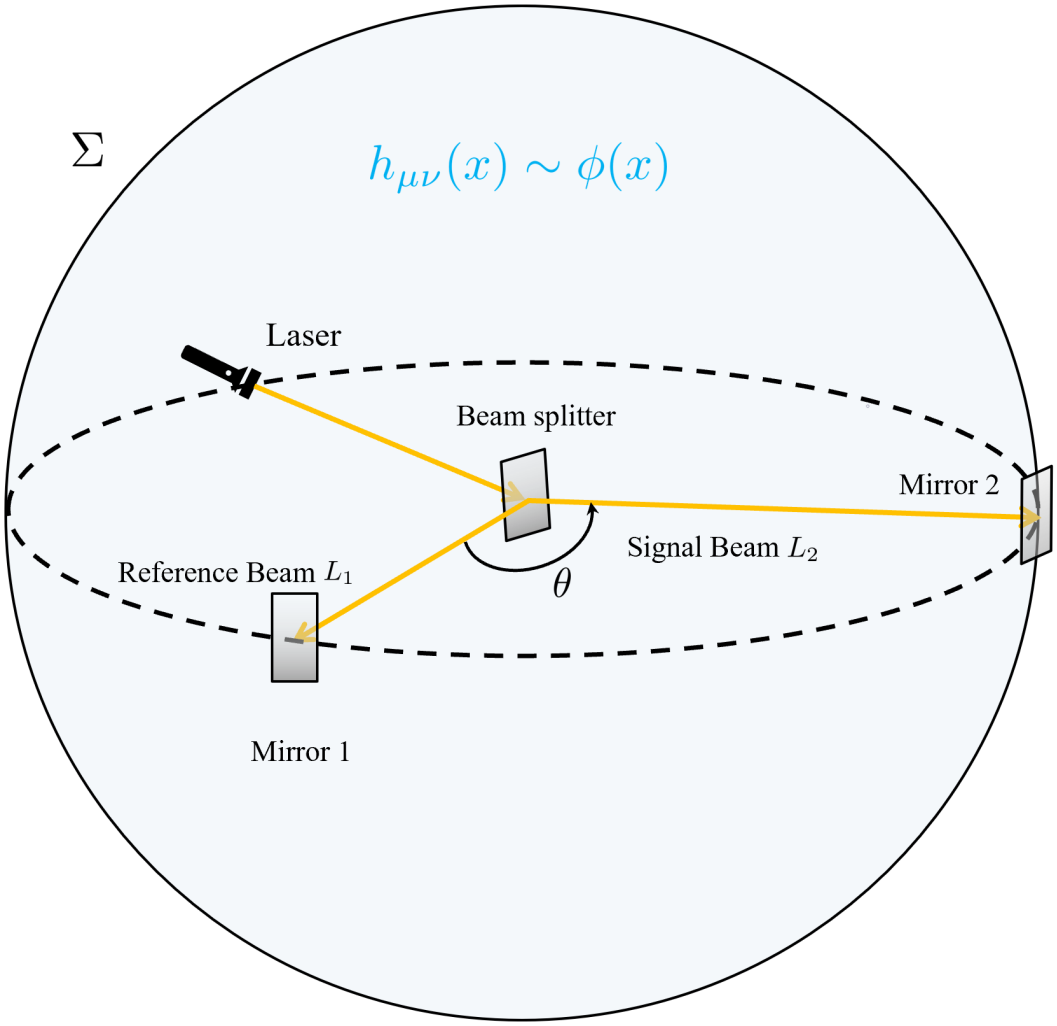

Figure 9.1: Setup of the interferometer.

of the boost symmetry of Σ, the entangling surface between B and its complement $\bar{B}$ [501, 484]. One can map B to Rindler space, so Σ is also a Rindler horizon. In the context of AdS/CFT, where $T_{\mu\nu}$ is the stress tensor of the boundary CFT, both the vacuum expectation value and the fluctuations of the modular Hamiltonian are known to obey an area law in vacuum [484, 502, 503]

$$\langle K \rangle = \langle \Delta K^2 \rangle = \frac{A(\Sigma)}{4G}\,, \tag{9.5}$$

where $A(\Sigma)$ is the area of Σ. One tempting interpretation of this relation is that $\langle K \rangle \equiv N$ counts the number of gravitational bits, or pixels, in the system, which is further motivated by the fact that the entanglement entropy $S_{ent} = \langle K \rangle$ is known to

hold in a CFT. The fluctuations of those N bits then satisfy "root-N" statistics:

$$\frac{|\Delta K|}{\langle K\rangle} = \frac{1}{\sqrt{N}}\,, \tag{9.6}$$

where $|\Delta K| = \sqrt{\langle \Delta K^2\rangle}$ represents the amplitude of the modular fluctuation.

While the precise relation $\langle K\rangle = \langle \Delta K^2\rangle$ is demonstrated only in the context of AdS/CFT, one can place a Randall-Sundrum brane in the (5-d) bulk of AdS, inducing gravity on the (flat 4-d) RS brane, and show that Eq. (9.5) holds on the 4-d brane [482]. The measuring apparatus can then be placed on the flat 4-d brane. Further, as shown in [481, 504, 482], gravity is approximately conformal near the horizon. For an interferometer, the light beams are probing the near-horizon geometry of the spherical entangling surface Σ bounding it (shown in Fig. 10.1), so Ref. [482] argued that the correlator of stress tensor takes the same form as any CFT. Thus, $\langle \Delta K^2\rangle$ follows Eq. (9.5), *i.e.,*

$$\begin{aligned}\langle \Delta K^2\rangle &\sim \int d^2y d^2y' \frac{dr\, dr' r\, r'}{((r-r')^2+(y-y')^2)^4} \\ &\sim A\int \frac{dr\, dr' r\, r'}{(r-r')^6} \sim \frac{A}{\delta^2} \sim \frac{A}{l_p^2}\,,\end{aligned} \tag{9.7}$$

where $\mathbf{y}$ denotes the transverse directions (corresponding to the coordinates on Σ), and $G \sim \delta^2$ corresponds to a UV cut-off in the theory at a distance scale $\delta \sim l_p$. In our case, $r - r' \sim \delta$ corresponds to the distance to the (unperturbed) spherical entangling surface Σ in our setup shown in Fig. 10.1. A similar relation holds for $\langle K\rangle$. More generally, as found in [505], an area law for entanglement entropy does not hold only for a CFT but also any massless scalar QFT, which also motivates the scalar model of geoentropic fluctuations in [497] and this work.

The idea of Ref. [497] was thus to model the gravitational effects of modular fluctuations with a massless scalar field, dubbed a "pixellon." Since pixellons are bosonic scalars, their creation and annihilation operators $(a, a^\dagger)$ satisfy the usual commutation relation

$$\left[a_{\mathbf{p}_1}, a^\dagger_{\mathbf{p}_2}\right] = (2\pi)^3\delta^{(3)}(\mathbf{p}_1 - \mathbf{p}_2)\,. \tag{9.8}$$

We are interested in modeling the impact of the (fluctuating) effective stress tensor in Eq. (9.13). We will do this by allowing for a non-zero occupation number $\sigma_{pix}(\mathbf{p})$,

$$\mathrm{Tr}\left(\rho_{pix} a^\dagger_{\mathbf{p}_1} a_{\mathbf{p}_2}\right) = (2\pi)^3\sigma_{pix}(\mathbf{p}_1)\delta^{(3)}(\mathbf{p}_1 - \mathbf{p}_2) \tag{9.9}$$

such that

$$\mathrm{Tr}\left(\rho_{pix}\{a_{\mathbf{p}_1}, a^{\dagger}_{\mathbf{p}_2}\}\right) = (2\pi)^3\left[1 + 2\sigma_{pix}(\mathbf{p}_1)\right]\delta^{(3)}(\mathbf{p}_1 - \mathbf{p}_2)\,. \tag{9.10}$$

The occupation number should be consistent with the modular energy fluctuation, Eq. (9.6), as we will check explicitly at the end of this section.

The pixellon couples to the metric and sources the stress tensor at second order in perturbations. In general, we can consider a metric of the form

$$g_{\mu\nu} = \eta_{\mu\nu} + \epsilon h_{\mu\nu} + \epsilon^2 H_{\mu\nu} + \dots\,, \tag{9.11}$$

where ϵ is a dimensionless parameter that denotes the order in perturbation theory. The vacuum Einstein Equation (EE) is, parametrically [1],

$$G_{\mu\nu} = \epsilon\left[\nabla^2 h\right]_{\mu\nu} + \epsilon^2\left(\left[\nabla^2 H\right]_{\mu\nu} - l_p^2 T_{\mu\nu}\right) + \dots = 0\,, \tag{9.12}$$

where the precise form of the equations of motion (*e.g.*, numerical prefactors in the time and spatial derivatives) will depend on the precise form of the metric that we consider below, and where the effective stress tensor is given by

$$T_{\mu\nu} \sim \frac{1}{l_p^2}\left[(\nabla h)^2\right]_{\mu\nu}\,. \tag{9.13}$$

At leading order in perturbation theory, the metric perturbation $h_{\mu\nu}$ satisfies the vacuum EE having a form

$$\left[\nabla^2 h\right]_{\mu\nu} = 0\,. \tag{9.14}$$

However, at second order, the effective stress tensor of $h_{\mu\nu}$ will source a non-zero metric perturbation $H_{\mu\nu}$, *i.e.*,

$$\left[\nabla^2 H\right]_{\mu\nu} = l_p^2 T_{\mu\nu}\,. \tag{9.15}$$

One can compute $\langle K\rangle$ from $\langle T_{\mu\nu}\rangle$, but as shown in [484], $\langle K\rangle$ does not gravitate and should be subtracted in the metric equation of motion (similar to a tadpole diagram in QFT). Thus, the vacuum expectation value of this stress tensor vanishes, $\langle T_{\mu\nu}\rangle = 0$, consistent with Eqs. (9.13)-(9.14). In contrast, it is expected to have nonzero fluctuations $\langle \Delta K^2\rangle \sim \langle T_{\alpha\beta}T_{\mu\nu}\rangle \neq 0$, which gravitate and lead to physical observables.

[1] This argument was formulated in private communication with E. Verlinde in the work leading to Ref. [484].

Although $\langle \Delta K^2 \rangle$ is directly related to the *vacuum* two-point function of $H_{\mu\nu}$ or four-point function of $h_{\mu\nu}$, the physical observable can be directly computed from the two-point function of $h_{\mu\nu}$ with a nontrivial density-of-states σ_{pix}. That is, we are using the language of linearized gravity in this work, while our result captures the nonlinearity in Eq. (9.15) and higher orders via σ_{pix}. To compute the fluctuations, we quantize the metric perturbations via the scalar field ϕ, which, to second order in perturbation theory, leads to a nonzero $\langle \Delta K^2 \rangle$, as shown at the end of this section. The major goal of this work is to compute the effects of such quantized metric perturbations on the interferometer depicted in Fig. 10.1.

More specifically, following Ref. [497], we model these energy fluctuations, in the volume of spacetime interrogated with an interferometer, with a thermal density matrix ρ_{pix}, as shown in Eqs. (9.9)-(9.10). The motivation for this choice is based on formal work [501] showing that the reduced density matrix ρ_V of the system V bounded by a sphere S^{d-1} or its casual development $\mathcal{D}$ can be mapped to the thermal density matrix ρ_β of the hyperbolic spacetime $R \times H^{d-1}$, which foliates AdS_{d+1}, in the asymptotic limit. A similar argument relating the vacuum state of any QFT in a causal diamond to a thermal density matrix can be found in [506].

Thus, following [497], we are motivated to define a thermal density matrix ρ_{pix} of pixellons using the definition in [507],

$$\rho_{pix} = \frac{1}{\mathcal{Z}} \exp\left[-\beta \int \frac{d^3\mathbf{p}}{(2\pi)^3} (\epsilon_{\mathbf{p}} - \mu) a^\dagger_{\mathbf{p}} a_{\mathbf{p}} \right] , \tag{9.16}$$

$$\mathcal{Z} = \prod_{\mathbf{p}} \frac{1}{1 - e^{-\beta(\epsilon_{\mathbf{p}} - \mu)}} , \tag{9.17}$$

where $\epsilon_{\mathbf{p}}$ is the energy of pixellons with momentum $\mathbf{p}$, and μ is the chemical potential counting background degrees of freedom associated with $\langle K \rangle$ [497].

Furthermore, as in Ref. [497], we identify the energy per degree-of-freedom as

$$\beta(\epsilon_{\mathbf{p}} - \mu) \equiv \beta\omega(p) \sim \frac{|\Delta K|}{\langle K \rangle} . \tag{9.18}$$

In four dimensions, according to Eq. (9.5),

$$\frac{|\Delta K|}{\langle K \rangle} = \frac{1}{\sqrt{\mathcal{N}}} \sim \frac{l_p}{L} , \tag{9.19}$$

suggesting that the energy fluctuation per degree-of-freedom is set by a ratio of UV and IR length scales. Since $\frac{l_p}{L} \ll 1$, we approximate the occupation number $\sigma(\mathbf{p})$ by

$$\sigma_{pix}(\mathbf{p}) = \frac{1}{e^{\beta\omega(\mathbf{p})} - 1} \approx \frac{1}{\beta\omega(\mathbf{p})} . \tag{9.20}$$

More specifically, we identify the IR length scale $1/L \sim \omega(\mathbf{p})$, so we take

$$\sigma_{pix}(\mathbf{p}) = \frac{a}{l_p \omega(p)}\,, \tag{9.21}$$

where a is the dimensionless number to be measured in an experiment, or fixed in a UV-complete theory. Here $a = 1/(2\pi)$ corresponds to an inverse temperature $\beta = 2\pi l_p$, giving a result most closely mirroring Refs. [30, 484, 497] in amplitude.

Note that $\sigma_{pix}(\mathbf{p})$ is not Lorentz invariant, but this is to be expected because the measurement of interest via a causal diamond picks out a frame. This is also not contradictory to our statement that we have computed a gauge invariant observable. It is because Lorentz transformations of $\sigma_{pix}(\mathbf{p})$ are global transformations of background Minkowski spacetime. After the interferometer picks a frame, the interferometer response is independent of how we describe metric perturbations, *i.e.*, independent of local coordinate transformations at scale of metric perturbations, which is what gauge invariance usually means in linearized gravity.

We now derive the dispersion relation for the scalar field from the metric in Eq. (9.2). We start from the linearized Einstein Hilbert action or Fierz-Pauli action [508]

$$\begin{aligned} S_{\rm FP} &= \frac{1}{2\kappa}\int d^4x\,\sqrt{-g}\;h_{\mu\nu}\left(G^{\mu\nu}[h_{\mu\nu}] - \kappa T^{\mu\nu}\right) \\ &= \frac{1}{4\kappa}\int d^4x\,\sqrt{-g}\;h_{\mu\nu}(\eta^{\mu\nu}\Box h - \Box h^{\mu\nu} \\ &\quad - 2\nabla^\mu\nabla^\nu h + 2\nabla_\rho\nabla^\mu h^{\nu\rho} - 2\kappa T^{\mu\nu}) + O(h^3)\,, \end{aligned} \tag{9.22}$$

where $\kappa = 8\pi G$. The Fierz-Pauli action can be derived by expanding the full metric $g_{\mu\nu}$ about the Minkowski metric $\eta_{\mu\nu}$, $g_{\mu\nu} = \eta_{\mu\nu} + h_{\mu\nu}$, and keeping the terms quadratic in $h_{\mu\nu}$ in the Einstein Hilbert action [508, 509]. Here, $h_{\mu\nu}$ is the metric perturbation associated with the pixellon ϕ. The terms linear in $h_{\mu\nu}$ are discarded because they can be written as a total derivative [509].

Instead of a functional of a general $h_{\mu\nu}$, $S_{\rm FP}$ in our model is a functional of the metric in Eq. (9.2) and thus a functional of ϕ, so the pixellon's action $S_{pix}[\phi]$ is

$$S_{pix}[\phi] \equiv S_{\rm FP}[h^{pix}_{\mu\nu}[\phi]]\,, \quad h^{pix}_{\mu\nu}\,dx^\mu dx^\nu = ds^2_{pix}\,, \tag{9.23}$$

which after plugging in Eq. (9.2) becomes

$$\begin{aligned} S_{pix}[\phi] &= \frac{1}{2\kappa}\int d^4x\,\sqrt{-g}\;\phi\left[\nabla^2 - 3\partial_t^2\right]\phi + \kappa\mathcal{L}_{\rm int}[\phi]\,, \\ \mathcal{L}_{\rm int}[\phi] &\equiv -h^{pix}_{\mu\nu}[\phi]T^{\mu\nu}\,. \end{aligned} \tag{9.24}$$

Then the equation of motion (EOM) of ϕ is derived by varying $\mathcal{L}_{pix}$ with respect to ϕ.

$$\left(\partial_t^2 - c_s^2\nabla^2\right)\phi = \frac{\kappa}{c_s^2}\frac{\delta\mathcal{L}_{\rm int}[\phi]}{\delta\phi}\,, \quad c_s \equiv \sqrt{\frac{1}{3}}\,. \tag{9.25}$$

Following the logic of Eqs. (9.12)-(9.13), to leading order in ϕ, the right-hand side of Eq. (9.25) vanishes. Although Eq. (9.25) is source-free, one may find that the effective stress tensor contains linear term in ϕ, which is a tadpole due to imposing the form of metric in Eq. (9.2) and can be subtracted off. Eq. (9.25) also implies that for the metric in Eq. (9.2), ϕ needs to have the dispersion relation

$$\omega = c_s|\mathbf{p}|\,, \quad c_s = \sqrt{\frac{1}{3}} \tag{9.26}$$

using the expansion $\phi = \int \frac{d^3\mathbf{p}}{(2\pi)^3}\,\phi(\mathbf{p})e^{-i\omega t + i\mathbf{p}\cdot\mathbf{x}}$. It is clear that ϕ is a sound mode with the sound speed $c_s = \sqrt{\frac{1}{3}}$. From Eq. (9.24), we also notice that to canonically normalize ϕ, we can define $\bar{\phi}$ such that

$$\phi = \sqrt{\kappa}\bar{\phi} = l_p\bar{\phi}\,. \tag{9.27}$$

As a consistency check, one can use the metric in Eq. (9.2) and the occupation number in Eq. (9.21) to confirm that $\langle\Delta K^2\rangle$ has the same scaling in Eq. (9.5). Although the physical observable is driven by the two-point function of ϕ as we will discuss in Sec. 9.3, $\langle\Delta K^2\rangle$ is driven by the four-point function of ϕ. One can see this by noting that $K^2 \sim (T_{\mu\nu})^2$ according to Eq. (9.4), while $T_{\mu\nu} \sim \frac{1}{l_p^2}\left[(\nabla\phi)^2\right]_{\mu\nu}$ according to Eq. (9.13). In Sec. 9.3, we find, utilizing the Ansatz Eq. (9.21) for the density of states, $\langle\phi^2\rangle \sim \frac{l_p}{L}$ [see Eq. (9.39)]. Thus, if we identify spatial gradients with the IR length scale $1/L$, we obtain $\langle\Delta K^2\rangle \sim \frac{L^2}{l_p^2} \sim \frac{A}{4G}$, as expected.

9.3 Time Delay in Pixellon Model

The major goal of this work is to compute an interferometer response to fluctuations in the pixellon model. Instead of using the Feynman-Vernon influence functional approach to compute the mirror's motion, *e.g.*, in [497, 509, 510], we compute the time delay of a light beam traveling a round trip directly.

In general, for a metric in the form

$$ds^2 = -(1-\mathcal{H}_0)dt^2 + (1+\mathcal{H}_2)dr^2 + 2\mathcal{H}_1 dt dr + \cdots\,, \tag{9.28}$$

we need to consider three effects: the shift in the clock rate, mirror motion, and light propagation. As discussed in detail in Appendix J, the shift in the clock's rate only

depends on $\mathcal{H}_0$, the mirror motion in the radial direction is affected by $\mathcal{H}_{0,1}$, and the light propagation is determined by all three components $\mathcal{H}_{0,1,2}$.

In Appendix K, we further show that if we take all of these three effects into consideration and sum up the resulting time delay for both outbound and inbound light, the total time delay T of a round trip is gauge invariant, so T is a physical quantity to measure. In this section, we compute the shift of T due to geoentropic fluctuations and its correlation function using the metric of the pixellon model in Eq. (9.2). To calculate time delay in a generic metric like Eq. (9.28), one can refer to Appendix J.

For the metric in Eq. (9.2), the only nonzero component in the $t-r$ sector of the metric is $\mathcal{H}_2$, so we only need to consider light propagation. Then for a light beam sent at time $t-L$ along the direction $\mathbf{n}$, its total time delay $T(t,\mathbf{n})$ of a round trip is completely determined by the pixellon field ϕ, *e.g.*,

$$\begin{aligned} T(t,\mathbf{n}) &= 2L + \frac{1}{2}\int_0^L dr\ \left[\phi(x)+\phi(x')\right], \\ x &\equiv (t-L+r, r\mathbf{n})\,,\ x' \equiv (t+L-r, r\mathbf{n})\,. \end{aligned} \tag{9.29}$$

We have chosen the start time to be at $t-L$ such that the time coordinate of x and x' are symmetric about t.

Since ϕ satisfies the massless free scalar wave equation with the sound speed $c_s = \frac{1}{\sqrt{3}}$ [*i.e.*, Eqs. (9.25) and (9.26)], the quantization for $\phi(x)$ should be

$$\phi(x) = l_p \int \frac{d^3\mathbf{p}}{(2\pi)^3}\frac{1}{\sqrt{2\omega(\mathbf{p})}}\left(a_{\mathbf{p}}e^{ip\cdot x} + a^\dagger_{\mathbf{p}}e^{-ip\cdot x}\right), \tag{9.30}$$

where l_p is to make $\bar{\phi}(x)$ canonically normalized, as discussed in Eq. (9.27). Creation and annihilation operators $a_{\mathbf{p}}$, $a^\dagger_{\mathbf{p}}$ satisfy the commutation relation in Eq. (9.8) with a thermal density matrix ρ_{pix} defined in Eqs. (9.16) and (9.21).

Let us define $\delta T(t,\mathbf{n})$ to be the correction to the total time delay $T(t,\mathbf{n})$. We write the auto-correlation of $\delta T(t,\mathbf{n})$ as

$$\begin{aligned} C(\Delta t,\theta) &\equiv \left\langle \frac{\delta T(t_1,\mathbf{n}_1)\delta T(t_2,\mathbf{n}_2)}{4L^2}\right\rangle, \\ \Delta t &\equiv t_1 - t_2\,,\quad \theta = \cos^{-1}\left(\mathbf{n}_1\cdot\mathbf{n}_2\right), \end{aligned} \tag{9.31}$$

and using Eq. (9.29), we obtain

$$\begin{aligned} C(\Delta t,\theta) = \frac{1}{16L^2}\int_0^L dr_1 \int_0^L dr_2 \\ \left\langle \left(\phi(x_1)+\phi(x_1')\right)\left(\phi(x_2)+\phi(x_2')\right)\right\rangle, \end{aligned} \tag{9.32}$$

where $\langle O \rangle$ is a shorthand notation for

$$\langle O \rangle = (\rho_{pix} O) \,. \tag{9.33}$$

We have assumed that $C(\Delta t, \theta)$ only depends on Δt, the difference of the time when the two beams are sent, and θ, the angular separation of two arms. We will see that this assumption is true.

Besides the correlation function in Eq. (9.31), a more physical correlation function is to first subtract the time delay of the first arm $T(t, \mathbf{n}_1)$ from the time delay of the second arm $T(t, \mathbf{n}_2)$, where two beams are sent at the same time t, and then correlate this difference of time delay at different beam-sent time:

$$\begin{aligned} C_{\mathcal{T}}(\Delta t, \theta) &\equiv \left\langle \frac{\mathcal{T}(t_1, \theta)\mathcal{T}(t_2, \theta)}{4L^2} \right\rangle \,, \\ \mathcal{T}(t, \theta) &\equiv T(t, \mathbf{n}_2) - T(t, \mathbf{n}_1) = \delta T(t, \mathbf{n}_2) - \delta T(t, \mathbf{n}_1) \,, \end{aligned} \tag{9.34}$$

such that

$$C_{\mathcal{T}}(\Delta t, \theta) = 2 \left[C(\Delta t, 0) - C(\Delta t, \theta) \right] \,. \tag{9.35}$$

Here, we treat the first arm as the reference beam and the second arm as the signal beam. Since the relation between $C(\Delta t, \theta)$ and $C_{\mathcal{T}}(\Delta t, \theta)$ is directly given by Eq. (9.35), we will focus on $C(\Delta t, \theta)$ in our calculations below. To compute $C(\Delta t, \theta)$ in Eq. (9.32), we need to first compute the correlation function of ϕ. Using Eq. (9.30), we obtain

$$\begin{aligned} \phi(x) + \phi(x') = l_p \int \frac{d^3\mathbf{p}}{(2\pi)^3} \frac{1}{\sqrt{2\omega(\mathbf{p})}} 2\cos\left[\omega(L - r)\right] \\ \left(a_{\mathbf{p}} e^{-i\omega t + i\mathbf{p}\cdot\mathbf{x}} + a^\dagger_{\mathbf{p}} e^{i\omega t - i\mathbf{p}\cdot\mathbf{x}} \right) \,. \end{aligned} \tag{9.36}$$

Then we have

$$\begin{aligned} &\left\langle \left(\phi(x_1) + \phi(x_1')\right) \left(\phi(x_2) + \phi(x_2')\right) \right\rangle \\ &= 4 l_p^2 \int \frac{d^3\mathbf{p}_1}{(2\pi)^3} \int \frac{d^3\mathbf{p}_2}{(2\pi)^3} \frac{1}{\sqrt{4\omega_1(\mathbf{p}_1)\omega_2(\mathbf{p}_2)}} \\ &\cos\left[\omega_1(L - r_1)\right] \cos\left[\omega_2(L - r_2)\right] \\ &\left[\langle a_{\mathbf{p}_1} a^\dagger_{\mathbf{p}_2} \rangle e^{-i(\omega_1 t_1 - \omega_2 t_2 - \mathbf{p}_1\cdot\mathbf{x}_1 + \mathbf{p}_2\cdot\mathbf{x}_2)} + c.c. \right] \,, \end{aligned} \tag{9.37}$$

where we have only kept the term proportional to $a^\dagger_{\mathbf{p}_1} a_{\mathbf{p}_2}$ and $a_{\mathbf{p}_1} a^\dagger_{\mathbf{p}_2}$ since the other terms are zero.

To evaluate Eq. (9.37), we need to calculate $\langle a^\dagger_{\mathbf{p}_1} a_{\mathbf{p}_2} \rangle$ and $\langle a_{\mathbf{p}_1} a^\dagger_{\mathbf{p}_2} \rangle$. The former is given directly by Eq. (9.9), $\langle a^\dagger_{\mathbf{p}_1} a_{\mathbf{p}_2} \rangle = (\rho_{pix} a^\dagger_{\mathbf{p}_1} a_{\mathbf{p}_2}) = (2\pi)^3 \sigma_{pix}(\mathbf{p}_1) \delta^{(3)}(\mathbf{p}_1 - \mathbf{p}_2)$.

Using both Eq. (9.9) and the commutation relation in Eq. (9.8), we find the latter to be

$$\begin{aligned}\langle a_{\mathbf{p}_1} a^\dagger_{\mathbf{p}_2}\rangle &= (2\pi)^3[1+\sigma_{pix}(\mathbf{p}_1)]\delta^{(3)}(\mathbf{p}_1-\mathbf{p}_2)\\ &\approx (2\pi)^3\sigma_{pix}(\mathbf{p}_1)\delta^{(3)}(\mathbf{p}_1-\mathbf{p}_2)\,,\end{aligned} \tag{9.38}$$

where we have used $\sigma_{pix}(\mathbf{p}) \gg 1$ at the last line. Then,

$$\begin{aligned}&\langle\left(\phi(x_1)+\phi(x_1')\right)\left(\phi(x_2)+\phi(x_2')\right)\rangle\\ &= 4l_p^2\int\frac{d^3\mathbf{p}}{(2\pi)^3}\frac{\sigma_{pix}(\mathbf{p})}{2\omega(\mathbf{p})}\cos\left[\omega(L-r_1)\right]\cos\left[\omega(L-r_2)\right]\\ &\quad\left[e^{-i\omega\Delta t+i\mathbf{p}\cdot\Delta\mathbf{x}}+c.c.\right]\,,\end{aligned} \tag{9.39}$$

where we have defined $\Delta\mathbf{x}\equiv\mathbf{x}_1-\mathbf{x}_2$. Notice that Eq. (9.37) is a complex function in general, so we usually need to symmetrize it over $\mathbf{x}_{1,2}$. Due to our approximation in Eq. (9.38), Eq. (9.39) is a real function, so the one after symmetrization over $\mathbf{x}_{1,2}$ is the same as Eq. (9.39). For simplicity, we will drop the term $c.c.$ and always assume that a complex conjugate is taken.

Finally, plugging Eq. (9.39) into Eq. (9.32), we obtain

$$\begin{aligned}C(\Delta t,\theta) = \frac{l_p^2}{4L^2}\int_0^L dr_1\int_0^L dr_2\int\frac{d^3\mathbf{p}}{(2\pi)^3}\frac{\sigma_{pix}(\mathbf{p})}{2\omega(\mathbf{p})}\\ \cos\left[\omega(L-r_1)\right]\cos\left[\omega(L-r_2)\right]e^{-i\omega\Delta t+i\mathbf{p}\cdot\Delta\mathbf{x}}\,.\end{aligned} \tag{9.40}$$

This is our main result, and we will work on applying it to existing interferometer configurations next.

9.4 Observational Signatures and Constraints

After plugging $\sigma_{pix}(\mathbf{p})$ in Eq. (9.21), Eq. (9.40) is reduced to

$$\begin{aligned}C(\Delta t,\theta) = \frac{al_p}{8L^2}\int_0^L dr_1\int_0^L dr_2\int\frac{d^3\mathbf{p}}{(2\pi)^3}\frac{1}{\omega^2(\mathbf{p})}\\ \cos\left[\omega(L-r_1)\right]\cos\left[\omega(L-r_2)\right]e^{-i\omega\Delta t+i\mathbf{p}\cdot\Delta\mathbf{x}}\,.\end{aligned} \tag{9.41}$$

In the next two subsections, we will study the power spectral density and angular correlation of Eq. (9.41) in more detail.

Power spectral density

We first study the power spectral density implied by Eq. (9.41). Carrying out the angular part of the momentum integral in Eq. (9.41), we have

$$\begin{aligned} C(\Delta t,\theta) &= \frac{a l_p}{32\pi^2 c_s^2 L^2}\int_0^L dr_1 \int_0^L dr_2 \int_0^\infty d|\mathbf{p}| \\ &\quad \cos\left[\omega(L-r_1)\right]\cos\left[\omega(L-r_2)\right] \\ &\quad e^{-i\omega\Delta t}\int_0^\pi d\vartheta\ \sin\vartheta e^{i|\mathbf{p}||\Delta\mathbf{x}|\cos\vartheta} \\ &= \frac{a l_p}{16\pi^2 c_s^2 L^2}\int_0^L dr_1 \int_0^L dr_2 \int_0^\infty d\omega \\ &\quad \cos\left[\omega(L-r_1)\right]\cos\left[\omega(L-r_2)\right] \\ &\quad \frac{\sin\left[\omega\mathcal{D}(r_1,r_2,\theta)/c_s\right]}{\omega\mathcal{D}(r_1,r_2,\theta)} e^{-i\omega\Delta t}\,, \end{aligned} \tag{9.42}$$

where we have defined

$$\mathcal{D}(r_1,r_2,\theta)\equiv|\Delta\mathbf{x}| = \sqrt{r_1^2+r_2^2-2r_1r_2\cos\theta}\,. \tag{9.43}$$

The additional factor of $\frac{1}{c_s^2}$ in Eq. (9.42) comes from using the dispersion relation in Eq. (9.26). $C_{\mathcal{T}}(\Delta t,\theta)$ is directly given by plugging Eq. (9.42) into Eq. (9.35). In Fig. 9.2, we have plotted $C_{\mathcal{T}}(\Delta t,\theta)$ over the separation angle θ of the interferometer for $\Delta t = 0$. Notice the signal is maximal when the interferometer arms are back-to-back.

Performing a Fourier transform of $C(\Delta t,\theta)$ with respect to Δt, we obtain the two-sided power spectral density $\tilde{C}(\omega,\theta)$ to be

$$\begin{aligned} \tilde{C}(\omega,\theta) &= \int_{-\infty}^\infty dt\ e^{-i\omega t}C(t,\theta) \\ &= \frac{a l_p}{8\pi c_s^2 L^2}\int_0^L dr_1\int_0^L dr_2 \frac{\sin\left[\omega\mathcal{D}(r_1,r_2,\theta)/c_s\right]}{\omega\mathcal{D}(r_1,r_2,\theta)} \\ &\quad \cos\left[\omega(L-r_1)\right]\cos\left[\omega(L-r_2)\right]\,. \end{aligned} \tag{9.44}$$

To evaluate the power spectral density of $C_{\mathcal{T}}(\Delta t,\theta)$, we can put Eq. (9.44) into Eq. (9.35) such that its power spectral density $\tilde{C}_{\mathcal{T}}(\omega,\theta)$ is

$$\tilde{C}_{\mathcal{T}}(\omega,\theta) = 2[\tilde{C}(\omega,0)-\tilde{C}(\omega,\theta)]\,. \tag{9.45}$$

In Fig. 9.3, we have plotted Eq. (9.45) over ωL for several different separation angles θ of the interferometer.

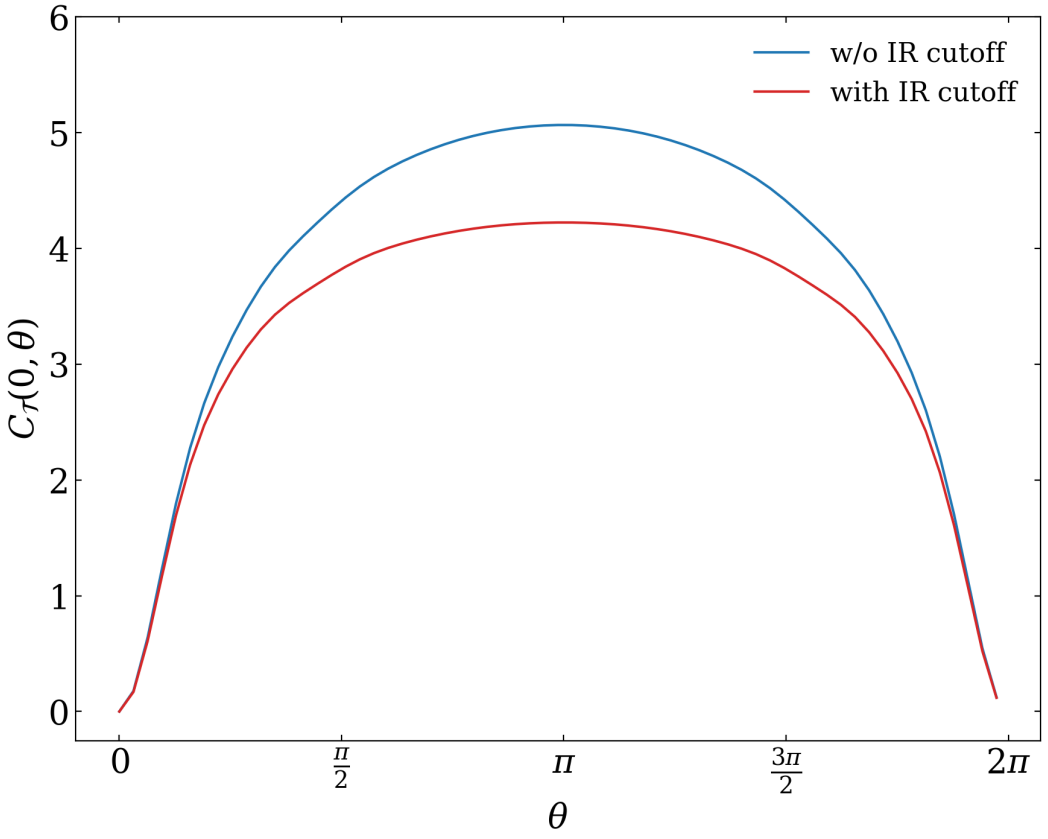

Figure 9.2: Equal-time correlation function $C_{\mathcal{T}}(0,\theta)$ [*i.e.*, Eq. (9.34)] of the pixellon model without IR cutoff in Eq. (9.41) (blue) and with an IR cutoff in Eq. (9.58) (red), where both curves are normalized by $\frac{8\pi^2 c_s^2 L}{a l_p}$.

In the limit $\omega \to 0$, Eqs. (9.44)-(9.45) reduce to

$$\tilde{C}(\omega,\theta) = \frac{a l_p}{8\pi c_s^3} + O(\omega^2 L^2)\,, \tag{9.46}$$

$$\tilde{C}_{\mathcal{T}}(\omega,\theta) = \frac{a l_p}{48\pi c_s^5}\omega^2 L^2(1-\cos\theta) + O(\omega^4 L^4)\,. \tag{9.47}$$

A major feature of $\tilde{C}(\omega,\theta)$ at low frequencies is that it is flat in frequency, corresponding to the spectrum of white noise. This feature is consistent with the "random walk intuition" of holographic effects in [86], as well as the random walk models in [511, 512]. On the other hand, although $\tilde{C}(\omega,\theta)$ is independent of ω at low frequency, $\tilde{C}_{\mathcal{T}}(\omega,\theta)$ is quadratic in ω. It is because, as one can directly observe from Eq. (9.46), the leading order term of $\tilde{C}(\omega,\theta)$ at low frequency is angle-independent. Thus, when subtracting the time delay of the first arm from the second arm, this leading order term cancels out, and the next order term, which is quadratic in ω and

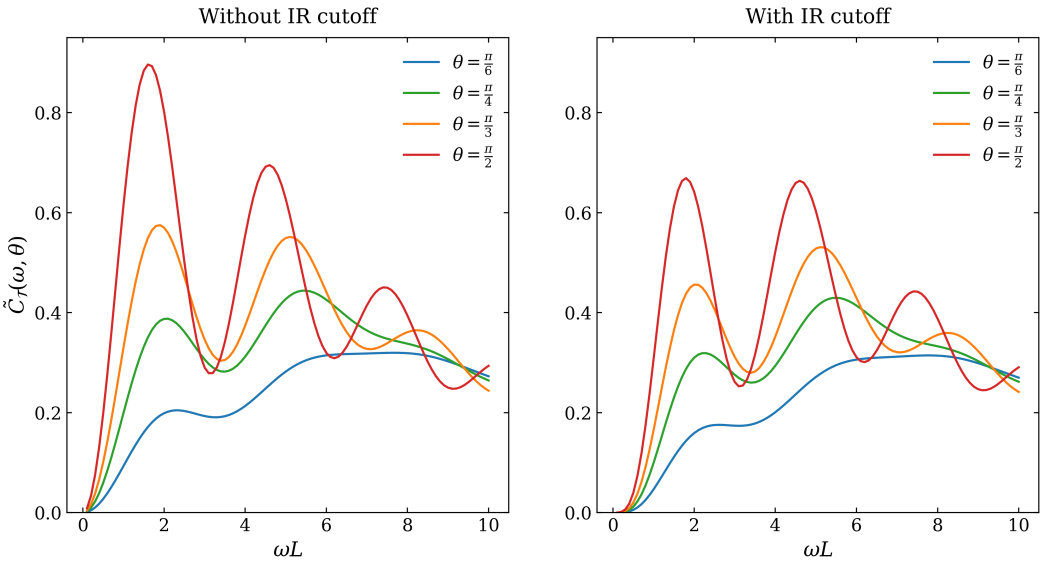

Figure 9.3: Power spectral density $\tilde{C}_{\mathcal{T}}(\omega,\theta)$ [*i.e.*, Eq. (9.45)] of the pixellon model without IR cutoff in Eq. (9.44) (left) and with an IR cutoff in Eq. (9.59) (right), where all the curves are normalized by $\frac{8\pi c_s^2}{a l_p}$.

has a nontrivial angular dependence, contributes to $\tilde{C}_{\mathcal{T}}(\omega,\theta)$.

In Eqs. (9.46)-(9.47), there are also additional factors of $\frac{1}{c_s}$ from the expansion of $\sin[\omega\mathcal{D}(r_1,r_2,\theta)/c_s]$ in Eq. (9.44). Since the leading order term in the expansion of $\sin[\omega\mathcal{D}(r_1,r_2,\theta)/c_s]$ is linear in its argument, it contributes an additional factor of $\frac{1}{c_s}$ to $\tilde{C}(\omega,\theta)$ in Eq. (9.46). On the other hand, as we explained above, this leading order term is angle-independent, so the next order term, which is cubic in its argument, contributes an additional factor of $\frac{1}{c_s^3}$ to $\tilde{C}_{\mathcal{T}}(\omega,\theta)$ in Eq. (9.47).

One last observation from Eqs. (9.46)-(9.47) is that both $\tilde{C}(\omega,\theta)$ and $\tilde{C}_{\mathcal{T}}(\omega,\theta)$ are regular in low frequency. In [30], an IR regulator at the scale of $\sim\frac{1}{L^2}$ was added to the 2D Laplacian on the sphere to regulate the angular correlation function as we will discuss in Sec. 9.4. To perform an analogous calculation and take into account other IR effects, such as information loss due to soft graviton loss, we will apply the procedures in this section to the pixellon model with an IR cutoff at the same scale as in [30] in Sec. 9.4.

Angular correlation

We now study the angular correlation implied by Eq. (9.41). It will be convenient to first decompose Eq. (9.41) into spherical harmonics and spherical Bessel functions.

Using

$$e^{i\mathbf{p}\cdot\mathbf{r}} = \sum_{\ell=0}^{\infty} i^l (2\ell+1) j_\ell(|\mathbf{p}|r) P_\ell(\cos\theta)\,, \quad \theta = \hat{\mathbf{p}}\cdot\hat{\mathbf{r}}\,, \tag{9.48}$$

and the addition theorem

$$P_\ell(\hat{\mathbf{p}}\cdot\mathbf{n}) = \frac{4\pi}{2\ell+1}\sum_m Y^{\ell m*}(\hat{\mathbf{p}}) Y^{\ell m}(\mathbf{n})\,, \tag{9.49}$$

we obtain

$$\begin{aligned} e^{i\mathbf{p}\cdot(\mathbf{x}_1-\mathbf{x}_2)} = & \sum_{\ell_1,m_1,\ell_2,m_2} 16\pi^2 i^{\ell_1}(-i)^{\ell_2} j_{\ell_1}(|\mathbf{p}|r_1) j_{\ell_2}(|\mathbf{p}|r_2) \\ & Y^{\ell_1 m_1 *}(\hat{\mathbf{p}}) Y^{\ell_2 m_2}(\hat{\mathbf{p}}) Y^{\ell_1 m_1}(\mathbf{n}_1) Y^{\ell_2 m_2 *}(\mathbf{n}_2)\,. \end{aligned} \tag{9.50}$$

Using $\int d\Omega\; Y^{\ell_1 m_1 *}(\hat{\mathbf{p}}) Y^{\ell_2 m_2}(\hat{\mathbf{p}}) = \delta^{\ell_1\ell_2}\delta^{m_1 m_2}$, we can integrate out all the angular dependence of $\mathbf{p}$, so

$$\begin{aligned} C(\Delta t,\theta) = & \frac{a l_p}{4\pi c_s^3 L^2}\sum_{\ell,m}\int_0^L dr_1 \int_0^L dr_2 \int_0^\infty d\omega \\ & \cos\left[\omega(L-r_1)\right]\cos\left[\omega(L-r_2)\right] \\ & j_\ell(\omega r_1/c_s) j_\ell(\omega r_2/c_s) \\ & Y^{\ell m}(\vartheta_1,\varphi_1) Y^{\ell m *}(\vartheta_2,\varphi_2) e^{-i\omega\Delta t}\,, \end{aligned} \tag{9.51}$$

where we have an additional factor of $\frac{1}{c_s^3}$ from replacing $\mathbf{p}$ with ω using Eq. (9.26). If we define the amplitude of each (ℓ, m) mode of the integrand to be

$$\begin{aligned} A_{\ell m}(\Delta t,\omega,r_1,r_2) \equiv\; & \cos\left[\omega(L-r_1)\right]\cos\left[\omega(L-r_2)\right] \\ & j_\ell(\omega r_1/c_s) j_\ell(\omega r_2/c_s) e^{-i\omega\Delta t}\,, \end{aligned} \tag{9.52}$$

Eq. (9.51) can be more compactly written as

$$\begin{aligned} C(\Delta t,\theta) = & \frac{a l_p}{4\pi c_s^3 L^2}\sum_{\ell,m}\int_0^L dr_1 \int_0^L dr_2 \int_0^\infty d\omega \\ & A_{\ell m}(\Delta t,\omega,r_1,r_2) Y^{\ell m}(\vartheta_1,\varphi_1) Y^{\ell m *}(\vartheta_2,\varphi_2)\,. \end{aligned} \tag{9.53}$$

Let us first look at the equal-time correlator by setting $\Delta t = 0$. The amplitude $c_{\ell m}$ of each (ℓ, m) mode of $C(0,\theta)$ is then given by integrating $A_{\ell m}(0,\omega,r_1,r_2)$ over ω and $r_{1,2}$ as indicated by Eq. (9.53), *i.e.*,

$$c_{\ell m} = \frac{a l_p}{4\pi c_s^3 L^2}\int_0^L dr_1 \int_0^L dr_2 \int_0^\infty d\omega\; A_{\ell m}(0,\omega,r_1,r_2)\,. \tag{9.54}$$

Since these integrals are hard to evaluate analytically, we have plotted the numerical result in Fig. 9.4. In Fig. 9.4, we have only plotted the modes starting from $\ell = 1$ since the $\ell = 0$ mode, which is angle-independent, is cancelled out in $C_{\mathcal{T}}(\Delta t, \theta)$ as explained in the previous section.

In Fig. 9.4, we have also shown the amplitude of each (ℓ, m) mode found in Ref. [30]. They argued that the angular part of $C(0, \theta)$ should be described by the Green's function of the 2D Laplacian on the sphere with an additional IR regulator at the scale of $\frac{1}{L^2}$. After decomposing the Green's function into spherical harmonics, one obtains

$$C(0, \theta) \propto \sum_{\ell,m} \frac{Y^{\ell m}(\vartheta_1, \varphi_1) Y^{\ell m *}(\vartheta_2, \varphi_2)}{\ell(\ell+1) + 1} \,. \tag{9.55}$$

Excellent agreement between the pixellon model and the expectation of Ref. [30] is observed.

As mentioned in Sec. 9.4, both $\tilde{C}(\omega, \theta)$ and $\tilde{C}_{\mathcal{T}}(\omega, \theta)$ in this work are regular when $\omega \to 0$, even without an IR regulator, *e.g.*, Eqs. (9.46)-(9.47). However, it will still be interesting to study the pixellon model with an IR cutoff due to IR effects from the physical size of the interferometer. We will consider the case with an IR cutoff in Sec. 9.4, but in this section, we first consider only the model without an IR cutoff. Thus, when comparing Eq. (9.54) to Ref. [30], we drop the additional 1 in the denominator of Eq. (9.55), which appears due to the insertion of an IR regulator. In this case, the amplitude of each (ℓ, m) mode becomes $\frac{1}{\ell(\ell+1)}$. In Fig. 9.4, one can observe that the angular correlation in this work is very close to the one in [30] without the IR regulator. Note that one also observes the same angular dependence in the shockwave geometry (*e.g.*, see Refs. [513, 514, 515, 500]), a connection we would like to study further in our future work.

One might also be interested in the amplitude $\tilde{c}_{\ell m}(\omega)$ of each (ℓ, m) mode of the power spectral density $\tilde{C}(\omega, \theta)$. Performing a Fourier transform of $C(\Delta t, \theta)$ in Eq. (9.53) and thus a Fourier transform of $A_{\ell m}(\Delta t, \omega, r_1, r_2)$ in Eq. (9.52), we obtain

$$\tilde{c}_{\ell m}(\omega) = \frac{a l_p}{2 c_s^3 L^2} \int_0^L dr_1 \int_0^L dr_2 \; A_{\ell m}(0, \omega, r_1, r_2) \,. \tag{9.56}$$

We have plotted $\tilde{c}_{\ell m}(\omega)$ starting from $\ell = 1$ in Fig. 9.5.

To determine an analytical representation of the amplitude of each (ℓ, m) mode, one can also look at $A_{\ell m}(0, \omega, r_1, r_2)$ at the end points $r_1 = r_2 = L$. If we integrate $A_{\ell m}(0, \omega, L, L)$ over ω, we find the amplitude of each (ℓ, m) mode at end points to

be

$$L\int_0^\infty d\omega\, A_{\ell m}(0,\omega,L,L) = \frac{\pi c_s}{2(2\ell+1)}\,, \tag{9.57}$$

which is the major contribution to $c_{\ell m}$ plotted in Fig. 9.4. Although Eq. (9.57) decreases more slowly than Eq. (9.55) over ℓ, we have additional suppression due to, for example, the factors of $\cos\left[\omega(L-r_{1,2})\right]$ in Eq. (9.52) when integrating $A_{\ell m}(0,\omega,r_1,r_2)$ over ω and $r_{1,2}$, so the total amplitude in Eq. (9.54) is very close to Eq. (9.55) without the IR regulator.

IR cutoff

In this section, we apply the calculations in the previous two sections to the pixellon model with an IR cutoff. As discussed above, although both $\tilde{C}(\omega,\theta)$ and $\tilde{C}_{\mathcal{T}}(\omega,\theta)$ are regular in the IR, we still expect an explicit IR cut-off to enter the calculation because of the finite size of the interferometer. We will also find that adding an IR cut-off gives a better agreement with the angular correlation of Eq. (9.55). For this reason, we place an IR cutoff at a scale $\sim \frac{1}{L^2}$, similar to [30], into Eq. (9.41), *e.g.*,

$$\begin{aligned} C(\Delta t,\theta) = \frac{a l_p}{8L^2}\int_0^L dr_1 \int_0^L dr_2 \int \frac{d^3\mathbf{p}}{(2\pi)^3}\frac{1}{\omega^2(\mathbf{p})+\frac{1}{L^2}} \\ \cos\left[\omega(L-r_1)\right]\cos\left[\omega(L-r_2)\right]e^{-i\omega\Delta t+i\mathbf{p}\cdot\Delta\mathbf{x}}\,. \end{aligned} \tag{9.58}$$

Following the same procedure in Sec. 9.4, we find that the power spectral density $\tilde{C}(\omega,\theta)$ in Eq. (9.44) is modulated by an additional factor in ω and L, *i.e.*,

$$\tilde{C}(\omega,\theta) \to \left(\frac{\omega^2}{\omega^2+\frac{1}{L^2}}\right)\tilde{C}(\omega,\theta)\,, \tag{9.59}$$

while $\tilde{C}_{\mathcal{T}}(\omega,\theta)$ is still given by Eq. (9.45). $C_{\mathcal{T}}(0,\theta)$ and $\tilde{C}_{\mathcal{T}}(\omega,\theta)$ with this IR cutoff are shown in Figs. 9.2 and 9.3, respectively.

One major effect of the IR cutoff is that the amplitude of $\tilde{C}(\omega,\theta)$ is suppressed at low frequency due to the modulation factor in Eq. (9.59), as one can directly observe in Fig. 9.3. For the same reason, the overall amplitude of $C_{\mathcal{T}}(\Delta t,\theta)$ in the case with an IR cutoff is smaller than the one without IR cutoff as depicted in Fig. 9.2. As frequency increases, the modulation factor goes to 1, so the amplitude of $\tilde{C}(\omega,\theta)$ in these two cases becomes nearly identical. In addition, as the separation angle θ decreases, the difference between these two cases also becomes smaller since interferometers with smaller θ are more sensitive to higher ℓ modes, which have higher characteristic frequency, and thus are less sensitive to the IR cutoff.

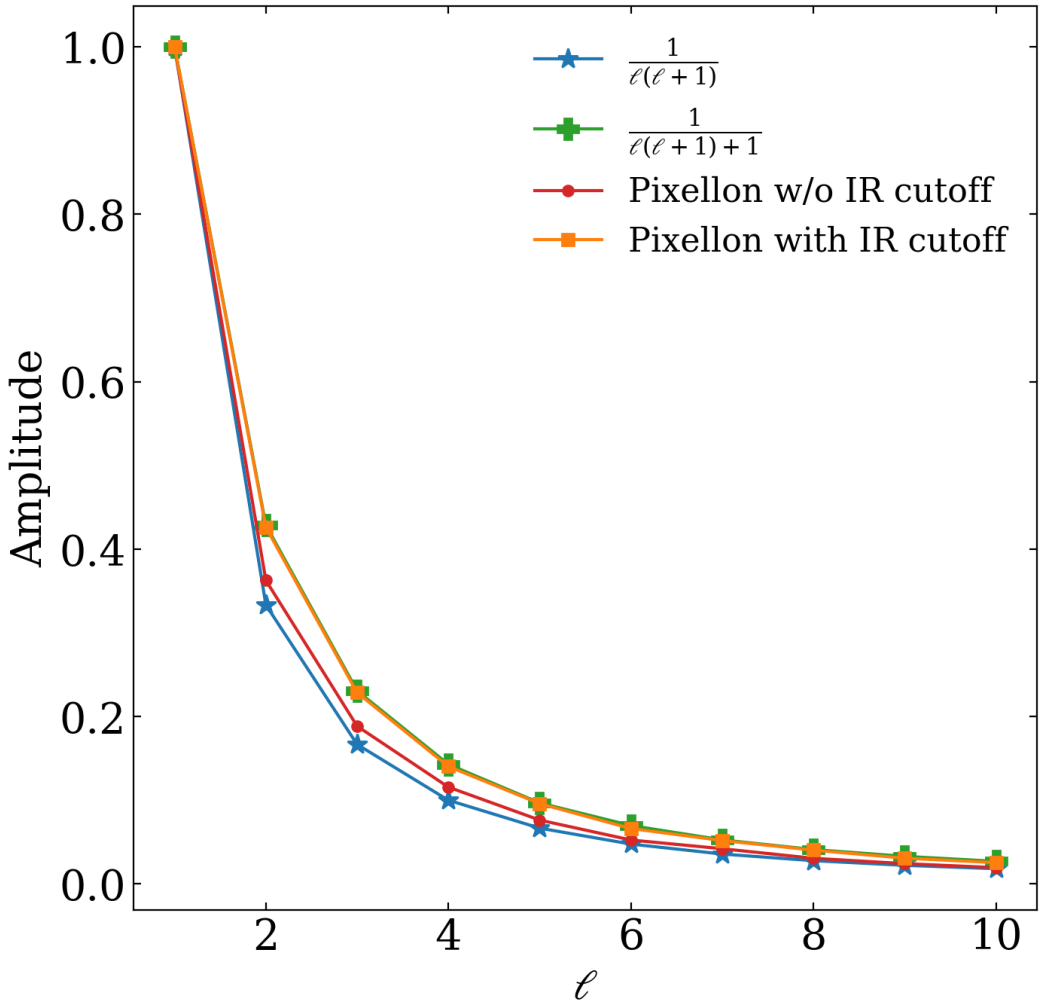

Figure 9.4: The amplitude of each (ℓ, m) mode of the equal-time correlation function $C(0,\theta)$ decomposed into spherical harmonics. The blue and green lines correspond to the amplitude in [30] [*i.e.*, Eq. (9.55)] without and with an IR regulator, respectively. The red and orange lines correspond to $c_{\ell m}$ [*i.e.*, Eq. (9.54)] of the pixellon model without IR cutoff in Eq. (9.52) and with an IR cutoff in Eq. (9.62), respectively. We have normalized the amplitude of each mode by the amplitude of the mode $\ell = 1$.

One can also determine the suppression factor due to the IR cutoff as $\omega \to 0$ by expanding Eq. (9.59), *e.g.*,

$$\tilde{C}(\omega,\theta) = \frac{a l_p}{8\pi c_s^3}\omega^2 L^2 + O(\omega^4 L^4)\,, \tag{9.60}$$

$$\tilde{C}_{\mathcal{T}}(\omega,\theta) = \frac{a l_p}{48\pi c_s^5}\omega^4 L^4 (1-\cos\theta) + O(\omega^6 L^6)\,. \tag{9.61}$$

The IR behaviors of both $\tilde{C}(\omega,\theta)$ and $\tilde{C}_{\mathcal{T}}(\omega,\theta)$ above are very different from the

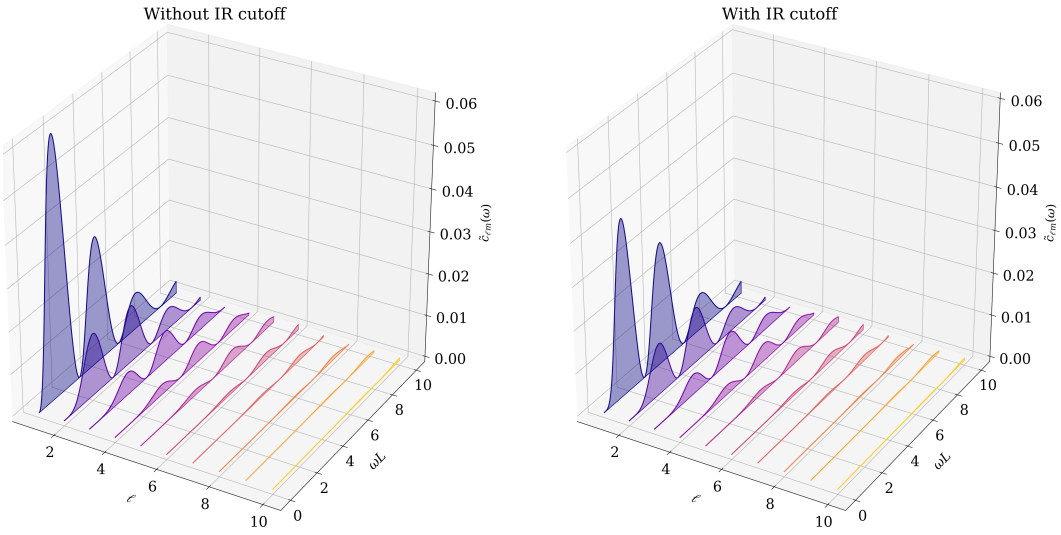

Figure 9.5: The amplitude $\tilde{c}_{\ell m}(\omega)$ [*i.e.*, Eq. (9.56)] of each (ℓ, m) mode of the power spectral density $\tilde{C}(\omega, \theta)$ decomposed into spherical harmonics. The left and right panels are for the pixellon model without IR cutoff in Eq. (9.52) and with an IR cutoff in Eq. (9.62), respectively. We have dropped the overall factor $\frac{al_p}{2c_s^3}$ in both plots.

case without an IR cutoff in Eq. (9.46)-(9.47) due to the additional factor of $\omega^2 L^2$ contributed by the modulation factor in Eq. (9.59). For this reason, one has to be cautious when constraining our model using detectors with peak sensitivity at low frequency, such as LIGO, as discussed in Sec. 9.4.

For the angular correlation, after decomposing Eq. (9.58) into spherical harmonics, we find that the amplitudes $c_{\ell m}$ and $\tilde{c}_{\ell m}(\omega)$ of each (ℓ, m) mode of $C(0, \theta)$ and $\tilde{C}(\omega, \theta)$ are given by Eqs. (9.54) and (9.56), respectively, but $A_{\ell m}(\Delta t, \omega, r_1, r_2)$ is modulated by the same factor in Eq. (9.59), *i.e.*,

$$A_{\ell m}(\Delta t, \omega, r_1, r_2) \to \left(\frac{\omega^2}{\omega^2 + \frac{1}{L^2}} \right) A_{\ell m}(\Delta t, \omega, r_1, r_2) \,. \tag{9.62}$$

We show both $c_{\ell m}$ and $\tilde{c}_{\ell m}(\omega)$ with the IR cutoff in Figs. 9.4 and 9.5, respectively.

Since the overall amplitude of $\tilde{C}(\omega, \theta)$ is suppressed at low frequency, the amplitude $\tilde{c}_{\ell m}(\omega)$ of different (ℓ, m) modes is also suppressed as shown in Fig. 9.5. In Fig. 9.4, one can also observe that the amplitude $c_{\ell m}$ falls off more slowly with ℓ in the case with an IR cutoff since low ℓ modes are more sensitive to this IR cutoff and hence are more suppressed. As noted previously, our model with the IR cutoff better agrees with the results in [30], though one should remain cautious until our model has been fully mapped to a UV-complete theory.

Existing constraints and future projections

In an effort to detect high frequency gravitational waves and quantum gravity signatures, several laboratory-sized interferometer experiments have been implemented to accurately detect tiny spacetime perturbations. The constraints from these experiments are often reported as upper limits on the one-sided noise strain $\sqrt{S_h(f)}$ of the photon round-trip time, obtained by analysing interference patterns. For stationary signals, the strain is defined as [516, 517]

$$\sqrt{S_h^{(n)}(f)} = \sqrt{2\int_{-\infty}^{\infty}\left\langle \frac{\Delta L(\tau)}{L}\frac{\Delta L(0)}{L}\right\rangle e^{-2\pi i f\tau}d\tau}\,, \tag{9.63}$$

which has units of $\mathrm{Hz}^{-1/2}$. This is related to Eq. (9.44) by Eq. (9.45), *i.e.*,

$$\sqrt{S_h(f)} = \sqrt{2\tilde{C}_{\mathcal{T}}\left(\omega, \theta = \frac{\pi}{2}\right)}\,, \tag{9.64}$$

where $\omega = 2\pi f$ and we assume a perpendicular arm configuration. Our power spectrum in Eq. (9.44) can be parameterized more conventionally by defining

$$\alpha \equiv \frac{2\pi}{c_s^2}a\,, \tag{9.65}$$

leading to the peak strain $\sqrt{S_h(f_{\rm peak})} \approx \sqrt{2\alpha l_p}/(4\pi) = \sqrt{\alpha}(2.62\times10^{-23})\ \mathrm{Hz}^{-1/2}$ [2]. Here $\alpha \sim 1$ gives the amplitude of the effect computed in [30, 484], and should be considered the natural benchmark [3].

We now compare our predicted strain to the experimental constraints from Holometer [516], GEO-600 [518], LIGO [519], and the projected sensitivity from LISA [520]. Since the four interferometers have different arm lengths, the predicted strain from our models will also differ between these experiments. The result assuming $\alpha = 1$ with or without the IR cutoff using Eqs. (9.44), (9.45), (9.59), (9.64), and (9.65) is plotted in Fig. 9.6. As expected, the tightest experimental limit comes from LIGO and Holometer measurements, which at 3σ significance, are roughly $\alpha \lesssim 3$ and $\alpha \lesssim 0.7$ (with IR cutoff), and $\alpha \lesssim 0.1$ and $\alpha \lesssim 0.6$ (w/o IR cutoff), respectively. On the other hand, our model is out of reach for GEO-600 and LISA.

Caltech and Fermilab are commissioning a joint theoretical and experimental initiative called Gravity from Quantum Entanglement of Space-Time (GQuEST), dedicated to probing the VZ effect proposed in Ref. [30]. This includes the construction

[2] This is related to the one-sided displacement spectrum by $S_L(f) = 2L^2\tilde{C}(f)$, which is peaked at $S_L(f_{\rm peak}) = \alpha l_p L^2/(8\pi^2)$.

[3] Since $\alpha = 1$ corresponds to $a = c_s^2/(2\pi)$, the finite propagation speed c_s has led us to make a corrected prescription of $\beta = l_p/a = 2\pi l_p/c_s^2$ in Eqs. (9.20) and (9.21).

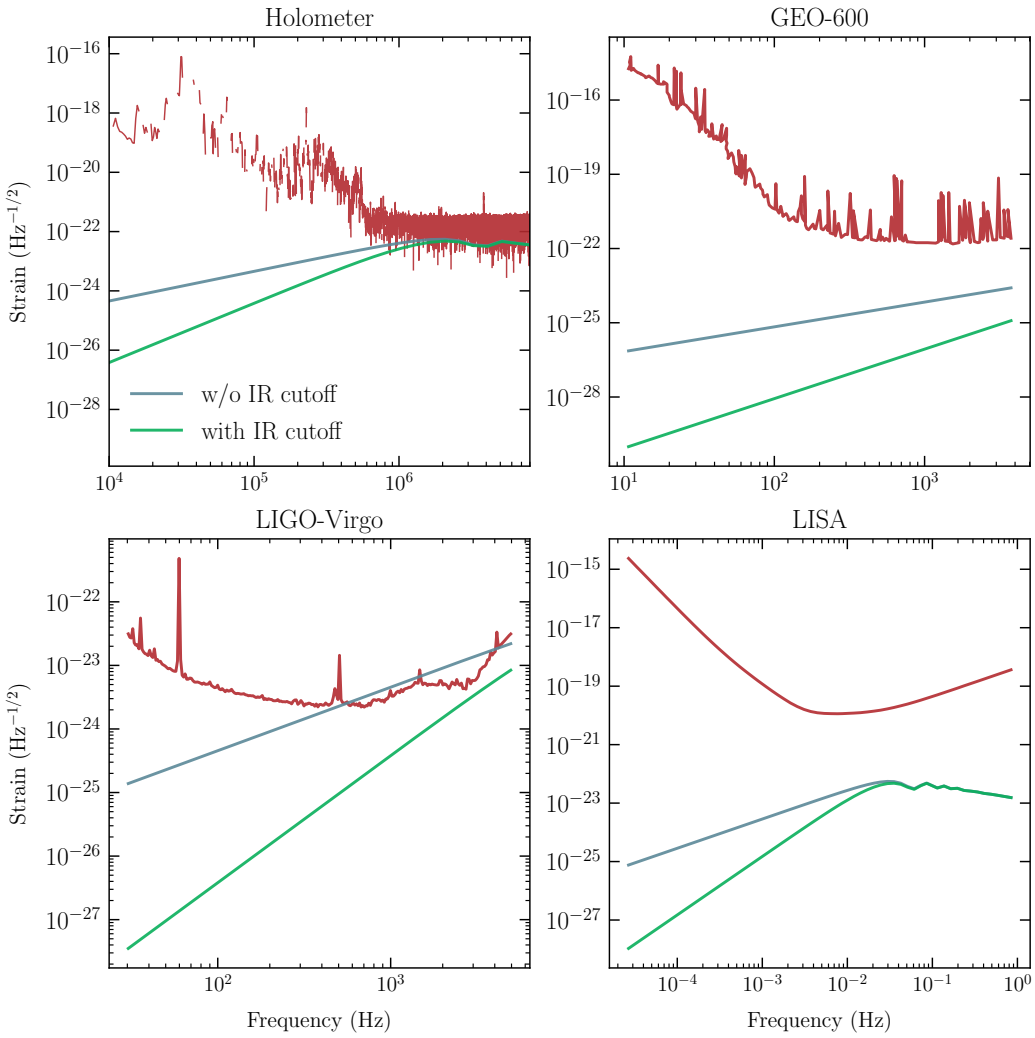

Figure 9.6: Strain comparison between model predictions (blue and green) and experimental / projection constraints (red). The model curves are computed using Eqs. (9.44), (9.45), (9.59), (9.64) and (9.65) assuming $\alpha = 1$, while the experimental curves are extracted from Refs. [516, 518, 519, 520]. The LIGO data shown here are obtained by the Livingston detector, but we note that the Hanford detector yields similar constraints.

of a tabletop optical Michelson interferometer with arm-length $L = 5$ m, with a novel read-out scheme with single photons rather than the usual interference effect. The advantage of this scheme is that sensitivity beats the standard quantum limit, with signal-to-noise ratio increasing linearly with integration time, rather than the usual square-root dependence. The experiment is projected to be able to constrain $\alpha \lesssim 1$ after 1000 s of background-free integration time, corresponding to a dark count rate of 10^{-3} Hz. We expect the constraint on α to tighten *linearly* with lower

dark count rate and longer integration time.

Some previous works on quantifying spacetime fluctuations (motivated by theories other than the VZ effect) argued that the predicted strain should not be directly compared against experimental constraints such as GEO-600 and LIGO [521], since transitional interferometer experiments often utilize Fabry-Perot cavities (*e.g.*, LIGO uses Fabry-Perot cavities within each arm, where the average light storage equals to 35.6 light round trips [522]) to boost the signal-to-noise ratio from astrophysical gravitational waves, while it is unclear whether quantum gravity signals, which are fundamental to spacetime itself, will benefit from additional light-crossings. Here we show that spacetime fluctuations based on Eq. (9.2) do accumulate over a Fabry-Perot cavity, thus justifying our direct strain comparison with gravitational experiments. A Fabry-Perot Michelson interferometer can be viewed as a linear device that measures the differential single-round-trip phase, $\Delta\Phi = \Phi_1 - \Phi_2$ between the two arms — regardless of whether this phase arises from gravitational waves, displacement of mirrors, or space-time fluctuations. This $\Delta\Phi$ is linearly transferred to the output field z, with noise N added:

$$z(f) = \mathcal{M}(f)\Delta\Phi(f) + N(f)\,. \tag{9.66}$$

In particular, $\mathcal{M}(f)$ contains the build-up (or suppression) of signal due to the Fabry-Perot cavity.

We now convert the strain-referred noise spectrum S_h published by LIGO to a spectrum for $\mathcal{T}$. In obtaining S_h (below 5 kHz, as shown in Fig. 9.6), LIGO used a long-wave-length approximation, and assumed that the wave has a + polarization (stretching along the x and squeezing along the y direction), and propagating along z — perpendicular to the detector plane (*e.g.*, adopted by Chapter 27.6 of [523]). In this case, in the Local Lorentz frame of the beam splitter, the first and second mirrors are going to be displaced by $\pm Lh/2$, leading to phase shifts of

$$\Phi_{1,2} = \pm\omega_0 Lh/c \tag{9.67}$$

and

$$\Delta\Phi = 2\omega_0 Lh/c\,. \tag{9.68}$$

In this way, the $\Delta\Phi$-referred spectrum is related to S_h published by LIGO via

$$\sqrt{S_{\Delta\Phi}} = \frac{2\omega_0 L}{c}\sqrt{S_h}\,. \tag{9.69}$$

We note that at higher frequencies, and/or for interferometers with longer arms, the conversion from h to Φ becomes less trivial. In our case, we have

$$\Delta\Phi(t) = \omega_0[\delta T(t, \mathbf{n}_1) - \delta T(t, \mathbf{n}_2)] = \omega_0 \mathcal{T}(t, \theta) \,. \tag{9.70}$$

We therefore have $\sqrt{S_{\Delta\Phi}} = \omega_0 \sqrt{S_{\mathcal{T}}}$ and thus

$$\sqrt{S_{\mathcal{T}}} = \frac{2L}{c} \sqrt{S_h} \,. \tag{9.71}$$

This allows us to straightforwardly relate our observable defined in Eqs. (9.34) and (9.45) to the quantity S_h constrained by LIGO. In LIGO, S_h is usually reported as a one-sided spectrum, so we need another factor of 2 when converting the two-sided spectrum $\tilde{C}_{\mathcal{T}}$ in Eq. (9.45) to the one-sided spectrum S_h, *i.e.,*

$$\sqrt{S_h} = \sqrt{S_{\mathcal{T}}} \Big/ \left(\frac{2L}{c}\right) = \sqrt{2\tilde{C}_{\mathcal{T}}\left(\omega, \theta = \frac{\pi}{2}\right)} \,, \tag{9.72}$$

which is consistent with the conversion in Eq. (9.64).

9.5 Conclusions

In this paper we have investigated the effects on the fluctuations in the time-of-arrival of a photon in an interferometer, due a scalar field coupled to the metric as in Eq. (9.2) with an occupation number given by Eq. (9.21). This simple scalar field is designed to model the behavior of vacuum fluctuations of the modular energy (*e.g.*, Ref. [484]) from shockwave geometries [500].

We showed that the interferometer observable had a power spectral density quadratically suppressed $\propto \omega^2$ or $\propto \omega^4$, depending on the IR regulator, at low frequency, and an angular correlation between the interferometer arms consistent with that proposed in Ref. [30], as expected from shockwave geometries.

In future work, we plan to more explicitly demonstrate the connection between shockwave geometries and interferometer observables, completing the bridge between the model presented here and the UV-complete theory.

Chapter 10

ASTRONOMICAL IMAGE BLURRING FROM TRANSVERSELY CORRELATED QUANTUM GRAVITY FLUCTUATIONS

This chapter is based on

[1] Vincent S. H. Lee, Kathryn M. Zurek, and Yanbei Chen. "Astronomical image blurring from transversely correlated quantum gravity fluctuations". In: *Phys. Rev. D* 109.8 (2024), p. 084005. DOI: 10.1103/PhysRevD.109.084005. arXiv: 2312.06757 [gr-qc].

10.1 Introduction

Although a consistent quantum mechanical description of spacetime geometry is not yet fully developed, it can be anticipated that spacetime geometry will have quantum fluctuations, which will manifest as uncertainties in the macroscopic distances traveled by light rays. Over a distance L, one naively expects that the length fluctuation is $\Delta L \sim l_p$ [524], where $l_p = \sqrt{8\pi G} = 10^{-34}$ m is the Planck length associated with the UV scale of gravity with G being the gravitational constant. However, it is possible for length fluctuations to accumulate over an entire path of length L, like a random walk, leading to an overall uncertainty of [525, 526]

$$\langle \Delta L^2 \rangle \sim l_p L \,. \tag{10.1}$$

More specifically, random walk can arise from a "spacetime foam" [527] model, in which the spacetime metric has independent, order-of-unity fluctuations at neighboring Planck-length intervals [528, 529]. During each Planck time $t_p = l_p/c$, a photon deviates from its classical path by a random step with zero average and $\sim l_p$ uncertainty [530, 531, 532]. After $N = L/l_p$ steps, the variance of the total distance traveled by the light ray is then given by $\Delta L \sim \sqrt{N} l_p$, consistent with Eq. (10.1).

It has been proposed that the phase front of starlight propagating in such a spacetime foam will be distorted and lead to blurring of telescope images [533, 534, 535, 536, 537, 538, 539, 540]. However, diffraction of light is known to be able to restore the transverse coherence of the phase front (see, e.g., Chapter 9 of Ref. [523]) and restore the quality of images for a large class of spacetime foam models [541].

If, however, quantum gravity is holographic, then the number of spacetime degrees of freedom in a region of spacetime is set by the area of its boundary, instead of

the volume of its bulk. This implies spatial correlations in the quantum degrees-of-freedom of spacetime, manifesting as correlations between metric fluctuations at different spacetime locations. In particular, Verlinde-Zurek (VZ) proposed how holographic theories could give rise to an accumulation of spacetime fluctuations consistent with Eq. 10.1 [30]. In the VZ theory, quantum degrees of freedom on the boundary of a causal diamond drive quantum fluctuations in the spacetime geometry inside the diamond, which in turn leads to fluctuations in the size of the causal diamond [484, 482, 6, 500]. In Ref. [30], VZ specifically considered the causal diamond generated by the union of the future and past domains of dependence, which in flat spacetime is simply a sphere.

For the radius L of the spatial sphere along any arbitrary direction, while they found a magnitude of fluctuation ΔL along the lightcone directions consistent with Eq. 10.1, they also discovered unique long distance (large angle) angular correlations between radii along different angular directions such that most of the power of the quantum fluctuations lies in the low angular harmonic modes. Decomposing the length fluctuation correlation between two points on a sphere with angular coordinates $\hat{\mathbf{\Omega}}$ and $\hat{\mathbf{\Omega}}'$ as a sum over spherical harmonics, the contribution from each mode exhibits a l^{-2} scaling for $l \gg 1$ [30], i.e.

$$\langle \Delta L(\hat{\mathbf{\Omega}}) \Delta L(\hat{\mathbf{\Omega}}') \rangle \sim \frac{l_p L}{4\pi} \sum_{lm} \frac{1}{l^2} Y_l^m(\mathbf{\Omega}) Y_l^{m*}(\mathbf{\Omega}') \,. \tag{10.2}$$

This is consistent with the 't Hooft uncertainty relation [542] that motivated the VZ proposal. In particular, the modular energy fluctuations that generate a length fluctuation of Eq. 10.2 [484] have been shown to have a physical origin in gravitational shockwaves produced by vacuum energy fluctuations [500, 543]. These gravitational shockwaves motivated the use of 't Hooft commutation relations as a way to quantize gravity at black hole horizons [544, 545, 542, 546], and has profound implications in various contexts of quantum gravity, including the AdS/CFT correspondence and black hole thermodynamics [547, 548].

As a consequence of the different correlation structure, while both spacetime foam and the VZ effect give rise to length fluctuations parametrically of the size of Eq. (10.1), they have different properties and observable signatures. For instance, the random walk model due to spacetime foam predicts spatial correlations in all directions consistent with Brownian motion for paths that are separated by more than l_p from each other, while the VZ effect has stronger correlations over large transverse distances up to L [30] as predicted by Eq. 10.2.

Since interferometers are extremely sensitive to tiny length fluctuations, they are the primary experimental candidates for detecting spacetime fluctuations [525, 549, 550, 532]. The correlation function (10.2) for radii emanating from the same origin alone is not sufficient to provide predictions for all experiments that can be performed in a spacetime, including for interferometers. For that general purpose, the Pixellon model was proposed [497], in which a breathing-mode metric perturbation is prescribed to provide consistent results with (10.2). The pixellon model has been applied to make predictions for current and future interferometer experiments [497, 7]. A summary of the VZ proposal is given in Ref. [86].

In addition to interferometers, it has been proposed that astronomical observations of distant stars can potentially constrain spacetime fluctuation thanks to the long propagation distance [533, 534, 535, 536, 537, 551]. The fluctuating spacetime between an astronomical object and a telescope acts as a fuzzy lens, leading to degradation in image quality. Hence the observation of a diffraction-limited image places an upper limit on the magnitude of the fluctuations. A diagram showing the propagation of light rays from a distant point source and the formation of its image in a telescope is given in Fig. 10.1.

Assuming no spatial correlations between fluctuations at points separated by more than l_p, the upper limit L for distance from a point source (a star, a galaxy, or a galaxy cluster) to the telescope, before the image of the star is blurred, can be naively estimated as $\sqrt{l_p L} \lesssim \lambda_0$, where λ_0 is the optical wavelength. For a cosmological distance of $L \sim$ Gpc, we have $\sqrt{l_p L} \sim 5 \times 10^{-5}$ m, which is already far greater than the wavelength of visible light.

This estimate has been used to argue that the random walk model is thus completely ruled out by, for instance, existing data from the Hubble Space Telescope (HST) [552, 553]. As an example, HST observed a star at a redshift of $z = 6.2$ [554] with distance $L \sim 28$ Gly from Earth[1], corresponding to a length fluctuation of order $\sqrt{l_p L} \sim 0.1$ mm, far exceeding the optical wavelength $\lambda_0 \sim 1\,\mu$m, and thus is expected to completely destroy the optical image of the star itself. However, in the case of spacetime foam, the constraining power of astronomical image blurring has been questioned in several papers [555, 556]. In particular, Ref. [541] argues that

[1]Here we quoted the *co-moving* distance, which is argued in Ref. [552] to be the correct distance measure for constraining spacetime foam as it measures the fabric of spacetime itself. However, as we will demonstrate in Sec. 10.4, the limits from image blurring are satisfied by many orders of magnitude for quantum gravity models that we are interested in, and thus our conclusion does not depend on the choice of distance measure.

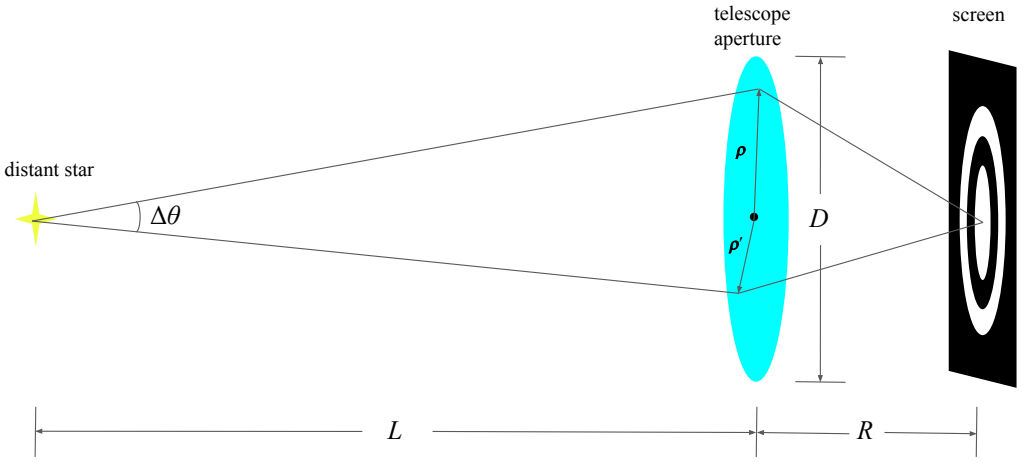

Figure 10.1: Diagram showing light rays originating from a distant star passing through the telescope aperture and forming a sharp image on the screen. Here the star-aperture distance, aperture diameter, and aperture-screen distance are denoted by L, D, and R, respectively. Two distinct points on the aperture, denoted by two-dimensional vectors $\boldsymbol{\rho}$ and $\boldsymbol{\rho}'$, span an angle of $\Delta\theta$. Typically $L \ggg R \gg D$. The diagram is not drawn to scale.

wave diffraction of photons with sub-Planckian energy as they propagate through spacetime introduces an extra factor of l_p/λ_0 in the level of fluctuations, completely eliminating any hope in constraining spacetime foam with any physical system.

In this work, we use the pixellon model [497, 7] realization of the VZ effect to show that length fluctuations given in Eq. (10.2) are not ruled out by the observations of astronomical images. The key idea is that while the phase shift relative to the classical photon path is large, the astrophysical image does not become blurred, since blurring depends not on the phase difference relative to the classical path, but rather on the phase difference between light rays hitting two typical points on the aperture, as illustrated in Fig. 10.1. Since the telescope size D is much smaller than the classical photon path length L, the phase difference across the aperture due to quantum fluctuations parameterized by Eq. (10.2) is much smaller, and thus cannot sufficiently decohere the light to prevent the formation of a sharp image. Using this argument plus a Riemann zeta regularization, we will demonstrate that for $L > D$, the maximum distance of propagation before the image is destroyed is given by

$$\sqrt{l_p L} \lesssim \frac{\lambda_0 L}{D}\,, \tag{10.3}$$

which is easily satisfied by any realistic telescope.[2]

It is natural to ask whether wave diffraction, as analyzed in Ref. [541] in the context of spacetime foam, affects our image blurring analysis when spatial correlations in the pixellon model are taken into account. However, since in the pixellon model, the energy associated with length fluctuations over a distance L mainly arises from scales $\sim 1/L$, which is much less than the optical frequency of a light ray, diffraction produces very little effect. This will be explicitly demonstrated using Huygens-Fresnel-Kirchhoff scalar diffraction theory [557].

The rest of the paper is organized as follows. In Sec. 10.2, using the pixellon model described in Refs. [497, 7], we derive the transverse correlations of fluctuations (more specifically, two-point correlation functions) in optical path lengths connecting a distant point source and points on the aperture of the telescope (see Fig. 10.1). In Sec. 10.3, we apply diffraction theory from the aperture of the telescope to the image plane and quantify the level of image degradation due to the pixellon-model-induced phase fluctuations. We also present some numerical results on the blurring effects as observed on an opaque screen. In Sec. 10.4, we consider the effects of diffraction between the point source and the telescope and show that they are subdominant for correlated fluctuations obtained in Sec. 10.3. Finally, in Sec. 10.5, we summarize our conclusions.

10.2 Transverse Correlations of Length Fluctuations of Light Rays from a Distant Star

In this section, we derive the transverse correlations of the distances traveled by light rays emitted from a distant point source. This source can either be a star or a galaxy, but for simplicity, we shall refer to it as a star. The setup is shown in Fig. 10.1. Assuming that the incident light is normal to the aperture plane, the blurring effect on the image provides a direct probe to the transverse correlation.

We commence with a brief review of the pixellon model as described in Refs [497, 7], but we emphasize that our analysis holds for any quantum gravity model that produces angular two-point correlation functions with a spherical harmonic decomposition in the form of Eq. (10.2). The pixellon model describes the breathing mode of a spherical entangling surface bounding a causal diamond [482, 6, 558]. Implications of the pixellon model on interferometer and astrophysical observables

[2] Note that inequality (10.3) can be formally violated when L is chosen to be a very small distance. However, that will violate the $L > D$ condition from which (10.3) was derived.

are studied in Refs [7, 559]. The metric fluctuation can be written as a scalar field in the radial component of the metric

$$ds^2 = -dt^2 + [1 - \phi(t, \mathbf{x})](dx^2 + dy^2 + dz^2)\,. \tag{10.4}$$

Decomposing the scalar field into Fourier components

$$\phi(t, \mathbf{x}) = l_p \int \frac{d^3\mathbf{p}}{(2\pi)^3} \frac{a_\mathbf{p} e^{-i\omega_\mathbf{p} t + i\mathbf{p}\cdot\mathbf{x}} + a^\dagger_\mathbf{p} e^{i\omega_\mathbf{p} t - i\mathbf{p}\cdot\mathbf{x}}}{\sqrt{2\omega_\mathbf{p}}}\,, \tag{10.5}$$

the creation and annihilation operators admit a two-point function of

$$\langle a_\mathbf{p} a^\dagger_{\mathbf{p}'} \rangle = (2\pi)^3 \left(1 + \frac{a}{l_p \omega_\mathbf{p}}\right) \delta^3(\mathbf{p} - \mathbf{p}')\,, \tag{10.6}$$

and an on-shell dispersion relation,

$$\omega_\mathbf{p} = c_s |\mathbf{p}|\,, \quad c_s \equiv 1/\sqrt{3}\,. \tag{10.7}$$

Here a is a constant characterizing the theoretical uncertainty of the model. Note that the second term in Eq. (10.6) corresponds to the pixellon occupation number and is much greater than unity. We refer readers to Refs. [497, 7, 559] for details of the pixellon model.

We now compute the two-point function of ϕ defined in Eq. (10.5) by using the correlation function (10.6) and the dispersion relation (10.7), obtaining

$$\begin{aligned}
&\langle \phi(t, \mathbf{x}) \phi(t', \mathbf{x}') \rangle \\
&= a l_p \int \frac{d^3\mathbf{p}}{(2\pi)^3} \frac{1}{\omega_\mathbf{p}^2} \cos\left[\omega_\mathbf{p}(t - t') - \mathbf{p}\cdot(\mathbf{x} - \mathbf{x}')\right] \\
&= \frac{\alpha l_p}{32\pi^2} \frac{1}{|\mathbf{x} - \mathbf{x}'|} \Theta\left(|\mathbf{x} - \mathbf{x}'| - c_s |t - t'|\right)\,,
\end{aligned} \tag{10.8}$$

where Θ is the Heaviside step function, and we have redefined the normalization constant to be $\alpha \equiv (2\pi/c_s^2)a$. Note that the benchmark of the theory is $\alpha \sim \mathcal{O}(1)$. Alternatively, we can apply the plane wave decomposition formula $e^{i\mathbf{p}\cdot\mathbf{x}} = 4\pi \sum_{lm} i^l j_l(|\mathbf{p}||\mathbf{x}|) Y_l^m(\hat{\mathbf{x}}) Y_l^{m*}(\hat{\mathbf{x}}')$ to Eq. (10.8), which gives

$$\begin{aligned}
\langle \phi(t, \mathbf{x}) \phi(t', \mathbf{x}') \rangle = \frac{\alpha l_p}{2\pi^2 c_s} \int_{-\infty}^{\infty} d\omega\, e^{-i\omega(t - t')} \\
\sum_{l=0}^{\infty} \sum_{m=-l}^{l} j_l\left(\frac{\omega|\mathbf{x}|}{c_s}\right) j_l\left(\frac{\omega|\mathbf{x}'|}{c_s}\right) Y_l^{m*}(\hat{\mathbf{x}}) Y_l^m(\hat{\mathbf{x}}')\,,
\end{aligned} \tag{10.9}$$

where we have integrated over the angular components of the momentum using the orthogonality relation of spherical harmonics, and extended to negative frequency using the identity $j_l(-x) = (-1)^l j_l(x)$. Remarkably, when $t = t'$, the integral over frequency in Eq. (10.9) can be performed exactly, leading to

$$\langle \phi(t,\mathbf{x})\phi(t,\mathbf{x}')\rangle = \frac{\alpha l_p}{2\pi}\sum_{l=0}^{\infty}\sum_{m=-l}^{l}\frac{1}{2l+1}Y_l^{m*}(\hat{\mathbf{x}})Y_l^m(\hat{\mathbf{x}}') \times\begin{cases}\dfrac{|\mathbf{x}|^l}{|\mathbf{x}'|^{l+1}} & \text{if } |\mathbf{x}|\le|\mathbf{x}'| \\ \dfrac{|\mathbf{x}'|^l}{|\mathbf{x}|^{l+1}} & \text{if } |\mathbf{x}|>|\mathbf{x}'|\end{cases}. \tag{10.10}$$

We now consider two photon paths originating from a distant star, extending over a distance L to two distinct points on the aperture with angular coordinates $\hat{\mathbf{\Omega}}$ and $\hat{\mathbf{\Omega}}'$. Clearly, when the aperture is much smaller than the star-telescope distance, $D \ll L$, the curvature of a sphere with radius L centered at the origin can be ignored when only the extent of the telescope is considered. The length shift of a photon path arriving at the telescope at time t is then given by integrating the linearized metric perturbation in Eq. (10.4) along the classical photon path,

$$\Delta L(t,\hat{\mathbf{\Omega}}) = -\frac{1}{2}\int_0^L dr\,\phi(t-L+r, r\hat{\mathbf{\Omega}})\,. \tag{10.11}$$

The two-point function of the accumulated length fluctuation is thus obtained by integrating Eq. (10.10) along radial coordinates r and r', leading to

$$\begin{aligned}&\langle \Delta L(t,\hat{\mathbf{\Omega}})\Delta L(t,\hat{\mathbf{\Omega}}')\rangle \\ &= \frac{1}{4}\int_0^L dr\int_0^L dr'\,\langle\phi(t-L+r,r\hat{\mathbf{\Omega}})\phi(t-L+r',r'\hat{\mathbf{\Omega}}')\rangle \\ &= \frac{1}{4}\int_0^L dr\int_0^L dr'\,\langle\phi(t,r\hat{\mathbf{\Omega}})\phi(t,r'\hat{\mathbf{\Omega}}')\rangle \\ &= \frac{\alpha l_p L}{4\pi}\sum_{l=0}^{\infty}\sum_{m=-l}^{l}\frac{1}{(l+1)(2l+1)}Y_l^{m*}(\hat{\mathbf{\Omega}})Y_l^m(\hat{\mathbf{\Omega}}')\,.\end{aligned} \tag{10.12}$$

Here the third line of Eq. (10.12) directly follows from the result in Eq. (10.8) and the triangle inequality, $|r\hat{\mathbf{\Omega}} - r'\hat{\mathbf{\Omega}}'| \ge |r-r'|$, alongside with $c_s < 1$. The l^{-2} scaling of the transverse correlation found here has been anticipated in Sec. 10.1, and is in accordance with previous works in Refs. [30, 500, 7, 558]. Using the addition theorem of spherical harmonics, $\sum_{m=-l}^{l} Y_l^{m*}(\hat{\mathbf{\Omega}})Y_l^m(\hat{\mathbf{\Omega}}') = \frac{2l+1}{4\pi}P_l(\hat{\mathbf{\Omega}}\cdot\hat{\mathbf{\Omega}}')$ where P_l

is the Legendre polynomial, we can rewrite Eq. (10.12) as

$$\langle \Delta L(t,\hat{\mathbf{\Omega}})\Delta L(t,\hat{\mathbf{\Omega}}')\rangle = \frac{\alpha l_p L}{16\pi^2}\sum_{l=0}^{\infty}\frac{1}{l+1}P_l(\cos\Delta\theta)\,, \tag{10.13}$$

where $\Delta\theta$ is the angular separation between $\hat{\mathbf{\Omega}}$ and $\hat{\mathbf{\Omega}}'$. Note that Eq. (10.13) is independent of time. Additionally, we note that the summation over l in Eq. (10.13) can be analytically performed to yield $\log(1+\csc(\Delta\theta/2))$, which diverges logarithmically as $\Delta\theta \to 0$.

Since both points are confined on the telescope, their separation is bounded by $\Delta\theta \lesssim D/L \ll 1$, and hence one can expand the Legendre polynomials for small argument, $P_l(\cos\Delta\theta) = 1 - \frac{1}{4}l(l+1)\Delta\theta^2 + \cdots$, and Eq. (10.13) becomes

$$\begin{aligned}&\langle \Delta L(\hat{\mathbf{\Omega}})\Delta L(\hat{\mathbf{\Omega}}')\rangle = \\ &\qquad \frac{\alpha l_p L}{16\pi^2}\left(\sum_{l=0}^{\infty}\frac{1}{l+1} - \frac{1}{4}\Delta\theta^2\sum_{l=0}^{\infty} l + \cdots\right)\,.\end{aligned} \tag{10.14}$$

The sums here are clearly divergent but can be properly regulated by some large Λ serving as a physical cutoff on the l-modes. As we will demonstrate in Sec. 10.3, the blurring effects from correlated fluctuations do not depend on the absolute phase of the light rays, but only the phase difference between two typical points on the aperture. The first sum in Eq. (10.14) is independent of $\Delta\theta$, and hence is an unimportant term that will drop out of the observable (i.e. the path difference between two points) by introducing a local counterterm, similar to an extrinsic energy quantity. The second sum in Eq. (10.14) depends on the system size, $\Delta\theta$, and has to be regulated accordingly. In particular, we do not expect our effective field theory description of the VZ effect, the pixellon model, to be valid at scales $l \gtrsim 1/\Delta\theta$. Imposing a cutoff on $l\Delta\theta$ then leads to the following regulated sums

$$\begin{aligned}&\langle \Delta L(\hat{\mathbf{\Omega}})\Delta L(\hat{\mathbf{\Omega}}')\rangle \\ &\to \frac{\alpha l_p L}{16\pi^2}\left(-\frac{1}{4}\Delta\theta^2\sum_{l=0}^{\infty} l e^{-l\Delta\theta/\Lambda} + \cdots\right) \\ &= \frac{\alpha l_p L}{16\pi^2}\left[-\frac{\Lambda^2}{4} + \frac{1}{48}\Delta\theta^2 + O\left(\frac{1}{\Lambda}\right) + O(\Delta\theta^4)\right]\,.\end{aligned} \tag{10.15}$$

The divergent parts are now all independent of $\Delta\theta$, and hence have to drop out of

the observable, which becomes

$$\begin{aligned}&\langle[\Delta L(\hat{\mathbf{\Omega}}) - \Delta L(\hat{\mathbf{\Omega}}')]^2\rangle \\ =&2[\Delta L(\hat{\mathbf{\Omega}})\Delta L(\hat{\mathbf{\Omega}}) - \Delta L(\hat{\mathbf{\Omega}})\Delta L(\hat{\mathbf{\Omega}}')] \\ =&-\frac{\alpha l_p L}{384\pi^2}\Delta\theta^2\,. \end{aligned} \tag{10.16}$$

Such a length fluctuation is strongly suppressed in astrophysical observations due to the extra factor $\Delta\theta^2 \lesssim (D/L)^2$.

Interestingly, one can directly arrive at the result in Eq. (10.16) by applying the following identity to Eq. (10.14)

$$\sum_{l=0}^{\infty} l = 1 + 2 + 3 + \cdots = -\frac{1}{12}\,. \tag{10.17}$$

This identity originates from the analytic continuation of the Riemann zeta function and is more familiar in the context of the Casimir force [560]. The Riemann zeta function, $\zeta(s) \equiv \sum_{n=1}^{\infty} n^{-s}$, is only convergent for $s > 1$, but can be analytically continued to include the entire complex plane except for a simple pole at $s = 0$. The identification amounts to $\zeta(-1) = -1/12$ by analytical continuation. This technique is known as the Zeta function regularization, which has been widely used to regulate divergent series in QFT and quantum gravity (e.g. see Ref. [22] for application to the gravitational path integral by Hawking). The divergent series is assigned a physical and finite value by analytic continuation, which always yields a unique value regardless of the actual renormalization scheme.

Returning to the image blurring analysis, analogous to the Casimir effect, the precise UV physics in Eq. (10.15) that cuts off $l\Delta\theta > \Lambda$ does not matter, since the quantum fluctuation that can be realistically measured by an experimental device is only sensitive to the IR physics. In addition, we note that while Eq. (10.16) appears to have a spurious minus sign, it will not affect the size of the image blurring effect, since the path difference only enters the observable as a phase of the light rays.

10.3 Blurring Effects from Correlated Fluctuations

In Sec. 10.2, we argued that the path difference between two light rays is the actual quantity responsible for blurring a sharp image from a distant star. We computed the variance of the path difference in Eq. (10.16) and found a severe suppression factor of $\sim \Delta\theta^2$. In this section, we justify this argument by an explicit computation of the blurring effect by the Huygens-Fresnel principle of wave optics to light propagation

from the telescope's aperture to the image plane. We find that the corresponding upper limits placed on the size of quantum fluctuation are given by Eq. (10.27), and are satisfied by many orders of magnitude.

In a typical astronomical observation, a telescope with size D is pointed towards the source such that the surface of the aperture is embedded in the transverse plane with respect to the propagation direction of the incoming photons, which points from the source to the telescope. (See Fig. 10.1 for an illustration of the system).

The source can then be treated as generating a perfect spherical wave. In the absence of perturbations (either astrophysical or quantum-gravity-induced), the incoming wave at the aperture of the telescope can be well-approximated as a plane wave. The intensity profile observed by the telescope is obtained by treating each point of the aperture as a spherical wavelet (Huygens-Fresnel principle) and computing their interference pattern by considering the path difference of each wavelet

$$I(\boldsymbol{\sigma}) \propto \left| \int_{\Omega_A} d^2\boldsymbol{\rho}\, e^{-i\mathbf{k}\cdot\boldsymbol{\rho}} \right|^2 , \tag{10.18}$$

where $I(\boldsymbol{\sigma})$ is the unperturbed image intensity at $\boldsymbol{\sigma}$ on the screen, Ω_A is the domain of the aperture, and we define $\mathbf{k} \equiv (2\pi/\lambda_0 R)\boldsymbol{\sigma}$ with R being the aperture-screen distance. Here we have assumed the far-field limit ($R \gg D$). Let $A = \pi(D/2)^2$ be the area of the aperture, the expression in Eq. (10.18) is more commonly written as the (squared) Fourier transform of the aperture function $w(\boldsymbol{\rho})$, defined to be 1 where the aperture is unblocked, and zero otherwise

$$\begin{aligned} I(\boldsymbol{\sigma}) &= \frac{I_0}{A^2} \left| \int_{-\infty}^{\infty} d^2\boldsymbol{\rho}\, w(\boldsymbol{\rho}) e^{-i\mathbf{k}\cdot\boldsymbol{\rho}} \right|^2 \\ &= \frac{I_0}{A^2} \left| \tilde{w}(\mathbf{k}) \right|^2 , \end{aligned} \tag{10.19}$$

where I_0 is the peak intensity of $I_{\text{ideal}}(\boldsymbol{\sigma})$. We now apply this to a circular aperture with a diameter D. Let $\gamma \ll 1$ be the angular position of $\boldsymbol{\sigma}$ relative to the origin, which is placed at the center of the aperture. Then the intensity profile is given by integrating Eq. (10.18)

$$\begin{aligned} I(\gamma) &= \frac{I_0}{\pi^2 (D/2)^4} \left| \int_0^{D/2} \rho d\rho \int_0^{2\pi} d\varphi\, e^{-i\frac{2\pi}{\lambda_0}\rho\gamma\sin\varphi} \right|^2 \\ &= 4I_0 \left[\frac{J_1(\pi\gamma D/\lambda_0)}{\pi\gamma D/\lambda_0} \right]^2 . \end{aligned} \tag{10.20}$$

The profile in Eq. (10.20) is known as the *Airy disk*, where the first minimum is located at $\gamma \approx 1.22\,\lambda_0/D$.

Image blurring happens when each wavelet from the aperture acquires a random fluctuating phase, $\Delta\Phi(\boldsymbol{\rho}) = (2\pi/\lambda_0)\Delta L(\boldsymbol{\rho})$. The resulting intensity now picks up a phase factor

$$I(\boldsymbol{\sigma}) = \frac{I_0}{A^2}\left|\int_{-\infty}^{\infty} d^2\boldsymbol{\rho}\, w(\boldsymbol{\rho}) e^{i\Delta\Phi(\boldsymbol{\rho})} e^{-i\mathbf{k}\cdot\boldsymbol{\rho}}\right|^2 , \tag{10.21}$$

with the expectation value

$$\langle I(\boldsymbol{\sigma})\rangle = \frac{I_0}{A^2}\int_{-\infty}^{\infty} d^2\boldsymbol{\rho}\int_{-\infty}^{\infty} d^2\boldsymbol{\rho}' \, w(\boldsymbol{\rho}) w(\boldsymbol{\rho}') e^{i(\Delta\Phi(\boldsymbol{\rho})-\Delta\Phi(\boldsymbol{\rho}'))} e^{-ik(\boldsymbol{\rho}-\boldsymbol{\rho}')} . \tag{10.22}$$

Defining $\sqrt{\langle\Delta\Phi^2\rangle} = \Delta\Phi_{\text{rms}}$, for uncorrelated noise, one expects significant image distortion to happen when $\Delta\Phi_{\text{rms}} \gtrsim \pi$. This is usually quantified using the Strehl ratio, defined as the ratio between the perturbed and unperturbed peak intensity, $S = \frac{\langle I(\theta=0)\rangle}{I_0}$, which is given by [561]

$$S = \frac{1}{A^2}\int_{-\infty}^{\infty} d^2\boldsymbol{\rho}\int_{-\infty}^{\infty} d^2\boldsymbol{\rho}' w(\boldsymbol{\rho}) w(\boldsymbol{\rho}') e^{-\frac{1}{2}D_\Phi(\boldsymbol{\rho},\boldsymbol{\rho}')} , \tag{10.23}$$

where we defined the two-point function $D_\Phi(\boldsymbol{\rho},\boldsymbol{\rho}') = |\langle[\Delta\Phi(\boldsymbol{\rho}) - \Delta\Phi(\boldsymbol{\rho}')]^2\rangle|$. It is clear that if $\Delta\Phi$ has no spatial correlation, then the Strehl ratio simply decays exponentially with the rms value of the phase [551], $S_{\text{uncorrelated}} = e^{-\Delta\Phi^2_{\text{rms}}}$. Requiring S to be close to unity then implies the rough estimate $\Delta\Phi_{\text{rms}} \lesssim 1$ and thus $\sqrt{l_p L} \lesssim \lambda_0$, ignoring $O(1)$ factors. This is a substantial level of fluctuations that have been ruled out, as we have discussed in Sec. 10.1.

If we now take transverse correlation into account, then Eq. (10.16) implies the phase difference variance to be

$$D_\Phi(\boldsymbol{\rho},\boldsymbol{\rho}') = 2\Phi^2_{\text{rms}}\frac{|\boldsymbol{\rho}-\boldsymbol{\rho}'|^2}{L^2} , \tag{10.24}$$

where $\Delta\Phi^2_{\text{rms}} = (1/192)(\alpha l_p L/\lambda_0^2)$. Combined with Eq. (10.23), one finds

$$S = \frac{1}{A^2}\int_{\Omega_A} d^2\boldsymbol{\rho}\int_{\Omega_A} d^2\boldsymbol{\rho}' e^{-\Delta\Phi^2_{\text{rms}}|\boldsymbol{\rho}-\boldsymbol{\rho}'|^2/L^2} . \tag{10.25}$$

Because $|\boldsymbol{\rho}| < D \ll L$, $D_\Phi(\boldsymbol{\rho},\boldsymbol{\rho}')$ in Eq. (10.24) is suppressed by an additional factor of $(D/L)^2$, which means the level of variation between $\Delta\Phi(\boldsymbol{\rho})$ across the

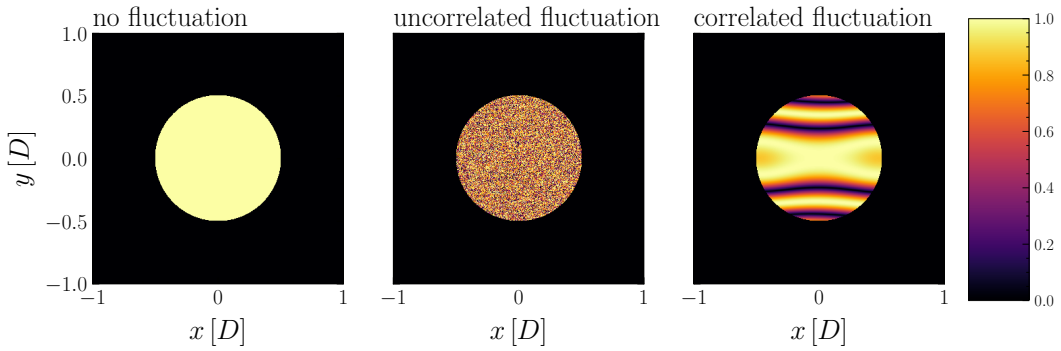

Figure 10.2: Plot of a realization of $\cos\Delta\Phi(r)$ on the aperture, generated in accordance with Eq. (10.24) assuming $\Delta\Phi_{\rm rms} = 2\pi$. The rightmost panel assumes $L = D$.

aperture is a factor D/L suppressed from $\Phi_{\rm rms}$. This drives the Strehl ratio strongly towards unity. More specifically, expanding the exponential in Eq. (10.25) gives

$$\begin{aligned} S &= 1 - \frac{1}{192}\frac{\alpha l_p}{\lambda_0^2 L}\frac{1}{A^2}\int_{\Omega_A} d^2\boldsymbol{\rho}\int_{\Omega_A} d^2\boldsymbol{\rho}'\,|\boldsymbol{\rho}-\boldsymbol{\rho}'|^2 \\ &= 1 - \frac{1}{768}\frac{\alpha l_p D^2}{\lambda_0^2 L}\,. \end{aligned} \tag{10.26}$$

The formation of a sharp image from a distant star indicates $S \approx 1$ in Eq. (10.26), and thus places a limit

$$\alpha \lesssim 3\times 10^{50}\left(\frac{\lambda_0}{1\,\mu\text{m}}\right)^2\left(\frac{L}{1\,\text{Gpc}}\right)\left(\frac{1\,\text{m}}{D}\right)^2\,, \tag{10.27}$$

which is clearly satisfied by many orders of magnitude in any realistic system with $\alpha \sim O(1)$.

We perform a numerical simulation by generating random fields $\Delta\Phi(\boldsymbol{\rho})$ across the aperture and producing the images as observed on the telescope's image plane by computing the Fourier transform in Eq. (10.21). We consider a circular aperture with a diameter of 1024 pixels, embedded in a 4096×4096-pixel square. The phase fluctuation is assumed to be a random Gaussian field with $\Delta\Phi_{\rm rms} = 0.1$, π and 2π. Correlated noise is generated to satisfy the variance in Eq. (10.24)[3] assuming $L/D = 1$ or 10. We show the distribution of $\cos\Delta\Phi(\boldsymbol{\rho})$ over the aperture in Fig. 10.2 and plot the observed image in Fig. 10.3. When the noise is uncorrelated, the Airy

[3]This can be achieved numerically, for example, by proposing that $\langle\Delta\Phi(\boldsymbol{\rho})\Delta\Phi(\boldsymbol{\rho}')\rangle = \Phi_{\rm rms}^2 e^{-|\boldsymbol{\rho}-\boldsymbol{\rho}'|^2/L^2} = (2\pi)^{-2}\int d^2\mathbf{k}\,G(\mathbf{k})e^{-i\mathbf{k}\cdot(\boldsymbol{\rho}-\boldsymbol{\rho}')}$, where $G(\mathbf{k}) = (\pi\Phi_{\rm rms}^2 L^2)e^{-L^2|\mathbf{k}|^2/4}$. Correlated noise can then be numerically simulated by filtering a realization of *uncorrelated* noise by the Green's function $G(\mathbf{k})$.

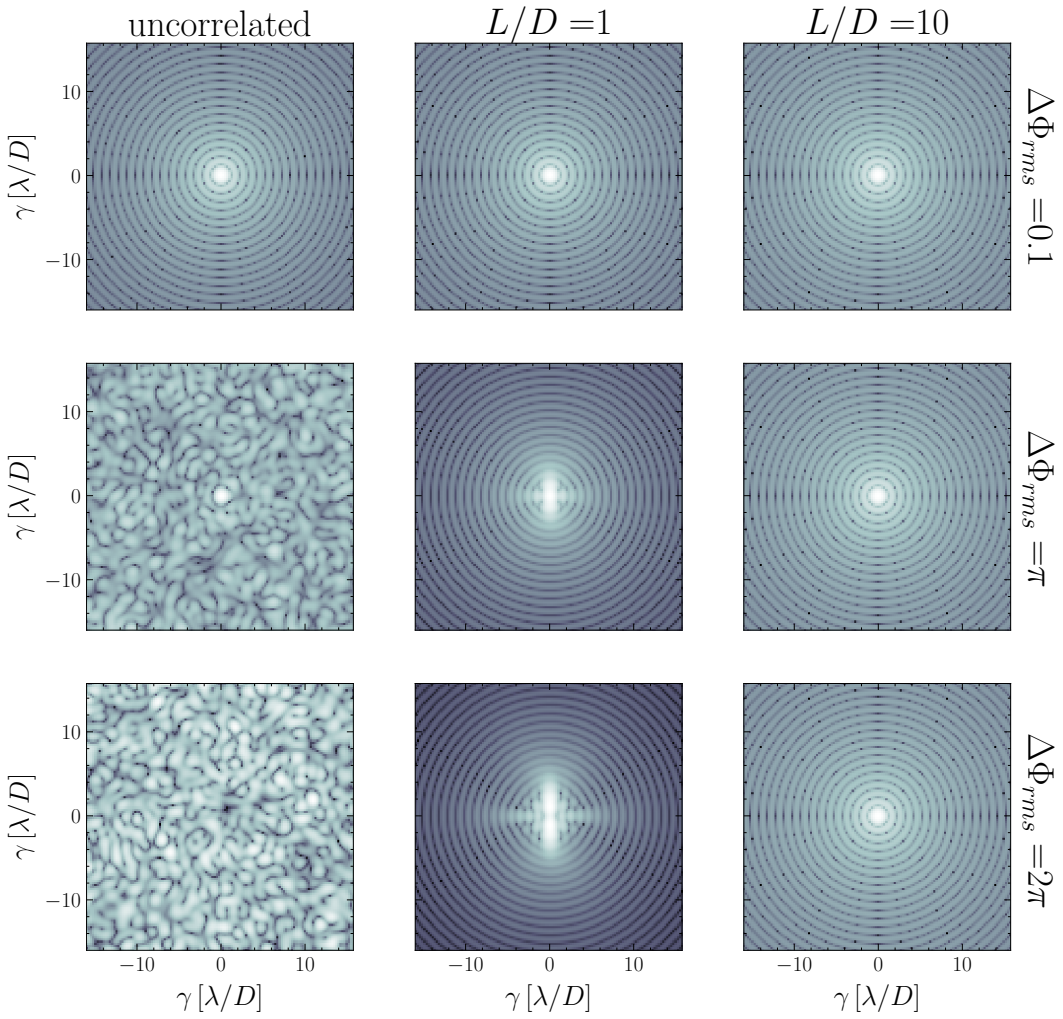

Figure 10.3: Images from a point object for various values of $\Delta\Phi_{\text{rms}}$ and correlation scale L, with correlation given by Eq. (10.24). The color represents $\log_{10}(I)$ with arbitrary normalization. The aperture is simulated with 1028×1028 pixels embedded in a 4096×4096 grid. The images are zoomed into the center 128×128 pixels to better resolve the Airy disks.

disk patterns from the point source are destroyed when $\Delta\Phi_{\rm rms} \gtrsim \pi$, corresponding to a small Strehl ratio. However, once spatial correlation is introduced to the noise, the Airy disk patterns are restored, showing that correlated length fluctuations are much harder to constrain by studying image blurring effects.

10.4 Effects of Diffraction

In Sec. 10.2, we treated photons from a distant star as point particles (with zero wavelength) following null rays until they reached the telescope. The sole contribution to the phase difference across the aperture is due to fluctuations in the distance covered by the rays. In other words, we have neglected the wave nature of the photons as they travel from the source to the telescope — even though in Sec. 10.3 we have incorporated that wave nature as light propagates from the aperture to the screen. In this section, we incorporate the wave nature of light rays more carefully by applying the Huygens- Fresnel-Kirchhoff scalar diffraction theory [557] to light propagation from the source to the telescope, which has been argued in Ref. [541] to significantly modify the blurring effect in the context of spacetime foam. A recent work that investigates the effects of spacetime fluctuations on light rays, taking into account the wave nature of photons, is given in Ref. [562].

We compute and compare the size of phase modulations on the telescope aperture, as well as their transverse correlations, explicitly in Fig. 10.4, and conclude that diffraction does not lead to qualitative changes in the observable if quantum gravity fluctuations have the high spatial correlation contained in the pixellon model.

Consider a scalar wave $\Phi(t, \mathbf{x})$ with angular frequency ω_0 propagating outwards in the radial direction with the metric in Eq. (10.4). The equation of motion of the scalar wave is given by $\frac{1}{\sqrt{-g}}\partial_\mu(g^{\mu\nu}\partial_\nu\Phi) = 0$. The leading order contributions of the derivatives is the frequency of the scalar wave ω_0, which allows us to take $\partial\phi \ll \partial\Phi$, leading to the familiar wave equation

$$\left[-(1-\phi(t,\mathbf{x}))\partial_t^2 + \nabla^2\right]\Phi(t,\mathbf{x}) = 0\,. \tag{10.28}$$

Note that one can also derive Eq. (10.28) by setting $ds^2 = 0$ in Eq. (10.4) and observing that the scalar wave travels with speed $dr/dt = (1-\phi)^{-1/2}$. Writing the wave as $\Phi(t,\mathbf{x}) = [\Phi_0(\mathbf{x}) + \psi(t,\mathbf{x})]e^{-i\omega_0 t}$, where $\Phi_0(\mathbf{x}) = e^{i\omega_0|\mathbf{x}|}/(4\pi|\mathbf{x}|)$ is an unperturbed spherical wave, and ψ is the time-dependent scattered wave. The wave equation to the first order gives

$$(\nabla^2 + \omega_0^2)\psi(t,\mathbf{x}) + (2i\omega_0\partial_t - \partial_t^2)\psi(t,\mathbf{x}) = \omega_0^2\phi(t,\mathbf{x})\Phi_0(\mathbf{x})\,. \tag{10.29}$$

We can decompose the scattered wave and the pixellon field into Fourier and harmonic modes, i.e. $\psi(t, r\hat{\mathbf{\Omega}}) = \int_{-\infty}^{\infty} d\omega\, e^{-i\omega t} \sum_{l=0}^{\infty} \sum_{m=-l}^{l} \psi_l^m(\omega, r) Y_l^m(\hat{\mathbf{\Omega}})$ and $\phi(t, r\hat{\mathbf{\Omega}}) = \int_{-\infty}^{\infty} d\omega\, e^{-i\omega t} \sum_{l=0}^{\infty} \sum_{m=-l}^{l} \phi_l^m(\omega, r) Y_l^m(\hat{\mathbf{\Omega}})$. Then Eq. (10.29) becomes

$$\left[\nabla_r^2 + (\omega_0 + \omega)^2 - \frac{l(l+1)}{r^2}\right] \psi_l^m(\omega, r) = \frac{\omega_0^2 e^{i\omega_0 r}}{4\pi r} \phi_l^m(\omega, r)\,. \tag{10.30}$$

Imposing a regularity condition at the origin and out-going wave boundary condition at infinity, we obtain a solution [541]

$$\begin{aligned}\psi_l^m(\omega, L) =& \frac{\omega_0^2(\omega_0 + \omega) h_l^{(1)}[(\omega_0 + \omega)L]}{4\pi} \\ & \int_0^L dr \left\{ r j_l[(\omega_0 + \omega)r] e^{i\omega_0 r} \phi_l^m(\omega, r) \right\}\,. \end{aligned} \tag{10.31}$$

On the other hand, the variance of the pixellon modes has been derived in Eq. (10.9)

$$\begin{aligned}&\langle \phi_l^m(\omega, r) \phi_{l'}^{m'*}(\omega', r') \rangle \\ &\quad = \frac{\alpha l_p}{2\pi^2 c_s} j_l\left(\frac{\omega r}{c_s}\right) j_l\left(\frac{\omega' r'}{c_s}\right) \delta_{ll'} \delta_{mm'} \delta(\omega - \omega')\,. \end{aligned} \tag{10.32}$$

The modulation as measured at the telescope can be written as $\xi(t, \hat{\mathbf{\Omega}}) \equiv \psi(t, L\hat{\mathbf{\Omega}})/\Phi_0(t, L\hat{\mathbf{\Omega}}) = 4\pi L \psi(t, L\hat{\mathbf{\Omega}}) e^{-i\omega_0 L}$. Combining Eq. (10.31) and Eq. (10.32), the variance of the modulation is given by

$$\begin{aligned}&\langle \xi(t, \hat{\mathbf{\Omega}}) \xi(t, \hat{\mathbf{\Omega}}') \rangle \\ &= \int_{-\infty}^{\infty} d\omega \sum_{l=0}^{\infty} \sum_{m=-l}^{l} |\xi_l^m(\omega)|^2 Y_l^m(\hat{\mathbf{\Omega}}) Y_l^{m'}(\hat{\mathbf{\Omega}}')\,, \end{aligned} \tag{10.33}$$

where

$$\begin{aligned}\left|\xi_l^m(\omega)\right|^2 =& \left|\omega_0^2(\omega_0 + \omega) L h_l^{(1)}[(\omega + \omega_0)L]\right|^2 \left(\frac{\alpha l_p}{2\pi^2 c_s}\right) \\ & \left| \int_0^L dr\, r e^{i\omega_0 r} j_l[(\omega_0 + \omega)r] j_l\left(\frac{\omega r}{c_s}\right) \right|^2\,. \end{aligned} \tag{10.34}$$

Here ξ_l^m's independence on m results from the spherical symmetry of the two-point function. While the integral over frequency in Eq. (10.34) is difficult to perform, we can estimate the variance in different regimes using asymptotic limits of Bessel functions. Realizing that each mode of the scattered wave $\psi_l^m(\omega)$ has a frequency of $\omega_0 + \omega$, significant blurring effects of the image can only be induced by scattered

waves with roughly the same frequency as the unperturbed wave, i.e. $\omega \lesssim \omega_0$. This leads to the following estimate for Eq. (10.34)

$$|\xi_l^m(\omega)|^2 \sim \left(\frac{\alpha l_p}{2\pi^2 c_s}\right) \times \begin{cases} \left(\frac{\omega_0 c_s}{2\omega}\right)^2 \frac{O(1)}{l} & \text{if } l \ll (\omega L/c_s), \omega_0 L \\ \left(\frac{C_l}{2l+1}\right)^2 \left(\frac{\omega L}{c_s}\right)^{2l} (\omega_0 L)^4 & \text{if } l \gg (\omega L/c_s),\ \omega_0 L \end{cases} , \tag{10.35}$$

where

$$C_l \equiv \frac{2^{l-1} l!}{(l+1)(2l+1)(2l)!} \ll 1 . \tag{10.36}$$

Here $O(1)$ in Eq. (10.35) denotes a number of order unity that has to be evaluated for each value of l. In Fig. 10.4 we plot $|\xi_l^m(\omega)^2|$ as a function of l in blue for different choices of $\omega_0 L$ and ωL (see caption), obtained by numerically integrating Eq. (10.34). Estimates in Eqs. (10.35)-(10.36) show that high l modes with $l \gg \omega_0 L$ are extremely suppressed by factors of $1/l!$ (more dramatic than an exponential suppression), which are negligible even when summed to $l \to \infty$. While we did not derive approximations in the intermediate l regime where $l \ll \omega L/c_s$ but $l \gg \omega_0 L$, it is clear from the right panel of Fig. 10.4 that these l-modes are also highly suppressed in this middle regime. Therefore, only the low l-modes satisfying $l \ll \omega L/c_s$ and $l \ll \omega_0 L$ will contribute to image blurring.

We now compare these new results with those obtained in Sec. 10.2, where the effects of diffraction are neglected. In that approximate treatment, the phase modulation as measured at the aperture, denoted by $\tilde{\xi}(t, \hat{\mathbf{\Omega}})$, was given by the photon path length fluctuation divided by the photon wavelength, i.e. $\tilde{\xi}(t, \hat{\mathbf{\Omega}}) = -(\omega_0/2) \int_0^L dr\, \phi(t, r\hat{\mathbf{\Omega}})$. We can obtain the mode decomposition of ξ by directly integrating Eq. (10.32) over the radial distance, obtaining

$$(\tilde{\xi}_l^m(\omega))^2 = \left(\frac{\alpha l_p}{2\pi^2 c_s}\right) \left(\frac{\omega_0}{2}\right)^2 \left[\int_0^L dr\, j_l\left(\frac{\omega r}{c_s}\right)\right]^2 . \tag{10.37}$$

This can be further approximated as

$$(\tilde{\xi}_l^m(\omega))^2 \approx \left(\frac{\alpha l_p}{2\pi^2 c_s}\right) \times \begin{cases} \frac{\pi}{2} \left(\frac{\omega_0 c_s}{2\omega}\right)^2 \frac{1}{l} & \text{if } l \ll (\omega L/c_s) \\ (C_l)^2 \left(\frac{\omega L}{c_s}\right)^{2l} (\omega_0 L)^2 & \text{if } l \gg (\omega L/c_s) \end{cases} . \tag{10.38}$$

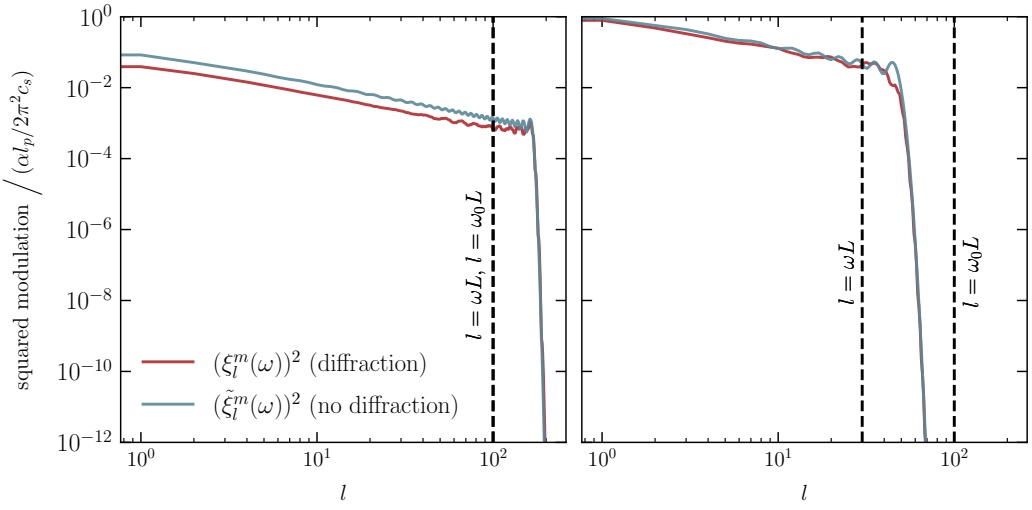

Figure 10.4: Plots of the modulations on the aperture, $(\xi_l^m(\omega))^2$ (red, Eq. (10.34)) and $(\tilde{\xi}_l^m(\omega))^2$ (blue, Eq. (10.37)), as functions of l with and without considering diffraction respectively. The curves are obtained by numerical integration. The left panel assumes $\omega_0 L = \omega L = 100$ while the right panel assumes $\omega_0 L = 100$ and $\omega L = 30$. The y-axes are normalized to $\alpha l_p/2\pi^2 c_s$.

where we also took the $l \gg 1$ limit with Stirling's approximation in the first entry. Comparing the result (10.35) from diffraction and the result (10.38) ignoring diffraction, one immediately observes that for both analyses, the high l-modes are severely suppressed, and will not produce any blurring effects. On the other hand, the amplitudes of the low l-modes in both analyses scale as $1/l$ with identical scalings in frequencies when $\omega \lesssim \omega_0$, and with numerical factors agreeing up to $O(1)$.

In Fig. 10.4 we plot in red the $|\tilde{\xi}_l^m(\omega)|^2$ obtained by numerically integrating Eq. (10.37) — and confirm that this agrees with the diffraction results (shown in blue) up to an $O(1)$ factor. We thus conclude that the diffraction effect does not qualitatively change the level and correlation structure of phase modulation on the telescope's aperture.

10.5 Conclusion

In this paper, we studied the effect of spacetime fluctuations from the VZ effect, specifically modeled by the pixellon field, on the blurring of astrophysical images. We concluded that it is not constrained by such observations. Even though the VZ effect, similar to the previously considered random walk models, leads to a root-mean-squared path length fluctuation of $\sim \sqrt{l_p L}$, we have shown that the transverse

correlation between phase modulations on the telescope's aperture will lead to a suppression factor of D/L, where D is the size of the aperture. More specifically, in Sec. 10.2, we used the pixellon model to compute the two-point correlation function of path length fluctuations on the telescope's aperture, and then employed a Zeta-function regularization technique to obtain UV-independent values for two-point correlations of phase fluctuations of light on the aperture. In Sec. 10.3, we applied scalar diffraction theory to convert this level of phase fluctuations to the level of image blurring, confirming that the VZ effect cannot be constrained by image blurring with foreseeable technology.

In Sec. 10.4, we incorporated the effect of diffraction on light propagation with spacetime fluctuations from the pixellon model. Unlike in Ref. [541] which considered a spacetime foam model of quantum fluctuations, diffraction does not qualitatively modify the correlation structure of light in the pixellon mode. In this way, diffraction alone does not provide a physical mechanism for the UV cutoff that underlies the Zeta-function regularization carried out in Sec. 10.2.

Note that our results are in contradiction to the claim made by Ref. [539], which incorrectly analyzed the model of Ref. [7] without properly renormalizing the UV divergence. One concludes that the VZ effect, as motivated by the 't Hooft commutation relations, can give rise to observably large effects in interferometers, while remaining consistent with the observations of images of distant stars.

Appendix A

SIGNAL GENERATION MONTE CARLO

Our goal is to compute the impact of a population of subhalos on the timing residuals measured in a PTA. The signal from an individual subhalo, given in Eq. (2.8), is a function of a few random variables, specifically: the subhalo mass, M, initial position, $\vec{r}^0$, and velocity, $\vec{v}$. To generate the full signal all of these variables must be generated for each subhalo. We assume that these probability distributions are independent and identically distributed (iid). With these assumptions the population can be generated by drawing random variables from three probability density functions (pdfs):

- $f_{\vec{r}}(\vec{r})$: the subhalo spatial distribution;
- $f_{\vec{v}(\vec{v})}$: the subhalo velocity distribution;
- $f_M(M)$: the subhalo mass distribution (related to the subhalo mass function, $d\tilde{n}/d\log M$ as described below),

all of which are normalized to 1: $\int dX f_X(X) = 1$. Since PTA searches are only sensitive to DM subhalos in the neighborhood of the solar system, we expect the position distribution to be uniform. Therefore we take $f_{\vec{r}=1/V}$, where V is the simulation volume. Practically this volume is limited by the total number of subhalos that can be kept in the simulation. The velocity distribution, $f_{\vec{v}(\vec{v})}$, is taken to be a Maxwell-Boltzmann distribution with $v_0 = 325$ km/s, $v_{\rm esc} = 600$ km/s, and the angular dependence assumed to be isotropic. The larger value of v_0 relative to the standard choice of ~ 200 km/s is chosen to account for the Earth or pulsar velocity relative to the Galactic rest frame.[1] Lastly, the mass distribution can be written in terms of the subhalo mass function as

$$f_M(M) = \frac{1}{\bar{n}M}\frac{d\tilde{n}}{d\log M}\,, \tag{A.1}$$

[1] This also introduces an anisotropy in the velocity distribution which creates spurious finite volume effects in the simulation. Since we do not expect the anisotropy to change our results significantly we ignore this effect.

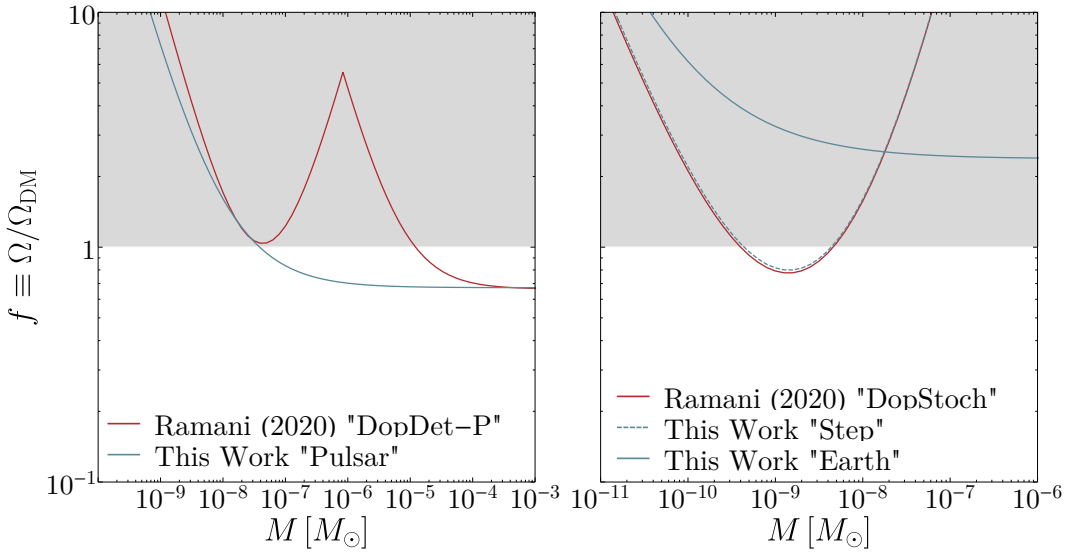

Figure A.1: Comparison of the PBH constraints between this work and [42]. The left panel compares the pulsar term results while the right panel compares the Earth term results. The meanings of the labels are described in the main text. The pulsar parameters used here are $N_p = 200$, $\Delta t = 2$, $t_{\rm rms} = 50$ and $T = 20$. The SNR thresholds are set to SNR = 4 for the pulsar term and SNR = 2 for the earth term for consistency with [42].

where $\overline{n} \equiv \int dM d\tilde{n}/dM$. The concentration parameters are then taken from the concentration-mass relationship, $c(M)$, as discussed in Sec. 2.4. We also generate the pulsar directions, $\hat{\vec{d}}$ in Eq. (2.8), from a uniform distribution on the sphere.

Given these pdfs, the Monte Carlo generates a large number (taken to be 1000 in our results) of different universe realizations and in each computes the total phase shift, Eq. (2.9), due to subhalos surrounding the Earth or pulsar. The total phase shift is computed on a uniform grid of time points with spacing equal to the cadence, Δt, and total number of points equal to $T/\Delta t$. The residual signal in each pulsar, h_I, is then computed by finding the best fit to the parameters ϕ^0, ν, and $\dot{\nu}$ in the timing model of (5.37) and subtracting the best fit timing model from the total phase shift. These h_I's are then used to compute the SNRs discussed in Sec. 2.2 for each realization. To draw constraints we take the $10^{\rm th}$ percentile SNR across universes. The statistical significance of a given SNR is discussed below in App. C.

The results derived here are more complete and subsume the previous works [43, 42]. To illustrate the differences with the previous results, in Fig. A.1 we compare the constraints on the fraction of DM in PBHs, $f = \Omega_{\rm PBH}/\Omega_{DM}$. The curves labelled "DopDet-P" in the left panel and "DopStoch" in the right panel are taken from [42],

which are analogous to the “pulsar term" and “Earth term" analysis presented in this work. The main difference between the more recent work, Ref. [42], and this analysis is how the signal is calculated. Previously the signal $h_I(t)$ and its autocorrelator were computed using analytic approximations, and the constraints were cut off when these were no longer good expressions. Here we explicitly generate the residual signal h_I which avoids the need of analytic simplifications. More specifically, for the “DopDet-P" curve in [42] the signal $\delta\phi(t)$ was approximated by the leading order term in the power series in the small (dynamic) and large (static) τ/T limits. By contrast, this work does not use the aforementioned approximations. This allows the constraint to smoothly interpolate between the two regimes and asymptote to the “DopDet-P" curves in both limits. Similarly, the “DopStoch" curve was obtained using an approximate form of the correlation function $R(t,t')$, which was derived analytically from the step function approximation of $\delta\phi(t)$. As shown in Fig. A.1, the constraint has a non-negligible deviation from this work, which is an indication that the approximations used in [42] is overly optimistic near the peak of the constraint. For an explicit comparison we ran the MC using the same approximate form of $\delta\phi(t)$ in [42], keeping only subhalos with impact parameter satisfying $b < \bar{v}T$. The resulting constraints are labelled “Step" in the right hand panel of Fig. A.1 and we see good agreement with the result in [42].

Appendix B

COMPARISON BETWEEN ANALYTIC AND NUMERICAL HALO MASS FUNCTION

In this appendix we compare the numerically derived HMF for axion models where the PQ symmetry is broken after inflation [118], against some commonly used analytic prescriptions. Specifically, we compare the numerical result against the analytic predictions of the Press-Schechter [106], and Sheth-Tormen [563] formalisms. The first one has been described in the main text, for convenience of reference we report here the differential halo mass fraction predicted by the PS formalism:

$$\frac{df_{PS}(M,z)}{d\ln M} = \sqrt{\frac{2}{\pi}}\nu(M,z)\exp\left(-\frac{\nu^2(M,z)}{2}\right)\frac{d\ln\sigma(M,z)}{d\ln M}\,, \tag{B.1}$$

where $\nu(M,z) \equiv \delta_c/\sigma(M,z)$. The Sheth-Tormen formalism instead predict a differential halo mass fraction given by

$$\frac{df_{ST}(M,z)}{d\ln M} = A\sqrt{\frac{a}{\pi}}\nu(M,z)\left[1+\left(\frac{1}{a\,\nu^2(M,z)}\right)^p\right]\exp\left(-\frac{a\,\nu^2(M,z)}{2}\right)\frac{d\ln\sigma(M,z)}{d\ln M}\,, \tag{B.2}$$

where the choice of parameters $A = 0.3222$, $a = 707$, and $p = 0.3$ has been showed to best reproduce the numerical results (at least for the the case of ΛCDM).

The results of the comparison, at four different redshifts, are shown in Fig. B.1. The agreement between numerical and analytic results is quite good, with the exception of the high mass regime where simulations start to lose sensitivity.

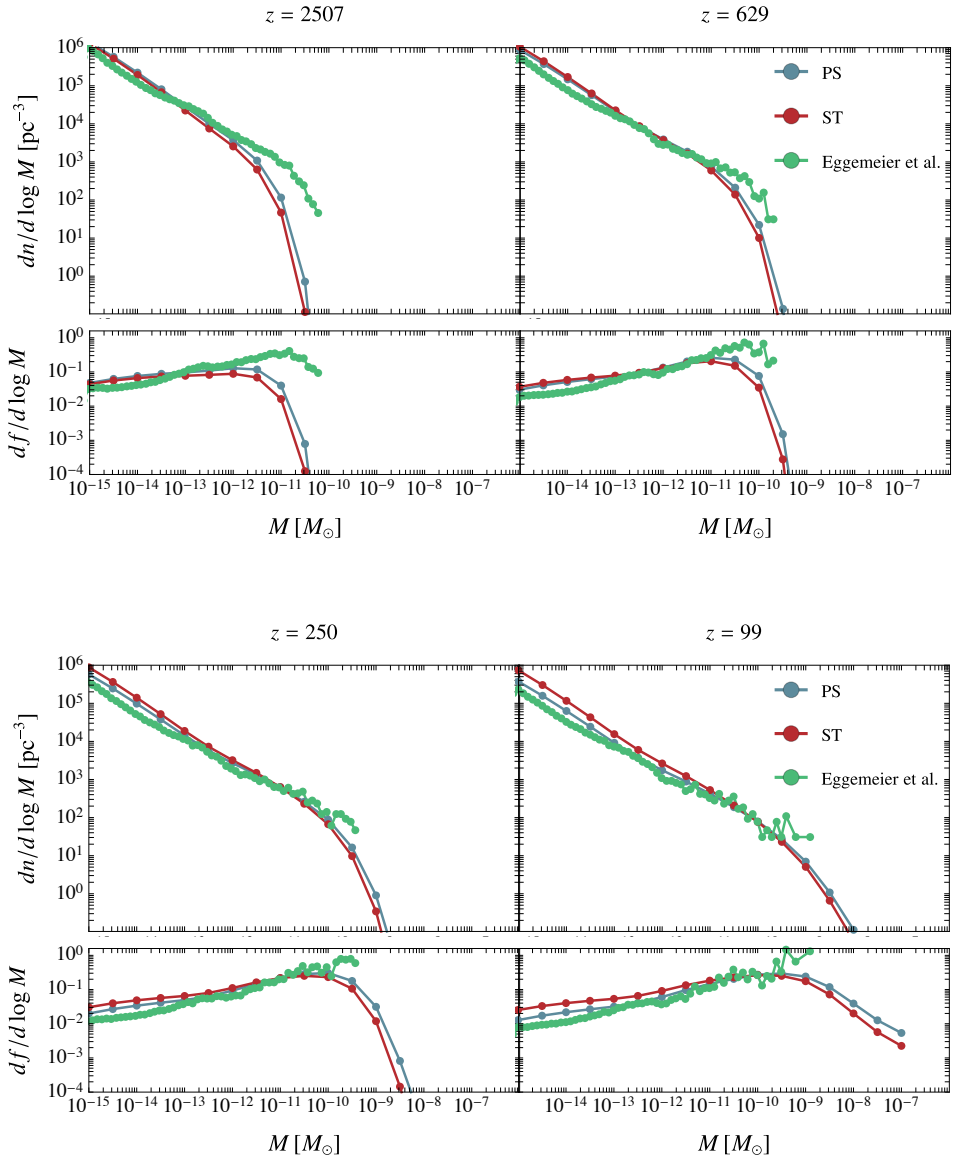

Figure B.1: Comparison between the HMF predicted by PS (blue) and the results of the numerical simulations (green) at four different redshifts. For comparison we also show the predictions of another analytical prescription (red) developed by Sheth & Tormen.

Appendix C

SNR STATISTICAL SIGNIFICANCE

In this section we discuss the statistical significance associated with a given observed value of the SNR, more specifically, we derive its p-value (*i.e* the probability that an SNR at least as large as the one observed is generated in presence of noise only).

In absence of a signal, the pulsar SNR given in (2.15) can be written as

$$\mathrm{SNR} = \frac{\left|\int dt\, n(t)\right|}{\left(\int dt dt' \langle n(t) n(t')\rangle\right)^{1/2}} = \frac{1}{\sqrt{T\widetilde{N}}}\left|\int dt\, n(t)\right| . \tag{C.1}$$

where we have drop the expectation value in the numerator because we want to study the full statistical distribution of the SNR, and ignored the filter functions for simplicity. Assuming that the noise is Gaussian, it is evident from the previous equation that the SNR in absence of a signal is distributed as the absolute value of a Gaussian variable with zero mean and unit standard deviation. From this follow that, given an array of N_P pulsars, the p-value for the pulsar term is

$$p(\mathrm{SNR}) = 1 - \left[\mathrm{erf}\left(\frac{\mathrm{SNR}}{\sqrt{2}}\right)^{N_P}\right] . \tag{C.2}$$

Assuming pulsar independent noise, the Earth SNR in absence of a signal takes the form

$$\mathrm{SNR} = \frac{\left|\sum_{I,J}\int dt dt' n_I(t) n_J(t')\right|}{\widetilde{N}\sqrt{2N_P(N_P-1)}} \tag{C.3}$$

where, as before, we have dropped the filter functions and the expectation value in the numerator. We now define

$$\rho \equiv \frac{\sum_I \int dt\, n_I(t)}{\sqrt{\widetilde{N} N_P T}} \tag{C.4}$$

which, by construction, is a Gaussian variable with zero mean and unit standard deviation. In terms of ρ, Eq. (C.3) can be rewritten as

$$\mathrm{SNR} = \frac{N_P}{\sqrt{2N_P(N_P-1)}}\rho^2 , \tag{C.5}$$

from which conclude that, in absence of signal, the Earth SNR follows a rescaled χ-squared distribution. Therefore, the p-value for the Earth term is given by

$$p(\mathrm{SNR}) = 1 - P(1/2, \frac{\sqrt{2N_P(N_P-1)}}{N_P}\,\mathrm{SNR}) \tag{C.6}$$

where $P(s,t)$ is the regularized gamma function.

Finally, when showing our final results in the main text, we express p-values in terms of standard deviations by using the relation

$$\sigma_{\mathrm{significance}}(p) = \sqrt{2}\mathrm{erf}^{-1}(1-2p)\,. \tag{C.7}$$

As an example, an SNR = 4 corresponds (both for the pulsar and Earth term) to a p-value of $p \sim 0.01$, and a signal significance of $\sigma_{\mathrm{significance}} \sim 2$.

Appendix D

CLASSICAL ORBITS AND $b_{\max}$ UNDER A LONG-RANGE INTERACTION

In this appendix we consider orbits of point-like DM about a static NS given both a gravitational and Yukawa force between them, as described in Sec. 5.1. Our primary goal is to identify the impact parameters of orbits that intersect the NS, which requires finding the location of centrifugal barriers. The barriers can occur at radii $r \gtrsim \lambda$ where the fifth force is starting to turn on, and at radii much smaller than the force range, where general and special relativity can be relevant. We begin with a reminder of the gravity-only case and then generalize to include the Yukawa interaction.

The general relativistic expression of energy conservation given a spherically symmetric star of mass M and a much lighter orbiting body of mass m comes from the constraint $p_\mu p^\mu = -m^2$. Employing the Schwarzschild metric and coordinates, $p_t = g_{tt} m \frac{dt}{d\tau} = -E = -m\gamma$ and $p_\phi = g_{\phi\phi} m \frac{d\phi}{d\tau} = L = \gamma m b v$ are conserved quantities along geodesics, where v is the asymptotic DM speed, $\gamma = 1/\sqrt{1-v^2}$, and b is the impact parameter. With these identifications the constraint reads,

$$\left(\frac{dr}{d\tau}\right)^2 = \frac{E^2}{m^2} - \left(\frac{(L/m)^2}{r^2} + 1\right)\left(1 - \frac{2GM}{r}\right). \tag{D.1}$$

Given a large enough impact parameter, DM streaming in from infinity with asymptotic speed v hits a centrifugal barrier, where $\frac{dr}{d\tau} \to 0$.

Given an additional attractive Yukawa interaction, the four-momentum constraint is the same, but $E \to E - V_{\rm Yuk}$. So orbits obey[1]

$$\left(\frac{dr}{d\tau}\right)^2 = \left(\frac{E - V_{\rm eff,+}}{m}\right)\left(\frac{E - V_{\rm eff,-}}{m}\right) \tag{D.2}$$

[1]The NS's fifth force charge could non-negligibly affect the general relativistic lapse function when $\frac{GQ_{\rm NS}^2}{R^2} =_n \left(\left(\frac{Q}{M/m_n}\right)_{\rm NS}\frac{GM}{R}\right)^2 \gtrsim 0.1$. So a consistency requirement is $\sqrt{n}\left(\frac{Q}{M/m_n}\right)_{\rm NS} \ll 1$. Since equivalence principle measurements restrict $_n \lesssim 10^{-11}$-10^{-9} for the force ranges we examine, the condition easily holds when baryonic charge (and not captured DM charge) dominates the total NS charge.

with[2]

$$\frac{V_{\text{eff},\pm}}{m} = -\frac{GM\tilde{\alpha}e^{-r/\lambda}}{r} \pm \sqrt{\left(1-\frac{2GM}{r}\right)\left(\frac{(L/m)^2}{r^2}+1\right)}. \tag{D.3}$$

The turning points, r_{min}, of unbound orbits—i.e. centrifugal barriers—occur at the maximum radial coordinate for which $V_{\text{eff},+} = E$. Solving the condition for the impact parameter, b, yields,

$$b(r_{\text{min}}) = r_{\text{min}}\sqrt{\frac{1+\frac{2GM}{r_{\text{min}}\gamma^2v^2}\left(1+e^{-r_{\text{min}}/\lambda}\right)+\left(\frac{GM}{r_{\text{min}}\gamma v}e^{-r_{\text{min}}/\lambda}\right)^2}{\left(1-\frac{2GM}{r_{\text{min}}}\right)}}. \tag{D.4}$$

DM focused through gravity alone breaches a NS surface iff $b < b(R)|_{\to 0} = R\sqrt{1+\frac{2GM/Rv^2}{1-2GM/R}} \approx \sqrt{\frac{2GMR/v^2}{1-2GM/R}}$.

For large $\tilde{\alpha}$, the exponential turn-on of the fifth force can lead to an additional partial centrifugal barrier at $r > \lambda$, and the peak of the inner centrifugal barrier near the Schwarzschild radius moves to larger radial coordinates. These behaviors are demonstrated in Fig. D.1, which shows examples of $V_{\text{eff},+}$ and E assuming $v = 10^{-3}$ for $\lambda = 10^{-11}$. When $\tilde{\alpha} = 20$ (orange), the centrifugal barrier appears first in the inner region where $r < \lambda$. When $\tilde{\alpha} = 50$ (purple), the centrifugal barrier appears in the outer region where $r > 2\lambda$. In these examples, DM orbits either hit a centrifugal barrier at $r > R$ or they intersect the neutron surface when $\frac{dr}{d\tau} > 0$; there are no orbits that just barely touch the NS surface.

The solid lines in Fig. D.1 correspond to conserved angular momentum $L = \gamma m b_{\text{max}} v$. For large , as can be seen in the figure, b_{max} and the coordinate of the barrier's peak, r_{b}, are the solutions to

$$V'_{\text{eff},+}(r_{\text{b}})|_{L=\gamma m b_{\text{max}} v} = 0, \qquad V_{\text{eff},+}(r_{\text{b}})|_{L=\gamma m b_{\text{max}} v} = \gamma m. \tag{D.5}$$

For very large there are two solutions, corresponding to the inner and outer barriers, respectively. The maximum impact parameter of DM that intersects the NS is the solution with smallest b_{max}.

Using $v^2 \ll \frac{GM}{R} \ll 1$ and $\lambda \gg R$, we find that a very good analytic approximation for b_{max} is given by the minimum of

$$b_{\text{max, inner}} \approx \frac{R}{v}\sqrt{\frac{\frac{2GM}{R}\left(1+\tilde{\alpha}e^{-R/\lambda}\right)+\left(\frac{GM}{R}\tilde{\alpha}e^{-R/\lambda}\right)^2}{\left(1-\frac{2GM}{R}\right)}} \tag{D.6}$$

[2] C.f. [564].

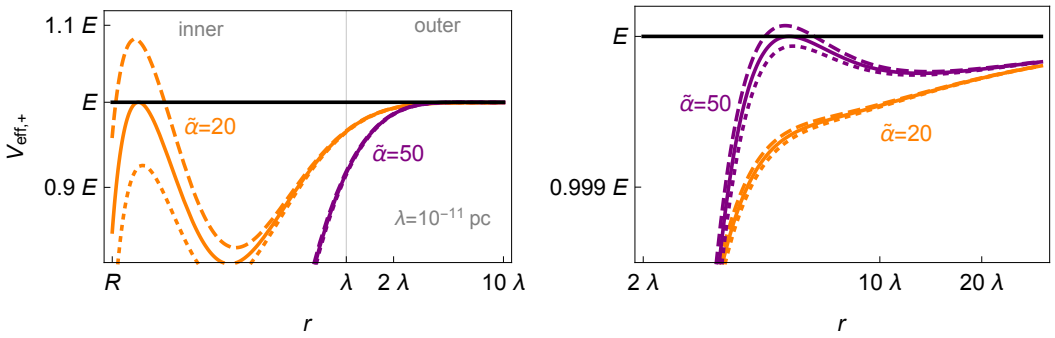

Figure D.1: $V_{\text{eff},+}$ as a function of DM radial coordinate when $b = b_{\max}$ (solid) and $b = 10^{\pm 0.01} b_{\max}$ (dashed/dotted), with $\lambda = 10^{-11}$, $v = 10^{-3}$, and $\tilde{\alpha} = 20$ (orange) or $\tilde{\alpha} = 50$ (purple). The right-hand plot shows only the outer region, with the vertical (logarithmic) scale magnified. In this example, the inner barrier determines $b_{\max}$ for $\tilde{\alpha} = 20$ while the outer barrier determines $b_{\max}$ for $\tilde{\alpha} = 50$. C.f. Fig. D.2.

and

$$b_{\max,\,\text{outer}} \approx \sqrt{\lambda x \left(\frac{2GM}{v^2} + \lambda x\right)} \quad \text{with} \quad x \approx \log\left(\frac{\tilde{\alpha}}{\frac{\lambda v^2}{GM} + \frac{1}{\log \tilde{\alpha}}}\right) \gtrsim 2 + \log 2, \tag{D.7}$$

so

$$b_{\max} = \min\left(b_{\max,\,\text{inner}}, b_{\max,\,\text{outer}}\right). \tag{D.8}$$

Fig. D.2 shows our analytic approximation in eq: b (color) alongside numerical solutions to eq: bmax numerical (black)[3] as a function of for three choices of force range, λ, assuming $v \sim 10^{-3}$, $R = 10$, and $\frac{GM}{R} = 0.2$. The inner barrier controls $b_{\max}$ at small $\tilde{\alpha}$. For $\tilde{\alpha} \gg 1$, $b_{\max}$ grows in proportion to $\tilde{\alpha}$ until it is cut to logarithmic growth because of the outer centrifugal barrier at radial distances greater than λ.

We end this appendix with a few comments on our analytic approximation and the behavior of $b_{\max}$. eq: b inner is the impact parameter for which the effective potential equals E at the NS surface in the $v \ll 1$ limit—i.e. $b(R)$ from eq: b of rmin. It is only a slight overestimate of the impact parameter for which the inner centrifugal barrier peaks at E (c.f. Fig. D.1), and it is exact in the limit $\to 0$. In the opposite limit and when $\lambda \gg R$, $b_{\max,\,\text{inner}} \approx \frac{GM}{v}\tilde{\alpha}$; the effective radius of the NS is approximately the geometric mean of the Coulomb classical and circular radii ($GM\tilde{\alpha}$ and $\frac{GM\tilde{\alpha}}{v^2}$, respectively). eq: b outer comes from analyzing the effective potential in the $\frac{GM}{r}, \frac{(L/m)^2}{r^2} \ll 1$ limit (the nonrelativistic limit), and $r_{\text{p}} \approx \lambda x$. For

[3]When $\frac{GM}{R} = 0.2$ and $\lambda \gg R$, $r_{\text{p}} \lesssim R$ when $\lesssim 6$, and $b_{\max}$ is given exactly by eq: b inner. The exact cutoff at small depends somewhat sensitively on $\frac{GM}{R}$.

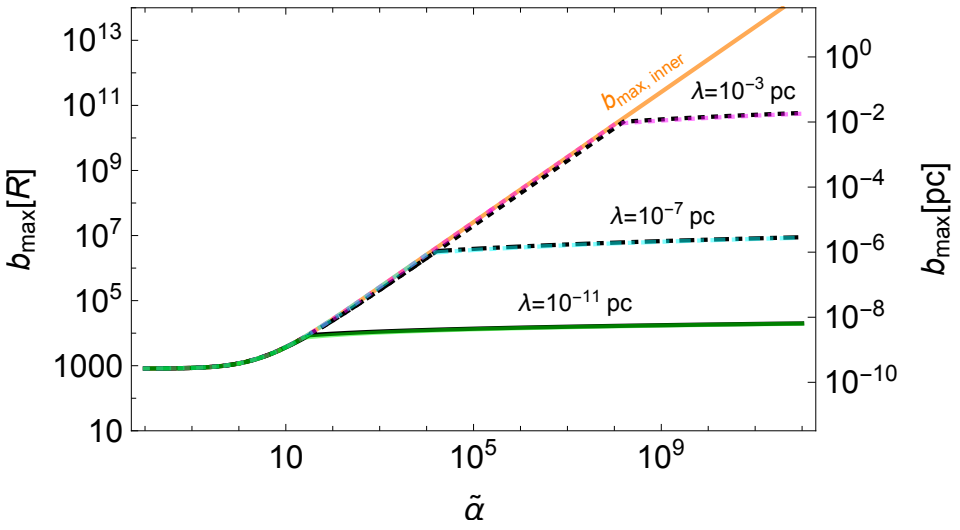

Figure D.2: Maximum impact parameter for which DM with asymptotic speed $v \sim 10^{-3}$ intersects a NS with circumferential radius R, assuming $\frac{GM}{R} = 0.2$, as a function of $\tilde{\alpha}$. The quoted λ values and right-hand scale assume $R = 10$. The black lines show (more exact) numerical results while the colored lines show our analytic approximation in eq: b, which agrees with the numerical results to within better than a factor of 2 in the entire range. The kink in the $b_{\rm max}$ curves correspond to the point where the outer centrifugal barrier at $r > \lambda$ occurs at smaller b than the inner barrier closer to $r \sim R$. C.f. Fig. D.1.

$x \lesssim 2$, the outer barrier does not exist. When the Yukawa force is much smaller than the gravitational force at the gravitational circular radius, $\tilde{\alpha} e^{-GM/v^2\lambda} \ll 1$, gravity is important in determining $b_{\rm max,\ outer}$, and $b_{\rm max,\ outer} \to \frac{1}{v}\sqrt{2\lambda GM \log(\tilde{\alpha} \log \tilde{\alpha})}$. In the opposite extreme, when $\tilde{\alpha} e^{-GM/v^2\lambda} > 1$, gravity is unimportant in determining the location of the barrier, and $b_{\rm max,\ outer} \to \lambda \log\left(\frac{\tilde{\alpha} GM}{\lambda v^2}\right)$. This latter case is the only one where $b_{\rm max} v$ evolves appreciably as a function of v; in all other limits discussed, $b_{\rm max} v$ is essentially constant.[4] When computing averages over the asymptotic DM velocity distribution, we use the fact that bv is nearly constant or—in the limit just discussed—mildly increasing (less than linearly) as a function of v.

[4]When $v \ll 1$, we expect $(L/m) \approx bv$ to be nearly independent of v for orbits that sweep near the NS surface because the kinetic energy at closest approach is essentially independent of v; it is instead dominated by the fifth force and gravitational potential energy loss.

Appendix E

TIMESCALE FOR NEUTRON STAR KINETIC HEATING FROM CAPTURED DARK MATTER

In this appendix we estimate the period of the first obit after DM is captured by depositing energy $\Delta E_{\rm graze}$ during a transit of a NS. Our approach is inspired by that in [303]. As long as the apastron of this orbit, $r_{\rm max}$, is large so that $\tilde{\alpha}\frac{GM}{r_{\rm max}}e^{-r_{\rm max}/\lambda}, \frac{GM}{r_{\rm max}} \ll 1$, a non-relativistic treatment yields a good estimate because then the DM is non-relativistic on parts of its trajectory near the apastron, where it spends the majority of its time. We proceed with a non-relativistic analysis.

The apastron is related to the DM's conserved non-relativistic energy, E, and orbital angular momentum magnitude, L, through

$$E = -\frac{GMm_X}{r_{\rm max}}(1+\tilde{\alpha}e^{-r_{\rm max}/\lambda}) + \frac{1}{2}\frac{L^2}{m_X r_{\rm max}^2}. \tag{E.1}$$

And the period of an orbit with apastron $r_{\rm max}$ and periastron $r_{\rm min}$ is

$$\Delta t = 2\int_{r_{\rm min}}^{r_{\rm max}} \frac{dr}{\dot{r}} = 2\int_{r_{\rm min}}^{r_{\rm max}} \left(\frac{2E}{m_X} + \frac{2GM}{r}\left(1+\tilde{\alpha}e^{-r/\lambda}\right) - \frac{(L/m_X)^2}{r^2}\right)^{-1/2} dr. \tag{E.2}$$

Assuming orbital angular momentum doesn't increase upon capture, $L_{\text{closed orbit}} \leq m_X b_{\rm max} v$, and the orbital angular momentum term negligibly affects the period of orbits with $r_{\rm max} \ggg R$, which are the orbits with the largest contribution to the total energy deposit timescale, we get

$$\Delta t \approx 2\int_0^{r_{\rm max}} \left(\frac{2GM(1+\tilde{\alpha}e^{-r/\lambda})}{r} - \frac{2GM(1+\tilde{\alpha}e^{-r_{\rm max}/\lambda})}{r_{\rm max}}\right)^{-1/2} dr. \tag{E.3}$$

The above equation is the period of a maximally eccentric orbit. It reduces to Kepler's third law, $\Delta t = 2\pi\frac{a^{3/2}}{\sqrt{GM}}$ for a maximally eccentric orbit, where $a = r_{\rm max}/2$, when the ratio of the fifth force to the gravitational force at the apastron is very small, $\tilde{\alpha}(1+\frac{r_{\rm max}}{\lambda})e^{-r_{\rm max}/\lambda} \ll 1$. To extremely good accuracy when the force ratio at the apastron is either very small or very large, we find the integral can be approximated as

$$\Delta t \approx \frac{\Delta t_\circ(r_{\rm max})}{2\sqrt{2}} = \frac{\pi}{\sqrt{2}}\frac{r_{\rm max}^{3/2}/\sqrt{GM}}{\sqrt{1+\tilde{\alpha}\left(1+\frac{r_{\rm max}}{\lambda}\right)e^{-r_{\rm max}/\lambda}}} \tag{E.4}$$

where $\Delta t_\circ$ is the period of a circular orbit with radius $r_{\rm max}$. eq: orbit period is an overestimate. The overestimate is most significant when the force ratio at the apastron is comparable to 1 and $\tilde{\alpha}$ is large, but it comes within a factor of 4 as long as $\tilde{\alpha} \lesssim 10^{30}$.

The apastron of the orbit after the first encounter, $r_{\rm max,1}$, is given by the solution to

$$\frac{1}{2}m_X v^2 - \Delta E_{\rm graze} = -\frac{GMm_X}{r_{\rm max,1}}\left(1+\tilde{\alpha}e^{-r_{\rm max,1}/\lambda}\right) + \frac{m_X}{2}\frac{(L_1/m_X)^2}{r_{\rm max,1}^2}. \tag{E.5}$$

A good estimate of the period of the first orbit after capture, Δt_1, is given by eq: orbit period evaluated at $r_{\rm max} = r_{\rm max,1}$ determined by eq: rmax1 with $L_1 = 0$ (a maximally eccentric orbit). We note that $r_{\rm max,1}$ is an increasing function of v and $r_{\rm max,1}(v) < r_{\rm max,1}(0)/(1 - v^2/v_{\rm max}^2)$ so that $\Delta t(v) \lesssim \frac{\Delta t(0)}{(1-v^2/v_{\rm cap}^2)^{3/2}}$. For asymptotic speeds up to about $0.8\, v_{\rm cap}$, $\Delta t_1(v) \approx \Delta t_1(0)$ is a good estimate; the period rapidly asymptotes to infinity thereafter, as $v \to v_{\rm cap}$.

Altogether, we have,

$$\Delta t_1(0) \approx GM\frac{\pi}{\sqrt{2}}\left(\frac{m_X}{\Delta E_{\rm graze}}\right)^{3/2}\frac{\left(1+\tilde{\alpha}e^{-r_{\rm max,1}/\lambda}\right)^{3/2}}{\sqrt{1+\tilde{\alpha}\left(1+\frac{r_{\rm max,1}}{\lambda}\right)e^{-r_{\rm max,1}/\lambda}}} \tag{E.6}$$

where we redefined $r_{\rm max,1}$ to be defined through eq: rmax1 with $v = 0, L_1 = 0$:

$$\Delta E_{\rm graze} = \frac{GMm_X}{r_{\rm max,\,1}}(1+e^{-r_{\rm max,\,1}/\lambda}). \tag{E.7}$$

When $r_{\rm max,1} \gg \lambda$ and $\frac{r_{\rm max,1}}{\lambda}\tilde{\alpha}e^{-r_{\rm max,1}/\lambda} \ll 1$, the period of the first orbit after capture is approximately $\Delta t_1 \approx GM\frac{\pi}{\sqrt{2}}\left(\frac{m_X}{\Delta E_{\rm graze}}\right)^{3/2}$. When $r_{\rm max,\,1} \sim \frac{GMm_X(1+)}{\Delta E_{\rm graze}} \ll \lambda$, $\Delta t_1 \approx GM\frac{\pi}{\sqrt{2}}\left(\frac{m_X}{\Delta E_{\rm graze}}\right)^{3/2}(1+\tilde{\alpha})$.

The timescale is the limiting factor in the tidal heating rate when $\Delta t_1 \gtrsim t_{\rm NS}$. From eq: orbit period, $r_{\rm max,1} > \left(\frac{\sqrt{2GM}}{\pi}\Delta t_1(0)\right)^{2/3}$ so $\Delta t_1 \gtrsim t_{\rm NS}$ requires $r_{\rm max} \gtrsim \left(t_{\rm NS}\sqrt{GM}\right)^{2/3} \sim 10\left(\frac{t_{\rm NS}}{}\right)^{2/3}$. For $\lambda \ll \left(t_{\rm NS}\sqrt{GM}\right)^{2/3}$ and $\tilde{\alpha} < \frac{\lambda}{\left(t_{\rm NS}\sqrt{GM}\right)^{2/3}}e^{\left(t_{\rm NS}\sqrt{GM}\right)^{2/3}/\lambda}$, we see $\Delta t_1 = t_{\rm NS}$ corresponds to the contour $\Delta t_1 = GM\frac{\pi}{\sqrt{2}}\left(\frac{m_X}{\Delta E_{\rm graze}}\right)^{3/2} = t_{\rm NS}$.

Appendix F

PULSAR GLITCHES

In principle DM can transfer both energy and angular momentum to pulsars. At most, DM can transfer its entire angular momentum, $m_X b v$, during a close-range interaction. This would cause a typical shift in the pulsar frequency—a glitch—of at most

$$\Delta\nu \approx \frac{|\Delta L_{\rm NS}|}{I_{\rm NS}} \approx \frac{m_X \langle b_{\rm max} v\rangle}{\frac{2}{5} M R^2} \approx 10^5 \left(\frac{m_X}{M}\right)\left(\frac{\langle b_{\rm max} v\rangle}{R}\right)\left(\frac{10\,{\rm km}}{R}\right){\rm Hz}. \tag{F.1}$$

Meanwhile, the DM glitch rate per NS is at most the DM flux, given by,

$$\dot{N}_{\rm glitch} \lesssim \frac{\rho_X}{m_X}\pi\langle b_{\rm max}^2 v\rangle \sim \frac{10^{-24}}{\rm yr}\frac{R^2}{(10\,{\rm km})^2}\frac{\rho_X}{0.4\,{\rm GeV/\,cm^3}}\frac{1.4 M_\odot}{M}\frac{10^{-3}}{v_p}\left(\frac{\langle b_{\rm max}^2 v\rangle v_p}{R^2}\right)\frac{M}{m_X}. \tag{F.2}$$

Consider $\Delta\nu \sim 10^{-9}$Hz as a benchmark.[1] Given gravity only, $\langle b_{\rm max} v\rangle/R \sim 1$, requiring $m_X/M \gtrsim 10^{-14}$ for a glitch of order 10^{-9}Hz or greater, and the rate for such glitches is order $\dot{N}_{\rm glitch} \sim \frac{10^{-10}}{\rm yr}$ or less for the fiducial parameters in (F.2).

However, the presence of a DM-NS fifth force with range greater than order a thousand kilometers opens up the possibility for larger $b_{\rm max}$; thus smaller m_X could cause detectable glitches at greater rates than in the gravity-only case just discussed. Given maximal kinetic heating, the coldest observed NS constrains $\tilde{\alpha} \lesssim 10^2$ for $\lambda \gtrsim 10^{-10}$ pc (see Eq. 5.33), corresponding to $\frac{\langle b_{\rm max} v\rangle}{R} \lesssim \frac{GM}{R} 10^2 \sim 20$. To get typical glitches of order 10^{-9}Hz or greater, one would require $\frac{m_X}{M} \gtrsim 10^{-15}$ and thus a glitch rate less than about 10^{-6} per NS per year.

To conclude, in principle, a DM-baryon fifth force may have given rise to an interesting DM-induced pulsar glitch phenomenon, but kinetic heating limits rule this out.

[1] Several convincing detections of frequency shifts as low as order $\Delta\nu \gtrsim 10^{-9}$Hz have been made [565, 566, 567]. See Ref. [568] for a discussion of thresholds.

Appendix G

PARAMETER RANGES AND LIMITS USED IN THE NEW PHYSICS SEARCH WITH NANOGRAV 15-YEAR DATASET

In this appendix, we specify the prior assumptions for all model parameters used in our analyses and report characteristic values for these parameters that we extract from the corresponding reconstructed 1D marginalized posterior distributions. In Table G.1, we list our prior assumptions for the pulsar-intrinsic red-noise parameters $A_{\rm red}$ and $\gamma_{\rm red}$ (A_a and γ_a in Eq. (6.4)) as well as for the SMBHB parameters and . In the latter case, we work with a bivariate normal distribution for $(\log_{10},)$ whose mean and covariance matrix are given by

$$\boldsymbol{\mu}_{\rm BHB} = \begin{pmatrix} -15.6 \\ 4.7 \end{pmatrix}, \qquad \sigma_{\rm BHB} = 10^{-1} \times \begin{pmatrix} 2.8 & -0.026 \\ -0.026 & 1.2 \end{pmatrix}, \tag{G.1}$$

which we obtain by fitting the $\log_{10}$ and distributions extracted from the SMBHB simulations in the `GWOnly-Ext` library in [344] (see Section 6.4). In Table G.2, we list our prior assumptions for the model parameters of all new-physics models considered in this work.

The Bayes estimator $\langle\theta\rangle$ of a parameter θ with marginalized 1D posterior probability distribution $P(\theta|\mathcal{D},\mathcal{H})$ corresponds to the expectation value with respect to the distribution $P(\theta|\mathcal{D},\mathcal{H})$, while the standard deviation σ_θ of the Bayes estimator corresponds to the positive square root of the associated variance σ_θ^2,

$$\begin{aligned} \langle\theta\rangle &= \int d\theta\, \theta\, P(\theta|\mathcal{D},\mathcal{H})\,, \\ \sigma_\theta^2 &= \langle\theta^2\rangle - \langle\theta\rangle^2 = \left[\int d\theta\, \theta^2\, P(\theta|\mathcal{D},\mathcal{H})\right] - \left[\int d\theta\, \theta\, P(\theta|\mathcal{D},\mathcal{H})\right]^2 . \end{aligned} \tag{G.2}$$

In practice, in a given analysis and for a given chain of MCMC samples, we compute the Bayes estimator and its standard deviation in terms of the corresponding sample mean and sample variance. The maximum posterior estimator $\theta_{\rm max}$ of a parameter θ with marginalized 1D posterior probability distribution $P(\theta|\mathcal{D},\mathcal{H})$ corresponds to the θ value where $P(\theta|\mathcal{D},\mathcal{H})$ reaches its global maximum across the predefined prior range,

$$P(\theta_{\rm max}|\mathcal{D},\mathcal{H}) = \max_\theta P(\theta|\mathcal{D},\mathcal{H})\,, \tag{G.3}$$

and the 68% Bayesian credible interval $\left[\theta_{68}^{\min}, \theta_{68}^{\max}\right]$ follows from integrating the posterior distribution $P(\theta|\mathcal{D}, \mathcal{H})$ over the regions of highest posterior density such that the integral returns an integrated probability of 68%,

$$\int_{\theta_{68}^{\min}}^{\theta_{68}^{\max}} d\theta \, P(\theta|\mathcal{D}, \mathcal{H}) = 0.68 \,, \tag{G.4}$$

where $P(\theta|\mathcal{D}, \mathcal{H}) > P_{68}$ for all $\theta \in \left[\theta_{68}^{\min}, \theta_{68}^{\max}\right]$ and some appropriate threshold P_{68}. Similarly, we can also construct 95% Bayesian credible intervals.

$$K\left(\theta_K\right) = \frac{P(\mathcal{D}|\theta_K, \mathcal{H})}{P(\mathcal{D}|\theta_0, \mathcal{H})} = \frac{1}{10} \,. \tag{G.5}$$

Note that, unlike all other quantities discussed in this section, the K ratio is not defined in terms of a posterior probability distribution, but rather in terms of a likelihood ratio, which makes it robust against our prior assumptions.

Parameter	Description	Prior
	Pulsar-Intrinsic Red Noise	
$A_{\rm red}$	red-noise power-law amplitude	log-Uniform $[-20, -11]$
$\gamma_{\rm red}$	red-noise power-law spectral index	Uniform $[0, 7]$
	Supermassive Black Bole Binaries (SMBHB)	
$(\log_{10} A_{\rm BHB}, \gamma_{BHB})$	SMBHB signal amplitude and slope	Normal$(\mu_{\rm BHB}, \sigma_{\rm BHB})$

Table G.1: Prior distributions for the pulsar-intrinsic red-noise parameters and the parameters of the astrophysical SMBHB signal. The mean and covariance matrix of the Gaussian prior distribution for $(\log_{10},)$ are given in Eq. (G.1). The red noise parameters are independent for each pulsar, while the SMBHB parameters are common across the PTA.

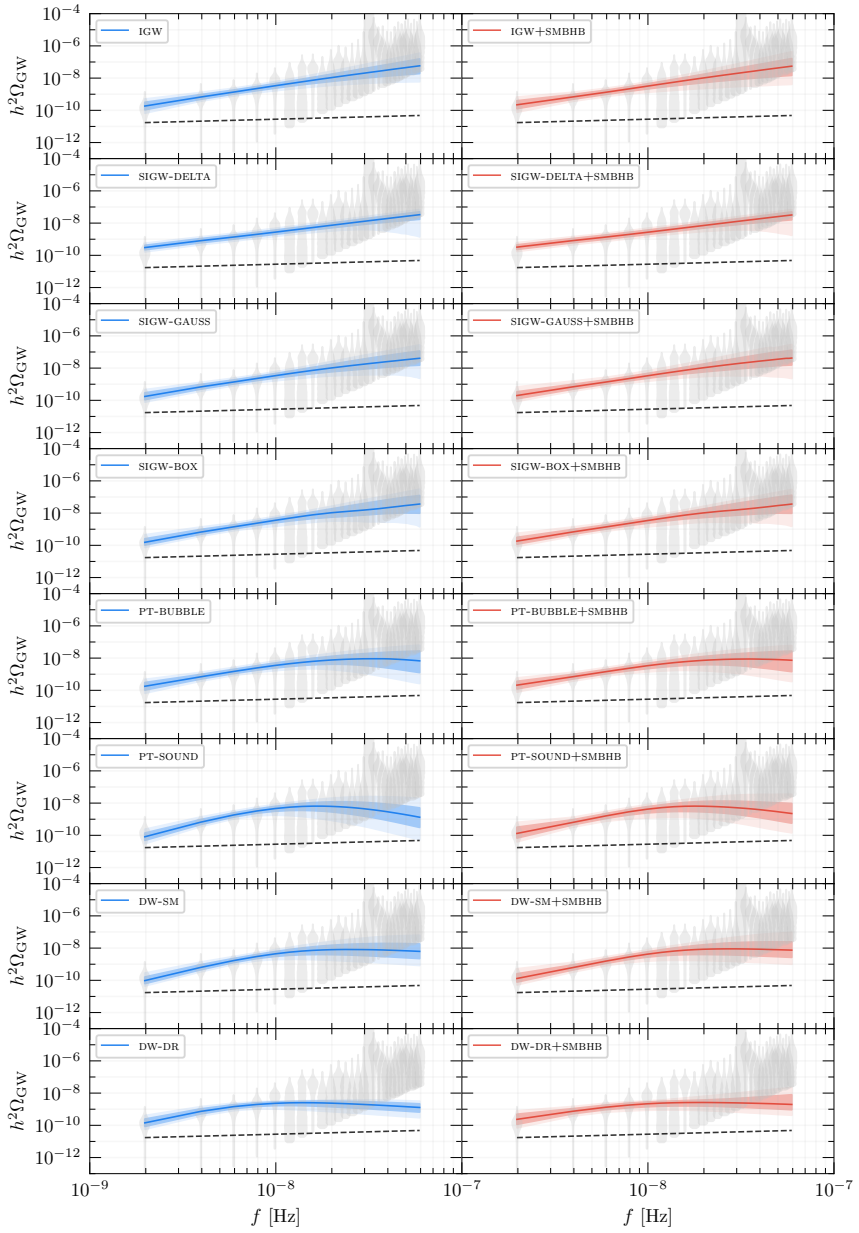

Figure G.1: Median GWB spectra (solid lines) for all new-physics models considered in this work except for the cosmic-string models, together with their 68% and 95% posterior envelopes. Median GWB spectra for the cosmic-string models are shown in Fig. G.2. In the left column (blue shading), we show the median GWB spectra for the new-physics models alone; in the right column (red shading), we combine the new-physics signals with the signal from SMBHBs. The gray violins are symmetrical representations of the 1D marginalized posterior probability density distributions of the GW energy density at each sampling frequency of the data. The dashed black lines show the GWB spectrum produced by inspiraling SMBHBs (see caption of Fig. 6.3).

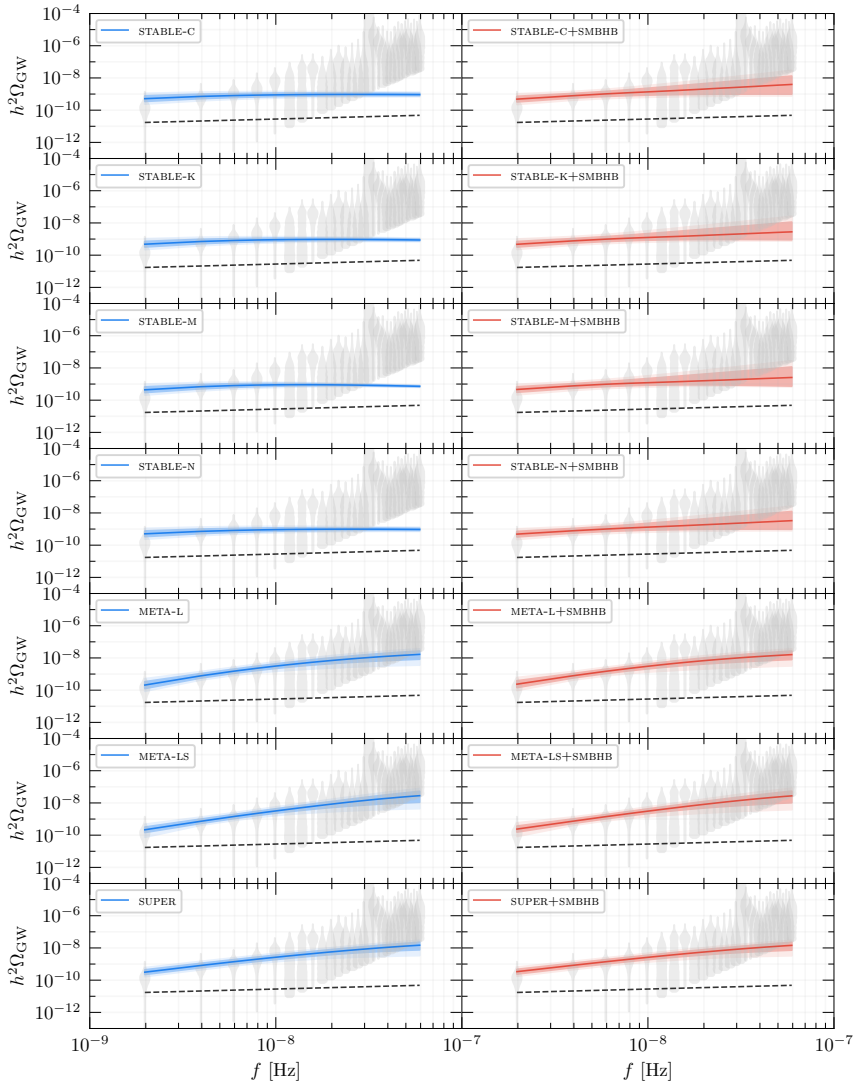

Figure G.2: Same as Fig. G.1 but for the cosmic-string models considered in this work.

Parameter	Description	Prior
	Cosmological phase transition (PT)	
T_* [GeV]	transition temperature	log-uniform $[-4, 4]$
α_*	transition strength	log-uniform $[-2, 1]$
H_*R_*	bubble separation	log-uniform $[-3, 0]$
a	low-frequency slope (PT-BUBBLES)	uniform $[1, 3]$
a	low-frequency slope (PT-SOUND)	uniform $[3, 5]$
b	high-frequency slope (PT-BUBBLES)	uniform $[1, 3]$
b	high-frequency slope (PT-SOUND)	uniform $[2, 4]$
c	spectral-shape width (PT-BUBBLES)	uniform $[1, 3]$
c	spectral-shape width (PT-SOUND)	uniform $[3, 5]$
	Primordial black holes (PBH-DYNAMIC)	
A	signal amplitude	log-uniform $[-20, -12]$
$T_0/T_{\rm obs}$	normalized time of closest approach	uniform $[0, 1]$
	Primordial black holes (PBH-STATIC)	
A	signal amplitude	log-uniform $[-21, -13]$

Table G.2: Priors distributions for the parameters of the new-physics models considered in this work. All paramters listed in this table are common across the PTA.

Appendix H

SUPPLEMENTARY MATERIAL IN THE NEW PHYSICS SEARCH WITH NANOGRAV 15-YEAR DATASET

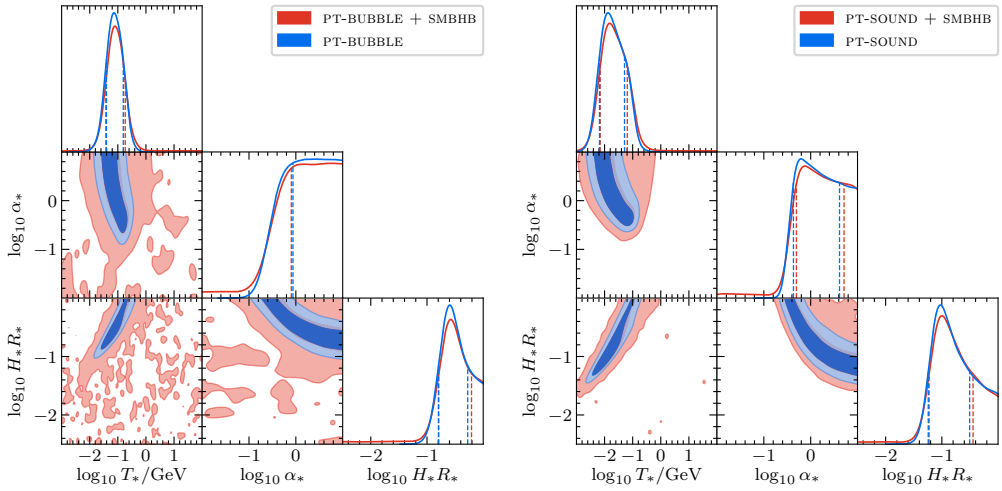

Figure H.1: Reconstructed posterior distributions for the PT-SOUND (left panel) and PT-BUBBLE models with a low-frequency slope fixed to the value predicted by causality, *i.e.*, $a = 3$.

Cosmological phase transitions

In the phase transition analysis discussed in the main text, we allow the low-frequency spectral index to float despite that causality predicts $a = 3$. We do this to capture possible double-peak spectral features with our simple power-law parametrization. However, it is not clear whether or not a strong and fast phase transition like the one needed to explain the observed signal could produce such a double-peak structure [402, 409]. Therefore, in Fig. H.1 we report the results of a phase transition analysis where we assume $a = 3$. Figure H.1 shows the reconstructed posterior distributions for the parameters α_*, T_*, and H_*R_* of the PT-SOUND and PT-BUBBLE models, both for the case where the PT is assumed to be the only source of GWs (blue contours) and for the scenario where we consider the superposition of the PT and SMBHBs signal (red contours). For the analyses where the SMBHB signal is included, we also report the posterior distributions for $A_{\rm BHB}$ and $\gamma_{\rm BHB}$. For the PT-SOUND model we notice very minor differences compared to the analysis in the

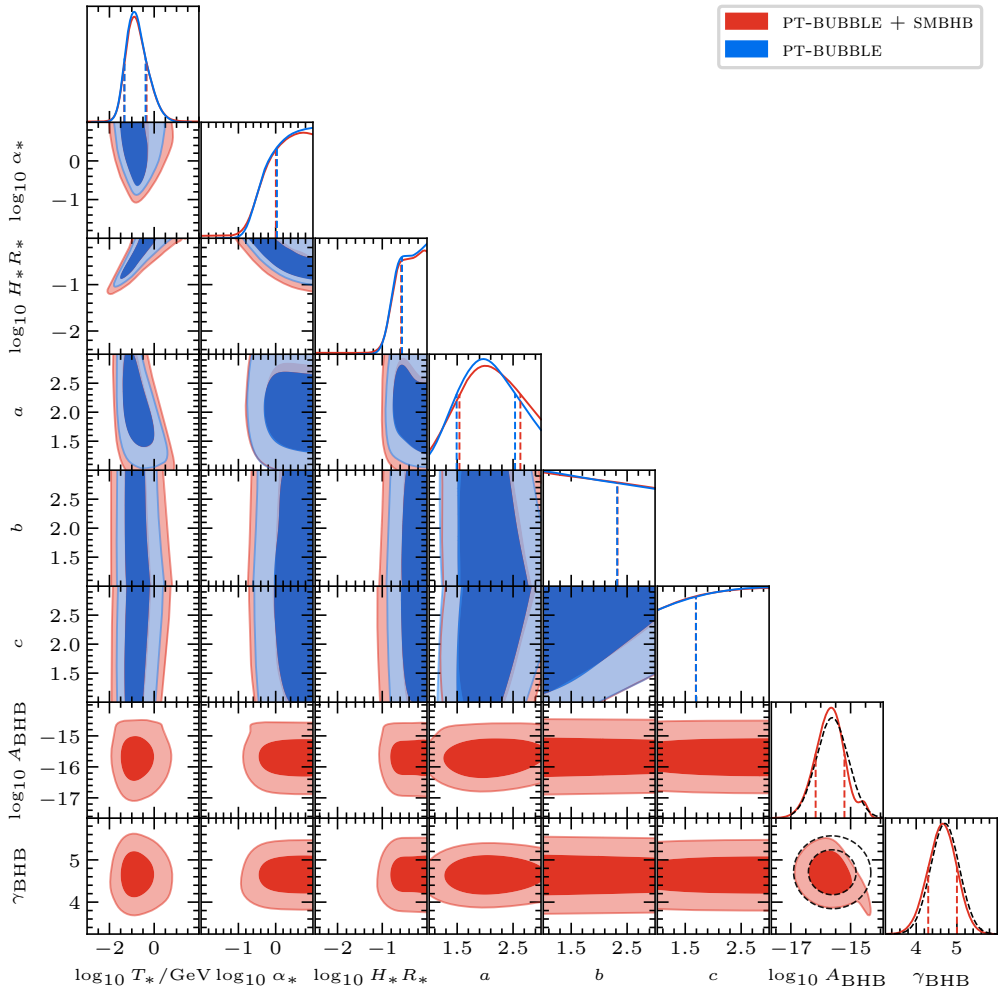

Figure H.2: Same as Fig. 6.4 but including the spectral shape parameters a, b, c and SMBHB parameters $A_{\rm BHB}$ and $\gamma_{\rm BHB}$.

main text. However, for the PT-BUBBLE model we notice how the posterior for T_* is peaked to slightly smaller values for the reasons explained in the main text.

In Figs. H.2 and H.3, we report the posterior distributions for all the parameters of the phase transition models, including the spectral shape parameters a, b, and c that were excluded from Fig. 6.4. As expected for the PT-BUBBLE model, the low-frequency slope is peaked around $a \sim 2$, which is the reconstructed slope of the GWB signal, while the posteriors for b and c are approximately flat. For the PT-SOUND model, the posterior for a is peaked around the lower limit of the prior range $a = 3$, and there is also a mild preference for larger values of the width parameter, as this would flatten the spectrum close to the peak.

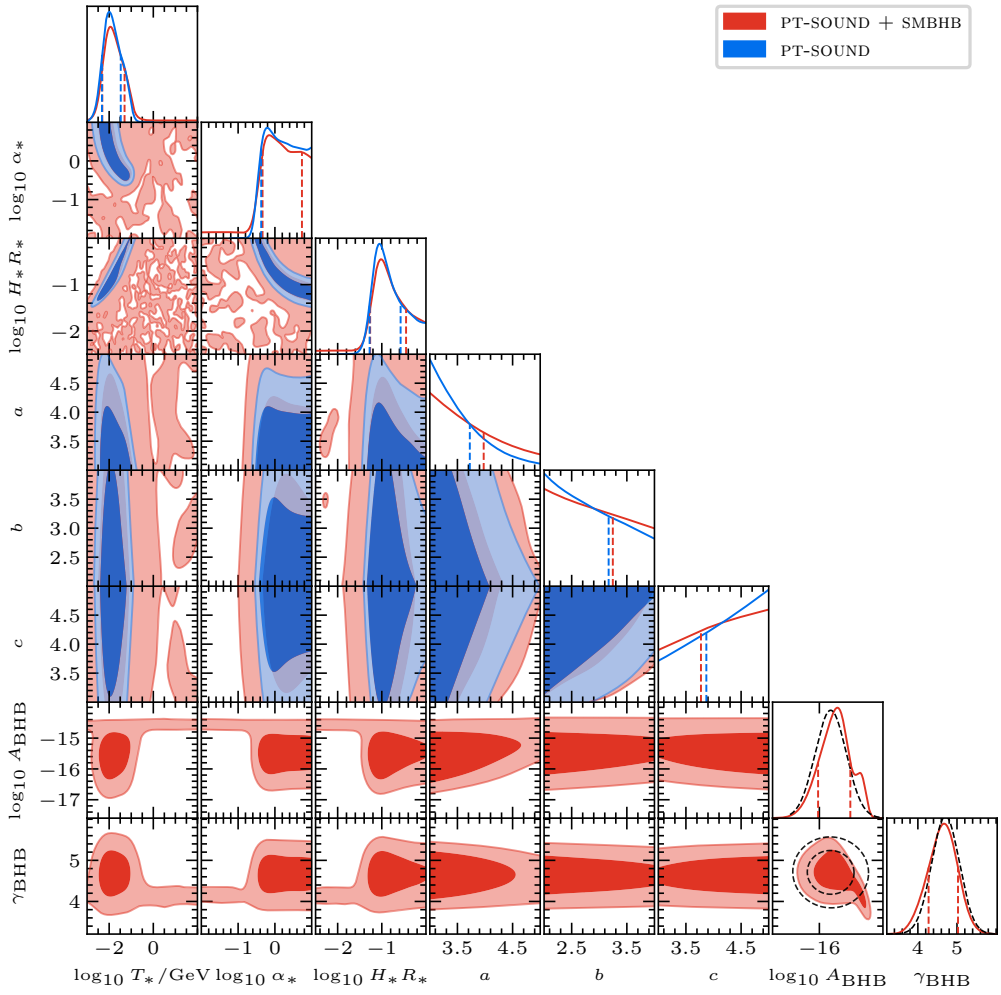

Figure H.3: Same as Fig. H.2 but for the PT-SOUND model.

Dark matter substructures

In this appendix we provide more details on the procedure that we followed to derive the constraints on $f_{\rm PBH}$ reported in Section 6.6.

Given a PBH with position relative to the pulsar given by $r(t) = r_0 + vt$, where r_0 and v are the initial PBH position and velocity, respectively, we can write the Doppler and Shapiro signals as

$$h_D(t) = \frac{GM}{v^2}\hat{\boldsymbol{d}} \cdot \left(\sqrt{1+x_D^2}\hat{\boldsymbol{b}}_D - \sinh^{-1}(x)\hat{\boldsymbol{v}}\right) \tag{H.1}$$

$$h_S(t) = 2GM \log(1+x_S^2)\,, \tag{H.2}$$

where $x_{\rm D} \equiv (t - t_{\rm D,0})/\tau_{\rm D}$ and $x_{\rm S} \equiv (t - t_{\rm S,0})/\tau_{\rm S}$. These expressions only include cubic terms in time t and have been previously derived in [43, 10]. For the static

limit in which $\tau \gg T_{\rm obs}$, these expressions can be expanded in series of t_0/τ. Since the $O(t^2)$ terms would be degenerate with the timing model, the measurable new-physics signal can then be parametrized as a term $\propto t^3$ as

$$h(t)_{\rm D(S)} = \frac{A_{\rm D\,(S),\,sta}}{\rm yr^2} t^3 \,, \tag{H.3}$$

where $A_{\rm D(S),\,sta}$ for both the Doppler and Shapiro static signal cases are dimensionless amplitudes given by

$$A_{\rm D,\,stat} = {\rm yr}^2 \frac{GM}{2v^2} \hat{\boldsymbol{d}} \cdot \left[\frac{t_{D,0}}{\tau_D^4} \frac{1}{(1+t_{D,0}^2/\tau_D^2)^{5/2}} \hat{\boldsymbol{b}}_D + \frac{1}{3\tau_D^3} \frac{1 - 2t_{D,0}^2/\tau_D^2}{(1+t_{D,0}^2/\tau_D^2)^{5/2}} \hat{\boldsymbol{v}} \right] \tag{H.4}$$

$$A_{\rm S,\,stat} = -{\rm yr}^2 \frac{4GM}{3} \frac{t_{S,0}}{\tau_S^4} \frac{3 - t_{S,0}^2/\tau_S^2}{(1+t_{S,0}^2/\tau_S^2)^3} \,. \tag{H.5}$$

For the Doppler case, in the dynamic limit when $\tau \ll T_{obs}$, the dominant contribution would come from the first term in Eq. (H.1) where $\sqrt{1+x_D^2} \propto |t - t_0|$. Upto linear order in x_D, we can write

$$h_{D,\rm dyn}(t) = A_{D,\rm dyn}(t - t_0)\Theta(t - t_0) \,, \tag{H.6}$$

where $A_{\rm D,dyn}$ is the dimensionless amplitude given by

$$A_{D,\rm dyn} = \frac{2GM}{\tau v^2} \hat{\boldsymbol{d}} \cdot \hat{\boldsymbol{b}}_D \,. \tag{H.7}$$

Given the expressions in Eqs. (H.1) and (H.2) for the Doppler and Shapiro signals, we use the MC developed in [9] to derive the distributions $p(\log_{10} A_I | f_{\rm PBH})$. Specifically, we proceed as follows:

• For each pulsar we generate a population of $N_{\rm PBH}$ PBHs, where $N_{\rm PBH}$ is implicitly defined by the relation

$$N_{\rm PBH} = f_{\rm PBH} \frac{\rho_{DM} V}{M_{\rm PBH}} \,, \tag{H.8}$$

where the simulation volume, V, is a sphere of radius $R = \bar{v} T_{obs}$ centered around the pulsar position for the Doppler signal and a cylinder with the same radius and height given by the Earth–pulsar distance for the Shapiro signal. Here $\bar{v} \simeq 340\, km/s$ is the average PBH velocity, and $T_{obs,I}$ is the observation time of the Ith pulsar.

• For each of these PBHs we generate a random initial position and velocity. Since PTA searches are only sensitive to DM subhalos in the neighborhood of the solar

system, we expect the position distribution to be uniform. Therefore, we use the probability density function $f(r) = 1/V$ to sample initial positions. To sample PBHs' velocity, we use a Maxwell–Boltzmann distribution with $v_0 = 325\,kms^{-1}$, $v_{esc} = 600\,kms^{-1}$, and the angular dependence assumed to be isotropic.

• The PBHs' signals are then classified as dynamic if they satisfy the condition $T_{obs,I} - \tau > t_0 > \tau$, and static otherwise.

• To evaluate $A_{\rm stat}$, we sum the static signals of all PBHs computed by using Eqs. (H.1) and (H.2), and we fit the resulting signal to a cubic polynomial in time to extract the t^3 term. To compute $A_{D,dyn}$, we take the closest transiting object and compute the signal amplitudes using Eq. (H.7).

All the previous points are repeated for 2.5×10^3 realizations to obtain the distributions $p(\log_{10} A_I|f_{\rm PBH})$. Given the conditional distributions $p(\log_{10} A_I|f_{\rm PBH})$ and the posterior distribution $p(\log_{10} A_I|\boldsymbol{\delta t})$ derived by analyzing our data, we can write

$$p\left(f_{\rm PBH}|\boldsymbol{\delta t}\right) = \prod_{I=1}^{N_P} \int p(f_{\rm PBH}|\log_{10} A_I) p\left(\log_{10} A_I|\boldsymbol{\delta t}\right) d\log_{10} A_I\,. \tag{H.9}$$

Then, using Bayes' theorem, we can rewrite

$$p\left(f_{\rm PBH}|\log_{10} A_I\right) = \frac{p\left(\log_{10} A_I|f_{\rm PBH}\right) p\left(f_{\rm PBH}\right)}{p\left(\log_{10} A_I\right)}\,. \tag{H.10}$$

Our priors on $p\left(f_{\rm PBH}\right)$ and $p\left(\log_{10} A_I\right)$ are uniform, which allows us to eventually write Eq. (H.9) as

$$p\left(f_{\rm PBH}|\boldsymbol{\delta t}\right) \propto \prod_{I=1}^{N_P} \int p(\log_{10} A_I|f_{\rm PBH}) p(\log_{10} A_I|\boldsymbol{\delta t})\; d\log_{10} A_I\,, \tag{H.11}$$

where the $\propto$ implies that the $p(f_{\rm PBH}|\delta t)$ would be subject to the normalization condition, $\int_0^\infty p(f_{\rm PBH}|\boldsymbol{\delta t})\; df_{\rm PBH} = 1$.

In the presence of a DM-baryon fifth force in the form of a Yukawa potential in Eq. (6.26), assuming point-mass DM, the pulsar frequency shift due to Doppler effect is given by [5]

$$\left(\frac{\delta\nu}{\nu}\right)_{\rm fifth} = \frac{\tilde{\alpha} G M}{\tau_D^2 v}\hat{d}\cdot\int \frac{1}{(1+x_D^2)^{3/2}}\left(1+\frac{b}{\lambda}\sqrt{1+x_D^2}\right) e^{-(b/\lambda)\sqrt{1+x_D^2}}(\hat{b}+x_D\hat{v})dx_D\,. \tag{H.12}$$

The integral in Eq. (H.12) has to be computed numerically, and the signal due to the fifth force can be computed by performing an additional integration over time and subtracting away degeneracies with timing model parameters. The total signal is the sum of the gravitational and the fifth-force contribution, $h_{D,\,\mathrm{total}}(t) = h_{D,\,\mathrm{fifth}}(t) + h_{D(S)}(t)$. In this analysis of the fifth-foce constraint, we only consider the scenario where the DM substructure makes up the entirety of the DM local density, which is equivalent to taking $f_{\mathrm{PBH}} = 1$ for the gravitational contribution. Parameterizing the signal as $h_{\mathrm{D,\,total}}(t) = \frac{A_{D,\,\mathrm{total}}}{\mathrm{yr}^2} t^3$ similar to the PBH case, the amplitude $A_{D,\,\mathrm{total}}$ is a random variable dependent on λ and $\tilde{\alpha}$. The probability distribution function $P(\log_{10} A_{D,\,\mathrm{total}}|\lambda, \tilde{\alpha})$ can be extracted again by Monte Carlo simulations and Bayes' theorem. Finally, the posterior distribution of $\tilde{\alpha}$ and λ, $P(\tilde{\alpha}, \lambda|\boldsymbol{\delta t})$, is given by the analog of Eq. (H.11)

$$p\,(\tilde{\alpha}, \lambda|\boldsymbol{\delta t}) \propto \prod_{I=1}^{N_P} \int p(\log_{10} A_I|\tilde{\alpha}, \lambda) p(\log_{10} A_I|\boldsymbol{\delta t})\; d\log_{10} A_I\,. \tag{H.13}$$

Appendix I

ANGULAR FACTORS

In this appendix we derive the mean values of angular factors involving dot and cross products between $\hat{\mathbf{v}}$, $\hat{\mathbf{b}}$ and $\hat{\mathbf{n}}$, assuming an isotropic distribution of $\hat{\mathbf{v}}$, and a uniform distribution of $\hat{\mathbf{b}}$ constrained on a plane perpendicular to $\hat{\mathbf{v}}$. We note that while the DM velocity in the lab frame has a preferred direction, the isotropic velocity distribution is a good approximation for analytic estimates, as verified by the Monte Carlo simulation.

Without loss of generality, we set $\hat{\mathbf{n}} = (0, 0, 1)$ on the z-axis. In spherical coordinates, we write $\hat{\mathbf{v}} = (\sin\theta\cos\phi, \sin\theta\sin\phi, \cos\theta)$. Since $\hat{\mathbf{b}}$ is constrained to be perpendicular to $\hat{\mathbf{v}}$, we can write $\hat{\mathbf{b}} = \cos\varphi\hat{\mathbf{b}}_1 + \sin\varphi\hat{\mathbf{b}}_2$, where $\hat{\mathbf{b}}_1 = (-\sin\phi, \cos\phi, 0)$ and $\hat{\mathbf{b}}_2 = (\cos\theta\cos\phi, \cos\theta\sin\phi, -\sin\theta)$ are orthogonal unit vectors that are perpendicular to $\hat{\mathbf{v}}$. Averages over an angular factor X are then computed by the integral

$$\langle X\rangle = \frac{1}{8\pi^2}\int_0^\pi \sin\theta d\theta \int_0^{2\pi} d\phi \int_0^{2\pi} d\varphi\, X(\theta, \phi, \varphi)\,. \tag{I.1}$$

One easily evaluates $\hat{\mathbf{v}}\cdot\hat{\mathbf{n}} = \cos\theta$, $\hat{\mathbf{b}}\cdot\hat{\mathbf{n}} = -\sin\theta\sin\varphi$, $|\hat{\mathbf{v}}\times\hat{\mathbf{n}}|^2 = \sin^2\theta$ and $|\hat{\mathbf{b}}\times\hat{\mathbf{n}}|^2 = \cos^2\phi + \cos^2\theta\sin^2\phi$, giving

$$\begin{aligned}\langle(\hat{\mathbf{v}}\cdot\hat{\mathbf{n}})^2\rangle &= \langle(\hat{\mathbf{b}}\cdot\hat{\mathbf{n}})^2\rangle = \frac{1}{3}\\ \langle|\hat{\mathbf{v}}\times\hat{\mathbf{n}}|^2\rangle &= \langle|\hat{\mathbf{b}}\times\hat{\mathbf{n}}|^2\rangle = \frac{2}{3}\,.\end{aligned} \tag{I.2}$$

Cross terms between $\hat{\mathbf{b}}$ and $\hat{\mathbf{v}}$ include $(\hat{\mathbf{b}}\cdot\hat{\mathbf{n}})(\hat{\mathbf{v}}\cdot\hat{\mathbf{n}}) = -\sin\theta\cos\theta\sin\varphi$ and $(\hat{\mathbf{b}}\times\hat{\mathbf{n}})\cdot(\hat{\mathbf{v}}\times\hat{\mathbf{n}}) = \sin\theta\cos\theta\sin\varphi$, which integrate to zero

$$\begin{aligned}\langle(\hat{\mathbf{b}}\cdot\hat{\mathbf{n}})(\hat{\mathbf{v}}\cdot\hat{\mathbf{n}})\rangle &= 0\\ \langle(\hat{\mathbf{b}}\times\hat{\mathbf{n}})\cdot(\hat{\mathbf{v}}\times\hat{\mathbf{n}})\rangle &= 0\,.\end{aligned} \tag{I.3}$$

Higher-order factors include $(\hat{\mathbf{b}}\cdot\hat{\mathbf{n}})^4 = \sin^4\theta\sin^4\phi$, $(\hat{\mathbf{v}}\cdot\hat{\mathbf{n}})^4 = \cos^4\theta$ and $(\hat{\mathbf{b}}\cdot\hat{\mathbf{n}})^2(\hat{\mathbf{v}}\cdot\hat{\mathbf{n}})^2 = \sin^2\theta\cos^2\theta\sin^2\varphi$,

$$\begin{aligned}\langle(\hat{\mathbf{b}}\cdot\hat{\mathbf{n}})^4\rangle &= \langle(\hat{\mathbf{v}}\cdot\hat{\mathbf{n}})^4\rangle = \frac{1}{5}\\ \langle(\hat{\mathbf{b}}\cdot\hat{\mathbf{n}})^2(\hat{\mathbf{v}}\cdot\hat{\mathbf{n}})^2\rangle &= \frac{1}{15}\,.\end{aligned} \tag{I.4}$$

For interferometers with two arms separated by $\Delta\theta$, we set $\hat{\mathbf{n}}_1 = (0, 0, 1)$ and $\hat{\mathbf{n}}_2 = (0, \sin\Delta\theta, \cos\Delta\theta)$, again without loss of generality. Then the angular differences between the two arms are

$$\begin{aligned}
\langle[(\hat{\mathbf{b}}\cdot\hat{\mathbf{n}}_1) - (\hat{\mathbf{b}}\cdot\hat{\mathbf{n}}_2)]^2\rangle &= \langle[(\hat{\mathbf{v}}\cdot\hat{\mathbf{n}}_1) - (\hat{\mathbf{v}}\cdot\hat{\mathbf{n}}_2)]^2\rangle = \frac{4}{3}\sin^2\left(\frac{\Delta\theta}{2}\right) \\
\langle[(\hat{\mathbf{b}}\cdot\hat{\mathbf{n}}_1)^2 - (\hat{\mathbf{b}}\cdot\hat{\mathbf{n}}_2)^2]^2\rangle &= \langle[(\hat{\mathbf{v}}\cdot\hat{\mathbf{n}}_1)^2 - (\hat{\mathbf{v}}\cdot\hat{\mathbf{n}}_2)^2]^2\rangle = \frac{4}{15}\sin^2\Delta\theta \\
\langle[(\hat{\mathbf{b}}\cdot\hat{\mathbf{n}}_1)(\hat{\mathbf{v}}\cdot\hat{\mathbf{n}}_1) - (\hat{\mathbf{b}}\cdot\hat{\mathbf{n}}_2)(\hat{\mathbf{v}}\cdot\hat{\mathbf{n}}_2)]^2\rangle &= \frac{1}{5}\sin^2\Delta\theta\,. \qquad \text{(I.5)}
\end{aligned}$$

Appendix J

PHOTON TIME DELAY IN LASER INTERFEROMETERS UNDER A GENERAL METRIC

In this appendix, we derive the time delay of a generic metric in Eq. (9.28). There are three effects, from the clock rate, the mirror motion, and the light propagation. Only when summing all three do we obtain the gauge invariant observable.

We start by computing the clock's rate. Since $g_{tt} = -(1 - \mathcal{H}_0)$, to the leading order, the proper time differs from the coordinate time by

$$\frac{d\tau}{dt} \approx 1 - \frac{1}{2}\mathcal{H}_0 \,. \tag{J.1}$$

Thus, for a clock with radial position r when there is no metric fluctuation, the difference $\delta\tau$ between the proper time and the coordinate time from $t = t_1$ to $t = t_2$ is

$$\delta\tau(t_1, t_2, r) = -\frac{1}{2}\int_{t_1}^{t_2} dt'\, \mathcal{H}_0(t', r) \,. \tag{J.2}$$

To account for the mirror's motion, we consider the geodesic equation of the mirror

$$0 = \frac{d^2x^\mu}{d\tau^2} + \Gamma^\mu_{\alpha\beta}\frac{dx^\alpha}{d\tau}\frac{dx^\beta}{d\tau} \approx \frac{d^2x^\mu}{d\tau^2} + \Gamma^\mu_{tt} + \Gamma^\mu_{ti}v^i + \cdots \,. \tag{J.3}$$

Since the velocity of the mirror $v^i \ll 1$, to the leading order, $\frac{d^2r}{dt^2} \approx -\Gamma^r_{tt}$. Using $\Gamma^\mu_{\alpha\beta} = \frac{1}{2}\eta^{\mu\nu}(\partial_\alpha h_{\beta\nu} + \partial_\beta h_{\alpha\nu} - \partial_\nu h_{\alpha\beta})$, we get

$$\Gamma^r_{tt} = \partial_t h_{tr} - \frac{1}{2}\partial_r h_{tt} = \partial_t\mathcal{H}_1 - \frac{1}{2}\partial_r\mathcal{H}_0 \,, \tag{J.4}$$

so for a mirror at radius r when there is no metric fluctuation, its radial position $r_{\rm M}$ at coordinate time t is

$$r_{\rm M}(t, r) \approx \int^t dt' \int^{t'} dt'' \left[\frac{1}{2}\partial_r\mathcal{H}_0(t'', r) - \partial_{t''}\mathcal{H}_1(t'', r)\right] . \tag{J.5}$$

For the light propagation, the geodesic equation of outgoing light is

$$\frac{dt^{\rm out}}{dr} \approx 1 + \frac{1}{2}\left(\mathcal{H}_0 + \mathcal{H}_2 + 2\mathcal{H}_1\right) \equiv 1 + \frac{1}{2}\mathcal{H}^{\rm out} \,, \tag{J.6}$$

and for ingoing light,

$$\frac{dt^{\rm in}}{dr} \approx -1 - \frac{1}{2}\left(\mathcal{H}_0 + \mathcal{H}_2 - 2\mathcal{H}_1\right) \equiv -1 - \frac{1}{2}\mathcal{H}^{\rm in} \,. \tag{J.7}$$

In total, the proper time $T^{\rm out}$ the light beam takes to reach the mirror is

$$\begin{aligned} T^{\rm out} &\approx \int_{0+r_{\rm M}(0,0)}^{L+r_{\rm M}(L,L)} dr \ \left[1+\frac{1}{2}\mathcal{H}^{\rm out}(r,r)\right] + \delta\tau(0,L,0) \\ &\approx L + r_{\rm M}(L,L) - r_{\rm M}(0,0) + \delta\tau(0,L,0) \\ &\quad + \frac{1}{2}\int_0^L dr\ \mathcal{H}^{\rm out}(r,r)\,. \end{aligned} \tag{J.8}$$

Similarly, for the ingoing light beam,

$$\begin{aligned} T^{\rm in} &\approx \int_{L+r_{\rm M}(L,L)}^{0+r_{\rm M}(2L,0)} dr \ \left[-1-\frac{1}{2}\mathcal{H}^{\rm in}(2L-r,r)\right] + \delta\tau(L,2L,0) \\ &\approx L + r_{\rm M}(L,L) - r_{\rm M}(2L,0) + \delta\tau(L,2L,0) \\ &\quad + \frac{1}{2}\int_0^L dr\ \mathcal{H}^{\rm in}(2L-r,r)\,. \end{aligned} \tag{J.9}$$

Then the total time delay T is given by summing up Eqs. (J.8) and (J.9), $T = T^{\rm out}+T^{\rm in}$.

Appendix K

GAUGE INVARIANCE OF PHOTON TIME DELAY IN LASER INTERFEROMETERS

In this appendix, we show that the total time delay $T = T^{\rm out} + T^{\rm in}$, where $T^{\rm out}$ and $T^{\rm in}$ are defined in Eqs. (J.8) and (J.9), of the light beam traveling a round trip is a gauge invariant quantity. Since the $t - r$ sector of any metric, *e.g.*, Eq. (9.28), will only be affected by the gauge transformations of coordinate t or r, we will show that T is invariant under these two types of gauge transformations.

Gauge transformations of coordinate t

First, let's consider gauge transformations $x^\mu \to x^\mu + \xi^\mu$, where only $\xi_t \neq 0$, so the metric becomes

$$\begin{aligned} ds^2 = & -(1 - \mathcal{H}_0 + 2\partial_t\xi_t)dt^2 + (1 + \mathcal{H}_2)dr^2 \\ & + 2(\mathcal{H}_1 - \partial_r\xi_t)dtdr + \cdots . \end{aligned} \tag{K.1}$$

Since h_{tt} is modified, $\frac{d\tau}{dt} \to \frac{d\tau}{dt} + \frac{1}{2}\partial_t\xi_t$, the difference between the proper time and the coordinate time becomes

$$\delta\tau(t_1, t_2, r) \to \delta\tau(t_1, t_2, r) + \xi_t(t_2, r) - \xi_t(t_1, r) . \tag{K.2}$$

The geodesics equations of light beam are modified into

$$\frac{dt^{\rm out}}{dr} \approx 1 + \frac{1}{2}\left(\mathcal{H}^{\rm out} - 2\partial_t\xi_t - 2\partial_r\xi_t\right) , \tag{K.3}$$

$$\frac{dt^{\rm in}}{dr} \approx -1 - \frac{1}{2}\left(\mathcal{H}^{\rm in} - 2\partial_t\xi_t + 2\partial_r\xi_t\right) . \tag{K.4}$$

For mirror's motion, let's define

$$\delta r^{\rm out} \equiv r_{\rm M}(L, L) - r_{\rm M}(0, 0) , \tag{K.5}$$

$$\delta r^{\rm in} \equiv r_{\rm M}(L, L) - r_{\rm M}(2L, 0) . \tag{K.6}$$

Since $\Gamma^r_{tt} \to \Gamma^r_{tt} - \partial_t\partial_r\xi_t + \partial_r\partial_t\xi_t = \Gamma^r_{tt}$ remains unchanged, $\delta r^{\rm out}_{\rm M} \to \delta r^{\rm out}_{\rm M}$ and $\delta r^{\rm in}_{\rm M} \to \delta r^{\rm in}_{\rm M}$. In total,

$$\begin{aligned} T^{\rm out} &\to T^{\rm out} + \xi_t(L, 0) - \xi_t(0, 0) - \int_0^L dr \ \left(\partial_t\xi_t + \partial_r\xi_t\right)|_{t=r} \\ &= T^{\rm out} + \xi_t(L, 0) - \xi_t(L, L) , \end{aligned} \tag{K.7}$$

$$\begin{aligned} T^{\text{in}} &\to T^{\text{in}} + \xi_t(2L,0) - \xi_t(L,0) + \int_0^L dr \ \left(\partial_r \xi_t - \partial_t \xi_t\right)|_{t=2L-r} \\ &= T^{\text{in}} - \xi_t(L,0) + \xi_t(L,L)\,, \end{aligned} \tag{K.8}$$

so the total time delay of a round trip $T \to T$ under the gauge transformation of coordinate t.

Gauge transformations of coordinate r

Next, let's consider gauge transformations $x^\mu \to x^\mu + \xi^\mu$ with $\xi_r \neq 0$ only. The metric then becomes

$$\begin{aligned} ds^2 = &-(1-\mathcal{H}_0)dt^2 + (1+\mathcal{H}_2 - 2\partial_r\xi_r)dr^2 \\ &+ 2(\mathcal{H}_1 - \partial_t\xi_r)dtdr + \cdots\,. \end{aligned} \tag{K.9}$$

The relation between the proper time and the coordinate time remains unchanged. The ingoing and outgoing light's geodesics are modified to be

$$\frac{dt^{\text{out}}}{dr} \approx 1 + \frac{1}{2}\left(\mathcal{H}^{\text{out}} - 2\partial_r\xi_r - 2\partial_t\xi_r\right)\,, \tag{K.10}$$

$$\frac{dt^{\text{in}}}{dr} \approx -1 - \frac{1}{2}\left(\mathcal{H}^{\text{in}} - 2\partial_r\xi_r + 2\partial_t\xi_r\right)\,. \tag{K.11}$$

Γ^r_{tt} now becomes $\Gamma^r_{tt} \to \Gamma^r_{tt} - \partial_t^2\xi_r$, so

$$\delta r^{\text{out}}_{\text{M}} \to \delta r^{\text{out}}_{\text{M}} + \xi_r(L,L) - \xi_r(0,0)\,, \tag{K.12}$$

$$\delta r^{\text{in}}_{\text{M}} \to \delta r^{\text{in}}_{\text{M}} + \xi_r(L,L) - \xi_r(2L,0)\,. \tag{K.13}$$

Then, in total,

$$\begin{aligned} T^{\text{out}} &\to T^{\text{out}} + \xi_r(L,L) - \xi_r(0,0) - \int_0^L dr \ \left(\partial_r\xi_r + \partial_t\xi_r\right)|_{t=r} \\ &= T^{\text{out}}\,, \end{aligned} \tag{K.14}$$

$$\begin{aligned} T^{\text{in}} &\to T^{\text{in}} + \xi_r(L,L) - \xi_r(2L,0) - \int_0^L dr \ \left(\partial_r\xi_r - \partial_t\xi_r\right)|_{t=2L-r} \\ &= T^{\text{in}}\,, \end{aligned} \tag{K.15}$$

so T also remains invariant under the gauge transformation of coordinate r. Thus, we have shown that T is a gauge invariant quantity.

BIBLIOGRAPHY

[1] Vincent S. H. Lee, Kathryn M. Zurek, and Yanbei Chen. "Astronomical image blurring from transversely correlated quantum gravity fluctuations". In: *Phys. Rev. D* 109.8 (2024), p. 084005. DOI: 10.1103/PhysRevD.109.084005. arXiv: 2312.06757 [gr-qc].

[2] Sander M. Vermeulen et al. "Photon Counting Interferometry to Detect Geontropic Space-Time Fluctuations with GQuEST". Apr. 2024. arXiv: 2404.07524 [gr-qc].

[3] Adeela Afzal et al. "The NANOGrav 15 yr Data Set: Search for Signals from New Physics". In: *Astrophys. J. Lett.* 951.1 (2023), p. L11. DOI: 10.3847/2041-8213/acdc91. arXiv: 2306.16219 [astro-ph.HE].

[4] Yufeng Du, Vincent S. H. Lee, Yikun Wang, and Kathryn M. Zurek. "Macroscopic dark matter detection with gravitational wave experiments". In: *Phys. Rev. D* 108.12 (2023), p. 122003. DOI: 10.1103/PhysRevD.108.122003. arXiv: 2306.13122 [astro-ph.CO].

[5] Moira I. Gresham, Vincent S. H. Lee, and Kathryn M. Zurek. "Astrophysical observations of a dark matter-Baryon fifth force". In: *JCAP* 02 (2023), p. 048. DOI: 10.1088/1475-7516/2023/02/048. arXiv: 2209.03963 [astro-ph.HE].

[6] Sergei Gukov, Vincent S. H. Lee, and Kathryn M. Zurek. "Near-horizon quantum dynamics of 4D Einstein gravity from 2D Jackiw-Teitelboim gravity". In: *Phys. Rev. D* 107.1 (2023), p. 016004. DOI: 10.1103/PhysRevD.107.016004. arXiv: 2205.02233 [hep-th].

[7] Dongjun Li, Vincent S. H. Lee, Yanbei Chen, and Kathryn M. Zurek. "Interferometer response to geontropic fluctuations". In: *Phys. Rev. D* 107.2 (2023), p. 024002. DOI: 10.1103/PhysRevD.107.024002. arXiv: 2209.07543 [gr-qc].

[8] Zaven Arzoumanian et al. "Searching for Gravitational Waves from Cosmological Phase Transitions with the NANOGrav 12.5-Year Dataset". In: *Phys. Rev. Lett.* 127.25 (2021), p. 251302. DOI: 10.1103/PhysRevLett.127.251302. arXiv: 2104.13930 [astro-ph.CO].

[9] Vincent S. H. Lee, Andrea Mitridate, Tanner Trickle, and Kathryn M. Zurek. "Probing Small-Scale Power Spectra with Pulsar Timing Arrays". In: *JHEP* 06 (2021), p. 028. DOI: 10.1007/JHEP06(2021)028. arXiv: 2012.09857 [astro-ph.CO].

[10] Vincent S. H. Lee, Stephen R. Taylor, Tanner Trickle, and Kathryn M. Zurek. "Bayesian Forecasts for Dark Matter Substructure Searches with

Mock Pulsar Timing Data". In: *JCAP* 08 (2021), p. 025. DOI: 10.1088/1475-7516/2021/08/025. arXiv: 2104.05717 [astro-ph.CO].

[11] Vincent S. H. Lee and Kathryn M. Zurek. "Proper Time Observables of General Gravitational Perturbations in Laser Interferometry-based Gravitational Wave Detectors". In: (Aug. 2024). arXiv: 2408.03363 [hep-ph].

[12] Georges Aad et al. "Observation of a new particle in the search for the Standard Model Higgs boson with the ATLAS detector at the LHC". In: *Phys. Lett. B* 716 (2012), pp. 1–29. DOI: 10.1016/j.physletb.2012.08.020. arXiv: 1207.7214 [hep-ex].

[13] Nima Arkani-Hamed. "Beyond the Standard Model theory". In: *Phys. Scripta T* 158 (2013). Ed. by Tord Ekelöf, p. 014023. DOI: 10.1088/0031-8949/2013/T158/014023.

[14] Joel N. Butler et al. "Report of the 2021 U.S. Community Study on the Future of Particle Physics (Snowmass 2021)". In: (Jan. 2023). DOI: 10.2172/1922503.

[15] Nathaniel Craig. "Naturalness: past, present, and future". In: *Eur. Phys. J. C* 83.9 (2023), p. 825. DOI: 10.1140/epjc/s10052-023-11928-7. arXiv: 2205.05708 [hep-ph].

[16] Vera C. Rubin, W. Kent Ford Jr., and Norbert Thonnard. "Extended rotation curves of high-luminosity spiral galaxies. IV. Systematic dynamical properties, Sa through Sc". In: *Astrophys. J. Lett.* 225 (1978), pp. L107–L111. DOI: 10.1086/182804.

[17] D. J. Eisenstein. "Dark energy and cosmic sound". In: *New Astron. Rev.* 49.7-9 (2005), pp. 360–365. DOI: 10.1016/j.newar.2005.08.005.

[18] Scott W. Randall, Maxim Markevitch, Douglas Clowe, Anthony H. Gonzalez, and Marusa Bradac. "Constraints on the Self-Interaction Cross-Section of Dark Matter from Numerical Simulations of the Merging Galaxy Cluster 1E 0657-56". In: *Astrophys. J.* 679 (2008), pp. 1173–1180. DOI: 10.1086/587859. arXiv: 0704.0261 [astro-ph].

[19] B. P. Abbott et al. "Observation of Gravitational Waves from a Binary Black Hole Merger". In: *Phys. Rev. Lett.* 116.6 (2016), p. 061102. DOI: 10.1103/PhysRevLett.116.061102. arXiv: 1602.03837 [gr-qc].

[20] R. P. Feynman. *Feynman lectures on gravitation*. Ed. by F. B. Morinigo, W. G. Wagner, and B. Hatfield. 1996.

[21] John F. Donoghue. "The effective field theory treatment of quantum gravity". In: *AIP Conf. Proc.* 1483.1 (2012). Ed. by Waldyr Alves Rodrigues, Richard Kerner, Gentil Pires, and Carols Pinheiro, pp. 73–94. DOI: 10.1063/1.4756964. arXiv: 1209.3511 [gr-qc].

[22] S. W. Hawking. “Zeta Function Regularization of Path Integrals in Curved Space-Time”. In: *Commun. Math. Phys.* 55 (1977), p. 133. DOI: 10.1007/BF01626516.

[23] S. W. Hawking. “Breakdown of Predictability in Gravitational Collapse”. In: *Phys. Rev. D* 14 (1976), pp. 2460–2473. DOI: 10.1103/PhysRevD.14.2460.

[24] Daniel Harlow. “Jerusalem Lectures on Black Holes and Quantum Information”. In: *Rev. Mod. Phys.* 88 (2016), p. 015002. DOI: 10.1103/RevModPhys.88.015002. arXiv: 1409.1231 [hep-th].

[25] Daniel Harlow et al. “TF1 Snowmass Report: Quantum gravity, string theory, and black holes”. In: (Oct. 2022). arXiv: 2210.01737 [hep-th].

[26] Aaron Buikema et al. “Sensitivity and performance of the Advanced LIGO detectors in the third observing run”. In: *Phys. Rev. D* 102.6 (2020), p. 062003. DOI: 10.1103/PhysRevD.102.062003. arXiv: 2008.01301 [astro-ph.IM].

[27] Stephen R. Taylor. “The Nanohertz Gravitational Wave Astronomer”. In: (May 2021). arXiv: 2105.13270 [astro-ph.HE].

[28] Gabriella Agazie et al. “The NANOGrav 15 yr Data Set: Evidence for a Gravitational-wave Background”. In: *Astrophys. J. Lett.* 951.1 (2023), p. L8. DOI: 10.3847/2041-8213/acdac6. arXiv: 2306.16213 [astro-ph.HE].

[29] Freeman Dyson. “Is a graviton detectable?” In: *Int. J. Mod. Phys. A* 28 (2013), p. 1330041. DOI: 10.1142/S0217751X1330041X.

[30] Erik P. Verlinde and Kathryn M. Zurek. “Observational signatures of quantum gravity in interferometers”. In: *Phys. Lett. B* 822 (2021), p. 136663. DOI: 10.1016/j.physletb.2021.136663. arXiv: 1902.08207 [gr-qc].

[31] B. P. Abbott et al. “LIGO: The Laser interferometer gravitational-wave observatory”. In: *Rept. Prog. Phys.* 72 (2009), p. 076901. DOI: 10.1088/0034-4885/72/7/076901. arXiv: 0711.3041 [gr-qc].

[32] Albert Abraham Michelson and Edward Williams Morley. “On the Relative Motion of the Earth and the Luminiferous Ether”. In: *Am. J. Sci.* 34 (1887), pp. 333–345. DOI: 10.2475/ajs.s3-34.203.333.

[33] Valerie Domcke and Joachim Kopp. “Electromagnetic (high-frequency) gravitational wave detectors: Interferometers revisited”. In: *58th Rencontres de Moriond on Very High Energy Phenomena in the Universe*. June 2024. arXiv: 2406.03244 [gr-qc].

[34] Michele Maggiore. *Gravitational Waves. Vol. 1: Theory and Experiments*. Oxford University Press, 2007. ISBN: 978-0-19-171766-6, 978-0-19-852074-0. DOI: 10.1093/acprof:oso/9780198570745.001.0001.

[35] V. De Luca, G. Franciolini, A. Kehagias, and A. Riotto. "On the Gauge Invariance of Cosmological Gravitational Waves". In: *JCAP* 03 (2020), p. 014. DOI: 10.1088/1475-7516/2020/03/014. arXiv: 1911.09689 [gr-qc].

[36] Malik Rakhmanov. "Response of test masses to gravitational waves in the local Lorentz gauge". In: *Phys. Rev. D* 71 (2005), p. 084003. DOI: 10.1103/PhysRevD.71.084003. arXiv: gr-qc/0406009.

[37] C. J. Moore, R. H. Cole, and C. P. L. Berry. "Gravitational-wave sensitivity curves". In: *Class. Quant. Grav.* 32.1 (2015), p. 015014. DOI: 10.1088/0264-9381/32/1/015014. arXiv: 1408.0740 [gr-qc].

[38] Craig Cahillane and Georgia Mansell. "Review of the Advanced LIGO Gravitational Wave Observatories Leading to Observing Run Four". In: *Galaxies* 10.1 (2022), p. 36. DOI: 10.3390/galaxies10010036. arXiv: 2202.00847 [gr-qc].

[39] Karl-Peter Marzlin. "Fermi coordinates for weak gravitational fields". In: *Phys. Rev. D* 50 (1994), pp. 888–891. DOI: 10.1103/PhysRevD.50.888. arXiv: gr-qc/9403044.

[40] Asher Berlin, Diego Blas, Raffaele Tito D'Agnolo, Sebastian A. R. Ellis, Roni Harnik, Yonatan Kahn, and Jan Schütte-Engel. "Detecting high-frequency gravitational waves with microwave cavities". In: *Phys. Rev. D* 105.11 (2022), p. 116011. DOI: 10.1103/PhysRevD.105.116011. arXiv: 2112.11465 [hep-ph].

[41] Joris P. W. Verbiest and G. M. Shaifullah. "Measurement uncertainty in pulsar timing array experiments". In: *Class. Quant. Grav.* 35.13 (2018), p. 133001. DOI: 10.1088/1361-6382/aac412.

[42] Harikrishnan Ramani, Tanner Trickle, and Kathryn M. Zurek. "Observability of Dark Matter Substructure with Pulsar Timing Correlations". In: *JCAP* 12 (2020), p. 033. DOI: 10.1088/1475-7516/2020/12/033. arXiv: 2005.03030 [astro-ph.CO].

[43] Jeff A. Dror, Harikrishnan Ramani, Tanner Trickle, and Kathryn M. Zurek. "Pulsar Timing Probes of Primordial Black Holes and Subhalos". In: *Phys. Rev. D* 100.2 (2019), p. 023003. DOI: 10.1103/PhysRevD.100.023003. arXiv: 1901.04490 [astro-ph.CO].

[44] Ethan R. Siegel, M. P. Hertzberg, and J. N. Fry. "Probing Dark Matter Substructure with Pulsar Timing". In: *Mon. Not. Roy. Astron. Soc.* 382 (2007), p. 879. DOI: 10.1111/j.1365-2966.2007.12435.x. arXiv: astro-ph/0702546.

[45] Pedro Schwaller. "Gravitational Waves from a Dark Phase Transition". In: *Phys. Rev. Lett.* 115.18 (2015), p. 181101. DOI: 10.1103/PhysRevLett.115.181101. arXiv: 1504.07263 [hep-ph].

[46] Stefano Profumo. "Astrophysical Probes of Dark Matter". In: *Theoretical Advanced Study Institute in Elementary Particle Physics: Searching for New Physics at Small and Large Scales*. 2013, pp. 143–189. DOI: 10.1142/9789814525220_0004. arXiv: 1301.0952 [hep-ph].

[47] Graciela B. Gelmini. "The Hunt for Dark Matter". In: *Theoretical Advanced Study Institute in Elementary Particle Physics: Journeys Through the Precision Frontier: Amplitudes for Colliders*. 2015, pp. 559–616. DOI: 10.1142/9789814678766_0012. arXiv: 1502.01320 [hep-ph].

[48] Mariangela Lisanti. "Lectures on Dark Matter Physics". In: *Theoretical Advanced Study Institute in Elementary Particle Physics: New Frontiers in Fields and Strings*. 2017, pp. 399–446. DOI: 10.1142/9789813149441_0007. arXiv: 1603.03797 [hep-ph].

[49] Tracy R. Slatyer. "Indirect Detection of Dark Matter". In: *Theoretical Advanced Study Institute in Elementary Particle Physics: Anticipating the Next Discoveries in Particle Physics*. 2018, pp. 297–353. DOI: 10.1142/9789813233348_0005. arXiv: 1710.05137 [hep-ph].

[50] Dan Hooper. "TASI Lectures on Indirect Searches For Dark Matter". In: *PoS* TASI2018 (2019), p. 010. arXiv: 1812.02029 [hep-ph].

[51] Tongyan Lin. "Dark matter models and direct detection". In: *PoS* 333 (2019), p. 009. DOI: 10.22323/1.333.0009. arXiv: 1904.07915 [hep-ph].

[52] Benjamin R. Safdi. "TASI Lectures on the Particle Physics and Astrophysics of Dark Matter". In: *PoS* TASI2022 (2024), p. 009. DOI: 10.22323/1.439.0009. arXiv: 2303.02169 [hep-ph].

[53] Jodi Cooley et al. "Report of the Topical Group on Particle Dark Matter for Snowmass 2021". In: (Sept. 2022). arXiv: 2209.07426 [hep-ph].

[54] V. C. Rubin, Jr. Ford W. K., and N. Thonnard. "Extended rotation curves of high-luminosity spiral galaxies. IV. Systematic dynamical properties, Sa -> Sc." In: 225 (Nov. 1978), pp. L107–L111. DOI: 10.1086/182804.

[55] J. Bekenstein and Mordehai Milgrom. "Does the missing mass problem signal the breakdown of Newtonian gravity?" In: *Astrophys. J.* 286 (1984), pp. 7–14. DOI: 10.1086/162570.

[56] Jacob D. Bekenstein. "Relativistic gravitation theory for the MOND paradigm". In: *Phys. Rev. D* 70 (2004). [Erratum: Phys.Rev.D 71, 069901 (2005)], p. 083509. DOI: 10.1103/PhysRevD.70.083509. arXiv: astro-ph/0403694.

[57] Mohammed Alzain. "MOND as a modification of Newtonian inertia". In: *J. Astrophys. Astron.* 38 (2017), p. 59. DOI: 10.1007/s12036-017-9479-0. arXiv: 1708.05385 [astro-ph.GA].

[58] Erik P. Verlinde. "Emergent Gravity and the Dark Universe". In: *SciPost Phys.* 2.3 (2017), p. 016. DOI: 10.21468/SciPostPhys.2.3.016. arXiv: 1611.02269 [hep-th].

[59] Benoit Famaey and Stacy McGaugh. "Modified Newtonian Dynamics (MOND): Observational Phenomenology and Relativistic Extensions". In: *Living Rev. Rel.* 15 (2012), p. 10. DOI: 10.12942/lrr-2012-10. arXiv: 1112.3960 [astro-ph.CO].

[60] Mordehai Milgrom. "MOND laws of galactic dynamics". In: *Mon. Not. Roy. Astron. Soc.* 437.3 (2014), pp. 2531–2541. DOI: 10.1093/mnras/stt2066. arXiv: 1212.2568 [astro-ph.CO].

[61] Tommaso Giannantonio, Ryan Scranton, Robert G. Crittenden, Robert C. Nichol, Stephen P. Boughn, Adam D. Myers, and Gordon T. Richards. "Combined analysis of the integrated Sachs-Wolfe effect and cosmological implications". In: *Phys. Rev. D* 77 (2008), p. 123520. DOI: 10.1103/PhysRevD.77.123520. arXiv: 0801.4380 [astro-ph].

[62] Douglas Clowe, Marusa Bradac, Anthony H. Gonzalez, Maxim Markevitch, Scott W. Randall, Christine Jones, and Dennis Zaritsky. "A direct empirical proof of the existence of dark matter". In: *Astrophys. J. Lett.* 648 (2006), pp. L109–L113. DOI: 10.1086/508162. arXiv: astro-ph/0608407.

[63] Brian D. Fields, Keith A. Olive, Tsung-Han Yeh, and Charles Young. "Big-Bang Nucleosynthesis after Planck". In: *JCAP* 03 (2020). [Erratum: JCAP 11, E02 (2020)], p. 010. DOI: 10.1088/1475-7516/2020/03/010. arXiv: 1912.01132 [astro-ph.CO].

[64] Edward W. Kolb and Michael S. Turner. *The Early Universe*. Vol. 69. 1990. ISBN: 978-0-201-62674-2. DOI: 10.1201/9780429492860.

[65] Julio F. Navarro, Carlos S. Frenk, and Simon D. M. White. "The Structure of cold dark matter halos". In: *Astrophys. J.* 462 (1996), pp. 563–575. DOI: 10.1086/177173. arXiv: astro-ph/9508025.

[66] Antonino Del Popolo and Morgan Le Delliou. "Small scale problems of the ΛCDM model: a short review". In: *Galaxies* 5.1 (2017), p. 17. DOI: 10.3390/galaxies5010017. arXiv: 1606.07790 [astro-ph.CO].

[67] Anze Slosar, Christopher Hirata, Uros Seljak, Shirley Ho, and Nikhil Padmanabhan. "Constraints on local primordial non-Gaussianity from large scale structure". In: *JCAP* 08 (2008), p. 031. DOI: 10.1088/1475-7516/2008/08/031. arXiv: 0805.3580 [astro-ph].

[68] Kris Pardo and David N. Spergel. "What is the price of abandoning dark matter? Cosmological constraints on alternative gravity theories". In: *Phys. Rev. Lett.* 125.21 (2020), p. 211101. DOI: 10.1103/PhysRevLett.125.211101. arXiv: 2007.00555 [astro-ph.CO].

[69] Marco Battaglieri et al. “US Cosmic Visions: New Ideas in Dark Matter 2017: Community Report”. In: *U.S. Cosmic Visions: New Ideas in Dark Matter*. July 2017. arXiv: 1707.04591 [hep-ph].

[70] Neal Dalal and Andrey Kravtsov. “Excluding fuzzy dark matter with sizes and stellar kinematics of ultrafaint dwarf galaxies”. In: *Phys. Rev. D* 106.6 (2022), p. 063517. DOI: 10.1103/PhysRevD.106.063517. arXiv: 2203.05750 [astro-ph.CO].

[71] T. Blaineau et al. “New limits from microlensing on Galactic black holes in the mass range 10 M⊙ < M < 1000 M⊙”. In: *Astron. Astrophys.* 664 (2022), A106. DOI: 10.1051/0004-6361/202243430. arXiv: 2202.13819 [astro-ph.GA].

[72] S. Tremaine and J. E. Gunn. “Dynamical Role of Light Neutral Leptons in Cosmology”. In: *Phys. Rev. Lett.* 42 (1979). Ed. by M. A. Srednicki, pp. 407–410. DOI: 10.1103/PhysRevLett.42.407.

[73] J. I. Read. “The Local Dark Matter Density”. In: *J. Phys. G* 41 (2014), p. 063101. DOI: 10.1088/0954-3899/41/6/063101. arXiv: 1404.1938 [astro-ph.GA].

[74] Lina Necib, Mariangela Lisanti, and Vasily Belokurov. “Inferred Evidence For Dark Matter Kinematic Substructure with SDSS-Gaia”. In: (July 2018). DOI: 10.3847/1538-4357/ab095b. arXiv: 1807.02519 [astro-ph.GA].

[75] Julio F. Navarro, Carlos S. Frenk, and Simon D. M. White. “A Universal density profile from hierarchical clustering”. In: *Astrophys. J.* 490 (1997), pp. 493–508. DOI: 10.1086/304888. arXiv: astro-ph/9611107.

[76] Hai-Nan Lin and Xin Li. “The Dark Matter Profiles in the Milky Way”. In: *Mon. Not. Roy. Astron. Soc.* 487.4 (2019), pp. 5679–5684. DOI: 10.1093/mnras/stz1698. arXiv: 1906.08419 [astro-ph.GA].

[77] James M. Overduin and P. S. Wesson. “Dark matter and background light”. In: *Phys. Rept.* 402 (2004), pp. 267–406. DOI: 10.1016/j.physrep.2004.07.006. arXiv: astro-ph/0407207.

[78] David N. Spergel and Paul J. Steinhardt. “Observational evidence for self-interacting cold dark matter”. In: *Phys. Rev. Lett.* 84 (2000), pp. 3760–3763. DOI: 10.1103/PhysRevLett.84.3760. arXiv: astro-ph/9909386.

[79] Felix Kahlhoefer, Kai Schmidt-Hoberg, Mads T. Frandsen, and Subir Sarkar. “Colliding clusters and dark matter self-interactions”. In: *Mon. Not. Roy. Astron. Soc.* 437.3 (2014), pp. 2865–2881. DOI: 10.1093/mnras/stt2097. arXiv: 1308.3419 [astro-ph.CO].

[80] Gianfranco Bertone and Dan Hooper. “History of dark matter”. In: *Rev. Mod. Phys.* 90.4 (2018), p. 045002. DOI: 10.1103/RevModPhys.90.045002. arXiv: 1605.04909 [astro-ph.CO].

[81] Nicolás Bernal, Matti Heikinheimo, Tommi Tenkanen, Kimmo Tuominen, and Ville Vaskonen. "The Dawn of FIMP Dark Matter: A Review of Models and Constraints". In: *Int. J. Mod. Phys. A* 32.27 (2017), p. 1730023. DOI: 10.1142/S0217751X1730023X. arXiv: 1706.07442 [hep-ph].

[82] Lawrence J. Hall, Karsten Jedamzik, John March-Russell, and Stephen M. West. "Freeze-In Production of FIMP Dark Matter". In: *JHEP* 03 (2010), p. 080. DOI: 10.1007/JHEP03(2010)080. arXiv: 0911.1120 [hep-ph].

[83] Simon Knapen, Tongyan Lin, and Kathryn M. Zurek. "Light Dark Matter: Models and Constraints". In: *Phys. Rev. D* 96.11 (2017), p. 115021. DOI: 10.1103/PhysRevD.96.115021. arXiv: 1709.07882 [hep-ph].

[84] Yonatan Kahn and Tongyan Lin. "Searches for light dark matter using condensed matter systems". In: *Rept. Prog. Phys.* 85.6 (2022), p. 066901. DOI: 10.1088/1361-6633/ac5f63. arXiv: 2108.03239 [hep-ph].

[85] Yonit Hochberg, Yonatan F. Kahn, Rebecca K. Leane, Surjeet Rajendran, Ken Van Tilburg, Tien-Tien Yu, and Kathryn M. Zurek. "New approaches to dark matter detection". In: *Nature Reviews Physics* 4.10 (Sept. 2022), pp. 637–641. DOI: 10.1038/s42254-022-00509-4.

[86] Kathryn M. Zurek. "Snowmass 2021 White Paper: Observational Signatures of Quantum Gravity". In: (May 2022). arXiv: 2205.01799 [gr-qc].

[87] J. D. Bekenstein. "Black holes and the second law". In: *Lett. Nuovo Cim.* 4 (1972), pp. 737–740. DOI: 10.1007/BF02757029.

[88] Jacob D. Bekenstein. "Black holes and entropy". In: *Phys. Rev. D* 7 (1973), pp. 2333–2346. DOI: 10.1103/PhysRevD.7.2333.

[89] Jacob D. Bekenstein. "Generalized second law of thermodynamics in black hole physics". In: *Phys. Rev. D* 9 (1974), pp. 3292–3300. DOI: 10.1103/PhysRevD.9.3292.

[90] Donald Marolf. "On the quantum width of a black hole horizon". In: *Springer Proc. Phys.* 98 (2005). Ed. by Josip Trampetic and Julius Wess, pp. 99–112. DOI: 10.1007/3-540-26798-0_9. arXiv: hep-th/0312059.

[91] Raphael Bousso and Geoff Penington. "Islands Far Outside the Horizon". In: (Dec. 2023). arXiv: 2312.03078 [hep-th].

[92] Edward Kolb. *The early universe*. New York: Westview Press, 1994. ISBN: 0201626748.

[93] Scott Dodelson. *Modern cosmology*. San Diego, California: Academic Press, An Imprint of Elsevier, 2003. ISBN: 0122191412.

[94] C.J. Hogan and M.J. Rees. "AXION MINICLUSTERS". In: *Phys. Lett. B* 205 (1988), pp. 228–230. DOI: 10.1016/0370-2693(88)91655-3.

[95] Edward W. Kolb and Igor I. Tkachev. "Axion miniclusters and Bose stars". In: *Phys. Rev. Lett.* 71 (1993), pp. 3051–3054. DOI: 10.1103/PhysRevLett.71.3051. arXiv: hep-ph/9303313.

[96] Adrienne L. Erickcek and Kris Sigurdson. "Reheating Effects in the Matter Power Spectrum and Implications for Substructure". In: *Phys. Rev. D* 84 (2011), p. 083503. DOI: 10.1103/PhysRevD.84.083503. arXiv: 1106.0536 [astro-ph.CO].

[97] JiJi Fan, Ogan Özsoy, and Scott Watson. "Nonthermal histories and implications for structure formation". In: *Phys. Rev. D* 90.4 (2014), p. 043536. DOI: 10.1103/PhysRevD.90.043536. arXiv: 1405.7373 [hep-ph].

[98] Peter W. Graham, Jeremy Mardon, and Surjeet Rajendran. "Vector Dark Matter from Inflationary Fluctuations". In: *Phys. Rev. D* 93.10 (2016), p. 103520. DOI: 10.1103/PhysRevD.93.103520. arXiv: 1504.02102 [hep-ph].

[99] Ken Van Tilburg, Anna-Maria Taki, and Neal Weiner. "Halometry from Astrometry". In: *JCAP* 07 (2018), p. 041. DOI: 10.1088/1475-7516/2018/07/041. arXiv: 1804.01991 [astro-ph.CO].

[100] Ana Diaz Rivero, Francis-Yan Cyr-Racine, and Cora Dvorkin. "Power spectrum of dark matter substructure in strong gravitational lenses". In: *Phys. Rev. D* 97.2 (2018), p. 023001. DOI: 10.1103/PhysRevD.97.023001. arXiv: 1707.04590 [astro-ph.CO].

[101] R.Benton Metcalf and Piero Madau. "Compound gravitational lensing as a probe of dark matter substructure within galaxy halos". In: *Astrophys. J.* 563 (2001), p. 9. DOI: 10.1086/323695. arXiv: astro-ph/0108224.

[102] Liang Dai and Jordi Miralda-Escudé. "Gravitational Lensing Signatures of Axion Dark Matter Minihalos in Highly Magnified Stars". In: *Astron. J.* 159.2 (2020), p. 49. DOI: 10.3847/1538-3881/ab5e83. arXiv: 1908.01773 [astro-ph.CO].

[103] Shant Baghram, Niayesh Afshordi, and Kathryn M. Zurek. "Prospects for Detecting Dark Matter Halo Substructure with Pulsar Timing". In: *Phys. Rev. D* 84 (2011), p. 043511. DOI: 10.1103/PhysRevD.84.043511. arXiv: 1101.5487 [astro-ph.CO].

[104] Hamish A. Clark, Geraint F. Lewis, and Pat Scott. "Investigating dark matter substructure with pulsar timing – I. Constraints on ultracompact minihaloes". In: *Mon. Not. Roy. Astron. Soc.* 456.2 (2016). [Erratum: Mon.Not.Roy.Astron.Soc. 464, 2468 (2017)], pp. 1394–1401. DOI: 10.1093/mnras/stv2743. arXiv: 1509.02938 [astro-ph.CO].

[105] Katelin Schutz and Adrian Liu. "Pulsar timing can constrain primordial black holes in the LIGO mass window". In: *Phys. Rev. D* 95.2 (2017), p. 023002. DOI: 10.1103/PhysRevD.95.023002. arXiv: 1610.04234 [astro-ph.CO].

[106] William H. Press and Paul Schechter. "Formation of galaxies and clusters of galaxies by selfsimilar gravitational condensation". In: *Astrophys. J.* 187 (1974), pp. 425–438. DOI: 10.1086/152650.

[107] Pablo A. Rosado, Alberto Sesana, and Jonathan Gair. "Expected properties of the first gravitational wave signal detected with pulsar timing arrays". In: *Mon. Not. Roy. Astron. Soc.* 451.3 (2015), pp. 2417–2433. DOI: 10.1093/mnras/stv1098. arXiv: 1503.04803 [astro-ph.HE].

[108] Tristan L. Smith and Robert Caldwell. "LISA for Cosmologists: Calculating the Signal-to-Noise Ratio for Stochastic and Deterministic Sources". In: *Phys. Rev. D* 100.10 (2019), p. 104055. DOI: 10.1103/PhysRevD.100.104055. arXiv: 1908.00546 [astro-ph.CO].

[109] Bruce Allen and Joseph D. Romano. "Detecting a stochastic background of gravitational radiation: Signal processing strategies and sensitivities". In: *Phys. Rev. D* 59 (1999), p. 102001. DOI: 10.1103/PhysRevD.59.102001. arXiv: gr-qc/9710117.

[110] Justin A. Ellis, Michele Vallisneri, Stephen R. Taylor, and Paul T. Baker. *ENTERPRISE: Enhanced Numerical Toolbox Enabling a Robust PulsaR Inference SuitE*. 2020. DOI: 10.5281/ZENODO.4059815.

[111] Fredrick A. Jenet and Joseph D. Romano. "Understanding the gravitational-wave Hellings and Downs curve for pulsar timing arrays in terms of sound and electromagnetic waves". In: *Am. J. Phys.* 83 (2015), p. 635. DOI: 10.1119/1.4916358. arXiv: 1412.1142 [gr-qc].

[112] R.w. Hellings and G.s. Downs. "Upper Limits on the Isotropic Gravitational Radiation Background from Pulsar Timing Analysis". In: *Astrophys. J. Lett.* 265 (1983), pp. L39–L42. DOI: 10.1086/183954.

[113] N. Aghanim et al. "Planck 2018 results. VI. Cosmological parameters". In: *Astron. Astrophys.* 641 (2020), A6. DOI: 10.1051/0004-6361/201833910. arXiv: 1807.06209 [astro-ph.CO].

[114] Edward W. Kolb and Igor I. Tkachev. "Large amplitude isothermal fluctuations and high density dark matter clumps". In: *Phys. Rev. D* 50 (1994), pp. 769–773. DOI: 10.1103/PhysRevD.50.769. arXiv: astro-ph/9403011.

[115] David Ellis, David J.E. Marsh, and Christoph Behrens. "Axion Miniclusters Made Easy". In: (June 2020). arXiv: 2006.08637 [astro-ph.CO].

[116] Volker Springel, Jie Wang, Mark Vogelsberger, Aaron Ludlow, Adrian Jenkins, Amina Helmi, Julio F. Navarro, Carlos S. Frenk, and Simon D.M. White. "The Aquarius Project: the subhalos of galactic halos". In: *Mon. Not. Roy. Astron. Soc.* 391 (2008), pp. 1685–1711. DOI: 10.1111/j.1365-2966.2008.14066.x. arXiv: 0809.0898 [astro-ph].

[117] Davide Fiacconi, Piero Madau, Doug Potter, and Joachim Stadel. "Cold Dark Matter Substructures in Early-Type Galaxy Halos". In: *Astrophys. J.* 824.2 (2016), p. 144. DOI: 10.3847/0004-637X/824/2/144. arXiv: 1602.03526 [astro-ph.GA].

[118] Benedikt Eggemeier, Javier Redondo, Klaus Dolag, Jens C. Niemeyer, and Alejandro Vaquero. "First Simulations of Axion Minicluster Halos". In: *Phys. Rev. Lett.* 125.4 (2020), p. 041301. DOI: 10.1103/PhysRevLett.125.041301. arXiv: 1911.09417 [astro-ph.CO].

[119] Jie Wang, Sownak Bose, Carlos S. Frenk, Liang Gao, Adrian Jenkins, Volker Springel, and Simon D.M. White. "Universal structure of dark matter haloes over a mass range of 20 orders of magnitude". In: *Nature* 585.7823 (2020), pp. 39–42. DOI: 10.1038/s41586-020-2642-9. arXiv: 1911.09720 [astro-ph.CO].

[120] C. Lacey and S. Cole. "Merger rates in hierarchical models of galaxy formation". In: *Monthly Notices of the Royal Astronomical Society* 262.3 (June 1993), pp. 627–649. DOI: 10.1093/mnras/262.3.627.

[121] Carlo Giocoli, Lidia Pieri, and Giuseppe Tormen. "Analytical Approach to Subhaloes Population in Dark Matter Haloes". In: *Mon. Not. Roy. Astron. Soc.* 387 (2008), pp. 689–697. DOI: 10.1111/j.1365-2966.2008.13283.x. arXiv: 0712.1476 [astro-ph].

[122] Frank C. van den Bosch, Go Ogiya, Oliver Hahn, and Andreas Burkert. "Disruption of Dark Matter Substructure: Fact or Fiction?" In: *Mon. Not. Roy. Astron. Soc.* 474.3 (2018), pp. 3043–3066. DOI: 10.1093/mnras/stx2956. arXiv: 1711.05276 [astro-ph.GA].

[123] Bradley J. Kavanagh, Thomas D.P. Edwards, Luca Visinelli, and Christoph Weniger. "Stellar Disruption of Axion Miniclusters in the Milky Way". In: (Nov. 2020). arXiv: 2011.05377 [astro-ph.GA].

[124] P.A.R. Ade et al. "Planck 2015 results. XX. Constraints on inflation". In: *Astron. Astrophys.* 594 (2016), A20. DOI: 10.1051/0004-6361/201525898. arXiv: 1502.02114 [astro-ph.CO].

[125] Simeon Bird, Hiranya V. Peiris, Matteo Viel, and Licia Verde. "Minimally Parametric Power Spectrum Reconstruction from the Lyman-alpha Forest". In: *Mon. Not. Roy. Astron. Soc.* 413 (2011), pp. 1717–1728. DOI: 10.1111/j.1365-2966.2011.18245.x. arXiv: 1010.1519 [astro-ph.CO].

[126] Torsten Bringmann, Pat Scott, and Yashar Akrami. "Improved constraints on the primordial power spectrum at small scales from ultracompact minihalos". In: *Phys. Rev. D* 85 (2012), p. 125027. DOI: 10.1103/PhysRevD.85.125027. arXiv: 1110.2484 [astro-ph.CO].

[127] James M. Bardeen, J.R. Bond, Nick Kaiser, and A.S. Szalay. "The Statistics of Peaks of Gaussian Random Fields". In: *Astrophys. J.* 304 (1986), pp. 15–61. DOI: 10.1086/164143.

[128] Sean M. Carroll, William H. Press, and Edwin L. Turner. "The Cosmological constant". In: *Ann. Rev. Astron. Astrophys.* 30 (1992), pp. 499–542. DOI: 10.1146/annurev.aa.30.090192.002435.

[129] Alejandro Vaquero, Javier Redondo, and Julia Stadler. "Early seeds of axion miniclusters". In: *JCAP* 04 (2019), p. 012. DOI: 10.1088/1475-7516/2019/04/012. arXiv: 1809.09241 [astro-ph.CO].

[130] Malte Buschmann, Joshua W. Foster, and Benjamin R. Safdi. "Early-Universe Simulations of the Cosmological Axion". In: *Phys. Rev. Lett.* 124.16 (2020), p. 161103. DOI: 10.1103/PhysRevLett.124.161103. arXiv: 1906.00967 [astro-ph.CO].

[131] Marco Gorghetto, Edward Hardy, and Giovanni Villadoro. "More Axions from Strings". In: (July 2020). arXiv: 2007.04990 [hep-ph].

[132] Kathryn M. Zurek, Craig J. Hogan, and Thomas R. Quinn. "Astrophysical Effects of Scalar Dark Matter Miniclusters". In: *Phys. Rev. D* 75 (2007), p. 043511. DOI: 10.1103/PhysRevD.75.043511. arXiv: astro-ph/0607341.

[133] Wolfram Ratzinger and Pedro Schwaller. "Whispers from the dark side: Confronting light new physics with NANOGrav data". In: *SciPost Phys.* 10.2 (2021), p. 047. DOI: 10.21468/SciPostPhys.10.2.047. arXiv: 2009.11875 [astro-ph.CO].

[134] Scott Dodelson. *Modern Cosmology*. Amsterdam: Academic Press, 2003. ISBN: 978-0-12-219141-1.

[135] Anne M. Green, Stefan Hofmann, and Dominik J. Schwarz. "The First wimpy halos". In: *JCAP* 08 (2005), p. 003. DOI: 10.1088/1475-7516/2005/08/003. arXiv: astro-ph/0503387.

[136] R. D. Peccei and Helen R. Quinn. "CP Conservation in the Presence of Instantons". In: *Phys. Rev. Lett.* 38 (1977), pp. 1440–1443. DOI: 10.1103/PhysRevLett.38.1440.

[137] Asimina Arvanitaki, Savas Dimopoulos, Marios Galanis, Luis Lehner, Jedidiah O. Thompson, and Ken Van Tilburg. "Large-misalignment mechanism for the formation of compact axion structures: Signatures from the QCD axion to fuzzy dark matter". In: *Phys. Rev. D* 101.8 (2020), p. 083014. DOI: 10.1103/PhysRevD.101.083014. arXiv: 1909.11665 [astro-ph.CO].

[138] Huangyu Xiao, Ian Williams, and Matthew McQuinn. "Simulations of axion minihalos". In: *Phys. Rev. D* 104.2 (2021), p. 023515. DOI: 10.1103/PhysRevD.104.023515. arXiv: 2101.04177 [astro-ph.CO].

[139] Bernard Carr, Kazunori Kohri, Yuuiti Sendouda, and Jun'ichi Yokoyama. "Constraints on primordial black holes". In: *Rept. Prog. Phys.* 84.11 (2021), p. 116902. DOI: 10.1088/1361-6633/ac1e31. arXiv: 2002.12778 [astro-ph.CO].

[140] C. Alcock et al. "The MACHO project: Microlensing results from 5.7 years of LMC observations". In: *Astrophys. J.* 542 (2000), pp. 281–307. DOI: 10.1086/309512. arXiv: astro-ph/0001272.

[141] P. Tisserand et al. "Limits on the Macho Content of the Galactic Halo from the EROS-2 Survey of the Magellanic Clouds". In: *Astron. Astrophys.* 469 (2007), pp. 387–404. DOI: 10.1051/0004-6361:20066017. arXiv: astro-ph/0607207.

[142] L. Wyrzykowski et al. "The OGLE View of Microlensing towards the Magellanic Clouds. IV. OGLE-III SMC Data and Final Conclusions on MACHOs". In: *Mon. Not. Roy. Astron. Soc.* 416 (2011), p. 2949. DOI: 10.1111/j.1365-2966.2011.19243.x. arXiv: 1106.2925 [astro-ph.GA].

[143] Hiroko Niikura et al. "Microlensing constraints on primordial black holes with Subaru/HSC Andromeda observations". In: *Nature Astron.* 3.6 (2019), pp. 524–534. DOI: 10.1038/s41550-019-0723-1. arXiv: 1701.02151 [astro-ph.CO].

[144] Kim Griest, Matthew J. Lehner, Agnieszka M. Cieplak, and Bhuvnesh Jain. "Microlensing of Kepler Stars as a Method of Detecting Primordial Black Hole Dark Matter". In: *Phys. Rev. Lett.* 107 (2011), p. 231101. DOI: 10.1103/PhysRevLett.107.231101. arXiv: 1109.4975 [astro-ph.CO].

[145] Kim Griest, Agnieszka M. Cieplak, and Matthew J. Lehner. "Experimental Limits on Primordial Black Hole Dark Matter from the First 2 yr of Kepler Data". In: *Astrophys. J.* 786.2 (2014), p. 158. DOI: 10.1088/0004-637X/786/2/158. arXiv: 1307.5798 [astro-ph.CO].

[146] Steven Clark, Bhaskar Dutta, Yu Gao, Louis E. Strigari, and Scott Watson. "Planck Constraint on Relic Primordial Black Holes". In: *Phys. Rev. D* 95.8 (2017), p. 083006. DOI: 10.1103/PhysRevD.95.083006. arXiv: 1612.07738 [astro-ph.CO].

[147] Djuna Croon, David McKeen, Nirmal Raj, and Zihui Wang. "Subaru-HSC through a different lens: Microlensing by extended dark matter structures". In: *Phys. Rev. D* 102.8 (2020), p. 083021. DOI: 10.1103/PhysRevD.102.083021. arXiv: 2007.12697 [astro-ph.CO].

[148] R. A. Allsman et al. "MACHO project limits on black hole dark matter in the 1-30 solar mass range". In: *Astrophys. J. Lett.* 550 (2001), p. L169. DOI: 10.1086/319636. arXiv: astro-ph/0011506.

[149] Hiroko Niikura, Masahiro Takada, Shuichiro Yokoyama, Takahiro Sumi, and Shogo Masaki. "Constraints on Earth-mass primordial black holes from OGLE 5-year microlensing events". In: *Phys. Rev. D* 99.8 (2019), p. 083503. DOI: 10.1103/PhysRevD.99.083503. arXiv: 1901.07120 [astro-ph.CO].

[150] Naoki Seto and Asantha Cooray. "Searching for primordial black hole dark matter with pulsar timing arrays". In: *Astrophys. J. Lett.* 659 (2007), pp. L33–L36. DOI: 10.1086/516570. arXiv: astro-ph/0702586.

[151] Kazumi Kashiyama and Naoki Seto. "Enhanced exploration for primordial black holes using pulsar timing arrays". In: *Monthly Notices of the Royal Astronomical Society* 426.2 (Oct. 2012), pp. 1369–1373. ISSN: 0035-8711. DOI: 10.1111/j.1365-2966.2012.21935.x. URL: http://dx.doi.org/10.1111/j.1365-2966.2012.21935.x.

[152] Kazumi Kashiyama and Masamune Oguri. "Detectability of Small-Scale Dark Matter Clumps with Pulsar Timing Arrays". In: (Jan. 2018). arXiv: 1801.07847 [astro-ph.CO].

[153] Justin A. Ellis, Michele Vallisneri, Stephen R. Taylor, and Paul T. Baker. *ENTERPRISE: Enhanced Numerical Toolbox Enabling a Robust PulsaR Inference SuitE*. Dec. 2019. ascl: 1912.015.

[154] A. Brazier et al. "The NANOGrav Program for Gravitational Waves and Fundamental Physics". In: (Aug. 2019). arXiv: 1908.05356 [astro-ph.IM].

[155] E.F. Keane et al. "A Cosmic Census of Radio Pulsars with the SKA". In: *PoS* AASKA14 (2015). Ed. by Tyler L. Bourke et al., p. 040. DOI: 10.22323/1.215.0040. arXiv: 1501.00056 [astro-ph.IM].

[156] Zaven Arzoumanian et al. "The NANOGrav 12.5 yr Data Set: Search for an Isotropic Stochastic Gravitational-wave Background". In: 905.2, L34 (Dec. 2020), p. L34. DOI: 10.3847/2041-8213/abd401. arXiv: 2009.04496 [astro-ph.HE].

[157] Alberto Sesana, Francesco Haardt, Piero Madau, and Marta Volonteri. "Low - frequency gravitational radiation from coalescing massive black hole binaries in hierarchical cosmologies". In: *Astrophys. J.* 611 (2004), pp. 623–632. DOI: 10.1086/422185. arXiv: astro-ph/0401543.

[158] Sarah Burke-Spolaor et al. "The Astrophysics of Nanohertz Gravitational Waves". In: *Astron. Astrophys. Rev.* 27.1 (2019), p. 5. DOI: 10.1007/s00159-019-0115-7. arXiv: 1811.08826 [astro-ph.HE].

[159] D. N. Matsakis, J. H. Taylor, and T. Marshall Eubanks. "A statistic for describing pulsar and clock stabilities." In: 326 (Oct. 1997), pp. 924–928.

[160] D. J. Helfand, R. N. Manchester, and J. H. Taylor. "Observations of pulsar radio emission. III. Stability of integrated profiles." In: 198 (June 1975), pp. 661–670. DOI: 10.1086/153644.

[161] X. J. Liu, C. G. Bassa, and B. W. Stappers. "High precision pulsar timing and spin frequency second derivatives". In: *Mon. Not. Roy. Astron. Soc.* 478.2 (2018), pp. 2359–2367. DOI: 10.1093/mnras/sty1202. arXiv: 1805.02892 [astro-ph.HE].

[162] Ross J. Jennings, James M. Cordes, and Shami Chatterjee. "Detecting Gravitational Scattering of Interstellar Objects Using Pulsar Timing". In: (Dec. 2019). DOI: 10.3847/1538-4357/ab64df. arXiv: 1910.08608 [astro-ph.HE].

[163] Henning Heiselberg. "Neutron star masses, radii and equation of state". In: (Jan. 2002). arXiv: astro-ph/0201465.

[164] S. Sivertsson, H. Silverwood, J. I. Read, G. Bertone, and P. Steger. "The localdark matter density from SDSS-SEGUE G-dwarfs". In: *Mon. Not. Roy. Astron. Soc.* 478.2 (2018), pp. 1677–1693. DOI: 10.1093/mnras/sty977. arXiv: 1708.07836 [astro-ph.GA].

[165] Z. Arzoumanian et al. "The NANOGrav Nine-year Data Set: Limits on the Isotropic Stochastic Gravitational Wave Background". In: *Astrophys. J.* 821.1 (2016), p. 13. DOI: 10.3847/0004-637X/821/1/13. arXiv: 1508.03024 [astro-ph.GA].

[166] Zaven Arzoumanian et al. "The NANOGrav Nine-year Data Set: Observations, Arrival Time Measurements, and Analysis of 37 Millisecond Pulsars". In: *Astrophys. J.* 813.1 (2015), p. 65. DOI: 10.1088/0004-637X/813/1/65. arXiv: 1505.07540 [astro-ph.IM].

[167] James M. Cordes. "Limits to PTA sensitivity: spin stability and arrival time precision of millisecond pulsars". In: *Classical and Quantum Gravity* 30.22, 224002 (Nov. 2013), p. 224002. DOI: 10.1088/0264-9381/30/22/224002.

[168] M. T. Lam et al. "The NANOGrav Nine-Year Data Set: Excess Noise in Millisecond Pulsar Arrival Times". In: *Astrophys. J.* 834.1 (2017), p. 35. DOI: 10.3847/1538-4357/834/1/35. arXiv: 1610.01731 [astro-ph.HE].

[169] M. L. Jones et al. "The NANOGrav Nine-year Data Set: Measurement and Analysis of Variations in Dispersion Measures". In: *Astrophys. J.* 841.2 (2017), p. 125. DOI: 10.3847/1538-4357/aa73df. arXiv: 1612.03187 [astro-ph.HE].

[170] Caterina Tiburzi, George Hobbs, Matthew Kerr, William Coles, Shi Dai, Richard Manchester, Andrea Possenti, Ryan Shannon, and Xiaopeng You. "A study of spatial correlations in pulsar timing array data". In: *Mon. Not. Roy. Astron. Soc.* 455.4 (2016), pp. 4339–4350. DOI: 10.1093/mnras/stv2143. arXiv: 1510.02363 [astro-ph.IM].

[171] E. S. Phinney. "A Practical theorem on gravitational wave backgrounds". In: (July 2001). arXiv: astro-ph/0108028.

[172] S. R. Taylor, P. T. Baker, J. S. Hazboun, Joseph J. Simon, and Sarah J. Vigeland. *enterprise extensions*. 2018. URL: https://github.com/nanograv/enterprise_extensions.

[173] Justin Ellis and Rutger van Haasteren. *PTMCMCSampler: Parallel tempering MCMC sampler package written in Python*. Dec. 2019. ascl: 1912.017.

[174] J. P. W. Verbiest et al. "The International Pulsar Timing Array: First Data Release". In: *Mon. Not. Roy. Astron. Soc.* 458.2 (2016), pp. 1267–1288. DOI: 10.1093/mnras/stw347. arXiv: 1602.03640 [astro-ph.IM].

[175] Michele Vallisneri. *libstempo: Python wrapper for Tempo2*. Feb. 2020. ascl: 2002.017.

[176] George Hobbs, R. Edwards, and R. Manchester. "Tempo2, a new pulsar timing package. 1. overview". In: *Mon. Not. Roy. Astron. Soc.* 369 (2006), pp. 655–672. DOI: 10.1111/j.1365-2966.2006.10302.x. arXiv: astro-ph/0603381.

[177] Russell T. Edwards, G. B. Hobbs, and R. N. Manchester. "Tempo2, a new pulsar timing package. 2. The timing model and precision estimates". In: *Mon. Not. Roy. Astron. Soc.* 372 (2006), pp. 1549–1574. DOI: 10.1111/j.1365-2966.2006.10870.x. arXiv: astro-ph/0607664.

[178] Jeffrey S. Hazboun, Joseph Simon, Xavier Siemens, and Joseph D. Romano. "Model Dependence of Bayesian Gravitational-Wave Background Statistics for Pulsar Timing Arrays". In: *Astrophys. J. Lett.* 905.1 (2020), p. L6. DOI: 10.3847/2041-8213/abca92. arXiv: 2009.05143 [astro-ph.IM].

[179] Nataliya K. Porayko et al. "Parkes Pulsar Timing Array constraints on ultralight scalar-field dark matter". In: *Phys. Rev. D* 98.10 (2018), p. 102002. DOI: 10.1103/PhysRevD.98.102002. arXiv: 1810.03227 [astro-ph.CO].

[180] R. S. Foster and D. C. Backer. "Constructing a Pulsar Timing Array". In: 361 (Sept. 1990), p. 300. DOI: 10.1086/169195.

[181] S. Detweiler. "Pulsar timing measurements and the search for gravitational waves". In: 234 (Dec. 1979), pp. 1100–1104. DOI: 10.1086/157593.

[182] M. V. Sazhin. "Opportunities for detecting ultralong gravitational waves". In: 22 (Feb. 1978), pp. 36–38.

[183] Scott Ransom et al. "The NANOGrav Program for Gravitational Waves and Fundamental Physics". In: vol. 51. Sept. 2019, 195, p. 195. arXiv: 1908.05356 [astro-ph.IM].

[184] G. Desvignes et al. "High-precision timing of 42 millisecond pulsars with the European Pulsar Timing Array". In: 458.3 (May 2016), pp. 3341–3380. DOI: 10.1093/mnras/stw483. arXiv: 1602.08511 [astro-ph.HE].

[185] M. Kerr et al. "The Parkes Pulsar Timing Array Project: Second data release". In: *arXiv e-prints*, arXiv:2003.09780 (Mar. 2020), arXiv:2003.09780. arXiv: 2003.09780 [astro-ph.IM].

[186] Bhal Chandra Joshi et al. “Precision pulsar timing with the ORT and the GMRT and its applications in pulsar astrophysics”. In: *Journal of Astrophysics and Astronomy* 39.4, 51 (Aug. 2018), p. 51. DOI: 10.1007/s12036-018-9549-y.

[187] B. B. P. Perera et al. “The International Pulsar Timing Array: second data release”. In: 490.4 (Dec. 2019), pp. 4666–4687. DOI: 10.1093/mnras/stz2857. arXiv: 1909.04534 [astro-ph.HE].

[188] K. J. Lee. “Prospects of Gravitational Wave Detection Using Pulsar Timing Array for Chinese Future Telescopes”. In: *Frontiers in Radio Astronomy and FAST Early Sciences Symposium 2015*. Ed. by L. Qain and D. Li. Vol. 502. Astronomical Society of the Pacific Conference Series. Feb. 2016, p. 19.

[189] M. Bailes et al. “MeerTime - the MeerKAT Key Science Program on Pulsar Timing”. In: *arXiv e-prints*, arXiv:1803.07424 (Mar. 2018), arXiv:1803.07424. arXiv: 1803.07424 [astro-ph.IM].

[190] Cherry Ng. “Pulsar science with the CHIME telescope”. In: *Pulsar Astrophysics the Next Fifty Years*. Ed. by P. Weltevrede, B. B. P. Perera, L. L. Preston, and S. Sanidas. Vol. 337. IAU Symposium. Aug. 2018, pp. 179–182. DOI: 10.1017/S1743921317010638. arXiv: 1711.02104 [astro-ph.IM].

[191] A. Sesana, F. Haardt, P. Madau, and M. Volonteri. “Low-Frequency Gravitational Radiation from Coalescing Massive Black Hole Binaries in Hierarchical Cosmologies”. In: 611 (Aug. 2004), pp. 623–632. DOI: 10.1086/422185. eprint: astro-ph/0401543.

[192] Sarah Burke-Spolaor et al. “The astrophysics of nanohertz gravitational waves”. In: 27.1, 5 (June 2019), p. 5. DOI: 10.1007/s00159-019-0115-7. arXiv: 1811.08826 [astro-ph.HE].

[193] Xavier Siemens, Vuk Mandic, and Jolien Creighton. “Gravitational-Wave Stochastic Background from Cosmic Strings”. In: 98.11, 111101 (Mar. 2007), p. 111101. DOI: 10.1103/PhysRevLett.98.111101. arXiv: astro-ph/0610920 [astro-ph].

[194] Jose J. Blanco-Pillado, Ken D. Olum, and Xavier Siemens. “New limits on cosmic strings from gravitational wave observation”. In: *Physics Letters B* 778 (Mar. 2018), pp. 392–396. DOI: 10.1016/j.physletb.2018.01.050. arXiv: 1709.02434 [astro-ph.CO].

[195] L. P. Grishchuk. “Amplification of gravitational waves in an isotropic universe”. In: *Soviet Journal of Experimental and Theoretical Physics* 40 (Sept. 1975), p. 409.

[196] Paul D. Lasky et al. “Gravitational-Wave Cosmology across 29 Decades in Frequency”. In: *Physical Review X* 6.1, 011035 (Jan. 2016), p. 011035. DOI: 10.1103/PhysRevX.6.011035. arXiv: 1511.05994 [astro-ph.CO].

[197] Sunny Vagnozzi. "Implications of the NANOGrav results for inflation". In: *Mon. Not. Roy. Astron. Soc.* 502.1 (2021), pp. L11–L15. DOI: 10.1093/mnrasl/slaa203. arXiv: 2009.13432 [astro-ph.CO].

[198] Jeffrey Winicour. "Gravitational Radiation from Relativistic Phase Transitions". In: 182 (June 1973), pp. 919–934. DOI: 10.1086/152193.

[199] C. J. Hogan. "Gravitational radiation from cosmological phase transitions". In: *Mon. Not. Roy. Astron. Soc.* 218 (1986), pp. 629–636.

[200] D. V. Deryagin, Dmitri Yu. Grigoriev, V. A. Rubakov, and M. V. Sazhin. "Possible Anisotropic Phases in the Early Universe and Gravitational Wave Background". In: *Mod. Phys. Lett. A* 1 (1986), pp. 593–600. DOI: 10.1142/S0217732386000750.

[201] Chiara Caprini, Ruth Durrer, and Xavier Siemens. "Detection of gravitational waves from the QCD phase transition with pulsar timing arrays". In: 82.6, 063511 (Sept. 2010), p. 063511. DOI: 10.1103/PhysRevD.82.063511. arXiv: 1007.1218 [astro-ph.CO].

[202] Archil Kobakhidze, Cyril Lagger, Adrian Manning, and Jason Yue. "Gravitational waves from a supercooled electroweak phase transition and their detection with pulsar timing arrays". In: *The European Physical Journal C* 77 (Mar. 2017). DOI: 10.1140/epjc/s10052-017-5132-y.

[203] Md F. Alam et al. "The NANOGrav 12.5-year Data Set: Observations and Narrowband Timing of 47 Millisecond Pulsars". In: *arXiv e-prints*, arXiv:2005.06490 (May 2020), arXiv:2005.06490. arXiv: 2005.06490 [astro-ph.HE].

[204] Zaven Arzoumanian et al. "The NANOGrav 12.5 yr Data Set: Search for an Isotropic Stochastic Gravitational-wave Background". In: 905.2, L34 (Dec. 2020), p. L34. DOI: 10.3847/2041-8213/abd401. arXiv: 2009.04496 [astro-ph.HE].

[205] H. Middleton, A. Sesana, S. Chen, A. Vecchio, W. Del Pozzo, and P. A. Rosado. "Massive black hole binary systems and the NANOGrav 12.5 yr results". In: 502.1 (Mar. 2021), pp. L99–L103. DOI: 10.1093/mnrasl/slab008. arXiv: 2011.01246 [astro-ph.HE].

[206] Nihan S. Pol et al. "Astrophysics Milestones For Pulsar Timing Array Gravitational Wave Detection". In: *arXiv e-prints*, arXiv:2010.11950 (Oct. 2020), arXiv:2010.11950. arXiv: 2010.11950 [astro-ph.HE].

[207] Ville Vaskonen and Hardi Veermäe. "Did NANOGrav See a Signal from Primordial Black Hole Formation?" In: *Phys. Rev. Lett.* 126 (5 Feb. 2021), p. 051303. DOI: 10.1103/PhysRevLett.126.051303. URL: https://link.aps.org/doi/10.1103/PhysRevLett.126.051303.

[208] V. De Luca, G. Franciolini, and A. Riotto. "NANOGrav Data Hints at Primordial Black Holes as Dark Matter". In: *Phys. Rev. Lett.* 126 (4 Jan. 2021), p. 041303. DOI: 10.1103/PhysRevLett.126.041303. URL: https://link.aps.org/doi/10.1103/PhysRevLett.126.041303.

[209] John Ellis and Marek Lewicki. "Cosmic String Interpretation of NANOGrav Pulsar Timing Data". In: *Phys. Rev. Lett.* 126 (4 Jan. 2021), p. 041304. DOI: 10.1103/PhysRevLett.126.041304. URL: https://link.aps.org/doi/10.1103/PhysRevLett.126.041304.

[210] Simone Blasi, Vedran Brdar, and Kai Schmitz. "Has NANOGrav Found First Evidence for Cosmic Strings?" In: *Phys. Rev. Lett.* 126 (4 Jan. 2021), p. 041305. DOI: 10.1103/PhysRevLett.126.041305. URL: https://link.aps.org/doi/10.1103/PhysRevLett.126.041305.

[211] Axel Brandenburg, Emma Clarke, Yutong He, and Tina Kahniashvili. "Can we observe the QCD phase transition-generated gravitational waves through pulsar timing arrays?" In: *arXiv e-prints*, arXiv:2102.12428 (Feb. 2021), arXiv:2102.12428. arXiv: 2102.12428 [astro-ph.CO].

[212] Andrii Neronov, Alberto Roper Pol, Chiara Caprini, and Dmitri Semikoz. "NANOGrav signal from magnetohydrodynamic turbulence at the QCD phase transition in the early Universe". In: 103.4, L041302 (Feb. 2021), p. L041302. DOI: 10.1103/PhysRevD.103.L041302. arXiv: 2009.14174 [astro-ph.CO].

[213] Shou-Long Li, Lijing Shao, Puxun Wu, and Hongwei Yu. "NANOGrav Signal from First-Order Confinement/Deconfinement Phase Transition in Different QCD Matters". In: *arXiv e-prints*, arXiv:2101.08012 (Jan. 2021), arXiv:2101.08012. arXiv: 2101.08012 [astro-ph.CO].

[214] Basabendu Barman, Amit Dutta Banik, and Avik Paul. "Implications of NANOGrav results and UV freeze-in in a fast-expanding Universe". In: *arXiv e-prints*, arXiv:2012.11969 (Dec. 2020), arXiv:2012.11969. arXiv: 2012.11969 [astro-ph.CO].

[215] Katsuya T. Abe, Yuichiro Tada, and Ikumi Ueda. "Induced gravitational waves as a cosmological probe of the sound speed during the QCD phase transition". In: *arXiv e-prints*, arXiv:2010.06193 (Oct. 2020), arXiv:2010.06193. arXiv: 2010.06193 [astro-ph.CO].

[216] Wolfram Ratzinger and Pedro Schwaller. "Whispers from the dark side: Confronting light new physics with NANOGrav data". In: *arXiv e-prints*, arXiv:2009.11875 (Sept. 2020), arXiv:2009.11875. arXiv: 2009.11875 [astro-ph.CO].

[217] Andrea Addazi, Yi-Fu Cai, Qingyu Gan, Antonino Marciano, and Kaiqiang Zeng. "NANOGrav results and Dark First Order Phase Transitions". In: *arXiv e-prints*, arXiv:2009.10327 (Sept. 2020), arXiv:2009.10327. arXiv: 2009.10327 [hep-ph].

[218] Yuichiro Nakai, Motoo Suzuki, Fuminobu Takahashi, and Masaki Yamada. "Gravitational Waves and Dark Radiation from Dark Phase Transition: Connecting NANOGrav Pulsar Timing Data and Hubble Tension". In: *arXiv e-prints*, arXiv:2009.09754 (Sept. 2020), arXiv:2009.09754. arXiv: 2009.09754 [astro-ph.CO].

[219] Matthew J. Strassler and Kathryn M. Zurek. "Echoes of a hidden valley at hadron colliders". In: *Phys. Lett. B* 651 (2007), pp. 374–379. DOI: 10.1016/j.physletb.2007.06.055. arXiv: hep-ph/0604261.

[220] Z. Chacko, Lawrence J. Hall, and Yasunori Nomura. "Acceleressence: dark energy from a phase transition at the seesaw scale". In: *JCAP* 10 (2004), p. 011. DOI: 10.1088/1475-7516/2004/10/011. arXiv: astro-ph/0405596.

[221] Marco Battaglieri et al. "US Cosmic Visions: New Ideas in Dark Matter 2017: Community Report". In: *arXiv e-prints*, arXiv:1707.04591 (July 2017), arXiv:1707.04591. arXiv: 1707.04591 [hep-ph].

[222] Shou-Long Li, Lijing Shao, Puxun Wu, and Hongwei Yu. "NANOGrav Signal from First-Order Confinement/Deconfinement Phase Transition in Different QCD Matters". In: (Jan. 2021). arXiv: 2101.08012 [astro-ph.CO].

[223] Ligong Bian, Rong-Gen Cai, Jing Liu, Xing-Yu Yang, and Ruiyu Zhou. "On the gravitational wave sources from the NANOGrav 12.5-yr data". In: (Sept. 2020). arXiv: 2009.13893 [astro-ph.CO].

[224] C. J. Moore, R. H. Cole, and C. P. L. Berry. "Gravitational-wave sensitivity curves". In: *Classical and Quantum Gravity* 32.1, 015014 (Jan. 2015), p. 015014. DOI: 10.1088/0264-9381/32/1/015014. arXiv: 1408.0740 [gr-qc].

[225] Planck Collaboration et al. "Planck 2018 results. VI. Cosmological parameters". In: 641, A6 (Sept. 2020), A6. DOI: 10.1051/0004-6361/201833910. arXiv: 1807.06209 [astro-ph.CO].

[226] E. S. Phinney. "A Practical Theorem on Gravitational Wave Backgrounds". In: *ArXiv Astrophysics e-prints* (Aug. 2001). eprint: astro-ph/0108028.

[227] R. W. Hellings and G. S. Downs. "Upper limits on the isotropic gravitational radiation background from pulsar timing analysis". In: 265 (Feb. 1983), pp. L39–L42. DOI: 10.1086/183954.

[228] Ryusuke Jinno and Masahiro Takimoto. "Gravitational waves from bubble collisions: An analytic derivation". In: *Phys. Rev. D* 95.2 (2017), p. 024009. DOI: 10.1103/PhysRevD.95.024009. arXiv: 1605.01403 [astro-ph.CO].

[229] Mark Hindmarsh, Stephan J. Huber, Kari Rummukainen, and David J. Weir. "Shape of the acoustic gravitational wave power spectrum from a first order phase transition". In: *Phys. Rev. D* 96.10 (2017). [Erratum: Phys.Rev.D 101,

089902 (2020)], p. 103520. DOI: 10.1103/PhysRevD.96.103520. arXiv: 1704.05871 [astro-ph.CO].

[230] Marek Lewicki and Ville Vaskonen. "Gravitational waves from colliding vacuum bubbles in gauge theories". In: (Dec. 2020). arXiv: 2012.07826 [astro-ph.CO].

[231] Daniel Cutting, Elba Granados Escartin, Mark Hindmarsh, and David J. Weir. "Gravitational waves from vacuum first order phase transitions II: from thin to thick walls". In: *Phys. Rev. D* 103.2 (2021), p. 023531. DOI: 10.1103/PhysRevD.103.023531. arXiv: 2005.13537 [astro-ph.CO].

[232] Chiara Caprini et al. "Science with the space-based interferometer eLISA. II: Gravitational waves from cosmological phase transitions". In: *JCAP* 04 (2016), p. 001. DOI: 10.1088/1475-7516/2016/04/001. arXiv: 1512.06239 [astro-ph.CO].

[233] Alberto Roper Pol, Sayan Mandal, Axel Brandenburg, Tina Kahniashvili, and Arthur Kosowsky. "Numerical simulations of gravitational waves from early-universe turbulence". In: *Phys. Rev. D* 102.8 (2020), p. 083512. DOI: 10.1103/PhysRevD.102.083512. arXiv: 1903.08585 [astro-ph.CO].

[234] Axel Brandenburg, Emma Clarke, Yutong He, and Tina Kahniashvili. "Can we observe the QCD phase transition-generated gravitational waves through pulsar timing arrays?" In: *Phys. Rev. D* 104.4 (2021), p. 043513. DOI: 10.1103/PhysRevD.104.043513. arXiv: 2102.12428 [astro-ph.CO].

[235] Pierre Binetruy, Alejandro Bohe, Chiara Caprini, and Jean-Francois Dufaux. "Cosmological Backgrounds of Gravitational Waves and eLISA/NGO: Phase Transitions, Cosmic Strings and Other Sources". In: *JCAP* 06 (2012), p. 027. DOI: 10.1088/1475-7516/2012/06/027. arXiv: 1201.0983 [gr-qc].

[236] Huai-Ke Guo, Kuver Sinha, Daniel Vagie, and Graham White. "Phase Transitions in an Expanding Universe: Stochastic Gravitational Waves in Standard and Non-Standard Histories". In: *JCAP* 01 (2021), p. 001. DOI: 10.1088/1475-7516/2021/01/001. arXiv: 2007.08537 [hep-ph].

[237] John Ellis, Marek Lewicki, and José Miguel No. "Gravitational waves from first-order cosmological phase transitions: lifetime of the sound wave source". In: *JCAP* 07 (2020), p. 050. DOI: 10.1088/1475-7516/2020/07/050. arXiv: 2003.07360 [hep-ph].

[238] David J. Weir. "Gravitational waves from a first order electroweak phase transition: a brief review". In: *Phil. Trans. Roy. Soc. Lond. A* 376.2114 (2018), p. 20170126. DOI: 10.1098/rsta.2017.0126. arXiv: 1705.01783 [hep-ph].

[239] Mark Hindmarsh and Mulham Hijazi. "Gravitational waves from first order cosmological phase transitions in the Sound Shell Model". In: *JCAP* 12 (2019), p. 062. DOI: 10.1088/1475-7516/2019/12/062. arXiv: 1909.10040 [astro-ph.CO].

[240] Jose R. Espinosa, Thomas Konstandin, Jose M. No, and Geraldine Servant. "Energy Budget of Cosmological First-order Phase Transitions". In: *JCAP* 06 (2010), p. 028. DOI: 10.1088/1475-7516/2010/06/028. arXiv: 1004.4187 [hep-ph].

[241] Arthur Kosowsky, Michael S. Turner, and Richard Watkins. "Gravitational radiation from colliding vacuum bubbles". In: *Phys. Rev. D* 45 (1992), pp. 4514–4535. DOI: 10.1103/PhysRevD.45.4514.

[242] Daniel Cutting, Mark Hindmarsh, and David J. Weir. "Gravitational waves from vacuum first-order phase transitions: from the envelope to the lattice". In: *Phys. Rev. D* 97.12 (2018), p. 123513. DOI: 10.1103/PhysRevD.97.123513. arXiv: 1802.05712 [astro-ph.CO].

[243] Marek Lewicki and Ville Vaskonen. "Gravitational wave spectra from strongly supercooled phase transitions". In: *Eur. Phys. J. C* 80.11 (2020), p. 1003. DOI: 10.1140/epjc/s10052-020-08589-1. arXiv: 2007.04967 [astro-ph.CO].

[244] Gideon Schwarz. "Estimating the Dimension of a Model". In: *Annals of Statistics* 6.2 (July 1978), pp. 461–464.

[245] Robert E. Kass and Adrian E. Raftery. "Bayes Factors". In: *Journal of the American Statistical Association* 90.430 (1995), pp. 773–795. DOI: 10.1080/01621459.1995.10476572.

[246] Daniel Cutting, Mark Hindmarsh, and David J. Weir. "Vorticity, kinetic energy, and suppressed gravitational wave production in strong first order phase transitions". In: *Phys. Rev. Lett.* 125.2 (2020), p. 021302. DOI: 10.1103/PhysRevLett.125.021302. arXiv: 1906.00480 [hep-ph].

[247] Particle Data Group et al. "Review of Particle Physics". In: *Progress of Theoretical and Experimental Physics* 2020.8, 083C01 (Aug. 2020), p. 083C01. DOI: 10.1093/ptep/ptaa104.

[248] Justin A. Ellis, Michele Vallisneri, Stephen R. Taylor, and Paul T. Baker. *ENTERPRISE: Enhanced Numerical Toolbox Enabling a Robust PulsaR Inference SuitE*. Dec. 2019. ascl: 1912.015.

[249] Jeffrey Hazboun, Joseph Romano, and Tristan Smith. "Hasasia: A Python package for Pulsar Timing Array Sensitivity Curves". In: *The Journal of Open Source Software* 4.42, 1775 (Oct. 2019), p. 1775. DOI: 10.21105/joss.01775.

[250] Michele Vallisneri. *libstempo: Python wrapper for Tempo2*. Feb. 2020. ascl: 2002.017.

[251] John D. Hunter. "Matplotlib: A 2D Graphics Environment". In: *Computing in Science and Engineering* 9.3 (May 2007), pp. 90–95. DOI: 10.1109/MCSE.2007.55.

[252] Justin Ellis and Rutger van Haasteren. *jellis18/PTMCMCSampler: Official Release*. Oct. 2017. DOI: 10.5281/zenodo.1037579. URL: https://doi.org/10.5281/zenodo.1037579.

[253] D. Nice et al. *Tempo: Pulsar timing data analysis*. Sept. 2015. ascl: 1509.002.

[254] George Hobbs and Russell Edwards. *Tempo2: Pulsar Timing Package*. Oct. 2012. ascl: 1210.015.

[255] Jing Luo et al. *PINT: High-precision pulsar timing analysis package*. Feb. 2019. ascl: 1902.007.

[256] E.G. Adelberger, B.R. Heckel, and A.E. Nelson. "Tests of the gravitational inverse-square law". In: *Annual Review of Nuclear and Particle Science* 53.1 (Dec. 2003), pp. 77–121. ISSN: 1545-4134. DOI: 10.1146/annurev.nucl.53.041002.110503. URL: http://dx.doi.org/10.1146/annurev.nucl.53.041002.110503.

[257] Edward Hardy, Robert Lasenby, John March-Russell, and Stephen M. West. "Big Bang Synthesis of Nuclear Dark Matter". In: *JHEP* 06 (2015), p. 011. DOI: 10.1007/JHEP06(2015)011. arXiv: 1411.3739 [hep-ph].

[258] Gordan Krnjaic and Kris Sigurdson. "Big Bang Darkleosynthesis". In: *Phys. Lett. B* 751 (2015), pp. 464–468. DOI: 10.1016/j.physletb.2015.11.001. arXiv: 1406.1171 [hep-ph].

[259] William Detmold, Matthew McCullough, and Andrew Pochinsky. "Dark Nuclei I: Cosmology and Indirect Detection". In: *Phys. Rev. D* 90.11 (2014), p. 115013. DOI: 10.1103/PhysRevD.90.115013. arXiv: 1406.2276 [hep-ph].

[260] Mark B. Wise and Yue Zhang. "Stable Bound States of Asymmetric Dark Matter". In: *Phys. Rev. D* 90.5 (2014). [Erratum: Phys.Rev.D 91, 039907 (2015)], p. 055030. DOI: 10.1103/PhysRevD.90.055030. arXiv: 1407.4121 [hep-ph].

[261] Moira I. Gresham, Hou Keong Lou, and Kathryn M. Zurek. "Early Universe synthesis of asymmetric dark matter nuggets". In: *Phys. Rev. D* 97.3 (2018), p. 036003. DOI: 10.1103/PhysRevD.97.036003. arXiv: 1707.02316 [hep-ph].

[262] Moira I. Gresham, Hou Keong Lou, and Kathryn M. Zurek. "Nuclear Structure of Bound States of Asymmetric Dark Matter". In: *Phys. Rev. D* 96.9 (2017), p. 096012. DOI: 10.1103/PhysRevD.96.096012. arXiv: 1707.02313 [hep-ph].

[263] Moira I. Gresham, Hou Keong Lou, and Kathryn M. Zurek. "Astrophysical Signatures of Asymmetric Dark Matter Bound States". In: *Phys. Rev. D* 98.9 (2018), p. 096001. DOI: 10.1103/PhysRevD.98.096001. arXiv: 1805.04512 [hep-ph].

[264] Moira I. Gresham and Kathryn M. Zurek. "Asymmetric Dark Stars and Neutron Star Stability". In: *Phys. Rev. D* 99.8 (2019), p. 083008. DOI: 10.1103/PhysRevD.99.083008. arXiv: 1809.08254 [astro-ph.CO].

[265] Dongok Kim, Younggeun Kim, Yannis K. Semertzidis, Yun Chang Shin, and Wen Yin. "Cosmic axion force". In: *Physical Review D* 104.9 (Nov. 2021). DOI: 10.1103/physrevd.104.095010. URL: https://doi.org/10.1103%2Fphysrevd.104.095010.

[266] Joel Bergé, Philippe Brax, Gilles Métris, Martin Pernot-Borràs, Pierre Touboul, and Jean-Philippe Uzan. "MICROSCOPE Mission: First Constraints on the Violation of the Weak Equivalence Principle by a Light Scalar Dilaton". In: *Phys. Rev. Lett.* 120.14 (2018), p. 141101. DOI: 10.1103/PhysRevLett.120.141101. arXiv: 1712.00483 [gr-qc].

[267] Pierre Fayet. "MICROSCOPE limits on the strength of a new force, with comparisons to gravity and electromagnetism". In: *Phys. Rev. D* 99.5 (2019), p. 055043. DOI: 10.1103/PhysRevD.99.055043. arXiv: 1809.04991 [hep-ph].

[268] Ahmet Coskuner, Dorota M. Grabowska, Simon Knapen, and Kathryn M. Zurek. "Direct Detection of Bound States of Asymmetric Dark Matter". In: *Phys. Rev. D* 100.3 (2019), p. 035025. DOI: 10.1103/PhysRevD.100.035025. arXiv: 1812.07573 [hep-ph].

[269] E. R. Siegel, M. P. Hertzberg, and J. N. Fry. "Probing dark matter substructure with pulsar timing". In: *Monthly Notices of the Royal Astronomical Society* 382.2 (Dec. 2007), pp. 879–885. DOI: 10.1111/j.1365-2966.2007.12435.x. URL: https://doi.org/10.1111%2Fj.1365-2966.2007.12435.x.

[270] Naoki Seto and Asantha Cooray. "Searching for Primordial Black Hole Dark Matter with Pulsar Timing Arrays". In: *The Astrophysical Journal* 659.1 (Mar. 2007), pp. L33–L36. DOI: 10.1086/516570. URL: https://doi.org/10.1086%2F516570.

[271] Hamish A. Clark, Geraint F. Lewis, and Pat Scott. "Investigating dark matter substructure with pulsar timing – I. Constraints on ultracompact minihaloes". In: *Monthly Notices of the Royal Astronomical Society* 456.2 (Dec. 2015), pp. 1394–1401. DOI: 10.1093/mnras/stv2743. URL: https://doi.org/10.1093%2Fmnras%2Fstv2743.

[272] Hamish A. Clark, Geraint F. Lewis, and Pat Scott. "Investigating dark matter substructure with pulsar timing – II. Improved limits on small-scale cosmology". In: *Monthly Notices of the Royal Astronomical Society* 456.2 (Dec.

2015), pp. 1402–1409. DOI: 10.1093/mnras/stv2529. URL: https://doi.org/10.1093%2Fmnras%2Fstv2529.

[273] Katelin Schutz and Adrian Liu. "Pulsar timing can constrain primordial black holes in the LIGO mass window". In: *Physical Review D* 95.2 (Jan. 2017). DOI: 10.1103/physrevd.95.023002. URL: https://doi.org/10.1103%2Fphysrevd.95.023002.

[274] Kazumi Kashiyama and Masamune Oguri. *Detectability of Small-Scale Dark Matter Clumps with Pulsar Timing Arrays*. 2018. DOI: 10.48550/ARXIV.1801.07847. URL: https://arxiv.org/abs/1801.07847.

[275] Masha Baryakhtar, Joseph Bramante, Shirley Weishi Li, Tim Linden, and Nirmal Raj. "Dark Kinetic Heating of Neutron Stars and An Infrared Window On WIMPs, SIMPs, and Pure Higgsinos". In: *Phys. Rev. Lett.* 119.13 (2017), p. 131801. DOI: 10.1103/PhysRevLett.119.131801. arXiv: 1704.01577 [hep-ph].

[276] Nirmal Raj, Philip Tanedo, and Hai-Bo Yu. "Neutron stars at the dark matter direct detection frontier". In: *Phys. Rev. D* 97.4 (2018), p. 043006. DOI: 10.1103/PhysRevD.97.043006. arXiv: 1707.09442 [hep-ph].

[277] Raghuveer Garani, Yoann Genolini, and Thomas Hambye. "New Analysis of Neutron Star Constraints on Asymmetric Dark Matter". In: *JCAP* 05 (2019), p. 035. DOI: 10.1088/1475-7516/2019/05/035. arXiv: 1812.08773 [hep-ph].

[278] Nicole F. Bell, Giorgio Busoni, and Sandra Robles. "Heating up Neutron Stars with Inelastic Dark Matter". In: *JCAP* 09 (2018), p. 018. DOI: 10.1088/1475-7516/2018/09/018. arXiv: 1807.02840 [hep-ph].

[279] Nicole F. Bell, Giorgio Busoni, and Sandra Robles. "Capture of Leptophilic Dark Matter in Neutron Stars". In: *JCAP* 06 (2019), p. 054. DOI: 10.1088/1475-7516/2019/06/054. arXiv: 1904.09803 [hep-ph].

[280] Raghuveer Garani and Julian Heeck. "Dark matter interactions with muons in neutron stars". In: *Phys. Rev. D* 100.3 (2019), p. 035039. DOI: 10.1103/PhysRevD.100.035039. arXiv: 1906.10145 [hep-ph].

[281] Javier F. Acevedo, Joseph Bramante, Rebecca K. Leane, and Nirmal Raj. "Warming Nuclear Pasta with Dark Matter: Kinetic and Annihilation Heating of Neutron Star Crusts". In: *JCAP* 03 (2020), p. 038. DOI: 10.1088/1475-7516/2020/03/038. arXiv: 1911.06334 [hep-ph].

[282] Aniket Joglekar, Nirmal Raj, Philip Tanedo, and Hai-Bo Yu. "Relativistic capture of dark matter by electrons in neutron stars". In: *Phys. Lett.* B (2020), p. 135767. DOI: 10.1016/j.physletb.2020.135767. arXiv: 1911.13293 [hep-ph].

[283] Basudeb Dasgupta, Aritra Gupta, and Anupam Ray. "Dark matter capture in celestial objects: light mediators, self-interactions, and complementarity with direct detection". In: *JCAP* 10 (2020), p. 023. DOI: 10.1088/1475-7516/2020/10/023. arXiv: 2006.10773 [hep-ph].

[284] Wai-Yee Keung, Danny Marfatia, and Po-Yan Tseng. "Heating neutron stars with GeV dark matter". In: *JHEP* 07 (2020), p. 181. DOI: 10.1007/JHEP07(2020)181. arXiv: 2001.09140 [hep-ph].

[285] Aniket Joglekar, Nirmal Raj, Philip Tanedo, and Hai-Bo Yu. "Dark kinetic heating of neutron stars from contact interactions with relativistic targets". In: *Phys. Rev. D* 102.12 (2020), p. 123002. DOI: 10.1103/PhysRevD.102.123002. arXiv: 2004.09539 [hep-ph].

[286] Nicole F. Bell, Giorgio Busoni, Theo F. Motta, Sandra Robles, Anthony W. Thomas, and Michael Virgato. "Nucleon Structure and Strong Interactions in Dark Matter Capture in Neutron Stars". In: *Phys. Rev. Lett.* 127.11 (2021), p. 111803. DOI: 10.1103/PhysRevLett.127.111803. arXiv: 2012.08918 [hep-ph].

[287] Nicole F. Bell, Giorgio Busoni, Sandra Robles, and Michael Virgato. "Improved Treatment of Dark Matter Capture in Neutron Stars II: Leptonic Targets". In: *JCAP* 03 (2021), p. 086. DOI: 10.1088/1475-7516/2021/03/086. arXiv: 2010.13257 [hep-ph].

[288] Raghuveer Garani, Aritra Gupta, and Nirmal Raj. "Observing the thermalization of dark matter in neutron stars". In: *Phys. Rev. D* 103.4 (2021), p. 043019. DOI: 10.1103/PhysRevD.103.043019. arXiv: 2009.10728 [hep-ph].

[289] Tarak Nath Maity and Farinaldo S. Queiroz. "Detecting bosonic dark matter with neutron stars". In: *Phys. Rev. D* 104.8 (2021), p. 083019. DOI: 10.1103/PhysRevD.104.083019. arXiv: 2104.02700 [hep-ph].

[290] David McKeen, Maxim Pospelov, and Nirmal Raj. "Neutron Star Internal Heating Constraints on Mirror Matter". In: *Phys. Rev. Lett.* 127.6 (2021), p. 061805. DOI: 10.1103/PhysRevLett.127.061805. arXiv: 2105.09951 [hep-ph].

[291] Cosmin Ilie and Caleb Levy. "Multicomponent multiscatter capture of dark matter". In: *Phys. Rev. D* 104.8 (2021), p. 083033. DOI: 10.1103/PhysRevD.104.083033. arXiv: 2105.09765 [astro-ph.CO].

[292] Cosmin Ilie and Jillian Paulin. "Analytic Approximations for the Velocity Suppression of Dark Matter Capture". In: *Astrophys. J.* 932.1 (2022), p. 46. DOI: 10.3847/1538-4357/ac651b. arXiv: 2107.00675 [astro-ph.CO].

[293] Nicole F. Bell, Giorgio Busoni, Sandra Robles, and Michael Virgato. "Improved Treatment of Dark Matter Capture in Neutron Stars". In: *JCAP* 09 (2020), p. 028. DOI: 10.1088/1475-7516/2020/09/028. arXiv: 2004.14888 [hep-ph].

[294] Joseph Bramante, Bradley J. Kavanagh, and Nirmal Raj. "Scattering Searches for Dark Matter in Subhalos: Neutron Stars, Cosmic Rays, and Old Rocks". In: *Phys. Rev. Lett.* 128.23 (2022), p. 231801. DOI: 10.1103/PhysRevLett.128.231801. arXiv: 2109.04582 [hep-ph].

[295] Sebastien Guillot, George G. Pavlov, Cristobal Reyes, Andreas Reisenegger, Luis E. Rodriguez, Blagoy Rangelov, and Oleg Kargaltsev. "Hubble Space Telescope Nondetection of PSR J2144–3933: The Coldest Known Neutron Star". In: *The Astrophysical Journal* 874.2 (Apr. 2019), p. 175. ISSN: 1538-4357. DOI: 10.3847/1538-4357/ab0f38. URL: http://dx.doi.org/10.3847/1538-4357/ab0f38.

[296] Zaven Arzoumanian et al. "The NANOGrav 11-year Data Set: High-precision Timing of 45 Millisecond Pulsars". In: *The Astrophysical Journal Supplement Series* 235.2 (Apr. 2018), p. 37. DOI: 10.3847/1538-4365/aab5b0. URL: https://doi.org/10.3847%2F1538-4365%2Faab5b0.

[297] Z. Arzoumanian et al. "The NANOGrav 11 Year Data Set: Pulsar-timing Constraints on the Stochastic Gravitational-wave Background". In: *The Astrophysical Journal* 859.1 (May 2018), p. 47. DOI: 10.3847/1538-4357/aabd3b. URL: https://doi.org/10.3847%2F1538-4357%2Faabd3b.

[298] A. Brazier et al. *The NANOGrav Program for Gravitational Waves and Fundamental Physics*. 2019. arXiv: 1908.05356 [astro-ph.IM].

[299] Hooman Davoudiasl. "Dark matter repulsion could thwart direct detection". In: *Phys. Rev. D* 96.9 (2017), p. 095019. DOI: 10.1103/PhysRevD.96.095019. arXiv: 1705.00028 [hep-ph].

[300] Hooman Davoudiasl, Peter B. Denton, and Julia Gehrlein. "Attractive scenario for light dark matter direct detection". In: *Phys. Rev. D* 102.9 (2020), p. 091701. DOI: 10.1103/PhysRevD.102.091701. arXiv: 2007.04989 [hep-ph].

[301] W. H. Press and S. A. Teukolsky. "On formation of close binaries by two-body tidal capture." In: 213 (Apr. 1977), pp. 183–192. DOI: 10.1086/155143.

[302] A. C. Fabian, J. E. Pringle, and M. J. Rees. "Tidal capture formation of binary systems and X-ray sources in globular clusters." In: *MNRAS* 172 (Aug. 1975), p. 15. DOI: 10.1093/mnras/172.1.15P.

[303] Paolo Pani and Abraham Loeb. "Tidal capture of a primordial black hole by a neutron star: implications for constraints on dark matter". In: *Journal of Cosmology and Astroparticle Physics* 2014.06 (June 2014), pp. 026–026. ISSN: 1475-7516. DOI: 10.1088/1475-7516/2014/06/026. URL: http://dx.doi.org/10.1088/1475-7516/2014/06/026.

[304] Curt Cutler and Lee Lindblom. "The Effect of Viscosity on Neutron Star Oscillations". In: 314 (Mar. 1987), p. 234. DOI: 10.1086/165052.

[305] Nils Andersson. "Modelling the dynamics of superfluid neutron stars". In: *Astrophys. Space Sci.* 308 (2007), pp. 395–402. DOI: 10.1007/s10509-007-9361-7. arXiv: astro-ph/0610192.

[306] E. Flowers and N. Itoh. "Transport properties of dense matter." In: 206 (May 1976), pp. 218–242. DOI: 10.1086/154375.

[307] E. Flowers and N. Itoh. "Transport properties of dense matter. II." In: 230 (June 1979), pp. 847–858. DOI: 10.1086/157145.

[308] William DeRocco, Marios Galanis, and Robert Lasenby. *Dark matter scattering in astrophysical media: collective effects*. 2022. arXiv: 2201.05167 [hep-ph].

[309] Dany Page, James M. Lattimer, Madappa Prakash, and Andrew W. Steiner. "Minimal cooling of neutron stars: A New paradigm". In: *Astrophys. J. Suppl.* 155 (2004), pp. 623–650. DOI: 10.1086/424844. arXiv: astro-ph/0403657.

[310] D.G. Yakovlev and C.J. Pethick. "Neutron Star Cooling". In: *Annual Review of Astronomy and Astrophysics* 42.1 (Sept. 2004), pp. 169–210. ISSN: 1545-4282. DOI: 10.1146/annurev.astro.42.053102.134013. URL: http://dx.doi.org/10.1146/annurev.astro.42.053102.134013.

[311] D. G. Yakovlev, K. P. Levenfish, and Yu. A. Shibanov. "Cooling neutron stars and superfluidity in their interiors". In: *Phys. Usp.* 42 (1999), pp. 737–778. DOI: 10.1070/PU1999v042n08ABEH000556. arXiv: astro-ph/9906456.

[312] T. A. Wagner, S. Schlamminger, J. H. Gundlach, and E. G. Adelberger. "Torsion-balance tests of the weak equivalence principle". In: *Class. Quant. Grav.* 29 (2012), p. 184002. DOI: 10.1088/0264-9381/29/18/184002. arXiv: 1207.2442 [gr-qc].

[313] Z. Arzoumanian et al. "THE NANOGRAV NINE-YEAR DATA SET: LIMITS ON THE ISOTROPIC STOCHASTIC GRAVITATIONAL WAVE BACKGROUND". In: *The Astrophysical Journal* 821.1 (Apr. 2016), p. 13. ISSN: 1538-4357. DOI: 10.3847/0004-637x/821/1/13. URL: http://dx.doi.org/10.3847/0004-637X/821/1/13.

[314] Jeffrey S. Hazboun, Joseph Simon, Xavier Siemens, and Joseph D. Romano. "Model Dependence of Bayesian Gravitational-wave Background Statistics for Pulsar Timing Arrays". In: *The Astrophysical Journal* 905.1 (Dec. 2020), p. L6. ISSN: 2041-8213. DOI: 10.3847/2041-8213/abca92. URL: http://dx.doi.org/10.3847/2041-8213/abca92.

[315] Bing Sun, Zhoujian Cao, and Lijing Shao. "Constraints on fifth forces through perihelion precession of planets". In: *Physical Review D* 100.8 (Oct. 2019). ISSN: 2470-0029. DOI: 10.1103/physrevd.100.084030. URL: http://dx.doi.org/10.1103/PhysRevD.100.084030.

[316] Lijing Shao, Norbert Wex, and Michael Kramer. "Testing the universality of free fall towards dark matter with radio pulsars". In: *Phys. Rev. Lett.* 120.24 (2018), p. 241104. DOI: 10.1103/PhysRevLett.120.241104. arXiv: 1805.08408 [gr-qc].

[317] Christopher W. Stubbs. "Experimental limits on any long range nongravitational interaction between dark matter and ordinary matter". In: *Phys. Rev. Lett.* 70 (2 Jan. 1993), pp. 119–122. DOI: 10.1103/PhysRevLett.70.119. URL: https://link.aps.org/doi/10.1103/PhysRevLett.70.119.

[318] Marius Cautun et al. "The Milky Way total mass profile as inferred from Gaia DR2". In: *Mon. Not. Roy. Astron. Soc.* 494.3 (2020), pp. 4291–4313. DOI: 10.1093/mnras/staa1017. arXiv: 1911.04557 [astro-ph.GA].

[319] Jonathan P. Gardner et al. "The James Webb Space Telescope". In: *Space Sci. Rev.* 123 (2006), p. 485. DOI: 10.1007/s11214-006-8315-7. arXiv: astro-ph/0606175.

[320] A. Weltman et al. "Fundamental physics with the Square Kilometre Array". In: *Publ. Astron. Soc. Austral.* 37 (2020), e002. DOI: 10.1017/pasa.2019.42. arXiv: 1810.02680 [astro-ph.CO].

[321] Chris Kouvaris. "WIMP Annihilation and Cooling of Neutron Stars". In: *Phys. Rev. D* 77 (2008), p. 023006. DOI: 10.1103/PhysRevD.77.023006. arXiv: 0708.2362 [astro-ph].

[322] Gianfranco Bertone and Malcolm Fairbairn. "Compact Stars as Dark Matter Probes". In: *Phys. Rev. D* 77 (2008), p. 043515. DOI: 10.1103/PhysRevD.77.043515. arXiv: 0709.1485 [astro-ph].

[323] Chris Kouvaris and Peter Tinyakov. "Can Neutron stars constrain Dark Matter?" In: *Phys. Rev. D* 82 (2010), p. 063531. DOI: 10.1103/PhysRevD.82.063531. arXiv: 1004.0586 [astro-ph.GA].

[324] Arnaud de Lavallaz and Malcolm Fairbairn. "Neutron Stars as Dark Matter Probes". In: *Phys. Rev. D* 81 (2010), p. 123521. DOI: 10.1103/PhysRevD.81.123521. arXiv: 1004.0629 [astro-ph.GA].

[325] Joseph Bramante, Antonio Delgado, and Adam Martin. "Multiscatter stellar capture of dark matter". In: *Phys. Rev. D* 96.6 (2017), p. 063002. DOI: 10.1103/PhysRevD.96.063002. arXiv: 1703.04043 [hep-ph].

[326] David McKeen, Maxim Pospelov, and Nirmal Raj. "Cosmological and astrophysical probes of dark baryons". In: *Phys. Rev. D* 103.11 (2021), p. 115002. DOI: 10.1103/PhysRevD.103.115002. arXiv: 2012.09865 [hep-ph].

[327] Michele Maggiore. "Gravitational wave experiments and early universe cosmology". In: *Phys. Rept.* 331 (2000), pp. 283–367. DOI: 10.1016/S0370-1573(99)00102-7. arXiv: gr-qc/9909001.

[328] Chiara Caprini and Daniel G. Figueroa. "Cosmological Backgrounds of Gravitational Waves". In: *Class. Quant. Grav.* 35.16 (2018), p. 163001. DOI: 10.1088/1361-6382/aac608. arXiv: 1801.04268 [astro-ph.CO].

[329] Nelson Christensen. "Stochastic Gravitational Wave Backgrounds". In: *Rept. Prog. Phys.* 82.1 (2019), p. 016903. DOI: 10.1088/1361-6633/aae6b5. arXiv: 1811.08797 [gr-qc].

[330] M. C. Guzzetti, N. Bartolo, M. Liguori, and S. Matarrese. "Gravitational waves from inflation". In: *Riv. Nuovo Cim.* 39.9 (2016), pp. 399–495. DOI: 10.1393/ncr/i2016-10127-1. arXiv: 1605.01615 [astro-ph.CO].

[331] Guillem Domènech. "Scalar Induced Gravitational Waves Review". In: *Universe* 7.11 (2021), p. 398. DOI: 10.3390/universe7110398. arXiv: 2109.01398 [gr-qc].

[332] Chen Yuan and Qing-Guo Huang. "A topic review on probing primordial black hole dark matter with scalar induced gravitational waves". In: *iScience 24, 102860 (2021)* (Mar. 2021). arXiv: 2103.04739 [astro-ph.GA].

[333] Chiara Caprini, M. Hindmarsh, S. Huber, et al. "Science with the space-based interferometer eLISA. II: Gravitational waves from cosmological phase transitions". In: *JCAP* 04 (2016), p. 001. DOI: 10.1088/1475-7516/2016/04/001. arXiv: 1512.06239 [astro-ph.CO].

[334] Chiara Caprini, M. Chala, G. C. Dorsch, et al. "Detecting gravitational waves from cosmological phase transitions with LISA: an update". In: *JCAP* 03 (2020), p. 024. DOI: 10.1088/1475-7516/2020/03/024. arXiv: 1910.13125 [astro-ph.CO].

[335] Mark B. Hindmarsh, Marvin Lüben, Johannes Lumma, and Martin Pauly. "Phase transitions in the early universe". In: *SciPost Phys. Lect. Notes* 24 (2021), p. 1. DOI: 10.21468/SciPostPhysLectNotes.24. arXiv: 2008.09136 [astro-ph.CO].

[336] Alexander Vilenkin. "Cosmic Strings and Domain Walls". In: *Phys. Rept.* 121 (1985), pp. 263–315. DOI: 10.1016/0370-1573(85)90033-X.

[337] M. B. Hindmarsh and T. W. B. Kibble. "Cosmic strings". In: *Rept. Prog. Phys.* 58 (1995), pp. 477–562. DOI: 10.1088/0034-4885/58/5/001. arXiv: hep-ph/9411342.

[338] Ken'ichi Saikawa. "A review of gravitational waves from cosmic domain walls". In: *Universe* 3.2 (2017), p. 40. DOI: 10.3390/universe3020040. arXiv: 1703.02576 [hep-ph].

[339] Maura A. McLaughlin. "The North American Nanohertz Observatory for Gravitational Waves". In: *Class. Quant. Grav.* 30 (2013), p. 224008. DOI: 10.1088/0264-9381/30/22/224008. arXiv: 1310.0758 [astro-ph.IM].

[340] Gabriella Agazie, A. Anumarlapudi, A. M. Archibald, et al. “The NANOGrav 15-year Data Set: Evidence for a Gravitational-Wave Background”. In: *Astrophys. J. Lett.* (2023). DOI: 10.3847/2041-8213/acdac6.

[341] Mohan Rajagopal and Roger W. Romani. “Ultra–Low-Frequency Gravitational Radiation from Massive Black Hole Binaries”. In: 446 (June 1995), p. 543. DOI: 10.1086/175813. arXiv: astro-ph/9412038 [astro-ph].

[342] Andrew H. Jaffe and Donald C. Backer. “Gravitational waves probe the coalescence rate of massive black hole binaries”. In: *Astrophys. J.* 583 (2003), pp. 616–631. DOI: 10.1086/345443. arXiv: astro-ph/0210148.

[343] J. Stuart B. Wyithe and Abraham Loeb. “Low-Frequency Gravitational Waves from Massive Black Hole Binaries: Predictions for LISA and Pulsar Timing Arrays”. In: 590.2 (June 2003), pp. 691–706. DOI: 10.1086/375187. arXiv: astro-ph/0211556 [astro-ph].

[344] Gabriella Agazie, A. Anumarlapudi, A. M. Archibald, et al. “PTArcade”. In: *arXiv* (2023). in preparation.

[345] Gabriella Agazie, M. F. Alam, A. M. Archibald, et al. “The NANOGrav 15-year Data Set: Observations and Timing of 68 Millisecond Pulsars”. In: *Astrophys. J. Lett.* (2023). DOI: 10.3847/2041-8213/acda9a.

[346] Andrei Khmelnitsky and Valery Rubakov. “Pulsar timing signal from ultralight scalar dark matter”. In: *JCAP* 02 (2014), p. 019. DOI: 10.1088/1475-7516/2014/02/019. arXiv: 1309.5888 [astro-ph.CO].

[347] N. K. Porayko and K. A. Postnov. “Constraints on ultralight scalar dark matter from pulsar timing”. In: *Physical Review D* 90.6 (Sept. 2014), p. 062008. DOI: 10.1103/PhysRevD.90.062008. URL: https://link.aps.org/doi/10.1103/PhysRevD.90.062008 (visited on 12/14/2022).

[348] Peter W. Graham, David E. Kaplan, Jeremy Mardon, Surjeet Rajendran, and William A. Terrano. “Dark Matter Direct Detection with Accelerometers”. In: *Phys. Rev. D* 93.7 (2016), p. 075029. DOI: 10.1103/PhysRevD.93.075029. arXiv: 1512.06165 [hep-ph].

[349] David E. Kaplan, Andrea Mitridate, and Tanner Trickle. “Constraining Fundamental Constant Variations from Ultralight Dark Matter with Pulsar Timing Arrays”. In: *Physical Review D* 106.3 (Aug. 2022). arXiv:2205.06817 [astro-ph, physics:hep-ph], p. 035032. ISSN: 2470-0010, 2470-0029. DOI: 10.1103/PhysRevD.106.035032. URL: http://arxiv.org/abs/2205.06817 (visited on 12/14/2022).

[350] Md F. Alam, Z. Arzoumanian, P. T. Baker, et al. “The NANOGrav 12.5 yr Data Set: Observations and Narrowband Timing of 47 Millisecond Pulsars”. In: *Astrophys. J. Suppl.* 252.1 (2021), p. 4. DOI: 10.3847/1538-4365/abc6a0. arXiv: 2005.06490 [astro-ph.HE].

[351] Zaven Arzoumanian, Adam Brazier, S. Burke-Spolaor, et al. "The NANOGrav 11-year Data Set: High-precision timing of 45 Millisecond Pulsars". In: *Astrophys. J. Suppl.* 235.2 (2018), p. 37. DOI: 10.3847/1538-4365/aab5b0. arXiv: 1801.01837 [astro-ph.HE].

[352] Ryan S. Park, William M. Folkner, James G. Williams, and Dale H. Boggs. "The JPL Planetary and Lunar Ephemerides DE440 and DE441". In: *"Astrophys. J."* 161.3, 105 (Mar. 2021), p. 105. DOI: 10.3847/1538-3881/abd414.

[353] Gabriella Agazie, A. Anumarlapudi, A. M. Archibald, et al. "The NANOGrav 15-Year Data Set: Detector Characterization and Noise Budget". In: *Astrophys. J. Lett.* (2023). DOI: 10.3847/2041-8213/acda88.

[354] Z. Arzoumanian, P. T. Baker, Adam Brazier, et al. "The NANOGrav 11-year Data Set: Pulsar-timing Constraints On The Stochastic Gravitational-wave Background". In: *Astrophys. J.* 859.1 (2018), p. 47. DOI: 10.3847/1538-4357/aabd3b. arXiv: 1801.02617 [astro-ph.HE].

[355] M. Vallisneri, S. R. Taylor, J. Simon, et al. "Modeling the uncertainties of solar-system ephemerides for robust gravitational-wave searches with pulsar timing arrays". In: *ApJ* (Jan. 2020). DOI: 10.3847/1538-4357/ab7b67. arXiv: 2001.00595 [astro-ph.HE].

[356] R. W. Hellings and G. S. Downs. "Upper limits on the isotropic gravitational radiation background from pulsar timing analysis." In: *Astrophys. J. Lett.* 265 (Feb. 1983), pp. L39–L42. DOI: 10.1086/183954.

[357] Rutger van Haasteren and Yuri Levin. "Understanding and analysing time-correlated stochastic signals in pulsar timing". In: *Monthly Notices of the Royal Astronomical Society* 428.2 (Oct. 2012), pp. 1147–1159. DOI: 10.1093/mnras/sts097. URL: https://doi.org/10.1093%5C%2Fmnras%5C%2Fsts097.

[358] Lindley Lentati, P. Alexander, M. P. Hobson, S. Taylor, J. Gair, S. T. Balan, and R. van Haasteren. "Hyper-efficient model-independent Bayesian method for the analysis of pulsar timing data". In: *Physical Review D* 87.10 (May 2013). DOI: 10.1103/physrevd.87.104021. URL: https://doi.org/10.1103%5C%2Fphysrevd.87.104021.

[359] Harold Jeffreys. *Theory of Probability*. Oxford University Press, 1961. ISBN: 9780191589676.

[360] Justin Ellis and Rutger van Haasteren. *jellis18/PTMCMCSampler: Official Release*. Oct. 2017. DOI: 10.5281/zenodo.1037579. URL: https://doi.org/10.5281/zenodo.1037579.

[361] Antony Lewis. "GetDist: a Python package for analysing Monte Carlo samples". In: (2019). arXiv: 1910.13970 [astro-ph.IM]. URL: https://getdist.readthedocs.io.

[362] Bradley P. Carlin and Siddhartha Chib. "Bayesian Model Choice via Markov Chain Monte Carlo Methods". In: *Journal of the Royal Statistical Society. Series B (Methodological)* 57.3 (1995), pp. 473–484. ISSN: 00359246. URL: http://www.jstor.org/stable/2346151 (visited on 01/27/2023).

[363] Simon J. Godsill. "On the Relationship between Markov Chain Monte Carlo Methods for Model Uncertainty". In: *Journal of Computational and Graphical Statistics* 10.2 (2001), pp. 230–248. ISSN: 10618600. URL: http://www.jstor.org/stable/1391010 (visited on 01/27/2023).

[364] S. Hee, W. J. Handley, M. P. Hobson, and A. N. Lasenby. "Bayesian model selection without evidences: application to the dark energy equation-of-state". In: *Monthly Notices of the Royal Astronomical Society* 455.3 (Nov. 2015), pp. 2461–2473. ISSN: 0035-8711. DOI: 10.1093/mnras/stv2217. eprint: https://academic.oup.com/mnras/article-pdf/455/3/2461/9377568/stv2217.pdf. URL: https://doi.org/10.1093/mnras/stv2217.

[365] B. Efron and R. Tibshirani. "An introduction to the bootstrap". In: *Statist. Sci.* 57.1 (1986), pp. 54–75. DOI: 10.1214/ss/1177013815.

[366] E. S. Phinney. "A Practical Theorem on Gravitational Wave Backgrounds". In: *arXiv e-prints*, astro-ph/0108028 (Aug. 2001), astro–ph/0108028. DOI: 10.48550/arXiv.astro-ph/0108028. arXiv: astro-ph/0108028 [astro-ph].

[367] José M. Bernardo and Adrian F.M. Smith. *Bayesian Theory*. Wiley, 2000. ISBN: 9780471494645.

[368] Adelchi Azzalini. *Statistical Inference: Based on the likelihood*. Boca Raton, London, New York, Washington D.C.: Chapman & Hall/CRC, 1996. ISBN: 978-0412606502.

[369] Andrea Mitridate et al. *PTArcade*. Apr. 2023. DOI: 10.5281/zenodo.7876429. URL: https://doi.org/10.5281/zenodo.7876429.

[370] Andrea Mitridate et al. "PTArcade". In: *arXiv* (2023). in preparation.

[371] John Kormendy and Luis C. Ho. "Coevolution (Or Not) of Supermassive Black Holes and Host Galaxies". In: *Ann. Rev. Astron. Astrophys.* 51 (2013), pp. 511–653. DOI: 10.1146/annurev-astro-082708-101811. arXiv: 1304.7762 [astro-ph.CO].

[372] Kazunori Akiyama, A. Alberdi, W. Alef, et al. "First M87 Event Horizon Telescope Results. I. The Shadow of the Supermassive Black Hole". In: *Astrophys. J. Lett.* 875 (2019), p. L1. DOI: 10.3847/2041-8213/ab0ec7. arXiv: 1906.11238 [astro-ph.GA].

[373] S. D. M. White and M. J. Rees. “Core condensation in heavy halos: a two-stage theory for galaxy formation and clustering”. In: *Monthly Notices of the Royal Astronomical Society* 183.3 (July 1978), pp. 341–358. ISSN: 0035-8711. DOI: 10.1093/mnras/183.3.341. eprint: https://academic.oup.com/mnras/article-pdf/183/3/341/2943374/mnras183-0341.pdf. URL: https://doi.org/10.1093/mnras/183.3.341.

[374] M. C. Begelman, R. D. Blandford, and M. J. Rees. “Massive black hole binaries in active galactic nuclei”. In: 287.5780 (Sept. 1980), pp. 307–309. DOI: 10.1038/287307a0.

[375] M. Enoki and M. Nagashima. “The Effect of Orbital Eccentricity on Gravitational Wave Background Radiation from Supermassive Black Hole Binaries”. In: *Progress of Theoretical Physics* 117.2 (Feb. 2007), pp. 241–256. DOI: 10.1143/PTP.117.241. arXiv: astro-ph/0609377 [astro-ph].

[376] Alberto Sesana, Alberto Vecchio, and Carlo Nicola Colacino. “The stochastic gravitational-wave background from massive black hole binary systems: implications for observations with Pulsar Timing Arrays”. In: *Mon. Not. Roy. Astron. Soc.* 390 (2008), p. 192. DOI: 10.1111/j.1365-2966.2008.13682.x. arXiv: 0804.4476 [astro-ph].

[377] B. Kocsis and A. Sesana. “Gas-driven massive black hole binaries: signatures in the nHz gravitational wave background”. In: *Monthly Notices of the Royal Astronomical Society* 411.3 (Mar. 2011), pp. 1467–1479. DOI: 10.1111/j.1365-2966.2010.17782.x. arXiv: 1002.0584 [astro-ph.CO].

[378] Luke Zoltan Kelley, Laura Blecha, Lars Hernquist, Alberto Sesana, and Stephen R. Taylor. “The Gravitational Wave Background from Massive Black Hole Binaries in Illustris: spectral features and time to detection with pulsar timing arrays”. In: *Mon. Not. Roy. Astron. Soc.* 471.4 (2017), pp. 4508–4526. DOI: 10.1093/mnras/stx1638. arXiv: 1702.02180 [astro-ph.HE].

[379] H. Middleton, A. Sesana, S. Chen, A. Vecchio, W. Del Pozzo, and P. A. Rosado. “Massive black hole binary systems and the NANOGrav 12.5 yr results”. In: *Mon. Not. Roy. Astron. Soc.* 502.1 (2021), pp. L99–L103. DOI: 10.1093/mnrasl/slab008. arXiv: 2011.01246 [astro-ph.HE].

[380] Luke Kelley et al. “holodeck”. In: *arXiv* (2023). in preparation.

[381] Adam R. Tomczak et al. “Galaxy Stellar Mass Functions from ZFOURGE/CANDELS: An Excess of Low-mass Galaxies since z = 2 and the Rapid Buildup of Quiescent Galaxies”. In: 783.2, 85 (Mar. 2014), p. 85. DOI: 10.1088/0004-637X/783/2/85. arXiv: 1309.5972 [astro-ph.CO].

[382] A. Sesana. “Systematic investigation of the expected gravitational wave signal from supermassive black hole binaries in the pulsar timing band.” In:

Monthly Notices of the Royal Astronomical Society 433 (June 2013), pp. L1–L5. DOI: 10.1093/mnrasl/slt034. arXiv: 1211.5375 [astro-ph.CO].

[383] Arthur Kosowsky, Michael S. Turner, and Richard Watkins. "Gravitational waves from first order cosmological phase transitions". In: *Phys. Rev. Lett.* 69 (1992), pp. 2026–2029. DOI: 10.1103/PhysRevLett.69.2026.

[384] Arthur Kosowsky and Michael S. Turner. "Gravitational radiation from colliding vacuum bubbles: envelope approximation to many bubble collisions". In: *Phys. Rev. D* 47 (1993), pp. 4372–4391. DOI: 10.1103/PhysRevD.47.4372. arXiv: astro-ph/9211004.

[385] Marc Kamionkowski, Arthur Kosowsky, and Michael S. Turner. "Gravitational radiation from first order phase transitions". In: *Phys. Rev. D* 49 (1994), pp. 2837–2851. DOI: 10.1103/PhysRevD.49.2837. arXiv: astro-ph/9310044.

[386] Chiara Caprini, Ruth Durrer, and Geraldine Servant. "Gravitational wave generation from bubble collisions in first-order phase transitions: An analytic approach". In: *Phys. Rev. D* 77 (2008), p. 124015. DOI: 10.1103/PhysRevD.77.124015. arXiv: 0711.2593 [astro-ph].

[387] Stephan J. Huber and Thomas Konstandin. "Gravitational Wave Production by Collisions: More Bubbles". In: *JCAP* 09 (2008), p. 022. DOI: 10.1088/1475-7516/2008/09/022. arXiv: 0806.1828 [hep-ph].

[388] Mark Hindmarsh, Stephan J. Huber, Kari Rummukainen, and David J. Weir. "Gravitational waves from the sound of a first order phase transition". In: *Phys. Rev. Lett.* 112 (2014), p. 041301. DOI: 10.1103/PhysRevLett.112.041301. arXiv: 1304.2433 [hep-ph].

[389] John T. Giblin Jr. and James B. Mertens. "Vacuum Bubbles in the Presence of a Relativistic Fluid". In: *JHEP* 12 (2013), p. 042. DOI: 10.1007/JHEP12(2013)042. arXiv: 1310.2948 [hep-th].

[390] John T. Giblin and James B. Mertens. "Gravitional radiation from first-order phase transitions in the presence of a fluid". In: *Phys. Rev. D* 90.2 (2014), p. 023532. DOI: 10.1103/PhysRevD.90.023532. arXiv: 1405.4005 [astro-ph.CO].

[391] Mark Hindmarsh, Stephan J. Huber, Kari Rummukainen, and David J. Weir. "Numerical simulations of acoustically generated gravitational waves at a first order phase transition". In: *Phys. Rev. D* 92.12 (2015), p. 123009. DOI: 10.1103/PhysRevD.92.123009. arXiv: 1504.03291 [astro-ph.CO].

[392] Edward Witten. "Cosmic Separation of Phases". In: *Phys. Rev. D* 30 (1984), pp. 272–285. DOI: 10.1103/PhysRevD.30.272.

[393] Xiao Xue, L. Bian, J. Shu, et al. “Constraining Cosmological Phase Transitions with the Parkes Pulsar Timing Array”. In: *Phys. Rev. Lett.* 127.25 (2021), p. 251303. DOI: 10.1103/PhysRevLett.127.251303. arXiv: 2110.03096 [astro-ph.CO].

[394] Li Li, Shao-Jiang Wang, and Zi-Yan Yuwen. “Bubble expansion at strong coupling”. In: *arXiv* (Feb. 2023). arXiv: 2302.10042 [hep-th].

[395] Wen-Yuan Ai, Benoit Laurent, and Jorinde van de Vis. “Model-independent bubble wall velocities in local thermal equilibrium”. In: *arXiv* (Mar. 2023). arXiv: 2303.10171 [astro-ph.CO].

[396] Tomasz Krajewski, Marek Lewicki, and Mateusz Zych. “Hydrodynamical constraints on bubble wall velocity”. In: *arXiv* (Mar. 2023). arXiv: 2303.18216 [astro-ph.CO].

[397] John Ellis, Marek Lewicki, and José Miguel No. “On the Maximal Strength of a First-Order Electroweak Phase Transition and its Gravitational Wave Signal”. In: *JCAP* 04 (2019), p. 003. DOI: 10.1088/1475-7516/2019/04/003. arXiv: 1809.08242 [hep-ph].

[398] John Ellis, Marek Lewicki, José Miguel No, and Ville Vaskonen. “Gravitational wave energy budget in strongly supercooled phase transitions”. In: *JCAP* 06 (2019), p. 024. DOI: 10.1088/1475-7516/2019/06/024. arXiv: 1903.09642 [hep-ph].

[399] Dietrich Bodeker and Guy D. Moore. “Electroweak Bubble Wall Speed Limit”. In: *JCAP* 05 (2017), p. 025. DOI: 10.1088/1475-7516/2017/05/025. arXiv: 1703.08215 [hep-ph].

[400] Jose R. Espinosa, Thomas Konstandin, Jose M. No, and Geraldine Servant. “Energy Budget of Cosmological First-order Phase Transitions”. In: *JCAP* 06 (2010), p. 028. DOI: 10.1088/1475-7516/2010/06/028. arXiv: 1004.4187 [hep-ph].

[401] Ryusuke Jinno and Masahiro Takimoto. “Gravitational waves from bubble collisions: An analytic derivation”. In: *Phys. Rev. D* 95.2 (2017), p. 024009. DOI: 10.1103/PhysRevD.95.024009. arXiv: 1605.01403 [astro-ph.CO].

[402] Mark Hindmarsh, Stephan J. Huber, Kari Rummukainen, and David J. Weir. “Shape of the acoustic gravitational wave power spectrum from a first order phase transition”. In: *Phys. Rev. D* 96.10 (2017). [Erratum: Phys.Rev.D 101, 089902 (2020)], p. 103520. DOI: 10.1103/PhysRevD.96.103520. arXiv: 1704.05871 [astro-ph.CO].

[403] John Ellis, Marek Lewicki, and José Miguel No. “Gravitational waves from first-order cosmological phase transitions: lifetime of the sound wave source”. In: *JCAP* 07 (2020), p. 050. DOI: 10.1088/1475-7516/2020/07/050. arXiv: 2003.07360 [hep-ph].

[404] Huai-Ke Guo, Kuver Sinha, Daniel Vagie, and Graham White. "Phase Transitions in an Expanding Universe: Stochastic Gravitational Waves in Standard and Non-Standard Histories". In: *JCAP* 01 (2021), p. 001. DOI: 10.1088/1475-7516/2021/01/001. arXiv: 2007.08537 [hep-ph].

[405] Marek Lewicki and Ville Vaskonen. "Gravitational wave spectra from strongly supercooled phase transitions". In: *Eur. Phys. J. C* 80.11 (2020), p. 1003. DOI: 10.1140/epjc/s10052-020-08589-1. arXiv: 2007.04967 [astro-ph.CO].

[406] Marek Lewicki and Ville Vaskonen. "Gravitational waves from colliding vacuum bubbles in gauge theories". In: *Eur. Phys. J. C* 81.5 (2021). [Erratum: Eur.Phys.J.C 81, 1077 (2021)], p. 437. DOI: 10.1140/epjc/s10052-021-09232-3. arXiv: 2012.07826 [astro-ph.CO].

[407] Daniel Cutting, Mark Hindmarsh, and David J. Weir. "Gravitational waves from vacuum first-order phase transitions: from the envelope to the lattice". In: *Phys. Rev. D* 97.12 (2018), p. 123513. DOI: 10.1103/PhysRevD.97.123513. arXiv: 1802.05712 [astro-ph.CO].

[408] Daniel Cutting, Elba Granados Escartin, Mark Hindmarsh, and David J. Weir. "Gravitational waves from vacuum first order phase transitions II: from thin to thick walls". In: *Phys. Rev. D* 103.2 (2021), p. 023531. DOI: 10.1103/PhysRevD.103.023531. arXiv: 2005.13537 [astro-ph.CO].

[409] Mark Hindmarsh and Mulham Hijazi. "Gravitational waves from first order cosmological phase transitions in the Sound Shell Model". In: *JCAP* 12 (2019), p. 062. DOI: 10.1088/1475-7516/2019/12/062. arXiv: 1909.10040 [astro-ph.CO].

[410] Yang Bai and Mrunal Korwar. "Cosmological constraints on first-order phase transitions". In: *Phys. Rev. D* 105.9 (2022), p. 095015. DOI: 10.1103/PhysRevD.105.095015. arXiv: 2109.14765 [hep-ph].

[411] Shihao Deng and Ligong Bian. "Constraining low-scale dark phase transitions with cosmological observations". In: *arXiv* (Apr. 2023). arXiv: 2304.06576 [hep-ph].

[412] Andrii Neronov, Alberto Roper Pol, Chiara Caprini, and Dmitri Semikoz. "NANOGrav signal from magnetohydrodynamic turbulence at the QCD phase transition in the early Universe". In: *Phys. Rev. D* 103.4 (2021), p. 041302. DOI: 10.1103/PhysRevD.103.L041302. arXiv: 2009.14174 [astro-ph.CO].

[413] Yuichiro Nakai, Motoo Suzuki, Fuminobu Takahashi, and Masaki Yamada. "Gravitational Waves and Dark Radiation from Dark Phase Transition: Connecting NANOGrav Pulsar Timing Data and Hubble Tension". In: *Phys. Lett. B* 816 (2021), p. 136238. DOI: 10.1016/j.physletb.2021.136238. arXiv: 2009.09754 [astro-ph.CO].

[414] Archil Kobakhidze, Cyril Lagger, Adrian Manning, and Jason Yue. "Gravitational waves from a supercooled electroweak phase transition and their detection with pulsar timing arrays". In: *Eur. Phys. J. C* 77.8 (2017), p. 570. DOI: 10.1140/epjc/s10052-017-5132-y. arXiv: 1703.06552 [hep-ph].

[415] Weishuang Linda Xu, Cora Dvorkin, and Andrew Chael. "Probing sub-GeV Dark Matter-Baryon Scattering with Cosmological Observables". In: *Phys. Rev. D* 97.10 (2018), p. 103530. DOI: 10.1103/PhysRevD.97.103530. arXiv: 1802.06788 [astro-ph.CO].

[416] M. Shafi Mahdawi and Glennys R. Farrar. "Constraints on Dark Matter with a moderately large and velocity-dependent DM-nucleon cross-section". In: *JCAP* 10 (2018), p. 007. DOI: 10.1088/1475-7516/2018/10/007. arXiv: 1804.03073 [hep-ph].

[417] G. Angloher, P. Bauer, A. Bento, et al. "Results on MeV-scale dark matter from a gram-scale cryogenic calorimeter operated above ground". In: *Eur. Phys. J. C* 77.9 (2017), p. 637. DOI: 10.1140/epjc/s10052-017-5223-9. arXiv: 1707.06749 [astro-ph.CO].

[418] Xingchen Xu and Glennys R. Farrar. "Resonant Scattering between Dark Matter and Baryons: Revised Direct Detection and CMB Limits". In: *arXiv* (Dec. 2020). arXiv: 2101.00142 [hep-ph].

[419] Daniel Green et al. "Snowmass Theory Frontier: Astrophysics and Cosmology". In: (Sept. 2022). arXiv: 2209.06854 [hep-ph].

[420] Kim Griest and Marc Kamionkowski. "Unitarity Limits on the Mass and Radius of Dark Matter Particles". In: *Phys. Rev. Lett.* 64 (1990), p. 615. DOI: 10.1103/PhysRevLett.64.615.

[421] Andrea Mitridate, Tanner Trickle, Zhengkang Zhang, and Kathryn M. Zurek. "Snowmass white paper: Light dark matter direct detection at the interface with condensed matter physics". In: *Phys. Dark Univ.* 40 (2023), p. 101221. DOI: 10.1016/j.dark.2023.101221. arXiv: 2203.07492 [hep-ph].

[422] D. Antypas et al. "New Horizons: Scalar and Vector Ultralight Dark Matter". In: *arXiv e-prints*, arXiv:2203.14915 (Mar. 2022), arXiv:2203.14915. DOI: 10.48550/arXiv.2203.14915. arXiv: 2203.14915 [hep-ex].

[423] Leonardo Badurina, Valerie Gibson, Christopher McCabe, and Jeremiah Mitchell. "Ultralight dark matter searches at the sub-Hz frontier with atom multigradiometry". In: 107.5, 055002 (Mar. 2023), p. 055002. DOI: 10.1103/PhysRevD.107.055002. arXiv: 2211.01854 [hep-ph].

[424] Bernard Carr, Florian Kuhnel, and Marit Sandstad. "Primordial Black Holes as Dark Matter". In: *Phys. Rev. D* 94.8 (2016), p. 083504. DOI: 10.1103/PhysRevD.94.083504. arXiv: 1607.06077 [astro-ph.CO].

[425] Mark B. Wise and Yue Zhang. "Yukawa Bound States of a Large Number of Fermions". In: *JHEP* 02 (2015). [Erratum: JHEP 10, 165 (2015)], p. 023. DOI: 10.1007/JHEP02(2015)023. arXiv: 1411.1772 [hep-ph].

[426] Alaina Attanasio et al. "Snowmass 2021 White Paper: The Windchime Project". In: *Snowmass 2021*. Mar. 2022. arXiv: 2203.07242 [hep-ex].

[427] D. Carney et al. "Mechanical Quantum Sensing in the Search for Dark Matter". In: *Quantum Sci. Technol.* 6 (2021), p. 024002. DOI: 10.1088/2058-9565/abcfcd. arXiv: 2008.06074 [physics.ins-det].

[428] B. P. Abbott et al. "Observation of Gravitational Waves from a Binary Black Hole Merger". In: 116.6, 061102 (Feb. 2016), p. 061102. DOI: 10.1103/PhysRevLett.116.061102. arXiv: 1602.03837 [gr-qc].

[429] Nancy Aggarwal et al. "Challenges and opportunities of gravitational-wave searches at MHz to GHz frequencies". In: *Living Reviews in Relativity* 24.1, 4 (Dec. 2021), p. 4. DOI: 10.1007/s41114-021-00032-5. arXiv: 2011.12414 [gr-qc].

[430] Aaron S. Chou et al. "First Measurements of High Frequency Cross-Spectra from a Pair of Large Michelson Interferometers". In: *Phys. Rev. Lett.* 117.11 (2016), p. 111102. DOI: 10.1103/PhysRevLett.117.111102. arXiv: 1512.01216 [gr-qc].

[431] Aaron Chou et al. "The Holometer: an instrument to probe Planckian quantum geometry". In: *Classical and Quantum Gravity* 34.6, 065005 (Mar. 2017), p. 065005. DOI: 10.1088/1361-6382/aa5e5c. arXiv: 1611.08265 [physics.ins-det].

[432] Lee McCuller. "Single-Photon Signal Sideband Detection for High-Power Michelson Interferometers". In: (Nov. 2022). arXiv: 2211.04016 [physics.ins-det].

[433] Evan D. Hall, Rana X. Adhikari, Valery V. Frolov, Holger Müller, and Maxim Pospelov. "Laser interferometers as dark matter detectors". In: 98.8 (Oct. 2018), p. 083019. DOI: 10.1103/PhysRevD.98.083019. eprint: 1605.01103.

[434] Joerg Jaeckel, Sebastian Schenk, and Michael Spannowsky. "Probing dark matter clumps, strings and domain walls with gravitational wave detectors". In: *Eur. Phys. J. C* 81.9 (2021), p. 828. DOI: 10.1140/epjc/s10052-021-09604-9. arXiv: 2004.13724 [astro-ph.CO].

[435] Chun-Hao Lee, Reinard Primulando, and Martin Spinrath. "Discovery prospects for heavy dark matter in KAGRA". In: *Phys. Rev. D* 107.3 (2023), p. 035029. DOI: 10.1103/PhysRevD.107.035029. arXiv: 2208.06232 [hep-ph].

[436] Naoki Seto and Asantha Cooray. "Search for small-mass black hole dark matter with space-based gravitational wave detectors". In: *Phys. Rev. D* 70 (2004), p. 063512. DOI: 10.1103/PhysRevD.70.063512. arXiv: astro-ph/0405216.

[437] Peter W. Graham, David E. Kaplan, Jeremy Mardon, Surjeet Rajendran, and William A. Terrano. "Dark Matter Direct Detection with Accelerometers". In: *Phys. Rev. D* 93.7 (2016), p. 075029. DOI: 10.1103/PhysRevD.93.075029. arXiv: 1512.06165 [hep-ph].

[438] Sebastian Baum, Michael A. Fedderke, and Peter W. Graham. "Searching for dark clumps with gravitational-wave detectors". In: *Phys. Rev. D* 106.6 (2022), p. 063015. DOI: 10.1103/PhysRevD.106.063015. arXiv: 2206.14832 [astro-ph.CO].

[439] Akio Kawasaki. "Search for kilogram-scale dark matter with precision displacement sensors". In: *Phys. Rev. D* 99 (2 Jan. 2019), p. 023005. DOI: 10.1103/PhysRevD.99.023005. URL: https://link.aps.org/doi/10.1103/PhysRevD.99.023005.

[440] E. G. Adelberger, Blayne R. Heckel, and A. E. Nelson. "Tests of the gravitational inverse square law". In: *Ann. Rev. Nucl. Part. Sci.* 53 (2003), pp. 77–121. DOI: 10.1146/annurev.nucl.53.041002.110503. arXiv: hep-ph/0307284.

[441] Javier F. Acevedo, Rebecca K. Leane, and Juri Smirnov. "Evaporation barrier for dark matter in celestial bodies". In: *JCAP* 04 (2024), p. 038. DOI: 10.1088/1475-7516/2024/04/038. arXiv: 2303.01516 [hep-ph].

[442] Joel Bergé, Martin Pernot-Borràs, Jean-Philippe Uzan, Philippe Brax, Ratana Chhun, Gilles Métris, Manuel Rodrigues, and Pierre Touboul. "MICROSCOPE's constraint on a short-range fifth force". In: *Classical and Quantum Gravity* 39.20, 204010 (Oct. 2022), p. 204010. DOI: 10.1088/1361-6382/abe142. arXiv: 2102.00022 [gr-qc].

[443] Dawid Brzeminski, Zackaria Chacko, Abhish Dev, Ina Flood, and Anson Hook. "Searching for a fifth force with atomic and nuclear clocks". In: 106.9, 095031 (Nov. 2022), p. 095031. DOI: 10.1103/PhysRevD.106.095031. arXiv: 2207.14310 [hep-ph].

[444] Soichiro Morisaki, Tomohiro Fujita, Yuta Michimura, Hiromasa Nakatsuka, and Ippei Obata. "Improved sensitivity of interferometric gravitational-wave detectors to ultralight vector dark matter from the finite light-traveling time". In: 103.5, L051702 (Mar. 2021), p. L051702. DOI: 10.1103/PhysRevD.103.L051702. arXiv: 2011.03589 [hep-ph].

[445] Lijing Shao, Norbert Wex, and Michael Kramer. "Testing the universality of free fall towards dark matter with radio pulsars". In: *Phys. Rev. Lett.* 120.24 (2018), p. 241104. DOI: 10.1103/PhysRevLett.120.241104. arXiv: 1805.08408 [gr-qc].

[446] T A Wagner, S Schlamminger, J H Gundlach, and E G Adelberger. "Torsion-balance tests of the weak equivalence principle". In: *Classical and Quantum Gravity* 29.18 (Aug. 2012), p. 184002. DOI: 10.1088/0264-9381/29/

18/184002. URL: https://doi.org/10.1088%5C%2F0264-9381%5C%2F29%5C%2F18%5C%2F184002.

[447] David N. Spergel and Paul J. Steinhardt. "Observational Evidence for Self-Interacting Cold Dark Matter". In: *Physical Review Letters* 84.17 (Apr. 2000), pp. 3760–3763. DOI: 10.1103/physrevlett.84.3760. URL: https://doi.org/10.1103%5C%2Fphysrevlett.84.3760.

[448] Felix Kahlhoefer, Kai Schmidt-Hoberg, Mads T. Frandsen, and Subir Sarkar. "Colliding clusters and dark matter self-interactions". In: *Monthly Notices of the Royal Astronomical Society* 437.3 (Nov. 2013), pp. 2865–2881. DOI: 10.1093/mnras/stt2097. URL: https://doi.org/10.1093%5C%2Fmnras%5C%2Fstt2097.

[449] Joel Bergé, Philippe Brax, Gilles Métris, Martin Pernot-Borràs, Pierre Touboul, and Jean-Philippe Uzan. "MICROSCOPE Mission: First Constraints on the Violation of the Weak Equivalence Principle by a Light Scalar Dilaton". In: *Phys. Rev. Lett.* 120 (14 Apr. 2018), p. 141101. DOI: 10.1103/PhysRevLett.120.141101. URL: https://link.aps.org/doi/10.1103/PhysRevLett.120.141101.

[450] Pierre Fayet. "MICROSCOPE limits on the strength of a new force with comparisons to gravity and electromagnetism". In: 99.5, 055043 (Mar. 2019), p. 055043. DOI: 10.1103/PhysRevD.99.055043. arXiv: 1809.04991 [hep-ph].

[451] Irwin I. Shapiro. "Fourth Test of General Relativity". In: 13.26 (Dec. 1964), pp. 789–791. DOI: 10.1103/PhysRevLett.13.789.

[452] Michael A. Fedderke, Peter W. Graham, and Surjeet Rajendran. "Asteroids for μHz gravitational-wave detection". In: *Phys. Rev. D* 105.10 (2022), p. 103018. DOI: 10.1103/PhysRevD.105.103018. arXiv: 2112.11431 [gr-qc].

[453] Sean M. Carroll. *Spacetime and Geometry*. Cambridge University Press, July 2019. ISBN: 978-0-8053-8732-2, 978-1-108-48839-6, 978-1-108-77555-7.

[454] Matthew Evans et al. "A Horizon Study for Cosmic Explorer: Science, Observatories, and Community". In: *arXiv e-prints*, arXiv:2109.09882 (Sept. 2021), arXiv:2109.09882. DOI: 10.48550/arXiv.2109.09882. arXiv: 2109.09882 [astro-ph.IM].

[455] Stefan Hild, Simon Chelkowski, and Andreas Freise. "Pushing towards the ET sensitivity using 'conventional' technology". In: *arXiv e-prints*, arXiv:0810.0604 (Oct. 2008), arXiv:0810.0604. DOI: 10.48550/arXiv.0810.0604. arXiv: 0810.0604 [gr-qc].

[456] S. Hild et al. "Sensitivity studies for third-generation gravitational wave observatories". In: *Classical and Quantum Gravity* 28.9, 094013 (May 2011), p. 094013. DOI: 10.1088/0264-9381/28/9/094013. arXiv: 1012.0908 [gr-qc].

[457] K. Ackley et al. “Neutron Star Extreme Matter Observatory: A kilohertz-band gravitational-wave detector in the global network”. In: 37, e047 (Nov. 2020), e047. DOI: 10.1017/pasa.2020.39. arXiv: 2007.03128 [astro-ph.HE].

[458] R. X. Adhikari et al. “A cryogenic silicon interferometer for gravitational-wave detection”. In: *Class. Quant. Grav.* 37.16 (2020), p. 165003. DOI: 10.1088/1361-6382/ab9143. arXiv: 2001.11173 [astro-ph.IM].

[459] Pau Amaro-Seoane et al. “Laser Interferometer Space Antenna”. In: *arXiv e-prints*, arXiv:1702.00786 (Feb. 2017), arXiv:1702.00786. DOI: 10.48550/arXiv.1702.00786. arXiv: 1702.00786 [astro-ph.IM].

[460] Asimina Arvanitaki and Andrew A. Geraci. “Detecting High-Frequency Gravitational Waves with Optically Levitated Sensors”. In: *Phys. Rev. Lett.* 110 (7 Feb. 2013), p. 071105. DOI: 10.1103/PhysRevLett.110.071105. URL: https://link.aps.org/doi/10.1103/PhysRevLett.110.071105.

[461] Nancy Aggarwal, George P. Winstone, Mae Teo, Masha Baryakhtar, Shane L. Larson, Vicky Kalogera, and Andrew A. Geraci. “Searching for New Physics with a Levitated-Sensor-Based Gravitational-Wave Detector”. In: *Phys. Rev. Lett.* 128.11 (2022), p. 111101. DOI: 10.1103/PhysRevLett.128.111101. arXiv: 2010.13157 [gr-qc].

[462] Michael J. Biercuk, Hermann Uys, Joe W. Britton, Aaron P. VanDevender, and John J. Bollinger. “Ultrasensitive detection of force and displacement using trapped ions”. In: *Nature Nanotechnology* 5.9 (Aug. 2010), pp. 646–650. DOI: 10.1038/nnano.2010.165. URL: https://doi.org/10.1038%2Fnnano.2010.165.

[463] Chris Timberlake, Giulio Gasbarri, Andrea Vinante, Ashley Setter, and Hendrik Ulbricht. “Acceleration sensing with magnetically levitated oscillators above a superconductor”. In: *Applied Physics Letters* 115.22 (Nov. 2019), p. 224101. DOI: 10.1063/1.5129145. URL: https://doi.org/10.1063%2F1.5129145.

[464] Charles W. Lewandowski, Tyler D. Knowles, Zachariah B. Etienne, and Brian D’Urso. “High sensitivity accelerometry with a feedback-cooled magnetically levitated microsphere”. In: *Phys. Rev. Applied* 15.1 (2021), p. 014050. DOI: 10.1103/PhysRevApplied.15.014050. arXiv: 2002.07585 [physics.app-ph].

[465] Fernando Monteiro, Wenqiang Li, Gadi Afek, Chang-ling Li, Michael Mossman, and David C. Moore. “Force and acceleration sensing with optically levitated nanogram masses at microkelvin temperatures”. In: *Phys. Rev. A* 101 (5 May 2020), p. 053835. DOI: 10.1103/PhysRevA.101.053835. URL: https://link.aps.org/doi/10.1103/PhysRevA.101.053835.

[466] Uroš Delić, Manuel Reisenbauer, Kahan Dare, David Grass, Vladan Vuletić, Nikolai Kiesel, and Markus Aspelmeyer. "Cooling of a levitated nanoparticle to the motional quantum ground state". In: *Science* 367.6480 (Feb. 2020), pp. 892–895. DOI: 10.1126/science.aba3993. URL: https://doi.org/10.1126%2Fscience.aba3993.

[467] Fernando Monteiro, Gadi Afek, Daniel Carney, Gordan Krnjaic, Jiaxiang Wang, and David C. Moore. "Search for composite dark matter with optically levitated sensors". In: *Phys. Rev. Lett.* 125.18 (2020), p. 181102. DOI: 10.1103/PhysRevLett.125.181102. arXiv: 2007.12067 [hep-ex].

[468] Felix Tebbenjohanns, Martin Frimmer, Vijay Jain, Dominik Windey, and Lukas Novotny. "Motional Sideband Asymmetry of a Nanoparticle Optically Levitated in Free Space". In: *Phys. Rev. Lett.* 124 (1 Jan. 2020), p. 013603. DOI: 10.1103/PhysRevLett.124.013603. URL: https://link.aps.org/doi/10.1103/PhysRevLett.124.013603.

[469] Jonghoon Ahn, Zhujing Xu, Jaehoon Bang, Peng Ju, Xingyu Gao, and Tongcang Li. "Ultrasensitive torque detection with an optically levitated nanorotor". In: *Nature Nanotechnology* 15.2 (Jan. 2020), pp. 89–93. DOI: 10.1038/s41565-019-0605-9. URL: https://doi.org/10.1038%5C%2Fs41565-019-0605-9.

[470] Daniel Carney, Sohitri Ghosh, Gordan Krnjaic, and Jacob M. Taylor. "Proposal for gravitational direct detection of dark matter". In: *Physical Review D* 102.7 (Oct. 2020). DOI: 10.1103/physrevd.102.072003. URL: https://doi.org/10.1103%5C%2Fphysrevd.102.072003.

[471] L. Gottardi et al. "Sensitivity of the spherical gravitational wave detector MiniGRAIL operating at 5 K". In: *Phys. Rev. D* 76 (2007), p. 102005. DOI: 10.1103/PhysRevD.76.102005. arXiv: 0705.0122 [gr-qc].

[472] Odylio Denys Aguiar. "The Past, Present and Future of the Resonant-Mass Gravitational Wave Detectors". In: *Res. Astron. Astrophys.* 11 (2011), pp. 1–42. DOI: 10.1088/1674-4527/11/1/001. arXiv: 1009.1138 [astro-ph.IM].

[473] Maxim Goryachev and Michael E. Tobar. "Gravitational Wave Detection with High Frequency Phonon Trapping Acoustic Cavities". In: *Phys. Rev. D* 90.10 (2014), p. 102005. DOI: 10.1103/PhysRevD.90.102005. arXiv: 1410.2334 [gr-qc].

[474] Maxim Goryachev, William M. Campbell, Ik Siong Heng, Serge Galliou, Eugene N. Ivanov, and Michael E. Tobar. "Rare Events Detected with a Bulk Acoustic Wave High Frequency Gravitational Wave Antenna". In: *Phys. Rev. Lett.* 127 (7 Aug. 2021), p. 071102. DOI: 10.1103/PhysRevLett.127.071102. URL: https://link.aps.org/doi/10.1103/PhysRevLett.127.071102.

[475] Raphael St-Gelais, Simon Bernard, Christoph Reinhardt, and Jack Sankey. *Swept-Frequency Drumhead Mechanical Resonators*. 2018. arXiv: 1808.10084 [physics.app-ph].

[476] Leonardo Badurina, Oliver Buchmueller, John Ellis, Marek Lewicki, Christopher McCabe, and Ville Vaskonen. "Prospective sensitivities of atom interferometers to gravitational waves and ultralight dark matter". In: *Philosophical Transactions of the Royal Society of London Series A* 380.2216, 20210060 (Feb. 2022), p. 20210060. DOI: 10.1098/rsta.2021.0060. arXiv: 2108.02468 [gr-qc].

[477] Peter W. Graham, Jason M. Hogan, Mark A. Kasevich, Surjeet Rajendran, and Roger W. Romani. "Mid-band gravitational wave detection with precision atomic sensors". In: (Nov. 2017). arXiv: 1711.02225 [astro-ph.IM].

[478] Mahiro Abe et al. "Matter-wave Atomic Gradiometer Interferometric Sensor (MAGIS-100)". In: *Quantum Sci. Technol.* 6.4 (2021), p. 044003. DOI: 10.1088/2058-9565/abf719. arXiv: 2104.02835 [physics.atom-ph].

[479] Yousef Abou El-Neaj et al. "AEDGE: Atomic Experiment for Dark Matter and Gravity Exploration in Space". In: *EPJ Quantum Technology* 7, 6 (Mar. 2020), p. 6. DOI: 10.1140/epjqt/s40507-020-0080-0. arXiv: 1908.00802 [gr-qc].

[480] L. Badurina et al. "AION: an atom interferometer observatory and network". In: 2020.5, 011 (May 2020), p. 011. DOI: 10.1088/1475-7516/2020/05/011. arXiv: 1911.11755 [astro-ph.CO].

[481] Sergey N. Solodukhin. "Conformal description of horizon's states". In: *Physics Letters B* 454.3 (1999), pp. 213–222. ISSN: 0370-2693. DOI: https://doi.org/10.1016/S0370-2693(99)00398-6. URL: https://www.sciencedirect.com/science/article/pii/S0370269399003986.

[482] Thomas Banks and Kathryn M. Zurek. "Conformal description of near-horizon vacuum states". In: *Phys. Rev. D* 104.12 (2021), p. 126026. DOI: 10.1103/PhysRevD.104.126026. arXiv: 2108.04806 [hep-th].

[483] Jan de Boer, Jarkko Järvelä, and Esko Keski-Vakkuri. "Aspects of capacity of entanglement". In: *Physical Review D* 99.6 (Mar. 2019). ISSN: 2470-0029. DOI: 10.1103/physrevd.99.066012. URL: http://dx.doi.org/10.1103/PhysRevD.99.066012.

[484] Erik Verlinde and Kathryn M. Zurek. "Spacetime Fluctuations in AdS/CFT". In: *JHEP* 04 (2020), p. 209. DOI: 10.1007/JHEP04(2020)209. arXiv: 1911.02018 [hep-th].

[485] Roman Jackiw. "Lower dimensional gravity". In: *Nuclear Physics B* 252 (1985), pp. 343–356. ISSN: 0550-3213. DOI: https://doi.org/10.1016/0550-3213(85)90448-1. URL: https://www.sciencedirect.com/science/article/pii/0550321385904481.

[486] Claudio Teitelboim. "Gravitation and hamiltonian structure in two spacetime dimensions". In: *Physics Letters B* 126.1 (1983), pp. 41–45. ISSN: 0370-2693. DOI: https://doi.org/10.1016/0370-2693(83)90012-6. URL: https://www.sciencedirect.com/science/article/pii/0370269383900126.

[487] Daniel Harlow and Daniel Jafferis. *The Factorization Problem in Jackiw-Teitelboim Gravity*. 2019. arXiv: 1804.01081 [hep-th].

[488] Juan Maldacena, Jeremy Michelson, and Andrew Strominger. "Anti-de Sitter fragmentation". In: *Journal of High Energy Physics* 1999.02 (Feb. 1999), pp. 011–011. ISSN: 1029-8479. DOI: 10.1088/1126-6708/1999/02/011. URL: http://dx.doi.org/10.1088/1126-6708/1999/02/011.

[489] Sean M. Carroll. *Spacetime and Geometry: An Introduction to General Relativity*. Cambridge University Press, 2019. DOI: 10.1017/97811087785.

[490] Andrew Svesko, Evita Verheijden, Erik P. Verlinde, and Manus R. Visser. "Quasi-local energy and microcanonical entropy in two-dimensional nearly de Sitter gravity". In: (Mar. 2022). arXiv: 2203.00700 [hep-th].

[491] Ahmed Almheiri and Joseph Polchinski. *Models of AdS2 Backreaction and Holography*. 2015. arXiv: 1402.6334 [hep-th].

[492] Gábor Sárosi. "AdS_2 holography and the SYK model". In: *PoS* Modave2017 (2018), p. 001. DOI: 10.22323/1.323.0001. arXiv: 1711.08482 [hep-th].

[493] Horacio Casini, Marina Huerta, and Robert C. Myers. "Towards a derivation of holographic entanglement entropy". In: *Journal of High Energy Physics* 2011.5 (May 2011). ISSN: 1029-8479. DOI: 10.1007/jhep05(2011)036. URL: http://dx.doi.org/10.1007/JHEP05(2011)036.

[494] Daniel Harlow. "Wormholes, emergent gauge fields, and the weak gravity conjecture". In: *Journal of High Energy Physics* 2016.1 (Jan. 2016). ISSN: 1029-8479. DOI: 10.1007/jhep01(2016)122. URL: http://dx.doi.org/10.1007/JHEP01(2016)122.

[495] Monica Guica and Daniel Jafferis. "On the construction of charged operators inside an eternal black hole". In: *SciPost Physics* 3.2 (Aug. 2017). ISSN: 2542-4653. DOI: 10.21468/scipostphys.3.2.016. URL: http://dx.doi.org/10.21468/SciPostPhys.3.2.016.

[496] Juan Maldacena, Douglas Stanford, and Zhenbin Yang. "Conformal symmetry and its breaking in two dimensional Nearly Anti-de-Sitter space". In: *PTEP* 2016.12 (2016), p. 12C104. DOI: 10.1093/ptep/ptw124. arXiv: 1606.01857 [hep-th].

[497] Kathryn M. Zurek. "On vacuum fluctuations in quantum gravity and interferometer arm fluctuations". In: *Phys. Lett. B* 826 (2022), p. 136910. DOI: 10.1016/j.physletb.2022.136910. arXiv: 2012.05870 [hep-th].

[498] Dominik Nickel and Dam T Son. "Deconstructing holographic liquids". In: *New Journal of Physics* 13.7 (July 2011), p. 075010. ISSN: 1367-2630. DOI: 10.1088/1367-2630/13/7/075010. URL: http://dx.doi.org/10.1088/1367-2630/13/7/075010.

[499] Michael Crossley, Paolo Glorioso, Hong Liu, and Yifan Wang. "Off-shell hydrodynamics from holography". In: *Journal of High Energy Physics* 2016.2 (Feb. 2016). ISSN: 1029-8479. DOI: 10.1007/jhep02(2016)124. URL: http://dx.doi.org/10.1007/JHEP02(2016)124.

[500] Erik Verlinde and Kathryn M. Zurek. "Modular fluctuations from shockwave geometries". In: *Phys. Rev. D* 106.10 (2022), p. 106011. DOI: 10.1103/PhysRevD.106.106011. arXiv: 2208.01059 [hep-th].

[501] Horacio Casini, Marina Huerta, and Robert C. Myers. "Towards a derivation of holographic entanglement entropy". In: *Journal of High Energy Physics* 2011.5 (Feb. 2011). arXiv: 1102.0440, p. 36. ISSN: 1029-8479. DOI: 10.1007/JHEP05(2011)036.

[502] Jan De Boer, Jarkko Järvelä, and Esko Keski-Vakkuri. "Aspects of capacity of entanglement". In: *Phys. Rev. D* 99.6 (2019), p. 066012. DOI: 10.1103/PhysRevD.99.066012. arXiv: 1807.07357 [hep-th].

[503] Yuki Nakaguchi and Tatsuma Nishioka. "A holographic proof of Rényi entropic inequalities". In: *JHEP* 12 (2016), p. 129. DOI: 10.1007/JHEP12(2016)129. arXiv: 1606.08443 [hep-th].

[504] Steven Carlip. "Effective conformal descriptions of black hole entropy: A review". In: *AIP Conference Proceedings*. AIP, 2012. DOI: 10.1063/1.4756962. URL: https://doi.org/10.1063%2F1.4756962.

[505] Mark Srednicki. "Entropy and area". In: *Physical Review Letters* 71.5 (Aug. 1993), pp. 666–669. DOI: 10.1103/physrevlett.71.666. URL: https://doi.org/10.1103%2Fphysrevlett.71.666.

[506] Ted Jacobson. "Entanglement Equilibrium and the Einstein Equation". In: *Physical Review Letters* 116.20 (May 2016). ISSN: 1079-7114. DOI: 10.1103/physrevlett.116.201101. URL: http://dx.doi.org/10.1103/PhysRevLett.116.201101.

[507] H. Casini and M. Huerta. "Entanglement entropy in free quantum field theory". In: *Journal of Physics A: Mathematical and Theoretical* 42.50 (Dec. 2009), p. 504007. ISSN: 1751-8113, 1751-8121. DOI: 10.1088/1751-8113/42/50/504007.

[508] Kurt Hinterbichler. "Theoretical aspects of massive gravity". In: *Reviews of Modern Physics* 84.2 (May 2012), pp. 671–710. ISSN: 1539-0756. DOI: 10.1103/revmodphys.84.671. URL: http://dx.doi.org/10.1103/RevModPhys.84.671.

[509] Maulik Parikh, Frank Wilczek, and George Zahariade. "Signatures of the Quantization of Gravity at Gravitational Wave Detectors". In: *arXiv:2010.08208* (Oct. 2020). arXiv: 2010.08208. URL: http://arxiv.org/abs/2010.08208.

[510] Jonathan W. Richardson et al. "Interferometric Constraints on Spacelike Coherent Rotational Fluctuations". In: *Physical Review Letters* 126.24 (June 2021). arXiv: 2012.06939, p. 241301. ISSN: 0031-9007, 1079-7114. DOI: 10.1103/PhysRevLett.126.241301.

[511] Giovanni Amelino-Camelia. "Gravity-wave interferometers as quantum-gravity detectors". In: *Nature* 398.6724 (Mar. 1999), pp. 216–218. DOI: 10.1038/18377. URL: https://doi.org/10.1038%2F18377.

[512] L. Diósi and B. Lukács. "Covariant evolution equation for the thermodynamic fluctuations". In: *Phys. Rev. A* 31 (5 May 1985), pp. 3415–3418. DOI: 10.1103/PhysRevA.31.3415. URL: https://link.aps.org/doi/10.1103/PhysRevA.31.3415.

[513] Gerard 't Hooft. "Strings from Gravity". In: *Physica Scripta* T15 (Jan. 1987), pp. 143–150. ISSN: 1402-4896. DOI: 10.1088/0031-8949/1987/T15/019.

[514] Tevian Dray and Gerard 't Hooft. "The gravitational shock wave of a massless particle". In: *Nuclear Physics B* 253 (Jan. 1985), pp. 173–188. ISSN: 0550-3213. DOI: 10.1016/0550-3213(85)90525-5.

[515] Gerard 't Hooft. "The scattering matrix approach for the quantum black hole, an overview". In: *International Journal of Modern Physics A* 11.26 (Oct. 1996). arXiv: gr-qc/9607022, pp. 4623–4688. ISSN: 0217-751X, 1793-656X. DOI: 10.1142/S0217751X96002145.

[516] Aaron Chou et al. "Interferometric constraints on quantum geometrical shear noise correlations". In: *Classical and Quantum Gravity* 34.16 (July 2017), p. 165005. DOI: 10.1088/1361-6382/aa7bd3. URL: https://doi.org/10.1088/1361-6382/aa7bd3.

[517] C J Moore, R H Cole, and C P L Berry. "Gravitational-wave sensitivity curves". In: *Classical and Quantum Gravity* 32.1 (Dec. 2014), p. 015014. DOI: 10.1088/0264-9381/32/1/015014. URL: https://doi.org/10.1088%2F0264-9381%2F32%2F1%2F015014.

[518] The LIGO Scientific Collaboration, The Virgo Collaboration, and The KAGRA Collaboration. "First joint observation by the underground gravitational-wave detector, KAGRA, with GEO600". In: (2022). DOI: 10.48550/ARXIV.2203.01270. URL: https://arxiv.org/abs/2203.01270.

[519] L. *et al.* McCuller. "LIGO's quantum response to squeezed states". In: *Phys. Rev. D* 104 (6 Sept. 2021), p. 062006. DOI: 10.1103/PhysRevD.104.062006. URL: https://link.aps.org/doi/10.1103/PhysRevD.104.062006.

[520] Stanislav Babak, Martin Hewitson, and Antoine Petiteau. "LISA Sensitivity and SNR Calculations". In: (2021). DOI: 10.48550/ARXIV.2108.01167. URL: https://arxiv.org/abs/2108.01167.

[521] Ohkyung Kwon and Craig J Hogan. "Interferometric tests of Planckian quantum geometry models". In: *Classical and Quantum Gravity* 33.10 (Apr. 2016), p. 105004. DOI: 10.1088/0264-9381/33/10/105004. URL: https://doi.org/10.1088/0264-9381/33/10/105004.

[522] The LIGO Scientific Collaboration. "LIGO: the Laser Interferometer Gravitational-Wave Observatory". In: *Reports on Progress in Physics* 72.7 (June 2009), p. 076901. DOI: 10.1088/0034-4885/72/7/076901. URL: https://doi.org/10.1088/0034-4885/72/7/076901.

[523] Kip S Thorne and Roger D Blandford. *Modern classical physics: optics, fluids, plasmas, elasticity, relativity, and statistical physics*. Princeton University Press, 2017.

[524] Charles W. Misner, K. S. Thorne, and J. A. Wheeler. *Gravitation*. San Francisco: W. H. Freeman, 1973. ISBN: 978-0-7167-0344-0, 978-0-691-17779-3.

[525] G. Amelino-Camelia. "Limits on the measurability of space-time distances in the semiclassical approximation of quantum gravity". In: *Mod. Phys. Lett. A* 9 (1994), pp. 3415–3422. DOI: 10.1142/S0217732394003245. arXiv: gr-qc/9603014.

[526] L. Diosi and B. Lukacs. "On the minimum uncertainty of space-time geodesics". In: *Phys. Lett. A* 142 (1989), p. 331. DOI: 10.1016/0375-9601(89)90375-7.

[527] John Archibald Wheeler. "Geons". In: *Phys. Rev.* 97 (2 Jan. 1955), pp. 511–536. DOI: 10.1103/PhysRev.97.511. URL: https://link.aps.org/doi/10.1103/PhysRev.97.511.

[528] S.W. Hawking, D.N. Page, and C.N. Pope. "Quantum gravitational bubbles". In: *Nuclear Physics B* 170.2 (1980). Volume B170 [FSI] No. 3 to follow in Approximately Two Months, pp. 283–306. ISSN: 0550-3213. DOI: https://doi.org/10.1016/0550-3213(80)90151-0. URL: https://www.sciencedirect.com/science/article/pii/0550321380901510.

[529] Abhay Ashtekar, Carlo Rovelli, and Lee Smolin. "Weaving a classical metric with quantum threads". In: *Physical Review Letters* 69.2 (July 1992), pp. 237–240. DOI: 10.1103/physrevlett.69.237. URL: https://doi.org/10.1103%2Fphysrevlett.69.237.

[530] Eugene P. Wigner. "Relativistic Invariance and Quantum Phenomena". In: *Rev. Mod. Phys.* 29 (1957), pp. 255–268. DOI: 10.1103/RevModPhys.29.255.

[531] H. Salecker and E. P. Wigner. "Quantum Limitations of the Measurement of Space-Time Distances". In: *Phys. Rev.* 109 (2 Jan. 1958), pp. 571–577. DOI: 10.1103/PhysRev.109.571. URL: https://link.aps.org/doi/10.1103/PhysRev.109.571.

[532] Ohkyung Kwon and Craig J. Hogan. "Interferometric Tests of Planckian Quantum Geometry Models". In: *Class. Quant. Grav.* 33.10 (2016), p. 105004. DOI: 10.1088/0264-9381/33/10/105004. arXiv: 1410.8197 [gr-qc].

[533] Richard Lieu and Lloyd W. Hillman. "The Phase coherence of light from extragalactic sources - direct evidence against first order quantum gravity fluctuations in time and space". In: *Astrophys. J. Lett.* 585 (2003), pp. L77–L80. DOI: 10.1086/374350. arXiv: astro-ph/0301184.

[534] Y. Jack Ng. "Selected topics in Planck scale physics". In: *Mod. Phys. Lett. A* 18 (2003), pp. 1073–1098. DOI: 10.1142/S0217732303010934. arXiv: gr-qc/0305019.

[535] Roberto Ragazzoni, Massimo Turatto, and Wolfgang Gaessler. "Lack of observational evidence for quantum structure of space - time at Planck scales". In: *Astrophys. J. Lett.* 587 (2003), pp. L1–L4. DOI: 10.1086/375046. arXiv: astro-ph/0303043.

[536] W. A. Christiansen, Y. Jack Ng, and H. van Dam. "Probing spacetime foam with extragalactic sources". In: *Phys. Rev. Lett.* 96 (2006), p. 051301. DOI: 10.1103/PhysRevLett.96.051301. arXiv: gr-qc/0508121.

[537] Eric S. Perlman, Y. Jack Ng, David J. E. Floyd, and Wayne A. Christiansen. "Using Observations of Distant Quasars to Constrain Quantum Gravity". In: *Astron. Astrophys.* 535 (2011), p. L9. DOI: 10.1051/0004-6361/201118319. arXiv: 1110.4986 [astro-ph.CO].

[538] E. S. Perlman, S. A. Rappaport, W. A. Christiansen, Y. J. Ng, J. DeVore, and D. Pooley. "New Constraints on Quantum Gravity from X-ray and Gamma-Ray Observations". In: *Astrophys. J.* 805.1 (2015), p. 10. DOI: 10.1088/0004-637X/805/1/10. arXiv: 1411.7262 [astro-ph.CO].

[539] Craig Hogan, Ohkyung Kwon, and Nathaniel Selub. "Angular spectrum of quantum fluctuations in causal structure". In: (Mar. 2023). arXiv: 2303.06563 [gr-qc].

[540] Eric Steinbring. "Holographic Quantum-Foam Blurring Is Consistent with Observations of Gamma-Ray Burst GRB221009A". In: *Galaxies* 11.6 (2023), p. 115. DOI: 10.3390/galaxies11060115.

[541] Yanbei Chen, Linqing Wen, and Yiqiu Ma. "Photons with sub-Planckian energy cannot efficiently probe space-time foam". In: *Phys. Rev. D* 90.6 (2014), p. 063011. DOI: 10.1103/PhysRevD.90.063011. arXiv: 1504.07509 [astro-ph.HE].

[542] Gerard 't Hooft. "The Scattering matrix approach for the quantum black hole: An Overview". In: *Int. J. Mod. Phys. A* 11 (1996), pp. 4623–4688. DOI: 10.1142/S0217751X96002145. arXiv: gr-qc/9607022.

[543] Temple He, Ana-Maria Raclariu, and Kathryn M. Zurek. "From Shockwaves to the Gravitational Memory Effect". In: (May 2023). arXiv: 2305.14411 [hep-th].

[544] Tevian Dray and Gerard 't Hooft. "The Gravitational Shock Wave of a Massless Particle". In: *Nucl. Phys. B* 253 (1985), pp. 173–188. DOI: 10.1016/0550-3213(85)90525-5.

[545] Tevian Dray and Gerard 't Hooft. "The Effect of Spherical Shells of Matter on the Schwarzschild Black Hole". In: *Commun. Math. Phys.* 99 (1985), pp. 613–625. DOI: 10.1007/BF01215912.

[546] Gerard 't Hooft. "Discreteness of Black Hole Microstates". In: (Sept. 2018). arXiv: 1809.05367 [gr-qc].

[547] Thomas G. Mertens, Gustavo J. Turiaci, and Herman L. Verlinde. "Solving the Schwarzian via the Conformal Bootstrap". In: *JHEP* 08 (2017), p. 136. DOI: 10.1007/JHEP08(2017)136. arXiv: 1705.08408 [hep-th].

[548] Ho Tat Lam, Thomas G. Mertens, Gustavo J. Turiaci, and Herman Verlinde. "Shockwave S-matrix from Schwarzian Quantum Mechanics". In: *JHEP* 11 (2018), p. 182. DOI: 10.1007/JHEP11(2018)182. arXiv: 1804.09834 [hep-th].

[549] Y. Jack Ng and H. van Dam. In: *Foundations of Physics* 30.5 (2000), pp. 795–805. DOI: 10.1023/a:1003745212871. URL: https://doi.org/10.1023%2Fa%3A1003745212871.

[550] Craig J. Hogan. "Measurement of Quantum Fluctuations in Geometry". In: *Phys. Rev. D* 77 (2008), p. 104031. DOI: 10.1103/PhysRevD.77.104031. arXiv: 0712.3419 [gr-qc].

[551] Eric S. Perlman, Saul A. Rappaport, Y. Jack Ng, Wayne A. Christiansen, John DeVore, and David Pooley. "New constraints on quantum foam models from X-ray and gamma-ray observations of distant quasars". In: *14th Marcel Grossmann Meeting on Recent Developments in Theoretical and Experimental General Relativity, Astrophysics, and Relativistic Field Theories*. Vol. 4. 2017, pp. 3935–3941. DOI: 10.1142/9789813226609_0523. arXiv: 1607.08551 [astro-ph.CO].

[552] Wayne A. Christiansen, Y. Jack Ng, David J. E. Floyd, and Eric S. Perlman. "Limits on Spacetime Foam". In: *Phys. Rev. D* 83 (2011), p. 084003. DOI: 10.1103/PhysRevD.83.084003. arXiv: 0912.0535 [astro-ph.CO].

[553] Steven V. W. Beckwith et al. "The Hubble Ultra Deep Field". In: *Astron. J.* 132 (2006), pp. 1729–1755. DOI: 10.1086/507302. arXiv: astro-ph/0607632.

[554] Brian Welch et al. “A highly magnified star at redshift 6.2”. In: 603.7903 (Mar. 2022), pp. 815–818. DOI: 10.1038/s41586-022-04449-y. arXiv: 2209.14866 [astro-ph.GA].

[555] D. H. Coule. “Quantum cosmological models”. In: *Class. Quant. Grav.* 22 (2005), R125–2308. DOI: 10.1088/0264-9381/22/12/R02. arXiv: gr-qc/0412026.

[556] Fay Dowker, Joe Henson, and Rafael Sorkin. “Discreteness and the transmission of light from distant sources”. In: *Phys. Rev. D* 82 (2010), p. 104048. DOI: 10.1103/PhysRevD.82.104048. arXiv: 1009.3058 [gr-qc].

[557] John David Jackson. *Classical Electrodynamics*. Wiley, 1998. ISBN: 978-0-471-30932-1.

[558] Yiwen Zhang and Kathryn M. Zurek. “Stochastic description of near-horizon fluctuations in Rindler-AdS”. In: *Phys. Rev. D* 108.6 (2023), p. 066002. DOI: 10.1103/PhysRevD.108.066002. arXiv: 2304.12349 [hep-th].

[559] Mathew W. Bub, Yanbei Chen, Yufeng Du, Dongjun Li, Yiwen Zhang, and Kathryn M. Zurek. “Quantum gravity background in next-generation gravitational wave detectors”. In: *Phys. Rev. D* 108.6 (2023), p. 064038. DOI: 10.1103/PhysRevD.108.064038. arXiv: 2305.11224 [gr-qc].

[560] H. B. G. Casimir and D. Polder. “The Influence of Retardation on the London-van der Waals Forces”. In: *Phys. Rev.* 73 (4 Feb. 1948), pp. 360–372. DOI: 10.1103/PhysRev.73.360. URL: https://link.aps.org/doi/10.1103/PhysRev.73.360.

[561] D. G. Sandler, S. Stahl, J. R. P. Angel, M. Lloyd-Hart, and D. McCarthy. “Adaptive optics for diffraction-limited infrared imaging with 8-m telescopes”. In: *J. Opt. Soc. Am. A* 11.2 (Feb. 1994), pp. 925–945. DOI: 10.1364/JOSAA.11.000925. URL: http://opg.optica.org/josaa/abstract.cfm?URI=josaa-11-2-925.

[562] B. Sharmila, Sander M. Vermeulen, and Animesh Datta. “Extracting electromagnetic signatures of spacetime fluctuations”. In: (June 2023). arXiv: 2306.17706 [gr-qc].

[563] Ravi K. Sheth and Giuseppe Tormen. “Large scale bias and the peak background split”. In: *Mon. Not. Roy. Astron. Soc.* 308 (1999), p. 119. DOI: 10.1046/j.1365-8711.1999.02692.x. arXiv: astro-ph/9901122.

[564] Marco Olivares, Joel Saavedra, Jose R. Villanueva, and Carlos Leiva. “Motion of charged particles on the Reissner-Nordström (Anti)-de Sitter black holes”. In: *Mod. Phys. Lett. A* 26 (2011), pp. 2923–2950. DOI: 10.1142/S0217732311037261. arXiv: 1101.0748 [gr-qc].

[565] A. A. Abdo et al. “PSR J0007+7303 in the CTA1 Supernova Remnant: New Gamma-Ray Results from Two Years of Fermi Large Area Telescope Observations”. In: 744.2, 146 (Jan. 2012), p. 146. DOI: 10.1088/0004-637X/744/2/146. arXiv: 1107.4151 [astro-ph.HE].

[566] A Basu, B Shaw, D Antonopoulou, M J Keith, A G Lyne, M B Mickaliger, B W Stappers, P Weltevrede, and C A Jordan. “The Jodrell bank glitch catalogue: 106 new rotational glitches in 70 pulsars”. In: *Monthly Notices of the Royal Astronomical Society* 510.3 (Nov. 2021), pp. 4049–4062. DOI: 10.1093/mnras/stab3336. URL: https://doi.org/10.1093%2Fmnras%2Fstab3336.

[567] Margaret A. Livingstone, Scott M. Ransom, Fernando Camilo, Victoria M. Kaspi, Andrew G. Lyne, Michael Kramer, and Ingrid H. Stairs. “X-ray and radio timing of the pulsar in 3C 58”. In: *The Astrophysical Journal* 706.2 (Nov. 2009), pp. 1163–1173. DOI: 10.1088/0004-637x/706/2/1163. URL: https://doi.org/10.1088%2F0004-637x%2F706%2F2%2F1163.

[568] C. M. Espinoza, D. Antonopoulou, B. W. Stappers, A. Watts, and A. G. Lyne. “Neutron star glitches have a substantial minimum size”. In: *Monthly Notices of the Royal Astronomical Society* 440.3 (Apr. 2014), pp. 2755–2762. DOI: 10.1093/mnras/stu395. URL: https://doi.org/10.1093%2Fmnras%2Fstu395.